NATIONAL TECHINCAL UNIVERSITY OF ATHENS
SCHOOL OF CIVIL ENGINEERING
LABORATORY FOR EARTHQUAKE ENGINEERING

ANALYTICAL AND EXPERIMENTAL INVESTIGATION OF COMPOSITE STRUCTURES FOR STATIC AND SEISMIC LOADS

PhD DISSERTATION

KYRIAKOPOULOS PANAGIOTIS

Supervisor

CONSTANTINOS SPYRAKOS

Emeritus Professor NTUA

ATHENS 2021

ΕΘΝΙΚΟ ΜΕΤΣΟΒΙΟ ΠΟΛΥΤΕΧΝΕΙΟ
ΣΧΟΛΗ ΠΟΛΙΤΙΚΩΝ ΜΗΧΑΝΙΚΩΝ
ΕΡΓΑΣΤΗΡΙΟ ΑΝΤΙΣΕΙΣΜΙΚΗΣ ΤΕΧΝΟΛΟΓΙΑΣ

ΑΝΑΛΥΤΙΚΗ ΚΑΙ ΠΕΙΡΑΜΑΤΙΚΗ ΔΙΕΡΕΥΝΗΣΗ ΣΥΜΜΙΚΤΩΝ ΚΑΤΑΣΚΕΥΩΝ ΥΠΟ ΣΤΑΤΙΚΑ ΚΑΙ ΣΕΙΣΜΙΚΑ ΦΟΡΤΙΑ

ΔΙΔΑΚΤΟΡΙΚΗ ΔΙΑΤΡΙΒΗ

ΚΥΡΙΑΚΟΠΟΥΛΟΥ ΠΑΝΑΓΙΩΤΗ

Επιβλέπων

ΚΩΝΣΤΑΝΤΙΝΟΣ ΣΠΥΡΑΚΟΣ

Ομότιμος Καθηγητής ΕΜΠ

ΑΘΗΝΑ 2021

NATIONAL TECHINCAL UNIVERSITY OF ATHENS
SCHOOL OF CIVIL ENGINEERING
LABORATORY FOR EARTHQUAKE ENGINEERING

ANALYTICAL AND EXPERIMENTAL INVESTIGATION OF COMPOSITE STRUCTURES FOR STATIC AND SEISMIC LOADS

PhD DISSERTATION

KYRIAKOPOULOS PANAGIOTIS

The dissertation is submitted to the School of Civil Engineering of the National Technical University of Athens in fulfilment of the requirements for the Degree of Doctor of Philosophy

ADVISORY COMMITTEE

1. C. SPYRAKOS, Professor Emeritus NTUA (supervisor)
2. C. ZERIS, Professor NTUA
3. I. ERMOPOULOS, Professor Emeritus NTUA

EXAMINATION COMMITTEE

1. C. SPYRAKOS, Professor Emeritus NTUA (supervisor)
2. C. ZERIS, Professor NTUA
3. I. ERMOPOULOS, Professor Emeritus NTUA
4. C. GANTES, Professor NTUA
5. P. THANOPOULOS, Lecturer NTUA
6. M. FRAGIADAKIS, As. Professor NTUA
7. N. LAGAROS, Professor NTUA

ATHENS 2021

ΕΘΝΙΚΟ ΜΕΤΣΟΒΙΟ ΠΟΛΥΤΕΧΝΕΙΟ
ΣΧΟΛΗ ΠΟΛΙΤΙΚΩΝ ΜΗΧΑΝΙΚΩΝ
ΕΡΓΑΣΤΗΡΙΟ ΑΝΤΙΣΕΙΣΜΙΚΗΣ ΤΕΧΝΟΛΟΓΙΑΣ

ΑΝΑΛΥΤΙΚΗ ΚΑΙ ΠΕΙΡΑΜΑΤΙΚΗ ΔΙΕΡΕΥΝΗΣΗ ΣΥΜΜΙΚΤΩΝ ΚΑΤΑΣΚΕΥΩΝ ΥΠΟ ΣΤΑΤΙΚΑ ΚΑΙ ΣΕΙΣΜΙΚΑ ΦΟΡΤΙΑ

ΔΙΔΑΚΤΟΡΙΚΗ ΔΙΑΤΡΙΒΗ

ΚΥΡΙΑΚΟΠΟΥΛΟΥ ΠΑΝΑΓΙΩΤΗ

Η διατριβή υποβλήθηκε στη Σχολή Πολιτικών Μηχανικών του Εθνικού Μετσόβιου Πολυτεχνείου προς εκπλήρωση των προϋποθέσεων του τίτλου του Διδάκτορος Μηχανικού

ΤΡΙΜΕΛΗΣ ΣΥΜΒΟΥΛΕΥΤΙΚΗ ΕΠΙΤΡΟΠΗ

1. Κ. ΣΠΥΡΑΚΟΣ, Ομότιμος Καθηγητής ΕΜΠ (επιβλέπων)
2. Χ. ΖΕΡΗΣ, Καθηγητής ΕΜΠ
3. Ι. ΕΡΜΟΠΟΥΛΟΣ, Ομότιμος Καθηγητής ΕΜΠ

ΕΠΤΑΜΕΛΗΣ ΕΞΕΤΑΣΤΙΚΗ ΕΠΙΤΡΟΠΗ

1. Κ. ΣΠΥΡΑΚΟΣ, Ομότιμος Καθηγητής ΕΜΠ επιβλέπων)
2. Χ. ΖΕΡΗΣ, Καθηγητής ΕΜΠ
3. Ι. ΕΡΜΟΠΟΥΛΟΣ, Ομότιμος Καθηγητής ΕΜΠ
4. Χ. ΓΑΝΤΕΣ, Καθηγητής ΕΜΠ
5. Π. ΘΑΝΟΠΟΥΛΟΣ, Λέκτορας ΕΜΠ
6. Μ. ΦΡΑΓΚΙΑΔΑΚΗΣ, Αν. Καθηγητής ΕΜΠ
7. Ν. ΛΑΓΑΡΟΣ, Καθηγητής ΕΜΠ

ΑΘΗΝΑ 2021

"…Είναι μεγάλος τούτος ο άνεμος

είναι πελώριος ετούτος ο άνεμος

είναι χαρούμενος, χαρούμενος, χαρούμενος,

ρίχνει τα τείχη που ύψωσαν ανάμεσα στους λαούς

ρίχνει τα τείχη του θανάτου

ρίχνει τα τείχη ανάμεσα στο νου και στην καρδιά

τα τείχη ανάμεσα σε σένα και σε μένα

κι ανοίγει διάπλατα πάνου από τον ένα κόσμο, του ήλιου παράθυρο.

Ακούστε πως σφυρίζει τούτος ο άνεμος

μέσα στις ματωμένες γειτονιές του κόσμου…"

Γιάννης Ρίτσος 1949-1951

"…This wind is big

it is huge this wind

it is joyful, joyful, joyful,

knocks down the walls raised between the peoples

knocks down the walls of death

knocks down the walls between the mind and the heart

the walls between you and me

and opens wide over the one world, the sun's window.

Listen how this wind whistles

in the bloodstained neighborhoods of the world…"

Yannis Ritsos 1949-1951

To my wife Antonia

and our sons Nestor & Odysseas

Acknowledgement

The present dissertation is the result of a hard and persistent work. During all these years certain individuals have guided, supported and aided me both scientifically and morally. To all these persons I would like to express my unlimited gratitude.

To begin with, I would like to thank my supervisor Prof. Constantinos Spyrakos that guided me throughout the research work from title's selection to this final outcome. His immense knowledge, motivation and patience have given me more power and spirit to excel in this demanding task. His experience and guidance helped me not only to complete this dissertation, but to become a better and more accomplished engineer. He is my mentor and I will always seek for his advice to overpass the difficulties that I will face throughout my career.

Apart from my Supervisor, I won't forget to express my gratitude to the remaining members of the advisory committee: Prof. Ioannis Ermopoulos and Prof. Christos Zeris, for encouraging me and sharing insightful suggestions. They all have played a major role in polishing and improving my research writing skills. Their guidance will be hard to forget throughout my life.

Special thanks to Prof. Ioannis Vayas and his laboratory team Dr. Xenofon Lignos and Stylianos Katsatsidis, for all the assistance during the experimental part of my PhD, in both planning and execution of the tests. Our collaboration was beyond expectations while they made everything look really easy and simple.

I would also like to acknowledge my colleagues from the laboratory for all the nice moments that we shared together. I will always be grateful for your contribution and impact to my research and my life.

My deepest gratitude is extended to the North to Simo Peltonen and Prof. Matti Leskela. Nothing would have happened without their unconditional help and support. I am grateful for every minute of your time spent to discuss about my problems.

I can barely find the words to thank my parents and my brother for their invaluable support. They have been my moral and financial support, especially in my very first steps. Their valuable lessons were a lighthouse to find my path in the difficult and dark times.

And last but not least, my deepest gratitude goes to my beloved wife Antonia. She was there since the beginning of my trip. She was there all these long sleepless nights when the analytical calculations didn't correlate with the experimental results. She was also there when they did. She was always listening to my problems and my stories, even though I am not so sure she could always understand me. And finally, the most important is that she made it possible to have a family with two handsome boys, the most handsome in my eyes, despite all the difficulties we have faced so far.

Abstract

In recent decades, a strong demand for efficient and economical structural elements is being observed. This demand led to an increase in the use of factory prefabricated elements, such as, e.g., concrete hollow core elements for slabs and composite steel beams and columns, which can be assembled on site. The use of standardized prefabricated elements concealed a higher quality standard associated with lower cost followed by a high degree of flexibility because of a wide range of possible combinations. The necessity for reduction of the floor height for high-rise buildings, namely, a reduction of the height between floors, without reducing the usable space, was anticipated in order to increase the total number of storeys for a given overall building height. Thus, parallel with prefabricated construction, a "new" more advanced structural system was born; the shallow floor system.

In the shallow floor system, the steel beam is placed within the thickness of the pre-cast concrete floor or the composite slab with profiled steel decks. This form of construction leads to a reduced clear building height and is, at the same time, beneficial for the building services that may run in any direction. In this system, also called slim or shallow floor, the decking elements are not supported on the upper flange of the steel member, as in traditional steel-concrete composite construction, but on the bottom plate. Thus, in the finished construction the steel members are fully or partially encased in the concrete slab.

The relatively small amount of research work related to shallow floor beams subjected to extreme loads, such as earthquakes or column loss scenarios, together with the lack of any relevant design guidance in the Eurocodes, as well as the numerous possibilities and combinations of steel sections and shapes that can be used, indicates the need to investigate this topic more extensively.

Existing research in the literature is solely related to the investigation of the flexural behavior of composite beams with asymmetric double-T steel profiles, while the imposed

load/displacement test sequences correspond to normal loading conditions. However, there is a need to examine the robustness of shallow-floor composite beams with hollow steel cross-sections under extreme loading conditions, shedding light to important factors, such as the shear connection between steel and concrete parts or the degree of confinement of the steel cross-section in cases of encased concrete. This dissertation elaborates on experimental investigations on shallow floor beams, called Deltabeams, carried out at the Institute of Steel Structures of the National Technical University of Athens (NTUA).

Deltabeam is a slim-floor composite beam which took its name by the Δ-shape of the hollow section steel beam, which is fully integrated into the concrete floor. The composite beam behaves as a steel beam at construction stages before the infilling concrete has reached the design strength. After the erection of the decking units on the outward ledges of the bottom plate, the beam is completely filled with concrete in situ through regularly spaced web openings, forming a composite element at service stage after concrete hardening.

Furthermore, three-dimensional (3D) Finite element models were created and calibrated with the experimental results. The good correlation of the numerical predictions with the experimental results gives an excellent opportunity to shed more light by further numerical analyses on the issues that could not be measured or indicated in the tests carried out and, thus, assist to a better understanding of the overall behavior of these beams. Finally, Deltabeams were successfully used as simply supported beams for the seismic design of an office building. Comparison of the results with a second model made by conventional monolithic concrete frames revealed the beneficial effect of the shallow floor construction, since, because of the lower height of Deltabeams, there was space for more storeys for the same overall building height.

Greek extended summary

Εκτενής περίληψη

Ιστορική αναδρομή

Η χρήση και η ανάπτυξη του δομικού χάλυβα ως δομικό υλικό είχαν τεράστια επιρροή στην εξέλιξη των βιομηχανοποιημένων κοινωνιών καθώς και στη δημιουργία του σύγχρονου τρόπου ζωής όπως τον βιώνουμε σήμερα. Οι σιδηρόδρομοι, οι γέφυρες, τα μεγάλα παραγωγικά εργοστάσια και τα κτήρια, δε θα είχαν ποτέ τη σημερινή μορφή τους χωρίς το δομικό χάλυβα.

Στις αρχές του 18ου αιώνα τρεις τύποι σιδηρούχων μετάλλων ήταν γνωστοί˙ ο κατεργασμένος σίδηρος, ο χυτοσίδηρος (μαντέμι) και ο χάλυβας. Ο κατεργασμένος σίδηρος χρησιμοποιόταν από τους σιδεράδες αρκετούς αιώνες για την κατασκευή προϊόντων όπως πύλες, κιγκλιδώματα, καρφιά και αλυσίδες. Αυτή η μορφή του υλικού έφτασε στο αποκορύφωμά της τη δεκαετία του 1860 ως το κυριότερο δομικό υλικό. Ο χυτοσίδηρος χρησιμοποιόταν κυρίως στην επιπλοποιία και στην κατασκευή μαγειρικών σκευών. Όντας ψαθυρός, δε χρησιμοποιήθηκε ως δομικό υλικό. Ο χάλυβας, μέχρι τα μέσα του 19ου αιώνα, χρησιμοποιόταν στην κατασκευή ακριβότερων και κομψότερων αντικειμένων, όπως ρολόγια και σπαθιά, λόγω του εξαιρετικά υψηλού κόστους παραγωγής του.

Το 1856 ο Henry Bessemer, ο οποίος θεωρείται ο πατέρας του σύγχρονου χάλυβα, εφηύρε μια μέθοδο με την εφαρμογή της οποίας κατέστη εφικτή μεγαλύτερη και οικονομικότερη παραγωγή χάλυβα. Ο συνδυασμός της μεθόδου, η οποία πήρε το όνομα του εφευρέτη της, με την εφεύρεση της «καμίνου ανοικτής εστίας» από τον Charles William Siemens το 1866, οδήγησε στην «εκθρόνιση» του κατεργασμένου σίδηρου, ως το κυριότερο κατασκευαστικό υλικό, από τον χάλυβα. Μία από τις τελευταίες διάσημες κατασκευές από κατεργασμένο σίδηρο είναι ο πύργος του Άιφελ (1889). Την ίδια περίοδο, κατασκευάστηκε στη Σκωτία η

γέφυρα Forth Bridge, η οποία ήταν η πρώτη μεγάλη κατασκευή από χάλυβα στη Βρετανία. Εγκαινιάστηκε το 1890 και είχε μήκος 2467 μ.

Στο Σικάγο στις αρχές του 19ου αιώνα τα κτήρια ήταν κατασκευασμένα κυρίως από ξύλο. Η μεγάλη πυρκαγιά του 1871 προκάλεσε τεράστιες καταστροφές. Περίπου 300 άτομα έχασαν τη ζωή τους, πάνω από 18000 κτήρια καταστράφηκαν και 100000 άνθρωποι (το ένα τρίτο του πληθυσμού της πόλης) έμειναν άστεγοι. Το διάστημα που ακολούθησε, το Σικάγο έγινε σημαντικό παράδειγμα ταχείας ανοικοδόμησης. Δεδομένου ότι οι κανονισμοί έναντι πυρκαγιάς ήταν πλέον αυστηρότεροι, γεννήθηκε η ανάγκη για καινούρια μη εύφλεκτα δομικά υλικά. Οι μηχανικοί βρήκαν τη λύση αυτού του προβλήματος στη χρήση του χάλυβα. Το Κτήριο Οικιακής Ασφάλισης, στο Σικάγο, κατασκευάστηκε το 1885 και, καθώς αποτελούταν από δέκα ορόφους, θεωρήθηκε ο πρώτος ουρανοξύστης. Ο σκελετός του κτηρίου αποτελούταν από χάλυβα. Η κατασκευή από χάλυβα δεν ήταν μόνο ελαφρύτερη από αυτή με τους οπτόπλινθους, οι οποίοι χρησιμοποιούνταν ευρέως στην κατασκευή κτηρίων, αλλά μπορούσε επιπλέον να παραλάβει περισσότερα φορτία. Ελαφρύτεροι τοίχοι ήταν συνδεδεμένοι στον χαλύβδινο σκελετό.

Στις αρχές του 20ου αιώνα ο δομικός χάλυβας έπρεπε να ανταγωνιστεί ένα καινούριο υλικό˙ το οπλισμένο σκυρόδεμα. Ο δομικός χάλυβας είχε υψηλή αντοχή, ολκιμότητα και συνέβαλε στην ταχύτερη ανέγερση της κατασκευής. Το οπλισμένο σκυρόδεμα είχε υψηλή δυσκαμψία, αντοχή έναντι θλίψης και φωτιάς και μικρότερο κόστος. Εν τέλει, η σύμμικτη κατασκευή από χάλυβα και οπλισμένο σκυρόδεμα, ένα νέο πιο εξελιγμένο δομικό σύστημα, προέκυψε όχι από τον ανταγωνισμό των δύο υλικών αλλά από τη συνεργασία τους.

Στα πρώτα βήματα των σύμμεικτων κατασκευών, δεν υπήρχε ξεκάθαρος διαχωρισμός μεταξύ των χαλύβδινων στοιχείων (μεταλλικές δοκοί και ράβδοι οπλισμού) και όλα έπρεπε να είναι υποχρεωτικά πλήρως εγκιβωτισμένα στο σκυρόδεμα. Τα πρώτα πειράματα σχετικά με τη σύνδεση και τη σχετική μετακίνηση μεταξύ των δύο υλικών πραγματοποιήθηκαν από τον Carl von Bach. Τα αποτελέσματα έδειξαν ότι υπήρχε μεγαλύτερη ολίσθηση μεταξύ των μεταλλικών δοκών και του σκυροδέματος σε σχέση με τις μεταλλικές ράβδους οπλισμού. Επιπλέον, η

εξόλκευση των πιο άκαμπτων χαλύβδινων στοιχείων προκαλούσε εκτεταμένες βλάβες στο σκυρόδεμα. Αυτές οι διαφορές έδωσαν το έναυσμα για την έναρξη της συζήτησης που αφορούσε το διαχωρισμό των δύο διαφορετικών χαλύβδινων στοιχείων.

Στην Ευρώπη, στο πρώτο μισό του 20ου αιώνα, η έρευνα επικεντρώθηκε κυρίως στη σύνδεση μεταξύ του χάλυβα και του σκυροδέματος. Κατά τη διάρκεια αυτής της περιόδου, εμφανίστηκαν οι πρώτες προτάσεις για μία μηχανική σύνδεση μεταξύ των δύο υλικών. Στην άλλη πλευρά του Ατλαντικού, στις ΗΠΑ, ο Julius Kahn έλαβε το δίπλωμα ευρεσιτεχνίας για μία σύμμεικτη δοκό παρόμοια με την πιο συνήθη σημερινή μορφή της. Η σύμμεικτη συμπεριφορά πραγματοποιούταν με τη χρήση καμπυλωμένων μεταλλικών λωρίδων συγκολλημένων στην άνω πλάκα της χαλύβδινης δοκού. Τα χρόνια που ακολούθησαν διεξήχθησαν πολλές πειραματικές εργασίες και σημειώθηκε μεγάλη πρόοδος, κυρίως στον τομέα της γεφυροποιίας. Παράλληλα συντάχθηκαν οι πρώτοι κανονισμοί σχετικοί με τις σύμμεικτες κατασκευές.

Την εισαγωγή των σύμμεικτων δοκών στη βιομηχανία της κατασκευής ακολούθησαν οι σύμμεικτες πλάκες. Ο συνδυασμός πλακών σκυροδέματος με χαλυβδόφυλλα, τα οποία συμπεριλαμβάνονταν στον υπολογισμό της αντοχής, εξάλειψε την ανάγκη χρήσης ξυλότυπου. Η εφαρμογή των χαλυβδόφυλλων συνδυαστικά ως μόνιμος ξυλότυπος και ενίσχυση στην πλάκα σκυροδέματος εφαρμόστηκε αρχικά στην Αμερική στις αρχές του 1950. Στο Ηνωμένο Βασίλειο η σύμμεικτη δόμηση εισήχθη τη δεκαετία του 1970 και είναι η πιο διαδεδομένη μορφή για την κατασκευή πλακών σε κτήρια από δομικό χάλυβα.

Τις τελευταίες δεκαετίες, κυρίως λόγω της παγκόσμιας οικονομικής κρίσης και των περιορισμών που απαιτούνται από του Κανονισμούς, αυξήθηκε η ζήτηση για πιο αποτελεσματικές και οικονομικές μεθόδους κατασκευής. Το γεγονός αυτό οδήγησε στη χρήση εργοστασιακά προκατασκευασμένων δομικών στοιχείων, τα οποία συναρμολογούνται στο εργοτάξιο. Η χρήση τυποποιημένων προκατασκευασμένων δομικών στοιχείων εξασφάλιζε ένα υψηλό επίπεδο ποιότητας με χαμηλό κόστος, συνακολουθούμενα από ένα μεγάλο βαθμό ευελιξίας λόγω του ευρέος φάσματος πιθανών συνδυασμών. Ως αποτέλεσμα της επιβολής της

μείωσης του ύψους των κτηρίων από τις αρχές, ένα τμήμα της κατασκευαστικής βιομηχανίας στόχευσε στη μείωση του ύψους μεταξύ των ορόφων, χωρίς τη μείωση του ωφέλιμου χώρου, με σκοπό την αύξηση του αριθμού των ορόφων, ως πλεονέκτημα έναντι των ανταγωνιστών τους. Έτσι, παράλληλα με την εμφάνιση της προκατασκευής ένα νέο προηγμένο δομικό σύστημα «γεννήθηκε». Το σύστημα αυτό αποτελείται από λεπτές σύμμεικτες κρυφοδοκούς οι οποίες στηρίζουν λεπτές πλάκες από σκυρόδεμα.

Με το νέο αυτό κατασκευαστικό σύστημα επιτυγχάνεται η ανέγερση κτηρίων με μικρότερο ύψος και, ταυτόχρονα, η επίπεδη -χωρίς κρέμαση δοκών- κάτω από την κάτω παρειά της πλάκας είναι καταλληλότερη για την τοποθέτηση των μηχανολογικών οδεύσεων. Η πλάκες πλέον δεν τοποθετούνται στο άνω πέλμα της μεταλλικής δοκού, όπως στις συμβατικές σύμμεικτες κατασκευές, αλλά στηρίζονται από το κάτω πέλμα της. Με αυτό τον τρόπο η χαλύβδινη δοκός είναι πλήρως ή μερικώς εγκιβωτισμένη στην πλάκα σκυροδέματος.

Στη Σκανδιναβία, και πιο συγκεκριμένα στη Σουηδία, στις αρχές της δεκαετίας του ’80 του προηγούμενου αιώνα, εμφανίστηκε το πρώτο σύστημα λεπτών σύμμεικτων πλακών με κρυφοδοκούς. Αυτή η νέα κατασκευαστική μέθοδος αύξησε το μερίδιο των μεταλλικών κατασκευών για χρήση γραφείων άνω του 50% της συνολικής αγοράς. Η πρώτη μορφή του εν λόγω συστήματος ονομαζόταν Δοκός Thor και αποτελούνταν από τμήματα διατομής U συγκολλημένα σε μία επίπεδη πλάκα. Το 1989 στη Φινλανδία, σχεδιάστηκε και εμφανίστηκε η δοκός Deltabeam. Πήρε το όνομά της από το σχήμα της διατομής της. Η σύνδεση μεταξύ σκυροδέματος και χάλυβα εξασφαλίζεται μέσω ράβδων οπλισμού που διέρχονται μέσα από οπές στους κορμούς. Δύο χρόνια μετά, το 1991, στο Ηνωμένο Βασίλειο αναπτύχθηκε η δοκός Slimflor η οποία αποτελείται από μία συνήθη μεταλλική διατομή υποστυλώματος συγκολλημένη σε μια χαλύβδινη πλάκα.

Οργάνωση της διατριβής

Το Κεφάλαιο 1 αποτελεί την εισαγωγή της διατριβής. Μέσω μιας σύντομης χρονικής αναδρομής περιγράφεται η εξέλιξη των χαλύβδινων κατασκευών, η αναβάθμισή τους σε σύμμεικτες με την εμφάνιση του οπλισμένου σκυροδέματος και εν τέλει ο πλήρης εγκιβωτισμός τους στην πλάκα σκυροδέματος. Επιπλέον στο Κεφάλαιο αυτό περιγράφεται και η διάρθρωση του κειμένου της διατριβής. Το Κεφάλαιο 2 περιγράφει τους Ευρωκώδικες με έμφαση σε εκείνα τα τμήματα που σχετίζονται με την καμπτική συμπεριφορά και το σχεδιασμό των σύμμεικτων δοκών. Επιπρόσθετα, στόχος του εν λόγω κεφαλαίου είναι να αναδείξει την έλλειψη διατάξεων και οδηγιών σχετικών με χαλύβδινες δοκούς πλήρως εγκιβωτισμένες στην πλάκα οπλισμένου σκυροδέματος. Στο Κεφάλαιο 3 πραγματοποιείται μια βιβλιογραφική ανασκόπηση με τις πιο σημαντικές και σχετικές, στην τρέχουσα έρευνα, πειραματικές δημοσιευμένες εργασίες πάνω σε σύμμεικτες δοκούς πλήρως εγκιβωτισμένες στην πλάκα σκυροδέματος. Αν και υπάρχει αρκετός αριθμός δημοσιεύσεων σχετικά με τη διατμητική συμπεριφορά των υπό διερεύνηση δοκών και την αντοχή τους έναντι πυρκαγιάς, δεν υπάρχουν πολλές εργασίες που να διερευνούν την καμπτική συμπεριφορά τους.

Στα Κεφάλαια 4 και 5 περιγράφεται το πειραματικό πρόγραμμα που ακολουθήθηκε στα πλαίσια της διδακτορικής διατριβής. Λεπτομερέστερα, στο Κεφάλαιο 4 εισάγεται η υπό διερεύνηση σύμμεικτη δοκός τραπεζοειδούς διατομής που για αυτό το λόγο ονομάζεται Deltabeam. Επιπλέον, παρουσιάζεται μια εκτεταμένη περιγραφή της πειραματικής διάταξης, που αποτελείται από το κύριο πλαίσιο, τις στηρίξεις, ένα υδραυλικό έμβολο και τις δοκούς-δοκίμια. Η γεωμετρία και οι λεπτομέρειες των δοκών καθώς και η προετοιμασία τους για τις δοκιμές περιγράφεται εκτενώς. Στη συνέχεια αναφέρονται οι μηχανικές ιδιότητες όλων των χρησιμοποιούμενων υλικών. Τέλος, περιγράφονται οι διατάξεις μέτρησης και οι θέσεις των οργάνων μέτρησης. Στο Κεφάλαιο 5 παρουσιάζονται τα αποτελέσματα των πειραμάτων. Για τον σκοπό αυτό δημιουργήθηκαν διαγράμματα στα οποία το φορτίο συσχετίζεται με τη μετατόπιση στο μέσο του ανοίγματος, την ολίσθηση μεταξύ του σκυροδέματος και της χαλύβδινης δοκού και τη διαμήκη παραμόρφωση των μεταλλικών πελμάτων σε συνδυασμό με μια λεπτομερή περιγραφή των πιο αξιοσημείωτων παρατηρήσεων του εκάστοτε πειράματος.

Στο Κεφάλαιο 6 παρουσιάζεται μια αναλυτική έρευνα με τη χρήση της μεθόδου πεπερασμένων στοιχείων (FEM). Τα τρισδιάστατα προσομοιώματα δημιουργήθηκαν με τη χρήση του λογισμικού Abaqus δίνοντας μεγάλη προσοχή στην ακριβή αναπαράσταση της γεωμετρίας, των υλικών και των συνοριακών συνθηκών. Τα στοιχεία των δοκιμίων τα οποία ήταν κατασκευασμένα από σκυρόδεμα και δομικό χάλυβα, αντιμετωπίστηκαν ως δύο ξεχωριστά στοιχεία στην προσομοίωση. Οι ιδιότητες της μεταξύ τους επαφής επιλέχθηκαν καταλλήλως ώστε τα δύο τμήματα να μπορούν να αποκολληθούν, αλλά να εμποδίζεται η διείσδυση του ενός στο άλλο. Επιπλέον, τα δύο τμήματα μπορούν να ολισθαίνουν το ένα σε σχέση με το άλλο, αναπτύσσοντας τριβή. Στη συνέχεια, για να βαθμονομηθούν τα προσομοιώματα και να επιλεγούν οι κατάλληλες παράμετροι που τα περιγράφουν, συγκρίθηκαν οι αναλυτικά υπολογισμένες καμπύλες φορτίου-μετατόπισης και φορτίου-παραμορφώσεων με τις αντίστοιχες πειραματικές. Επιπρόσθετα, γίνεται και σύγκριση, στο κεφάλαιο αυτό, διαγραμμάτων, των οποίων οι καμπύλες αποτελούν το μέσο όρο των πειραματικών και αναλυτικών αποτελεσμάτων, που αποδεικνύει την αξιοπιστία και αποτελεσματικότητα των αναλυτικών προσομοιωμάτων.

Στη συνέχεια, εξετάζεται αναλυτικά η συμπεριφορά και ο σχεδιασμός ενός πραγματικού κτιρίου έναντι σεισμικών φορτίων στο Κεφάλαιο 7. Διεξήχθησαν δύο διαφορετικές αναλύσεις. Τα κατακόρυφα στοιχεία του κτιρίου είναι τοιχεία οπλισμένου σκυροδέματος τα οποία συνδέονται, στην πρώτη περίπτωση, με τις δοκούς Deltabeams και στη δεύτερη με συμβατικές δοκούς οπλισμένου σκυροδέματος. Οι δοκοί Deltabeams συνδέονται με τα τοιχεία με στηρίξεις μεταφοράς τέμνουσας. Ως αποτέλεσμα, μόνο κατακόρυφα φορτία μεταφέρονται από τις δοκούς στα κατακόρυφα στοιχεία. Παρουσιάζεται επίσης η σύγκριση των αποτελεσμάτων. Τέλος εφαρμόζεται η πρόταση της παρούσας διατριβής με τη χρήση προσομοιώματος για τον αναλυτικό υπολογισμό της αντοχής της ενισχυμένης, με χρήση οπλισμών, διατομής.

Το Κεφάλαιο 8 συνοψίζει την έρευνα που διεξήχθη σε αυτή τη διατριβή και καταλήγει σε συμπεράσματα από την αξιολόγηση των αποτελεσμάτων. Επιπλέον, συμπεριλαμβάνονται ορισμένες προτάσεις για τα επόμενα βήματα της έρευνας σχετικά με τα Deltabeams (π.χ. διερεύνηση της αντοχής έναντι αρνητικών ροπών).

Πειραματική διερεύνηση

Οι δοκοί Deltabeams είναι λεπτές σύμμεικτες δοκοί πλήρως εγκιβωτισμένες στην πλάκα και πήραν το όνομά τους από το σχήμα της διατομής τους. Η δυστρεψία τους είναι αρκετά υψηλή ώστε να επιτρέπει την τοποθέτηση βαρέων στοιχείων στις προεξοχές της μεταλλικής πλάκας του κάτω πέλματος χωρίς επιπλέον στήριξη. Είναι σχεδιασμένες να χρησιμοποιούνται ως δομικά στοιχεία και μπορούν να συνδυαστούν με όλους τους γενικούς τύπους πλακών σκυροδέματος.

Οι δοκοί Deltabeams συμπεριφέρονται ως αμιγώς μεταλλικές πριν το σκυρόδεμα αποκτήσει την απαιτούμενη αντοχή. Κατά τη διάρκεια της σκυροδέτησης των πλακών, οι δοκοί πληρώνονται με σκυρόδεμα μέσω τακτών ανοιγμάτων στις μεταλλικές πλάκες του κορμού, σχηματίζοντας έτσι μία σύμμεικτη διατομή μετά τη σκλήρυνση του σκυροδέματος. Η αντοχή της σύμμεικτης διατομής έναντι διάτμησης είναι μεγαλύτερη της αντίστοιχης αντοχής της μεταλλικής δοκού πριν τη σκυροδέτηση, λόγω της συνεισφοράς του σκυροδέματος. Πολλαπλά πειράματα έχουν αποδείξει ότι η δοκός Deltabeam έχει υψηλή πυραντοχή, η οποία εξαρτάται από το πάχος της μεταλλικής πλάκας του κάτω πέλματος και τον αριθμό των ράβδων πυροπροστασίας που τοποθετούνται μέσα στον πυρήνα της δοκού. Ο οπλισμός πυροπροστασίας αντισταθμίζει την απώλεια αντοχής του κάτω πέλματος κατά τη διάρκεια της πυρκαγιάς και ως εκ τούτου, συνήθως, δε χρειάζεται πρόσθετη εξωτερική πυροπροστασία.

Ο τελικός στόχος του ερευνητικού προγράμματος είναι η δημιουργία μιας αμιγώς πλαισιωτής κατασκευής με δοκούς Deltabeams το οποίο θα έχει επαρκή αντοχή και πλαστιμότητα έναντι σεισμικών φορτίων ή/και πιθανοτήτων διαδοχικής κατάρρευσης. Στην παρούσα διατριβή παρουσιάζεται το πρώτο μέρος της έρευνας, το οποίο σχετίζεται με την καμπτική συμπεριφορά της σύμμεικτης δοκού Deltabeam έναντι θετικών ροπών (εφελκυσμός κάτω πέλματος). Ο μικρός αριθμός επιστημονικών δημοσιεύσεων σχετιζόμενων με τις λεπτές σύμμεικτες πλάκες με κρυφοδοκούς από χάλυβα καθώς και η παντελής έλλειψη οδηγιών στους Ευρωκώδικες, καθιστά την πειραματική διερεύνηση αναγκαία. Η πειραματική διερεύνηση έλαβε μέρος στο Εργαστήριο Μεταλλικών Κατασκευών του Εθνικού Μετσόβιου Πολυτεχνείου (Αθήνα), όπου

εξετάστηκε η συμπεριφορά δεκατριών αμφιέρειστων δοκών χωρισμένων σε τέσσερις ομάδες, ανάλογα με τον τύπο της διατομής τους (Εικόνα 1). Αρκετοί σημαντικοί παράγοντες, όπως το μέγεθος των χαλύβδινων διατομών, οι λεπτομέρειες των οπλισμών, η διάταξη των διατμητικών ήλων και η γεωμετρία της πλάκας σκυροδέματος μελετήθηκαν μέσω της πειραματικής διερεύνησης. Όλα τα δοκίμια είχαν μήκος 7700 mm.

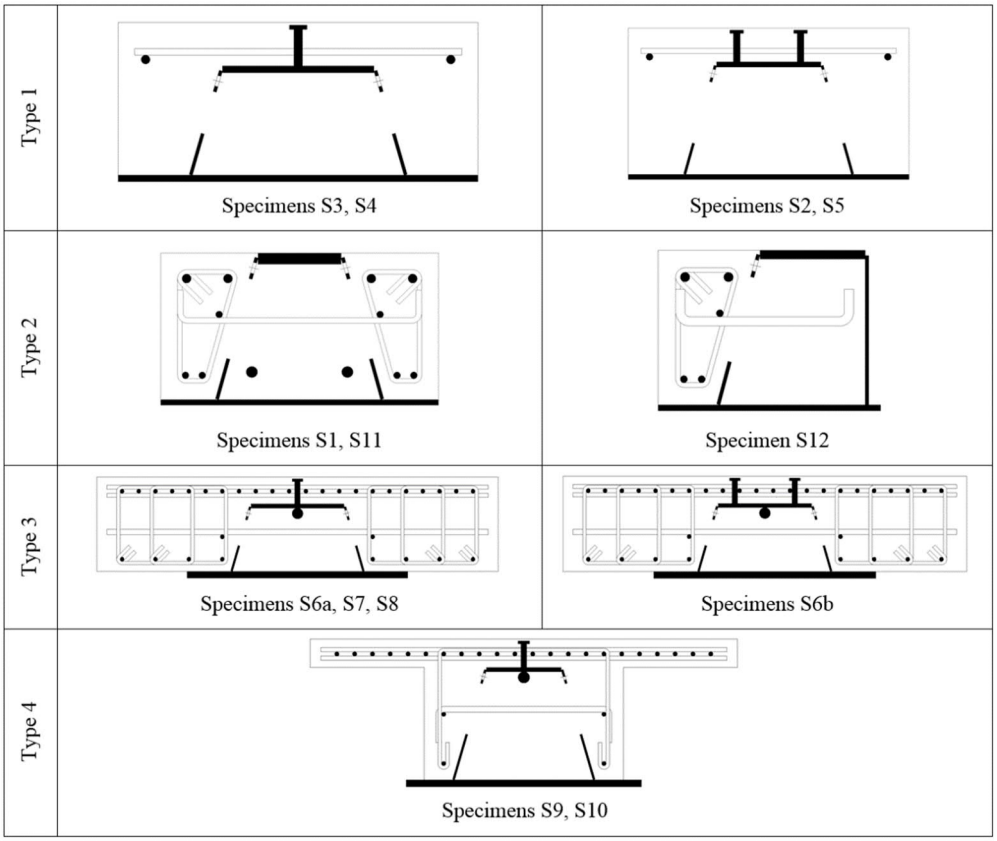

Εικ. 1- Ομαδοποίηση των δοκών ανάλογα με τη διατομή τους

Η πειραματική διάταξη αποτελείτο από ένα άκαμπτο πλαίσιο, ένα υδραυλικό έμβολο, τις στηρίξεις, οι οποίες σχεδιάστηκαν αποκλειστικά για τα πειράματα, και τέλος τα δοκίμια (Εικόνα 2). Το άκαμπτο πλαίσιο κατασκευάστηκε από τέσσερα ισχυρά μεταλλικά υποστυλώματα HE 600M συνδεδεμένα με τέσσερις δοκούς τύπου HE 600M κατά τη διαμήκη διεύθυνση των δοκιμίων και με τέσσερις δοκούς διατομής διπλού U στην εγκάρσια διεύθυνση. Οι συνθήκες στήριξης σχεδιάστηκαν ως «αρθρώσεις». Δύο λεπτές πλάκες από inox χάλυβα και teflon χρησιμοποιήθηκαν ανάμεσα στις στηρίξεις και τις δοκούς για την όσο το δυνατό μείωση της τριβής. Η απόσταση μεταξύ των κεντροβαρικών αξόνων των στηρίξεων ήταν 7200 mm.

Εικ. 2- Πειραματική διάταξη

Κατά τη διάρκεια των πειραμάτων μετρήθηκε η κατακόρυφη μετακίνηση στο μέσο των δοκιμίων με τη χρήση δύο επιμηκυνσιομέτρων εκατέρωθεν της διατομής. Η τελική καμπύλη φορτίου- μετακίνησης υπολογίστηκε ως ο μέσος όρος των δύο αυτών μετρήσεων. Επιπλέον, μετρήθηκαν οι παραμορφώσεις του κάτω μεταλλικού πέλματος σε όλες τις δοκούς και του άνω πέλματος στις περιπτώσεις που αυτό ήταν δυνατόν και η ολίσθηση μεταξύ του σκυροδέματος και της μεταλλικής δοκού σε έξι σημεία κατά μήκους της. Οι αρχικές τιμές των μετρήσεων όλων των οργάνων μηδενίστηκαν με αποτέλεσμα οι μετρήσεις να περιέχουν μόνο τις διαφορές λόγω του κατακόρυφου φορτίου και όχι την επιρροή του ιδίου βάρους των δοκών. Τέλος οι παραμορφώσεις των στηρίξεων παρακολουθούνταν καθ' όλη τη διάρκεια των πειραμάτων. Οι τιμές των μετρήσεων αυτών ήταν σχεδόν μηδενικές και δεν επηρέασαν τη συνολική πορεία των πειραμάτων.

Εφαρμόστηκαν δύο χρονοϊστορίες φόρτισης. Και οι δύο αποτελούνταν αρχικά από τρεις κύκλους, με μετακίνηση ίση με 27 mm (ΟΚΛ). Η διάρκεια κάθε κύκλου ήταν δέκα λεπτά. Στη συνέχεια ακολουθούσε η μονότονη φόρτιση μέχρι το τέλος των πειραμάτων (ΟΚΑ) η οποία αποτελούνταν από δύο τμήματα με διαφορετικό ρυθμό επιβαλλόμενης παραμόρφωσης. Στην πρώτη χρονοϊστορία (Εικόνα 3) υπήρχε ένα τμήμα με χαμηλή ταχύτητα φόρτισης μέχρι τα 100

mm. Έπειτα η ταχύτητα αυξήθηκε μέχρι το τέλος του πειράματος. Στη δεύτερη χρονοϊστορία (Εικόνα 4) το πρώτο αργό τμήμα της μονότονης φόρτισης επιμηκύνθηκε μέχρι τα 150 mm.

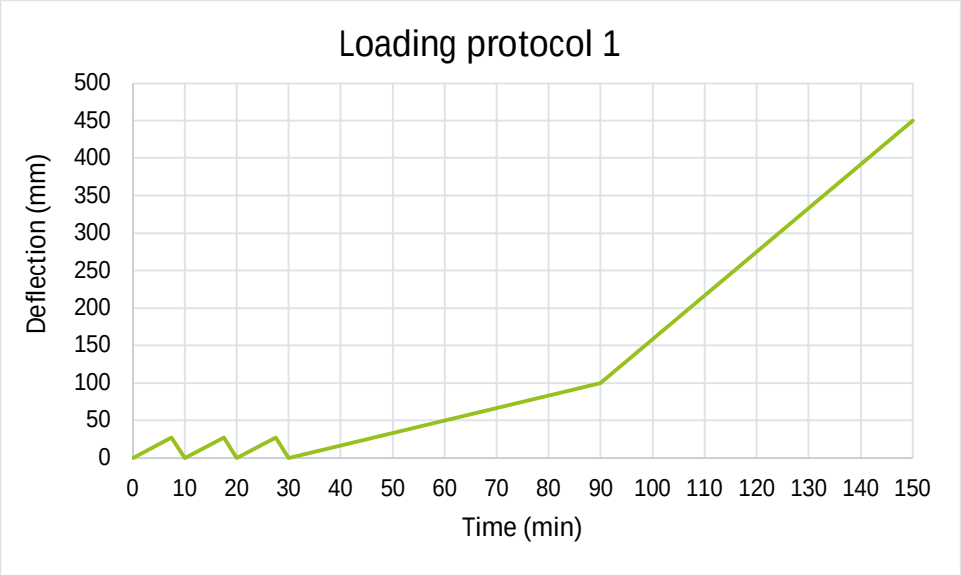

Εικ. 3- Πρώτη χρονοϊστορία φόρτισης

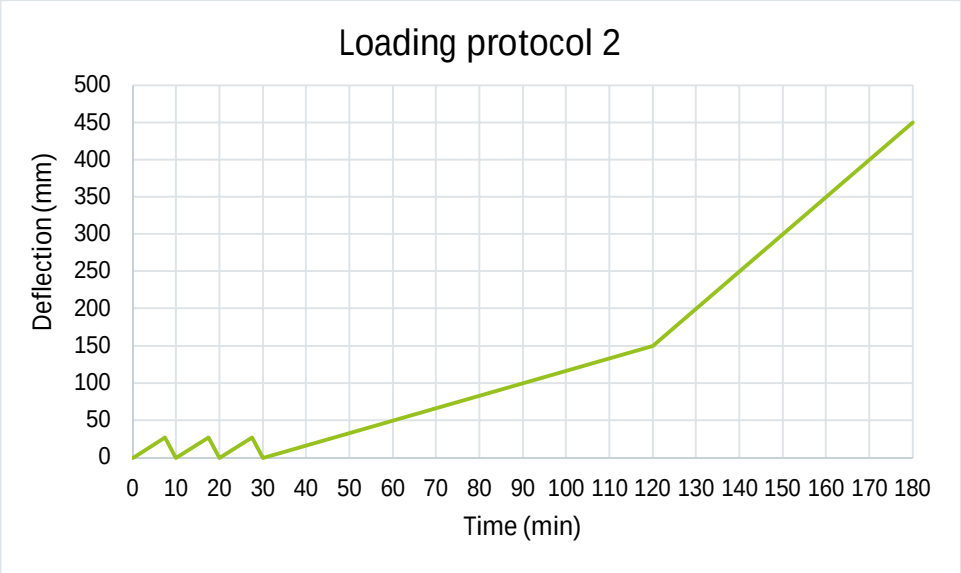

Εικ. 4- Δεύτερη χρονοϊστορία φόρτισης

Πειραματικά αποτελέσματα.

- **Δοκίμια διατομής Τύπου** 1

Οι διατομές Τύπου 1 ήταν οι λιγότερο οπλισμένες και αντιπροσωπεύουν τον τρέχοντα τρόπο χρήσης των δοκών. Αυτός ο παράγοντας είχε πολλή μεγάλη επίδραση στη συμπεριφορά τους.

i. **Δοκός** S2

Οι πρώτες ρωγμές εμφανίστηκαν σε μετατόπιση ίση με 23 mm στον δεύτερο κύκλο λειτουργικότητας (Εικόνα 3). Όταν η μετατόπιση έφτασε τα 117 mm (495 kN) οι διαμήκεις ράβδοι στη θλιβόμενη ζώνη λύγισαν δημιουργώντας βλάβες στο σκυρόδεμα. Λόγω έλλειψης συνδετήρων η βλάβη στο σκυρόδεμα ήταν εκτεταμένη και δεν αποτράπηκε ο λυγισμός του άνω πέλματος. Αυτοί οι παράγοντες προκάλεσαν μία απότομη πτώση στην αντοχή της δοκού έως το 60% του μέγιστου φορτίου, προσδίδοντας στο δοκίμιο μία μη πλάστιμη συμπεριφορά (Εικόνα 5). Η μέγιστη τιμή της ολίσθησης μεταξύ του σκυροδέματος και της μεταλλικής δοκού που μετρήθηκε ήταν 1.9 mm και σημειώθηκε στο μέγιστο φορτίο. Μετά την εκτεταμένη ρηγμάτωση του σκυροδέματος μειώθηκε ο βαθμός διατμητικής σύνδεσης μεταξύ σκυροδέματος και μεταλλικής δοκού, με αποτέλεσμα να μειωθούν και οι τιμές της ολίσθησης.

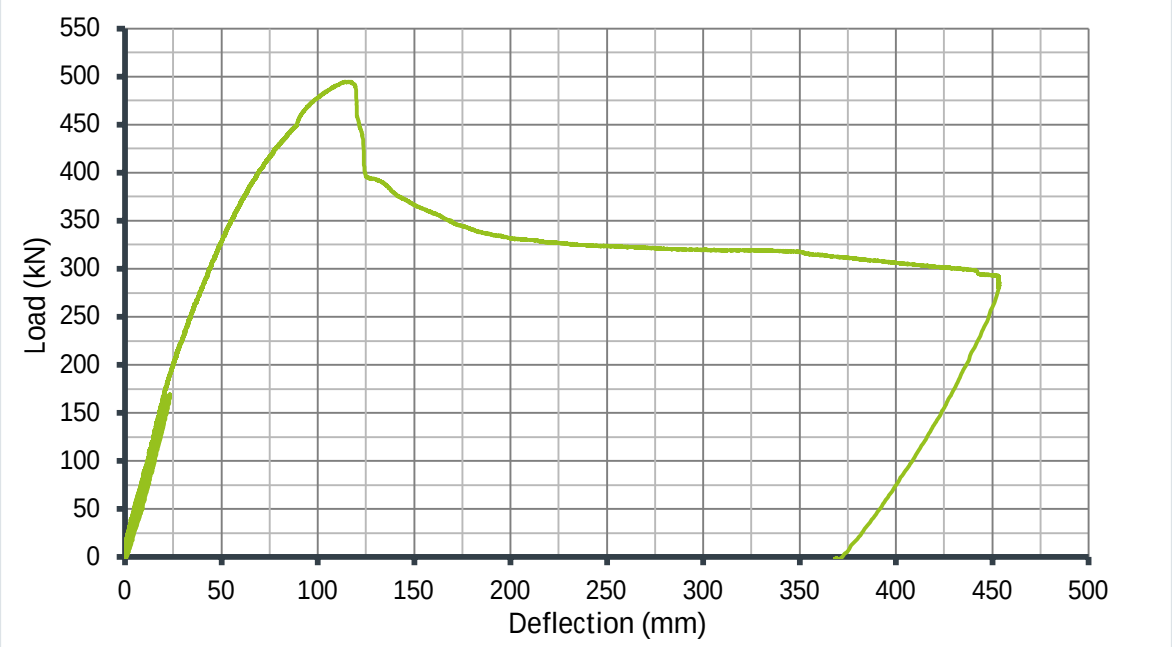

Εικ. 5- S2- Καμπύλη φορτίου-μετατόπισης

ii. **Δοκός** S3

Οι πρώτες ρωγμές εμφανίστηκαν σε μετατόπιση ίση με 20 mm στον δεύτερο κύκλο λειτουργικότητας. Οι πρώτες θλιπτικές ρωγμές παρατηρήθηκαν σε μετατόπιση ίση με 105 mm. Στη μετατόπιση που αντιστοιχεί στο μέγιστο φορτίο εμφανίστηκε λυγισμός στις θλιβόμενες διαμήκεις ράβδους με αποτέλεσμα τη θραύση του σκυροδέματος. Η έλλειψη συνδετήρων οδήγησε σε εκτενείς βλάβες στο σκυρόδεμα. Ακολούθως οι πλάκες του άνω πέλματος και των κορμών της μεταλλικής δοκού λύγισαν τοπικά με αποτέλεσμα τη μείωση του φορτίου κατά 43% (Εικόνα 6). Η μέγιστη ολίσθηση ήταν ίση με 2.2 mm και μετρήθηκε πλησίον της περιοχής φόρτισης. Οι παραμορφώσεις στο κάτω πέλμα κατανέμονται σχεδόν ομοιόμορφα με τα σημεία σύνδεσης του πέλματος με τους κορμούς να έχουν ελαφρώς υψηλότερες τιμές.

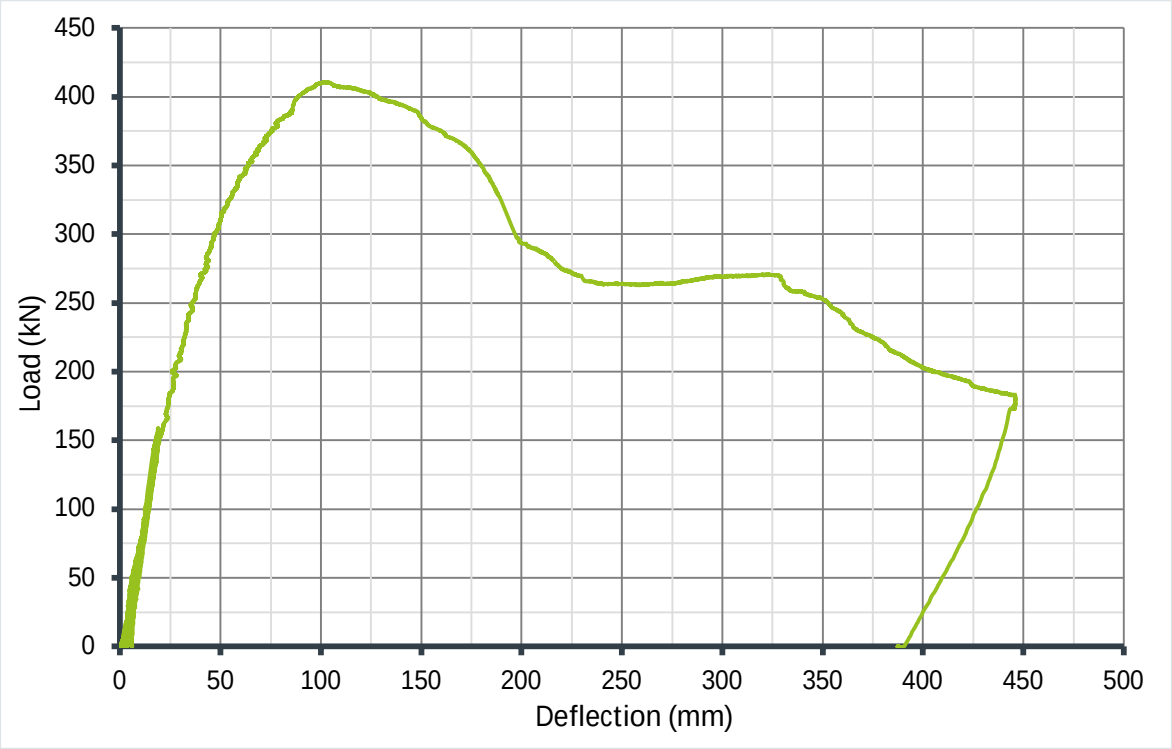

Εικ. 6- S3- Καμπύλη φορτίου-μετατόπισης

iii. **Δοκός** S4

Οι πρώτες ρωγμές εμφανίστηκαν σε μετατόπιση ίση με 20 mm στον πρώτο κύκλο λειτουργικότητας. Οι πρώτες θλιπτικές ρωγμές στην άνω παρειά του σκυροδέματος παρατηρήθηκαν σε μετατόπιση ίση με 100 mm λόγω λυγισμού των θλιβόμενων διαμήκων ράβδων. Η θραύση του σκυροδέματος και ο τοπικός λυγισμός του άνω πέλματος της

μεταλλικής δοκού δεν αποφεύχθηκαν. Η τιμή του φορτίου στο τέλος του πειράματος ήταν ίση με το 72% της μέγιστης τιμής του (Εικόνα 7). Η μέγιστη ολίσθηση ήταν ίση με 1.0 mm και μετρήθηκε στα όργανα πλησίον της περιοχής φόρτισης. Οι παραμορφώσεις στο κάτω πέλμα κατανέμονται σχεδόν ομοιόμορφα με τα σημεία ένωσης του πέλματος με τους κορμούς να έχουν ελαφρώς υψηλότερες τιμές.

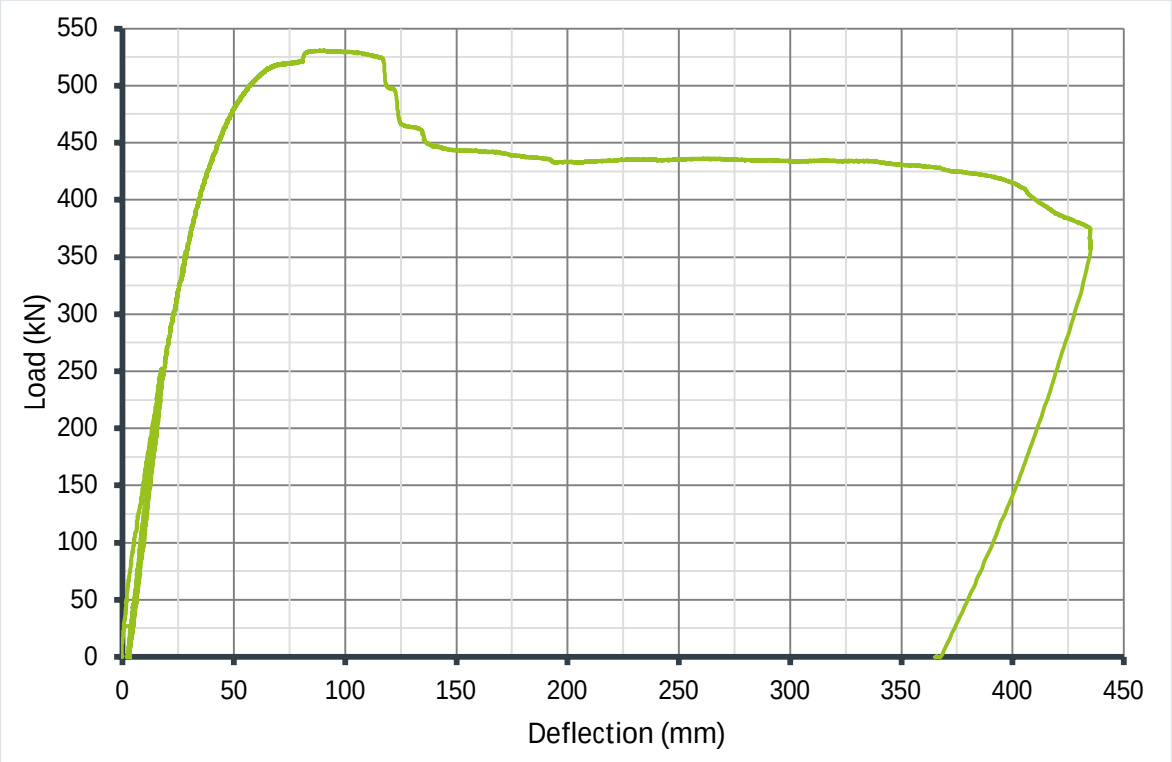

Εικ. 7- S4- Καμπύλη φορτίου-μετατόπισης

iv. **Δοκός** S5

Η δοκός S5 δεν ήταν εντελώς ευθυγραμμισμένη στην αρχή του πειράματος πιθανότερα λόγω των συγκολλήσεων των μεταλλικών πλακών που απαρτίζουν τη δοκό Deltabeam. Όταν η μετατόπιση έφτασε τα 105 mm (527 kN) οι διαμήκεις ράβδοι στη θλιβόμενη ζώνη λύγισαν προκαλώντας βλάβες στο σκυρόδεμα. Όπως και στις προηγούμενες δοκούς του ίδιου τύπου, λόγω έλλειψης συνδετήρων η βλάβη στο σκυρόδεμα ήταν εκτεταμένη και ο λυγισμός του άνω πέλματος δεν αποτράπηκε. Αυτοί οι παράγοντες προκάλεσαν μία απότομη πτώση στην αντοχή της δοκού ίση με 25% του μέγιστου φορτίου (Εικόνα 8). Η μέγιστη τιμή της ολίσθησης μεταξύ του σκυροδέματος και της μεταλλικής δοκού που μετρήθηκε ήταν 1.12 mm και σημειώθηκε στο μέγιστο φορτίο πλησίον της περιοχής φόρτισης. Οι παραμορφώσεις στο κάτω πέλμα στα

πρώτα βήματα του πειράματος κατανέμονται σχεδόν ομοιόμορφα. Με την αύξηση της μετατόπισης παρατηρήθηκε σημαντική άνοδος των τιμών της παραμόρφωσης στα σημεία ένωσης του κάτω πέλματος με τους κορμούς.

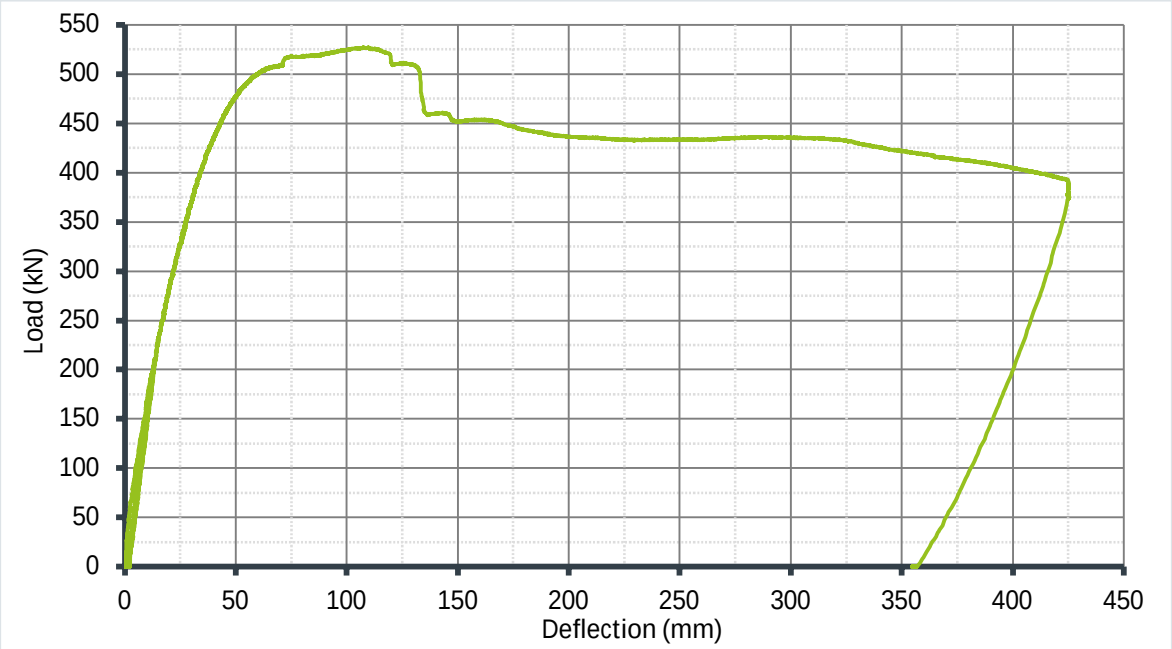

Εικ. 8- S5- Καμπύλη φορτίου-μετατόπισης

v. **Συγκριτικά αποτελέσματα δοκών Τύπου** 1

Στην Εικόνα 9 συγκρίνονται οι ανηγμένες καμπύλες φορτίου- μετακίνησης. Μόλις το φορτίο έφτασε στη μέγιστη τιμή του, οι δοκοί δεν μπόρεσαν να παραλάβουν μεγαλύτερο φορτίο λόγω της σύνθλιψης του σκυροδέματος και συνεπακολούθως της εμφάνισης τοπικού λυγισμού στις πλάκες του άνω πέλματος και των κορμών. Όπως φαίνεται στα αποτελέσματα, η διαφοροποίηση στις σειρές των διατμητικών ήλων δεν οδήγησε σε διαφοροποίηση των αποτελεσμάτων. Επιπλέον το μέγιστο φορτίο είναι ανάλογο του μεγέθους της διατομής της Deltabeam.

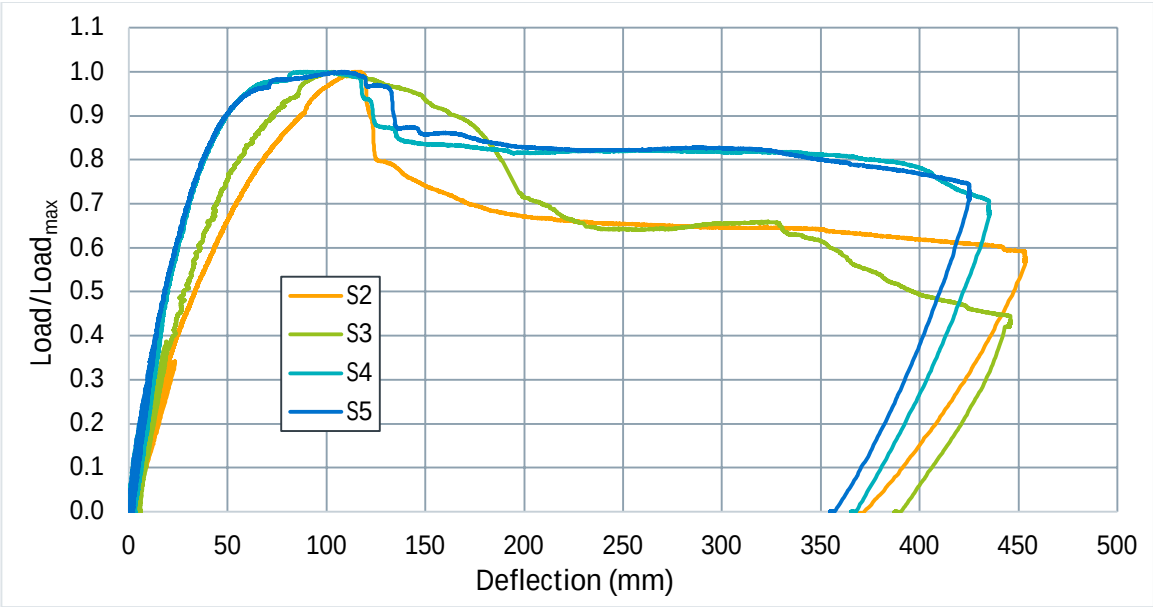

Εικ. 9- Ανηγμένα διαγράμματα φορτίου-μετατόπισης των δοκών Τύπου 1

- **Δοκίμια διατομής Τύπου** 2

Τα δοκίμια που ανήκουν σε αυτή την ομάδα είναι οπλισμένα. Οι κλωβοί των οπλισμών είναι τοποθετημένοι στο σκυρόδεμα που περιβάλλει εξωτερικά τη μεταλλική δοκό. Επιπλέον δεν υπάρχει στρώση σκυροδέματος πάνω από την άνω πλάκα της Deltabeam, με την άνω παρειά της να είναι εμφανής.

i. **Δοκός** S1

Οι πρώτες τριχοειδείς ρωγμές εμφανίστηκαν στο κάτω μέρος του δοκιμίου σε μετατόπιση ίση με 25 mm μετά τους κύκλους λειτουργικότητας. Η διάταξη των ρωγμών στο τέλος του πειράματος ήταν καμπτική. Το πείραμα σταμάτησε όταν η τιμή της μετακίνησης ήταν ίση με 448 mm διότι το έμβολο έφτασε στο μέγιστο όριο διαδρομής. Η δοκός αύξησε την αντοχή της καθ' όλη τη διάρκεια του πειράματος (Εικόνα 10). Η χρήση συνδετήρων εμπόδισε την εκτεταμένη σύνθλιψη του σκυροδέματος και την περιόρισε μόνο στη ζώνη της επικάλυψης. Η ολίσθηση μεταξύ των δύο υλικών παρέμεινε σε πολύ χαμηλές τιμές με τη μέγιστη να είναι ίση με 0.61 mm. Οι παραμορφώσεις παρουσιάζουν παρόμοιες τιμές, κατ' απόλυτη τιμή, και στα οκτώ σημεία μέτρησης, οδηγώντας στο συμπέρασμα μίας συμμετρικής κατανομής τους κατά το μήκος και το πλάτος του δοκιμίου.

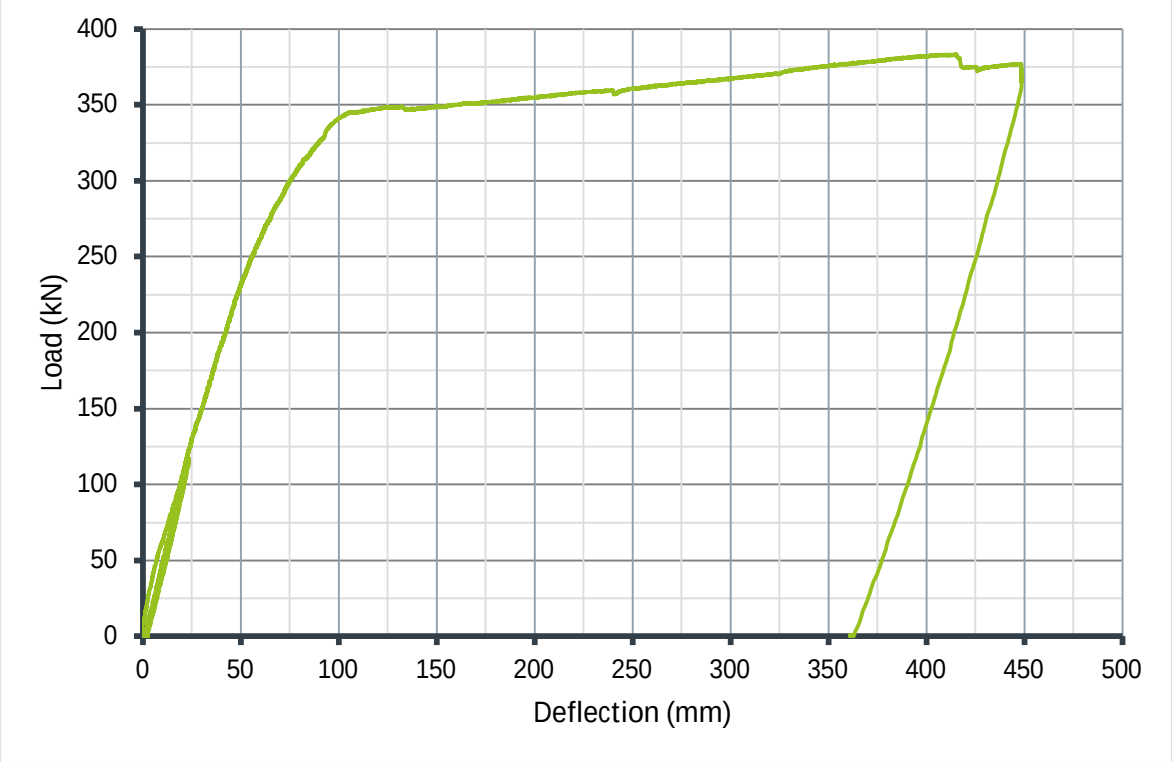

Εικ. 10- S1- Καμπύλη φορτίου-μετατόπισης

ii. **Δοκός** S11

Οι πρώτες τριχοειδείς εφελκυστικές ρωγμές εμφανίστηκαν σε μετατόπιση ίση με 18 mm μετά τους κύκλους λειτουργικότητας. Σε μετακίνηση ίση με 65 mm εμφανίστηκαν ρωγμές στην άνω παρειά του σκυροδέματος λόγω θλιπτικών τάσεων. Το πείραμα σταμάτησε όταν η τιμή της μετακίνησης ήταν ίση με 445 mm (Εικόνα 11) διότι το έμβολο έφτασε στο μέγιστο όριο διαδρομής. Η δοκός αύξησε την αντοχή της καθ' όλη τη διάρκεια του πειράματος. Η χρήση συνδετήρων εμπόδισε την εκτεταμένη σύνθλιψη του σκυροδέματος και την περιόρισε μόνο στη ζώνη της επικάλυψης. Η ολίσθηση μεταξύ των δύο υλικών παρέμεινε σε πολύ χαμηλές τιμές, με τη μέγιστη να είναι ίση με 0.40 χιλ. Οι εφελκυστικές παραμορφώσεις έχουν υψηλότερες τιμές από τις αντίστοιχες θλιπτικές δείχνοντας ότι η θέση του ουδέτερου άξονα βρίσκεται πάνω από το μέσον της διατομής.

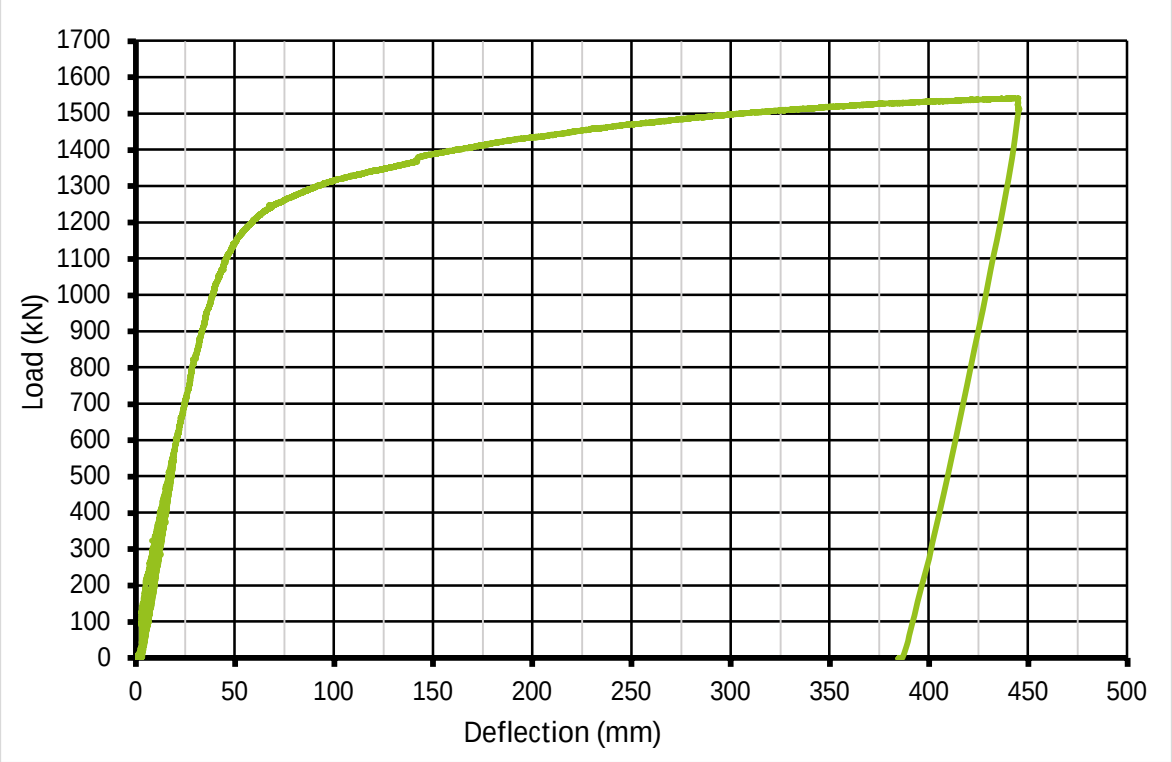

Εικ. 11- S11- Καμπύλη φορτίου-μετατόπισης

iii. **Δοκός** S12

Οι πρώτες τριχοειδείς ρωγμές εμφανίστηκαν στο κάτω μέρος της δοκού σε μετατόπιση ίση με 21 mm των δύο πρώτων κύκλων λειτουργικότητας. Η διαφορά με τις προηγούμενες δοκούς είναι ότι οι ρωγμές εμφανίστηκαν στην άνω παρειά των άκρων της δοκού πιθανότερα λόγω στρέψης. Το πείραμα σταμάτησε όταν η τιμή της μετακίνησης ήταν ίση με 416 mm (Εικόνα 12) πάλι επειδή το έμβολο έφτασε στο μέγιστο όριο διαδρομής. Η δοκός διατήρησε την αντοχή της καθ' όλη τη διάρκεια του πειράματος. Η χρήση συνδετήρων εμπόδισε την εκτεταμένη σύνθλιψη του σκυροδέματος και την περιόρισε μόνο στη ζώνη της επικάλυψης. Στο τέλος του πειράματος παρατηρήθηκε στρέψη περί τον διαμήκη άξονα λόγω έλλειψης συμμετρίας της διατομής. Η ολίσθηση μεταξύ των δύο υλικών παρέμεινε σε πολύ χαμηλές τιμές με τη μέγιστη να είναι ίση με 0.27 mm. Η διαφορά μεταξύ των θλιπτικών και εφελκυστικών παραμορφώσεων φανερώνει ότι ο ουδέτερος άξονας είναι πιο κοντά στην άνω παρειά της δοκού.

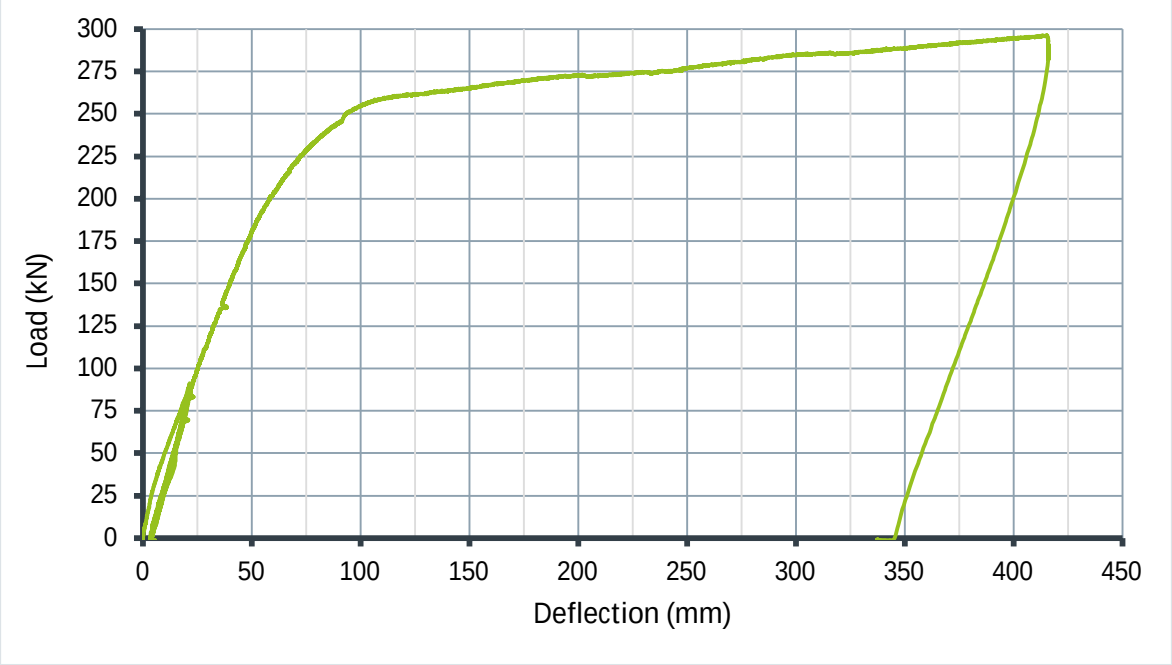

Εικ. 12- S12- Καμπύλη φορτίου-μετατόπισης

iv. **Συγκριτικά αποτελέσματα δοκών Τύπου** 2

Όλα τα δοκίμια Τύπου 2 απέδωσαν υψηλή πλαστιμότητα. Μετά τη μετατόπιση διαρροής παρουσίασαν κράτυνση με σταθερή κλίση μέχρι το τέλος των πειραμάτων, χωρίς καθόλου μείωση της αντοχής τους. Η εικόνα του σκυροδέματος μετά το πέρας των πειραμάτων ήταν καλή, με τη θραύση του σκυροδέματος να περιορίζεται στην επικάλυψη. Στην εικόνα 13 συγκρίνονται οι ανηγμένες καμπύλες φορτίου- μετακίνησης για τις τρεις δοκούς.

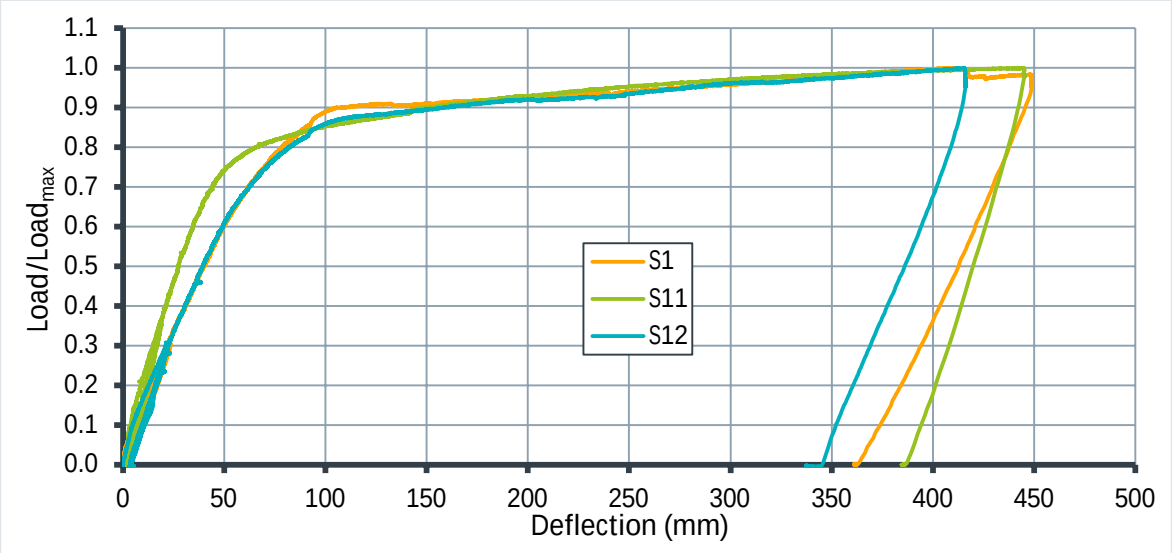

Εικ. 13- Ανηγμένα διαγράμματα φορτίου-μετατόπισης των δοκών Τύπου 2

➢ **Δοκίμια διατομής Τύπου** 3

Τα δοκίμια που ανήκουν σε αυτή την ομάδα είναι εκείνα με τον περισσότερο οπλισμό. Επίσης, η πλάκα του σκυροδέματος έχει μεγαλύτερο πλάτος ίσο με 1200 mm.

i. **Δοκός** S6a

Οι πρώτες ρωγμές παρουσιάστηκαν σε μετακίνηση ίση με 25 mm μετά τους κύκλους λειτουργικότητας. Σε μετακίνηση ίση με 100 mm, κάτω από την πλάκα φόρτισης, μία εγκάρσια ράβδος κάμφθηκε, με αποτέλεσμα τη δημιουργία ρωγμής στην άνω παρειά του σκυροδέματος. Η πλάκα του κάτω πέλματος διέρρευσε όταν η μετακίνηση έφτασε τα 98 mm. Το πείραμα σταμάτησε στα 452 mm λόγω των δυνατοτήτων του εμβόλου. Όπως φαίνεται στην Εικόνα 14 η συμπεριφορά της δοκού ήταν σχεδόν ελαστο-πλαστική με τις μικρές διακυμάνσεις να οφείλονται στις ρηγματώσεις του σκυροδέματος. Μετά την αφαίρεση του θρυμματισμένου σκυροδέματος, φανερώθηκε ότι οι θλιβόμενες διαμήκεις ράβδοι λύγισαν τοπικά. Όμως οι χρήση συνδετήρων περιόρισε το μήκος του λυγισμού, με αποτέλεσμα αυτό να μην επηρεάζει τη γενική συμπεριφορά της δοκού. Η ολίσθηση μεταξύ του σκυροδέματος και της μεταλλικής δοκού ήταν μεγαλύτερη με μέγιστη τιμή ίση με 4.74 mm. Μέχρι τη μετακίνηση των 100 mm οι παραμορφώσεις ήταν ομοιόμορφα κατανεμημένες στο πλάτος της μεταλλικής πλάκας του κάτω πέλματος. Για μεγαλύτερες όμως μετακινήσεις η παραμόρφωση στο μέσο της πλάκας είναι αυξημένη σε σχέση με τα άκρα της.

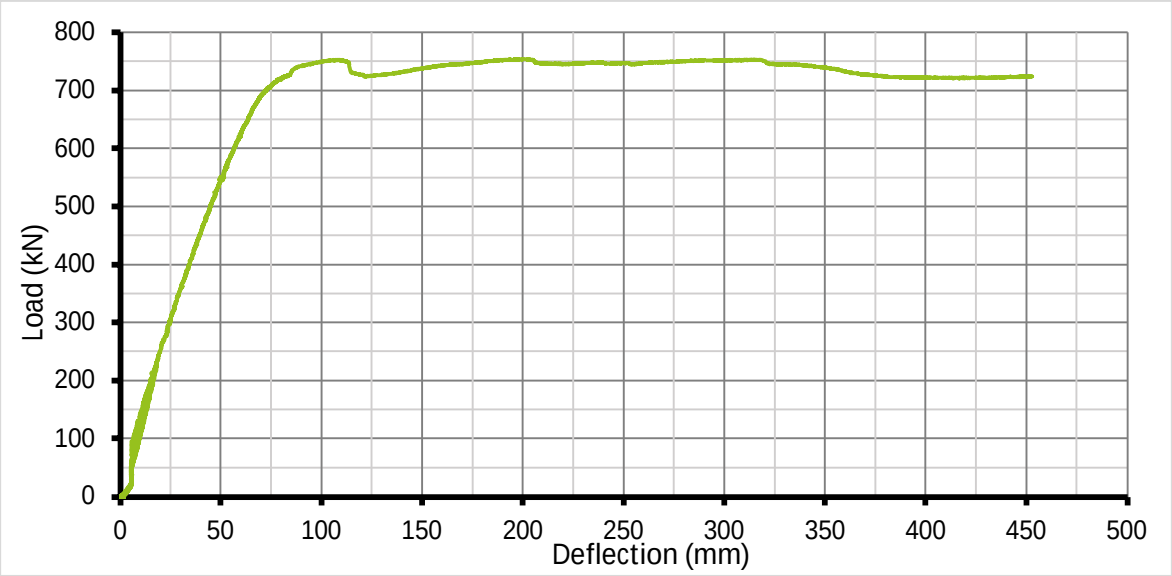

Εικ. 14- S6a- Καμπύλη φορτίου-μετατόπισης

ii. **Δοκός** S6b

Η διαφορά του δοκιμίου S6b με το S6a έγκειται στη διπλή σειρά διατμητικών ήλων. Αυτή η παράμετρος δε διαφοροποίησε αισθητά τα αποτελέσματα. Οι πρώτες ρωγμές παρουσιάστηκαν σε μετακίνηση ίση με 25 mm μετά τους κύκλους λειτουργικότητας. Σε μετακίνηση ίση με 119 mm, κάτω από την πλάκα φόρτισης, μία εγκάρσια ράβδος κάμφθηκε με αποτέλεσμα τη δημιουργία ρωγμής στην άνω παρειά του σκυροδέματος. Η πλάκα του κάτω πέλματος διέρρευσε όταν η μετακίνηση έφτασε τα 98 mm. Το πείραμα σταμάτησε στα 447 mm λόγω της μέγιστης διαδρομής του εμβόλου. Στην Εικόνα 15 παρουσιάζεται η καμπύλη φορτίου-μετατόπισης. Μετά την αφαίρεση του θρυμματισμένου σκυροδέματος, φανερώθηκε ότι οι θλιβόμενες διαμήκεις ράβδοι λύγισαν τοπικά. Όμως η χρήση συνδετήρων περιόρισε το μήκος του λυγισμού με αποτέλεσμα να μην έχει επιρροή στη γενική συμπεριφορά της δοκού. Ο μεγαλύτερος αριθμός διατμητικών ήλων επηρέασε αισθητά την ολίσθηση μεταξύ των δύο υλικών μειώνοντάς τη στα περίπου 1.5 mm. Οι παραμορφώσεις ήταν σχεδόν ομοιόμορφα κατανεμημένες στο πλάτος της μεταλλικής πλάκας του κάτω πέλματος σε όλη τη διάρκεια του πειράματος.

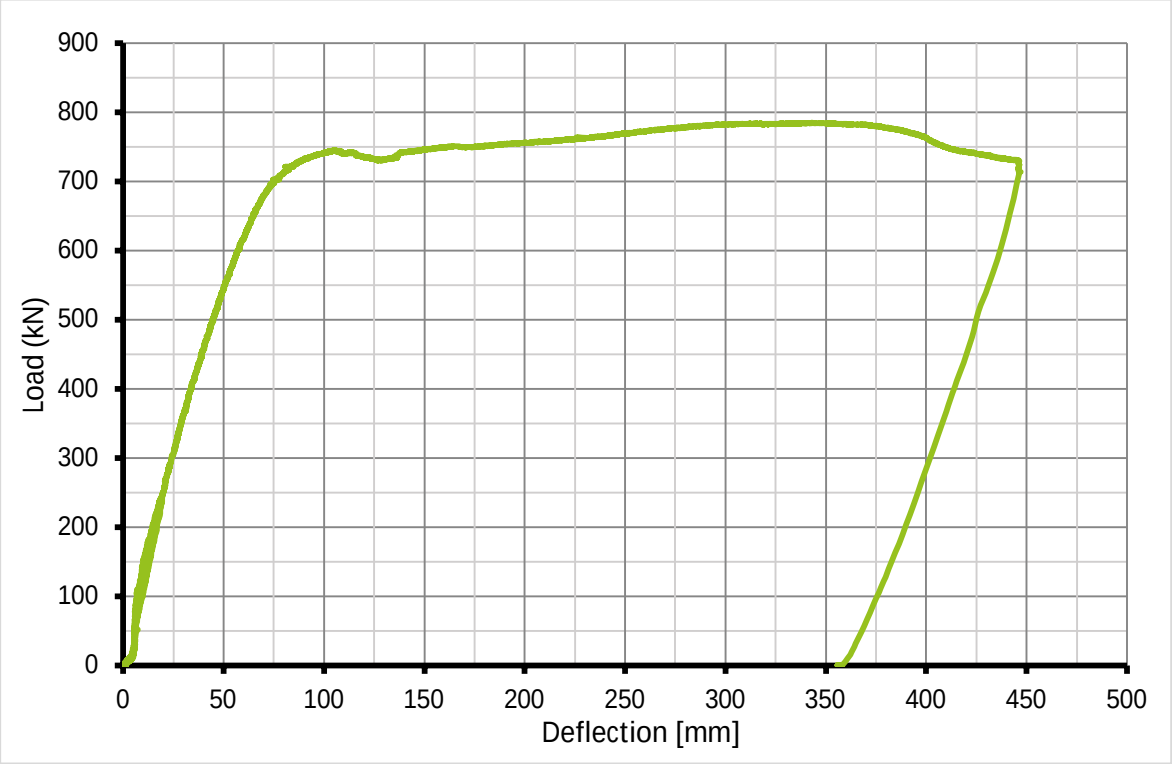

Εικ. 15- S6b- Καμπύλη φορτίου-μετατόπισης

iii. **Δοκός** S7

Οι πρώτες ρωγμές παρουσιάστηκαν σε μετακίνηση ίση με 17 mm στον πρώτο κύκλο λειτουργικότητας. Σε μετακίνηση ίση με 114 mm, κάτω από την πλάκα φόρτισης, μία εγκάρσια ράβδος κάμφθηκε με αποτέλεσμα τη δημιουργία ρωγμής στην άνω παρειά του σκυροδέματος. Το πείραμα σταμάτησε στα 432 mm λόγω της μέγιστης διαδρομής του εμβόλου. Στην Εικόνα 16 παρουσιάζεται η καμπύλη φορτίου-μετατόπισης. Μετά την αφαίρεση του θρυμματισμένου σκυροδέματος, παρατηρήθηκε ότι οι θλιβόμενες διαμήκεις ράβδοι λύγισαν τοπικά. Όμως η χρήση συνδετήρων περιόρισε το μήκος του λυγισμού με αποτέλεσμα να μην έχει επιρροή στη γενική συμπεριφορά της δοκού. Η ολίσθηση μεταξύ των δύο υλικών μετρήθηκε περίπου ίση με 3.0 mm. Οι παραμορφώσεις ήταν σχεδόν ομοιόμορφα κατανεμημένες στο πλάτος της μεταλλικής πλάκας του κάτω πέλματος με τις τιμές στο μέσο της δοκού ελαφρώς αυξημένες.

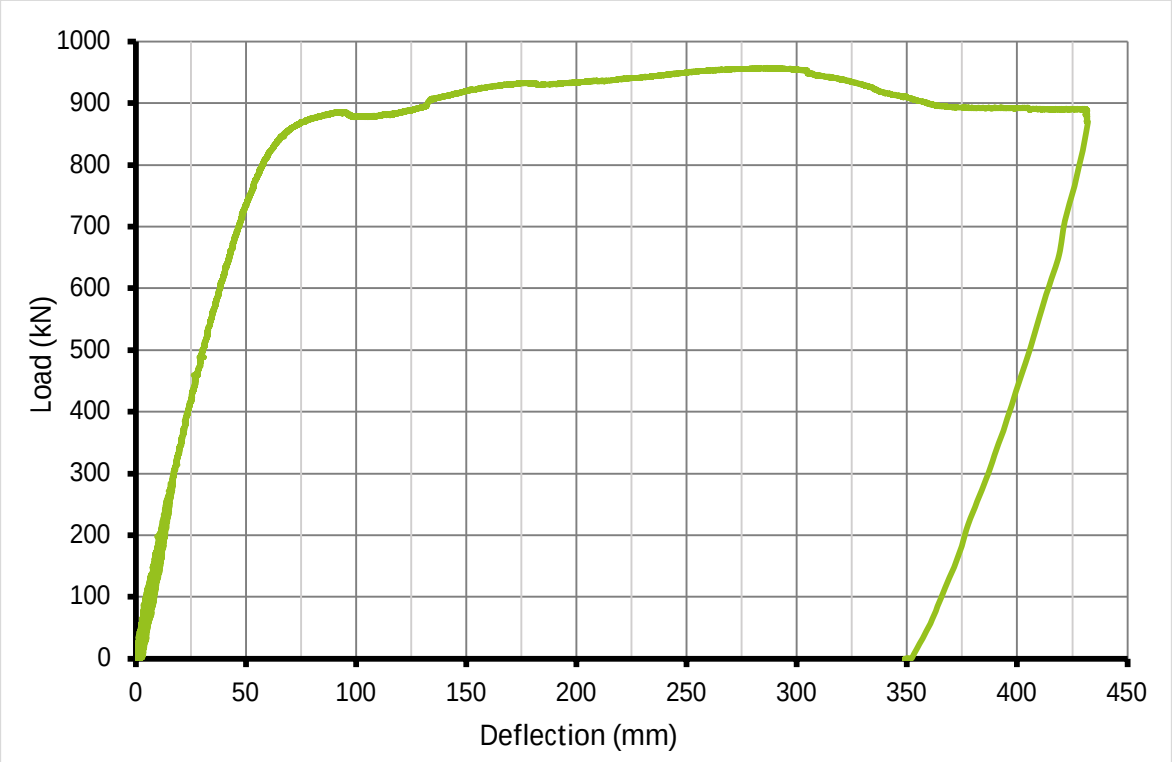

Εικ. 16- S7- Καμπύλη φορτίου-μετατόπισης

iv. **Δοκός** S8

Οι πρώτες τριχοειδείς ρωγμές εμφανίστηκαν σε μετακίνηση ίση με 19 mm η οποία ήταν η μέγιστη για τους κύκλους λειτουργικότητας. Σε μετακίνηση ίση με 85 mm, οι πρώτες θλιπτικές ρωγμές εμφανίστηκαν κάτω από την πλάκα φόρτισης. Το πείραμα σταμάτησε στα 445 mm

λόγω της μέγιστης διαδρομής του εμβόλου. Μετά τη διαρροή, το φορτίο αυξήθηκε με σταθερή κλίση μέχρι το τέλος του πειράματος (Εικόνα 17). Η πυκνή όπλιση διατήρησε τη ρηγμάτωση του σκυροδέματος στην επικάλυψη. Μετά την αφαίρεση του θρυμματισμένου σκυροδέματος, παρατηρήθηκε ότι οι θλιβόμενες διαμήκεις ράβδοι λύγισαν τοπικά. Όμως η χρήση συνδετήρων περιόρισε το μήκος του λυγισμού με αποτέλεσμα να μην επηρεάζει τη γενική συμπεριφορά της δοκού. Η ολίσθηση μεταξύ των δύο υλικών μετρήθηκε περίπου ίση με 3.89 mm. Οι παραμορφώσεις ήταν σχεδόν ομοιόμορφα κατανεμημένες στο πλάτος της μεταλλικής πλάκας του κάτω πέλματος, με τις τιμές στις συνδέσεις με τις πλάκες των κορμών ελαφρώς αυξημένες.

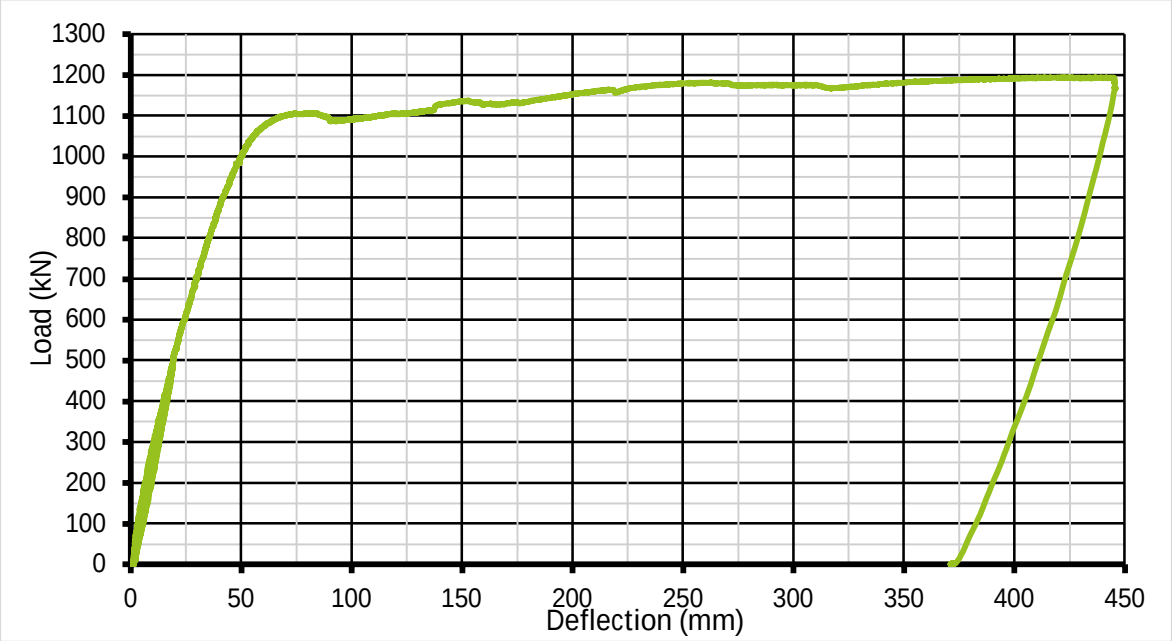

Εικ. 17- S8- Καμπύλη φορτίου-μετατόπισης

v. **Συγκριτικά αποτελέσματα δοκών Τύπου** 3

Όλα τα δοκίμια Τύπου 3 είχαν πλάστιμη συμπεριφορά. Μετά τη μετακίνηση διαρροής οι καμπύλες είναι σχεδόν οριζόντιες μέχρι το τέλος των πειραμάτων χωρίς μείωση του φορτίου. Οι μικρές διακυμάνσεις στην πλαστική περιοχή των καμπύλων οφείλονται στις ρηγματώσεις του σκυροδέματος. Η εικόνα του σκυροδέματος μετά το πέρας των πειραμάτων ήταν καλή με τη θραύση του σκυροδέματος να περιορίζεται στην επικάλυψη. Στην εικόνα 18 συγκρίνονται οι ανηγμένες καμπύλες φορτίου- μετακίνησης για τις τρεις δοκούς.

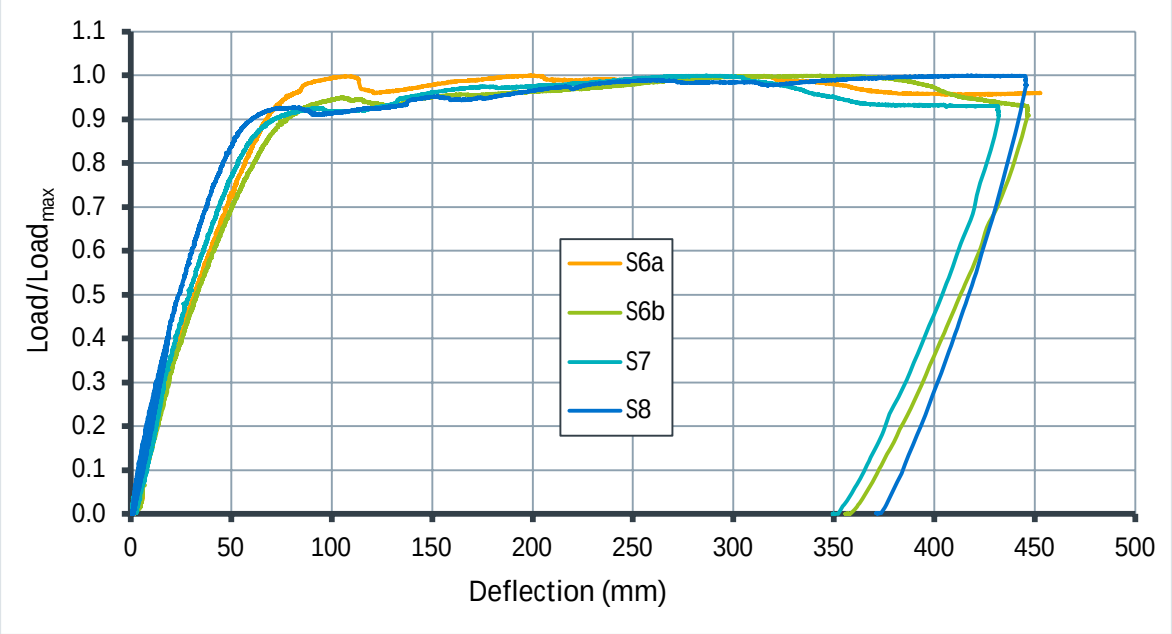

Εικ. 18- Ανηγμένα διαγράμματα φορτίου-μετατόπισης των δοκών Τύπου 3

- **Δοκίμια διατομής Τύπου** 4

Τα δοκίμια που ανήκουν σε αυτή την ομάδα προσομοιάζουν το συνδυασμό των Deltabeams με προκατασκευασμένες προεντεταμένες πλάκες σκυροδέματος.

i. **Δοκός** S9

Οι πρώτες τριχοειδείς ρωγμές εμφανίστηκαν σε μετακίνηση ίση με 19 mm στους κύκλους λειτουργικότητας. Σε μετακίνηση ίση με 95 mm, οι πρώτες θλιπτικές ρωγμές εμφανίστηκαν στο ένα άκρο της πλάκας σκυροδέματος. Αμέσως μετά την εμφάνιση των ρωγμών η πλάκα στο τμήμα αυτό αστόχησε, γεγονός που αποτυπώθηκε στην καμπύλη φορτίου-μετακίνησης ως μία μείωση του φορτίου της τάξεως των 75 kN (Εικόνα 19). Το φορτίο παρέμεινε σταθερό για τα επόμενα περίπου 100 mm όταν αστόχησε και το δεύτερο άκρο της πλάκας με επιπλέον μείωση του φορτίου ίση με 80 kN. Ακολούθως το φορτίο αυξανόταν σταθερά μέχρι το τέλος του πειράματος. Το πείραμα σταμάτησε στα 463 mm λόγω της μέγιστης διαδρομής του εμβόλου. Οι ανοικτοί συνδετήρες αποδείχθηκαν αποτελεσματικοί προστατεύοντας το σκυρόδεμα στο κεντρικό κυρίως τμήμα της δοκού. Η ολίσθηση μεταξύ των δύο υλικών μετρήθηκε ίση με 3.02 mm. Οι παραμορφώσεις ήταν σχεδόν ομοιόμορφα κατανεμημένες στο πλάτος της μεταλλικής

πλάκας του κάτω πέλματος. Στο τέλος του πειράματος παρουσιάστηκε μία μεγάλη αύξηση των παραμορφώσεων στο μέσο της δοκού.

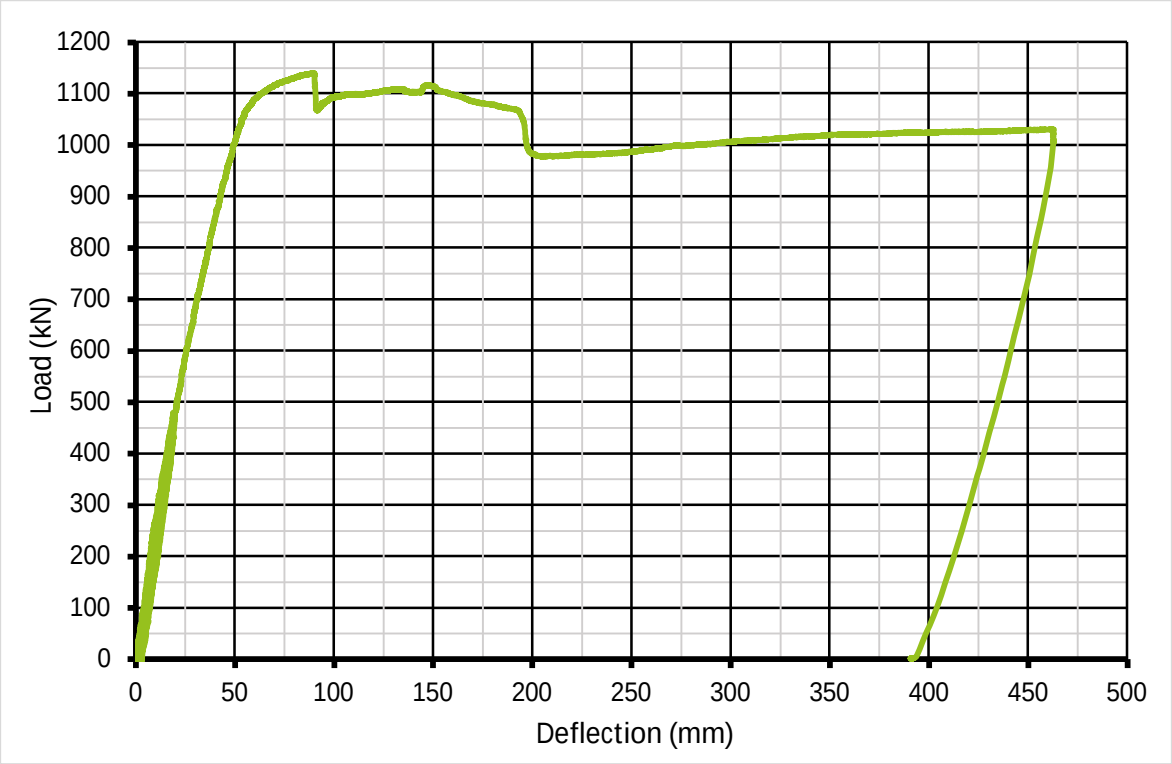

Εικ. 19- S9- Καμπύλη φορτίου-μετατόπισης

ii. **Δοκός** S10

Η συμπεριφορά του δοκιμίου S10 ήταν παρόμοια με αυτή του S9. Οι πρώτες τριχοειδείς ρωγμές εμφανίστηκαν στον πρώτο κύκλο λειτουργικότητας σε μετακίνηση ίση με 20 mm στο κάτω μέρος της δοκού. Σε μετακίνηση ίση με 80 mm, το σκυρόδεμα στο ένα εκ των δύο άκρων αστόχησε οδηγώντας σε μείωση του φορτίου ίση με 55 kN (Εικόνα 20). Το φορτίο παρέμεινε σταθερό για τα επόμενα περίπου 85 mm όταν αστόχησε και το δεύτερο άκρο της πλάκας με επιπλέον μείωση του φορτίου περίπου ίση με 100 kN. Έπειτα το φορτίο παρέμεινε σταθερό μέχρι το τέλος του πειράματος. Το πείραμα σταμάτησε στα 460 mm λόγω της μέγιστης διαδρομής του εμβόλου. Οι ανοικτοί συνδετήρες αποδείχθηκαν αποτελεσματικοί, προστατεύοντας το σκυρόδεμα στο κεντρικό κυρίως τμήμα της δοκού. Η ολίσθηση μεταξύ των δύο υλικών μετρήθηκε ίση με 3.35 mm. Οι παραμορφώσεις ήταν σχεδόν ομοιόμορφα κατανεμημένες στο πλάτος της μεταλλικής πλάκας του κάτω πέλματος.

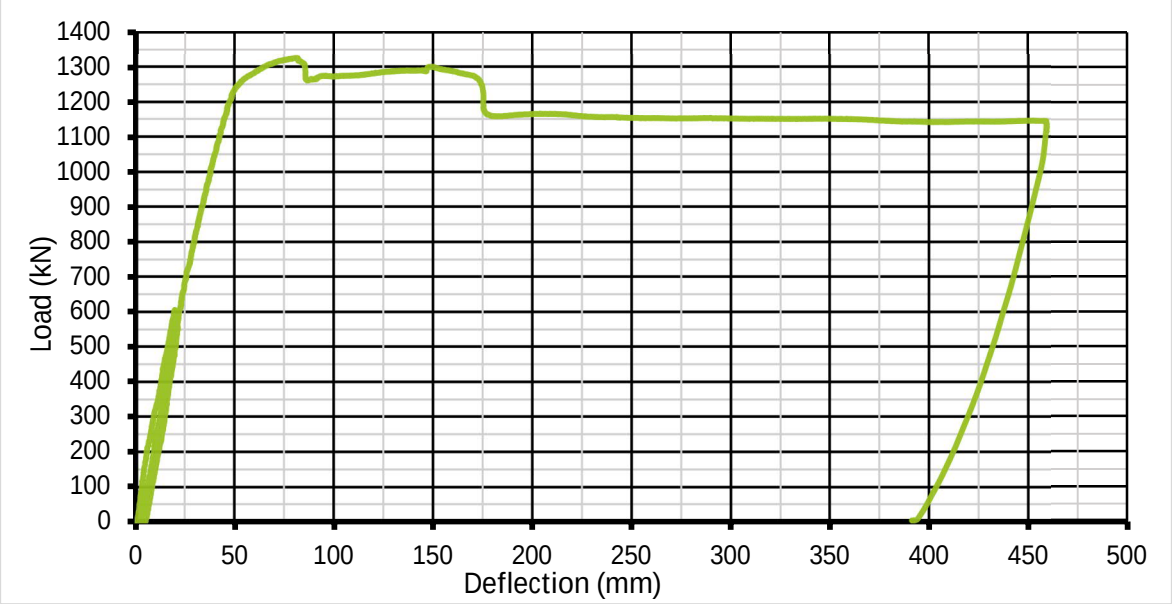

Εικ. 20- S10- Καμπύλη φορτίου-μετατόπισης

iii. **Συγκριτικά αποτελέσματα δοκών Τύπου** 4

Τα δοκίμια Τύπου 4 εμφάνισαν παρόμοια συμπεριφορά. Μετά το μέγιστο φορτίο, τα δύο άκρα της πλάκας σκυροδέματος αστόχησαν λόγω θλίψης, προκαλώντας δύο διαδοχικές μειώσεις στην αντοχή των δοκών. Το γεγονός ότι η πλάκα του σκυροδέματος είχε ίδιες διαστάσεις και οπλισμό και στα δύο δοκίμια εξηγεί τις ίσες μειώσεις. Έπειτα, το κεντρικό κομμάτι και στις δύο περιπτώσεις κατάφερε να διατηρήσει την αντοχή του αναπτύσσοντας πλάστιμη συμπεριφορά. Στην εικόνα 21 συγκρίνονται οι ανηγμένες καμπύλες φορτίου- μετακίνησης για τις δύο δοκούς.

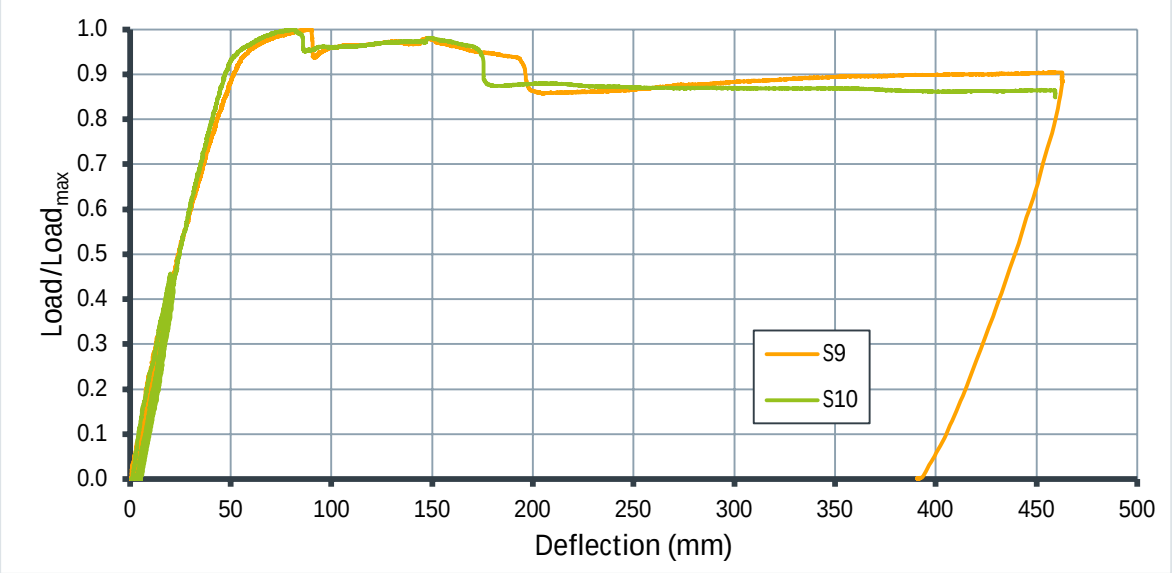

Εικ. 21- Ανηγμένα διαγράμματα φορτίου-μετατόπισης των δοκών Τύπου 4

Αναλυτική διερεύνηση των πειραματικών αποτελεσμάτων με τη μέθοδο των πεπερασμένων στοιχείων

Η μέθοδος των πεπερασμένων στοιχείων (FEM) καλύπτει σχεδόν όλο το φάσμα των αναλύσεων συμπεριλαμβανομένης της στατικής και δυναμικής ανάλυσης, της θερμικής συμπεριφοράς συστημάτων, της κίνησης υγρών κ.α. Δεδομένου ότι αυτή η μέθοδος είναι μία αριθμητική προσέγγιση, τα αποτελέσματα που λαμβάνονται με τη διενέργεια μιας ανάλυσης με τη χρήση της μεθόδου συνήθως δεν ταυτίζονται απόλυτα με τα πειραματικά αποτελέσματα. Παρόλα αυτά, μία πολύ ακριβής λύση μπορεί να επιτευχθεί με την ανάλυση ενός προσομοιώματος, βασισμένη στις αρχές της μεθόδου.

Σε γενικές γραμμές η μέθοδος των πεπερασμένων στοιχείων ακολουθεί από βήματα:

i. Διακριτοποίηση του προσομοιώματος. Το πρώτο βήμα αποτελεί η διακριτοποίηση των διαφόρων τμημάτων του συνεχούς μέσου σε πεπερασμένα στοιχεία και η περιγραφή των συνοριακών συνθηκών. Το πρώτο βήμα είναι ιδιαίτερα σημαντικό για την ακρίβεια των αποτελεσμάτων.

ii. Καθορισμός των καταστατικών ιδιοτήτων των πεπερασμένων στοιχείων.

iii. Καθορισμός της γενικής εξίσωσης ισορροπίας. Όλες οι επιμέρους εξισώσεις του κάθε στοιχείου πρέπει να συζευχθούν.

iv. Επίλυση της γενικής εξίσωσης δυνάμεων-μετακινήσεων. Από την επίλυση της εξίσωσης υπολογίζονται οι μετακινήσεις στους συνοριακούς κόμβους των πεπερασμένων στοιχείων. Η επίλυση της γενικής εξίσωσης μπορεί να πραγματοποιηθεί με άμεσες ή επαναλαμβανόμενες μεθόδους.

v. Υπολογισμός πρόσθετων αποτελεσμάτων. Σε πολλά προβλήματα απαιτείται ο υπολογισμός, εκτός των μετακινήσεων που υπολογίστηκαν, επιπλέον παραμέτρων όπως οι ανηγμένες παραμορφώσεις, οι τάσεις, οι σχετικές ολισθήσεις κ.α.

Τα προσομοιώματα που μορφώθηκαν για την αναλυτική διερεύνηση των δοκιμίων με τη χρήση του λογισμικού Abaqus αποτελούνται από πέντε τρισδιάστατα ανεξάρτητα μέρη, ένα για το σκυρόδεμα, ένα για τη μεταλλική δοκό, ένα για τους οπλισμούς και δύο άκαμπτα για τις στηρίξεις και την πλάκα φόρτισης. Η αναλύσεις πραγματοποιήθηκαν για τα δοκίμια με διατομές Τύπου 2, 3 και 4. Η έλλειψη οπλισμών στις δοκούς Τύπου 1, κατέστησε το σκυρόδεμα ένα υπολογιστικά ασταθές υλικό με αποτέλεσμα το βήμα της ανάλυσης να γίνει τόσο μικρό ώστε η ανάλυση να είναι αδύνατον να ολοκληρωθεί.

Επιλέχθηκε ένας «γενικός τύπος διεπιφάνειας σύνδεσης» για την αλληλεπίδραση μεταξύ των μερών. Το Abaqus ορίζει αυτόματα μία επιφάνεια κατάλληλη για την περιγραφή της επαφής. Για την ολοκλήρωση του ορισμού της αλληλεπίδρασης μεταξύ των μερών του προσομοιώματος, πρέπει να οριστούν και οι ιδιότητές της. Οι ιδιότητες ορίστηκαν με τέτοιο τρόπο ώστε οι επιφάνειες τις επαφής να μην διαπερνούν η μία την άλλη και παράλληλα να μπορούν να αποκολληθούν αν το απαιτήσει η ανάλυση. Η εφαπτομενική συμπεριφορά των αλληλεπιδρωσών επιφανειών ορίστηκε με δύο διαφορετικούς τρόπους. Μεταξύ του σκυροδέματος και της μεταλλικής δοκού εφαρμόστηκε τριβή με συντελεστή ίσο με 0.4. Μεταξύ των στηρίξεων και της πλάκας του κάτω πέλματος της δοκού Deltabeam ο συντελεστής τριβής ορίστηκε ίσος με μηδέν για την πιστότερη προσομοίωση των πειραμάτων.

Για τη διακριτοποίηση της μεταλλικής δοκού και του σκυροδέματος χρησιμοποιήθηκαν τρισδιάστατα εξαεδρικά στερεά στοιχεία. Οι στηρίξεις και η πλάκα φόρτισης προσομοιώθηκαν με επιφανειακά άκαμπτα στοιχεία. Τέλος η διακριτοποίηση του οπλισμού έγινε με μονοδιάστατα γραμμικά στοιχεία ράβδων.

Επιλέχθηκε, το κλασικό αριθμητικό προσομοίωμα για μέταλλα με όλκιμη συμπεριφορά (Von Mises) σε συνδυασμό με κράτυνση σταθερής κλίσης για τον ορισμό του χάλυβα της μεταλλικής δοκού και των οπλισμών.

Η πραγματική καταστατική σχέση τάσεων-παραμορφώσεων υπολογίστηκε από τις αντίστοιχες μηχανικές τιμές, οι οποίες ελήφθησαν από πειράματα μεταλλικών δειγμάτων σε εφελκυσμό, στα οποία οι μηχανικές τιμές υπολογίζονται διαιρώντας τα πειραματικά φορτία με

τη διατομή των δοκιμίων. Επισημαίνεται ότι η εν λόγω διατομή δεν παραμένει σταθερή καθ' όλη τη διάρκεια του πειράματος. Οι αναλυτικές εξισώσεις που χρησιμοποιήθηκαν για τη μετατροπή των μηχανικών τιμών στις αντίστοιχες πραγματικές είναι οι ακόλουθες:

$$\sigma_{true} = \sigma_{engineering} * (1 + \varepsilon_{engineering})$$

$$\varepsilon_{true} = \ln(1 + \varepsilon_{engineering})$$

όπου

σ_{true} είναι η πραγματική τάση

ε_{true} είναι η πραγματική παραμόρφωση

$\sigma_{engineering}$ είναι η μηχανική τάση

$\varepsilon_{engineering}$ είναι η μηχανική παραμόρφωση

Η συμπεριφορά του σκυροδέματος είναι γενικά σύνθετη. Η πολυπλοκότητα έγκειται κυρίως στη μη γραμμική συμπεριφορά του έναντι πολυαξονικής καταπόνησης, ανισοτροπική μείωση της δυσκαμψίας, διαδοχική ρηγμάτωση λόγω εφελκυστικών τάσεων και παραμορφώσεων, αλληλεπίδραση μεταξύ σκυροδέματος και οπλισμού κ.α. Η πρόοδος στις υπολογιστικές δυνατότητες των σύγχρονων υπολογιστών οδήγησε στη δημιουργία διαφόρων προσομοιωμάτων, τα οποία να περιέχουν τις προαναφερθείσες πολυπλοκότητες. Για τον προσδιορισμό της συμπεριφοράς του σκυροδέματος στο Abaqus χρησιμοποιήθηκε το προσομοίωμα «Concrete Damaged Plasticity» (CDP). Οι δύο κύριοι μηχανισμοί αστοχίας είναι η ρηγμάτωση λόγω εφελκυσμού και η θραύση λόγω θλίψης. Για τη δημιουργία της καμπύλης τάσεων-παραμορφώσεων για μονοαξονική θλίψη χρησιμοποιήθηκαν οι εξισώσεις που παρέχονται από τον Ευρωκώδικα 2. Η μη-ελαστική εφελκυστική συμπεριφορά του σκυροδέματος καθορίστηκε από την ενέργεια θραύσης. Με τη χρήση της ενέργειας θραύσης η συμπεριφορά του υλικού δε συσχετίζεται με το μήκος του ρηγματωμένου στοιχείου. Με αυτό τον τρόπο αποφεύγονται προβλήματα σύγκλισης κατά την επίλυση.

Η επιβαλλόμενη μετακίνηση εφαρμόστηκε στα προσομοιώματα μέσω ενός άκαμπτου μέρους το οποίο προσομοιώνει τη μεταλλική πλάκα στη βάση του εμβόλου. Η χρονοϊστορία φόρτισης που χρησιμοποιήθηκε ήταν η ίδια με τη χρονοϊστορία των πειραμάτων. Το άκαμπτο μέρος που χρησιμοποιήθηκε για την προσομοίωση των στηρίξεων δεσμεύτηκε έναντι μετακίνησης και στροφής προς όλες τις κατευθύνσεις.

Στη συνέχεια παρουσιάζονται οι καμπύλες φορτίου- μετακίνησης για κάθε δοκό των Τύπων 2, 3 και 4. Με χρήση της μεθόδου της γραμμικής παρεμβολής υπολογίστηκαν οι μέσοι όροι των πειραματικών και αναλυτικών αποτελεσμάτων τόσο για κάθε τύπο διατομής ξεχωριστά όσο και για όλες τις δοκούς συνολικά (Εικόνες 22- 25). Το σφάλμα μεταξύ των πειραματικών και αναλυτικών αποτελεσμάτων υπολογίστηκε μικρότερο από 5%. Για να εκτιμηθεί καλύτερα η συσχέτιση μεταξύ αναλυτικών και πειραματικών αποτελεσμάτων, υπολογίστηκε ο συντελεστής συσχέτισης χρησιμοποιώντας την αναλυτική σχέση του Pearson:

$$\boldsymbol{r} = \frac{\boldsymbol{n}\sum \boldsymbol{xy} - (\sum \boldsymbol{x})(\sum \boldsymbol{y})}{\sqrt{\boldsymbol{n}(\sum \boldsymbol{x^2}) - (\sum \boldsymbol{x})^2}\sqrt{\boldsymbol{n}(\sum \boldsymbol{y^2}) - (\sum \boldsymbol{y})^2}}$$

όπου

n ο αριθμός των αποτελεσμάτων

x τα πειραματικά αποτελέσματα

y τα αναλυτικά αποτελέσματα

Ο συντελεστής συσχέτισης χρησιμοποιείται για να εξηγήσει πόσο μπορεί ένας παράγοντας να μεταβληθεί λόγω της σχέσης του με έναν άλλον και το εύρος τιμών του είναι μεταξύ 0 και 1. Η τιμή 1 υποδεικνύει μια τέλεια αντιστοιχία και ως εκ τούτου ένα πολύ αξιόπιστο μοντέλο για μελλοντικές προβλέψεις. Αντιθέτως, η τιμή 0 δείχνει ότι το προσομοίωμα αποτυγχάνει εντελώς στην πρόβλεψη των πραγματικών τιμών. Όσο πιο μικρή είναι η απόσταση του συντελεστή από τη μονάδα τόσο πιο αξιόπιστη είναι η συσχέτιση μεταξύ των δύο αποτελεσμάτων και κατ' επέκταση το προσομοίωμα. Στη συγκεκριμένη διερεύνηση ο συντελεστής συσχέτισης

υπολογίστηκε ίσος με 0.996. Αυτό δηλώνει ότι το προσομοίωμα των πεπερασμένων στοιχείων μπορεί να υπολογίσει με αυξημένη ακρίβεια τη συμπεριφορά παρόμοιων δοκών.

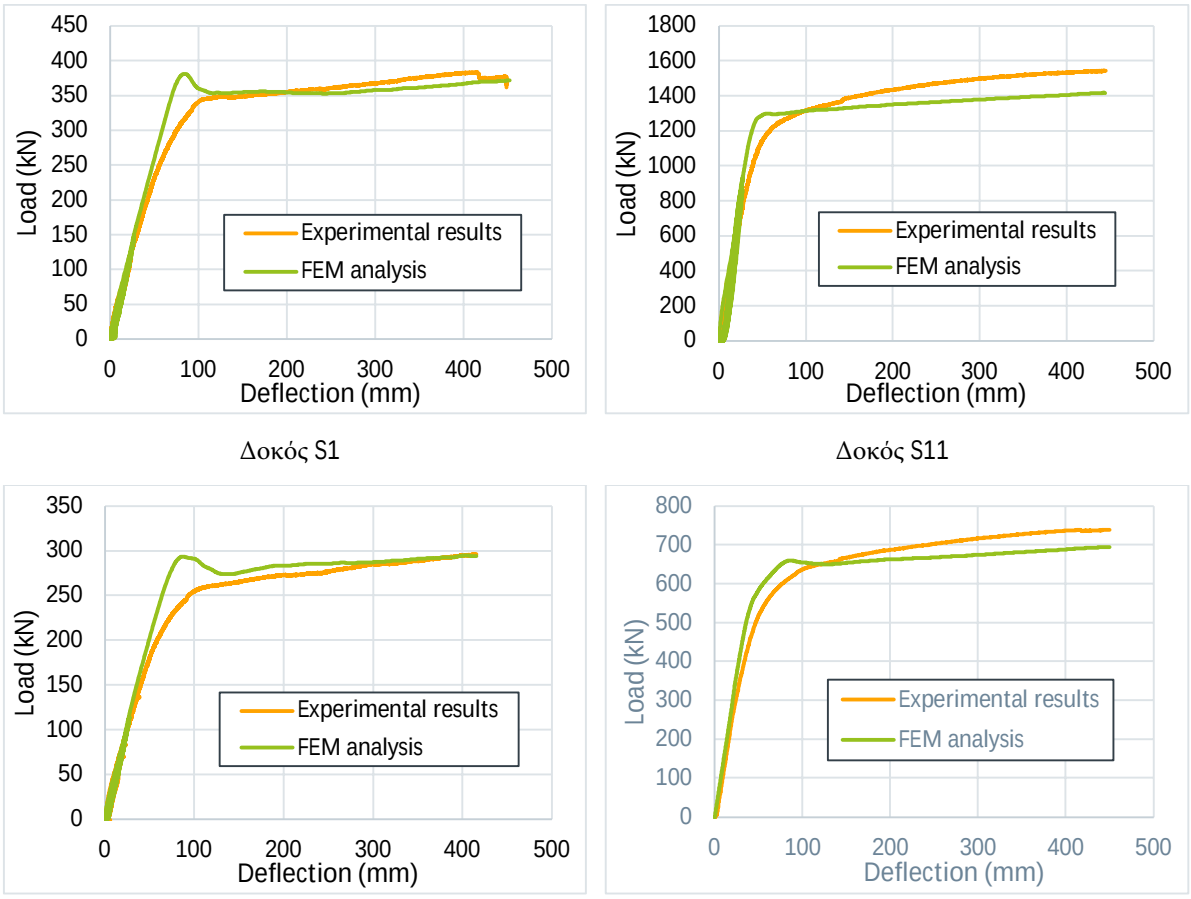

Εικ. 22- Σύγκριση πειραματικών και αναλυτικών αποτελεσμάτων για τις δοκούς Τύπου 2

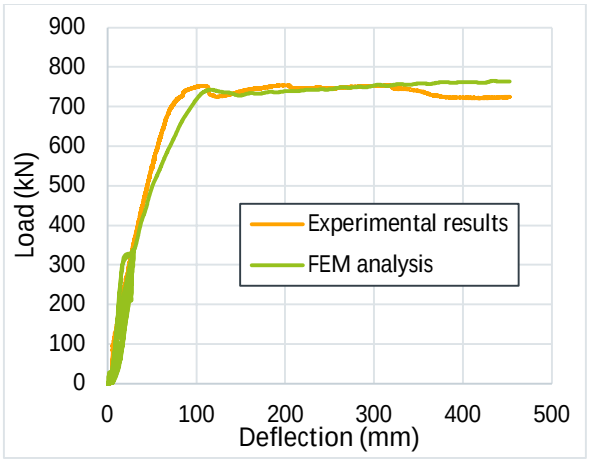

Δοκός S6a

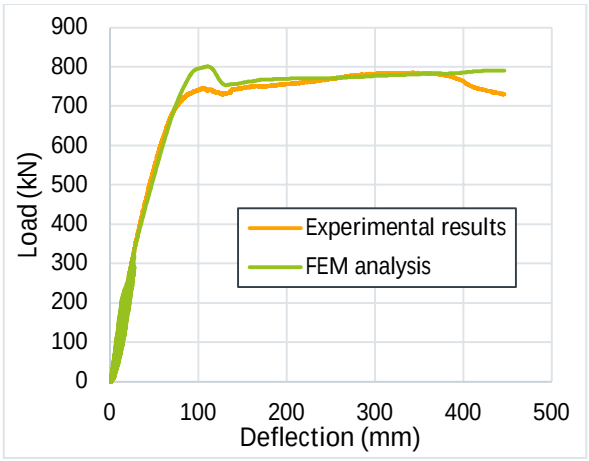

Δοκός S6b

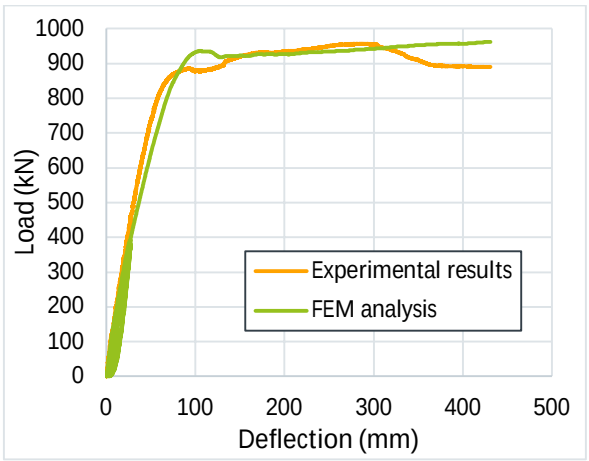

Δοκός S7

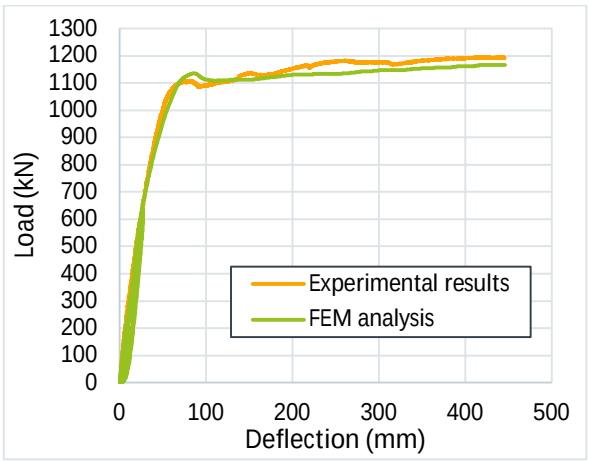

Δοκός S8

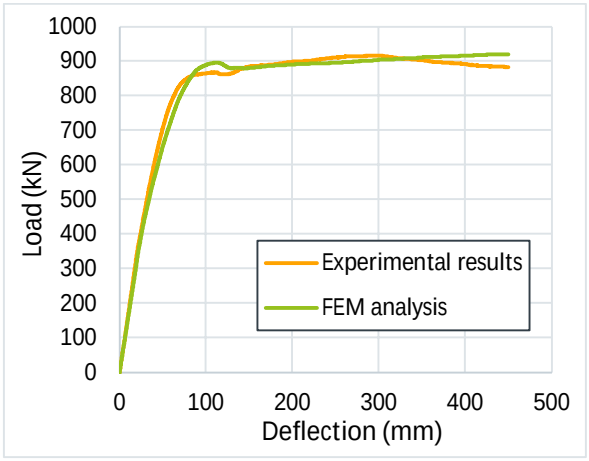

Μέσος όρος δοκών Τύπου 3

Εικ. 23- Σύγκριση πειραματικών και αναλυτικών αποτελεσμάτων για τις δοκούς Τύπου 3

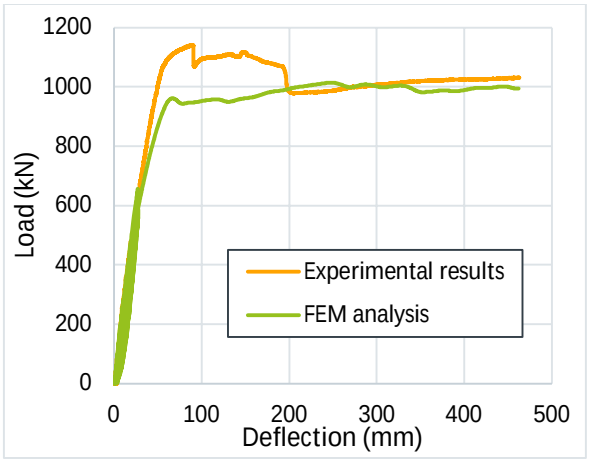

Δοκός S9

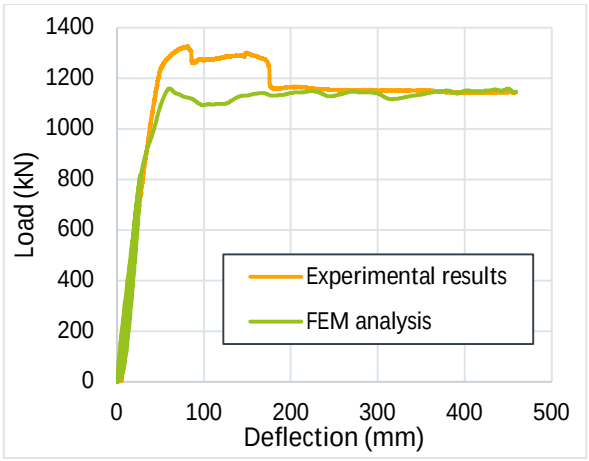

Δοκός S10

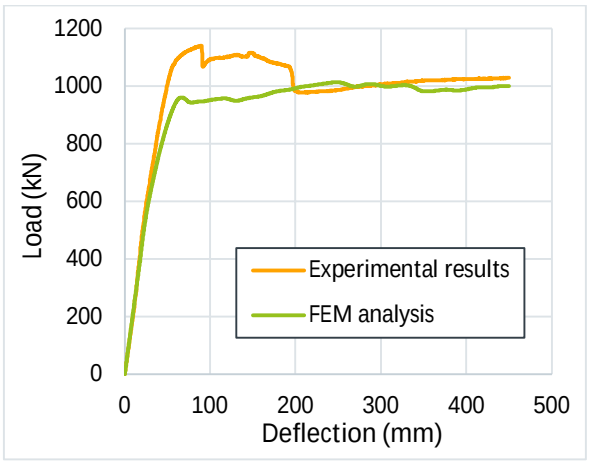

Μέσος όρος δοκών Τύπου 4

Εικ. 24- Σύγκριση πειραματικών και αναλυτικών αποτελεσμάτων για τις δοκούς Τύπου 4

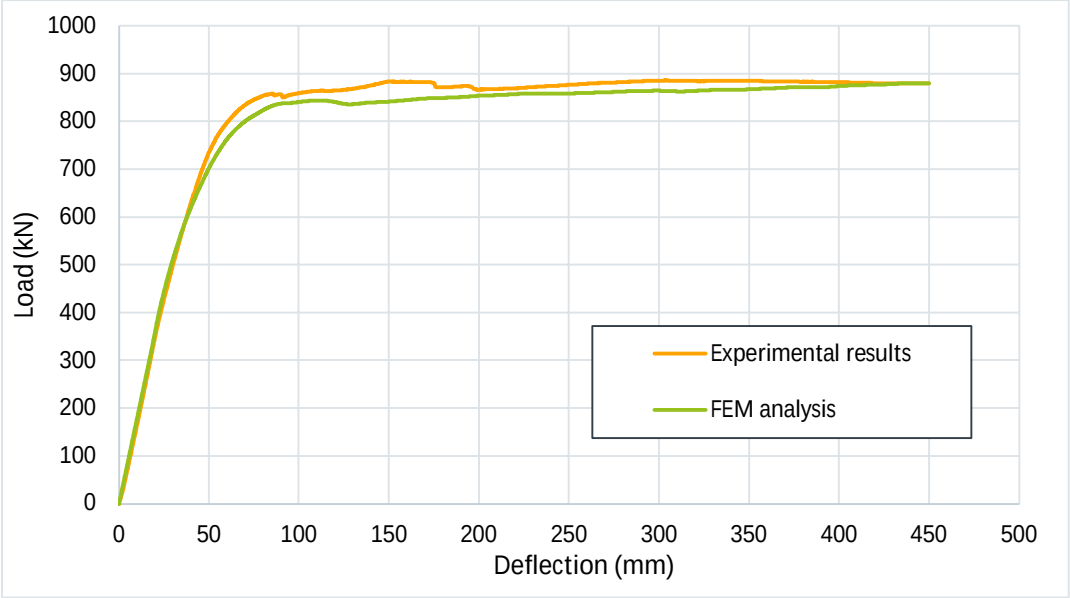

Εικ. 25- Σύγκριση συνολικών αποτελεσμάτων

Μετά την πιστοποίηση της εγκυρότητας του προσομοιώματος, διερευνήθηκε η σημασία της προστασίας που παρέχει στους κορμούς της δοκού Deltabeam το εξωτερικό περισφιγμένο σκυρόδεμα και η επιρροή του στη γενική συμπεριφορά της δοκού. Η διερεύνηση έγινε στο προσομοίωμα της δοκού S11 (Προσομοίωμα 1), με την πειραματική διατομή να αποτελεί το βασικό προσομοίωμα για τον έλεγχο των αποτελεσμάτων. Η κύρια διαφορά των προσομοιωμάτων της διερεύνησης με το προσομοίωμα αναφοράς είναι η απουσία του εξωτερικού σκυροδέματος. Ο παράγοντας υπό διερεύνηση ήταν το πάχος των κορμών των Deltabeams. Το Προσομοίωμα 2 έχει την ίδια διατομή με το προσομοιώμα αναφοράς χωρίς το εξωτερικό οπλισμένο σκυρόδεμα. Στο Προσομοίωμα 3, έχουν συγκολληθεί δύο ράβδοι οπλισμού διαμέτρου 20 mm σε κάθε πλάκα του κορμού. Τέλος το Προσομοίωμα 4 έχει αυξημένο πάχος κορμών ίσο με 8 mm.

Στην Εικόνα 26 παρουσιάζεται η σύγκριση των διαγραμμάτων φορτίου- μετακίνησης. Όλες οι δοκοί χωρίς εξωτερικά οπλισμένο σκυρόδεμα εμφάνισαν τοπικό λυγισμό. Αρχικά, ο λυγισμός εμφανίστηκε στις πλάκες του κορμού και στη συνέχεια στην πλάκα του άνω πέλματος. Τα αποτελέσματα έδειξαν πως όταν οι κορμοί ήταν «ισχυρότεροι» η συμπεριφορά των δοκών ήταν καλύτερη και ο λυγισμός εμφανίστηκε σε μεγαλύτερες τιμές μετακίνησης. Παρ' όλα αυτά, ο κίνδυνος για λυγισμό εξαλείφεται οριστικά μόνο όταν εμποδίζεται η πλευρική μετακίνηση των μεταλλικών πλακών του κορμού.

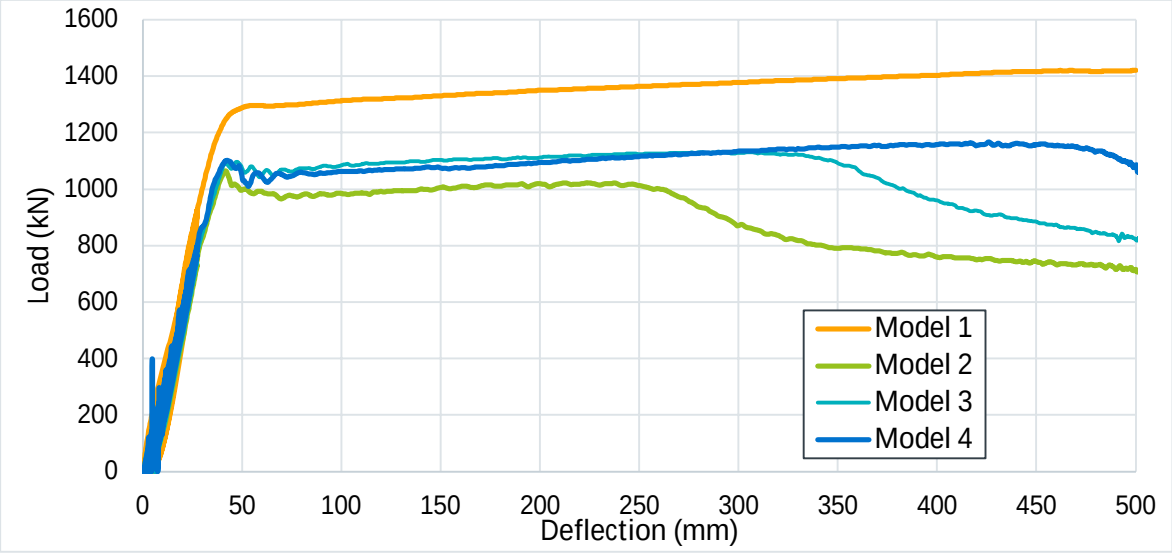

Εικ. 26- Σύγκριση συνολικών πρόσθετης διερεύνησης

Σχεδιασμός κτηρίου έναντι σεισμού

Πραγματοποιήθηκαν και συγκρίθηκαν δύο διαφορετικές επιλύσεις για το σχεδιασμό ενός κτηρίου γραφείων. Στην πρώτη ανάλυση χρησιμοποιήθηκαν οι δοκοί Deltabeams ενώ στη δεύτερη χρησιμοποιήθηκαν συνήθεις δοκοί οπλισμένου σκυροδέματος. Η παρουσίαση των αποτελεσμάτων περιορίζεται στο σχεδιασμό έναντι κάμψης των κύριων δομικών στοιχείων. Παρόλα αυτά ο σχεδιασμός πραγματοποιήθηκε ακολουθώντας και εφαρμόζοντας όλες τις οδηγίες των σχετιζόμενων Ευρωκωδίκων.

Η αρχική αρχιτεκτονική κάτοψη παρουσιάζεται στην Εικόνα 27. Το συνολικό μήκος του κτηρίου είναι 21.25 m και το συνολικό πλάτος του 17.80 m. Το καθαρό ύψος μεταξύ των ορόφων θεωρήθηκε ότι είναι 3.00 m. Η κάτοψη του σχεδιαστικού προσομοιώματος παρουσιάζεται επίσης στην Εικόνα 27.

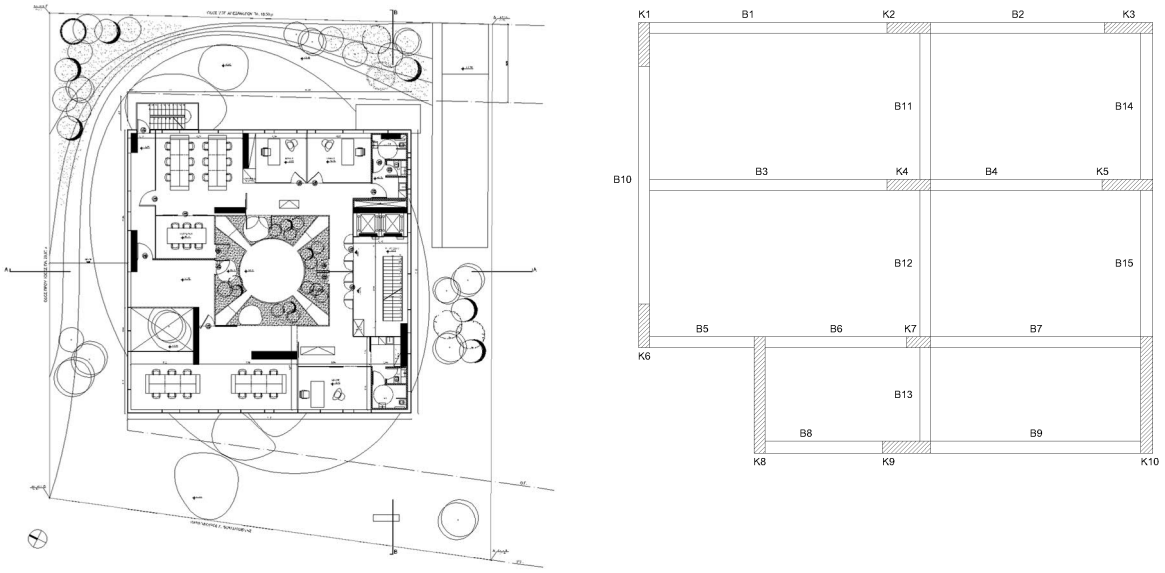

Εικ. 27- Κάτοψη τυπικού ορόφου και ισοδύναμου προσομοιώματος

Η τοποθεσία του εν λόγω κτηρίου βρίσκεται σε Σεισμική ζώνη Ι με εδαφική επιτάχυνση σχεδιασμού ίση με 0.16g. Το έδαφος είναι κατηγορίας Β. Σύμφωνα με τον πίνακα 5.1 του Ευρωκώδικα 1998-1:2004 ο συντελεστής συμπεριφοράς για τον υπολογισμό της οριζόντιας σεισμικής συνιστώσας σχεδιασμού επιλέχθηκε ίσος με 3.0. Αντιστοίχως, ο συντελεστής συμπεριφοράς για τον υπολογισμό της κατακόρυφης συνιστώσας επιλέχθηκε ίσος με 1.5, όπως συνιστάται.

- **Προσομοίωμα με χρήση δοκών** Deltabeams

Όπως προαναφέρθηκε, οι δοκοί Deltabeams συνδέονται με τα κατακόρυφα τοιχεία οπλισμένου σκυροδέματος με τρόπο τέτοιο που να επιτρέπει τη μεταφορά μόνο των κατακόρυφων φορτίων. Επομένως, οι Deltabeams σχεδιάστηκαν μόνο έναντι του στατικού συνδυασμού των μόνιμων και κινητών φορτίων. Ο σχεδιασμός του κτηρίου πραγματοποιήθηκε σε τρία στάδια. Αρχικά, το προσομοίωμα του τυπικού ορόφου κατασκευάστηκε με τη χρήση του λογισμικού που δημιουργήθηκε από την Peikko για τον σχεδιασμό των δοκών Deltabeams. Οι δοκοί, οι οποίες προσομοιώθηκαν ως αμφιέρειστες, στο πρώτο στάδιο της ανέγερσης συμπεριφέρονται ως μεταλλικές. Στο επόμενο στάδιο τοποθετούνται προκατασκευασμένες πλάκες σκυροδέματος στη μεταλλική πλάκα του κάτω πέλματος των δοκών. Τέλος, το τρίτο στάδιο περιέχει τη σκυροδέτηση και τη δημιουργία μίας επιπλέον στρώσης σκυροδέματος πάνω από τις μεταλλικές δοκούς. Έπειτα οι δοκοί σχεδιάστηκαν για όλες τις φάσεις της κατασκευής έναντι κάμψης, διάτμησης, πυρκαγιάς τόσο στην οριακή κατάσταση αστοχίας όσο και στην οριακή κατάστασης λειτουργικότητας. Το πάχος των προκατασκευασμένων πλακών και της επιπλέον στρώσης σκυροδέματος διαστασιολογήθηκε ίσο με 200 mm και 80 mm, αντίστοιχα. Η γεωμετρία των επιλεγμένων Deltabeams παρουσιάζεται αναλυτικά στον Πίνακα 1. Στον Πίνακα 2 φαίνεται η σχεδιαστική αντοχή έναντι κάμψης κάθε δοκού.

Οι διαστάσεις και το εμβαδόν των κατακόρυφων οπλισμών των τοιχείων παρουσιάζεται στον Πίνακα 3. Κάθε τοιχείο προσομοιώθηκε με τη χρήση ενός ραβδωτού στοιχείου στο κέντρο του. Η διατομή του κάθε στοιχείου σχεδιάστηκε στο Section Designer σύμφωνα με τον Πίνακα 3. Η ένωση των τοιχείων με τις εκατέρωθεν δοκούς γίνεται με τη χρήση οριζόντιων άκαμπτων γραμμικών στοιχείων, τα οποία συνδέουν το άκρο της κάθε δοκού με τον άνω κόμβο του τοιχείου. Τα άκαμπτα αυτά στοιχεία έχουν την ίδια διατομή με τις δοκούς που ακολουθούν, για την αποφυγή υπολογιστικών προβλημάτων λόγω ανεπιθύμητων ασυνεχειών, με θεωρητικά άπειρη δυσκαμψία. Η μάζα και το βάρος τους έχουν μηδενική τιμή, καθώς η χρήση τους είναι μόνο για την προσομοίωση του τοιχείου. Για κάθε δοκό Deltabeam αποδεσμευτήκαν οι περιορισμοί σε στροφή στα άκρα του για την ακριβέστερη προσομοίωση των πραγματικών στηρίξεων.

Πίνακας 1- Γεωμετρία των Deltabeams

Δοκός	**Πλάτος άνω πέλματος** (mm)	**Πάχος άνω πέλματος** (mm)	**Πλάτος κάτω πέλματος** (mm)	**Πάχος κάτω πέλματος** (mm)	**Ύψος μεταλλικών δοκών** (mm)	**Συνολικό ύψος** (mm)
B1	180	14	390	7	300	380
B2	180	14	365	7	200	280
B3	230	25	660	14	300	380
B4	270	16	660	12	220	300
B5	180	10	365	5	200	280
B6	278	10	660	8	200	280
B7	270	16	660	10	220	300
B8	180	10	365	5	200	280
B9	180	10	380	5	250	330
B10	180	30	405	16	320	400
B11	278	10	660	5	200	280
B12	278	10	660	5	200	280
B13	278	10	660	5	200	280
B14	180	10	365	5	200	280
B15	180	10	365	5	200	280

Πίνακας 2- Αντοχή σχεδιασμού έναντι κάμψης

Δοκός	Deltabeam	Ροπή σχεδιασμού (kNm)	Αντοχή σχεδιασμού (kNm)	Ποσοστό (%)
B1	DR30-270	413.4	486.15	85.0
B2	DR20-245	211.8	276.86	76.5
B3	D30-400	809.6	952.52	85.0
B4	D22-400	410.7	561.47	73.1
B5	DR20-245	76.3	182.66	41.8
B6	D20-400	231.4	405.06	57.1
B7	D22-400	518.9	555.86	93.4
B8	DR20-245	65.5	182.63	35.9
B9	DR25-260	217.8	304.16	71.6
B10	DR32-285	822.5	882.36	93.2
B11	D20-400	66.3	297.82	22.3
B12	D20-400	67.5	297.82	22.7
B13	D20-400	26.9	297.82	9.0
B14	DR20-245	36.1	182.63	19.8
B15	DR20-245	36.7	182.63	20.1

Πίνακας 3- Λεπτομέρειες των τοιχείων

Τοιχείο	**Μήκος** (m)	**Πλάτος** (m)	**Κατακόρυφος οπλισμός** $A_{s,v}$ (cm^2)
K1	1.80	0.45	137.44
K2	1.80	0.45	169.90
K3	2.00	0.45	117.81
K4	1.80	0.45	117.81
K5	2.10	0.45	197.04
K6	1.80	0.45	137.44
K7	1.00	0.45	49.09
K8	4.80	0.45	221.67
K9	2.00	0.50	197.04
K10	4.80	0.50	246.30

Η φασματική ανάλυση πραγματοποιήθηκε με τη χρήση των εκατό πρώτων ιδιομορφών για τον υπολογισμό των σεισμικών φορτίων. Οι ιδιοπερίοδοι και το ποσοστό συμμετοχής της μάζας περιγράφονται στον Πίνακα 4. Οι τρεις πρώτες ιδιομορφές και τα ιδιοσχήματά τους φαίνονται στην Εικόνα 28. Το άθροισμα των ποσοστών της δρώσας μάζας για τις δύο οριζόντιες μεταφορικές παραμορφώσεις (UX και UY) και της στρεπτικής παραμόρφωσης κατά των κατακόρυφο άξονα (RZ) υπερβαίνει το 90% που απαιτείται από τον κανονισμό.

Πίνακας 4- Ιδιομορφές και ποσοστό ιδιομορφικής μάζας πρώτου προσομοιώματος

Ιδιομορφή	**Ιδιοπερίοδος** (sec)	UX	UY	UZ	RX	RY	RZ
1	1.275	0.753	0.002	0.000	0.001	0.190	0.001
2	1.175	0.002	0.668	0.000	0.259	0.000	0.006
3	0.962	0.001	0.009	0.000	0.002	0.000	0.688
Σύνολο	Με χρήση 100 ιδιομορφών	0.980	0.977	0.773	0.882	0.859	0.960

Ο έλεγχος των διατομών έγινε με όρους αλληλεπίδρασης ροπών και αξονικής. Το μέγιστο ποσοστό αλληλεπίδρασης υπολογίστηκε ίσο με 0.563, μικρότερο της μονάδας. Πρέπει να τονιστεί ότι ο σχεδιασμός δεν είναι ο βέλτιστος δυνατός αλλά μία πρώτη διερεύνηση αν το σύστημα με δοκούς Deltabeam και ισχυρά τοιχεία με τις κατάλληλες συνδέσεις μπορεί να παραλάβει επαρκώς τα κατακόρυφα και σεισμικά φορτία.

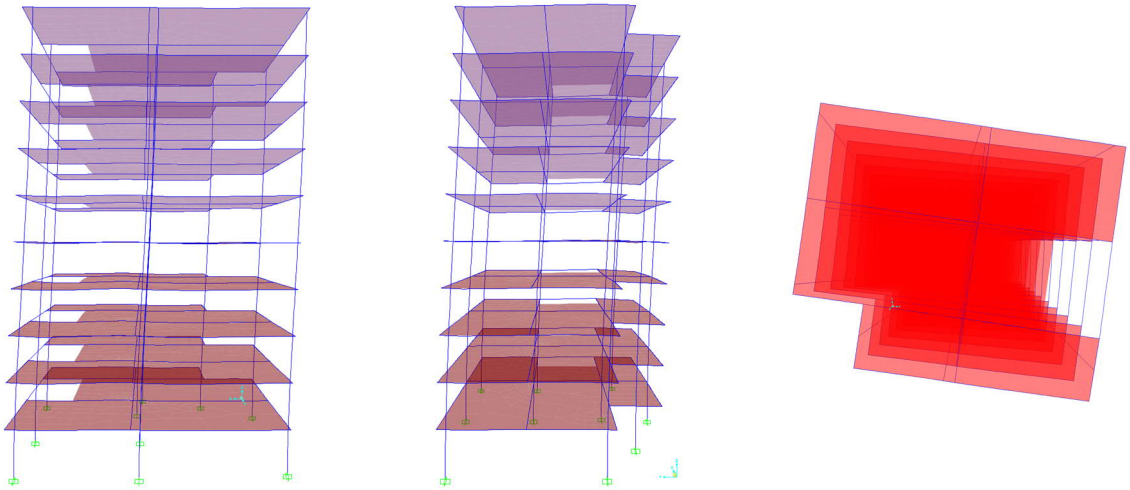

Ιδιομορφή 1 Ιδιομορφή 2 Ιδιομορφή 3

Εικ. 28- Ιδιοσχήματα των τριών πρώτων κύριων ιδιομορφών του πρώτου προσομοιώματος

- **Προσομοίωμα με δοκών οπλισμένου σκυροδέματος**

Στην περίπτωση με τις δοκούς από οπλισμένο σκυρόδεμα πραγματοποιήθηκε μόνο μία ανάλυση με τη χρήση του SAP2000. Η γεωμετρία των τοιχείων και ο οπλισμός τους διατηρήθηκαν ίδια με την προηγούμενη ανάλυση. Εκ νέου, για λόγους απλοποίησης, μόνο μία διατομή χρησιμοποιήθηκε για όλες τις δοκούς οι οποία σχεδιάστηκε έναντι του πιο κρίσιμου συνδυασμού φορτίων.

Η διατομή της δοκού σχεδιάστηκε επίσης στο Section Designer. Το ύψος και το πλάτος της είναι 0.7 m και 0.35 m, αντίστοιχα. Ως διαμήκης οπλισμός, 24 ράβδοι με διάμετρο 18 mm (A_s=61.08 cm^2) μοιράστηκαν εξίσου στην πάνω και κάτω παρειά της δοκού. Η διατομή των δοκών οδήγησε σε ένα νέο ύψος ορόφου ίσο με 3.7 m. Σαν αποτέλεσμα, το τελικό προσομοίωμα αποτελείται από εννέα ορόφους με συνολικό ύψος 33.3 m.

Και σε αυτή την περίπτωση η φασματική ανάλυση πραγματοποιήθηκε με τη χρήση των εκατό πρώτων ιδιομορφών. Οι ιδιοπερίοδοι και το ποσοστό συμμετοχής της μάζας περιγράφονται στον Πίνακα 5. Οι τρεις πρώτες ιδιομορφές και τα ιδιοσχήματά τους φαίνονται στην Εικόνα 29. Το άθροισμα των ποσοστών της δρώσας μάζας για τις διευθύνσεις υπερβαίνει και εδώ το 90% που απαιτείται.

Ο έλεγχος των διατομών έγινε παρομοίως με όρους αλληλεπίδρασης ροπών και αξονικής. Το μέγιστο ποσοστό αλληλεπίδρασης για τις δοκούς υπολογίστηκε ίσο με 0.957 οριακά μικρότερο της μονάδας. Για τα τοιχεία το νέο μέγιστο ποσοστό αλληλεπίδρασης είναι ίσο με 0.632 αυξημένο κατά 12.25%.

Πίνακας 5- Ιδιομορφές και ποσοστό ιδιομορφικής μάζας δεύτερου προσομοιώματος

Ιδιομορφή	**Ιδιοπερίοδος** (sec)	UX	UY	UZ	RX	RY	RZ
1	0.949	0.065	0.640	0.000	0.210	0.014	0.004
2	0.907	0.720	0.058	0.000	0.021	0.160	0.002
3	0.683	0.001	0.009	0.000	0.001	0.000	0.730
Σύνολο	Με χρήση 100 ιδιομορφών	0.990	0.990	0.900	0.940	0.930	0.970

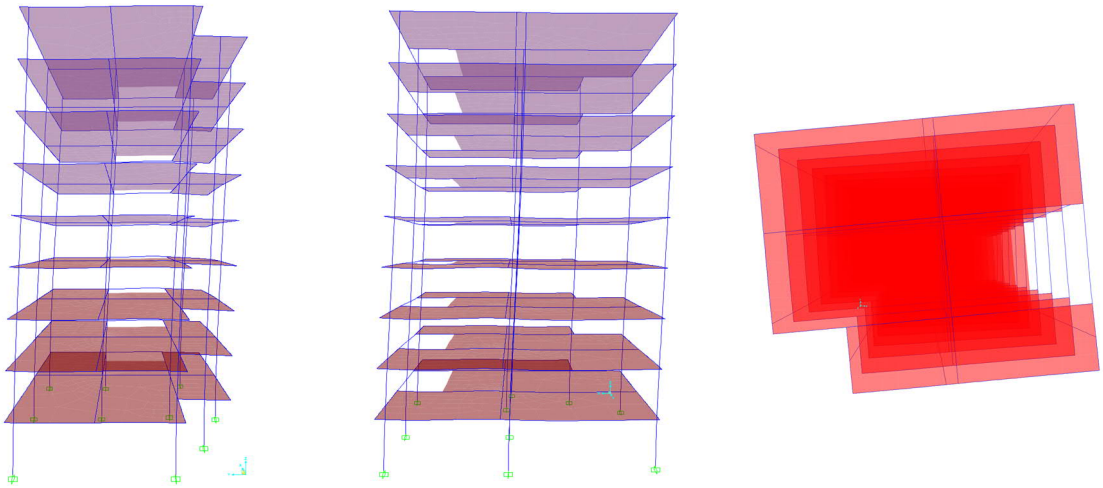

Ιδιομορφή 1 Ιδιομορφή 2 Ιδιομορφή 3

Εικ. 29- Ιδιοσχήματα των τριών πρώτων κύριων ιδιομορφών του δεύτερου προσομοιώματος

- **Σύγκριση αποτελεσμάτων**

Η επεξεργασία των αποτελεσμάτων και η σύγκριση μεταξύ των δύο αναλύσεων οδήγησε στα ακόλουθα συμπεράσματα. Πρωτίστως, η κύρια διαφορά εντοπίζεται στη διαφορά των ορόφων. Το προσομοίωμα με τις δοκούς Deltabeam αποτελείτο από δέκα ορόφους με συνολικό ύψος 34.0 m ενώ το προσομοίωμα με τις δοκούς από οπλισμένο σκυρόδεμα αποτελείτο από εννέα ορόφους και συνολικό ύψος 33.3 m.

Το δεύτερο προσομοίωμα με τον μονολιθικό σκελετό, όπως αναμενόταν, ήταν πιο δύσκαμπτο από το πρώτο. Η αύξηση της δυσκαμψίας, και κατ' επέκτασιν η μείωση των τιμών των ιδιοπεριόδων, είναι σημαντική γιατί μπορεί να οδηγήσει σε μεγαλύτερα σεισμικά φορτία. Η μείωση στις τιμές των ιδιοπεριόδων ήταν της τάξης του 25.57%, 22.81% και 29.00% για τις τρεις πρώτες ιδιομορφές αντίστοιχα. Επιπλέον, όπως φαίνεται στις Εικόνες 28 και 29, η διεύθυνση των δύο πρώτων ιδιομορφών άλλαξε. Τα ποσοστά της δρώσας μάζας για τις τρεις πρώτες ιδιομορφές ήταν σχεδόν τα ίδια, παρουσιάζοντας όμως διαφορές στις τιμές των αθροισμάτων των εκατό πρώτων ιδιομορφών με αυτές της μονολιθικής κατασκευής να είναι αυξημένες. Παρατηρήθηκε ανακατανομή των φορτίων λόγω των διαφορετικών στατικών συστημάτων, χωρίς αυτό να συντελεί σε μεγάλες αλλαγές στους συντελεστές αλληλεξάρτησης.

- **Εφαρμογή της παρούσας έρευνας**

Για την εφαρμογή των ευρημάτων της παρούσας έρευνας δημιουργήθηκε ένα αναλυτικό προσομοίωμα για τον υπολογισμό της αντοχής σε κάμψη των ενισχυμένων Deltabeams σύμφωνα με τη στερεοπλαστική θεωρία. Σύμφωνα με αυτή τη θεωρία τα εξωτερικά φορτία κατανέμονται στα επιμέρους τμήματα της διατομής ανάλογα με την αντοχή τους, δεδομένου ότι η διατομή είναι Κατηγορίας 1 ή 2 και υπάρχει πλήρης αλληλεπίδραση μεταξύ των ξεχωριστών τμημάτων. Η πιο κοινή μέθοδος για τον υπολογισμό της πλαστικής αντοχής σε κάμψη είναι η διαίρεση της διατομής σε μικρότερα ορθογωνικά σχήματα με πάχος ίσο με Δz. Σε κάθε σχήμα αντιστοιχεί ένα εμβαδόν $\Delta A_i = b_i \Delta z_i$, ανάλογα με το πλάτος του και μία μέγιστη αντοχή f_i σε σχέση με το υλικό. Η καμπτική ροπή του κάθε σχήματος σε σχέση με τον ουδέτερο άξονα είναι:

$$\Delta M_i = \Delta A_i f_i (z_i - z_o)$$

Η τελική αντοχή έναντι κάμψης υπολογίζεται από το άθροισμα των επιμέρους ροπών των σχημάτων.

$$M_{pl,Rd} = \sum \Delta M_i$$

Η αρχική διατομή τροποποιείται σε μία ισοδύναμη Η τμηματοποίηση της ισοδύναμης διατομής σύμφωνα με τα διάφορα υλικά παρουσιάζεται στην Εικόνα 30.

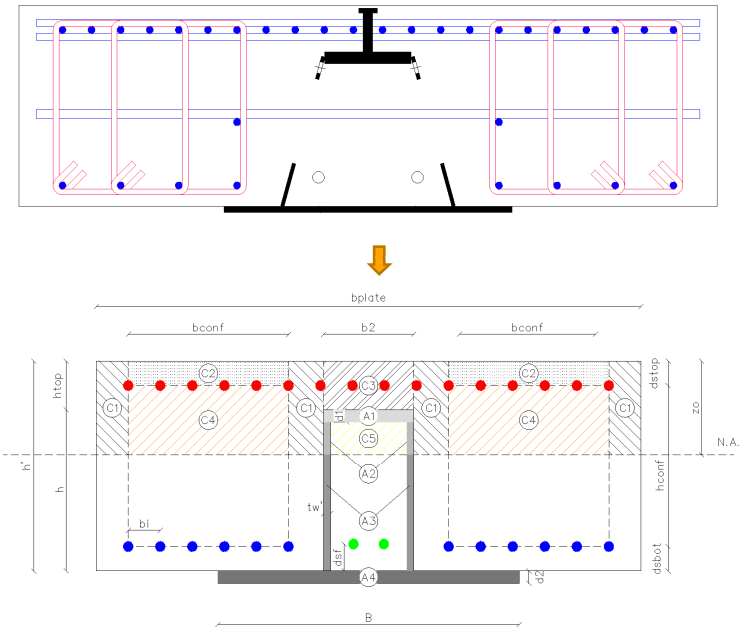

Εικ. 30- Ισοδύναμη διατομή για τον υπολογισμό της αντοχής σχεδιασμού σε κάμψη

Για την επικύρωση της ορθότητας του αναλυτικού προσομοιώματος υπολογίστηκαν οι αντοχές τον πειραματικών δοκιμίων, με τις πραγματικές τιμές των υλικών και όχι με αυτές του σχεδιασμού, και συγκρίθηκαν με τα πειραματικά αποτελέσματα. Η καλή συσχέτιση των υπολογισμών με τα πειραματικά αποτελέσματα επικυρώνει την ακρίβεια του αριθμητικού προσομοιώματος και το καθιστά αξιόπιστο. Στην Εικόνα 31 παρουσιάζεται ενδεικτικά η σύγκριση των αποτελεσμάτων για τις δοκούς Τύπου 3.

Το επόμενο βήμα που πραγματοποιήθηκε ήταν η αναβάθμιση των διατομών των Deltabeam που προέκυψαν από το σχεδιασμό του πρώτου προσομοιώματος σε διατομές Τύπου 3, όπως προαναφέρθηκε, με τέτοιο τρόπο ώστε δοκοί με μικρότερο ύψος να μπορούν να παραλάβουν τα ίδια φορτία. Οι υπολογισμοί αφορούσαν μόνο το σχεδιασμό έναντι κάμψης και όχι έναντι τέμνουσας ή φωτιάς.

Οι καινούριες διατομές των Deltabeam, τα νέα συνολικά ύψη και οι αντίστοιχες αντοχές σχεδιασμού παρουσιάζονται στον Πίνακα 5. Με τη χρήση των ενισχυμένων διατομών το συνολικό ύψος κάθε ορόφου μειώθηκε από τα 3.4 m στα 3.33 m. Η μείωση του συνολικού ύψους του κτηρίου ήταν ίση με 0.7 m.

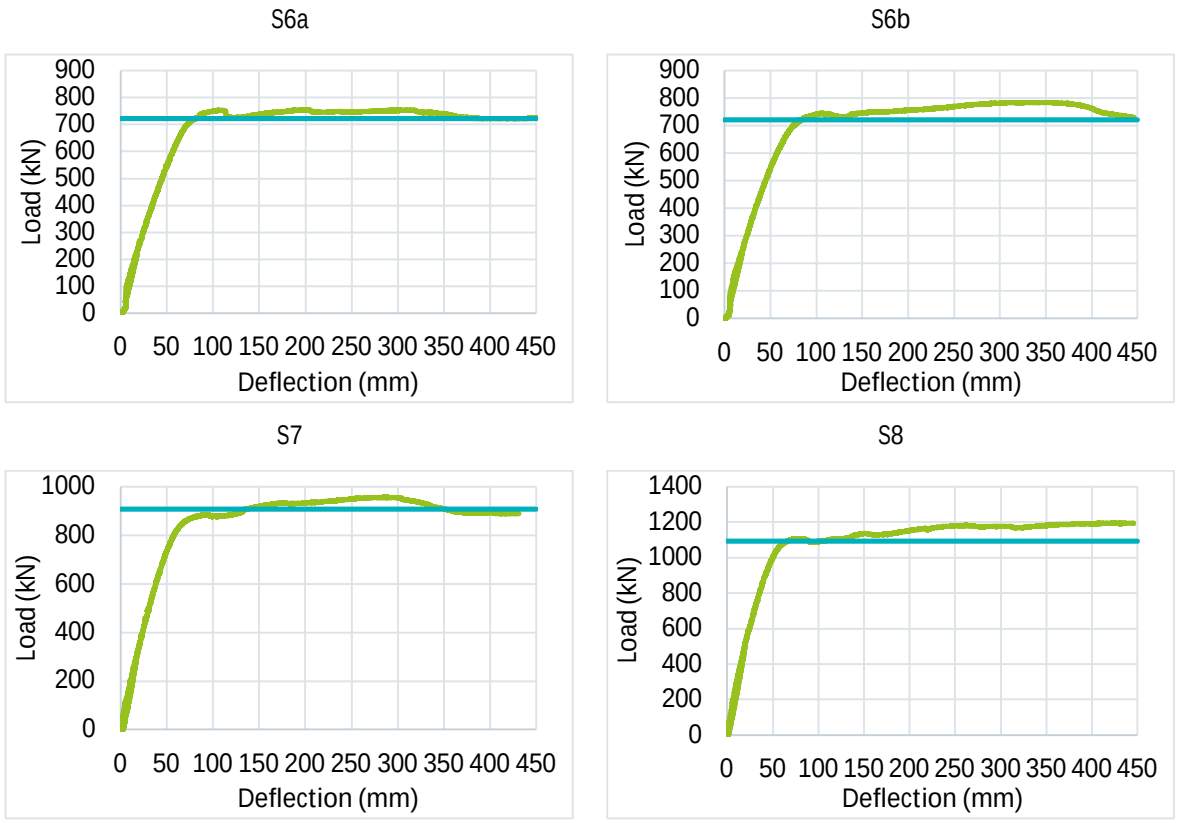

Εικ. 31- Σύγκριση πειραματικών και αναλυτικών αποτελεσμάτων για τις δοκούς Τύπου 3

Πίνακας 6- Σύγκριση των διαστασιολογημένων δοκών με τις αντίστοιχες ενισχυμένες

Δοκός	**Ροπη σχεδιαμού** (kNm)	Deltabeam	**Συνολικό ύψος** (mm)	**Αντοχή** (kNm)	Deltabeam	**Συνολικό ύψος** (mm)	**Αντοχή** (kNm)
B1	413.4	DR30-270	380	486.15	DR22-250	300	436.33
B2	211.8	DR20-245	280	276.86	DR20-245	280	412.46
B3	809.6	D30-400	380	952.52	D22-400	300	839.19
B4	410.7	D22-400	300	561.47	D20-400	280	667.80
B5	76.3	DR20-245	280	182.66	DR20-245	280	279.20
B6	231.4	D20-400	280	405.06	D20-400	280	507.20
B7	518.9	D22-400	300	555.86	D20-400	280	612.44
B8	65.5	DR20-245	280	182.63	DR20-245	280	279.20
B9	217.8	DR25-260	330	304.16	DR20-245	280	344.01
B10	822.5	DR32-285	400	882.36	DR25-260	330	886.07
B11	66.3	D20-400	280	297.82	D20-400	280	429.83
B12	67.5	D20-400	280	297.82	D20-400	280	429.83
B13	26.9	D20-400	280	297.82	D20-400	280	429.83
B14	36.1	DR20-245	280	182.63	DR20-245	280	279.20
B15	36.7	DR20-245	280	182.63	DR20-245	280	279.20

Συμπεράσματα

Τα κύρια συμπεράσματα της παρούσας διατριβής είναι τα ακόλουθα:

1. Ο μικρός αριθμός δημοσιεύσεων σχετικών με την πειραματική διερεύνηση της καμπτικής συμπεριφοράς λεπτών σύμμεικτων κρυφοδοκών και η έλλειψη αναφορών στους Ευρωκώδικες για τις εν λόγω δοκούς, αναδεικνύει την ανάγκη για πιο εκτεταμένη διερεύνηση του θέματος.

2. Τα πειραματικά αποτελέσματα δείχνουν ότι οι δοκοί Deltabeam σε συνδυασμό με την κατάλληλη όπλιση, προσφέρουν μία εξαιρετικά πλάστιμη συμπεριφορά. Η ολίσθηση μεταξύ του σκυροδέματος και της μεταλλικής δοκού παρέμεινε σε χαμηλές τιμές και η ακεραιότητα των δοκιμίων διατηρήθηκε σε υψηλά επίπεδα μέχρι το τέλος των πειραμάτων. Η ευεργετική αυτή συμπεριφορά υποδηλώνει ότι η χρήση ενισχυμένων με οπλισμούς Deltabeams ενδείκνυται για χρήση τους σε τυχηματικά φορτία και/ή προστασία έναντι διαδοχικής κατάρρευσης.

3. Γενικά τα δοκίμια ίδιου τύπου παρουσίασαν ποιοτικά παρόμοια συμπεριφορά. Η αντοχή των δοκών ήταν ανάλογη του ύψους τους. Οι υψηλότερες διατομές επέτρεψαν την άσκηση μεγαλύτερων φορτίων.

4. Τα δοκίμια με την ίδια διατομή αλλά διαφορετικό αριθμό σειρών από διατμητικούς ήλους, είχαν παρόμοια συμπεριφορά, αποδεικνύοντας ότι η διατμητική σύνδεση μεταξύ του σκυροδέματος και της μεταλλικής δοκού ήταν πλήρης και η πρόσθετη σειρά διατμητικών ήλων δεν επηρέασε τα αποτελέσματα.

5. Δημιουργήθηκαν εννέα προσομοιώματα με τη μέθοδο των πεπερασμένων στοιχείων και βαθμονομήθηκαν με τα πειραματικά δεδομένα. Η συσχέτιση μεταξύ των πειραματικών και αναλυτικών αποτελεσμάτων ήταν υψηλή. Το ποσοστό σφάλματος ήταν μικρότερο του 5% και ο συντελεστής συσχέτισης ίσος με 0.996, καθιστώντας το προσομοίωμα αξιόπιστο για παραμετρική επίλυση και επέκτασή της σε άλλες γεωμετρίες και υλικά.

6. Πραγματοποιήθηκε πρόσθετη διερεύνηση για την επιρροή των παραμέτρων και των χαρακτηριστικών που χρησιμοποιούνται κατά τον ορισμό του σκυροδέματος. Η γωνία διαστολής ψ επηρέασε αναλογικά την αντοχή του σκυροδέματος. Αύξηση της τιμής της γωνίας διαστολής είχε ως αποτέλεσμα την αύξηση του φορτίου. Σε μετακινήσεις όπου οι παραμορφώσεις ξεπερνούσαν την οριακή παραμόρφωση του σκυροδέματος, η επιρροή του συγκεκριμένου παράγοντα δεν ήταν σημαντική. Ο παράγοντας K_c, ο οποίος είναι ο λόγος της δεύτερης αναλλοίωτης του τανυστή των τάσεων επί της εφελκυστικής συνιστώσας προς την αντίστοιχη της θλιπτικής συνιστώσας για κάθε δεδομένη τιμή του ισοτροπέα τέτοια ώστε η μέγιστη κύρια τάση να είναι αρνητική, επηρέασε τη συνολική συμπεριφορά του σκυροδέματος και την ικανότητά του για παραμόρφωση. Χαμηλότερες τιμές της εν λόγω παραμέτρου είχαν ως αποτέλεσμα την προς τα πάνω μετατόπιση του πλαστικού τμήματος της καμπύλης φορτίου-μετακίνησης.

7. Η περαιτέρω αναλυτική διερεύνηση ανέδειξε τη σημασία της πλευρικής προστασίας που παρέχει το εξωτερικό οπλισμένο σκυρόδεμα στις μεταλλικές πλάκες του κορμού, γεγονός που επηρεάζει τη γενική συμπεριφορά της δοκού. Σε όλα τα προσομοιώματα χωρίς πλευρική προστασία εμφανίστηκε τοπικός λυγισμός. Αρχικά, ο λυγισμός εμφανίστηκε στις πλάκες του κορμού και στη συνέχεια επεκτάθηκε στην πλάκα του άνω πέλματος. Τα αποτελέσματα έδειξαν πως όταν οι πλάκες του κορμού είχαν μεγαλύτερο πάχος, και κατ' επέκταση υψηλότερη αντοχή, η συμπεριφορά της δοκού ήταν καλύτερη και ο τοπικός λυγισμός εμφανίστηκε σε μεγαλύτερες μετακινήσεις. Παρόλα αυτά ο κίνδυνος του τοπικού λυγισμού εξαλείφεται εντελώς μόνο όταν δεσμεύεται η πλευρική μετακίνηση των πλακών του κορμού. Η συγκεκριμένη δέσμευση παρέχεται από το εξωτερικό τμήμα του σκυροδέματος και την περίσφιγξη λόγω των συνδετήρων.

8. Οι δοκοί Deltabeam χρησιμοποιήθηκαν επιτυχώς, ως αμφιέρειστες, για το σχεδιασμό ενός κτηρίου γραφείων, έναντι κατακόρυφων φορτίων και σεισμού. Η σύγκριση των αποτελεσμάτων με τα αντίστοιχα ενός δεύτερου προσομοιώματος το οποίο κατασκευάστηκε με χρήση μονολιθικών πλαισίων οπλισμένου σκυροδέματος, ανέδειξε

τα πλεονεκτήματα των λεπτών σύμμεικτων κρυφοδοκών, αφού λόγω του μικρότερου ύψους των Deltabeams υπήρχε περιθώριο για την προσθήκη ενός πρόσθετου ορόφου έναντι των εννέα της συμβατικής κατασκευής από οπλισμένο σκυρόδεμα.

Συνοπτική λίστα προτεινόμενης έρευνας

1. Το πρώτο μέρος του πειραματικού προγράμματος για τη δημιουργία ενός πλαισίου με χρήση των Deltabeams, το οποίο να μπορεί να παραλάβει επαρκώς ροπές, ολοκληρώθηκε με επιτυχία. Ως επόμενο βήμα του προγράμματος προτείνεται η διερεύνηση της καμπτικής συμπεριφοράς των Deltabeams έναντι αρνητικών ροπών για τις κρίσιμες ζώνες πλησίον των συνδέσεων με τα κατακόρυφα στοιχεία. Τέλος απαιτείται ο σχεδιασμός μίας κατάλληλης σύνδεσης παραλαβής ροπής με τα υποστυλώματα σύμφωνα με τις οδηγίες των Ευρωκωδίκων.

2. Ο σχεδιασμός ενός κτηρίου με Deltabeams ανέδειξε τη δυνατότητα της χρήσης τους, σε συνδυασμό με ισχυρά κατακόρυφα δομικά στοιχεία, στο σχεδιασμό έναντι σεισμικών φορτίων. Κατά συνέπεια, η αντίστοιχη σύνδεση δοκού-κατακόρυφου στοιχείου πρέπει να διερευνηθεί διεξοδικά τόσο πειραματικά όσο και αναλυτικά.

3. Τα βαθμονομημένα προσομοιώματα πεπερασμένων στοιχείων μπορούν και πρέπει να χρησιμοποιηθούν περαιτέρω για μία εις βάθος διερεύνηση παραμέτρων και παραγόντων (περίσφιγξη του σκυροδέματος στον πυρήνα των δοκών, αλληλεπίδραση μεταξύ του σκυροδέματος και της μεταλλικής δοκού, διατμητική σύνδεση και ολίσθηση, κατανομές τάσεων και παραμορφώσεων κα), των οποίων η παρακολούθηση δεν ήταν εφικτή κατά τη διάρκεια των πειραμάτων. Αυτή η γνώση είναι απαραίτητη για την ολοκληρωμένη κατανόηση της καθολικής συμπεριφοράς.

Table of contents

List of Figures

List of Tables

1

Introduction

1.1 Historical background

Structural steel as a building material and its development had a huge influence on the evolution of the industrialized world and the creation of modern way of life as we know it today. Railways, bridges, large production factories and buildings would have never taken their current form without structural steel.

At the beginning of 18th century three types of ferrous metal were known; wrought iron, cast iron and steel. Wrought iron had been used by blacksmiths for centuries to create products like gates, railings, nails and chains. This form of iron reached its peak in the 1860s, when it was on the edge to become the major structural material. Cast Iron was mainly used for furniture and cooking equipment. Being very brittle, it failed to be used as a structural material. Steel until the middle of 19th century was mainly used for the creation of more expensive and elegant products like watches and swords due to its extremely high production cost.

Henry Bessemer, who is considered as the father of modern steel, invented a method in 1856, that took its name, which led to a more economical production and larger quantities of steel [1]. Combined with the "open hearth furnace", an invention of Charles William Siemens on 1866 [2], resulted in the "dethronement" of wrought iron as the main structural material by steel. One of the last wide-known structures built by wrought iron was the Eiffel Tower on 1889. At the same time, the Forth Bridge in Scotland was build being the first major structure in Britain to be constructed of steel [3]. The bridge opened in March of 1890 and its total length was 2467 m.

In Chicago, during the 19th century, the buildings were mainly constructed by timber. The Great Chicago Fire in 1871 caused a huge damage that is still appalling more than a century later. Nearly 300 persons died, 18,000 buildings were destroyed, 100,000 people (one-third of the city) were homeless and property loss valued at 200,000,000 $ (about a third of the valuation of the city) [4]. Afterwards, Chicago became a major example of reconstruction. With the regulations against fire situation having been stricter, new non-combustible materials were required. The engineers found the solution to their problems on steel. The Home Insurance Building was built in 1885 and was 10 stories high, being the very first skyscraper. The structural frame of the building was made by steel. Construction of steel was not only lighter than that made of brick, which was commonly used in the construction of buildings, but it could carry more weight. Lighter masonry walls were hanged from the steel frame.

At the beginning of the 20th century structural steel had to compete a newborn material, the reinforced concrete. Structural steel had high strength and was ductile and faster to erect. Reinforced concrete had high rigidity, compressive strength, fire resistance and durability as well as being more economical [5]. A new more advanced structural system was created, not from the competition of structural steel and concrete, but from their cooperation; the steel-concrete composite system.

A report written by Paul Christophe [6] includes several composite elements, mainly slabs and beam-slab systems. A characteristic example is the floor proposed by Mathias Koenen, where the steel sections at the bottom carried the tensile forces and the arching concrete at the top was responsible for the compressive ones.

At the very first steps of composite structural elements, there was not a distinction between the steel parts cooperating with concrete (rigid steel elements or steel rebars) and all of them had to be encased in concrete [7]. The first tests related to the bonding and the relative movement between the two materials were conducted by Carl von Bach [8]. The results showed that smaller relative slip was measured between the concrete and the steel rebars, than in the case of rigid steel sections. In addition, the extrusion of the rigid steel elements caused extensive

damage to the concrete body. This outcome gave birth to the discussion about the distinction between the concrete elements with steel rebars and rigid steel parts.

In Europe, the first half of 20th century, research was mainly concentrated on the bonding between the two elements. During this period, the first proposals appeared related to a mechanical bonding between steel and concrete. On the other side of the Atlantic, in the US, Julius Kahn obtained a patent [9] in 1926 for a composite beam remarkably similar to the currently used most common form (figure 1.1). The composite behavior is achieved through "tongues", as referred to the patent text, which are curved steel stripes welded on the top plate of the steel beam.

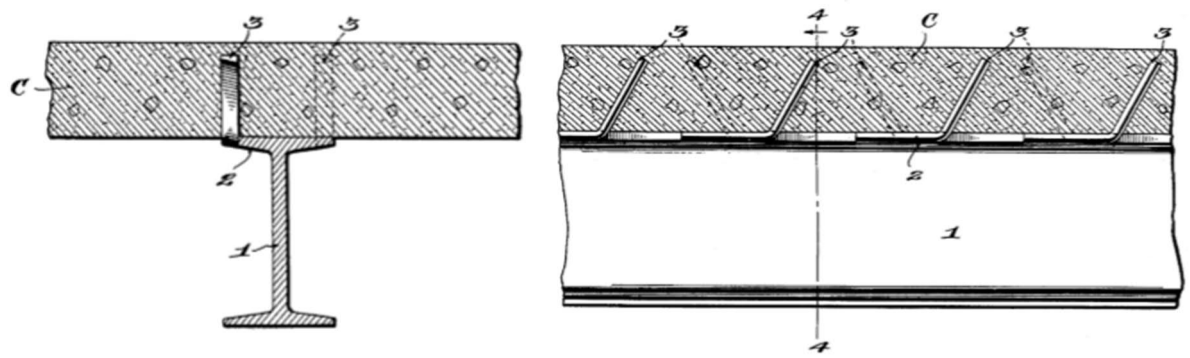

Fig. 1.1- Composite beam on Kahn's patent

The following years a lot of experimental research was conducted and advances were made, mainly in the bridge construction industry. In parallel, the first codes were enforced in relation to the composite beams, such as the design provisions of the American Association of State Highway Officials (AASHO) in 1941 [10].

The introduction of steel- concrete composite beams to the construction industry was followed by the introduction of composite slabs. The combination of concrete slabs with profiled steel sheeting, which was taken into account in strength calculations, eliminated the need for wooden formwork. The application of profiled steel sheeting as both permanent formwork and reinforcement to the concrete slab was first developed in America in the early 1950s. In the United Kingdom they were introduced in the 1970s, with this system becoming the most widespread form of floor system for steel framed office buildings.

In recent decades, partly due to the economic crisis and the limitations of enforced Code regulations, a strong demand for efficient and economical structures has emerged [11]. This has led to factory fabricated structural elements, like concrete hollow core elements for slabs and steel beams and columns for the structural framework, which were assembled on site. The use of prefabricated standardized elements concealed a higher standard of quality with lower costs, followed by a high degree of construction flexibility due to the wide range of possible combinations. Since authorities imposed the reduction on the height of the floors in high-rise buildings, a part of the construction industry aimed to the reduction of height clearance between floors, without reducing the useful space, in order to increase the total number of storeys, as an advantage against their competitors. So, in parallel with the appearance of prefabricated construction, a "new" more advanced composite structural system was born; the shallow composite floor system.

In the shallow floor system, the steel beam is encased within the depth of the pre-cast concrete floor or composite slab, with profiled steel decks [12]. This form of construction allows for the erection of buildings with lower height and, simultaneously, the flat soffit is beneficial for the building services extending in any direction. In this system, also called slim floor, the slab elements are not placed on the upper plate of a steel beam, as in traditional composite construction, but are supported by its bottom plate. Thus, finally, the steel beam is fully or partially encased within the concrete slab.

In Scandinavia, and more specifically in Sweden, in the early 1980s, the first slim floor system appeared. That method of construction increased the market share of steel structures for office buildings in Sweden to over 50% [13]. This original slim floor concept (also called the "Thor-beam", see figure 1.2a), consisted of two U-shaped sections welded to a flat plate. Additional plates are welded to the top flanges to provide the shear connection. In 1989 in Finland, the "Deltabeam" was launched (figure 1.2b), taking its name by its cross-section shape. The shear connection between steel and concrete is ensured through connector bars that pass through regularly spaced web openings. Two years later, in 1991, in UK, the Slimflor beam was developed (figure 1.2c), which consisted of a universal column section welded to a steel plate.

Recently, interest has been concentrated on the asymmetric hot-rolled steel beam (Fig. 1.2d) in the UK, and on the asymmetric welded steel beam in Finland.

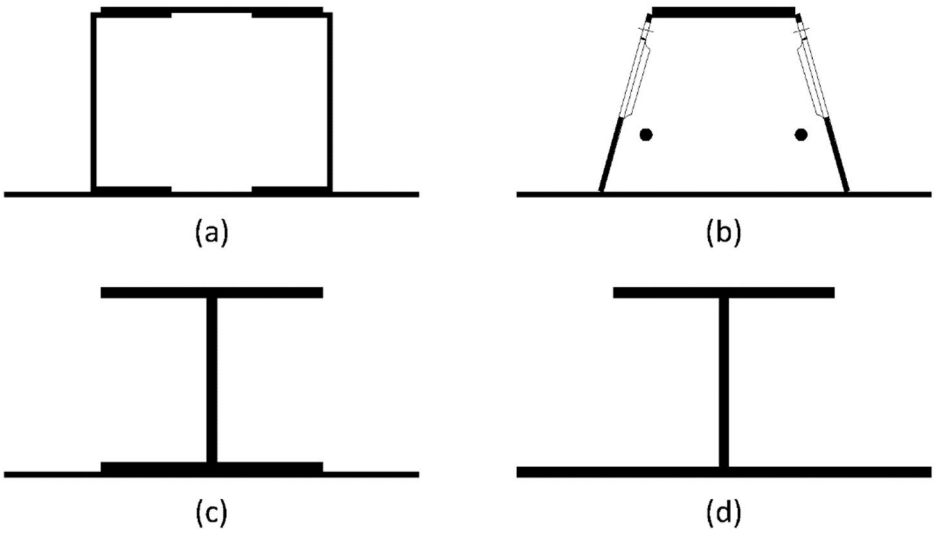

Fig. 1.2 – Different types of shallow (slim) floor beams (steel cross-section): (a) Thor-Beam, (b) Deltabeam, (c) Slimflor and (d) Asymmetric Slim Floor beam

1.2 Dissertation organization

The structure of this dissertation consists of eight Chapters. The present Chapter, Chapter 1, is an introduction to shallow (slim) floor composite beams. In addition, the objectives and the steps of this research are described.

Chapter 2 presents the references of Eurocodes to steel-concrete composite beams. More specifically, the second Chapter includes the information provided by EN 1994-1-1 and EN 1998-1 related to the flexural behavior, the structural details and the designing methods of composite beams. An additional aim of this Chapter is to state the lack of norms and guidelines in Eurocodes related to the shallow floor beams.

In Chapter 3 a literature review is provided, of the most relevant, to the current research, experimental investigations on shallow floor beams. It is thus identified that, although there was a sufficient number of publications related to the shear behavior of shallow floor beams and their resistance against fire, there haven't been many research projects investigating the flexural behavior of such type of beams.

Chapters 4 and 5 describe the experimental procedure that, as part of the present work, aims at bridging the gap of knowledge above. In more detail, in Chapter 4 the shallow floor composite beam under investigation, called Deltabeam, is introduced. Furthermore, there is an extensive description of the experimental set-up (reaction frame, supports, hydraulic actuator) and the specimens investigated in the present work: the geometry and the details of the test specimens, their preparation for the tests, the mechanical properties of all materials used are included and finally, the experimental measurements and the positions of the measuring instruments are described. In Chapter 5 the results of the tests are presented, in terms of: Load-deflection, load-strain and load-slip (between the concrete and the steel part) curves, created for each specimen, combined with a detailed description of the most remarkable highlights of the testing procedure.

In Chapter 6 a numerical investigation is described, using the Finite Element Method (FEM). To this purpose, three dimensional models were developed in Abaqus software with particular emphasis given in the most accurate representation of the geometry, the materials and the boundary conditions. Afterwards, in order to calibrate the models and choose the appropriate parameters in the input data, the analytically predicted load-deflection and load-strain curves were compared with the experimental ones.

Subsequently, the behavior and the design of a building against a seismic loading scenario are investigated in Chapter 7. Two different analyses were conducted. In the first one Deltabeams were used. The model of the second analysis was created with the use of reinforced concrete beams. The comparison of the results is presented.

Chapter 8 summarizes the research conducted in this dissertation and draws conclusions from the assessment of the experimental, numerical and design results. Furthermore, some proposals for the further steps of the research related to Deltabeams are included.

2

Bending behavior and design of composite beams according to Eurocodes

In this chapter the most important requirements of Eurocodes 4 and 8 related to the flexural behavior of composite beams are presented.

2.1 Eurocode 4 (EN 1994-1-1) [14]

2.1.1 Scope and terms

The scope of Eurocode 4 is described in section 1.1. It "applies to the design of composite structures and members for buildings and civil engineering works. It complies with the principles and requirements for the safety and serviceability of structures, the basis of their design and verification that are given in EN 1990 - Basis of structural design". Part 1-1 gives general instructions for the design of composite structures and rule for buildings. In Table 2.1 some basic terms are presented as described in section 1.5.2.

A composite beam as defined in Eurocode 4 is a composite member created by structural steel and reinforced concrete and it is subjected mainly to bending and shear. Beams with steel webs encased by reinforced concrete, in which shear connection exists between the concrete and steel components are referred as partially-encased beams (figure 2.1).

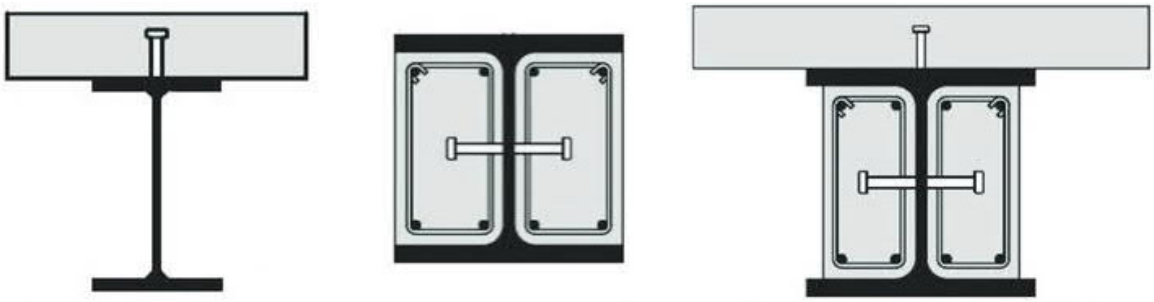

(a) Composite section with slab

(b) Partially encased section without slab

(c) Partially encased section with slab

Fig. 2.1- Typical cross-sections of composite beams

Table 2.1- Basic terms and definitions used in EN1994-1-1

No	Term	Definition
1	Composite member	A structural member with components of concrete and of structural or cold-formed steel, interconnected by shear connection so as to limit the longitudinal slip between concrete and steel and the separation of one component from the other
2	Shear connection	An interconnection between the concrete and steel components of a composite member that has sufficient strength and stiffness to enable the two components to be designed as parts of a single structural member
3	Composite behavior	Behavior which occurs after the shear connection has become effective due to hardening of concrete
4	Composite beam	A composite member subjected mainly to bending
5	Composite column	A composite member subjected mainly to compression or to compression and bending
6	Composite slab	A slab in which profiled steel sheets are used initially as permanent shuttering and subsequently combine structurally with the hardened concrete and act as tensile reinforcement in the finished floor
7	Composite frame	A framed structure in which some or all of the elements are composite members and most of the remainder are structural steel members
8	Composite joint	A joint between a composite member and another composite, steel or reinforced concrete member, in which reinforcement is taken into account in design for the resistance and the stiffness of the joint
9	Propped structure or member	A structure or member where the weight of concrete elements is applied to the steel elements which are supported in the span, or is carried independently until the concrete elements are able to resist stresses
10	Un-propped structure or member	A structure or member in which the weight of concrete elements is applied to steel elements which are unsupported in the span

2.1.2 Bending resistance of composite beams

In order to choose the method that will be used to calculate the bending resistance of a composite cross-section, two important factors should be taken into account; the shear connection between concrete and steel parts and the classification of the steel cross-section.

To maintain the contact between the concrete and steel parts, shear connectors and transverse reinforcement must be used. To prevent separation of the two materials shear connectors should be able to resist a nominal ultimate tensile force, perpendicular to the plane of the steel flange, at least equal to the 10% of their ultimate shear resistance.

EN 1994-1-1, just like EN 1993-1-1 [15] for steel structures, classifies the composite sections into 4 Classes. The scope of the classification is to define if local buckling will affect the resistance and rotation capacity of the composite cross-section. The classification of the composite sections is made on the basis of whether the cross sections will be able to reach the plastic moment and their rotational capacity (figure 2.2) [16].

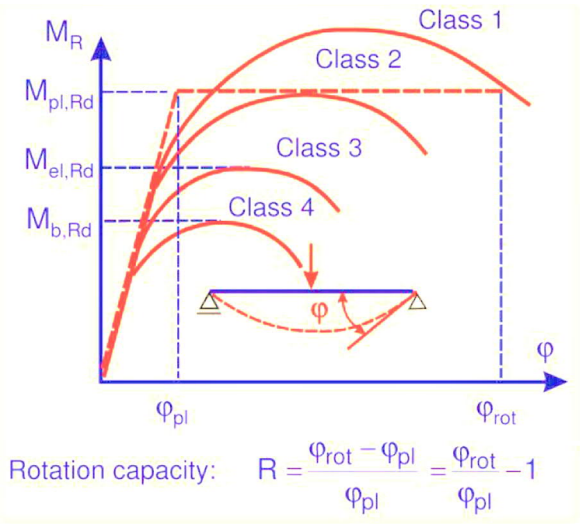

Class	Bending resistance
1 and 2	Plastic
3	Elastic
4	Elastic taking into account local buckling

Fig. 2.2- Definition of classes of composite sections

- Class 1- The section can form a plastic hinge and has sufficient rotational capacity to maintain this plastic moment over a considerable range of in-plane rotation (ductility)
- Class 2- The section can develop plastic resistance but has limited rotational capacity to act as a hinge

- Class 3- The section can develop elastic resistance of the full cross-section
- Class 4 - Local buckling of slender elements reduces the elastic resistance; the section can develop elastic resistance of an effective cross-section, smaller than the full section.

The classification of a cross-section depends on the width to thickness ratio of the steel parts totally or partially under compression (figures 2.3 and 2.4). The steel part in compression with the least favorable class, determines the class of the whole composite cross-section. The overall behavior of the cross section can be improved and can be placed in a more favorable class, provided that the performance of the steel element under compression is improved by attaching it to a reinforced concrete element.

Composite sections with concrete encasement are also classified in accordance with Table 5.2 of EN 1994-1-1/§5.5.3 (figure 2.5). The encasing concrete for these cases should be "reinforced, mechanically connected to the steel section, and capable of preventing buckling of the web and of any part of the compression flange towards the web". These requirements are fulfilled if:

- The concrete reinforcement is assembled by longitudinal bars and stirrups, and/or welded mesh
- The requirements identified in figure 2.5 are satisfied
- The concrete between the flanges is mechanically connected to the web by stirrups welded to the webs, by bars (D_{min}= 6mm) through holes on the web and/or by welding studs (D_{min}= 10mm) to the web. (figure 2.6)
- The longitudinal spacing between two consecutive studs or bars through web holes is maximum 400 mm. Additionally, these studs and bars must have a maximum distance from the inner face of the nearest flange equal to 200 mm.

Internal compression parts

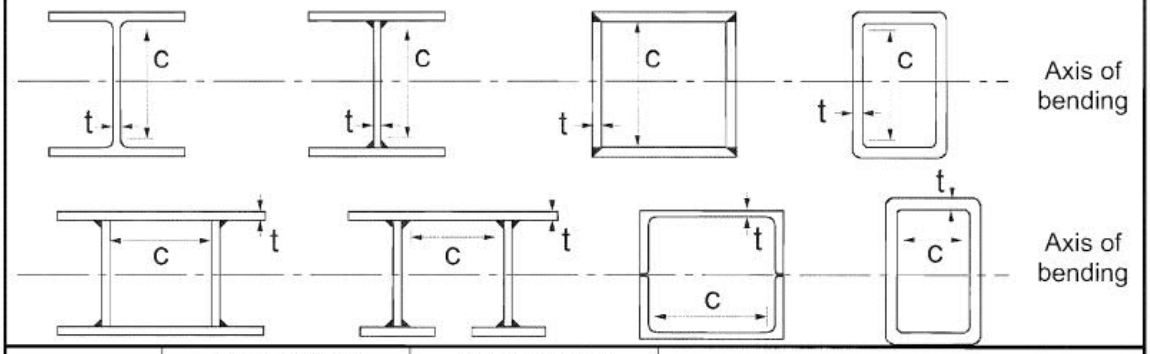

Class	Part subject to bending	Part subject to compression	Part subject to bending and compression
Stress distribution in parts (compression positive)	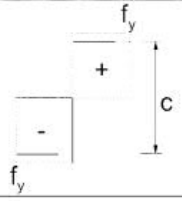	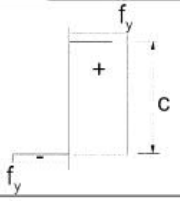	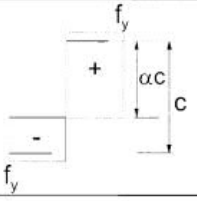
1	$c/t \le 72\varepsilon$	$c/t \le 33\varepsilon$	when $\alpha > 0{,}5$: $c/t \le \frac{396\varepsilon}{13\alpha - 1}$ when $\alpha \le 0{,}5$: $c/t \le \frac{36\varepsilon}{\alpha}$
2	$c/t \le 83\varepsilon$	$c/t \le 38\varepsilon$	when $\alpha > 0{,}5$: $c/t \le \frac{456\varepsilon}{13\alpha - 1}$ when $\alpha \le 0{,}5$: $c/t \le \frac{41{,}5\varepsilon}{\alpha}$
Stress distribution in parts (compression positive)	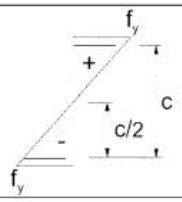	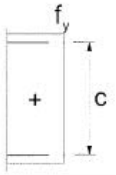	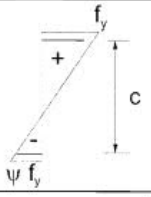
3	$c/t \le 124\varepsilon$	$c/t \le 42\varepsilon$	when $\psi > -1$: $c/t \le \frac{42\varepsilon}{0{,}67 + 0{,}33\psi}$ when $\psi \le -1^{*)}$: $c/t \le 62\varepsilon(1-\psi)\sqrt{(-\psi)}$

$\varepsilon = \sqrt{235/f_y}$	f_y	235	275	355	420	460
	ε	1,00	0,92	0,81	0,75	0,71

*) $\psi \le -1$ applies where either the compression stress $\sigma \le f_y$ or the tensile strain $\varepsilon_y > f_y/E$

Fig. 2.3- Maximum width-to-thickness ratios for internal compression parts (taken in whole from Ref[15])

Outstand flanges

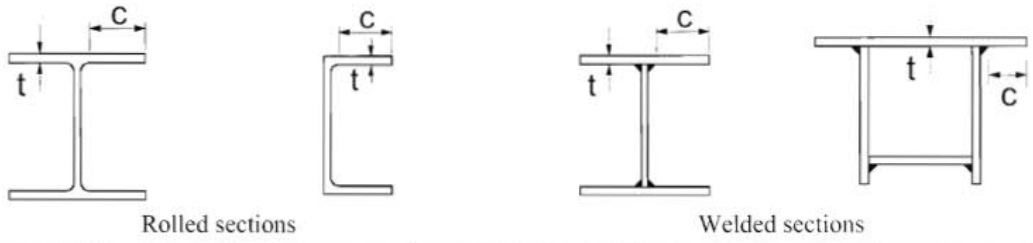

Class	Part subject to compression	Part subject to bending and compression	
		Tip in compression	Tip in tension
Stress distribution in parts (compression positive)	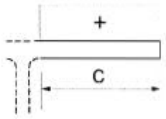	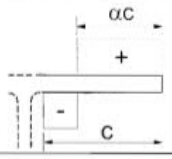	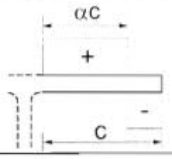
1	$c/t \le 9\varepsilon$	$c/t \le \frac{9\varepsilon}{\alpha}$	$c/t \le \frac{9\varepsilon}{\alpha\sqrt{\alpha}}$
2	$c/t \le 10\varepsilon$	$c/t \le \frac{10\varepsilon}{\alpha}$	$c/t \le \frac{10\varepsilon}{\alpha\sqrt{\alpha}}$
Stress distribution in parts (compression positive)	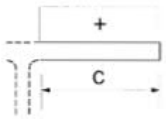	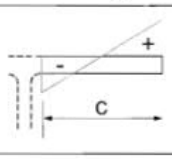	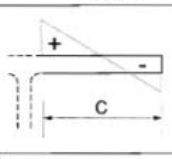
3	$c/t \le 14\varepsilon$	$c/t \le 21\varepsilon\sqrt{k_\sigma}$ For k_σ see EN 1993-1-5	

$\varepsilon = \sqrt{235/f_y}$	f_y	235	275	355	420	460
	ε	1,00	0,92	0,81	0,75	0,71

Fig. 2.4- Maximum width-to-thickness ratios for outstand flanges (taken in whole from Ref[15])

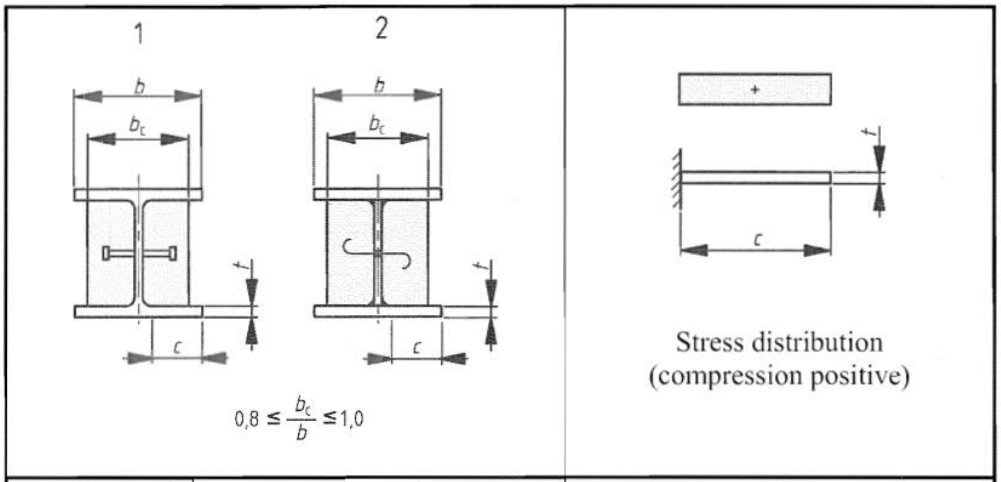

Class	Type	Limit
1	(1) rolled or (2) welded	$c/t \le 9\varepsilon$
2		$c/t \le 14\varepsilon$
3		$c/t \le 20\varepsilon$

Fig. 2.5- Maximum width-to-thickness ratios for internal compression parts (taken in whole from Ref[15])

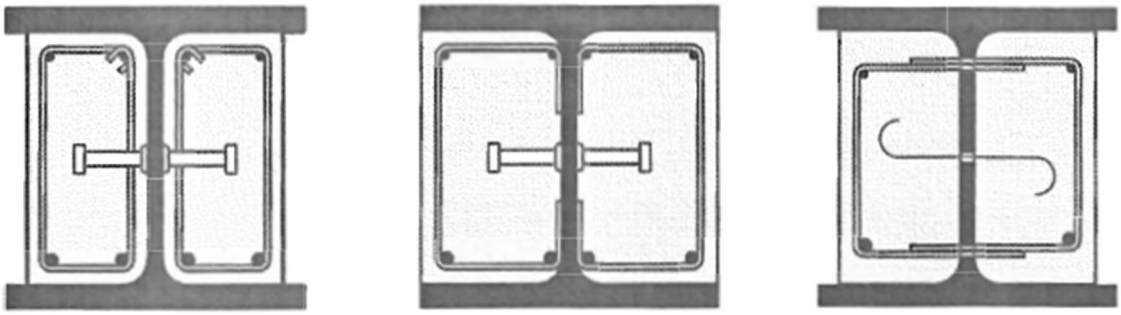

Closed stirrups | Open stirrups welded to the web | Stirrups through the web

Fig. 2.6- Arrangement of stirrups

In order to calculate the bending resistance of a composite cross section, EN 1944-1-1 provides three different approaches; calculation using rigid plastic theory, non-linear theory and elastic analysis. In the absence of pre-stressing by tendons, the design bending resistance of a composite cross-section, classified in Class 1 or Class 2, can be determined by the rigid-plastic theory, while elastic analysis and non-linear theory can be used for all classes of composite beams (EN 1994-1-1/§6.2.1.1).

2.1.2.1 Plastic resistance to bending

It can be proved that in plastic analysis, when all the individual parts of the composite cross-section have yielded, an external load (axial force, moment etc.) is distributed among these parts according to their resistance [17]. It should be reminded that in order to apply plastic analysis, the cross-section should be Class 1 or 2 while full interaction between structural steel, reinforcement and concrete is assumed. The stresses used for each material are:

- Concrete under compression $0.85 f_{cd} = 0.85\, f_{ck}/\gamma_c = 0.85\, f_{ck}/1.5$
- Concrete under tension $f_{ctd} = 0$
- Structural steel $f_{yd} = f_{yk}/\gamma_M = f_{yk}/1.0$
- Reinforcement steel $f_{sd} = f_{sk}/\gamma_s = f_{sk}/1.15$

where,

f_{cd} and f_{ck} are the design and characteristic cylinder compressive concrete strength respectively (see EN 1992-1-1, Table 2 [18])

f_{ctd} is the design tensile strength of concrete

f_{yd} and f_{yk} are the design and characteristic yield strength of structural steel, respectively

f_{sd} and f_{sk} are the design and characteristic yield strength of reinforcing steel, respectively

A minimum area of longitudinal reinforcement is required at the effective width of the concrete slab and should satisfy the following condition:

$$A_s \geq \rho_s A_c \quad \text{with} \quad \rho_s = \delta \frac{f_y}{235} \frac{f_{ctm}}{f_{sk}} \sqrt{k_c}$$

where,

A_c is the effective area of the concrete flange

f_y is the nominal value of the yield strength of the structural steel

f_{sk} is the characteristic yield strength of the reinforcement

f_{ctm} is the mean tensile strength of the concrete

δ is equal to 1.1 for Class 1 cross-sections and 1.0 for Class 2 cross-sections

k_c is a coefficient equal to $k_c = \frac{1}{1+\frac{h_c}{2z_0}} + 0.3 \leq 1$ with z_0 the distance of the mass center of the concrete plate to the mass center of the composite cross-section and h_c the thickness of the plate (figure 2.7)

The most common method to calculate the plastic bending resistance is the fiber method. According to this method the cross-section is divided in fibers of Δz thickness (figure 2.7). Each fiber has an area $\Delta A_i = b_i \Delta z_i$ and an ultimate strength f_i. The position of the neutral axis is defined through the solution of the forces resultant set equal to zero, practically meaning that the compressive forces are equal to the tensile ones. The moment at each fiber related to the neutral axis is $\Delta M_i = \Delta A_i f_i (z_i - z_0)$. The final bending resistance of the cross-section is the sum of the individual moments.

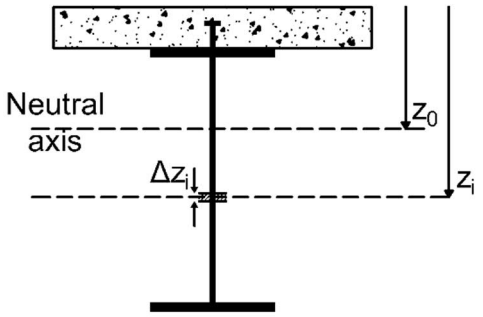

$$M_{pl,Rd} = \sum_i \Delta M_i$$

Fig. 2.7- Calculation of bending resistance using the fiber method

For the calculation of the positive bending resistance three cases are distinguished depending on the position of the neutral axis:

i. The neutral axis is within the concrete plate
ii. The neutral axis is within the top plate of the steel section
iii. The neutral axis is within the web plate of the steel section

For the calculation of the negative (i.e. tension by the top outer concrete fiber) bending resistance the neutral axis is, most commonly, within the web plate of the steel section. The concrete plate is fully under tension and so its influence to the bending resistance is ignored. The final cross-section consists of the steel beam and the reinforcement of the concrete plate (figure 2.8).

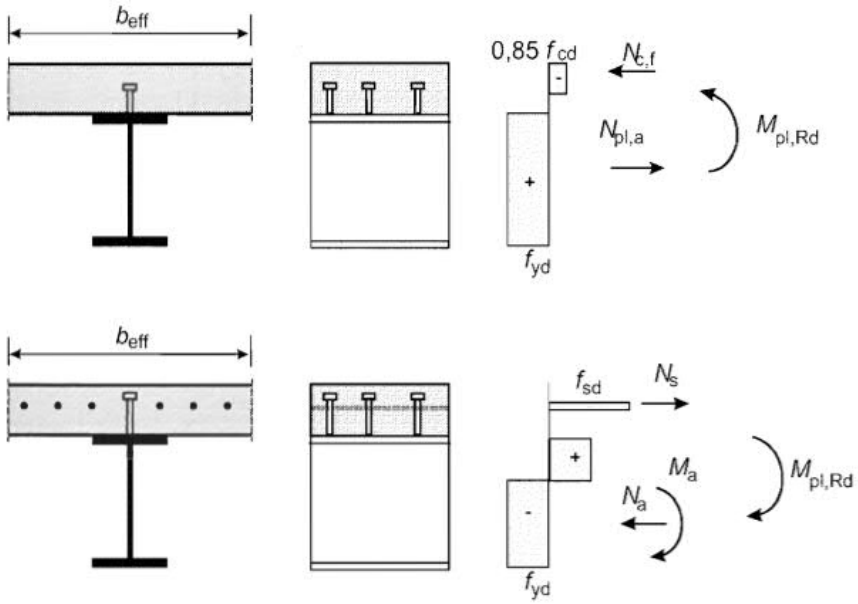

Fig. 2.8- Examples of plastic stress distributions in positive (top) and negative (bottom) bending

In cases that ductile shear connectors are used, the compressive force in the concrete flange $N_{c,f}$ should be reduced by a factor η to a value equal to $N_c = \eta N_{c,f}$ [19]. The ratio $\eta = N_c/N_{c,f}$ is the degree of shear connection and varies from zero (0), when there is no connection between the two parts (only the resistance of the steel section is considered) and one (1) when there is full shear connection between the steel beam and the concrete plate.

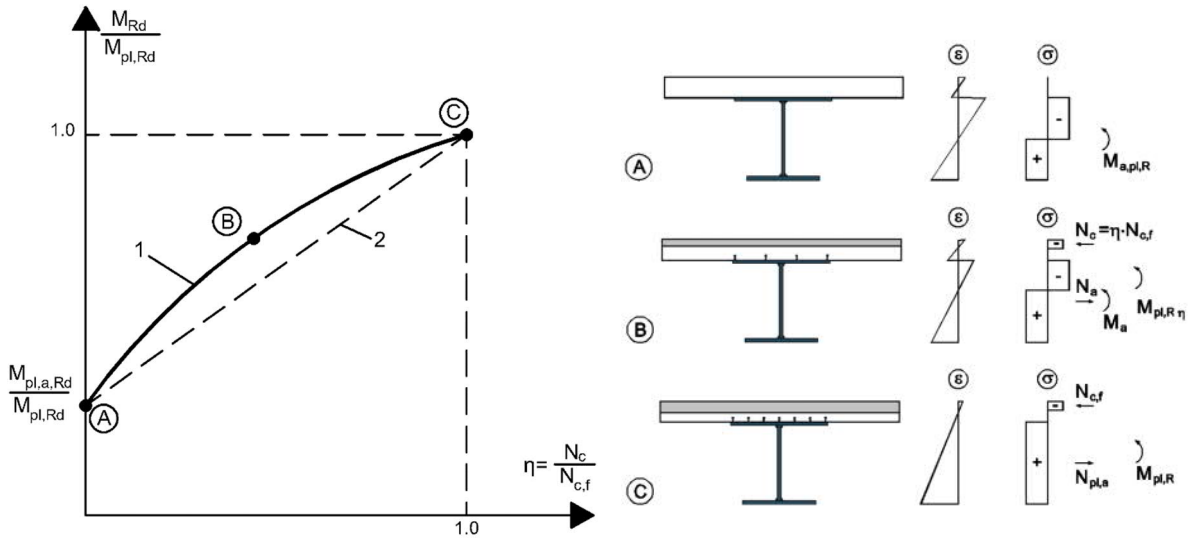

Fig. 2.9- Relation between M_{Rd} and N_c for partial shear connection

The relation between M_{Rd} and N_c is calculated by curve 1 (ABC) as is presented in figure 2.9, where $M_{pl,a,Rd}$ and $M_{pl,Rd}$ are the design plastic resistances to positive bending of the steel section alone and the composite cross-section with full shear connection, respectively. Alternatively, the simplified and conservative method is provided by using curve 2 (AC) in figure 2.9, where

$$M_{Rd} = M_{pl,Rd} + \eta\left(M_{pl,Rd} - M_{pl,a,Rd}\right)$$

2.1.2.2 Non-linear resistance to bending

In EN 1994-1-1/§6.2.1.4 the possibility to use non-linear theory for the calculation of the bending resistance, and thus take into account the actual stress-strain relationship of the materials, is provided. The stress-strain curves should be derived from:

- EN 1992-1-1/§3.1.7 for concrete under compression
- EN 1992-1-1/§3.2.7 for reinforcement steel
- EN 1993-1-1/§5.4.3 for structural steel

When the concrete flange of a Class 1 or Class 2 composite cross-section is fully under compression, the non-linear bending resistance M_{Rd} can be related to the compressive force in the concrete according to the following formulas (figure 2.10) for propped (the weight of concrete elements is applied to the steel sections which are supported in the span) and un-propped (the weight of concrete elements is applied to the steel sections which are unsupported in the span) constructions:

$$M_{Rd} = M_{a,Ed} + \left(M_{el,Rd} - M_{a,Rd}\right)\frac{N_c}{N_{c,el}} \qquad \text{for } N_c \leq N_{c,el}$$

$$M_{Rd} = M_{el,Ed} + \left(M_{pl,Rd} - M_{el,Rd}\right)\frac{N_c - N_{c,el}}{N_{c,f} - N_{c,el}} \qquad \text{for } N_{c,el} \leq N_c \leq N_{c,f}$$

with $M_{el,Ed} = M_{a,Ed} + kM_{c,Ed}$

where,

$M_{a,Ed}$ is the design bending moment applied to the steel section

$M_{c,Ed}$ is the design bending moment applied to the composite section

k is a factor which ensures that the stress limits for the materials are reached (f_{cd} for concrete in compression, f_{yd} for structural steel and f_{sd} for reinforcement steel).

$M_{c,el}$ is the compressive force in the concrete flange corresponding to the moment $M_{el,Rd}$

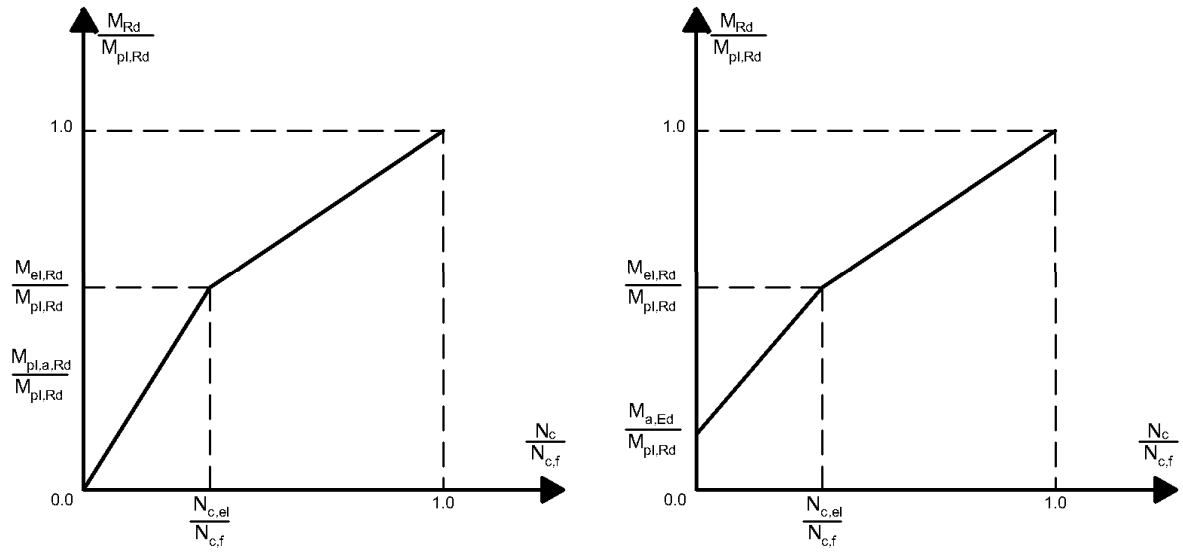

Fig. 2.10- Simplified relationship between M_{Rd} and N_c for propped (left) and unpropped (right) constructions

2.1.2.3 Elastic resistance to bending

According to section 6.2.1.5 of EN 1994-1-1, the elastic bending resistance is the minimum bending moment to reach the maximum stresses f_{cd}, f_{yd} and f_{sd} in the cross-section for concrete, structural steel and reinforcement steel, respectively. During elastic analysis, the distribution of the stresses in the individual parts, is conducted proportionally to their stiffness. Due to the linearity of the procedure, the stresses created by the axial force and the bending moment can be calculated separately and then be summed.

The principal assumption in this case is that the loading history is taken into account, meaning that the stress state in the steel member is calculated first and then the stresses of the composite member are added [20], following erection stage.

2.2 Eurocode 8 (EN 1998-1) [21]

2.2.1 Scope and terms

EN 1998 covers the design and construction of civil engineering buildings in areas with seismic activity. "Its purpose is to ensure that in the event of earthquakes:

- human lives are protected
- damage is limited
- important structures remain operational"

Specifically, EN 1998-1 covers the design of buildings in seismic regions. In Table 2.2 some basic terms are presented as described in section 1.5.2 of EN 1998-1.

Table 2.2- Basic terms and definitions used in EN1998-1-1

No	Term	Definition
1	Behavior factor	A factor that reduces the forces obtained from a linear analysis in order to take into account the non-linear response of a structure due to the material, the structural system and the design procedures.
2	Dissipative structure	A structure which is able to absorb energy by means of ductile hysteretic behavior and/or by other mechanisms.
3	Dissipative zones	Predefined parts of a structure where the dissipative capabilities are mainly located.
4	Importance factor	A factor which defines the importance of a building related to the consequences of its failure.
5	Non-dissipative structure	A structure designed against a seismic situation by considering a linear material behavior.
6	Non-structural element	An element or system that is not considered a load carrying element in the design procedure.
7	Primary seismic members	Members of the structural system, that resists the seismic action, which are modelled in the analysis and are fully designed and detailed according to the rules of EN 1998.
8	Secondary seismic members	Members that are not considered a part of the structural system that resists the seismic action and whose strength and stiffness against seismic actions are neglected.

2.2.2 Specific rules for composite steel concrete buildings

2.2.2.1 General

Three design concepts are available for the designer in terms of seismic energy dissipation by the building:

- Concept a Low-dissipative structural behavior.
- Concept b Dissipative structural behavior with composite dissipative zones
- Concept c Dissipative structural behavior with steel dissipative zones

These concepts are related to the structural ductility class and the behavior factor q (Table 2.3). Composite buildings that are designed against earthquakes shall be designed according to these concepts.

Table 2.3- Design concepts, structural ductility classes and values of behavior factors

Design concept	Structural ductility class	Range of the reference values of the behavior factor q
Concept a	DCL (Low)	≤ 1.5 - 2
Concept b or c	DCM (Medium)	≤ 4 Limited by the values of Table 2.6
	DCH (High)	Only limited by the values of Table 2.6

In concept a, the resistance of the members and the connections can be calculated according to EN 1993 and EN 1994 without any additional requirements. The action effects can be calculated by an elastic analysis without considering the non-linear behavior of the materials, provided that the initial moment of inertia of the elements in parts of the beam spans is reduced due to concrete cracking. In concepts b and c, the elements of the structure that are in the dissipative zones are allowed to develop inelastic deformations and thus the non-linear behavior of the materials should be taken into account. The target of the design rules for dissipating composite structures is to ensure the development of reliable local plastic mechanisms (dissipative zones, also called critical regions) and of a global plastic mechanism that will dissipate as much energy as possible under the seismic actions.

2.2.2.2 Materials

- Concrete

The lowest concrete class that is allowed to be used in dissipative zones is C20/25, while the highest concrete class that is covered by EN 1998 is C40/50. If higher classes are used, then the design is not within the scope of EN 1998.

- Reinforcing steel

According to Table C.1 of EN 1992-1-1 (Table 2.4), class B or C steel should be used for the reinforcement in the plastic resistance of dissipative zones for ductility class DCM and only

class C steel is allowed for ductility class DCH. Only ribbed bars are allowed in regions with high stresses, excluding the closed stirrups or cross ties.

Table 2.4- Properties of reinforcement

Product form		Bars and de-coiled rods			Wire Fabrics			Requirement or quantile value (%)
Class		A	B	C	A	B	C	-
Characteristic yield strength f_{yk} or $f_{0.2k}$		400 to 600						5.0
Minimum value of k=$(f_t/f_y)_k$		≥1.05	≥1.08	≥1.15 <1.35	≥1.05	≥1.08	≥1.15 <1.35	10.0
Characteristic strain at maximum force, ε_{uk} (%)		≥2.5	≥5.0	≥7.5	≥2.5	≥5.0	≥7.5	10.0
Bendability		Bend/Rebend test			-			
Shear strength		-			0.25 Af_{yk} (A is area of wire)			Minimum
Maximum deviation from nominal mass (individual bar or wire) (%)	Nominal bar size (mm)							5.0
	≤8	±6.0						
	>8	±4.5						

- Structural steel

Structural steel must be according to the standards of EN 1993. Nominal values of the yield strength f_y and the ultimate strength f_u can be obtained directly by the product standard ($f_y=R_{eH}$ and $f_u=R_m$) or by using the values provided in the following Table 2.5. In order to ensure that structural steel has a required minimum ductility the following conditions must be fulfilled:

- fu/fy ≥ 1.10
- the elongation at failure on a gauge length is equal to $5.65\sqrt{A_0}$ and is not less than 15% (A_0 is the original cross-section area)
- the ultimate strain ε_u should be greater than $15\varepsilon_y$ ($\varepsilon_y = f_y / E$ is the yield strain)

These limits presented are the recommended values. More precise values are defined in National Annexes.

Table 2.5- Nominal values of yield and ultimate tensile strength for structural steel

Standard and steel grade	Nominal thickness of the element t (mm)			
	t ≤ 40 mm		40 mm < t ≤ 80 mm	
	f_y [N/mm^2]	f_u [N/mm^2]	f_y [N/mm^2]	f_u [N/mm^2]
EN 10025-2				
S 235	235	360	215	360
S 275	275	430	255	410
S 355	355	490	335	470
S 450	440	550	410	550
EN 10025-3				
S 275 N/NL	275	390	255	370
S 355 N/NL	355	490	335	470
S 420 N/NL	420	520	390	520
S 460 N/NL	460	540	430	540
EN 10025-4				
S 275 M/ML	275	370	255	360
S 355 M/ML	355	470	335	450
S 420 M/ML	420	520	390	500
S 460 M/ML	460	540	430	530
EN 10025-5				
S 235 W	235	360	215	340
S 355 W	355	490	335	490
EN 10025-6				
S 460 Q/QL/QL1	460	570	440	550

2.2.2.3 Structural types and behavior factors

Seismic codes, such as EN 1998-1, in order to calculate the ductility of a structure, introduce the behavior factor q, based on the materials used and the structural system, which accounts for the energy dissipation capacity of the structure. The behavior factor is calculated using the following formula:

$$q = \frac{F_e}{F_d}$$

where F_e is the maximum horizontal load caused by the earthquake that would be developed at the structure if it had adequate strength to behave elastically during the seismic action and F_d

is the maximum design horizontal load. The values of the behavior factor in relation to the structural system are presented in Table 2.6. Each structural system is described in the following sections.

Table 2.6- Upper limits to reference values of behavior systems regular in elevation

Structural Type	Ductility class	
	DCM	DCH
a) Moment resisting frames	4	$5\alpha_u/\alpha_1$
b) Frame with concentric bracings		
Diagonal bracings	4	4
V-bracings	2	2.5
c) Frame with eccentric bracings	4	$5\alpha_u/\alpha_1$
d) Inverted pendulum	2	$2^{\alpha}{}_u/\alpha_1$
e) Composite structural systems		
Composite walls (Type 1 and Type 2)	$3\alpha_u/\alpha_1$	$4\alpha_u/\alpha_1$
Composite or concrete walls coupled by steel or composite beams (Type 3)	$3\alpha_u/\alpha_1$	$4.5\alpha_u/\alpha_1$
f) Composite steel plate shear walls	$3\alpha_u/\alpha_1$	$4\alpha_u/\alpha_1$

where α_1 is the value that magnifies only the horizontal seismic design action (all other design actions remain constant) until the development of the first plastic hinge and α_u is the value by which the horizontal seismic design action is multiplied in order to have a mechanism on the structure and an overall unstable behavior. If the building has not regularity in elevation the values of Table 2.6 are reduced by 20%. Indicative values of the ratio α_u/α_1 in the absence of appropriate calculations, in relation to the structural system are presented in figures 2.11- 2.17

a) Moment resisting frames

In moment resisting frames the horizontal forces are resisted by generally flexural members (figure 2.11).

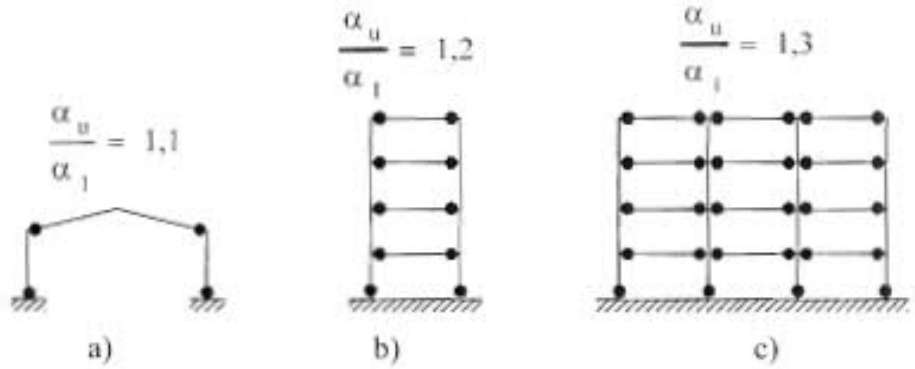

Fig. 2.11- Moment resisting frames (dissipative zones in beams and at the bottom of columns)

b) Composite concentrically braced frames

In frames with concentric bracings the horizontal forces are resisted by members subjected to axial forces (figures 2.12- 2.13).

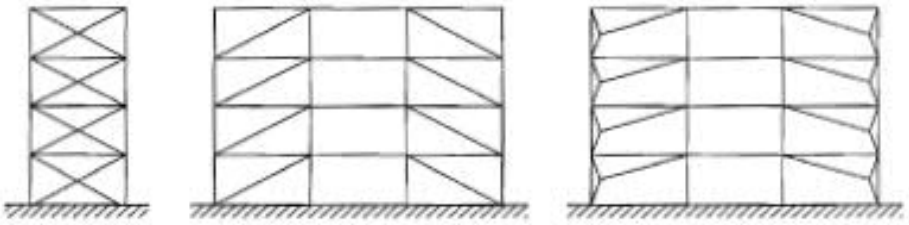

Fig. 2.12- Frames with concentric diagonal bracings (dissipative zones in tension diagonals only)

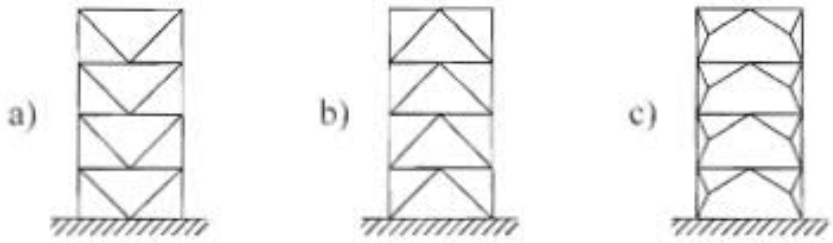

Fig. 2.13- Frames with concentric V-bracings (dissipative zones in tension and compression diagonals)

c) Composite eccentrically braced frames

In frames with eccentric bracings the horizontal forces are resisted by members subjected to axial forces (figure 2.14), but only in cases that the layout allows energy dissipation in seismic links (cyclic bending or cyclic shear).

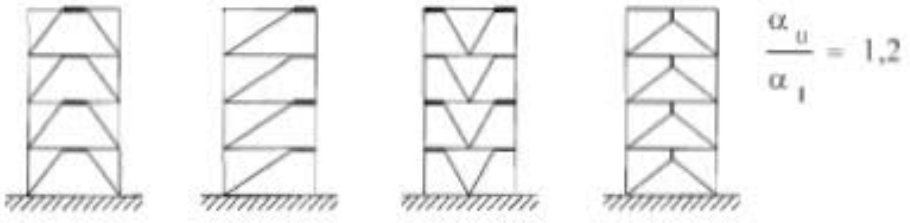

Fig. 2.14- Frames with eccentric bracings (dissipative zones in bending or shear links)

d) Inverted pendulum structures

In this category belong the structures that half or more of their mass is concentrated in the upper third of their height or structures where dissipation of energy is located mainly at the bottom of a single building element (figure 2.15).

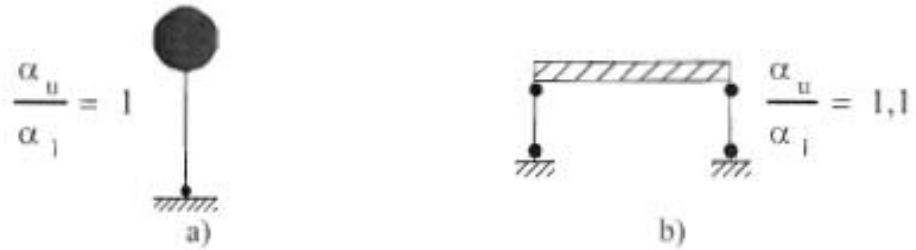

Fig. 2.15- Inverted pendulum (dissipative zones a) at the column base or b) in columns where $N_{ed}/N_{pl,Rd}<0.3$)

e) Composite structural systems

Composite structural systems are those which behave essentially as reinforced concrete walls and may belong to one of the following types:

- Type 1 is a steel or composite frame combined with concrete infill panels connected to the steel structure (figure 2.16a)
- Type 2 is a reinforced concrete wall strengthened with encased steel parts working as vertical edge reinforcement (figure 2.16b)
- Type 3 include two or more shear walls connected with steel or composite beams (figure 2.17)

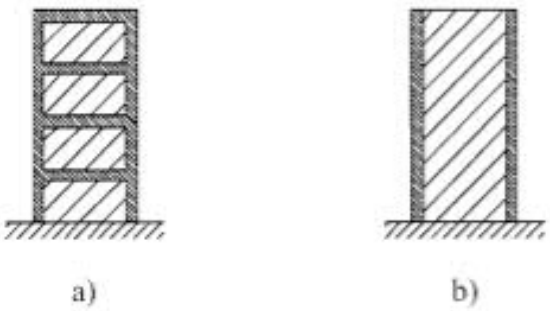

Fig. 2.16- Composite walls a) type 1 and b) type 2

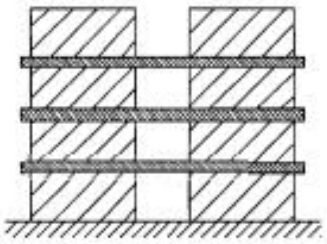

Fig. 2.17- Composite or concrete walls coupled by steel or composite beams (type 3)

f) Composite steel plate shear walls

This category includes shear walls consisting of a vertical steel plate, continuous along the height of the building, with reinforced concrete encasement on one or both faces of the plate and of the structural steel or composite boundary members.

2.2.3 Design criteria and detailing rules for dissipative structural behavior

Primary composite seismic members, which must comply with the instructions of EN 1994-1-1:2004, are designed with reference to a global plastic mechanism that determines the location of the dissipative and non-dissipative zones.

In order to ensure adequate ductility for members under compression or bending some requirements must be fulfilled. The width to thickness ratio of the steel components must be restricted according to the cross-sectional classes described in a previous section (§2.1.2) while the steel dissipative zones and the non-encased steel parts of composite members must comply

with the requirements of Table 2.7. Additionally, Table 2.8 describes the requirements for the dissipative zones of encased composite members

Table 2.7- Limitations on cross-sectional class of dissipative elements depending on ductility class and reference behavior factor

Ductility class	Reference value of behavior factor q	Required cross- sectional class
DCM	1.5<q≤2	Class 1, 2 or 3
	2<q≤4	Class 1 or 2
DCH	q>4	Class 1

Table 2.8- Relation between behavior factor and slenderness limits of walls of sections in dissipative zones of encased composite structures

Ductility Class of structure	DCM		DCH
Reference value of behavior factor q	q ≤ 1.5-2	1.5-2 < q ≤ 4	q > 4
Partially encased H or I section			
Fully encased H or I section			
flange outstand limits c/t_f	20 ε	14 ε	9 ε
Filled rectangular section			
h/t limits	52 ε	38 ε	24 ε
Filled circular sections			
d/t limits	90 ε^2	85 ε^2	80 ε^2

The geometric references are described in the following figure 2.18.

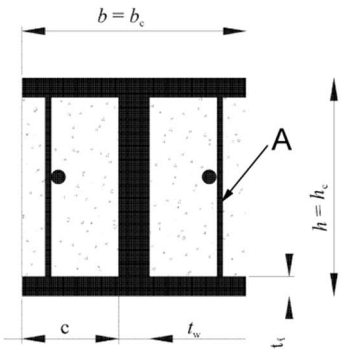

Fig. 2.18- Detail of transverse reinforcement, with the additional straight bars (links) welded to the flanges.

Special care is also taken by EN 1998-1 for the integrity of the concrete slab during an earthquake when yielding takes place in the bottom part of the steel section and/or in the steel reinforcement of the slab. Full or partial shear connection between the concrete slab and the steel beam can be adopted, provided that the minimum degree of shear connection η, as defined in section 2.1.2.1, is not less than 0.8 and the total resistance of the connectors within any negative moments region is not less than the plastic resistance of the reinforcement bars in the slab. The design resistance of the shear connectors obtained from EN 1994-1-1 must be reduced by 25%. An additional reduction of shear connectors resistance, k_r, is needed when a profile steel sheeting with ribs transverse to the supporting beams is used, as given in figure 2.19. When non-ductile shear connectors are used, full shear connection is required.

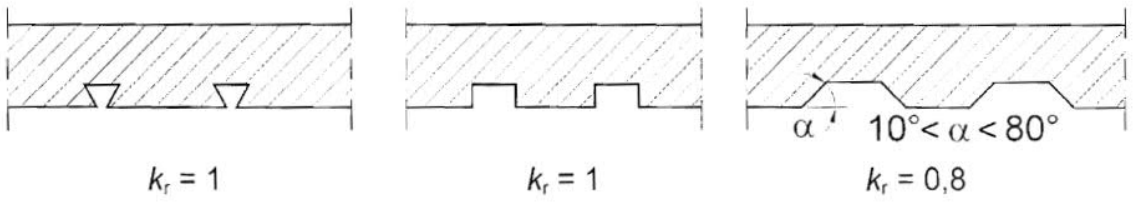

Fig. 2.19- Values of the rib shape efficiency factor k_r

Finally, in order for a composite beam to be considered as ductile, the following condition must apply:

$$x/d < \varepsilon_{cu2}/(\varepsilon_{cu2} + \varepsilon_a)$$

where

x is the distance between the outer concrete compression fiber and the plastic neutral axis

d is the height of the composite section

ε_{cu2} is the ultimate compressive strain of concrete according to EN 1994-1-1:2004

ε_a is the total strain in steel at Ultimate Limit State

This expression is fulfilled if the values of x/d ratio are less than the limits included in Table 2.9.

Table 2.9- Limit values of x/d for ductility of beams with slab

Ductility class	q	f_y (N/mm^2)	x/d upper limit
DCM	1.5 < q ≤ 4	355	0.27
	1.5 < q ≤ 4	235	0.36
DCH	q > 4	355	0.20
	q > 4	235	0.27

3

Literature review

The purpose of this chapter is to present the most important and relevant experimental investigations related to the flexural behavior of shallow (slim) floor composite beams. The small number of publications with test results of this type of beams subjected to bending loads combined with the lack of any reference on the Eurocodes, as well as the numerous possibilities and combinations of steel sections and shapes available, indicates that this topic should be investigated more extensively.

3.1 Flexural capacity of the encased (slim floor) composite beam with deep deck plate [22]

In this paper the authors presented the results from the investigation of the flexural behavior of slim-floor beams. 8 full-scale specimens with span length 6m were tested and their shapes and details are presented in figure 3.1 and Table 3.1. The load (in the form of displacement control) was applied at two points L/4 away from the supports creating a 4-point bending set-up.

Table 3.1- Details of specimens

Specimen	h	h_d	h_t	d	H-section	t_p	b	b_1	L	Shear stud	Loading type
SB200	230	140	30	200	H200x200x12x8	15	200	550	1500	without	concentric
SB250-A	340	250	90	250	H250x250x14x9		250	525	1500	with	concentric
SB250-B										without	
SB300-A			40	300	H300x305x15x15		305	525	1500	without	concentric
SB300-B								122.5	750		
SB300-C								525	1500		eccentric
SB300-D	390	300	90	300				497.5	1500	with	concentric
SB300-E										without	

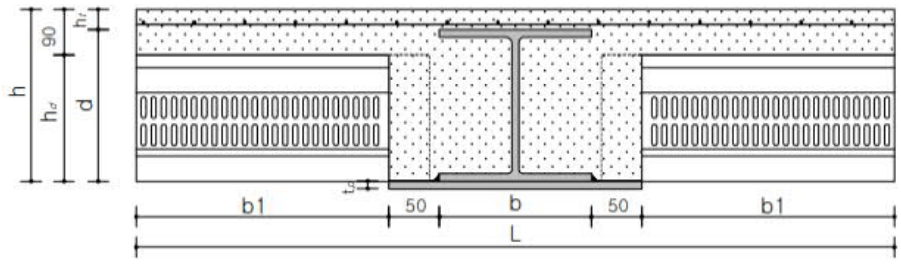

(a) SB200, SB300-A, B, C (Loading type, effective width of slab)

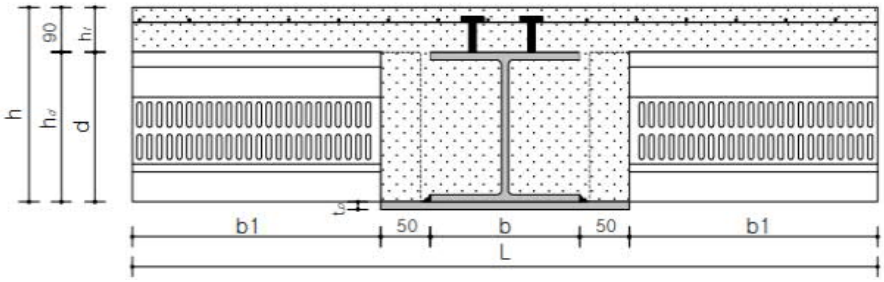

(b) SB-250A, B, SB300-D, E (with or without shear connector)

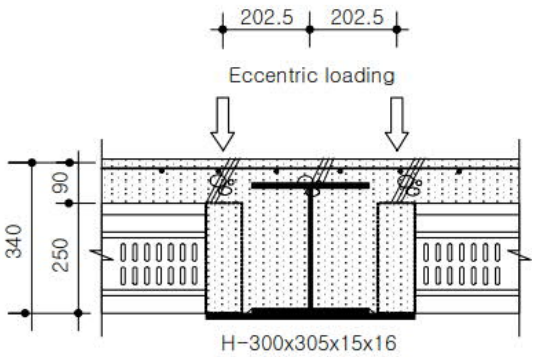

(c) SB300-C (Eccentric loading)

Fig. 3.1- Shape and dimensions of specimens

In figure 3.2 the load-deflection curve for each specimen is presented. In addition, each graph contains the analytical curves of the bare steel and fully composite beams. Finally, the load- slip (measured at the end of the beams) curve is also included.

A comparison of the stiffness after initial cracking and ultimate loads was conducted between the composite beam and the bare steel one (figure 3.3). Specimens without studs had 1.11 to 2.52 times higher stiffness than the bare steel beams. The corresponding ratio for the ultimate load varied between 1.65 and 2.18.

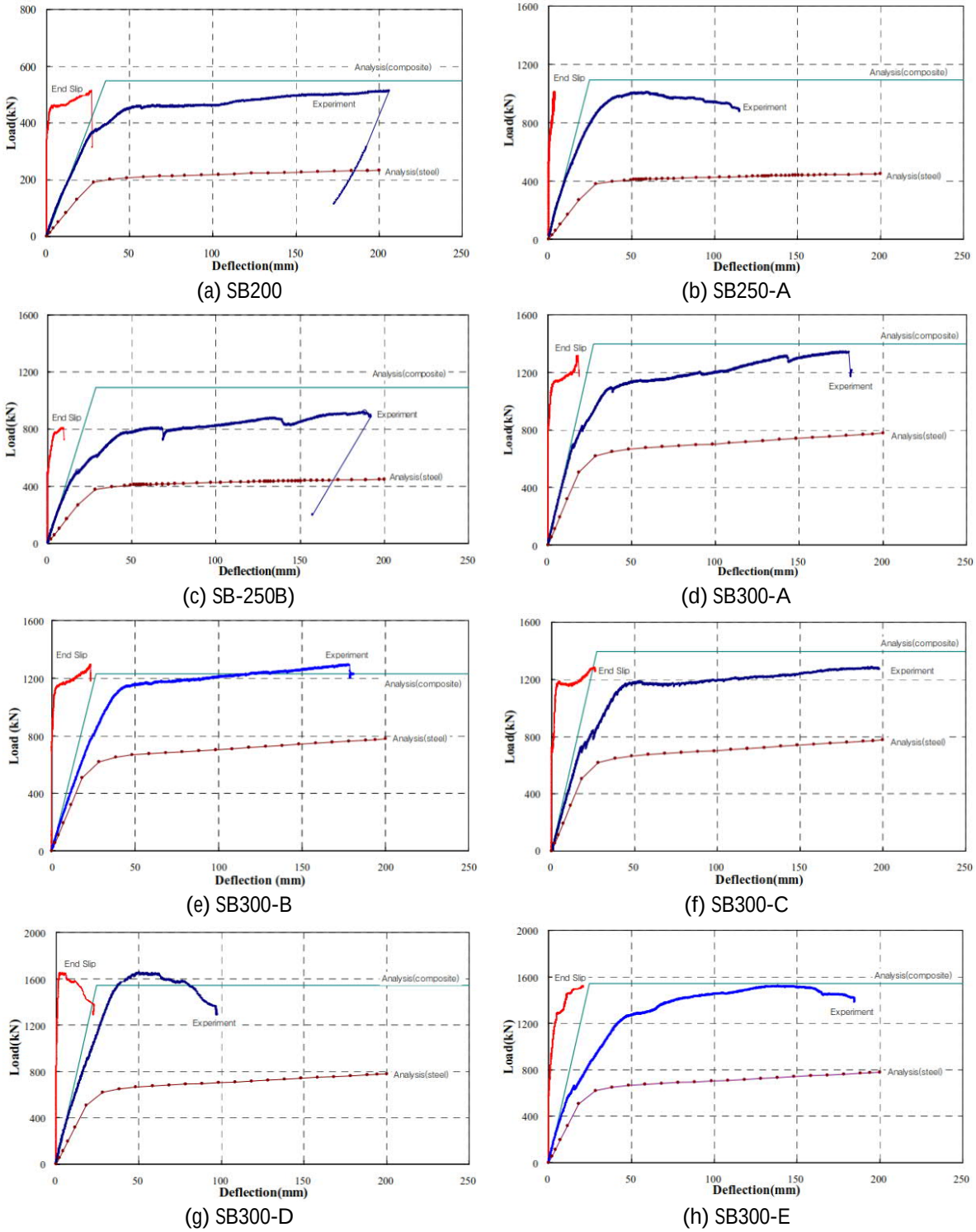

(a) SB200 (b) SB250-A

(c) SB-250B) (d) SB300-A

(e) SB300-B (f) SB300-C

(g) SB300-D (h) SB300-E

Fig. 3.2- Load-deflection curves

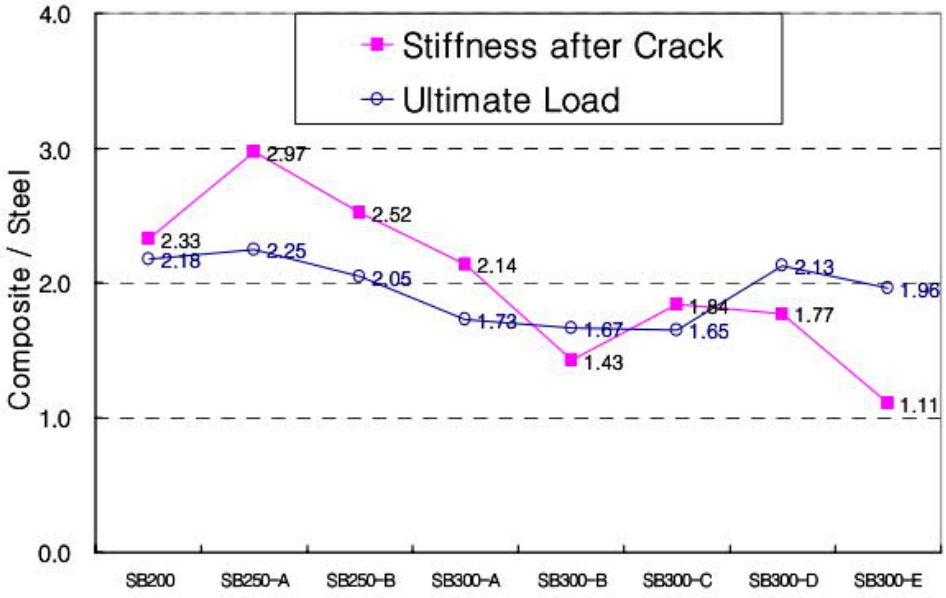

Fig. 3.3- Stiffness and strength against steel beam

Finally, the authors draw the following conclusions:

- Micro-cracks appeared along the length of the beams. However, no serious concrete separation occurred even using the minimum reinforcement.
- For the composite beams with partial shear connection, the initial slip load was proportional to the depth of the concrete topping and the shear bond area provided by the steel beams.
- The shear resisting capacity of the composite beams was increased by about 50% due to mechanical bond between the concrete and the steel beam.
- Shear bond stresses varied between 1.20 and 1.45 N/mm^2 at maximum load. The composite ratios ranged from 0.53 to 0.96 times compared with composite beams with full shear connection.

3.2 Loading capacity of composite slim frame beams [23]

Wang et al. investigated the bending capacity, flexural stiffness and the influence of the ratio of reinforcement of two slim frame beams with deep deck under monotonic loading. The cross sections of the beams are illustrated in figure 3.4. Both specimens have the same geometry but

differ in the reinforcement ratio. The span of the specimens was 6 m and the width of concrete slab was 0.75 m. The set-up of the test is shown in figure 3.5

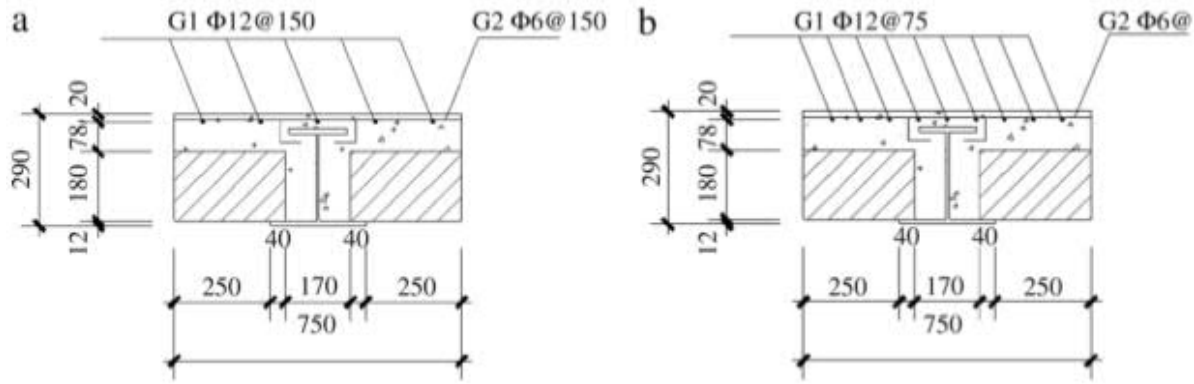

Fig. 3.4- Cross sections of the tested specimens

Fig. 3.5- Test setup

The properties of concrete, structural steel and reinforcement steel are presented in Table 3.2 and Table 3.3, respectively.

Table 3.2- Material properties of concrete

Specimen	Cubic crushing strength $f_{cu,k}$ (N/mm^2)	Young's modulus E (10^3 N/mm^2)	Design value of axial compressive strength f_c (N/mm^2)
FSB1	34.27	29.00	14.30
FSB2	32.87	28.56	14.30

Table 3.3- Material properties of structural and reinforcement bars

Material	Yield strength f_y (N/mm^2)	Young's modulus E (10^3 N/mm^2)	Yield strain ($\mu\varepsilon$)	Ultimate strength f_u (N/mm^2)	Design strength f (N/mm^2)
Q235-B	313.74	202	1471	508.18	215
D12 bars	370.30	190	2254	556.69	215
D6 bars	401.34	279	-	577.79	215

Results showed that in the elastic stage, the composite sections were following Bernoulli's principle both in the positive and negative moment region. In the ultimate limit state, the flanges and most of the webs of the steel section yielded, as did the reinforcement bars. Plastic hinges were developed at beam ends and mid-span, while the frame composite beam demonstrated significant ductility (figure 3.6). The load-deflection curves of the two specimens were the same in the elastic stage, which indicates that the ratio of the reinforcement had a small effect on the stiffness of the composite beam. The main reason is that the stiffness of the whole beam largely depends on the stiffness of the sagging moment region. The higher ultimate capacity was manifested by the beam with the higher reinforcement ratio because the ultimate capacity of the composite beam is determined by the resistance of both sagging and hogging moment regions.

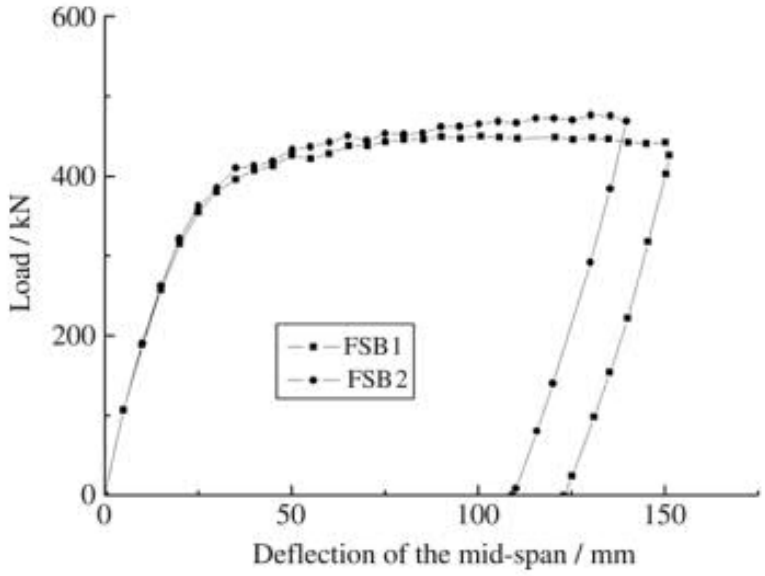

Fig. 3.6- Load deflection curves

Subsequently, based on the experimental results, formulas of calculating the bending capacity and flexural stiffness in the hogging moment region of the slim beam with deep deck were proposed. A design method of the frame slim beam had been developed by combining these formulas with existing ones for the estimation of the ultimate loading capacity in the sagging moment region.

3.3 Flexural behavior of shallow cellular composite floor beams with innovative shear connection [24]

Shiming Chen et al. investigated the role that the shear connection plays in the overall behavior of the composite slim floor system. Usually, in slim floor beams the longitudinal shear transfer is assumed by the bonding between the concrete and the steel part. This is in contrast with the ordinary composite beams, where the shear connection is achieved mainly with shear studs welded at the top plate of the steel part. Yet, this adhesive strength between concrete and steel is small. For this reason and in order to establish an effective shear connection for the composite slim floor beams, modified steel beams with a row of circular openings within the steel web combined with transverse steel reinforcing bars were used in the experiments in this study (figure 3.7).

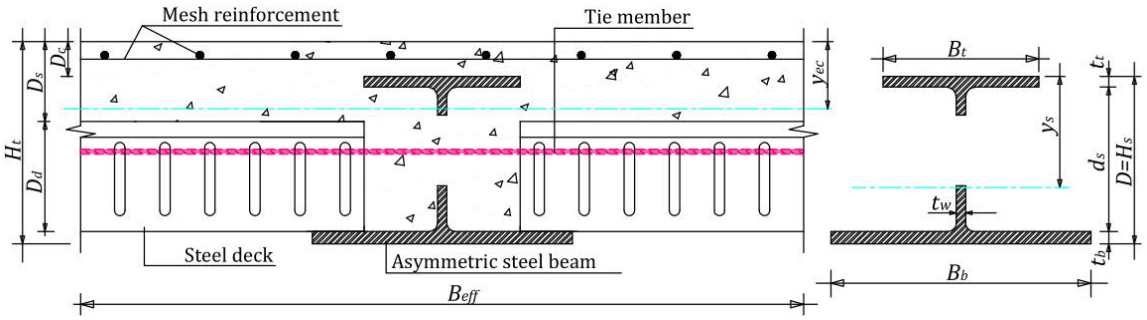

Fig. 3.7- Geometrical configuration of shallow cellular beam with shear connection arrangement

Four full-scaled shallow cellular composite beams were tested as simply supported under four-point loading conditions. The scope of these tests was to investigate the load bearing behavior, the shear capacity and the longitudinal shear transferring mechanism occurring in this type of beams, while the results helped in the development of a design method.

The beams were simply supported with a length of 4200 mm. Three major factors were considered for the individual specimens: shape of the steel cross section, opening of steel web and concrete topping above the steel beam. The geometry of the specimens is presented in figures 3.8 and 3.9. The amount of reinforcement and the position of the bars differ from one specimen configuration to another.

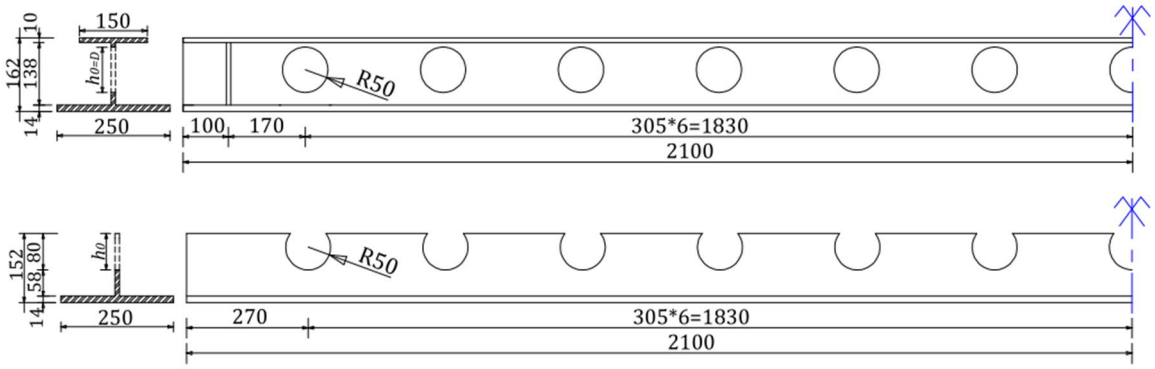

Fig. 3.8- Geometrical characteristics of the steel beams of specimens SCSFB 1 and SCSFB 2 with circular web openings (top) and specimens SCSFB 3 and SCSFB 4 with clothoidal web openings (bottom)

The behavior of all specimens was comparable; linear elastic during the initial loading stage followed by the yielding and the ultimate failure. In Table 3.4, the loads at the yielding point and the maximum loads are presented. Additionally, the maximum deflection values measured at the mid-spans are included in Table 3.4.

Table 3.4- Load and deflection behavior

Specimen	Load values at the yielding point (kN)	Maximum load values (kN)	Maximum deflection values (mm)
SCSFB 1	250.0	349.0	133.3 (span/30)
SCSFB 2	190.0	264.7	120.4 (span/33)
SCSFB 3	160.0	255.1	93.3 (span/43)
SCSFB 4	110.0	154.4	132.9 (span/30)

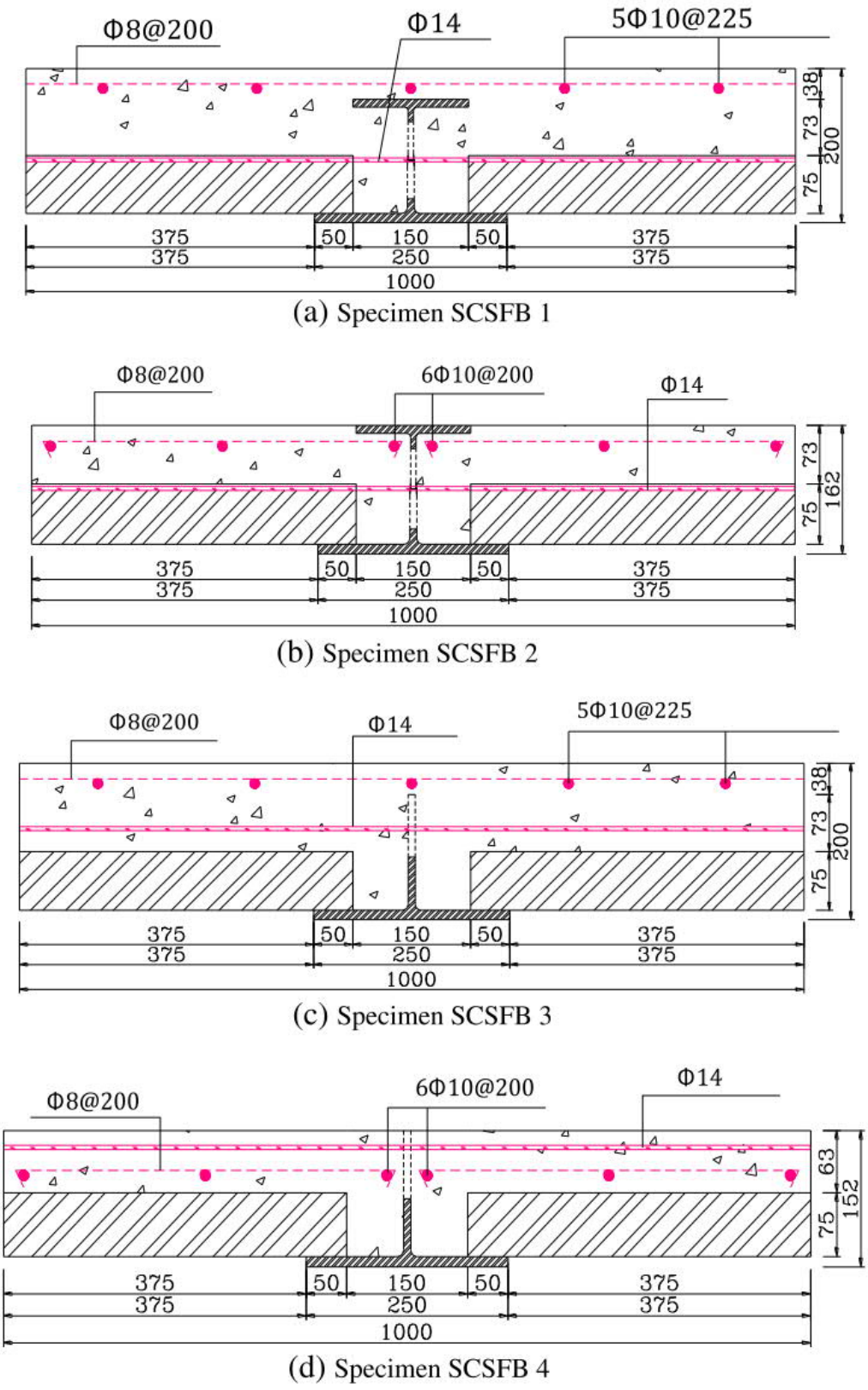

Fig. 3.9- Geometrical characteristics of composite cross-sections

The load- deflection curves are presented in figure 3.10. Nonlinear and ductile behavior can be observed for all specimens.

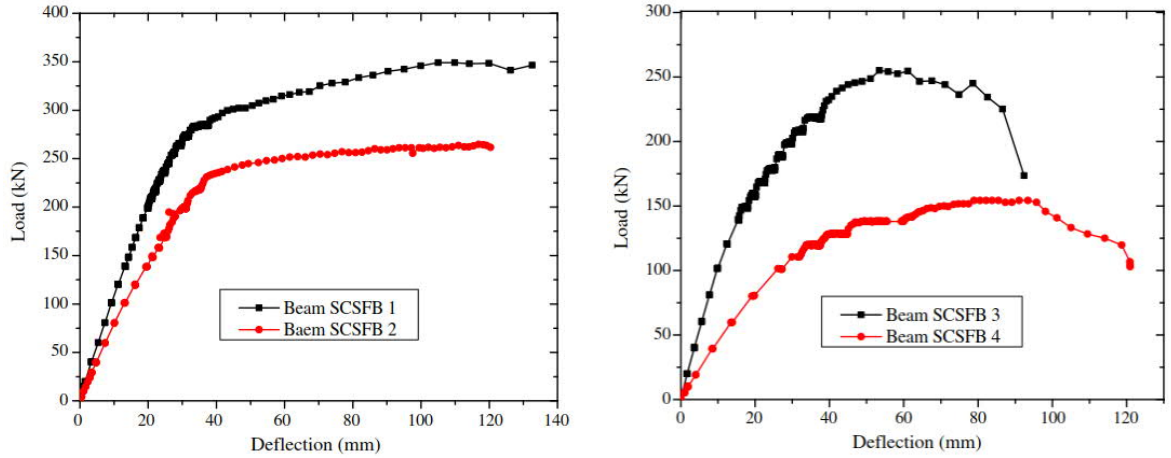

Fig. 3.10- Load- deflection curves

Slips between concrete and steel were measured and are presented in figure 3.11. For specimens SCSFB 1 and 3 slips were measured at the two ends while for specimens SCSFB 2 and 4 slips were measured at the beam ends (S1 and S2), mid-span (S3) and at the two-quarter-spans (S2 and S4).

The cracks pattern and the failure of the specimens were carefully examined after the test. Based on the observation two failure mechanisms were identified.

- The flexural failure of specimens SCSFB 1 and 2. This failure mode was characterized by the permanent deformation and the attaining of the plastic moment. The crushing of the concrete on the top of the slab was also an indication of the flexural failure.
- The shear failure of specimens SCSFB 3 and 4. These modes were characterized by the diagonal shear cracks and the failure of the shear connections. The full plastic moment of the sections was not reached due to prior failure in shear.
- Finally, models for the calculation of the bending resistance and the design of the shear connection were proposed.

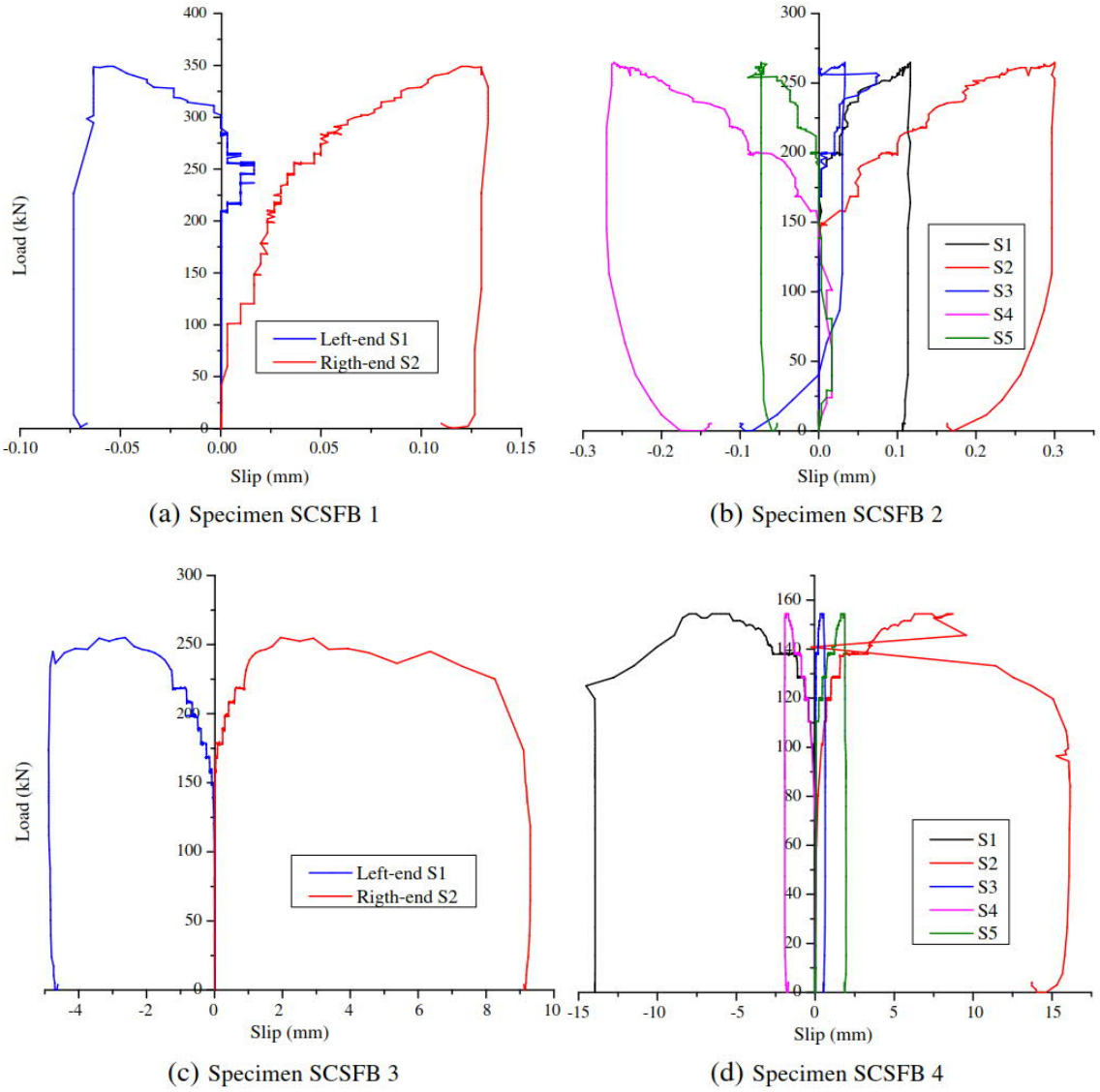

(a) Specimen SCSFB 1 (b) Specimen SCSFB 2

(c) Specimen SCSFB 3 (d) Specimen SCSFB 4

Fig. 3.11- Load- slip curves of the specimens

3.4 Flexural behavior of composite slim floor beams [25]

In this paper, the authors presented the results from the experimental investigation of the flexural behavior of slim-floor beams with different arrangements of shear connectors. Afterwards, the results were compared with the results from previously conducted tests of beams subjected to shear.

Nine specimens were tested under a four-point loading configuration and in this paper the results of six beams named BT1a, BT3, BT4, BT6, BT7 and BT8 were presented. A HEB200

steel beam section was encased in the concrete slab of 240 mm depth (figure 3.12). A 400 x 15 mm steel plate was welded at the bottom plate of the steel beam. The span between the supports was 6000 mm and each load point was located 2250 mm from each support. The shear connection between the steel part and the concrete was established with steel bars, 1200 mm long, passing through holes opened at the webs with 40 mm diameter. The different types of shear connection between the beams is presented in Table 3.5.

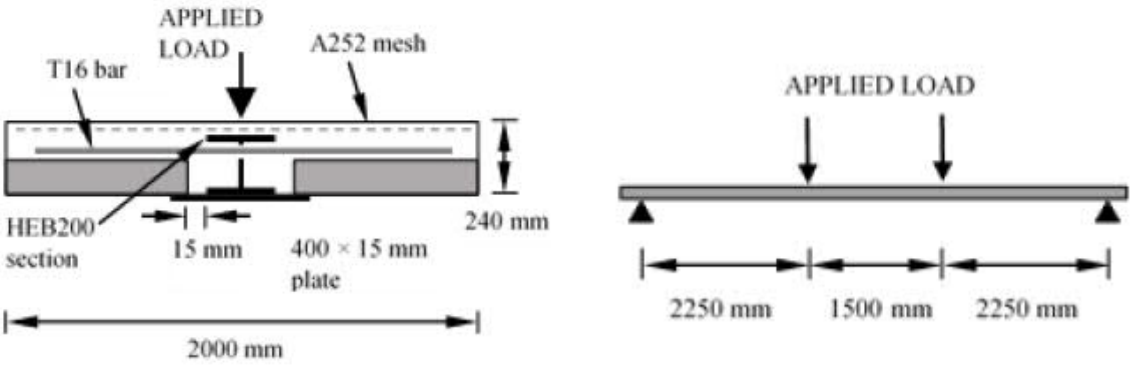

Fig. 3.12- Cross-section (left) and side (right) view of typical specimen

Table 3.5- Shear connection type of specimens

Specimen	Shear connection type
BT1a	Designed to provide a shear connection equal to 40%
BT3	Designed to provide a shear connection equal to 100%
BT4	Designed to provide a shear connection equal to 25%
BT6	No shear connectors
BT7	Horizontal shear studs welded on the beam web
BT8	Diameter of the holes on the beam web equal to 80 mm

The overall behavior of the specimens was quite similar (figure 3.13). At the beginning of all tests the stiffness of the specimens was high and linear. As the applied load was further increased the stiffness was reduced. During the final stage of the procedure the load reached a constant value while the deflection was increasing until the beams could not withstand any more deformation. The maximum deflection of all the specimens exceeded the value of 150 mm, which corresponds to a normalized ratio equal to span/40.

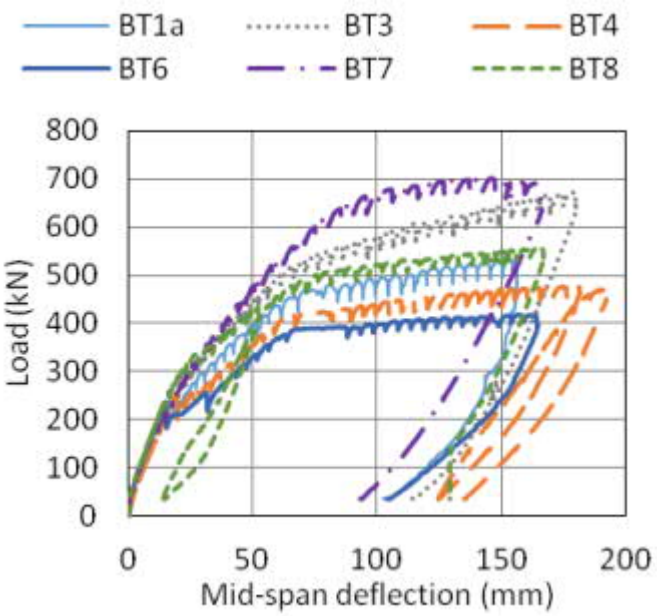

Specimen	Maximum Load (kN)
BT1a	502
BT3	645
BT4	461
BT6	405
BT7	676
BT8	538

Fig. 3.13- Relationship between load and mid-span deflection

Figure 3.14 presents the relationship between the load and the slips between steel and concrete measured at the ends of each beam. The maximum slips for all cases were between 10- 20 mm, values higher than the 6 mm limit defined by Eurocode 4 for ductile shear connectors. The shear connectors, that consisted by the transverse steel bar and the surrounding concrete at each web hole, resisted the relative movement between the concrete plate and the steel beam maintaining the composite action between the two components.

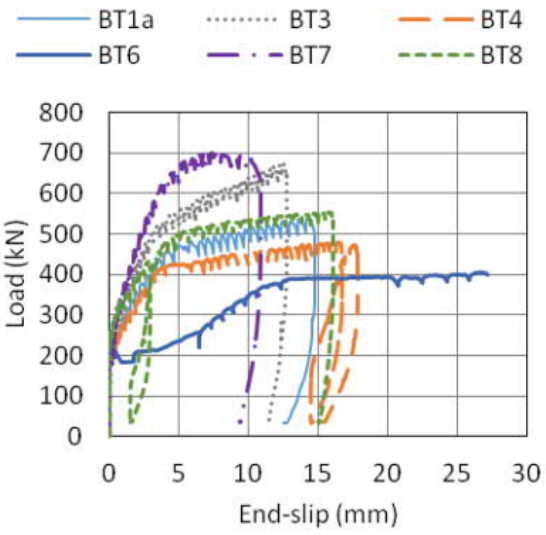

Fig. 3.14- Relationship between load and end-slips

3.5 Service and ultimate behaviour of slim floor beams- An experimental study [26]

In this study, the authors intended to provide new experimental data for the service "long-term" as well as the ultimate behavior of slim floor beams. Two slim floor samples were prepared with identical concrete and steel geometries but following a different loading history. One specimen remained unloaded (SF1) in order to investigate the influence of shrinkage and the other (SF2) was constantly loaded to investigate the influence of creep and shrinkage. The composite cross-section was assembled by a HEB200 steel beam, a steel plate welded under the bottom flange and a concrete T-shaped slab with width equal to 2000 mm. A square welded wire fabric mesh was used over the top plate of the steel beam for top reinforcement, while transverse bars passing through holes opened on the web of the steel part were used to establish the shear connection between concrete and steel (figure 3.15).

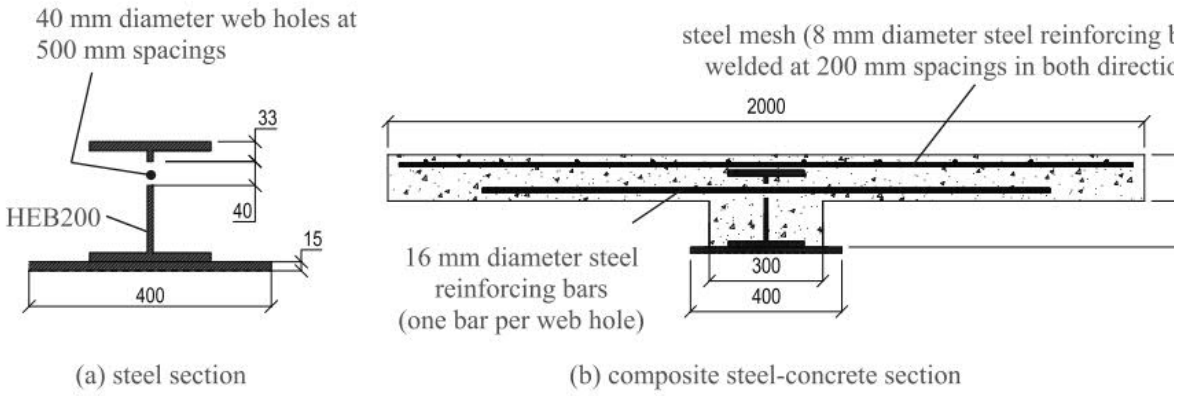

Fig. 3.15- Cross sectional geometry of the slim floor samples

Specimens SF1 and SF2 were monitored for about 10 months. SF1 was not loaded for the entire duration of the "long-term" test. A load of 300 kN was applied on SF2, three months after casting. Before carrying out the bending tests the condition of the specimens was monitored. In the case of SF1 small deflections were observed at the mid-span during the first 3-4 months due to shrinkage (figure 3.16a). After that, a transversal crack at the concrete plate lead to a sudden reduction of the deflection. That deflection value was constant till the end of the monitoring. In the case of SF2, similar behavior was recorded for the first months before the

application of the sustained load. After the application of the load the mid-span deflection increased as expected (figure 3.16b).

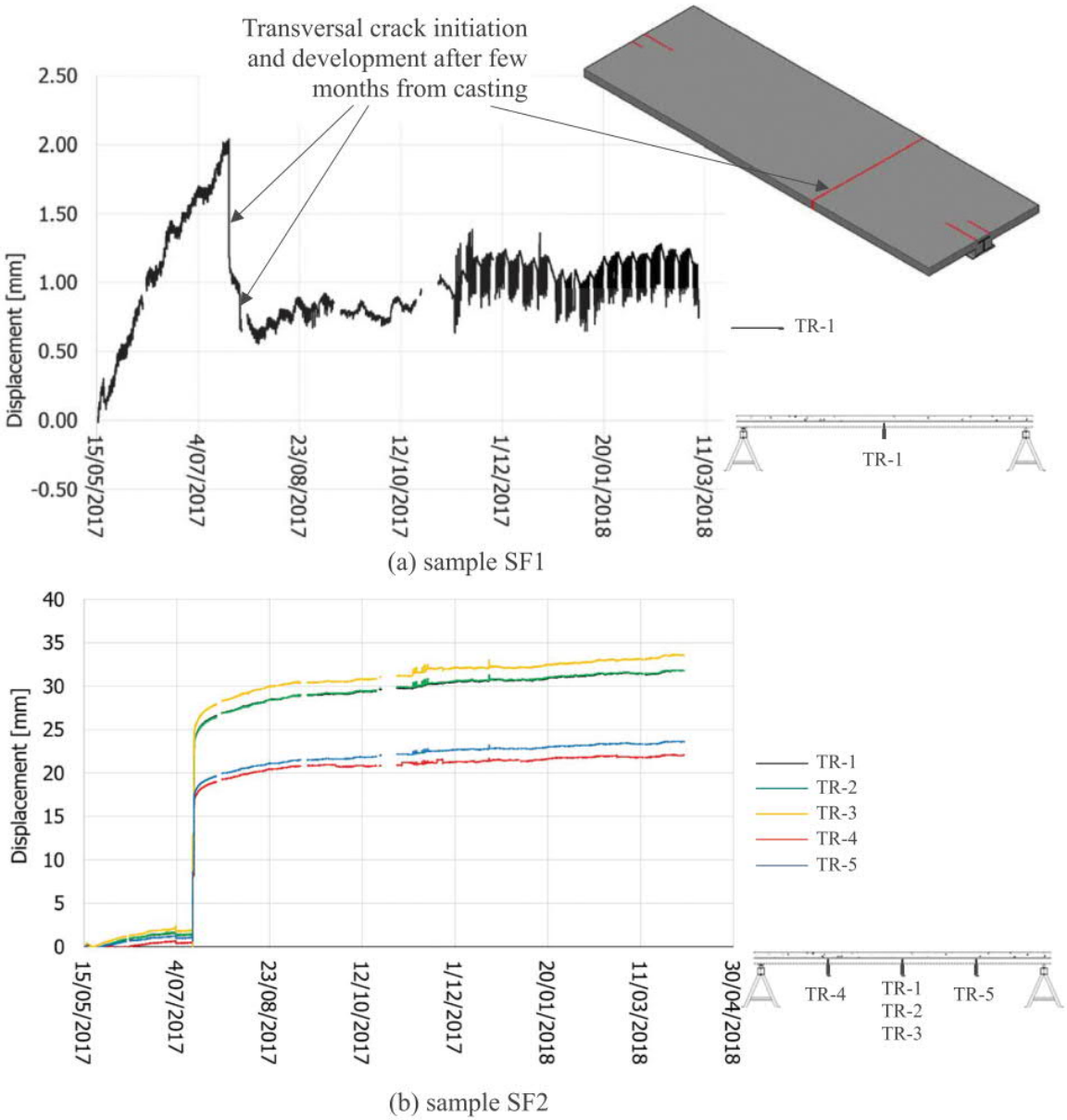

Fig. 3.16- "Long-term" experiment: deflection measurements

After the end of the "long-term" experiment, the flexural behavior of the beams was investigated to failure under a four-point loading configuration (figure 3.17). Both specimens manifested similar behavior during these ultimate tests. The maximum load values for SF1 and SF2 were 536.4 kN and 562.7 kN, respectively. Both specimens demonstrated ductile behavior. The tests were terminated when a softening behavior was observed at the load- deflection curves at a deflection of about 380 mm (figure 3.18).

Fig. 3.17- Test setup

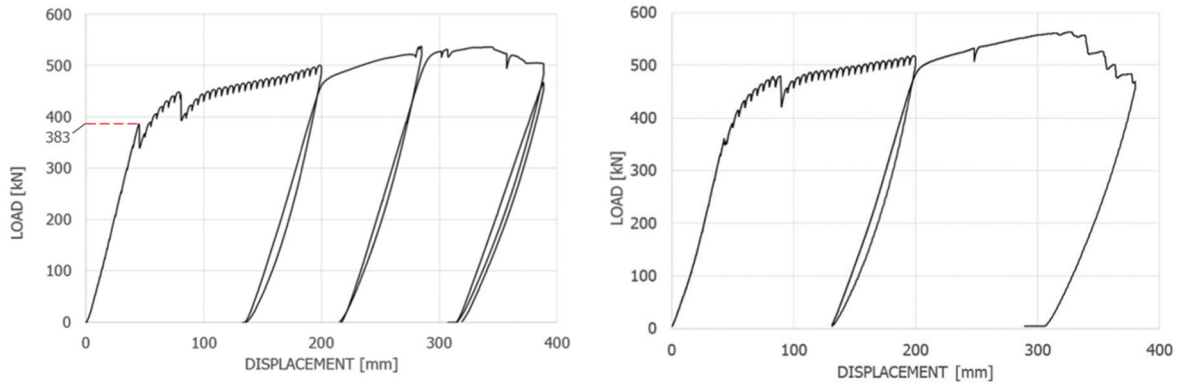

Fig. 3.18- Ultimate experiment: deflection measurements of SF1 (left) and SF2 (right)

Despite the different loading history during the “long-term” experiment, specimens had similar ultimate response, regarding both flexural behavior and failure mode attributed to crushing of the top concrete. The final conclusion drawn was that for this geometry and detailing, the creep effects were not significant.

4

Experimental set-up

4.1 Introduction

Deltabeam is a slim-floor composite beam which took its name by its shape (figure 4.1) and is fully integrated into the floor. Its torsional stiffness is high enough to allow the assembly of heavy elements on the ledges of the bottom plate without extra support. It is designed to be used as structural element combined with all general concrete slab forms: hollow-core slabs, filigree slabs, composite steel decking, trapezoidal steel decking slabs and cast-in-situ concrete slabs (figure 4.2).

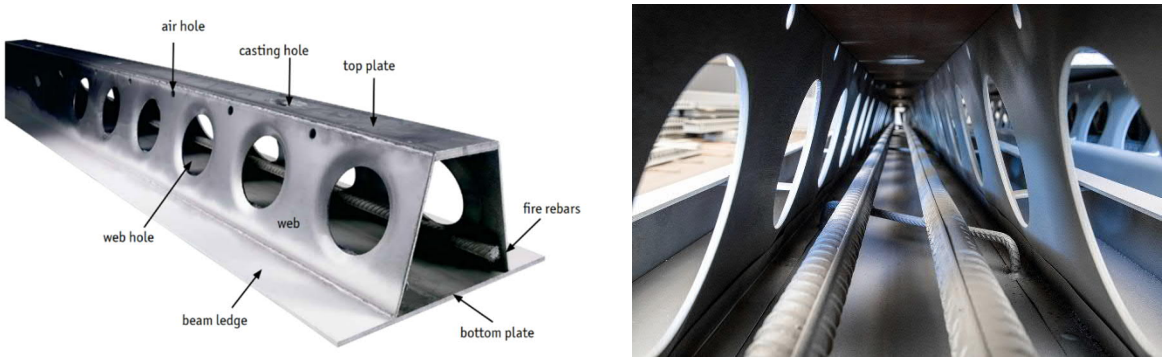

Fig. 4.1- Deltabeam

Deltabeams act as steel beams before the infill concrete has reached the required strength. After placement of the hollow-core slabs or the erection of the in-situ concrete slabs, the beams are completely filled with concrete on-site through regularly spaced web openings, thus forming a composite structure after the concrete has hardened (figure 4.3). The shear resistance of the composite cross-section is considerably higher than that of the steel part because of the

contribution of the core concrete. Experimental test results from the investigation of the shear strength of Deltabeams are reported by Leskela et al. [27].

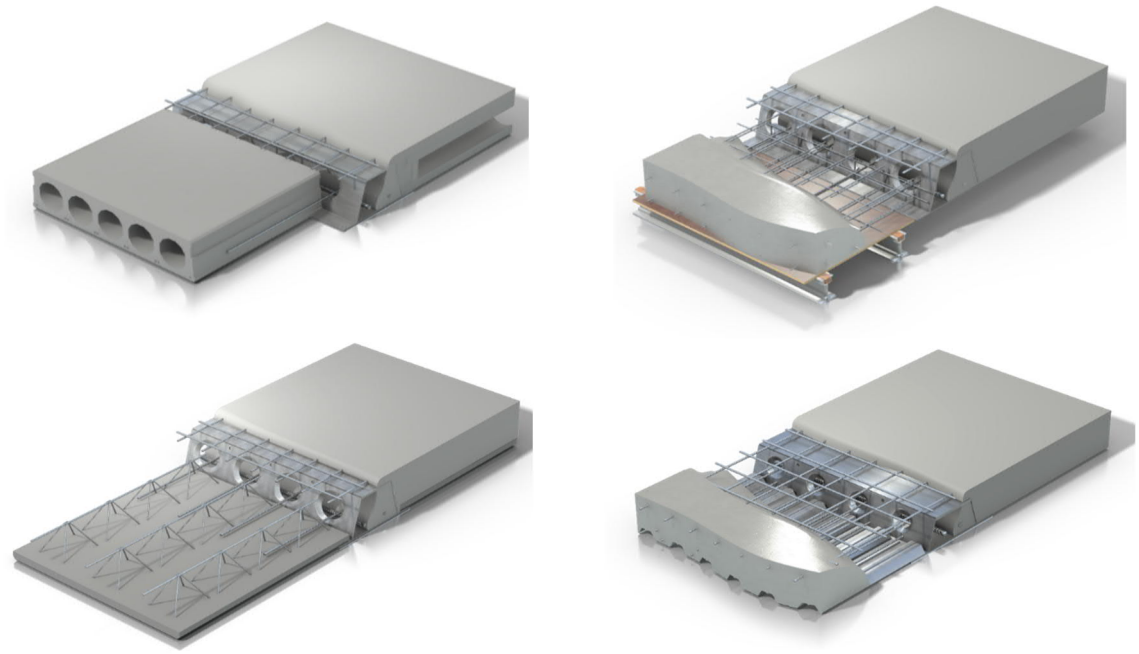

Fig. 4.2- Various slab types combined with Deltabeam

(a) (b)

(c) (d)

Fig. 4.3- Construction stages using Deltabeams

Multiple fire tests [28] have proven Deltabeam to have an excellent fire resistance (rate higher than R180), that depends on the thickness of the bottom plate and the number of fire rebars located inside the boxed core of the beam. The fire rebars compensate the strength loss of the bottom plate, meaning that additional external fire protection is not normally needed (figure 4.1). Deltabeams enable the covering of large open spaces and constitute a most suitable solution for multi-story buildings such as offices, hospitals, schools, hotels, car parks, shopping centers, and residential buildings.

4.2 Scope of the experimental project

Deltabeams can be used as single-span beams or in multi-span beam construction. In multi-span beam construction, Gerber connections are used to connect the beams. Connection of Deltabeams with columns is currently achieved with corbels or with bolts and welds at the top of a column (figure 4.4). In that way, only vertical reactions can be successfully transferred to the vertical structural elements from the beams.

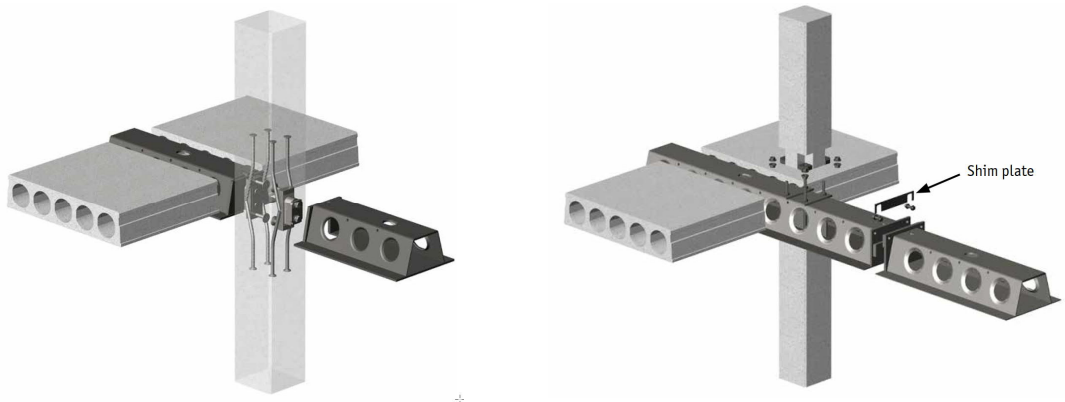

Fig. 4.4- Typical connections of Deltabeams

The scope of the experimental test program is to create a full moment frame that will provide adequate ductility and resistance in order to be used for designs against seismic loads or column loss scenarios. This chapter presents the specifiments used in order to experimentally investigate the positive (sagging) bending resistance of the beams.

4.3 Test specimens

4.3.1 Geometry and details of specimens

The experimental investigation of the response of Deltabeams under sagging bending was carried out at the Institute of Steel Structures of the National Technical University of Athens (NTUA). The specimens were divided in four types regarding the detailing of their section, as given in figure 4.5. With these four types, various parameters, such as, use of different steel profiles, reinforcing details, arrays of shear studs and concrete shapes, were investigated during the experiments. The experimental part of this investigation consists of 13 full scale specimens tested as simply supported beams under 3-point loads. All specimens were 7700 mm long. The distance between the central axis of the supports was 7200 mm.

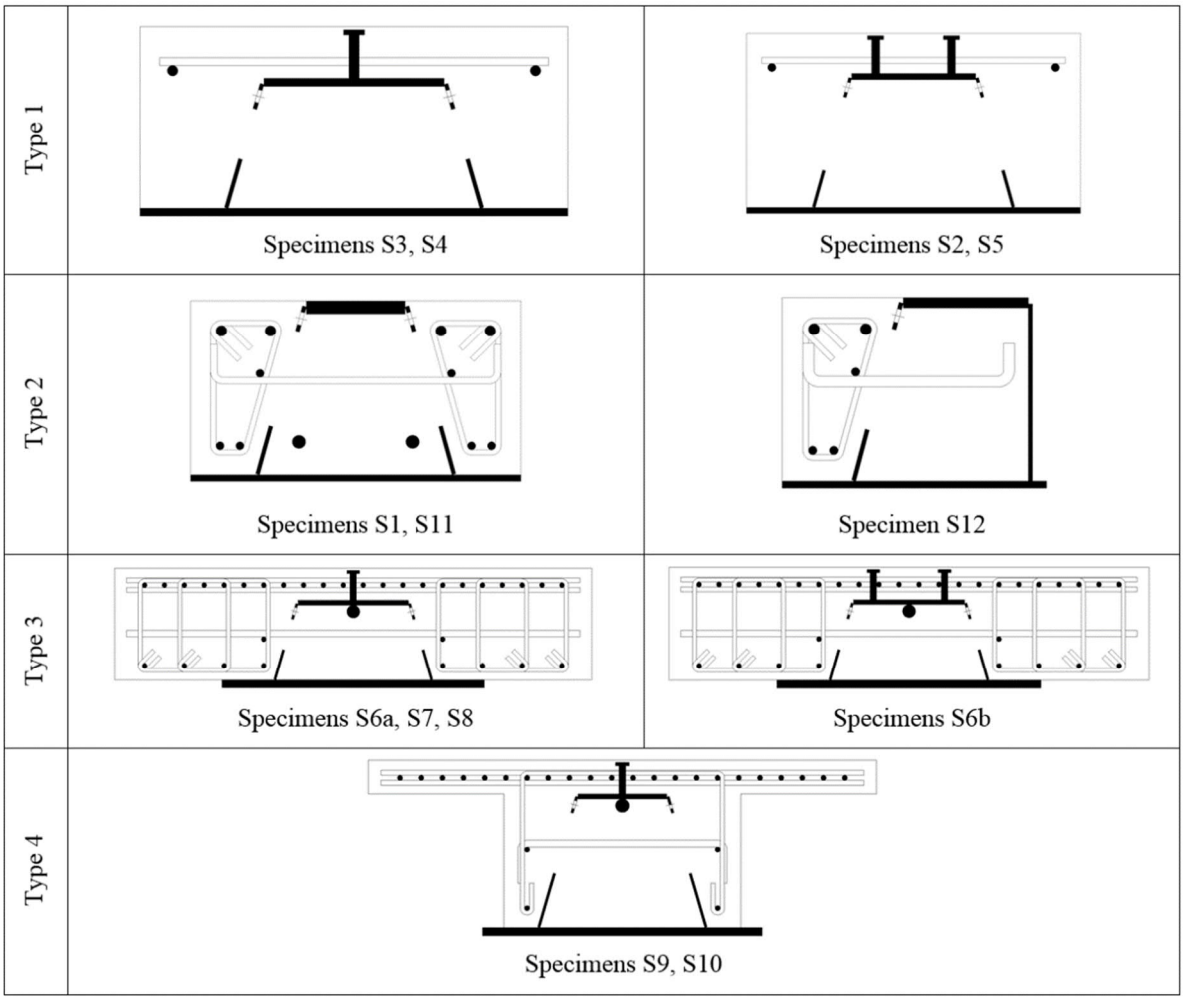

Fig. 4.5- Section types of test specimens

- Type 1 specimens

S2 and S3 specimens have the same steel cross section profile. Their main difference is that S3 has one row of shear studs and S2 has two (figure 4.6). S4 and S5 have also the same steel cross section profile with one and two rows of shear stud respectively. The studs that are used in both beams are M16 per 100 mm. Two transverse bars are placed to the left and right of each stud (figure 4.7). Two longitudinal rebars with diameter of 16 mm support the transverse bars. Also, only S2 has 4 additional fire rebars with diameter 32 mm.

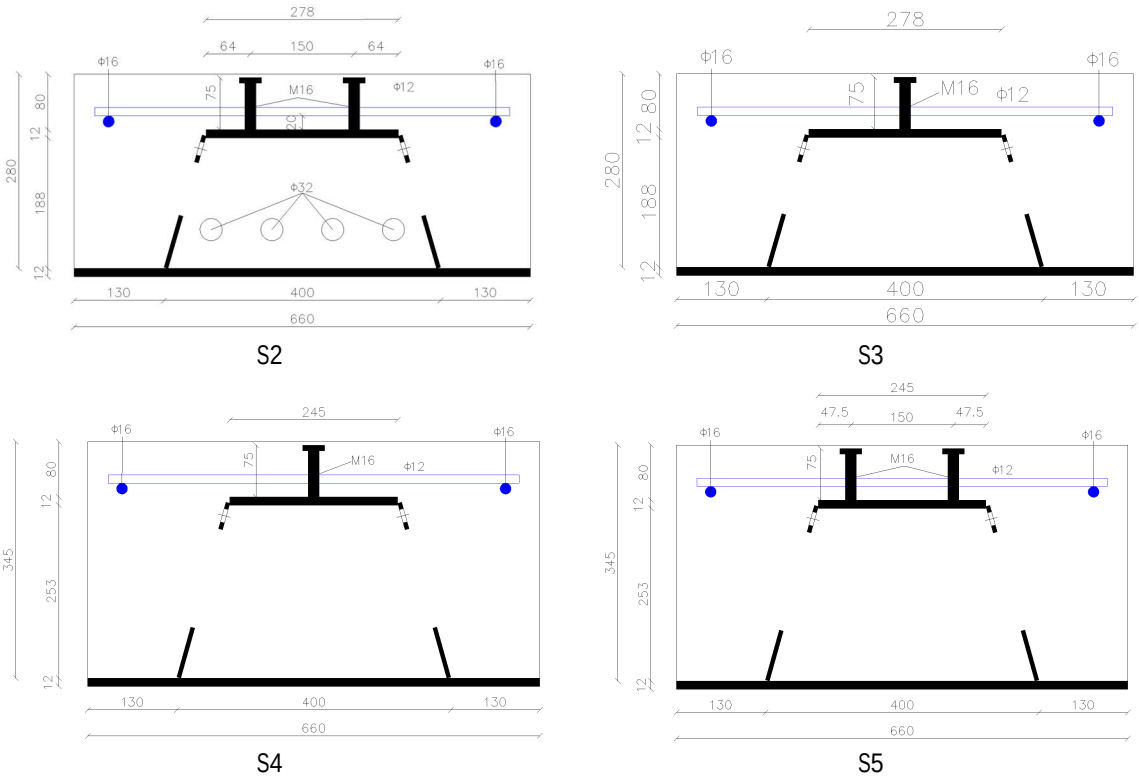

Fig. 4.6- Type 1 cross sections

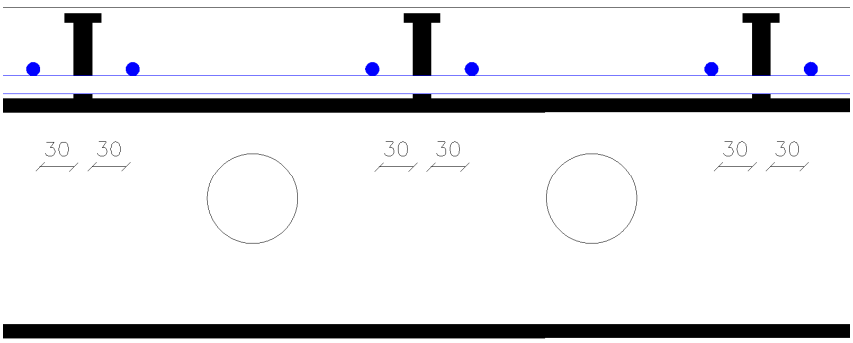

Fig. 4.7- Side view detail of Type 1 specimens

- Type 2 specimens

Type 2 specimens are relatively more heavily reinforced than those of type 1. S1 has four longitudinal rebars with 16 mm diameter at the top, two on each side of the steel cross section. Similarly, S1 has two and S11 has six rebars with the same diameter. At the bottom of the concrete part all specimens have two rebars on each side with 12 mm diameter. It should be noted that S12 is an edge-type Deltabeam, therefore it has concrete only on one side (figure 4.8). Connector bars are placed through the web holes to ensure the shear connection between the steel beam and the concrete. The diameters of the connector bars are 10, 20 and 16 mm for S1, S11 and S12 respectively. One longitudinal bar with 12 mm diameter is used on each side to support the connector bars. Stirrups with 8 mm diameter at 100 mm are used for all specimens of this type. Finally, for S1 and S11 two fire rebars are used. The diameters of the fire rebars for S1 is 20 mm and for S11 is 32 mm.

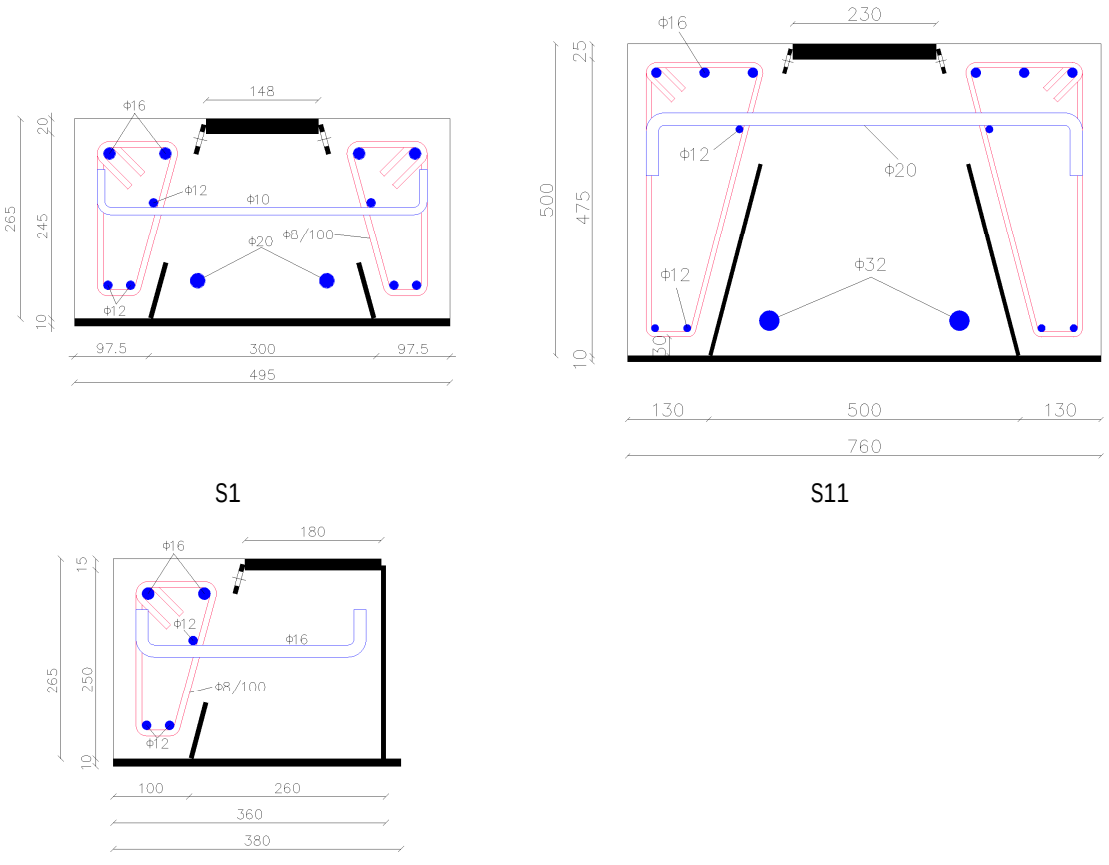

Fig. 4.8- Type 2 cross sections

- Type 3 specimens

Type 3 specimens are the most heavily reinforced specimens. Also, the specimens had a wider concrete part with a width equal to 1200 mm (figure 4.10). The main difference between the beams of this type was the steel cross section profile used, while the detailing of the reinforcement was the same for all specimens. Inside the critical region, a length of 3300 mm at the middle of the span, a bar mesh was placed at the concrete topping above the steel section. The mesh consisted of twenty-two longitudinal rebars and two transverse bars per 100 mm above and below of the longitudinal ones. The diameter of all bars of the mesh was 12 mm. Outside of the critical region the longitudinal rebars were reduced to twelve and only the top transverse bars were retained at 300 mm spacing (figure 4.9). At the bottom of the concrete plate eight longitudinal bars were used. Two stirrups were used at each side of the plate to confine the concrete. The diameter of the stirrups was 10 mm and their distance was 100 mm inside the critical region and 300 mm outside of it. Again, connector bars of 16 mm diameter were used to establish the shear connection between the concrete and the steel beam. To enhance the shear connection also M16 shear studs were used. The distance between the central axis of the studs was 100 mm and 300 mm for the critical and non-critical region respectively. Beams S6a and S6b differed in the number of shear studs' rows, with S6a having one and S6b two rows, respectively. Finally, a rebar with 32 mm diameter was welded at the bottom surface of the top plate along the critical region in order to avoid local buckling phenomena due to compression.

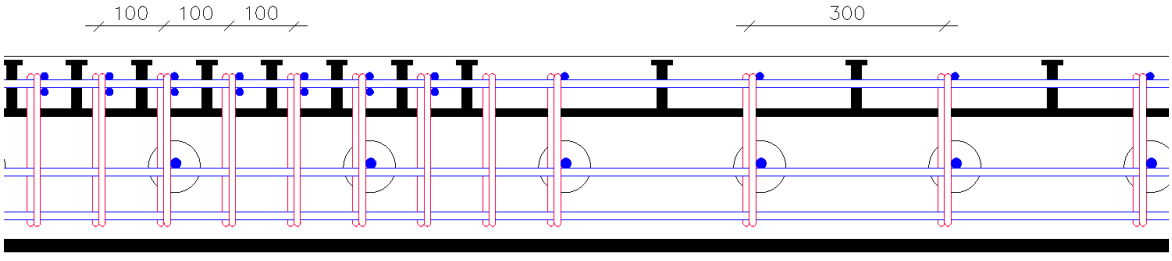

Fig. 4.9- Side view detail of Type 3 specimens

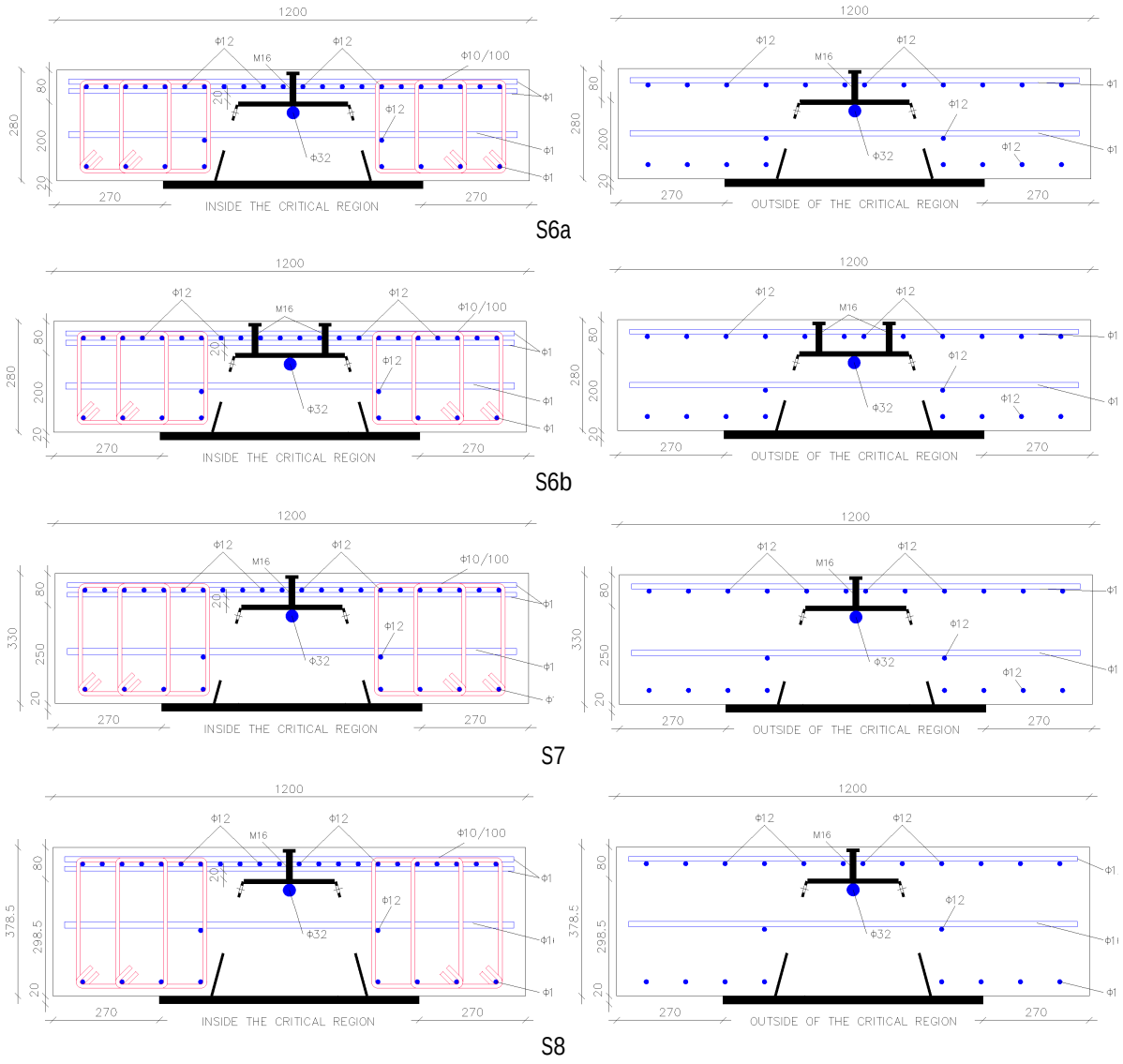

Fig. 4.10- Type 3 cross sections

- Type 4 specimens

Type 4 specimens were a “modified” version of type 3 beams. The main difference was the shape of the concrete plate (figure 4.11). The reason of this change was to make a beam capable to collaborate with precast concrete plate elements. The rebar mesh at the topping was the same with the previous type. Open stirrups were used in these two specimens. The diameter of the stirrups was 10 mm and their distance was 100 mm inside the critical region and 300 mm outside of it. The connector bars were also modified due to the lack of anchorage space. The diameter of the bars was 16 mm. M16 shear studs were welded at the top plate as well. Finally, a rebar with 32 mm diameter was welded at the bottom surface of the top plate along the critical region.

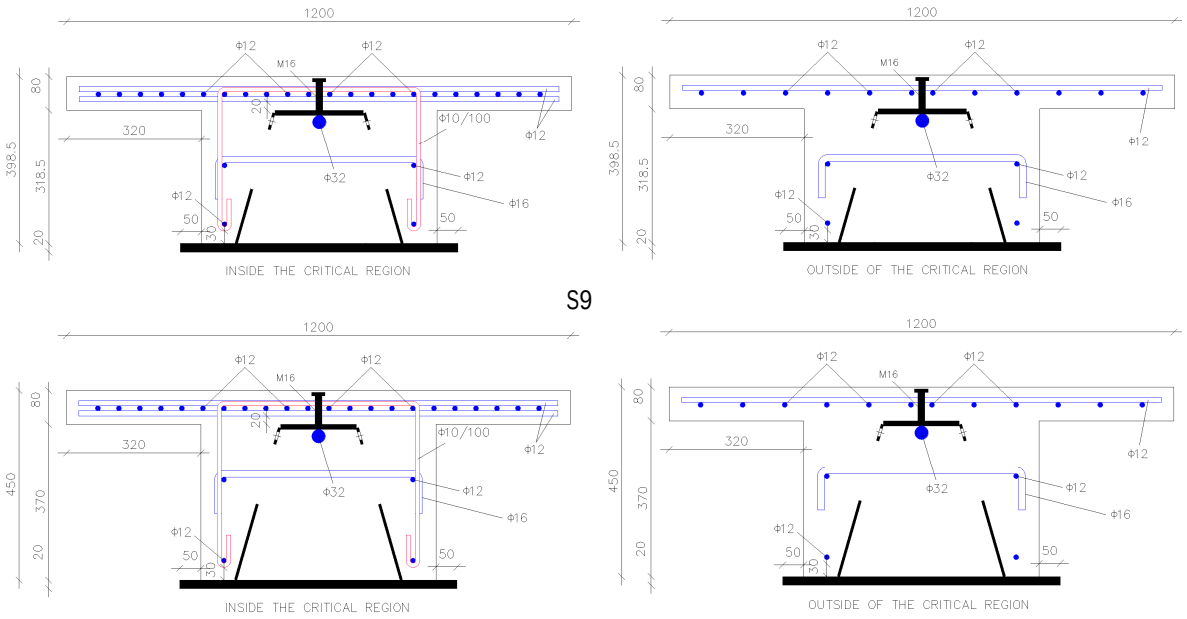

Fig. 4.11- Type 4 cross sections

In Table 4.1 the geometric dimensions of the steel profiles are presented.

Table 4.1- Dimensions of steel sections

Specimens	Delta beam	t_{fb}	b_{fb}	t_{ft}	b_{ft}	h	Cross section type
		(mm)					
S1	D26-300-20-10	10	495	20	148	265	Type 2
S2	D20-400-12-12	12	660	12	278	200	Type 1
S3	D20-400-12-12	12	660	12	278	200	Type 1
S4	D26-400-12-12	12	660	12	245	265	Type 1
S5	D26-400-12-12	12	660	12	245	265	Type 1
S6a	D20-400-12-20	20	660	12	278	200	Type 3
S6b	D20-400-12-20	20	660	12	278	200	Type 3
S7	D25-400-12-20	20	660	12	255	250	Type 3
S8	D30-400-12-20	20	660	12	230	300	Type 3
S9	D32-400-12-20	20	660	12	210	320	Type 4
S10	D37-400-12-20	20	660	12	180	370	Type 4
S11	D50-500-25-10	10	760	25	230	500	Type 2
S12	DR26-260-15-10	10	380	15	180	265	Type 2

4.3.2 Thickness measurements of Deltabeams

The thickness of all Deltabeams was measured in order to verify the actual plate thickness and was compared with the nominal values. Each Deltabeam was composed of four plates, one upper flange, one bottom flange and two webs. Accordingly, the plate thicknesses were measured at various positions across and along the plates. Table 4.2 presents average values of the measured thicknesses.

Table 4.2- Measured thicknesses of steel sections

Specimens		Plate thickness (mm)							
		t_1	$t_{1,nom}$	t_2	$t_{2,nom}$	t_3	$t_{3,nom}$	t_4	$t_{4,nom}$
S1	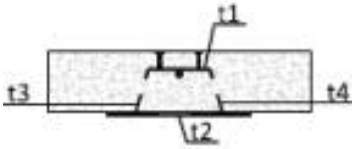	20.06	20	10.07	10	6.05	6	6.05	6
S2		12.06	12	12.07	12	5.99	6	6.02	6
S3		12.40	12	12.05	12	5.98	6	5.98	6
S4		12.30	12	12.20	12	6.05	6	6.05	6
S5		12.07	12	10.55	12	6.00	6	6.01	6
S6a		12.81	12	20.46	20	6.02	6	6.11	6
S6b		12.62	12	20.87	20	6.06	6	6.03	6
S7		12.81	12	20.69	20	6.10	6	6.15	6
S8		12.89	12	20.73	20	6.15	6	6.15	6
S9		12.84	12	20.48	20	6.11	6	6.20	6
S10		12.58	12	20.80	20	6.07	6	6.13	6
S11		25.05	25	10.39	10	6.07	6	6.06	6
S12		15.54	15	10.08	10	6.10	6	6.30	6

4.4 Preparation of test specimens

Deltabeams delivered at the laboratory included the fire reinforcement within the steel box (figure 4.12). All other reinforcement and the formwork were erected in the Laboratory (figure 4.13). Subsequently, the specimens were concreted during one day (figure 4.14-4.15). The delivery and the tests were divided into two series. The first one was parted by S1, S2, S3, S4, S5 and S12 and the second one with the remaining specimens S6a, S6b, S7, S8, S9, S10 and S11.


Fig. 4.12- Arrival of the specimens at the laboratory


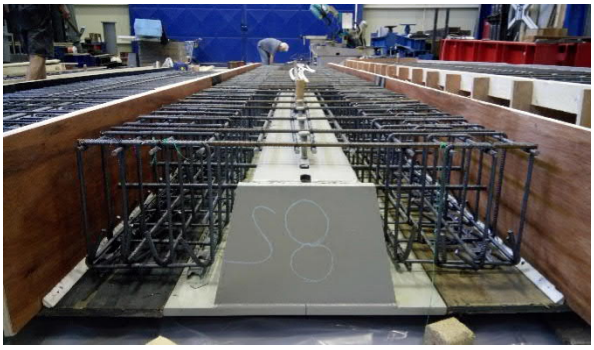

Fig. 4.13- Placement of the formwork and the reinforcement


Fig. 4.14- Concreting of specimens


Fig. 4.15- Vibration of concrete

4.5 Material properties

4.5.1 Structural steel

The delivery of the test beams was accompanied by material certificates provided by the producers of the steel material. The certificates included the chemical composition and the mechanical properties of the test specimens and they were corresponding to each different steel coil used to fabricate the steel beams. Tables 4.3 and 4.4 depict the mechanical properties of the structural steel material used for the Deltabeam boxes as extracted from the certificates for the first and second series respectively.

Table 4.3- Mechanical properties of the structural steel of the first series of specimens

Plate thickness (mm)	Grade to EN 10025 [29]	Yield stress f_y (MPa)	Tensile strength f_u (MPa)	Elongation at failure ε_u (%)
6	S 355J2 + N	408	533	28.1
10	S 355J2 + N	432	560	27.2
15	S 355J2 + N	391	530.5	25
20	S 355J2 + N	430.5	530	25

Table 4.4- Mechanical properties of the structural steel of the second series of specimens

Plate thickness (mm)	Grade to EN 10025	Yield stress f_y (MPa)	Tensile strength f_u (MPa)	Elongation at failure ε_u (%)
6	S 355J2 + N	410.4	537	28.3
10	S 355J2 + N	372.5	536	33.5
15	S 355J2 + N	428.5	553.8	26
20	S 355J2 + N	382.3	535.2	27.8
25	S 355J2 + N	370	489	37

4.5.2 Fire reinforcement bars

The mechanical properties of the fire reinforcement were provided by the accompanying certificate and are given in Tables 4.5 and 4.6. The actual properties comply with the relevant Eurocode provisions for reinforcing steel.

Table 4.5- Mechanical properties of the fire reinforcement of the first series of specimens

Diameter ø (mm)	Grade to EN 10025	Yield stress f_y (MPa)	Tensile strength f_u (MPa)	Elongation strain at maximum force A_{gt} (ε_u %)
20	B500B	563	654	11.1
32	B500B	586	690	10.3

Table 4.6- Mechanical properties of the fire reinforcement of the second series of specimens

Diameter ø (mm)	Grade to EN 10025	Yield stress f_y (MPa)	Tensile strength f_u (MPa)	Elongation strain at maximum force A_{gt} (ε_u %)
32	B500B	625	732	14.6

4.5.3 Other reinforcement

The mechanical properties of the longitudinal reinforcement outside the steel box and the transverse bars were determined by testing at the laboratory. The tensile tests have been performed in the universal testing machine type INSTRON 300LX. The test set-up is shown in figure 4.16. The tests were carried out in accordance with ISO 6892 [30] and ISO 15630-1 [31]. The results of the tensile tests are presented in figure 4.17 and Table 4.7.

Fig. 4.16- Set-up for the tensile tests of the bars

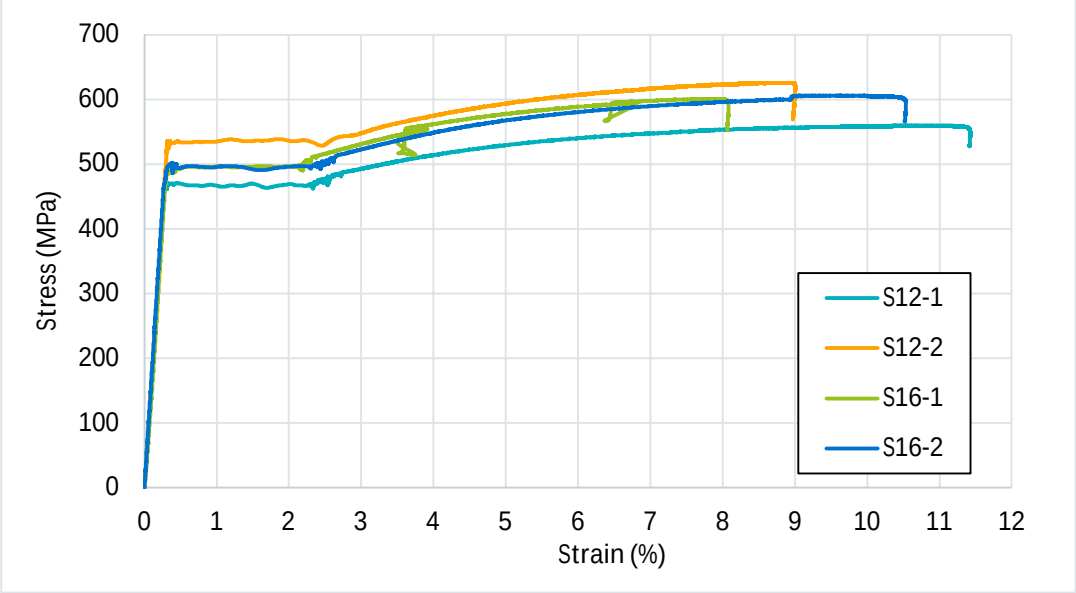

Fig. 4.17- Results of the tensile tests

Table 4.7- Mechanical properties of the reinforcement bars

Diameter ø (mm)	Grade to EN 10025	Yield stress f_y (MPa)	Tensile strength f_u (MPa)	Elongation strain at maximum force A_{gt} (ε_u %)
12	B500B	549.42	642.79	10.73
16	B500B	522.91	631.20	10.80

4.5.4 Shear studs

Shear studs were used according to EN ISO 13918 [32]. The mechanical properties of the studs in the test specimens, as provided by the accompanying certificate, issued according to DIN EN 20024/3.1, are given for both series of specimens in Table 4.8.

Table 4.8- Mechanical properties of the shear studs

Yield stress f_y (MPa)	Tensile strength f_u (MPa)	Elongation at failure ε_u (%)
459	484	21

4.5.5 Concrete

Concrete was of nominal grade C30/37 according to EN 1992-1-1. It was delivered to the Laboratory by two concrete mixers per series of specimens. From each mixer three cylindrical

specimens (Φ15/30), in total six (6), were taken at the day of concreting (figure 4.18). The specimens were then cured in accordance with EN 12390 [33] and at 28 days subjected to compression test (figure 4.19- 4.20). The resulting compressive strength is shown in Tables 4.9 and 4.10.

Table 4.9- Concrete compressive tests of the first series of specimens

No	Diameter (mm)	Height (mm)	Mass (g)	Force P (kN)	Strength f_c (MPa)
1	149	294	12754	546	30.9
2	149	291	12602	608.6	34.4
3	149	294	12757	558	31.6
4	149	289	12350	745	42.2
5	149	291	12515	626	35.4
6	149	288	12824	758	42.9
			Average value		36.23

The average value of the measured concrete strength is 36.23 MPa and the standard deviation 5.18 MPa.

Table 4.10- Concrete compressive tests of the second series of specimens

No	Diameter (mm)	Height (mm)	Mass (g)	Force P (kN)	Strength f_c (MPa)
1	149	290	12521	638.9	36.64
2	149	293	12566	702.2	40.27
3	149	293	12350	691.7	39.67
4	149	291	12529	708	40.61
5	149	290	12789	700.4	40.17
6	149	289	12755	619	35.50
			Average value		38.81

Fig. 4.18- Creating the cylindrical specimens

Fig. 4.19- Preparation of the concrete specimens for the tests

Fig. 4.20- Compression tests of the concrete specimens

4.6 Test set-up

The experimental set-up consists of the test reaction frame, a computer controlled hydraulic actuator and the test specimens. The test rig, available in the Steel Structures Laboratory of NTUA, was appropriately modified to receive the test specimens. The description of the test rig is divided into two parts; the main steel frame and the supports.

4.6.1 Reaction frame

The reaction steel frame consists of four large columns HE 600M resting on the strong floor of the Laboratory that are connected in both directions by rolled and built-up steel beams (figure 4.21). Four HE 600M are used along the direction of the specimens and four double U400 along the transversal one.

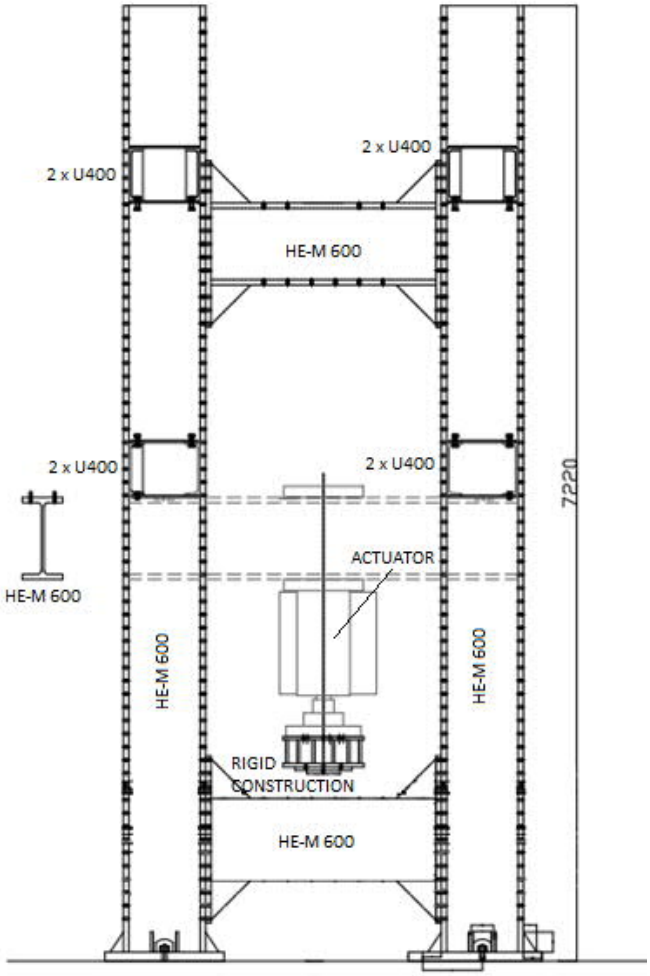

Fig. 4.21- Reaction steel frame of the test set-up

4.6.2 Specimen supports

4.6.2.1 Details and geometry

The supporting conditions should represent “hinged” supports, free of longitudinal restrain. The supports were accordingly specifically designed and fabricated for these tests (figures 4.22-4.23). They should:

- provide a rigid vertical support along the entire specimen’s width
- allow the free development of end rotations
- allow free longitudinal sliding of the specimen
- be used for all specimens heights without moving of the actuator

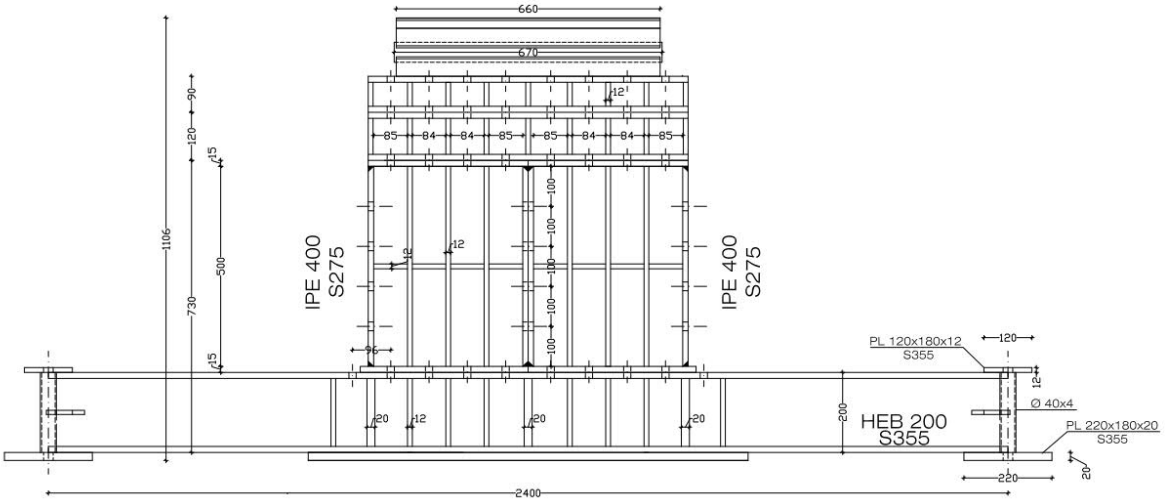

Fig. 4.22- Elevation of the support

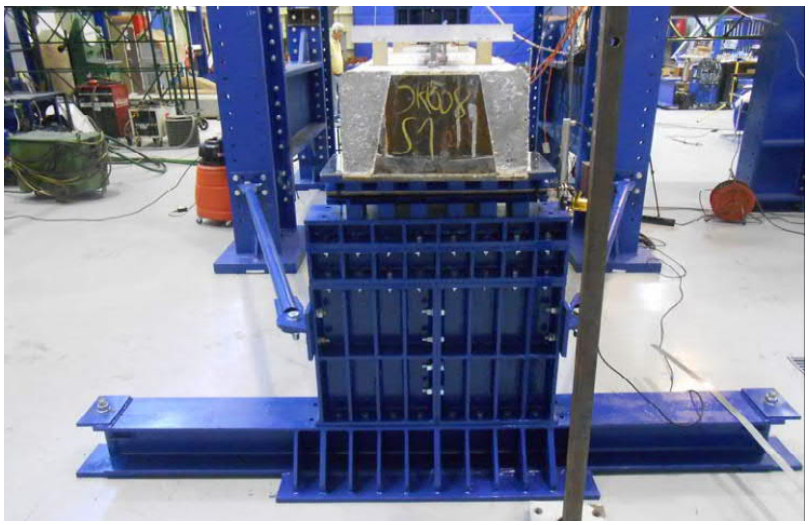

Fig. 4.23- Support structure

Accordingly, the supports consisted of a rigid stiffened steel structure anchored at the strong floor. Free rotation of the specimens was allowed by a steel cylinder located between two semi-circular guides, with free gliding allowed, through the provision of a stainless-steel plate resting on teflon (figures 4.24-4.25).

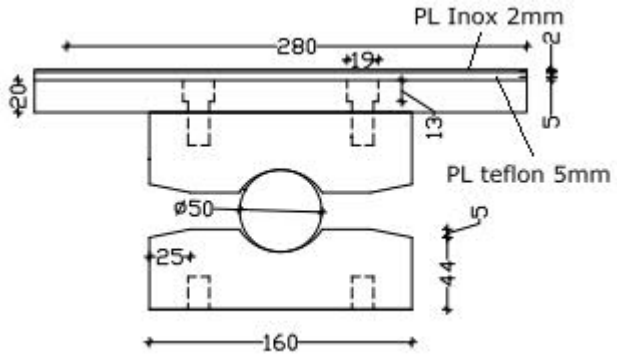

Fig. 4.24- Details of the hinge

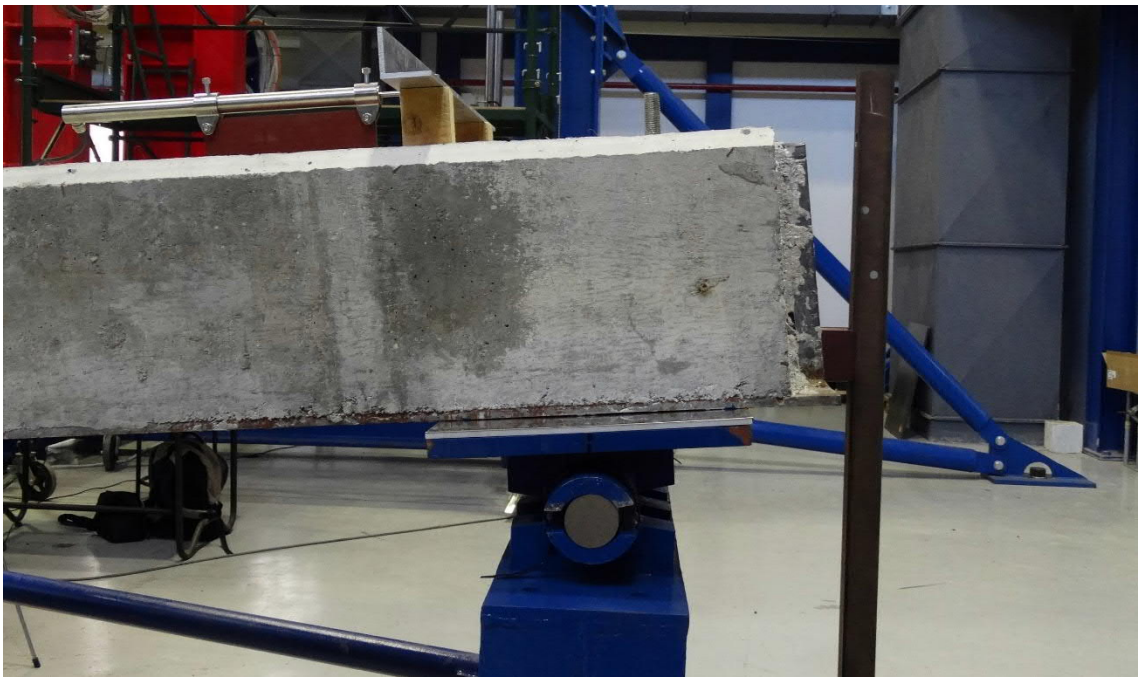

Fig. 4.25- Details of the hinge

The support construction was restrained in the longitudinal direction by two horizontal braces (figures 4.26-4.27). The width of the end supports was such that the actual length of the test specimen from support-to-support axis was 7200 mm.

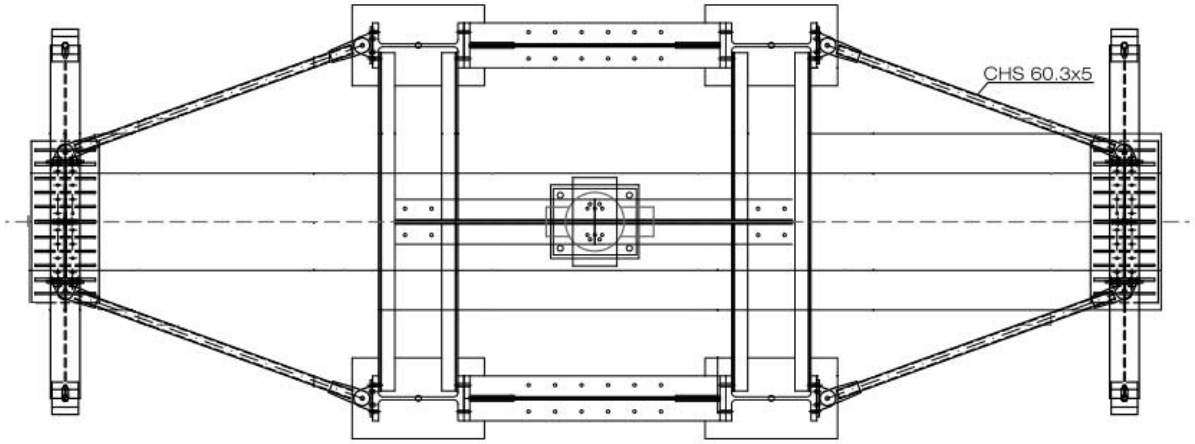

Fig. 4.26- Plan view of the set-up

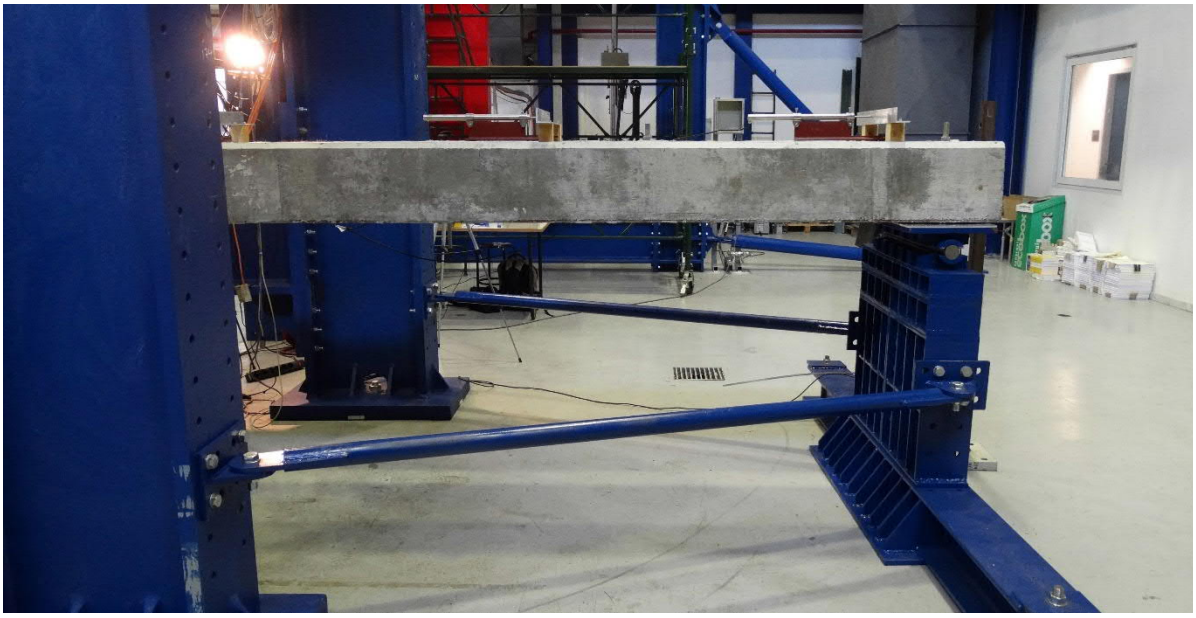

Fig. 4.27- Horizontal braces

4.6.2.2 Analytical investigation

An analytical investigation of the hinge's behavior was conducted using the Abaqus FEA software. The hinge stresses and deformation were checked in combination with the biggest and smallest Deltabeams. In figure 4.28 some views of the FE model can be seen. In figures 4.29 and 4.30 the Von Mises stresses and the deformation of hinge's diameter are presented respectively.

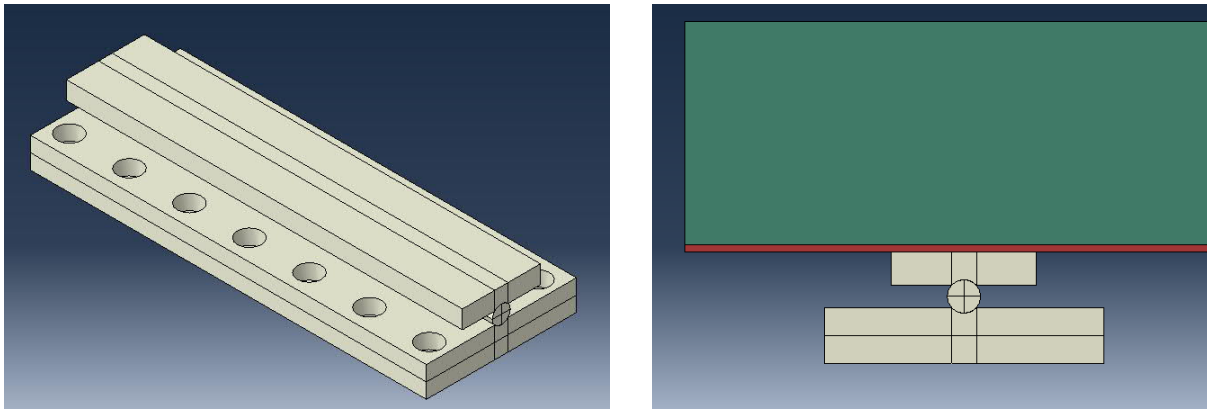

Fig. 4.28- Views of the model

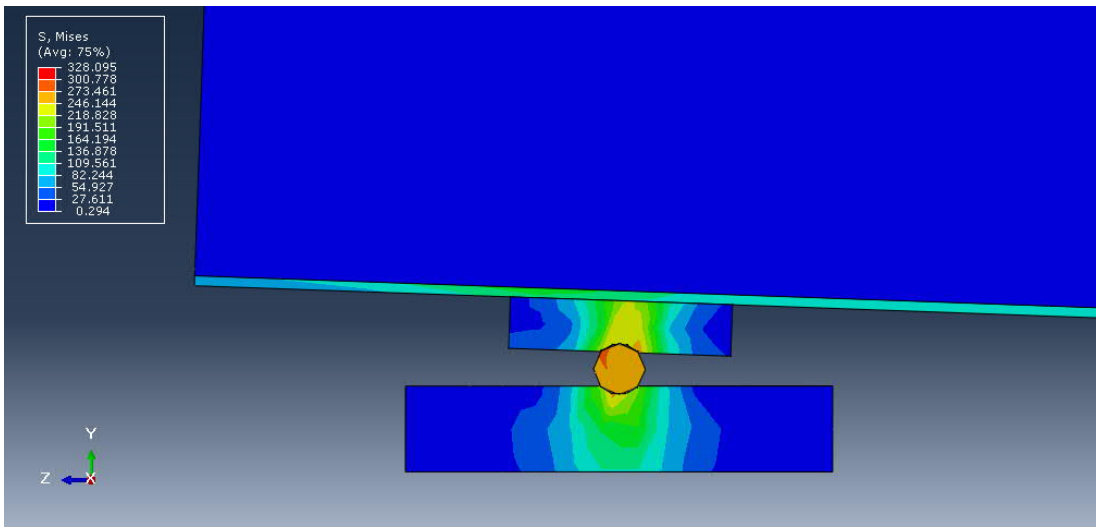

Fig. 4.29- Von Mises stresses on the hinge

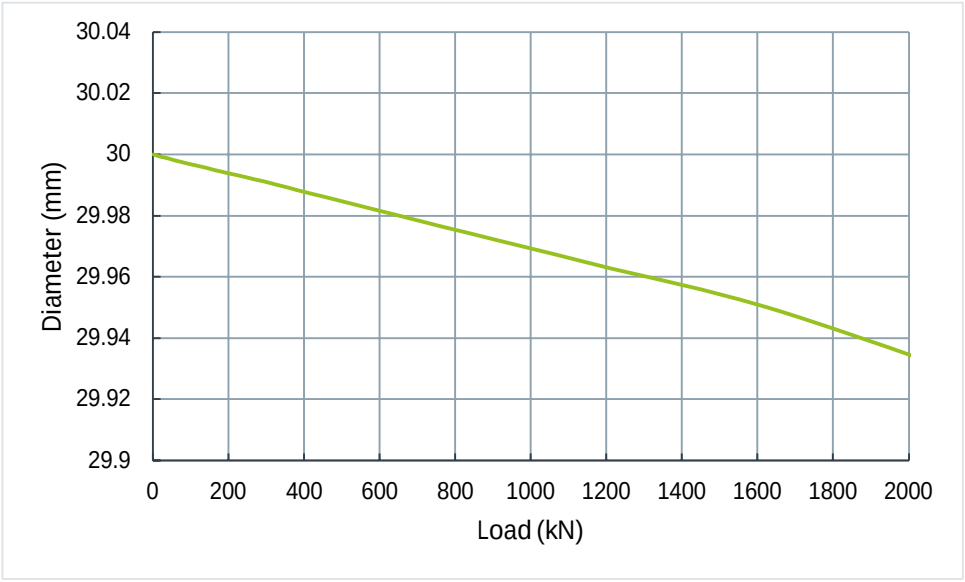

Fig. 4.30- Deformation of hinge's diameter

4.6.3 Loading actuator

The actuator is a computer controlled hydraulic cylinder with a load capacity of 2.500 kN and a maximum stroke of 500 mm positioned vertically on a rigid beam. The load was introduced to the specimen by means of a rigid loading element (figure 4.31). The dimensions of the contact area between the rigid load introduction and the specimen were 250 x 350 mm in the longitudinal and transverse direction, accordingly.

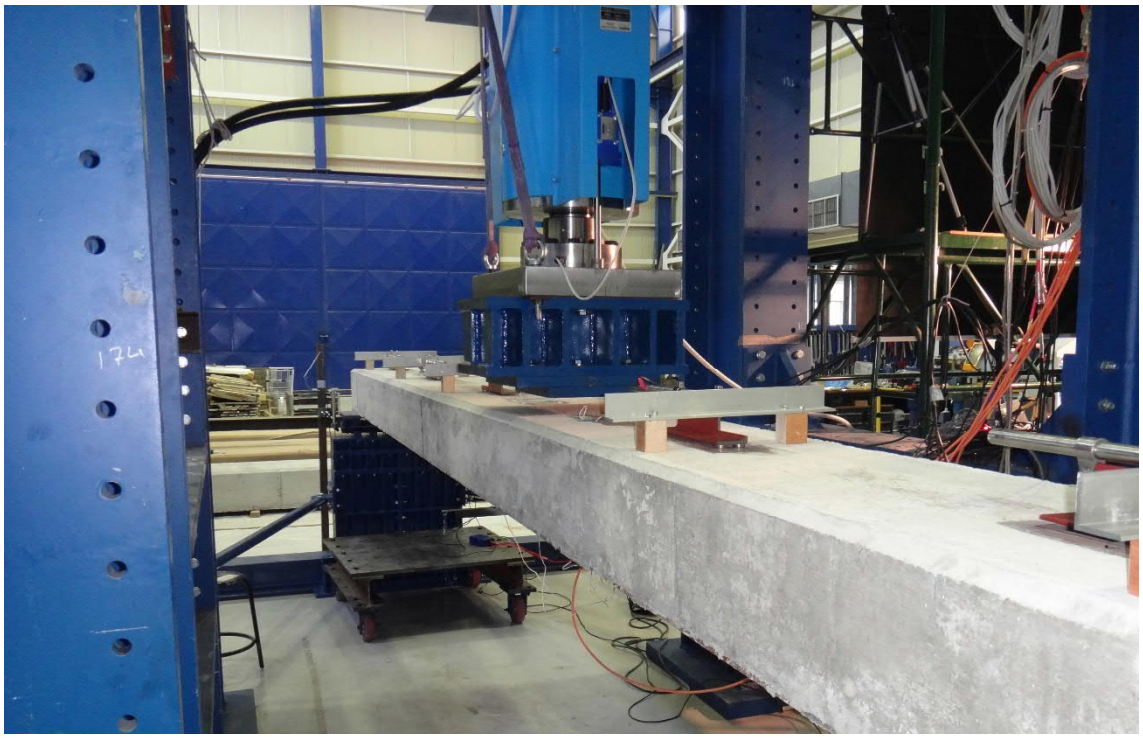

Fig. 4.31- Rigid block at the bottom of the loading actuator

4.7 Experimental measurements

4.7.1 General

The experimental measurements included deflection, strain and slip measurements. Additionally, rotations at two cross sections were measured. All measurements, including the equipment applied, are described in the following. It should be said that the recordings of all instruments were set to zero (0) immediately before the start of the loading protocol, therefore, all measurements do not include the effects of the self-weight of the test beams and include only the effects of the applied concentrated load.

4.7.2 Deflections at mid-span and at supports

An aluminum bar from angle section was placed transversely to the specimen at mid-span and supported by magnets to the specimen's steel flange (figure 4.32). This was the top flange for specimens S1, S11 and S12 and the bottom flange for specimens with topping. The deflections on both sides of the specimens at mid-span were measured by transducers resting on the floor that were connected to this transverse angle. The total rotation of the beams was measured with two inclinometers (figure 4.33).

Fig. 4.32- Wires for the measurement of deflection at the mid-span

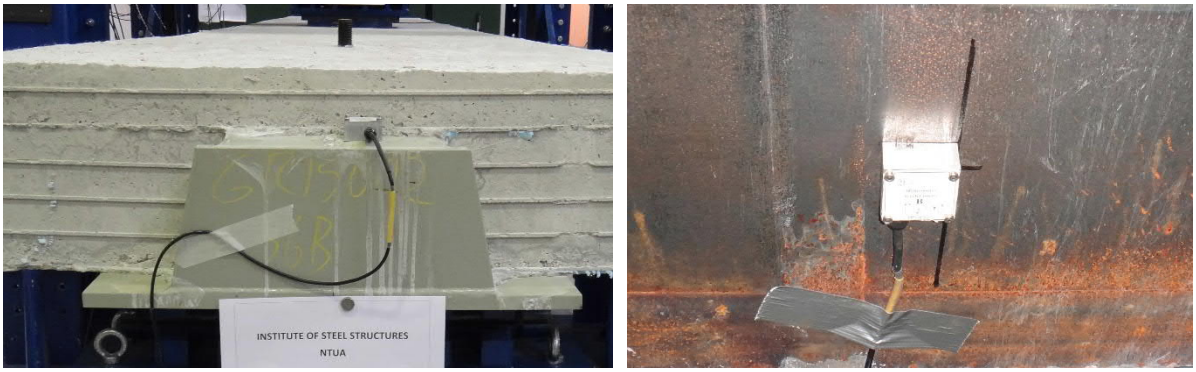

Fig. 4.33- Inclinometers at the end (left) and bottom (right) plates

4.7.3 Strain measurements of the steel flanges

Strains of the steel flanges were measured in sections A and B on either sides of the loaded area, at a relative distance of 700 mm from the load (figure 4.34). Strains were measured at two positions of the flanges for specimen S1, S11 and S12, i.e. 8 measurements, where there was access to both flanges, whereas, for the remaining specimens, only at three positions of the bottom flanges to which there was access, i.e. 6 measurements (figures 4.34-4.35).

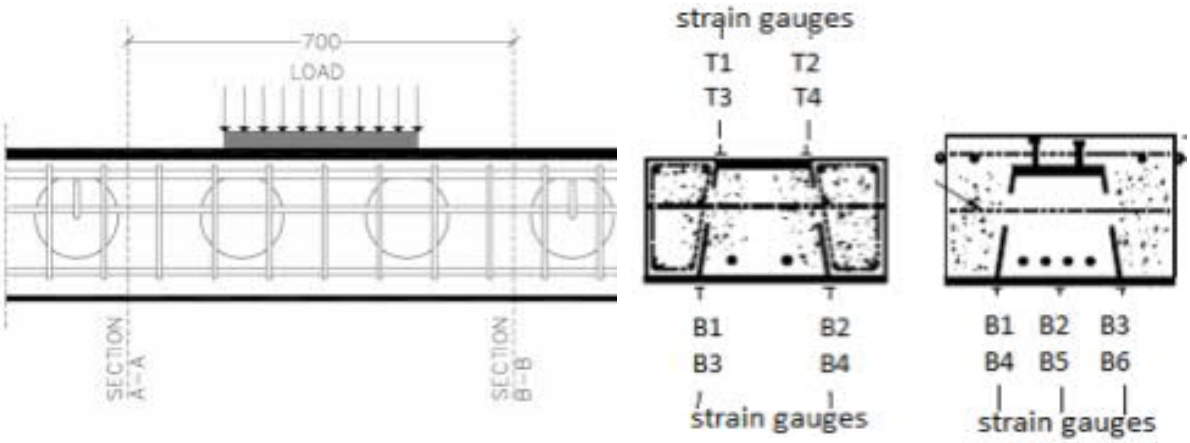

(a) (b)

Fig. 4.34- Strain measurements in longitudinal (a) and transverse (b) direction

Fig. 4.35- Strain gauges at the top (left) and bottom (right) plates

4.7.4 Strain measurements of the concrete

Compressive strains of the concrete were measured in the loaded area at a gauge length of 700 mm. The measurements were performed by LVDTs between aluminum angles that were fastened 40 mm below the top surface of the concrete (figure 4.36).

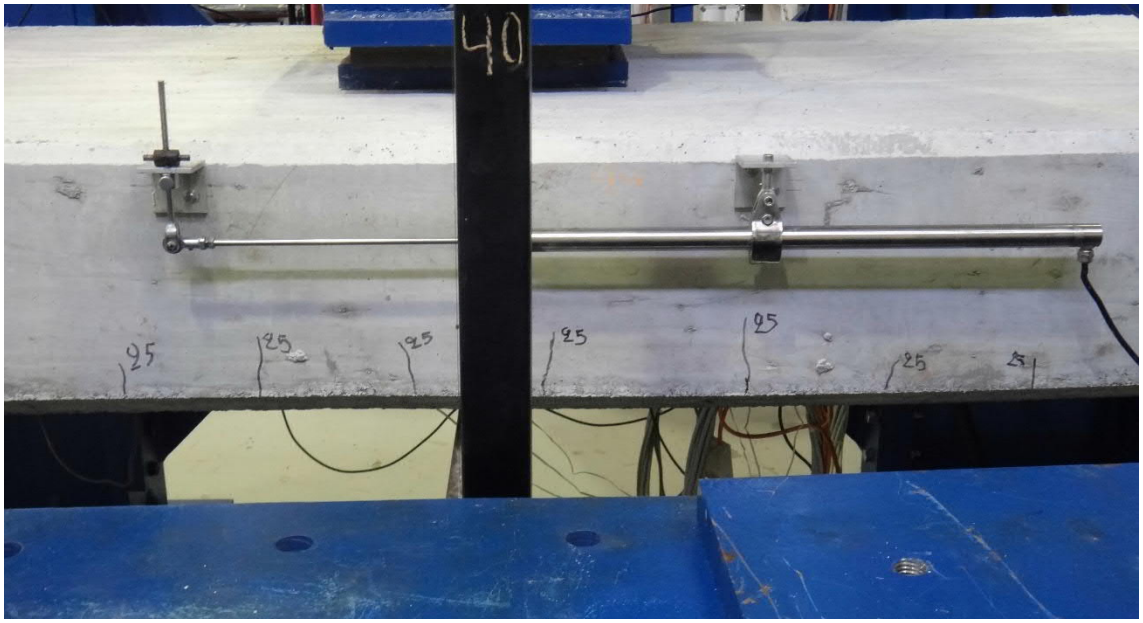

Fig. 4.36- Strain measurements of concrete in the loaded area

4.7.5 Slip measurements between steel beam and concrete

Slip between concrete and steel beams were measured at six sections, three on each side of the specimen, coincident with the positions of the holes at the webs of the box (figure 4.37).

Subsequently steel angles were mounted by magnets at exactly the same position as the aluminum angles. Slip was measured by LVDTs which were fasten to the steel angles and were connected to the aluminum bars (figure 4.38).

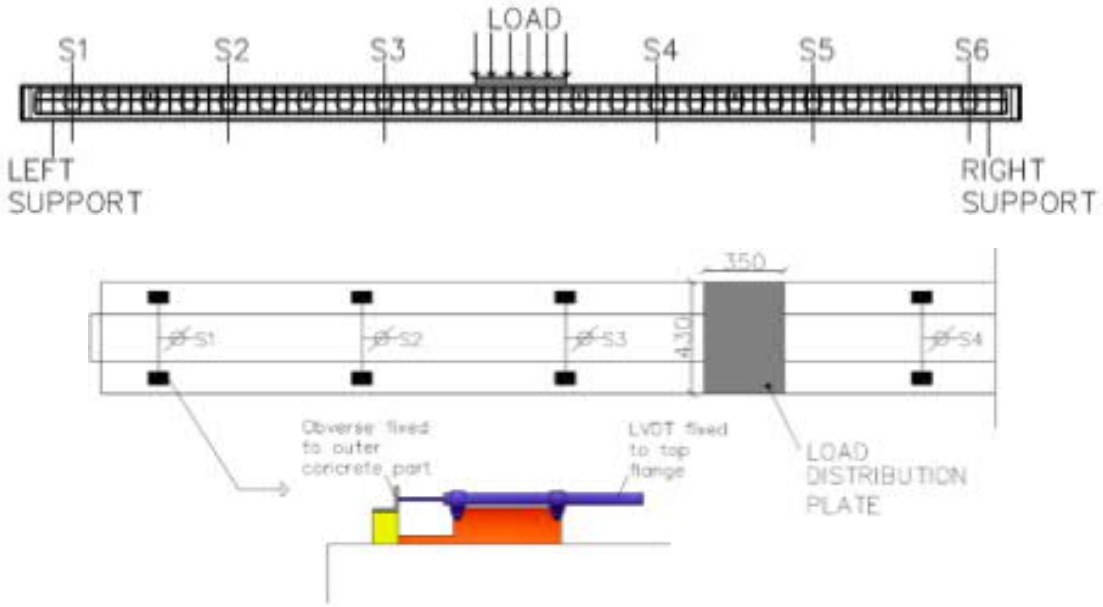

Fig. 4.37- Position of instruments for slip measurements

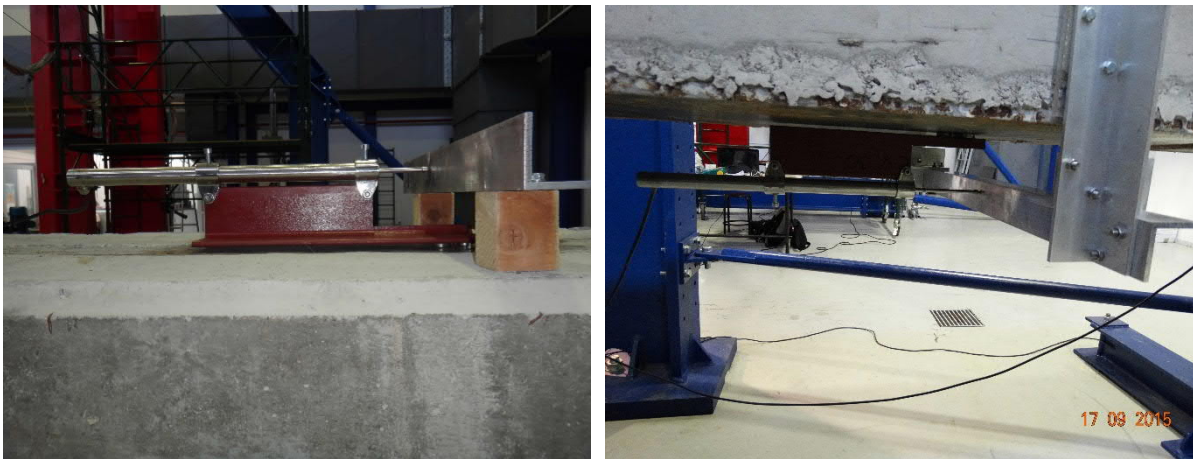

Fig. 4.38- Slip measurements between steel part and concrete

4.8 Loading procedure

Two (2) loading protocols were used for the tests. Loading protocol 1 was applied at specimens S1, S2, S3, S4, S5, S6a and S12 and loading protocol 2 at specimens S6b, S7, S8, S9, S10 and S11. Loading was imposed displacement controlled.

- Loading protocol 1

The loading protocol included three (3) cycles at serviceability level displacement 27 mm, which is approximately L/260, where L is equal to 7200 mm. After that the displacement increased with two different speeds, one slower, in the range 0 to 100 mm and one faster, in the range 100 to 450 mm. The duration of each loading-unloading phase for the three 3 cycles was 7.5+2.5=10 minutes, the duration of loading in the range 0- 100 mm and in the range 100- 450 mm was 1 hour. The total duration of the test was accordingly 2.5 hours. The loading speed for the 3 cycles was 0.06 mm/sec, in the range 0- 100 mm 0.0278 mm/sec and in the range 100- 450 mm 0.0972 mm/sec (figure 4.39).

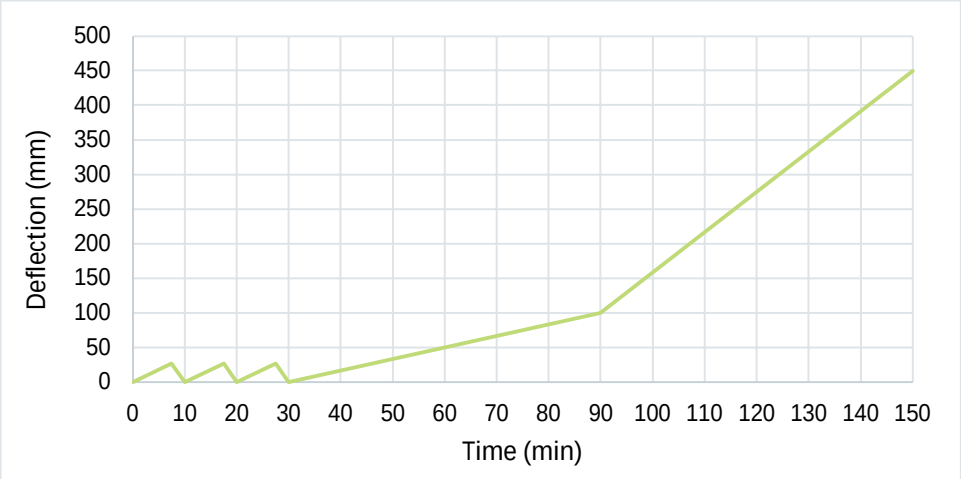

Fig. 4.39- Loading protocol 1

- Loading protocol 2

This loading protocol included also three (3) cycles at serviceability level displacement 27 mm and after that the displacement increased with two different speeds, one slower, in the range 0 to 150 mm and one faster, in the range 150 to 450 mm. The duration of each loading-unloading phase for the three 3 cycles was 7.5+2.5=10 minutes, the duration of loading in the range 0- 150 mm was 1.5 hour and in the range 150- 450 mm was 1 hour. The total duration of the test was accordingly 3 hours. The loading speed for the 3 cycles was 0.06 mm/sec, in the range 0- 150 mm 0.0278 mm/sec and in the range 150- 450 mm 0.0972 mm/sec (figure 4.40).

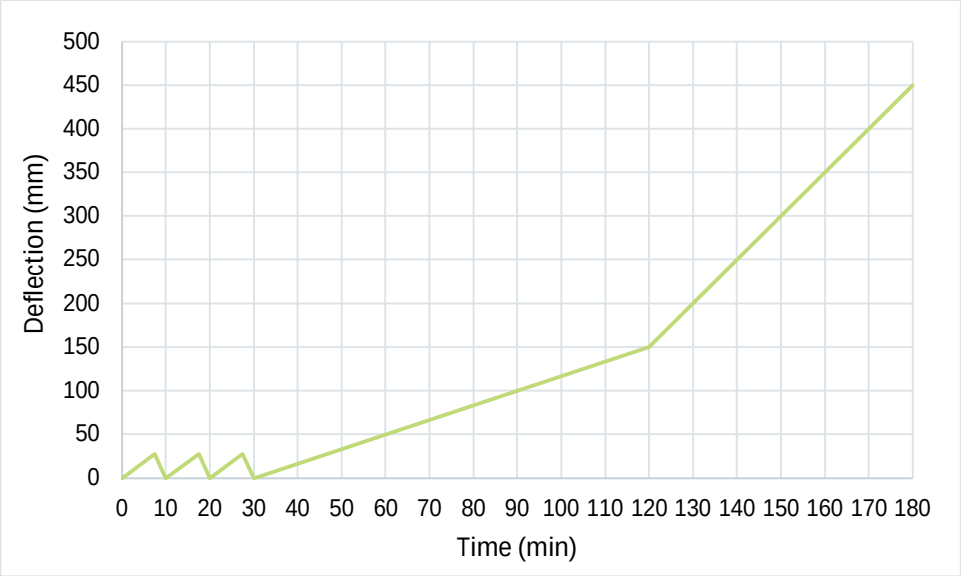

Fig. 4.40- Loading protocol 2

5

Experimental results

All specimens, cross-section dimensions and reinforcement details are described in detail in section 4.3.1.

5.1 Type 1 sections

Type 1 sections were the least reinforced specimens and represent the current configuration of the beams. This factor had a greatly influential effect on their behavior as demonstrated in the following test results. When the maximum load was reached failure occurred, that is, the concrete under compression was crushed due to the lack of longitudinal and transversal reinforcement, leading to buckling of the web and top plates, as explained in detail in the following sections.

5.1.1 Specimen S2

First cracks occurred at a deflection of 23 mm (165 kN) at the second circle of phase 1 (figure 5.1). In figure 5.2 the crack pattern at 50 mm (325 kN) is presented. When the maximum load was reached at a deflection of 117 mm (495 kN) the longitudinal rebars at the compression zone buckled, causing spalling of the concrete (figure 5.3). Due to the absence of stirrups the failure of the concrete was extensive (figure 5.4) and buckling at the top plate of the steel beam was not prevented (figure 5.5). These factors caused a dramatic and sudden drop of the beam strength (ultimate load was 60% of the maximum load), leading to an overall non-ductile behavior. Also, this behavior is clearly described by the load- deflection and moment- rotation curves shown on figures 5.6 and 5.7.

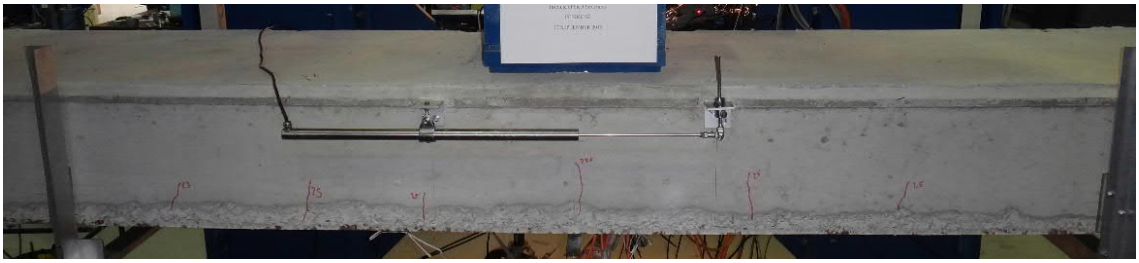

Fig. 5.1- S2- Cracks at deflection of 23 mm (fig. 5.6 and 5.7, points A and A')

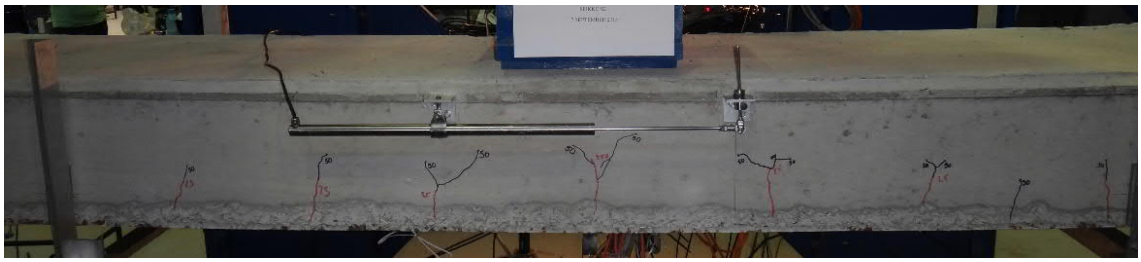

Fig. 5.2- S2- Cracks at deflection of 50 mm (fig. 5.6 and 5.7, points B and B')

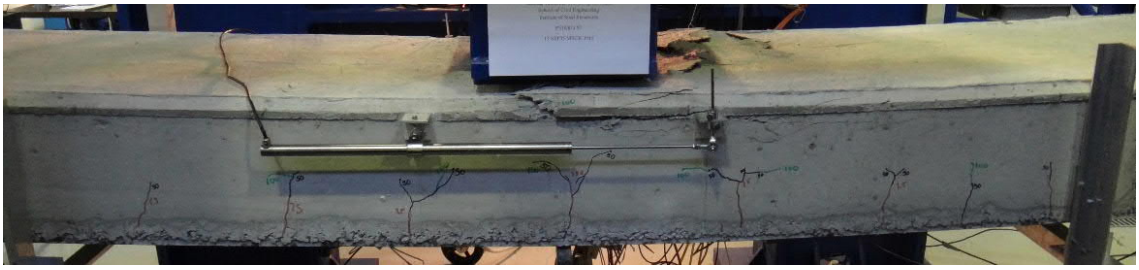

Fig. 5.3- S2- Tensile and compressive cracks at deflection of 117 mm (fig. 5.6 and 5.7, points C and C')

Fig. 5.4- S2- The beam top mid span at the end of the test (fig. 5.6 and 5.7, points D and D')

Fig. 5.5- S2- Buckling of the top plate

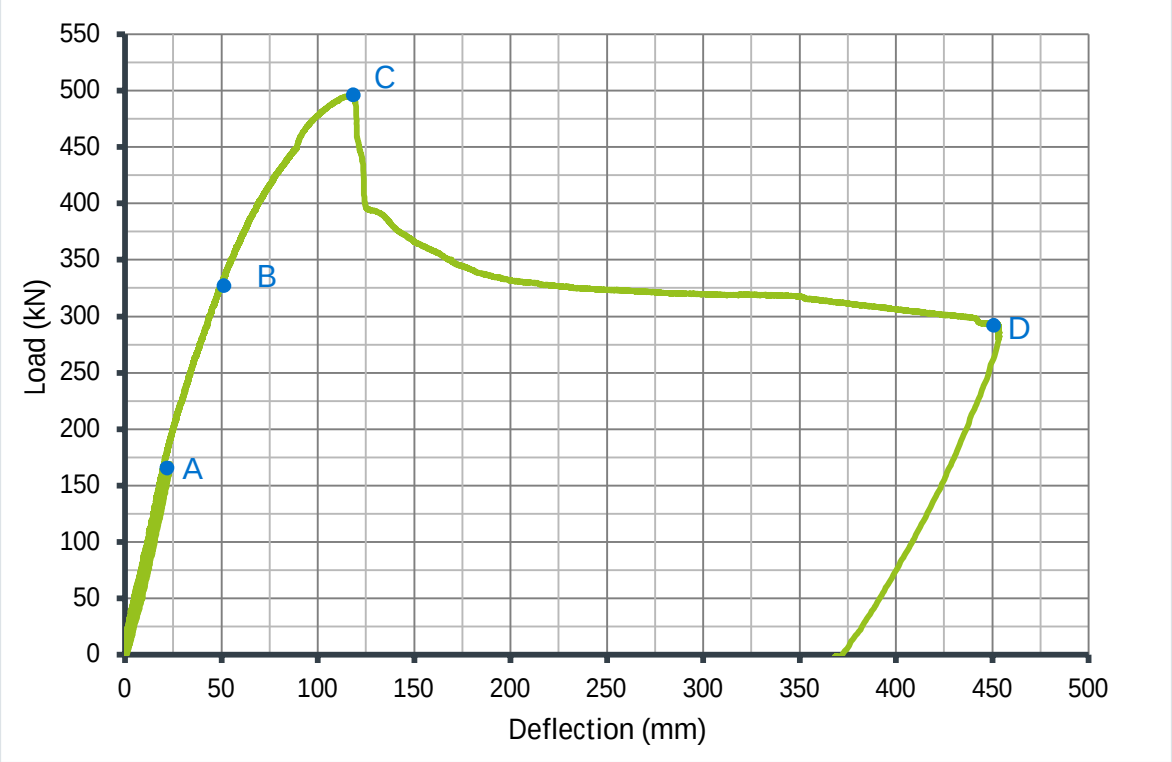

Fig. 5.6- S2- Average load- deflection curve

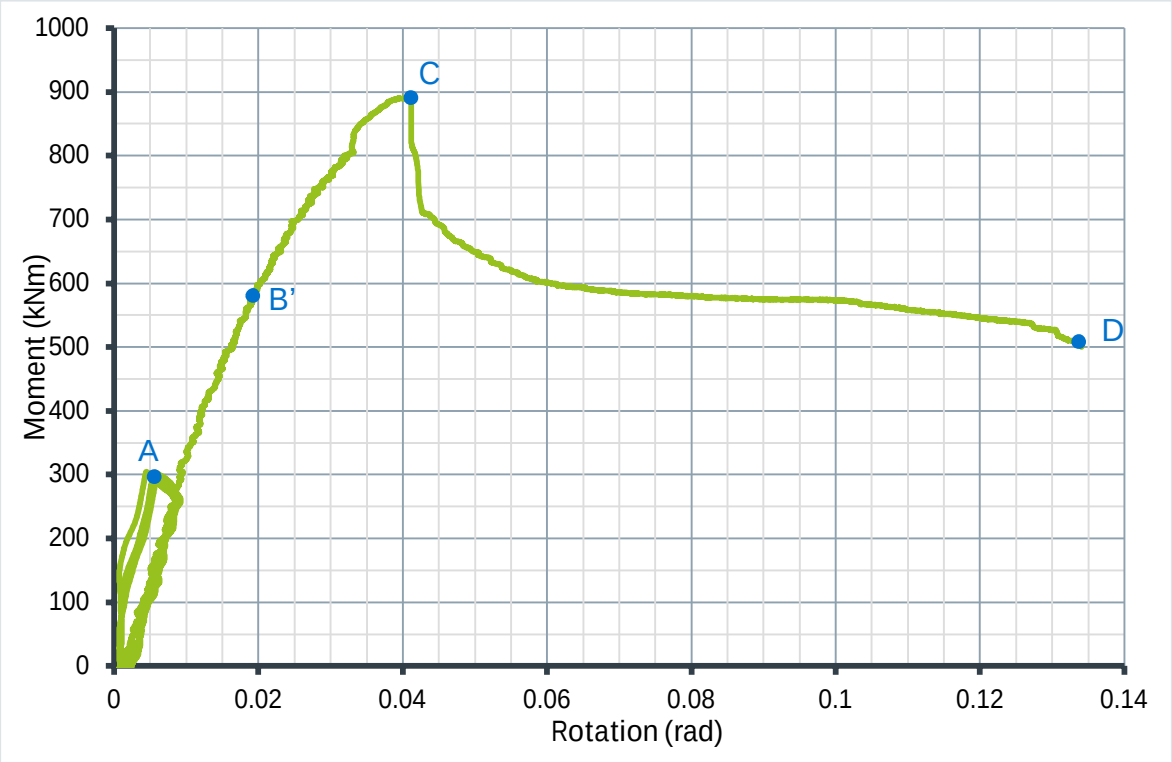

Fig. 5.7- S2- Average moment- rotation curve (inclinometer)

In figure 5.8 the slips between the concrete and the steel beam are presented. The measurements were valid up to the maximum load where the maximum slip values were measured, while at that point, the slips started decreasing. The maximum slips were observed at S4 (1.35 mm) and S5 (1.91 mm) at the right half of the beam where the failure occurred. Also, the maximum slips for each side of the beam, right and left of the loading area, were at their middle (S2 and S5) of each half, while the smallest were at the supports (S1 and S6). In figure 5.9, the propagation of slips along the longitudinal direction of the beam for four different deflection values is presented.

Load- strain curves are shown in figure 5.10. The strain gauges which measured the highest values were the ones placed at the intersection of the bottom plate with the web plates (B1, B4 and B6). This can be clarified by figure 5.11, which presents the propagation of strains across the bottom plate width for sections A-A and B-B (positions of strain gauges left and right of the loading area), for various deflection values.

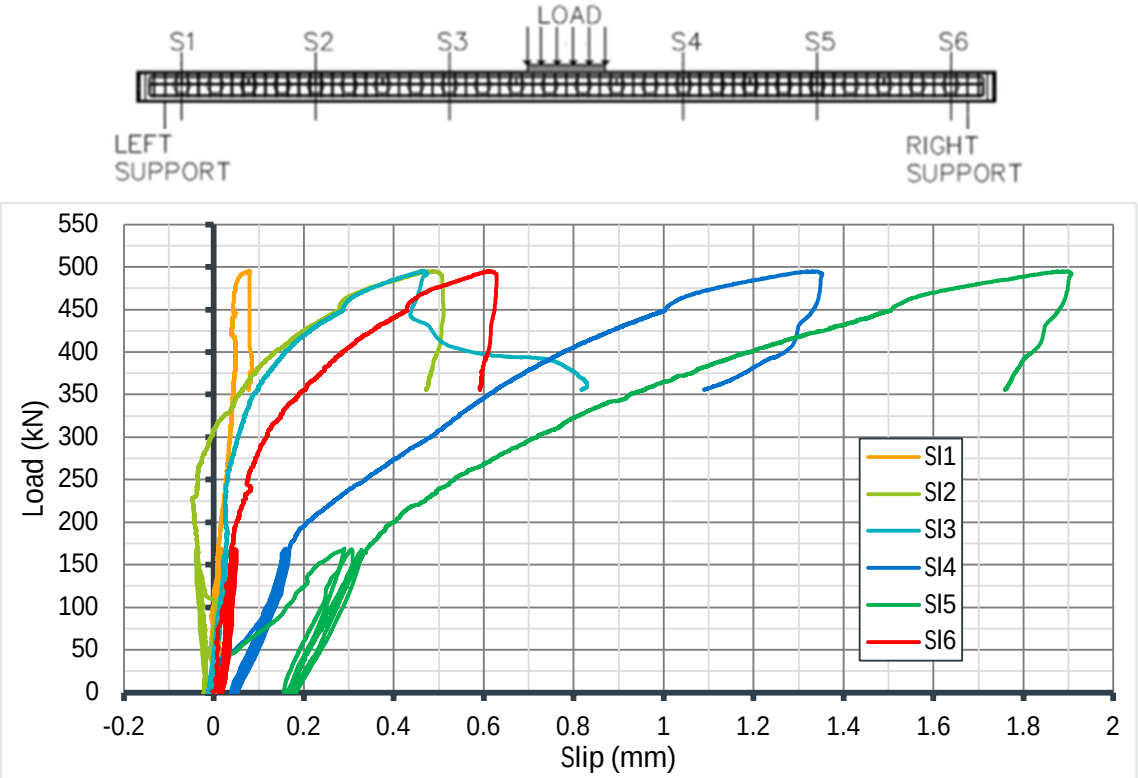

Fig. 5.8- S2- Load- slip curves

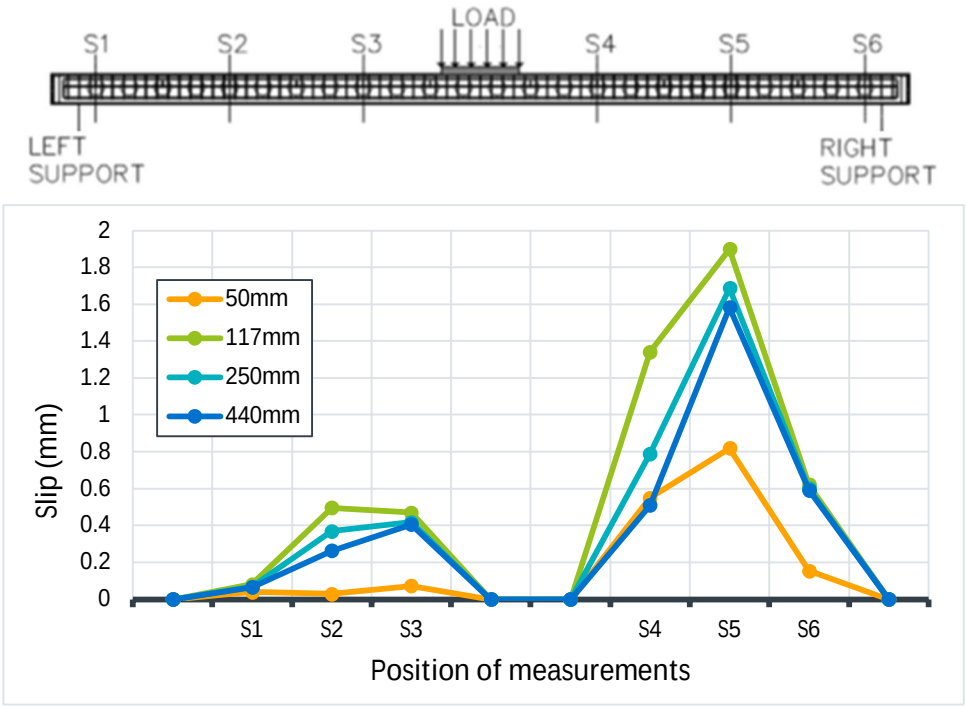

Fig. 5.9- S2- Slip propagation for different deflection values

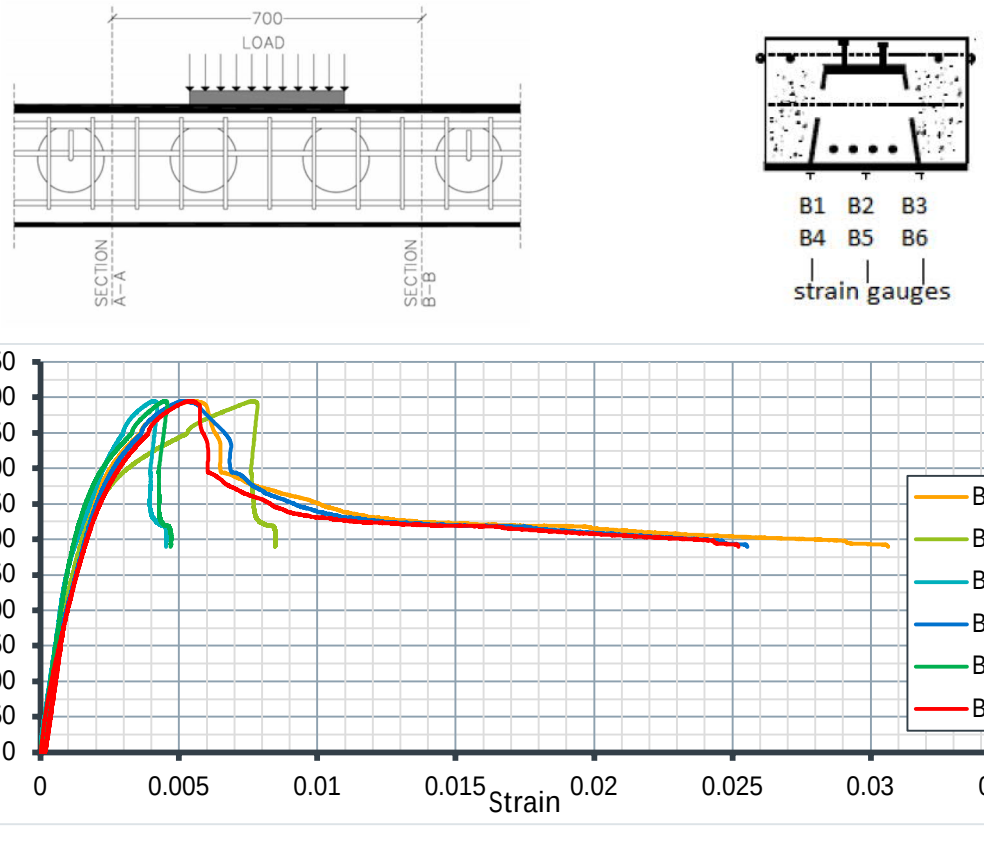

Fig. 5.10- S2- Strains at the bottom plate of the beam

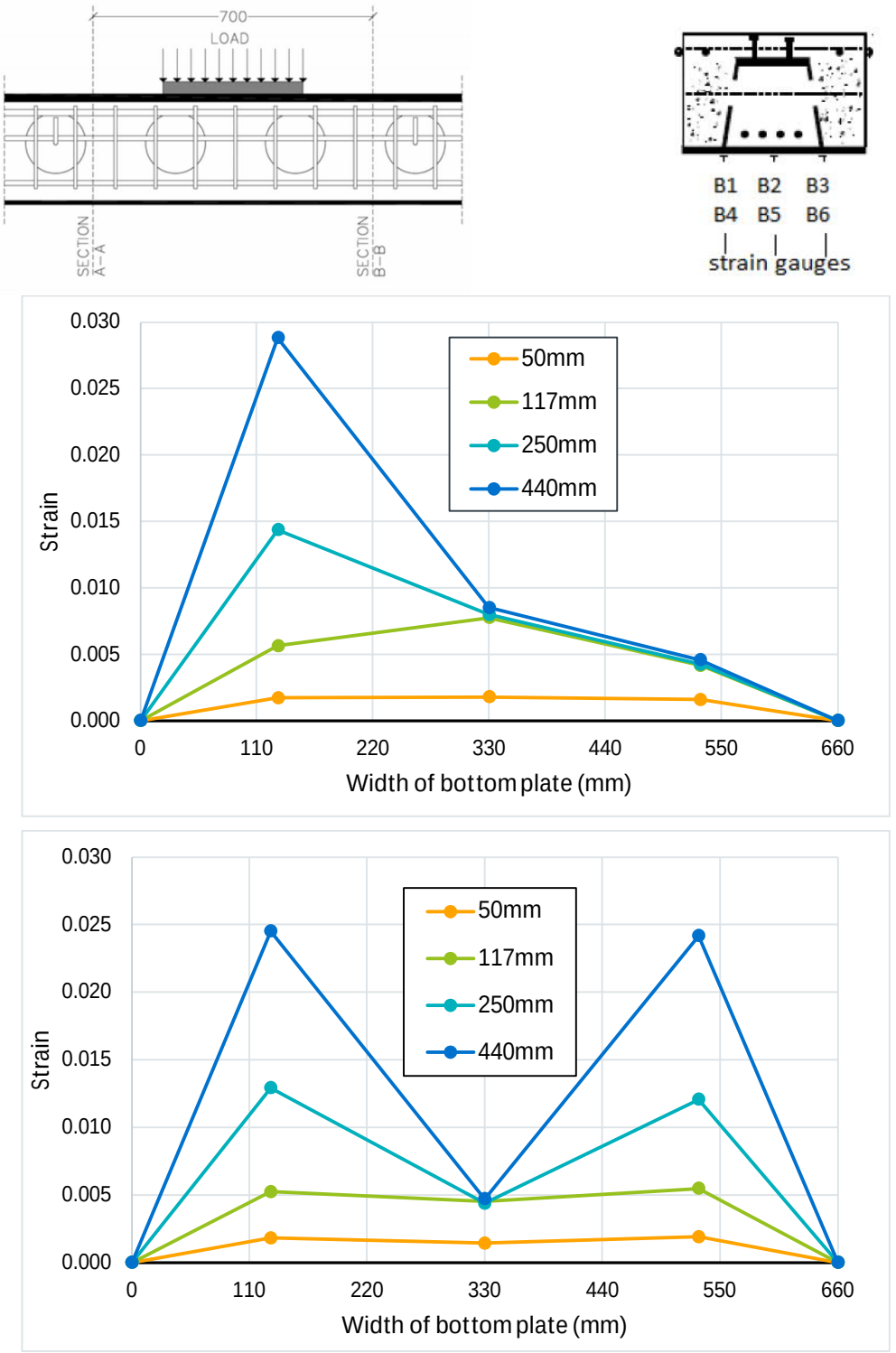

Fig. 5.11- S2- Strains along the bottom plate at sections A-A (top) and B-B (bottom) for various deflections

5.1.2 Specimen S3

First cracks occurred at a deflection of 20 mm (165 kN) at the second circle of phase 1 (figure 5.12). In figures 5.13 and 5.14 the crack pattern at 50 mm and 100 mm is presented. The first compressive crack was observed at a deflection of 105 mm (figure 5.15). At that deflection corresponds the maximum load, when the longitudinal rebars at the compression zone buckled causing spalling of the concrete. Due to the absence of stirrups the failure on the concrete was extensive (figure 5.16). The top plate also buckled due to the lack of confinement (figure 5.17). The reduction of the ultimate load was 43% of the maximum load, leading again to a non-ductile behavior (figures 5.18 and 5.19).

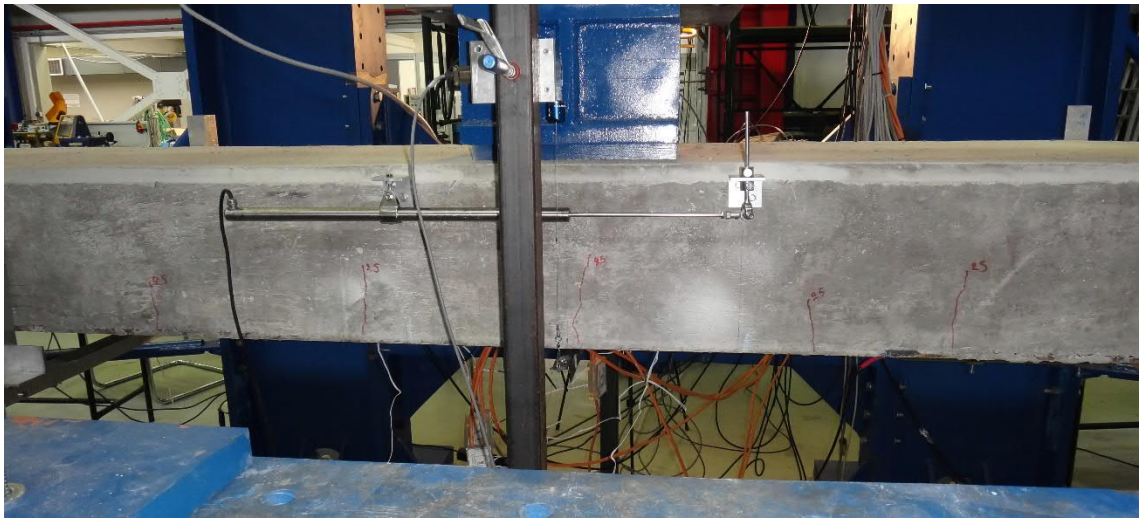

Fig. 5.12- S3- Cracks at deflection of 20 mm (fig. 5.18 and 5.19, points A and A')

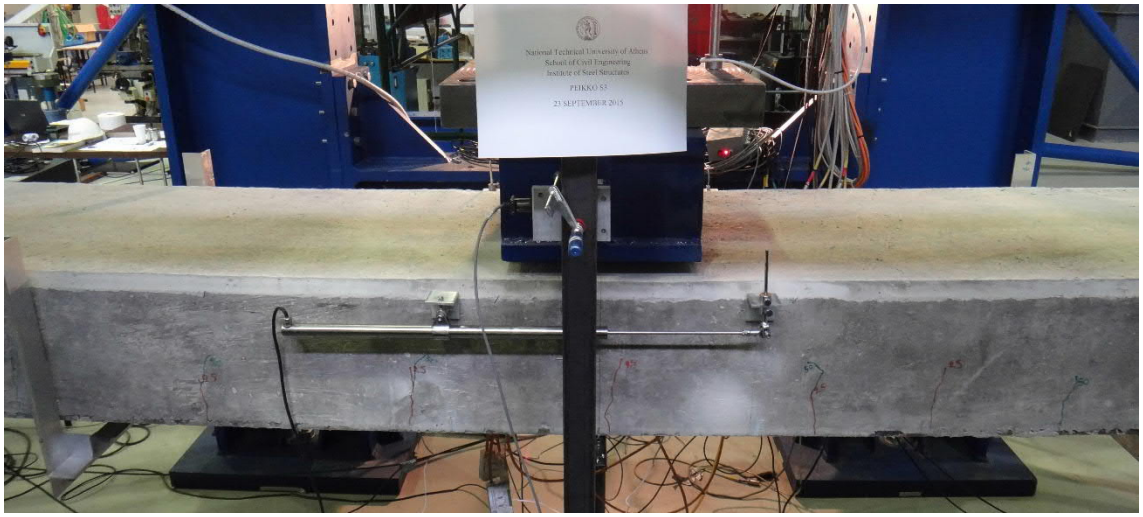

Fig. 5.13- S3- Cracks at deflection of 50 mm (fig. 5.18 and 5.19, points B and B')

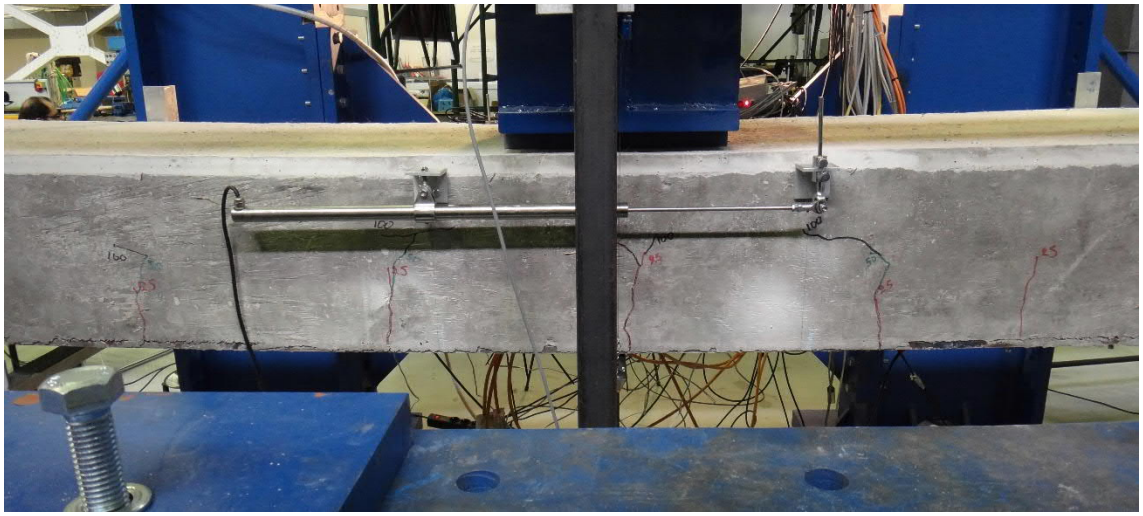

Fig. 5.14- S3- Cracks at deflection of 100 mm (fig. 5.18 and 5.19, points C and C')

Fig. 5.15- S3- Compressive cracks at deflection of 105 mm (fig. 5.18 and 5.19, points C and C')

Fig. 5.16- S3- Specimen at the end of the test (fig. 5.18 and 5.19, points D and D')

Fig. 5.17- S3- Buckling at the top plate of the steel beam

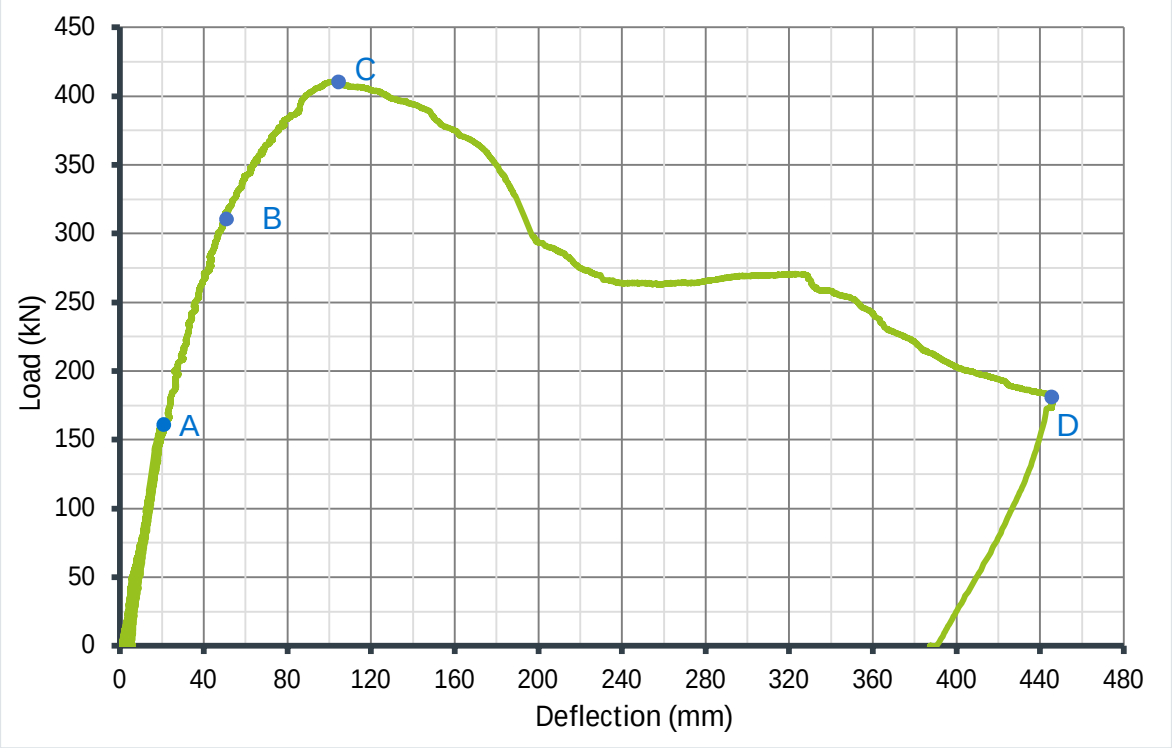

Fig. 5.18- S3- Average load- deflection curve

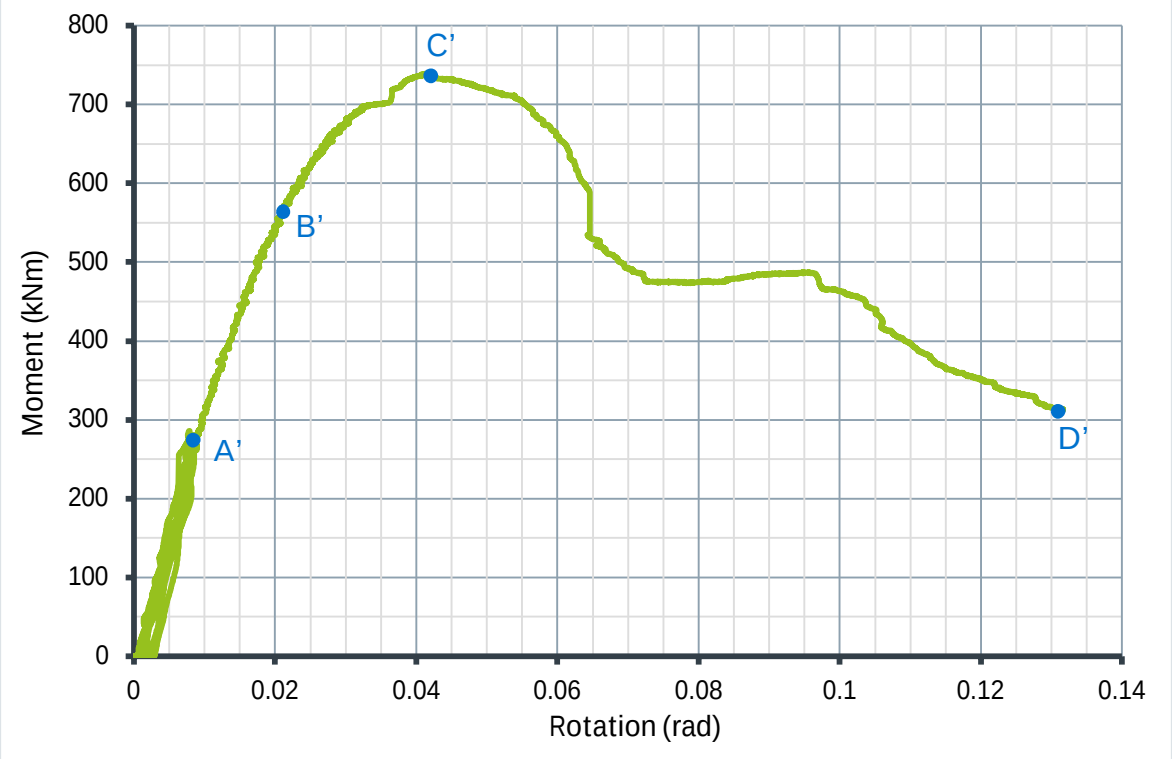

Fig. 5.19- S3- Average moment- rotation curve (Inclinometer)

In figure 5.20 the slips between the concrete and the steel beam are presented up to the maximum load. The maximum slips were observed at S3 (2.38 mm) and S4 (2.35 mm) by the LVTDs next to the loading area. In figure 5.21, the propagation of slips along the longitudinal direction of the beam for four different deflection values is presented.

Load- strain curves are shown in figure 5.22. The strains are distributed almost equally along the bottom plate of the steel beam, with the areas under the webs (B1, B3, B4 and B6) having slightly higher values. This is also observed in figure 5.23 where the propagation of strains across the bottom plate, for sections A-A and B-B (positions of strain gauges left and right of the loading area), for various deflection values is presented.

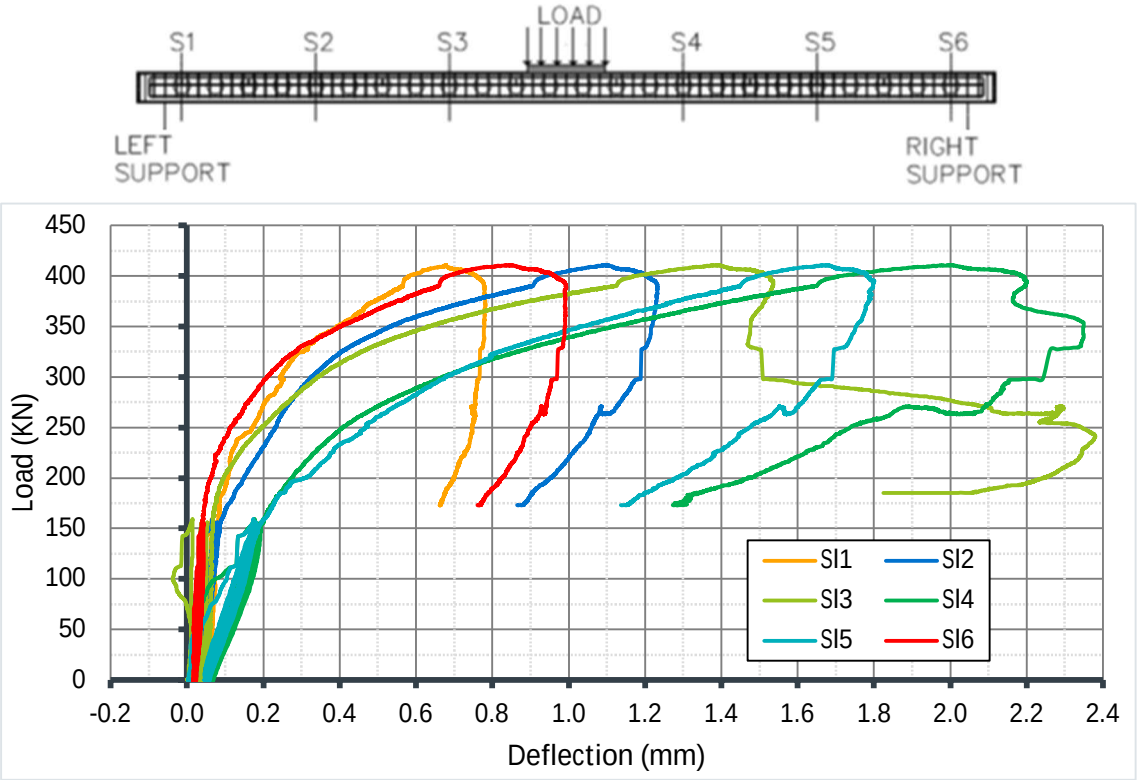

Fig. 5.20- S3- Load- slip curves

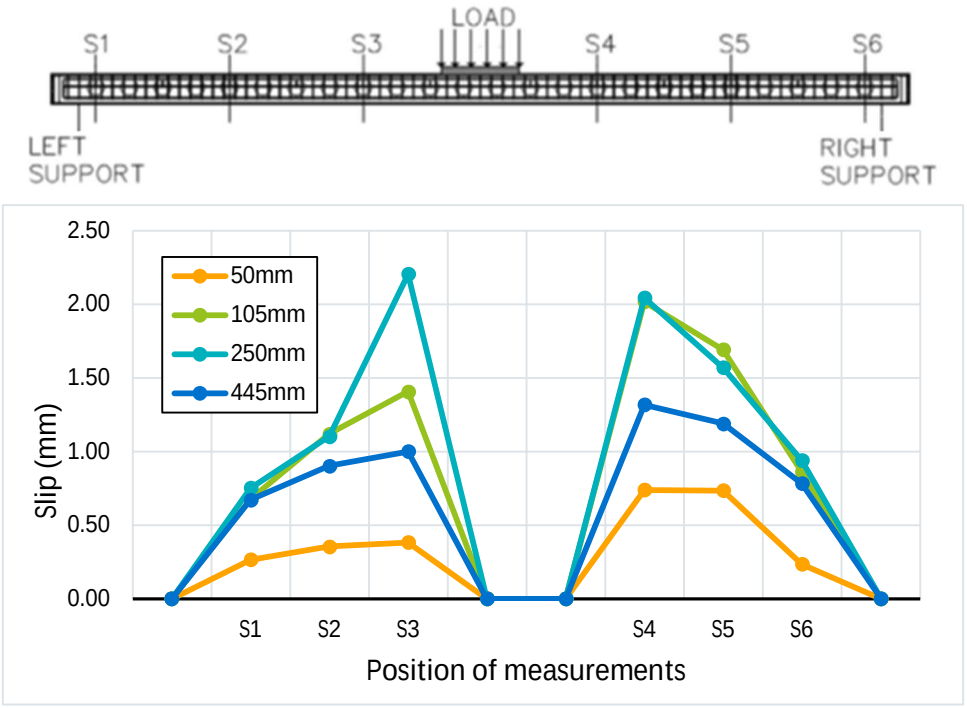

Fig. 5.21- S3- Slip propagation for different deflection values

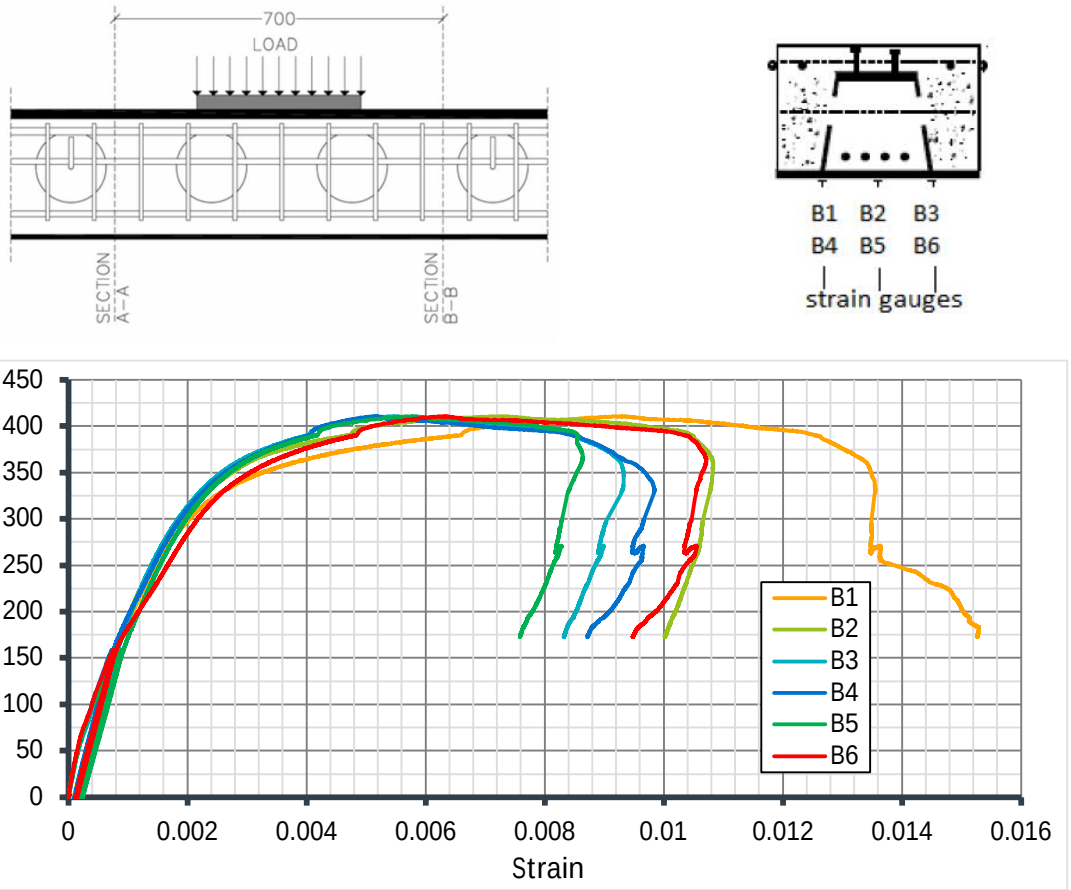

Fig. 5.22- S3- Tensile strains at the bottom plate of the beam

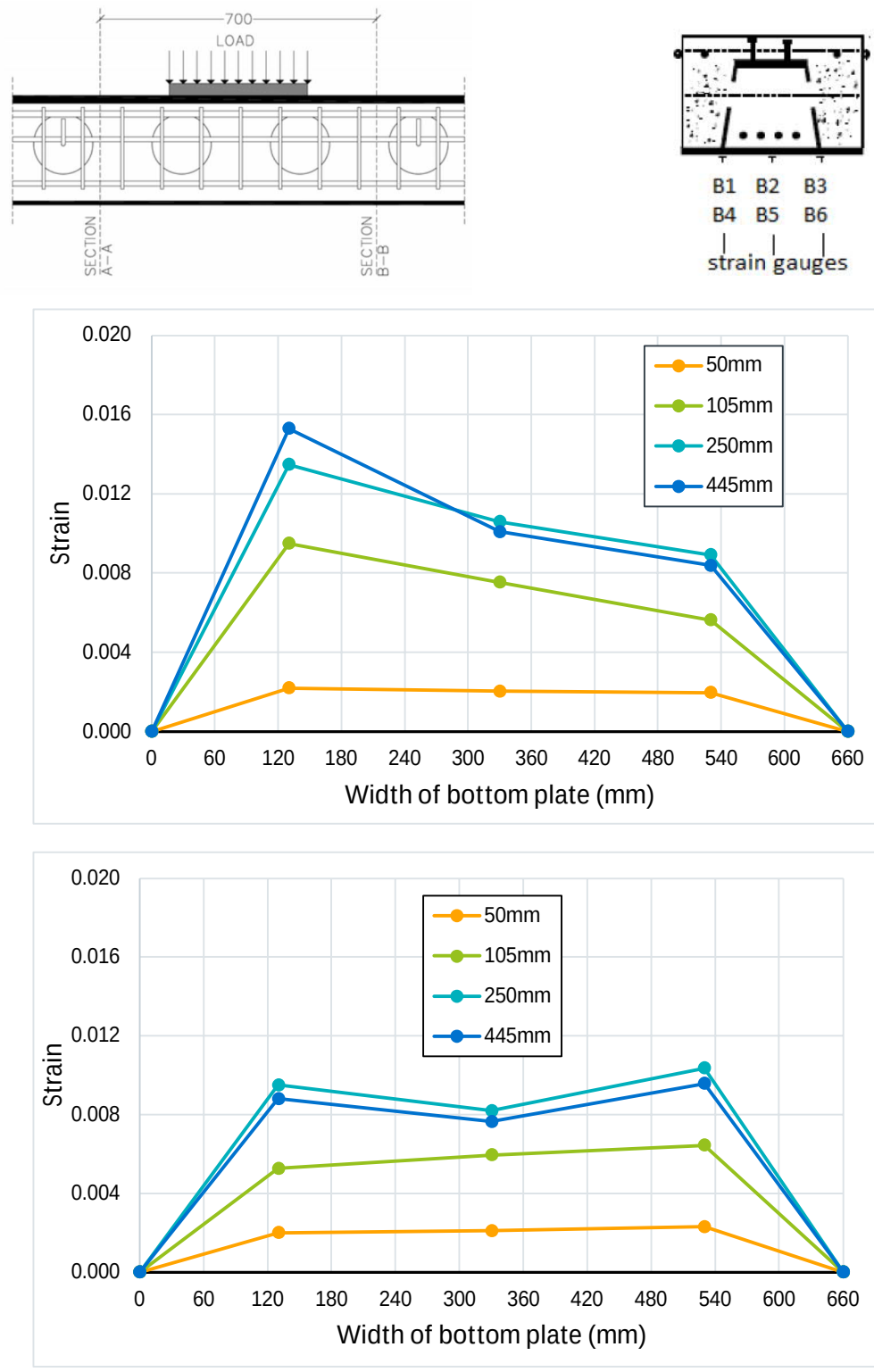

Fig. 5.23- S3- Strains along the bottom plate at sections A-A (top) and B-B (bottom) for various deflections

5.1.3 Specimen S4

First cracks occurred at a deflection of 20 mm (240 kN) at the first serviceability circle (figure 5.24). In figures 5.25 and 5.26 the crack pattern at 50 mm (480 kN) and 100 mm (531 kN) is presented. Also, at deflection equal to 100 mm, the first compressive cracks were seen at the top of the concrete (figure 5.27), when the longitudinal rebars at the compression zone buckled causing spalling of the concrete (figure 5.28). The spalling of the concrete and thereby the buckling of the top steel plate were not prevented (figure 5.29). The ultimate load dropped at 72% of the maximum load (figures 5.30 and 5.31).

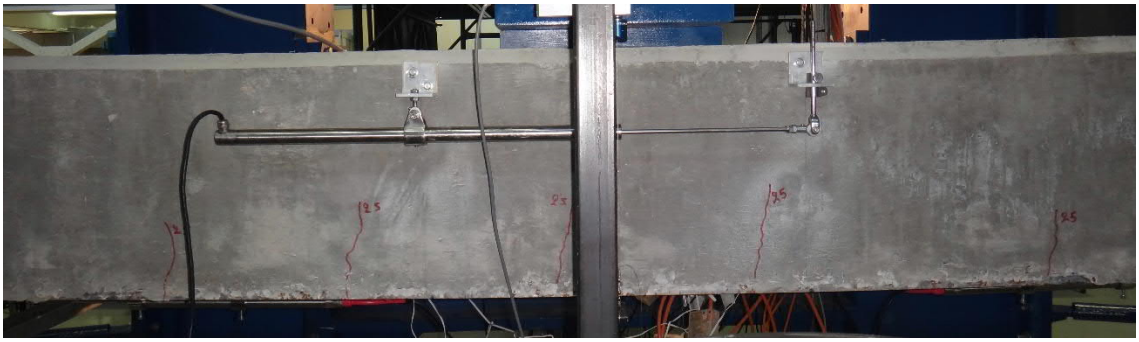

Fig. 5.24- S4- Cracks at deflection of 20 mm (fig. 5.30 and 5.31, points A and A')

Fig. 5.25- S4- Cracks at deflection of 50 mm (fig. 5.30 and 5.31, points B and B')

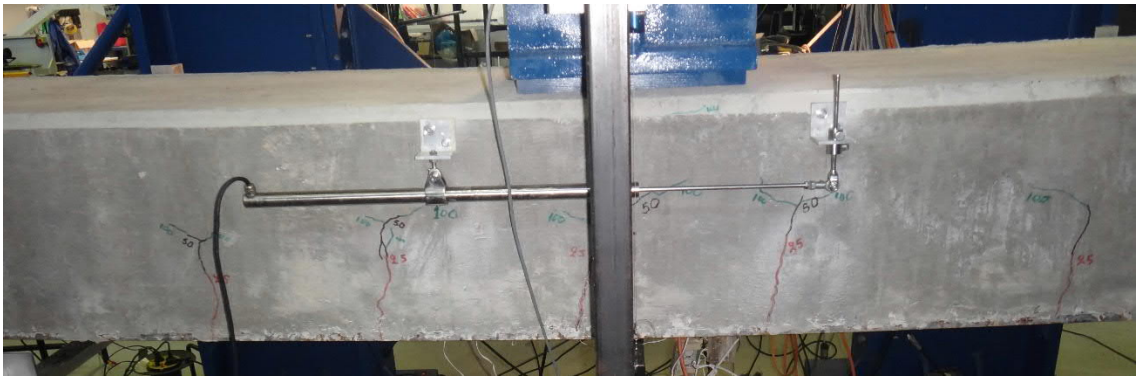

Fig. 5.26- S4- Cracks at deflection of 100 mm (fig. 5.30 and 5.31, points C and C')

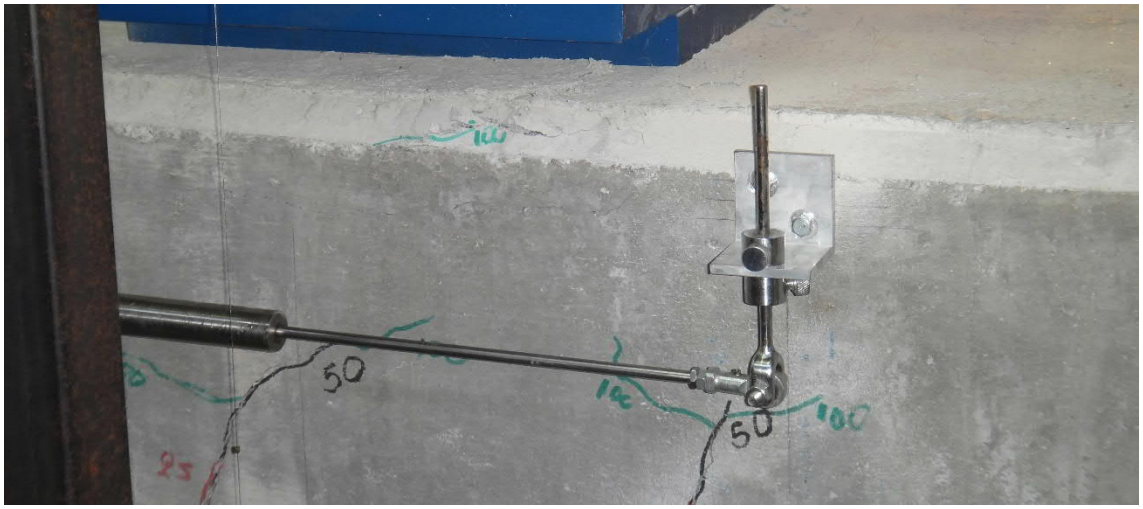

Fig. 5.27- S4- Compressive cracks at deflection of 100 mm (fig. 5.30 and 5.31, points C and C')

Fig. 5.28- S4- Buckling of rebars at the end of the test (fig. 5.30 and 5.31, points D and D')

Fig. 5.29- S4- Buckling at the top plate of the steel beam

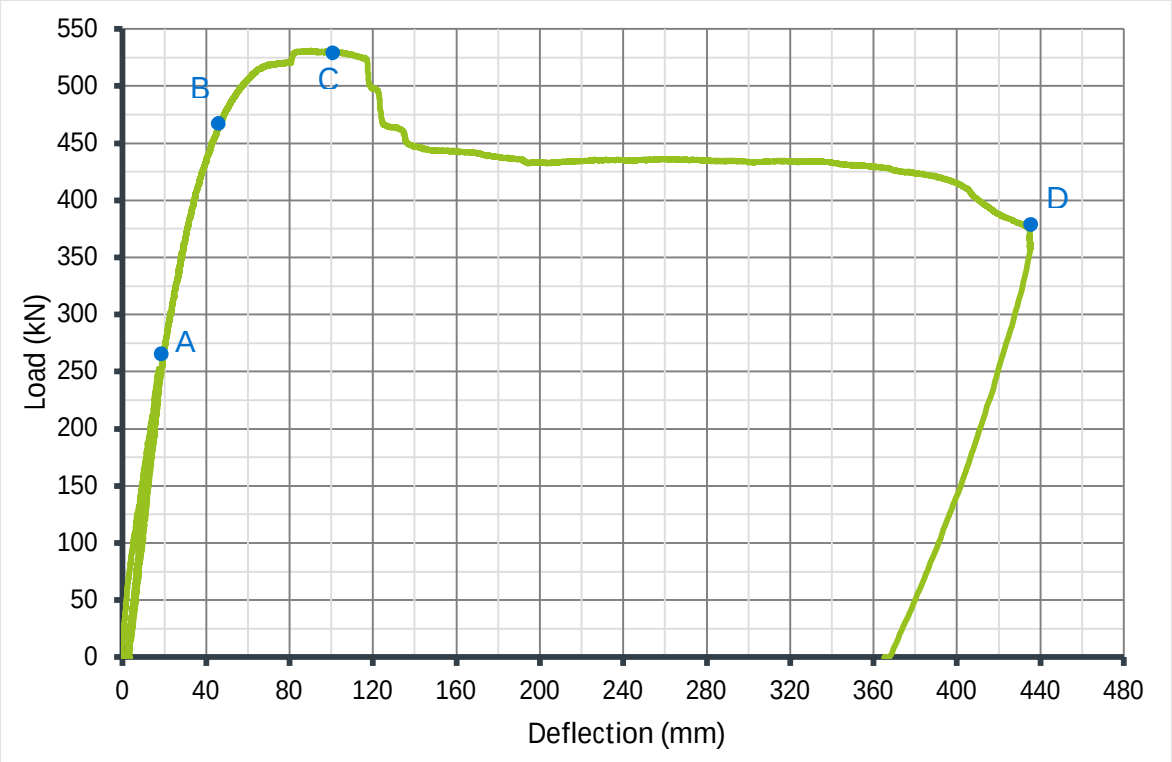

Fig. 5.30- S4- Average load- deflection curve

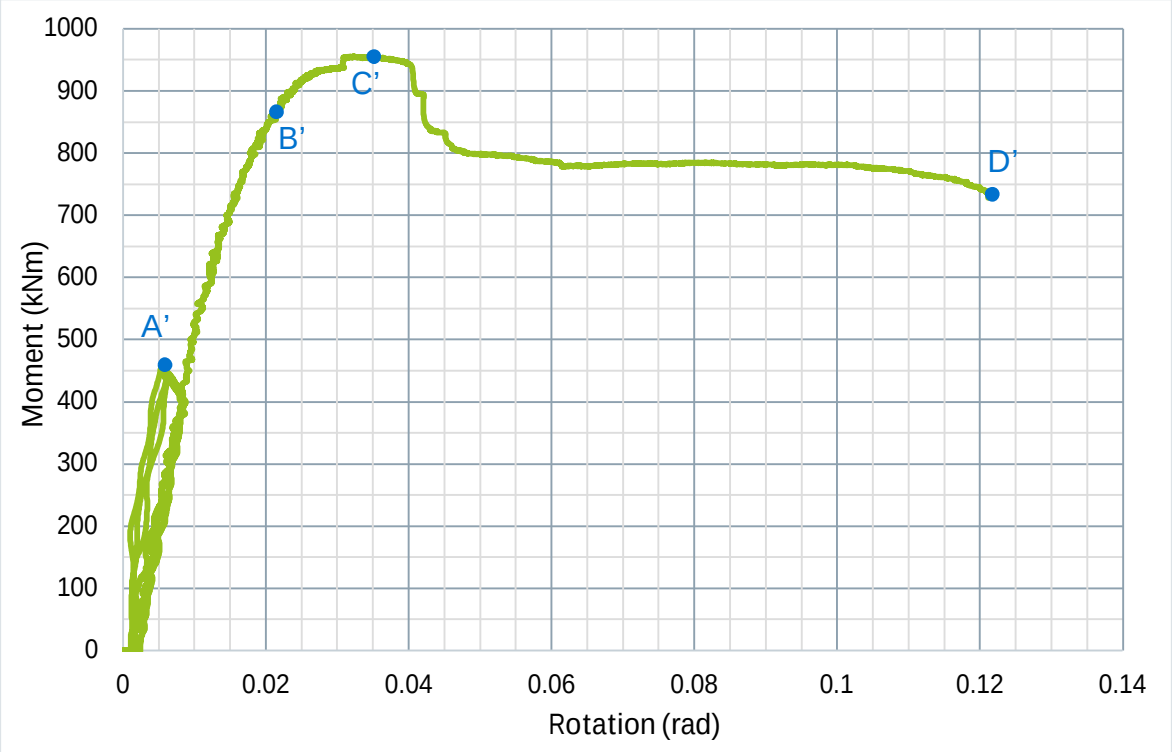

Fig. 5.31- S4- Average moment- rotation curve (Inclinometer)

The slips between the concrete and the steel beam are presented in figure 5.32 up to the maximum load. The maximum slips were observed at S4 (1.13 mm) and S5 (0.95 mm) by the LVTDs in the right side of the loading area (figure 5.33).

Load- strain curves are shown in figure 5.34. It can be observed that at the beginning of the deformation when the beam was behaving elastically (50 mm), the strains are equally distributed along the width of the bottom plate. After the maximum load was reached (100 mm), when the failing mechanism begun, the distribution of the strains is not symmetrical. In figure 5.35, where the propagation of strains across the bottom plate width, for sections A-A and B-B (positions of strain gauges left and right of the loading area), for various deflection values is presented, it can be observed that the maximum strains are measured at the tree of the four strain gauges (B1, B4 and B6) under the web plates.

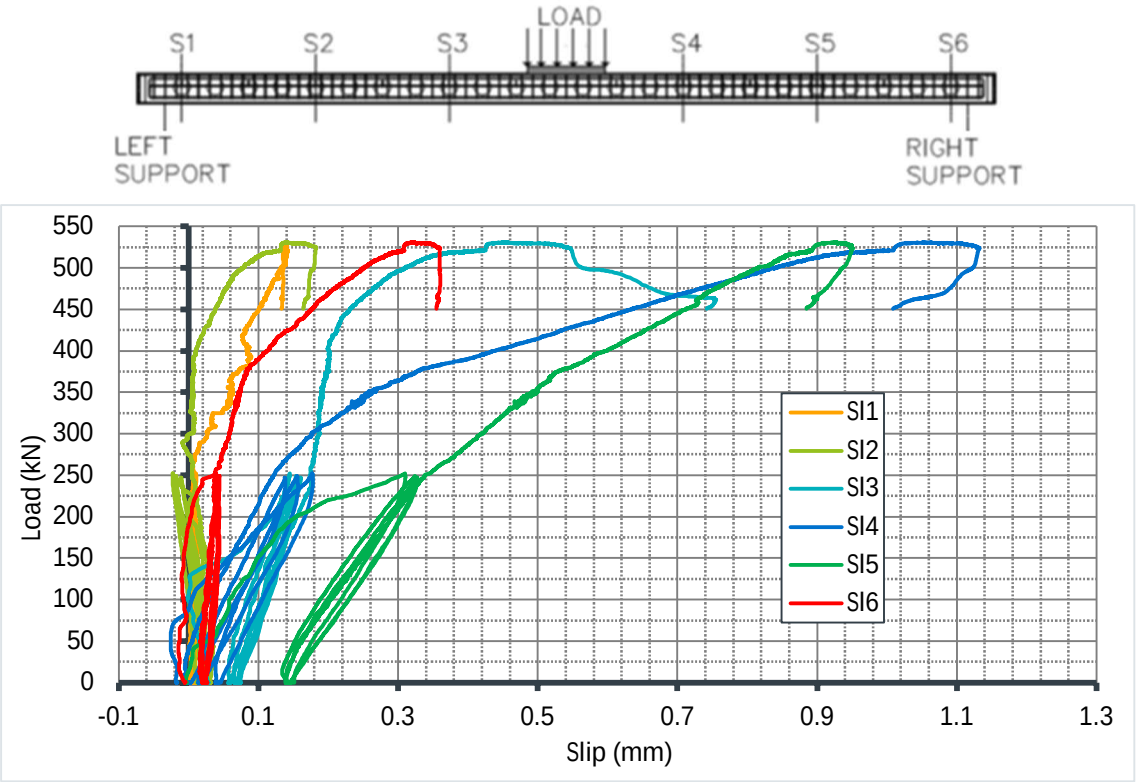

Fig. 5.32- S4- Load- slip curves

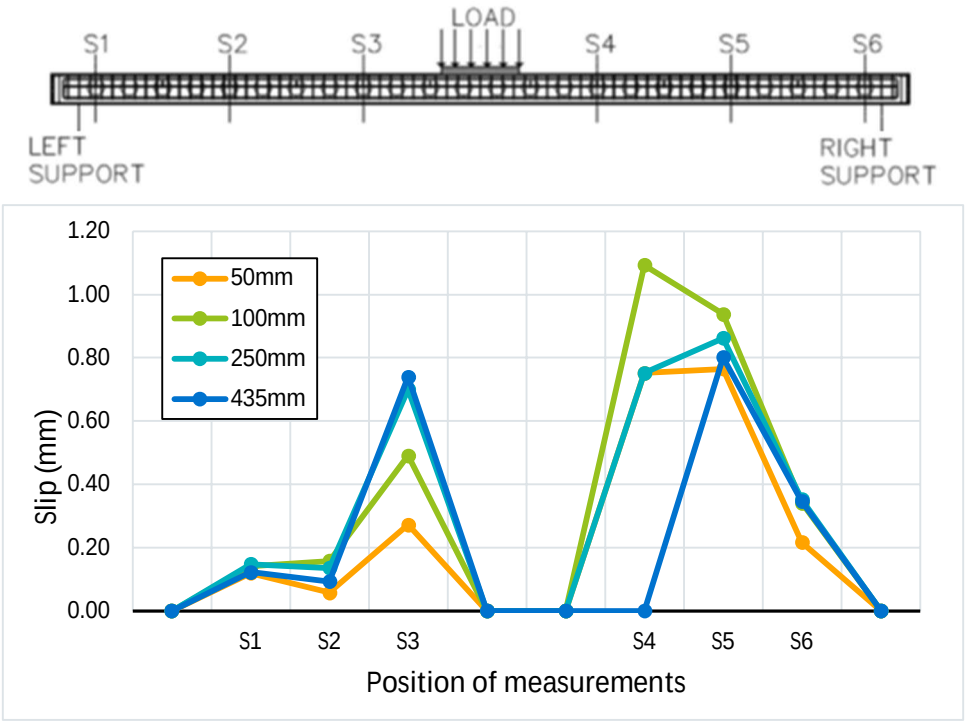

Fig. 5.33- S4- Slip propagation for different deflection values

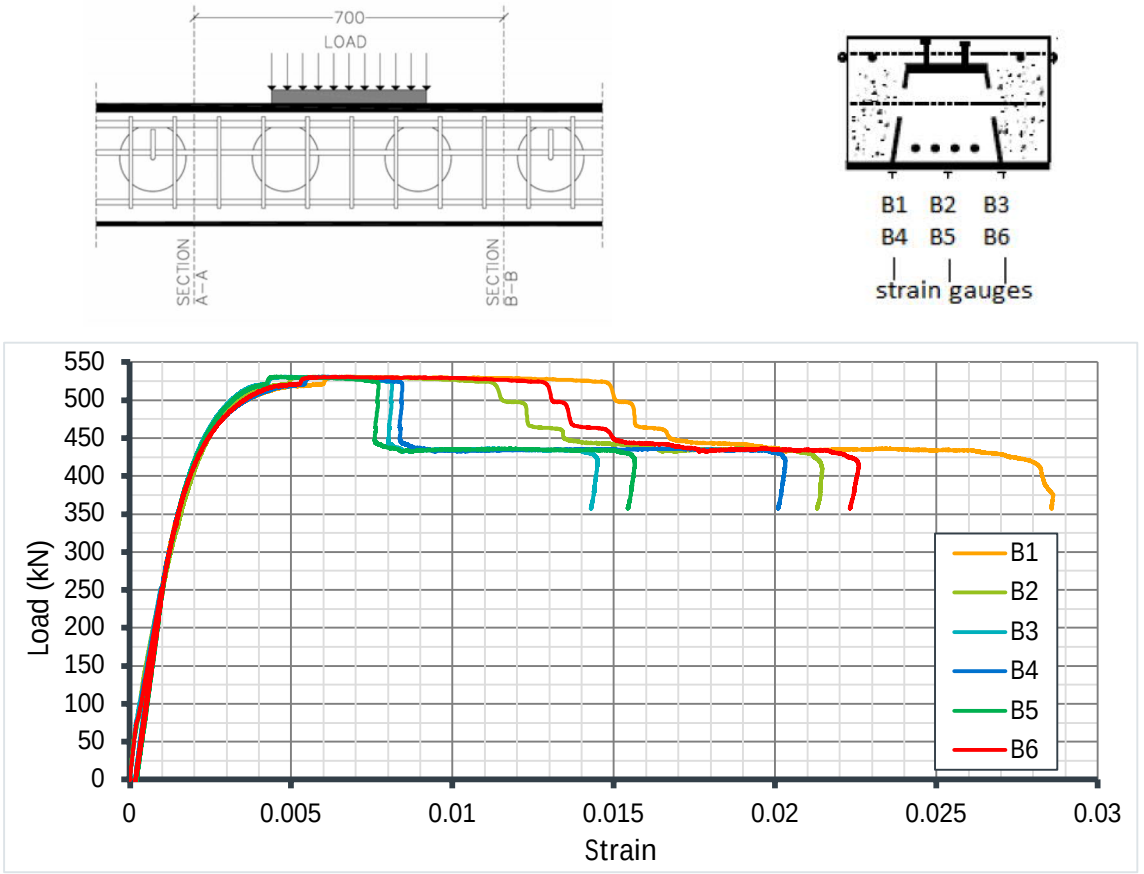

Fig. 5.34- S4- Tensile strains at the bottom plate of the beam

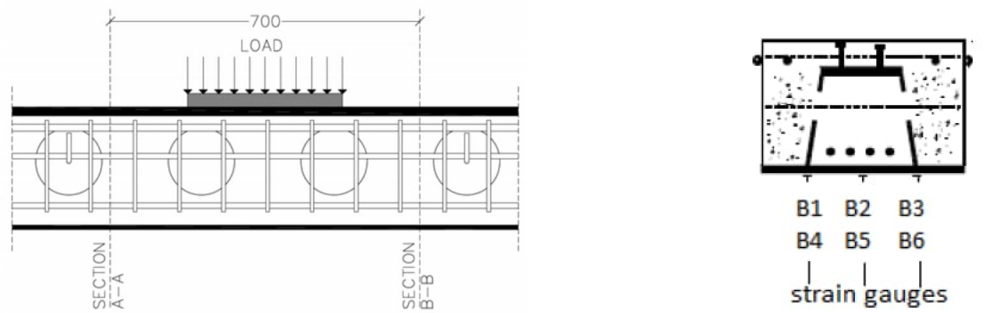

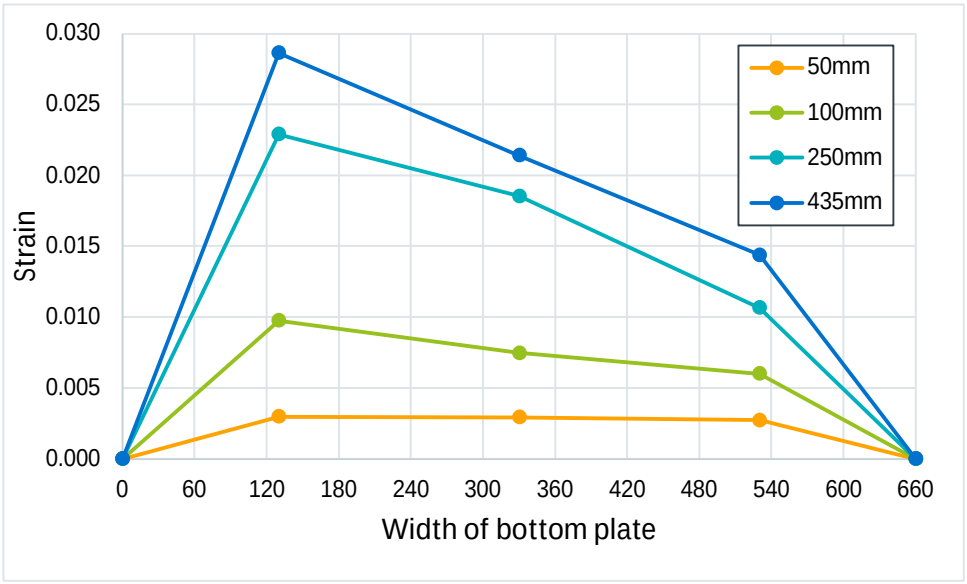

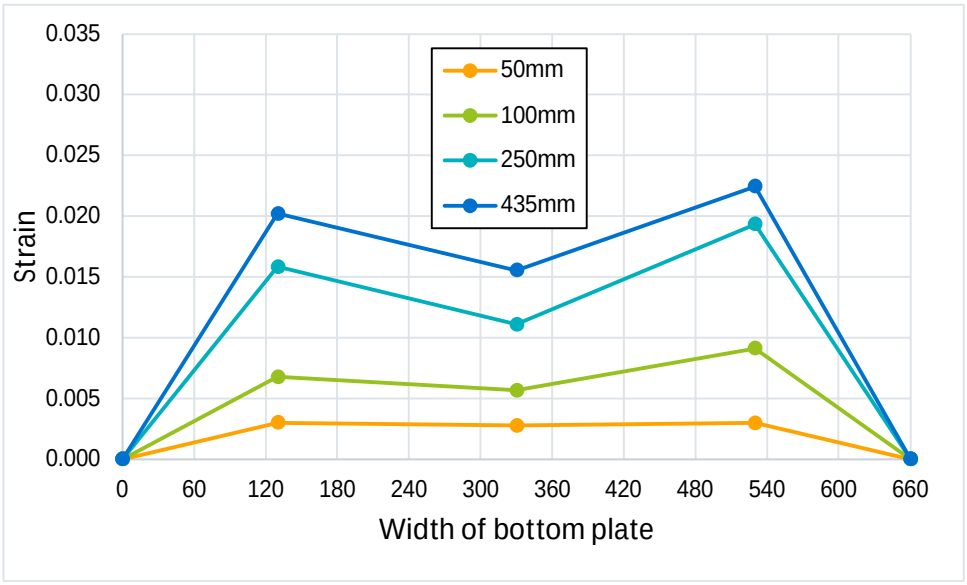

Fig. 5.35- S4- Strains along the bottom plate at sections A-A (top) and B-B (bottom) for various deflections

5.1.4 Specimen S5

S5 specimen was not totally aligned at the beginning of the test. A small torsion existed, probably due to the welding of the steel plates. First cracks occurred at a deflection of 15 mm (203 kN) at the second circle of phase 1 (figure 5.36). In figures 5.37 and 5.38 the crack pattern at 50 mm (477 kN) and 100 mm (524 kN) is presented. When the maximum load was reached at a deflection of 105 mm (527 kN) the longitudinal rebars at the compression zone buckled causing extensive spalling to the concrete (figures 5.39- 5.40). Again, the top plate buckled (figure 5.41). The ultimate load was reduced at 75% of the maximum load (figures 5.42- 5.43).

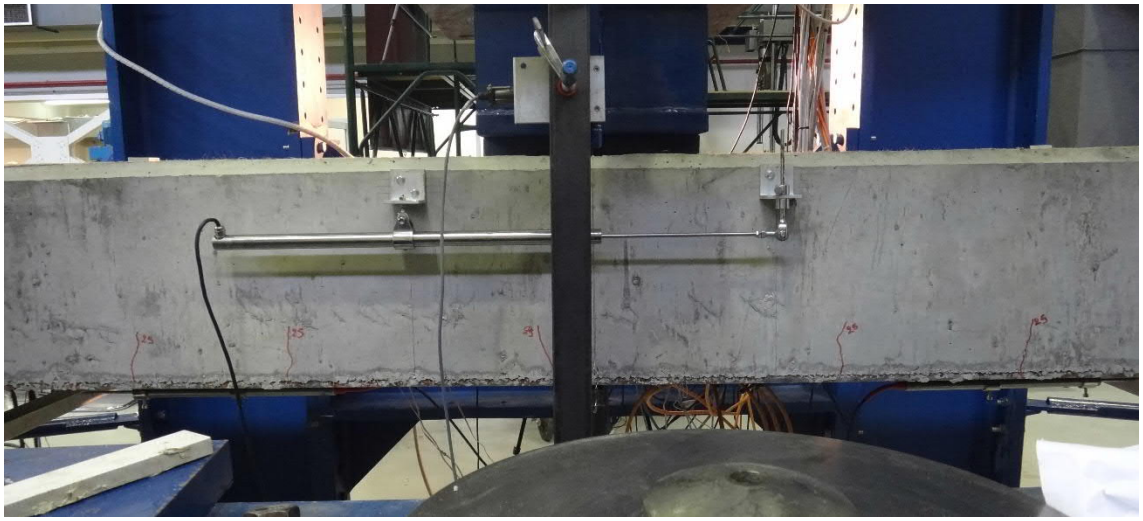

Fig. 5.36- S5- Cracks at deflection of 15 mm (fig. 5.42 and 5.43, points A and A')

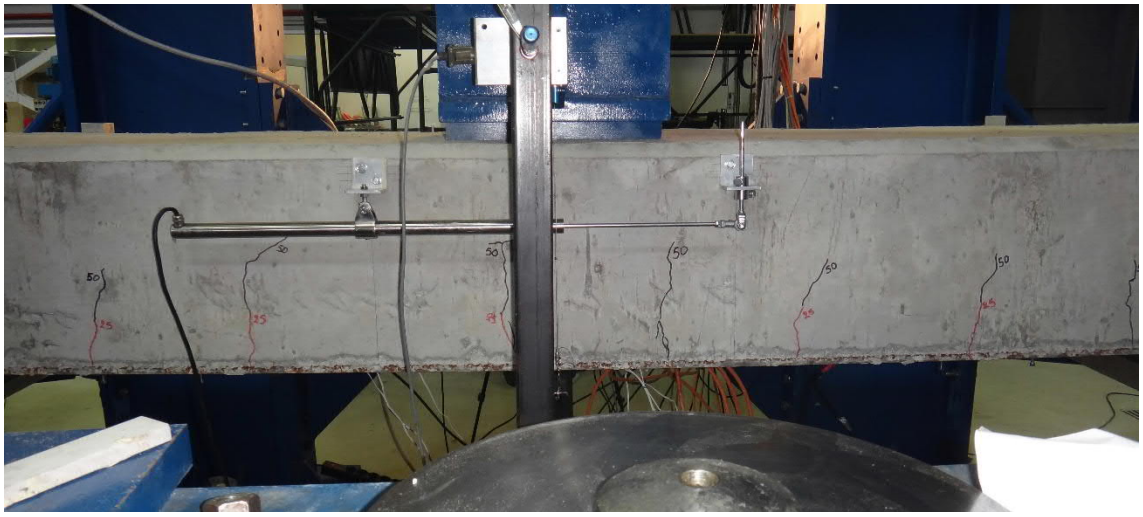

Fig. 5.37- S5- Cracks at deflection of 50 mm (fig. 5.42 and 5.43, points B and B')

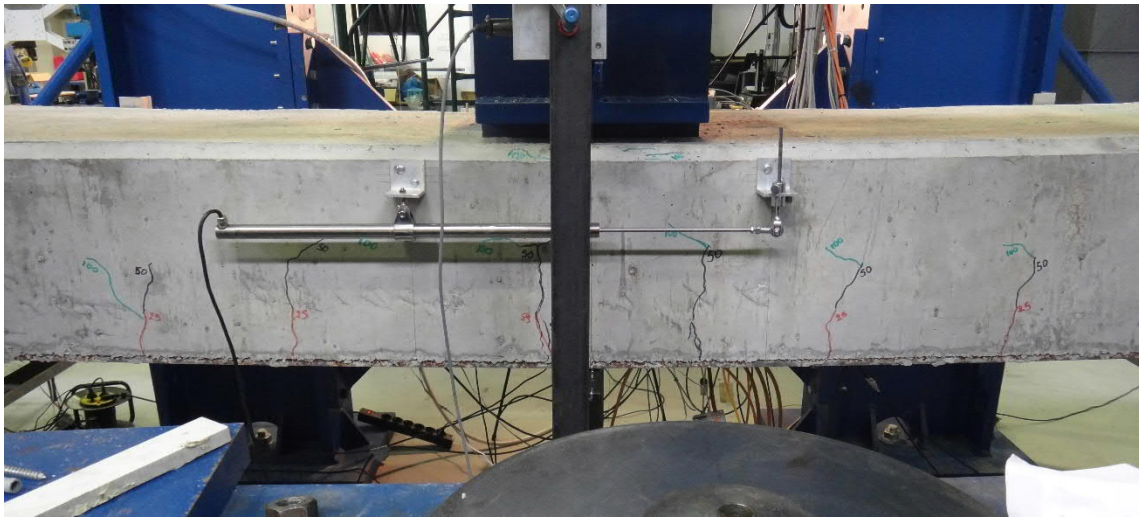

Fig. 5.38- S5- Cracks at deflection of 100 mm (fig. 5.42 and 5.43, points C and C')

Fig. 5.39- S5- Compressive cracks at deflection of 105 mm (fig. 5.42 and 5.43, points C and C')

Fig. 5.40- S5- Buckling of longitudinal rebars at the end of the test (fig. 5.42 and 5.43, points D and D')

Fig. 5.41- S5- Buckling at the top plate of the steel beam

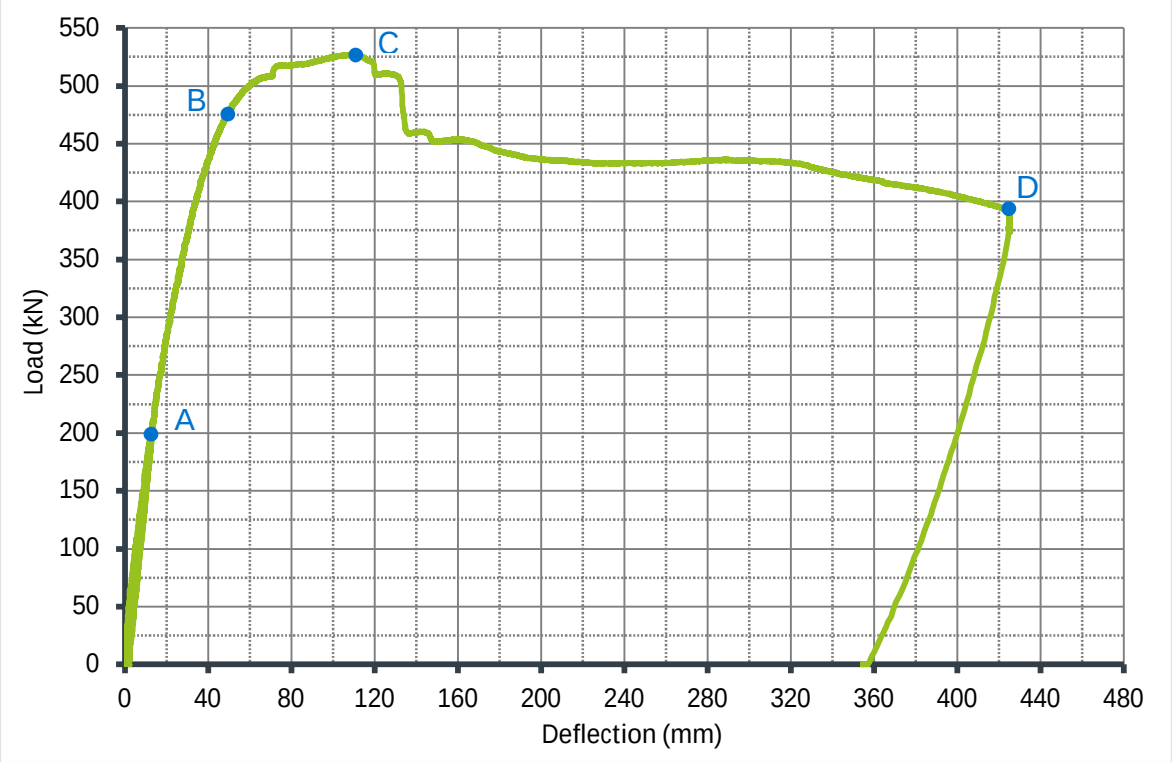

Fig. 5.42- S5- Average load- deflection curve

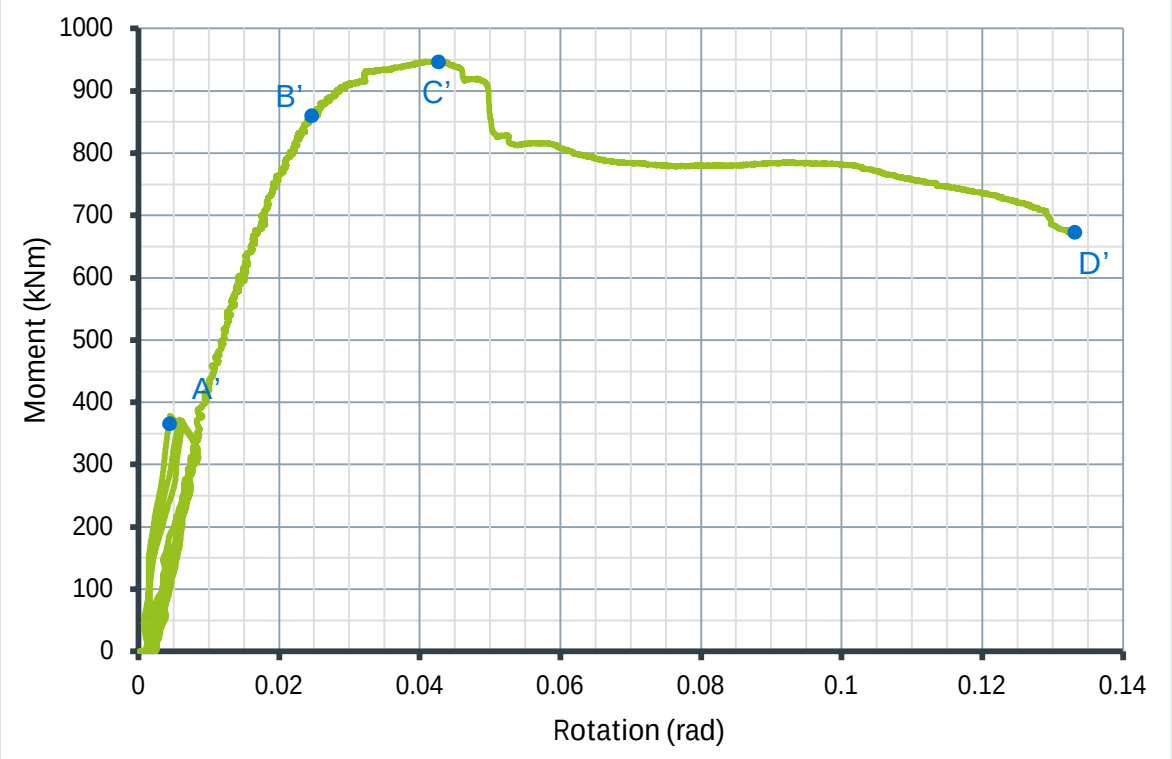

Fig. 5.43- S5- Average moment- rotation curve (Inclinometer)

The slips between the concrete and the steel beam are presented in figure 5.44 up to the maximum load. The maximum slips were observed at S4 (1.16 mm) and S3 (1.00 mm) by the LVTDs next to the loading area (figure 5.45). Slips at the right half of the beam, where the failure occurred, were bigger for deflections up to the maximum load. At the end of the test the values measured on that side were reduced, while the values measured at the left side maintained an increasing rate.

Load- strain curves are presented in figure 5.46. It can be observed that at the beginning of the deformation when the beam was behaving elastically (50 mm), the strains are equally distributed along the width of the bottom plate. When the maximum load was reached (100 mm) and the failing mechanism begun, the distribution ceased to be symmetrical. In figure 5.47 the propagation of strains across the bottom plate, for sections A-A and B-B (positions of strain gauges left and right of the loading area), for various deflection values is presented.

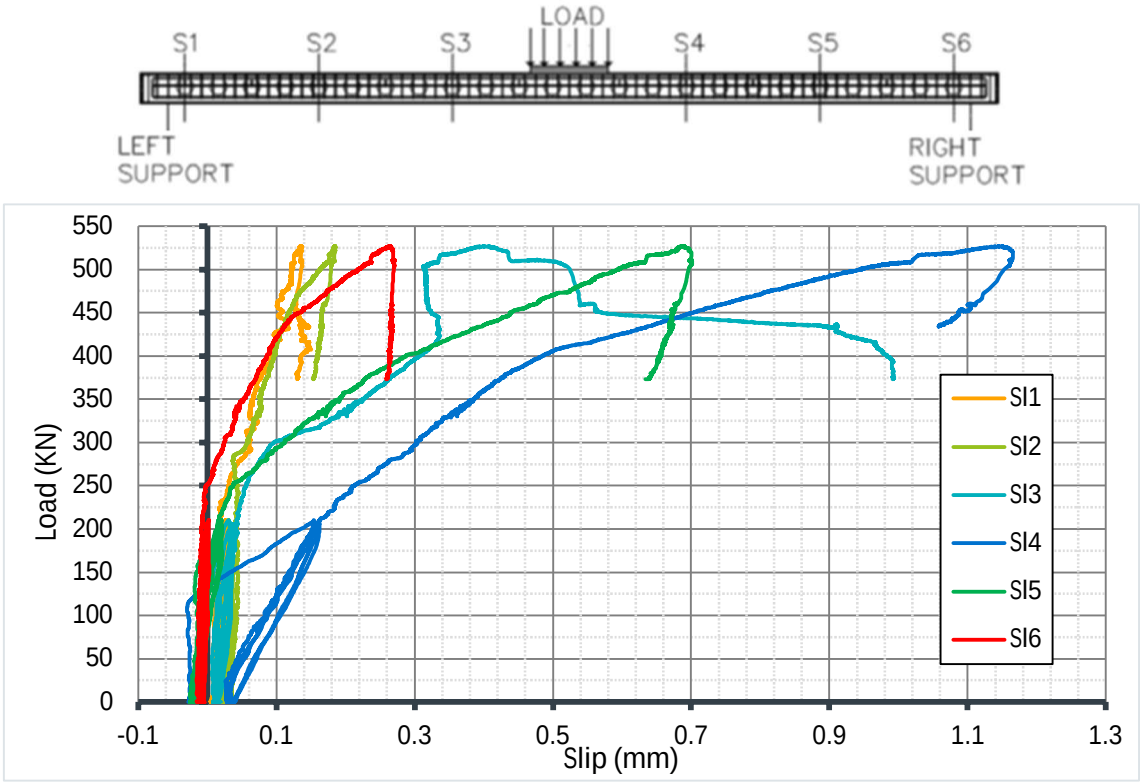

Fig. 5.44- S5- Load- slip curves

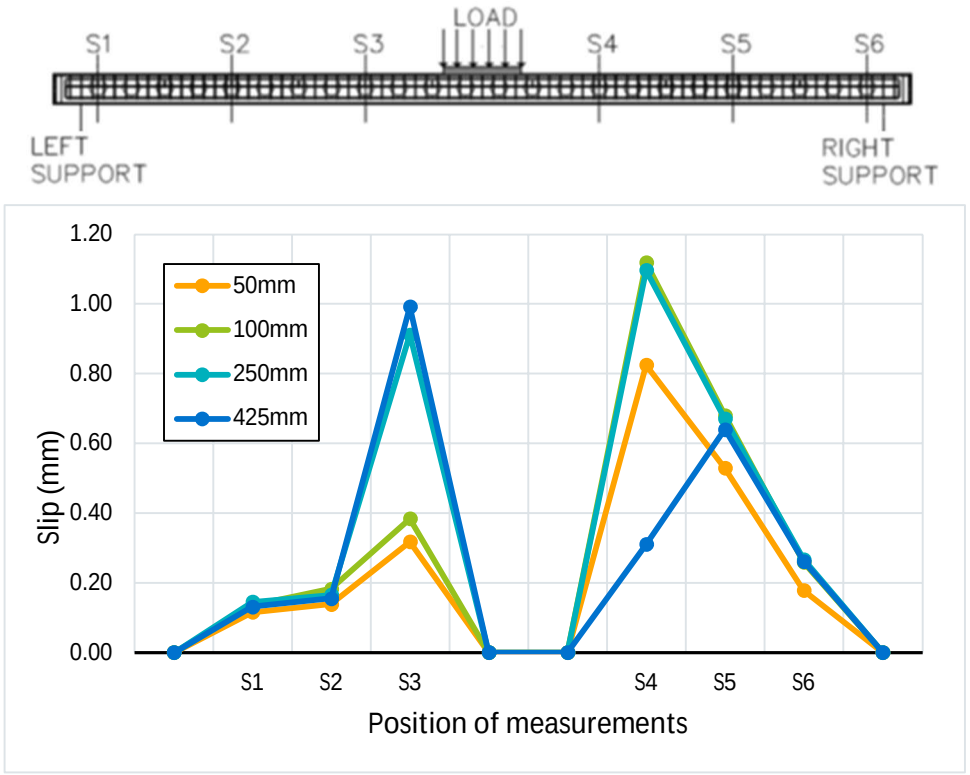

Fig. 5.45- S5- Slip propagation for different deflection values

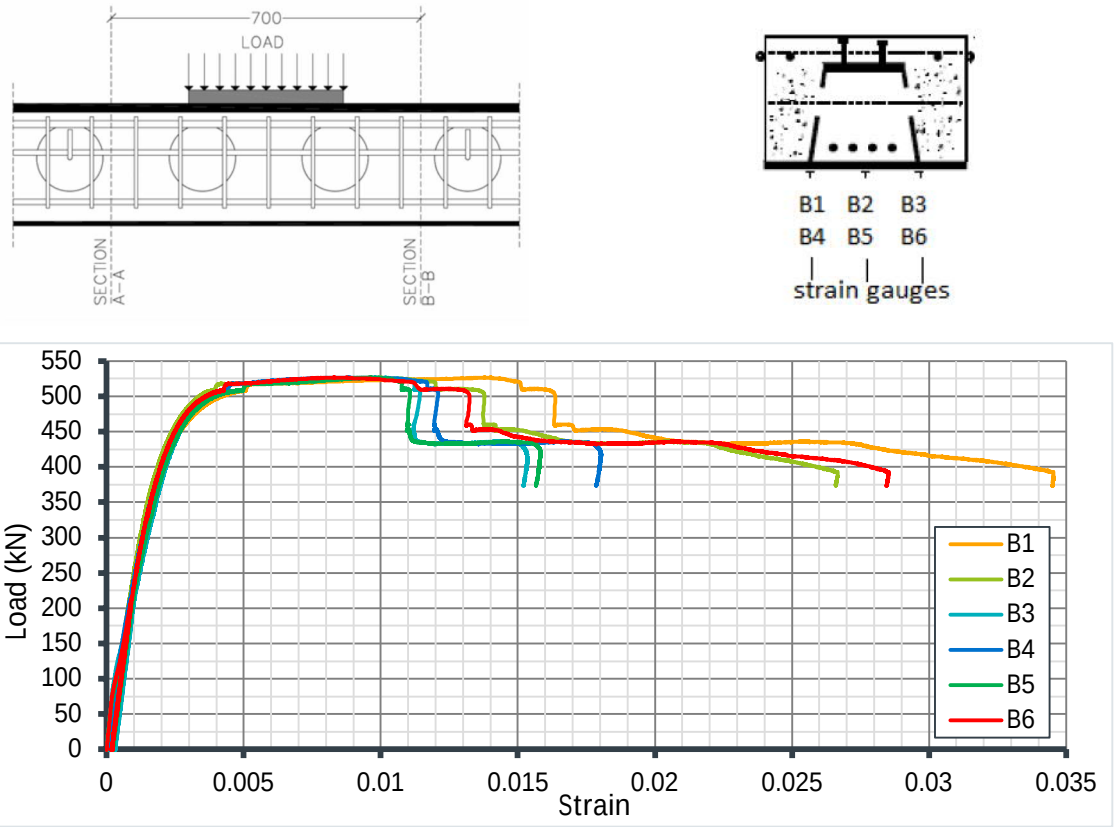

Fig. 5.46- S5- Tensile strains at the bottom plate of the beam

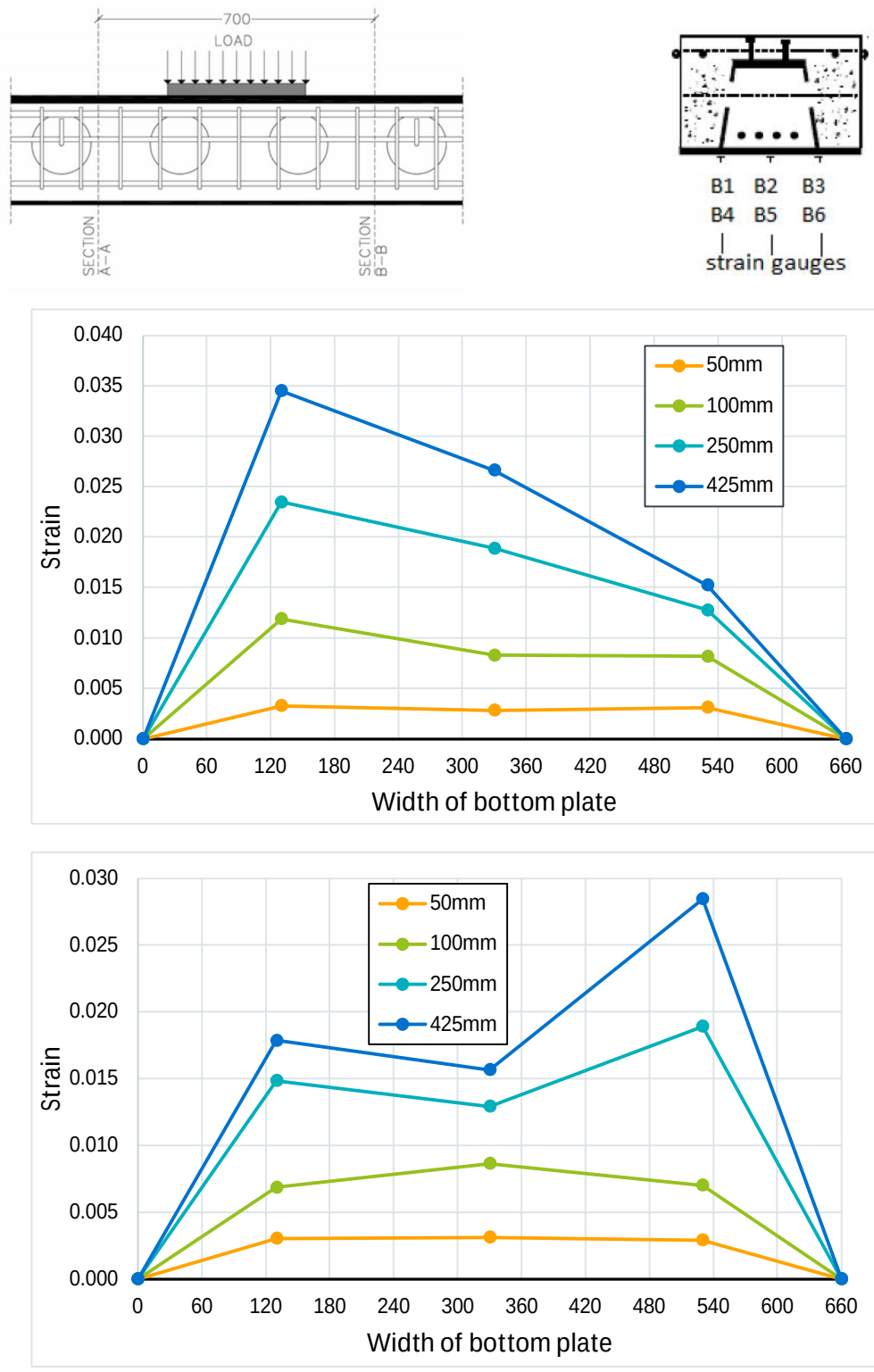

Fig. 5.47- S5- Strains along the bottom plate at sections A-A (top) and B-B (bottom) for various deflections

5.1.5 Comparative results

In figures 5.48 and 5.49 the load- deflection and the normalized load- deflection curves for all Type 1 specimens are presented, respectively. The overall behavior, as described previously, was the same for all beams. After the maximum load was reached, the beams could not undertake any additional load due to concrete crushing and buckling of the top plate. Another conclusion that can be drawn is that the different number of shear studs rows (S3 and S4 have one and S2 and S5 have two) did not affect the behavior of the beams.

Specimens S4 and S5 have identical curves and the difference of the maximum loads of S2 and S3 attributed to the fire rebars placed at the concrete core of S2. Additionally, it can be observed that the maximum load is relative to the size of the beam. The beams with the higher cross section (S4 and S5) led to higher load values than S2 and S3. An increase of 23% at the height of the beams led to 28% higher load values.

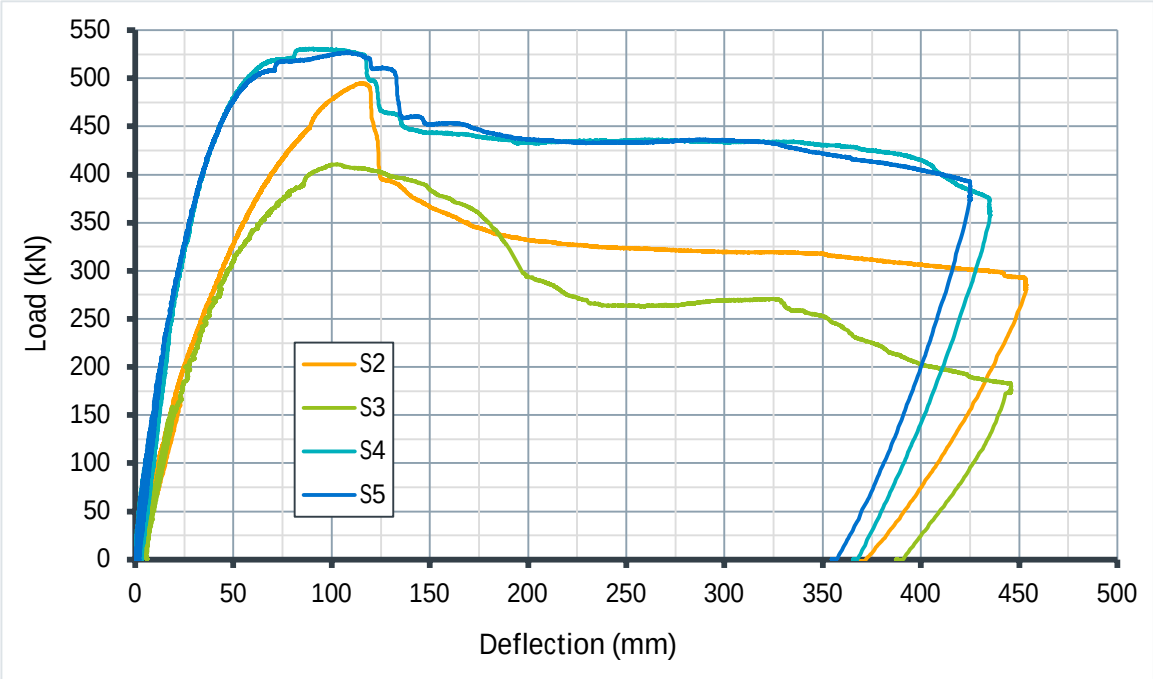

Fig. 5.48- Type 1 load- deflection curves

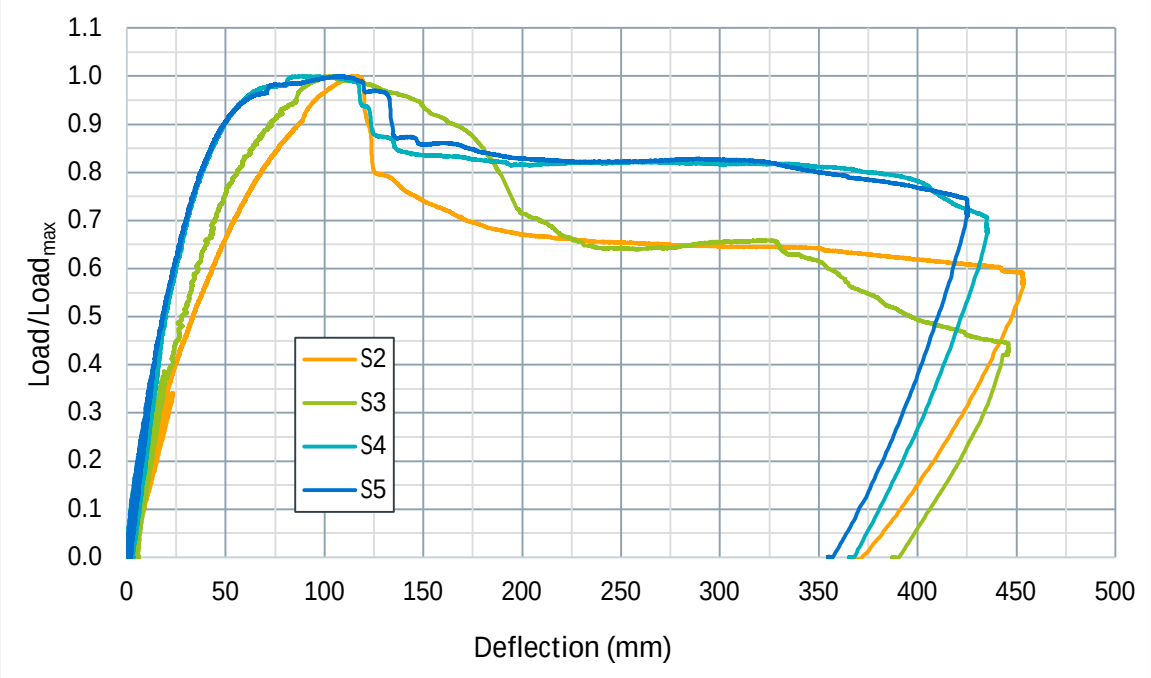

Fig. 5.49- Normalized Type 1 load- deflection curves

5.2 Type 2 sections

All specimens of this type had a flexural hardening behavior. The flexural strength was increasing until the end of the tests. It should be noted that all tests of type 2 specimens were terminated at a deflection of 450 mm because the maximum stroke of the actuator was reached. Ductility values for S1, S11 and S12 were equal to 6.4, 9.0 and 6.0, respectively, with yielding point indicated at the point where load is equal to 75% of the maximum load. Specimens at the end of the tests were in perfect condition. The concrete did not crush. The reinforcement cages (stirrups and longitudinal rebars) created conditions of three-dimensional confining stresses that constrained further crushing of concrete under the loading plate. That can lead to the assumption that even higher values of ductility could be reached. In the next paragraphs, an extensive description of the results for each Type 2 specimen is presented.

5.2.1 Specimen S1

First hair-line cracks appeared at a deflection of 25 mm after the serviceability circles (figure 5.50). In figures 5.51- 5.53 the crack pattern at 50 mm, 100 mm and 200 mm is presented,

respectively. At a deflection of 65mm, cracks were created between the contact surfaces of steel and concrete at the top faces of the beam's ends (figure 5.54). Same cracks occurred at the middle of the beam at a deflection of 100 mm (figure 5.55). The test ended at a deflection of 448mm because the loading actuator reached its maximum displacement capacity. The beam maintained its strength until the end of the test with no degradation (figures 5.57- 5.58). In figure 5.56 the condition of the beam can be seen after removing the crushed part of the concrete. The usage of the stirrups prevented further crushing of the concrete and limited the failure at the cover area.

Fig. 5.50- S1- Hair-line cracks at deflection of 25 mm (fig. 5.57 and 5.58, points A and A')

Fig. 5.51- S1- Cracks at deflection of 50 mm (fig. 5.57 and 5.58, points B and B')

Fig. 5.52- S1- Cracks at deflection of 100 mm (fig. 5.57 and 5.58, points D and D')

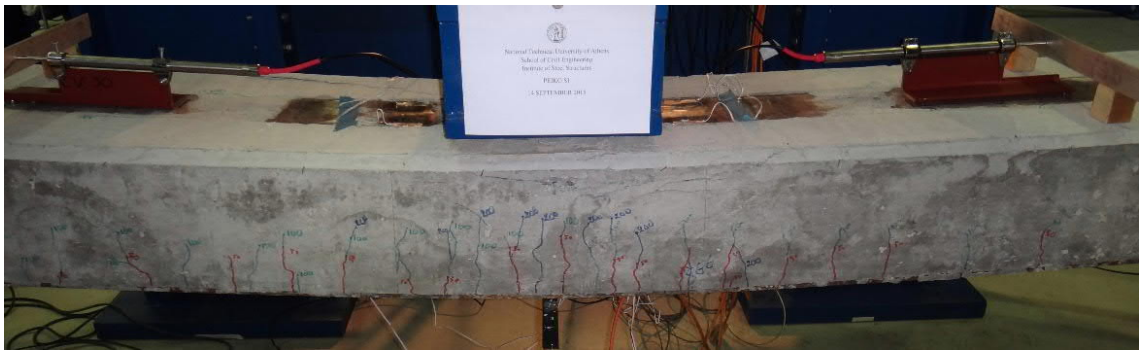

Fig. 5.53- S1- Cracks at deflection of 200 mm (fig. 5.57 and 5.58, points E and E')

Fig. 5.54- S1- Cracks between concrete and steel at 65 mm deflection (fig. 5.57 and 5.58, points C and C')

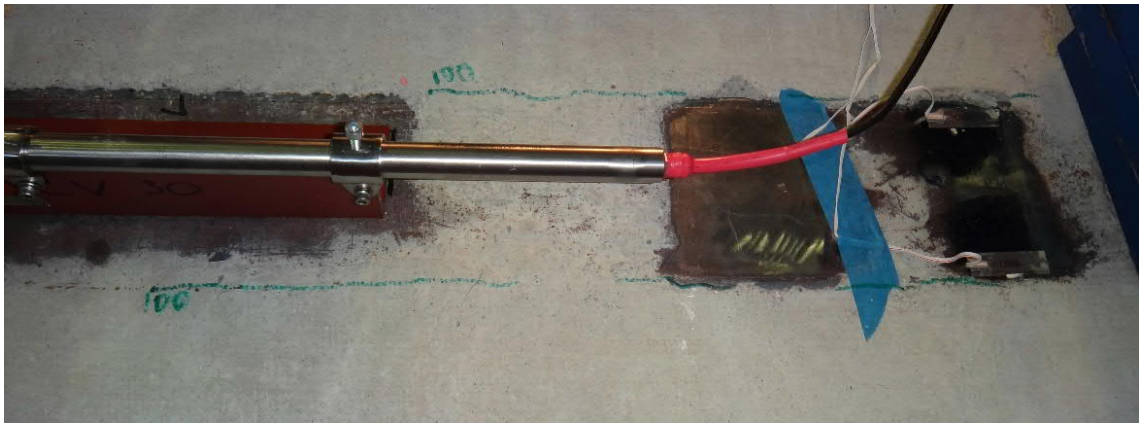

Fig. 5.55- S1- Cracks between concrete and steel at 100 mm deflection (fig. 5.57 and 5.58, points D and D')

Fig. 5.56- S1- The specimen at the end of the test (fig. 5.57 and 5.58, points F and F')

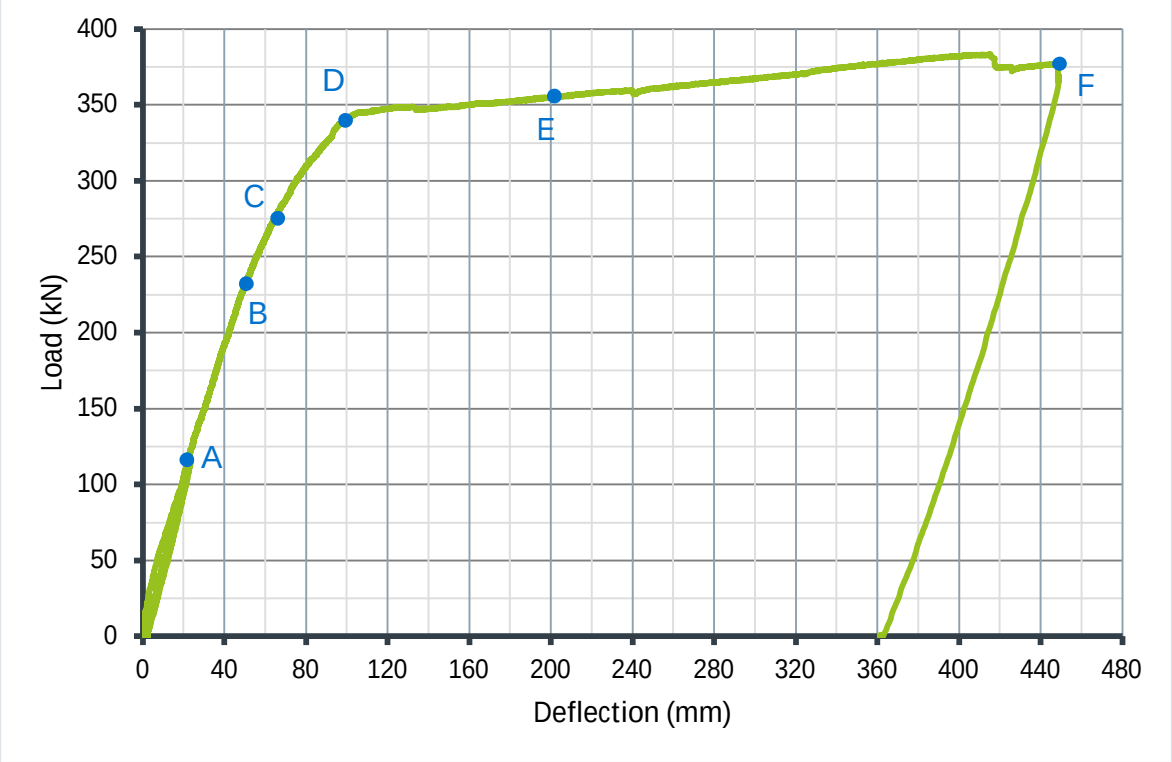

Fig. 5.57- S1- Average load- deflection curve

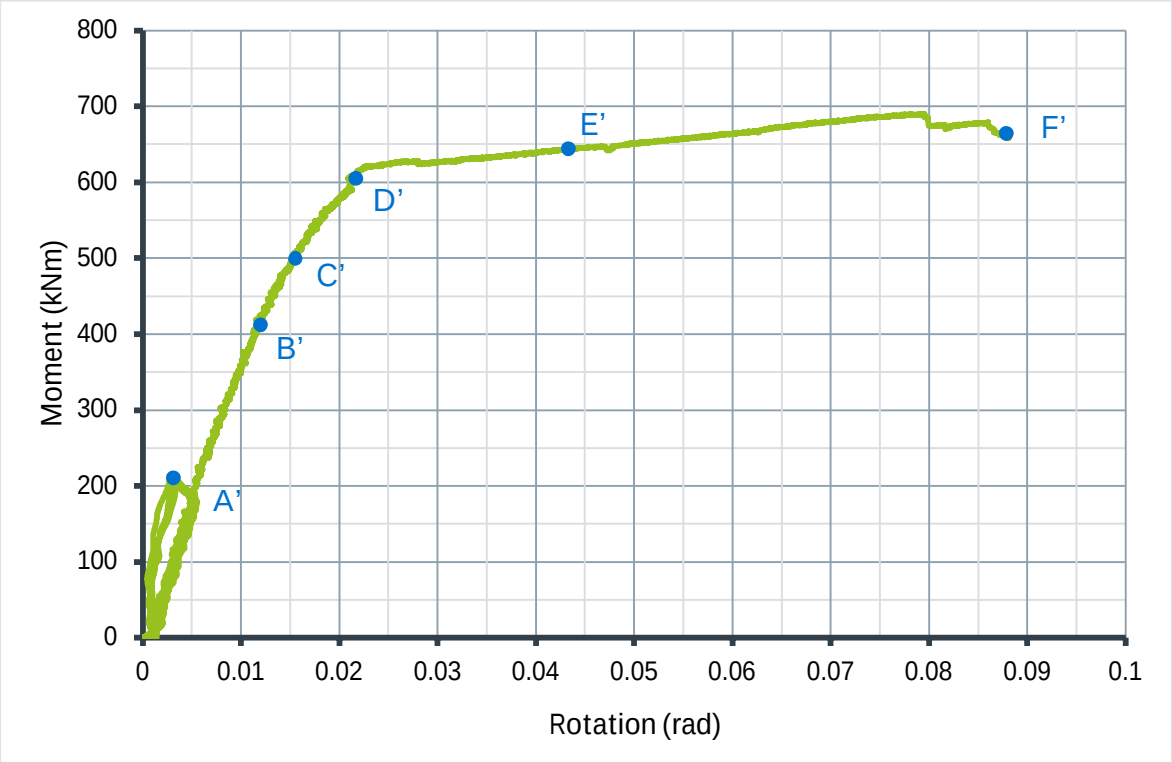

Fig. 5.58- S1- Average moment- rotation curve (Inclinometer)

The slips between the concrete and the steel beam remained in very low values (figure 5.59). Maximum slips were observed at S3 (0.61 mm) and S4 (0.44 mm). The slips measured by the remaining instruments (S1, S2, S5 and S6) were almost zero (figure 5.60).

Load- strain curves are presented in figure 5.61. In figures 5.62 and 5.63 the propagation of strains is presented at the intersections of web plates with the bottom and top plates, for different deflection values. It can be observed that strains have relatively similar values at all 8 measurement points, leading to the conclusion of a symmetrical distribution of the deformation.

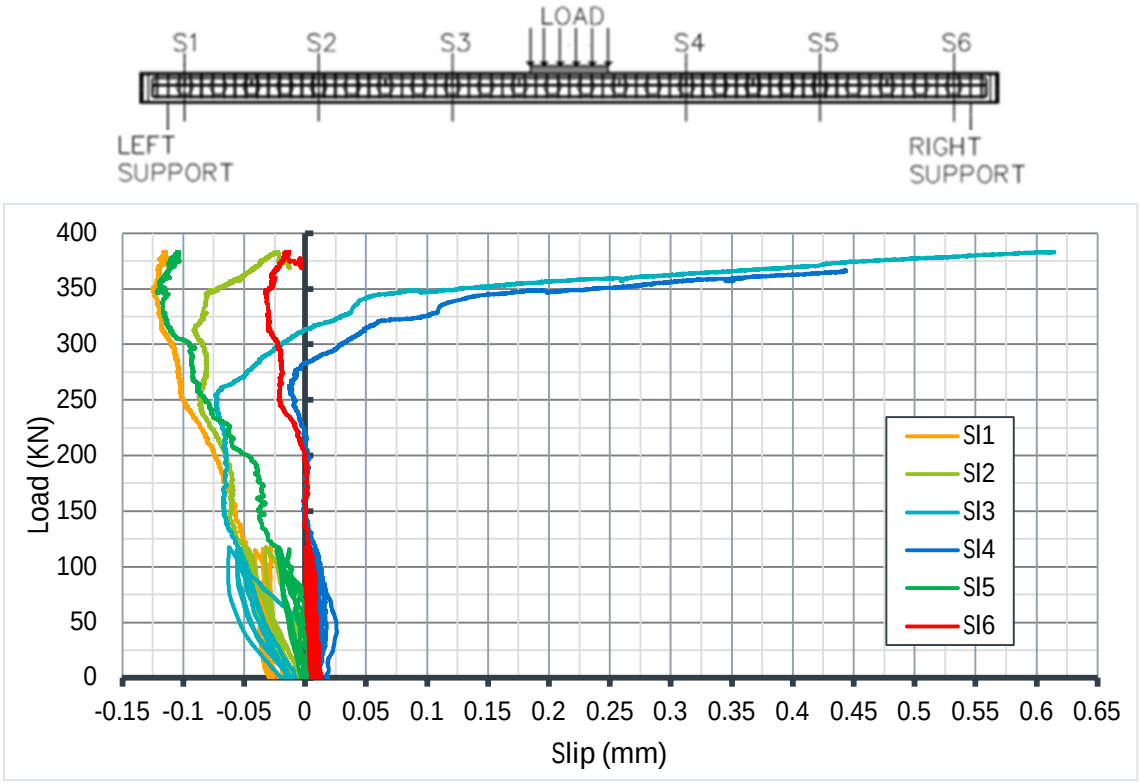

Fig. 5.59- S1- Load- slip curves

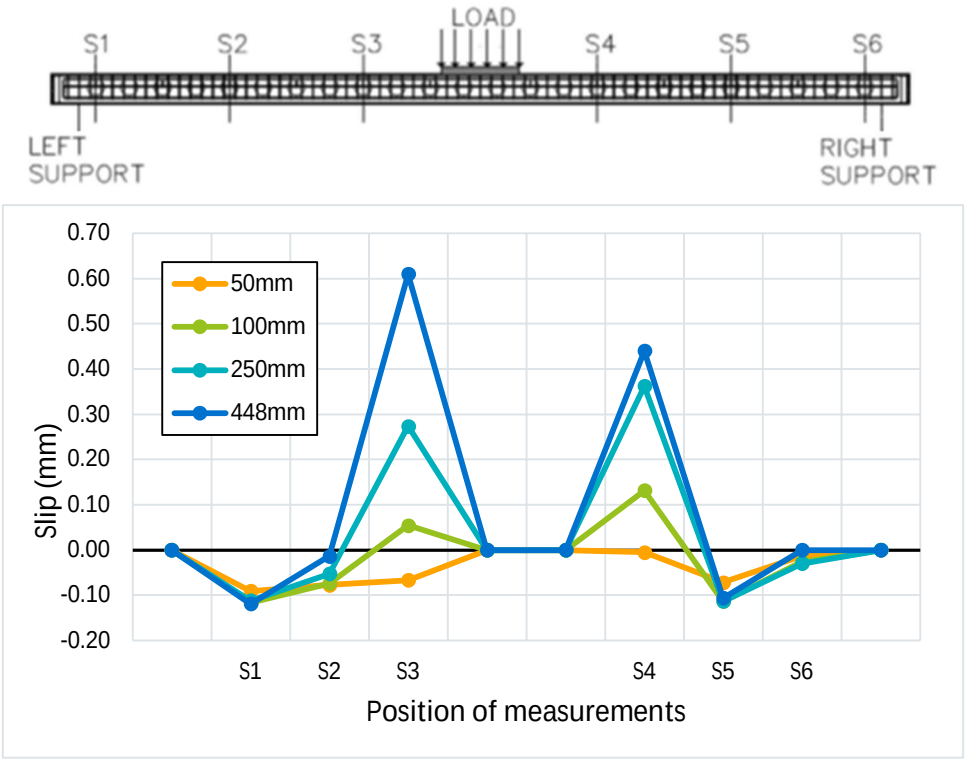

Fig. 5.60- S1- Slip propagation for different deflection values

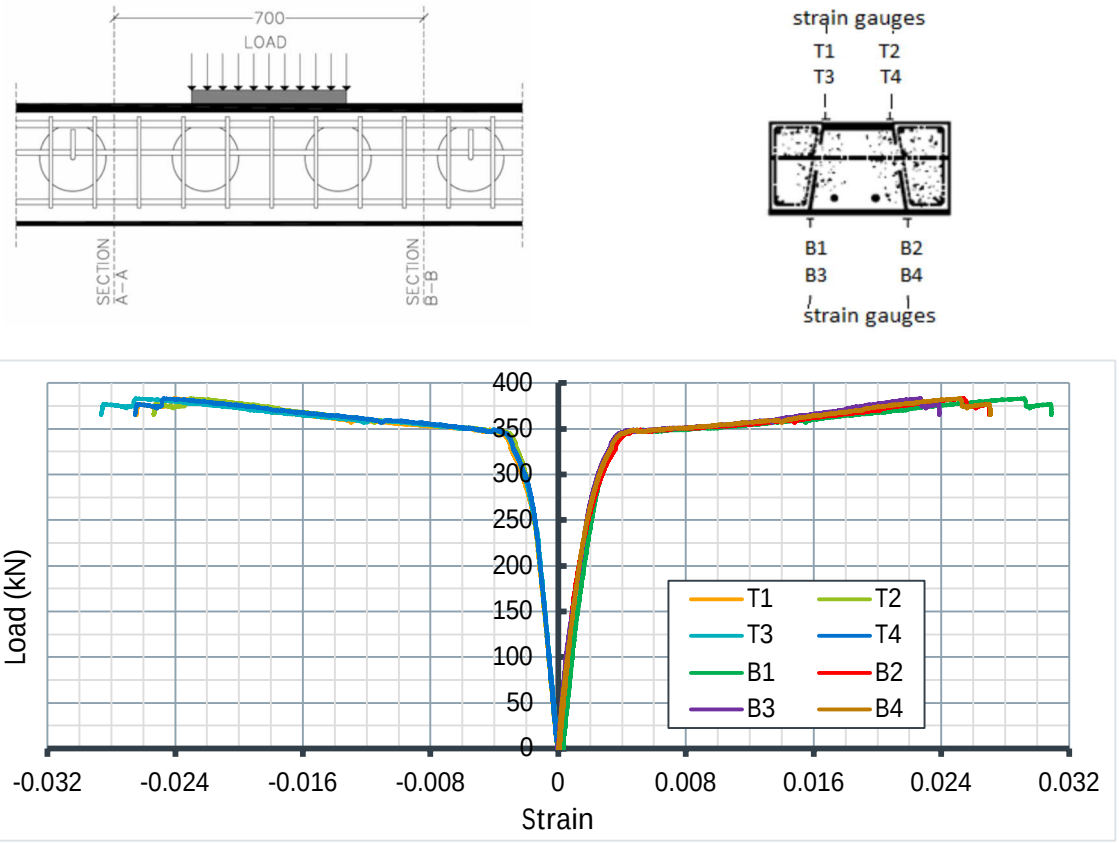

Fig. 5.61- S1- Strains at the top and bottom plates of the beam

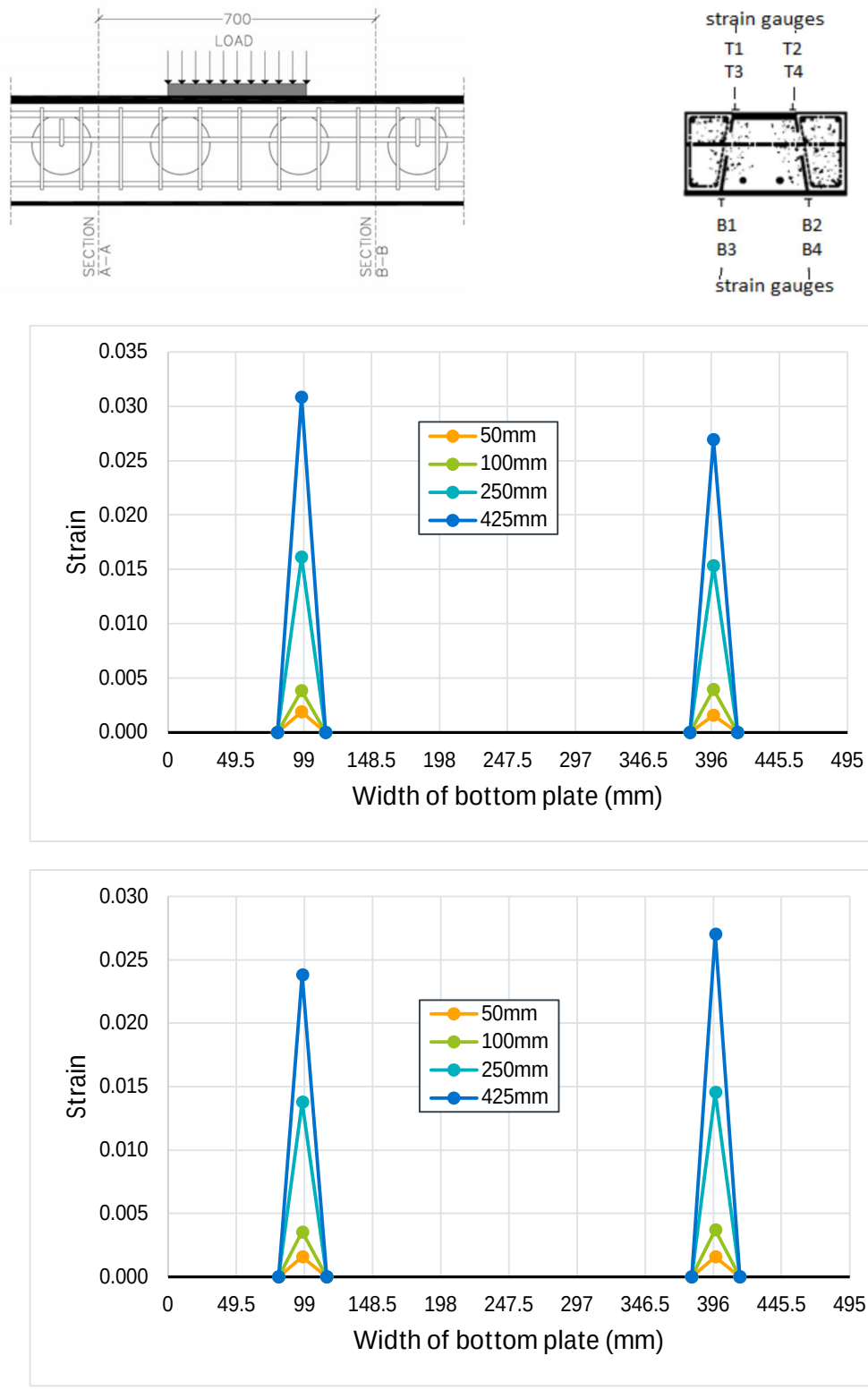

Fig. 5.62- S1- Strains along the bottom plate at sections A-A (top) and B-B (bottom) for various deflections

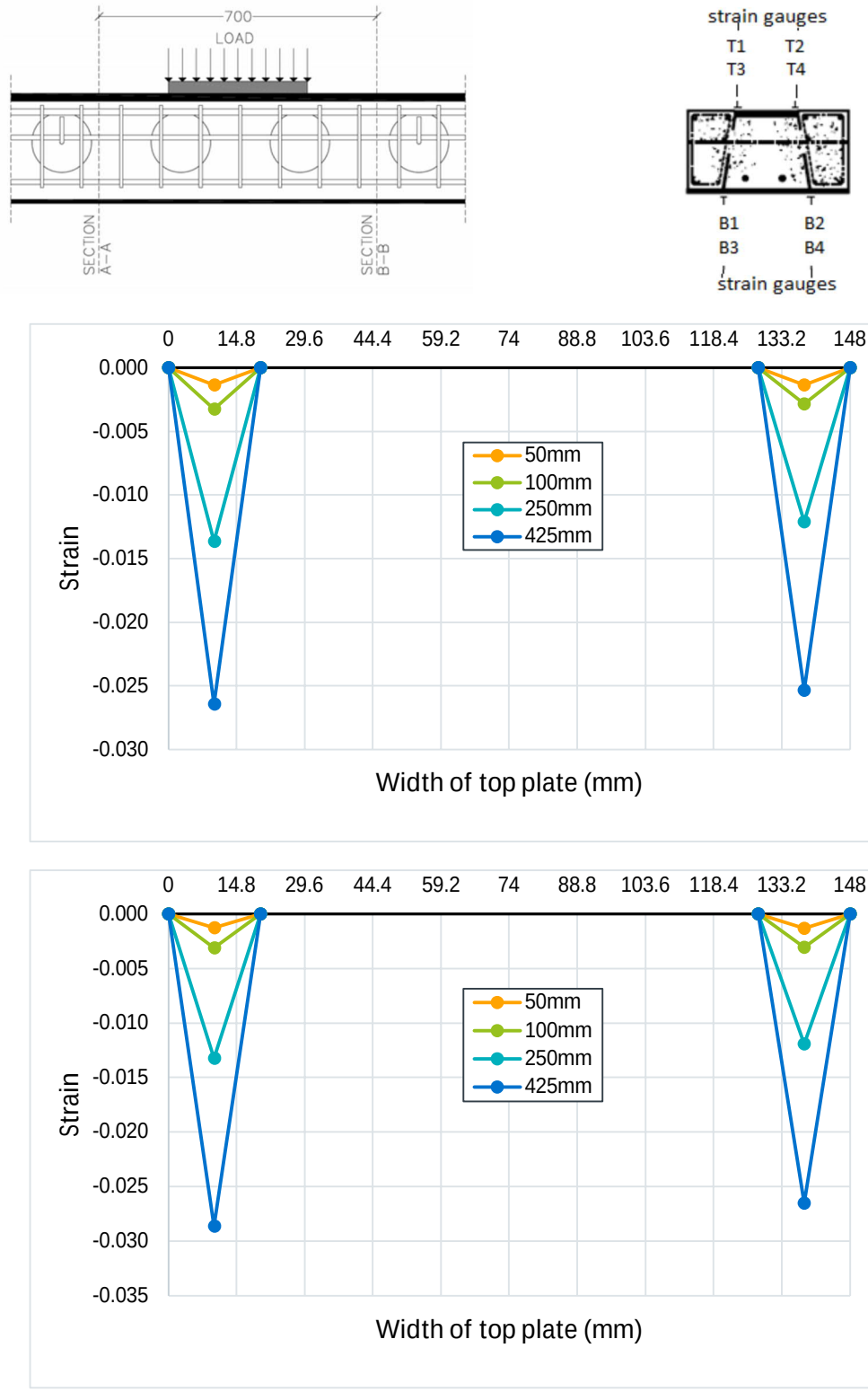

Fig. 5.63- S1- Strains along the top plate at sections A-A (top) and B-B (bottom) for various deflections

5.2.2 Specimen S11

First hair-line cracks appeared at a deflection of 18 mm (521 kN) after the serviceability circles (figure 5.64). In figures 5.65- 5.66 and 5.68-5.69 the crack pattern at 25 mm (709 kN), 50 mm (1142 kN), 100 mm (1316 kN) and 150 mm (1388 kN) is presented, respectively. At a deflection of 65mm (1231 kN), cracks were created at the concrete due to compressive stresses (figure 5.67). The test ended at a deflection of 445mm (1510 kN) because the loading actuator reached its maximum displacement capacity. The beam maintained its strength until the end of the test with no degradation (figures 5.71 and 5.72). In figure 5.70 the condition of the beam, after removing the crushed part of the concrete, can be observed. The usage of stirrups prevented the extensive crushing of the concrete and limited the failure at the cover area.

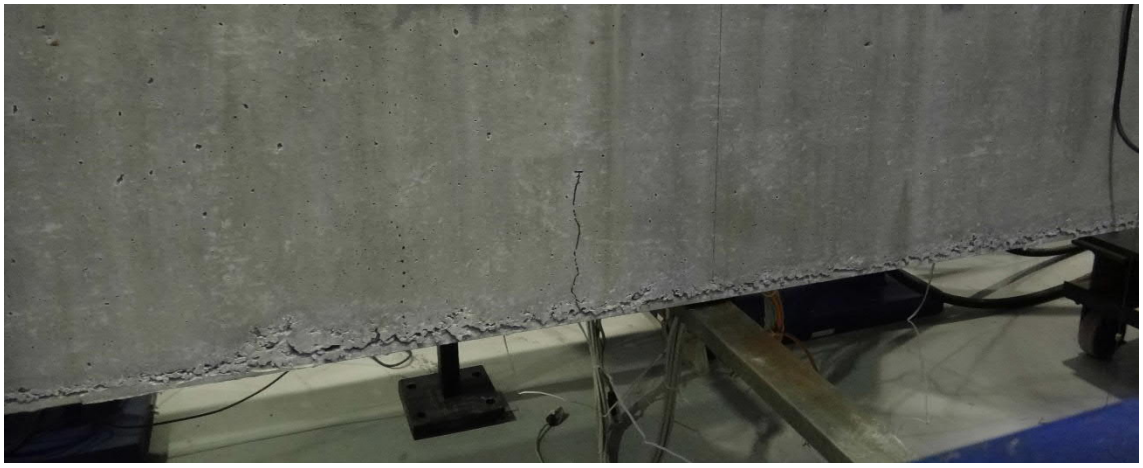

Fig. 5.64- S11- Hair-line cracks at deflection of 18 mm (fig. 5.71 and 5.72, points A and A')

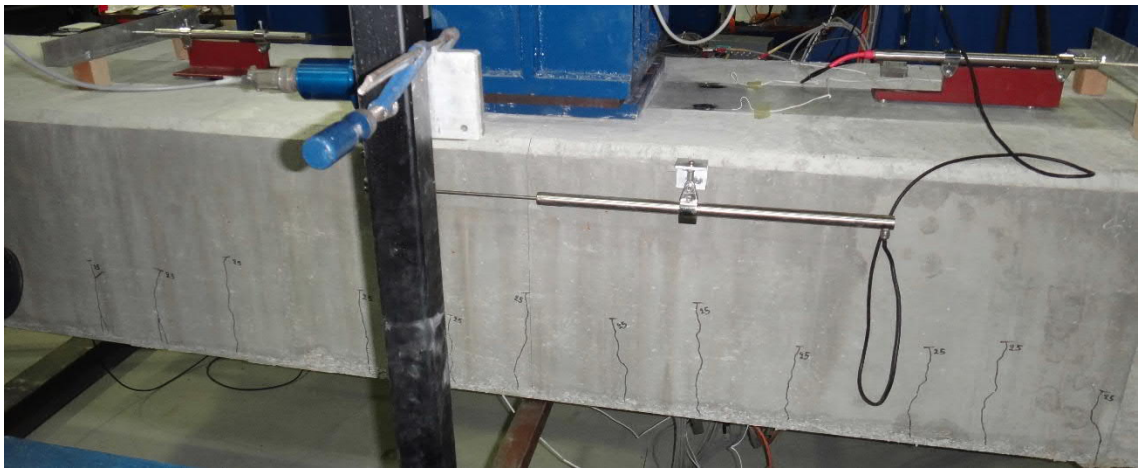

Fig. 5.65- S11- Cracks at deflection of 25 mm (fig. 5.71 and 5.72, points B and B')

Fig. 5.66- S11- Cracks at deflection of 50 mm (fig. 5.71 and 5.72, points C and C')

Fig. 5.67- S11- Cracks due to compression at deflection of 65 mm (fig. 5.71 and 5.72, points D and D')

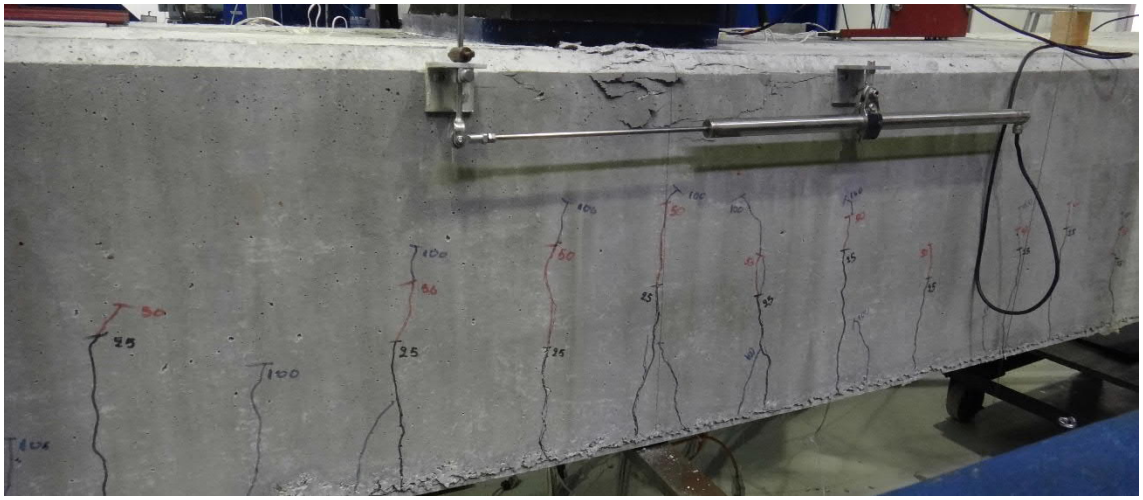

Fig. 5.68- S11- Cracks at deflection of 100 mm (fig. 5.71 and 5.72, points E and E')

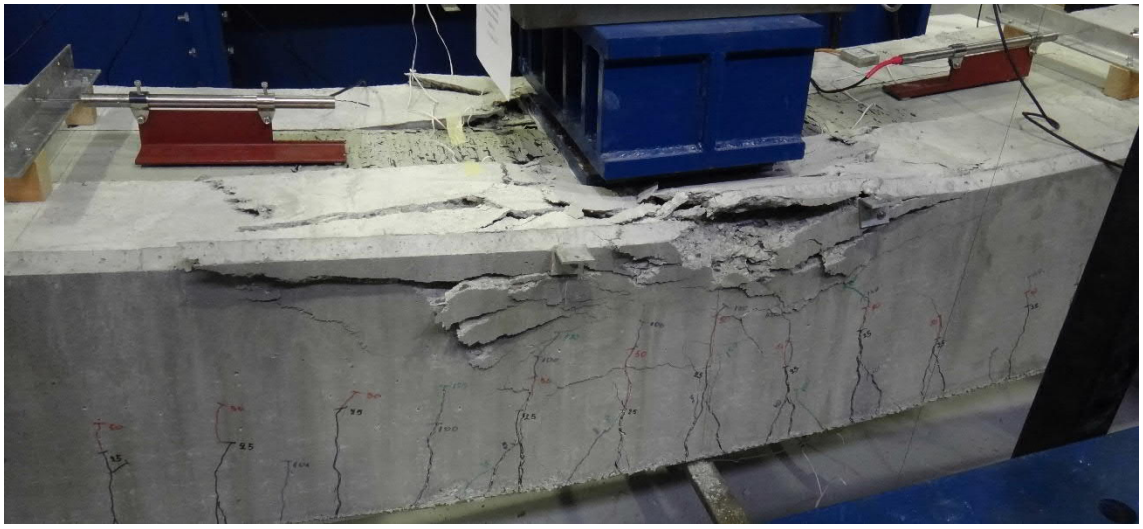

Fig. 5.69- S11- Cracks at deflection of 150 mm (fig. 5.71 and 5.72, points F and F')

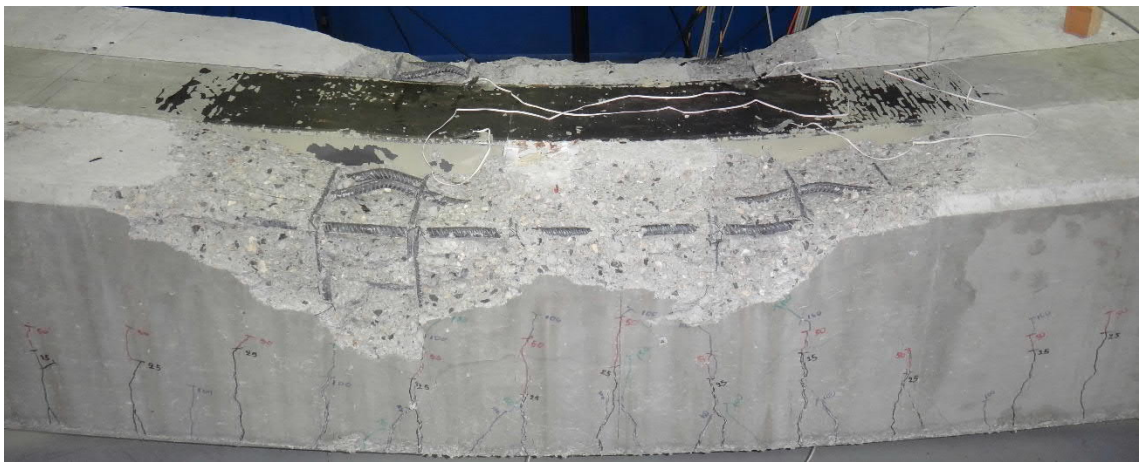

Fig. 5.70- S11- The specimen at the end of the test (fig. 5.71 and 5.72, points G and G')

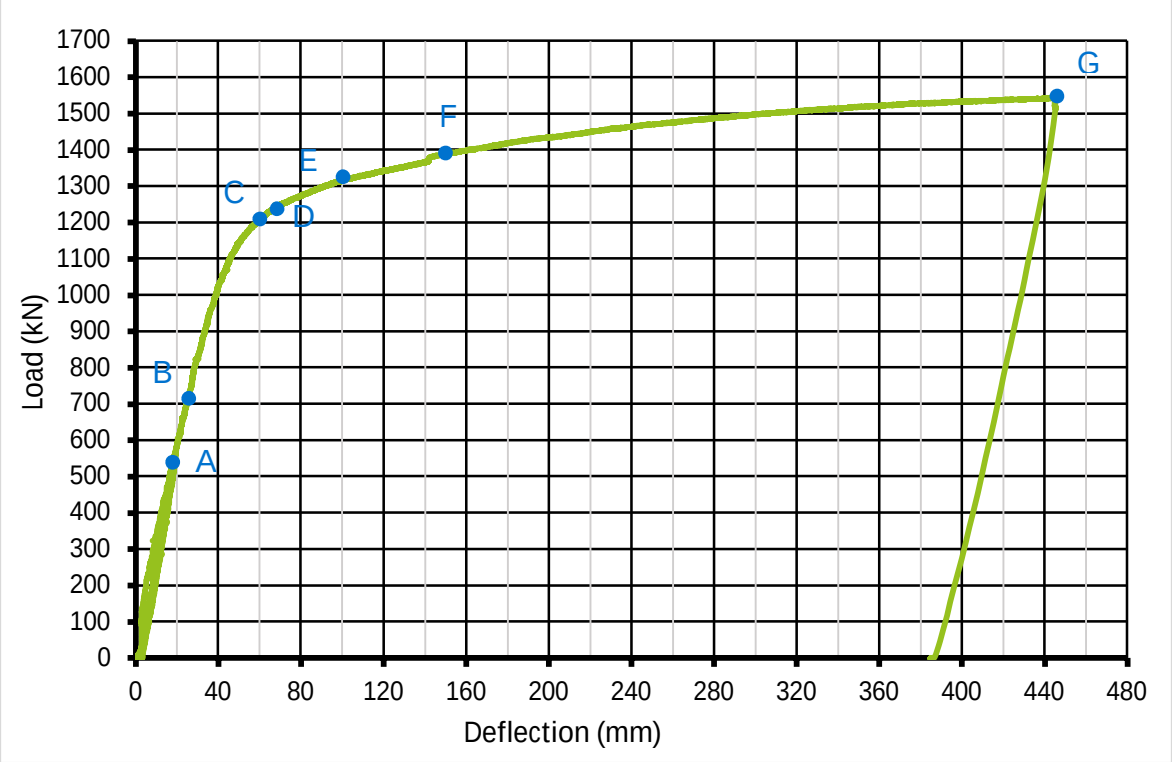

Fig. 5.71- S11- Average load- deflection curve

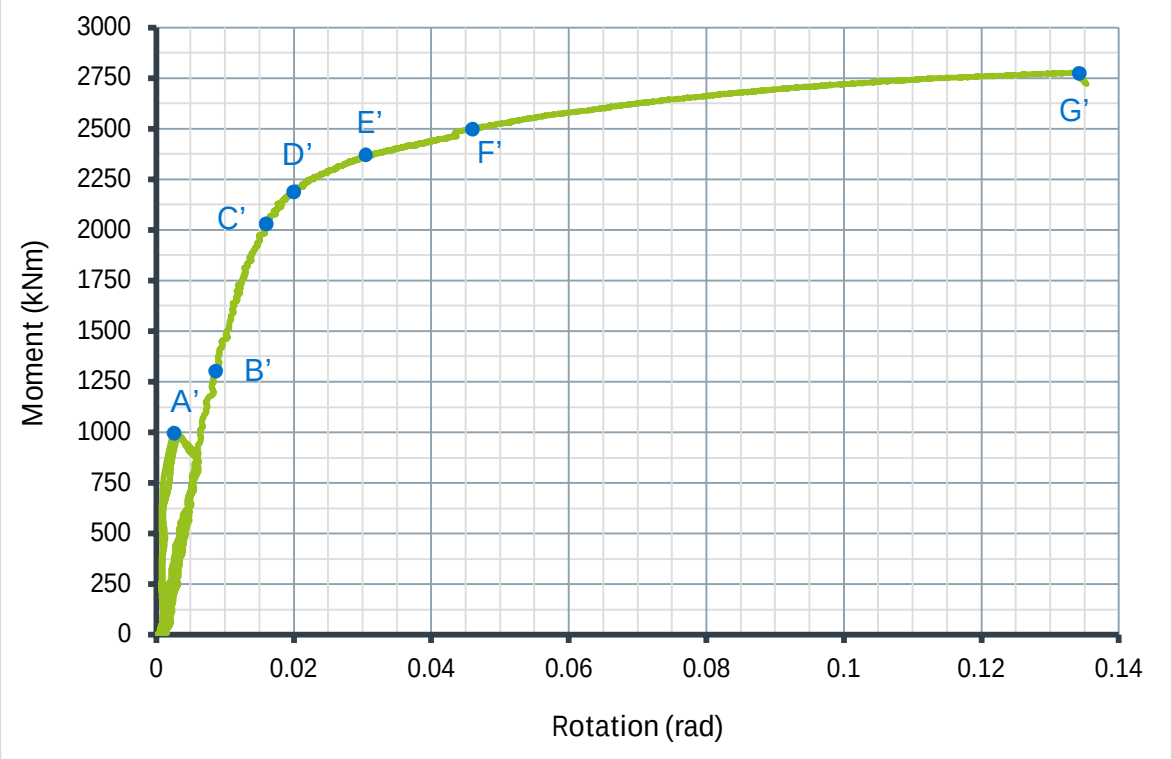

Fig. 5.72- S11- Average moment- rotation curve (Inclinometer)

The slips between the concrete and the steel beam remained in very low values (figure 5.73). Maximum slips were observed at S4 (0.40 mm) and S5 (0.33 mm). Generally, the slips where not symmetrical, but because of the very small values no additional conclusions can be drawn (figure 5.74).

Load- strain curves are presented in figure 5.75. In figures 5.76 and 5.77 the propagation of strains is presented at the intersections of web plates with the bottom and top plates, for different deflection values. It can be observed that tensile strains at the bottom plate have much higher values than the corresponding compressive strains at the top plate, meaning that the neutral axis is located higher than the mid-height of the cross section.

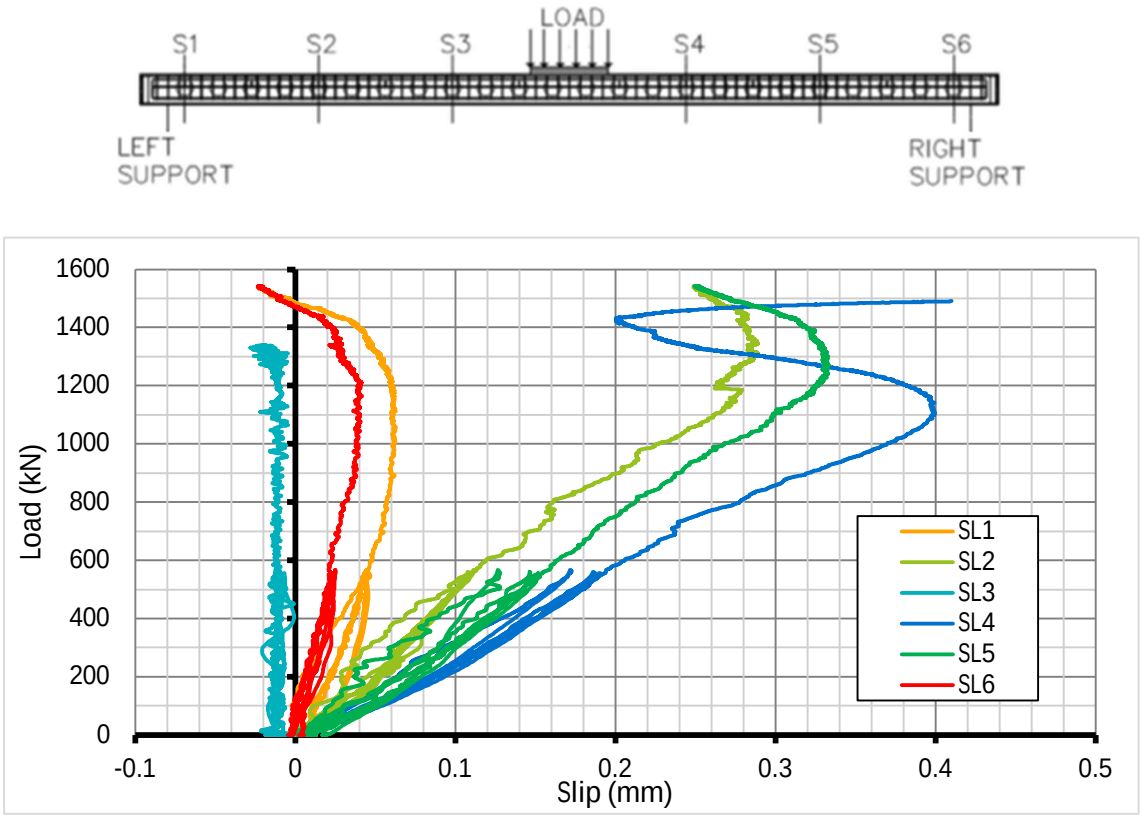

Fig. 5.73- S11- Load- slip curves

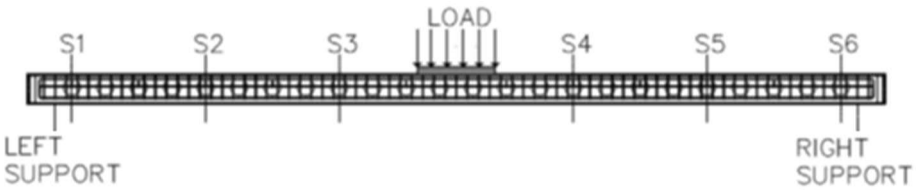

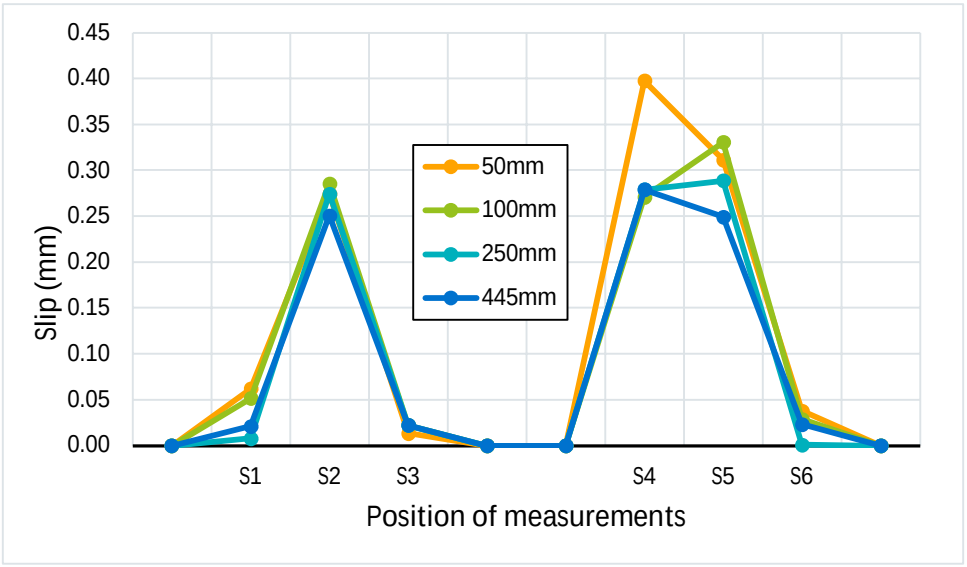

Fig. 5.74- S11- Slip propagation for different deflection values

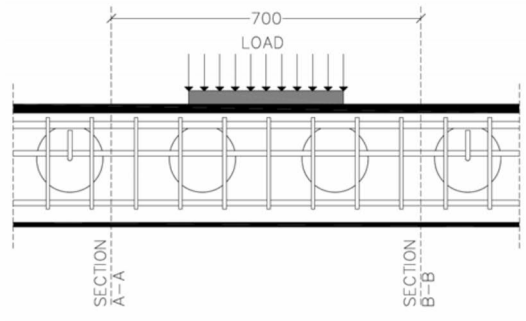

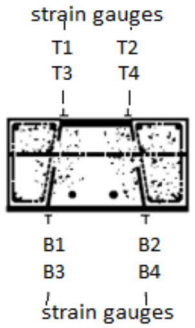

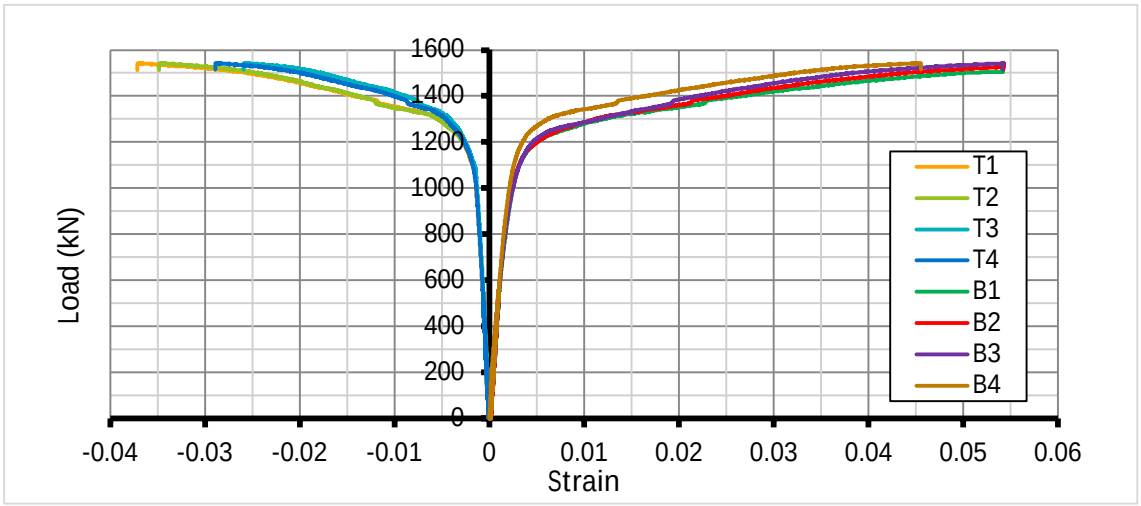

Fig. 5.75- S11- Strains at the top and bottom plates of the beam

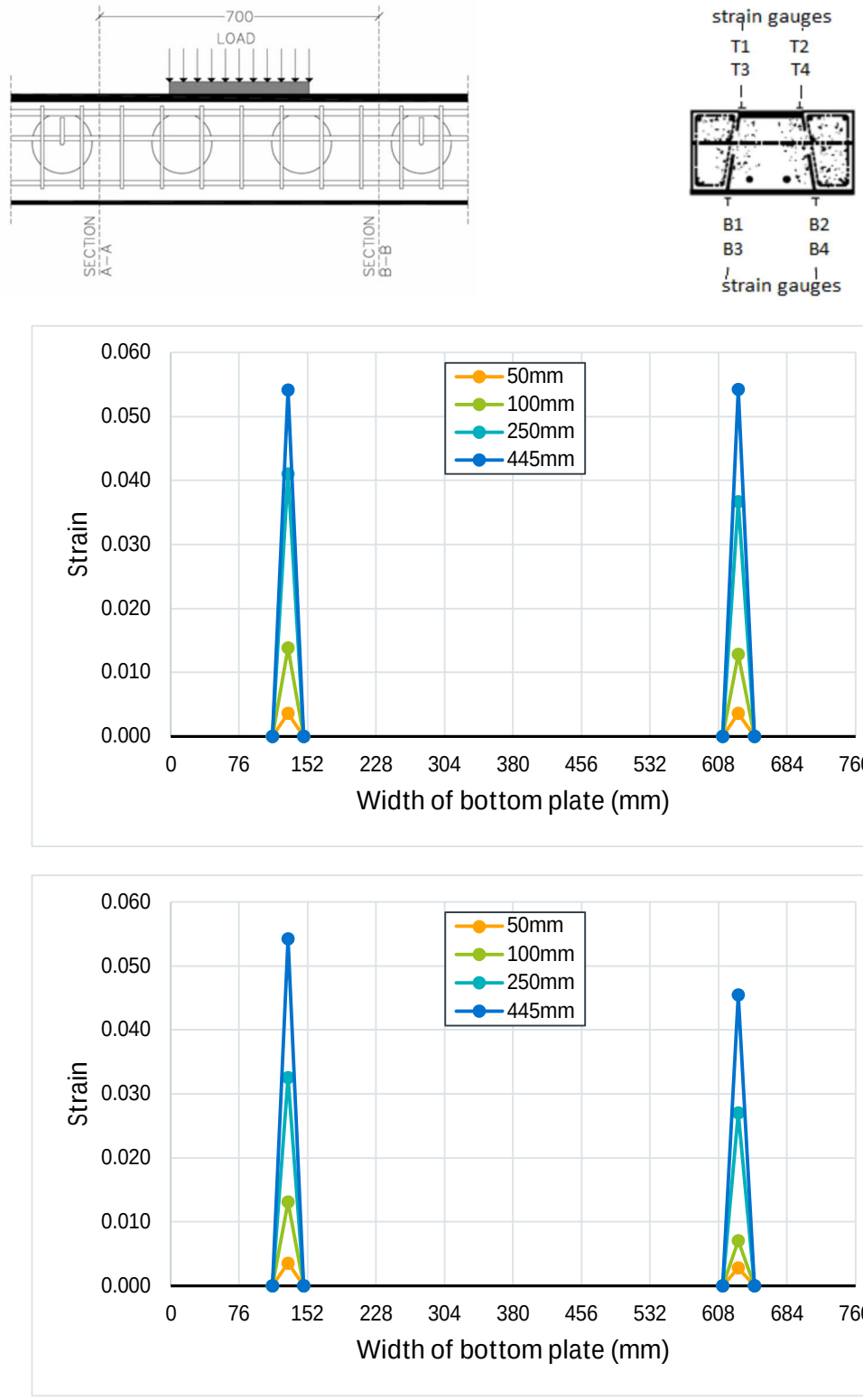

Fig. 5.76- S11- Strains along the bottom plate at sections A-A (top) and B-B (bottom) for various deflections

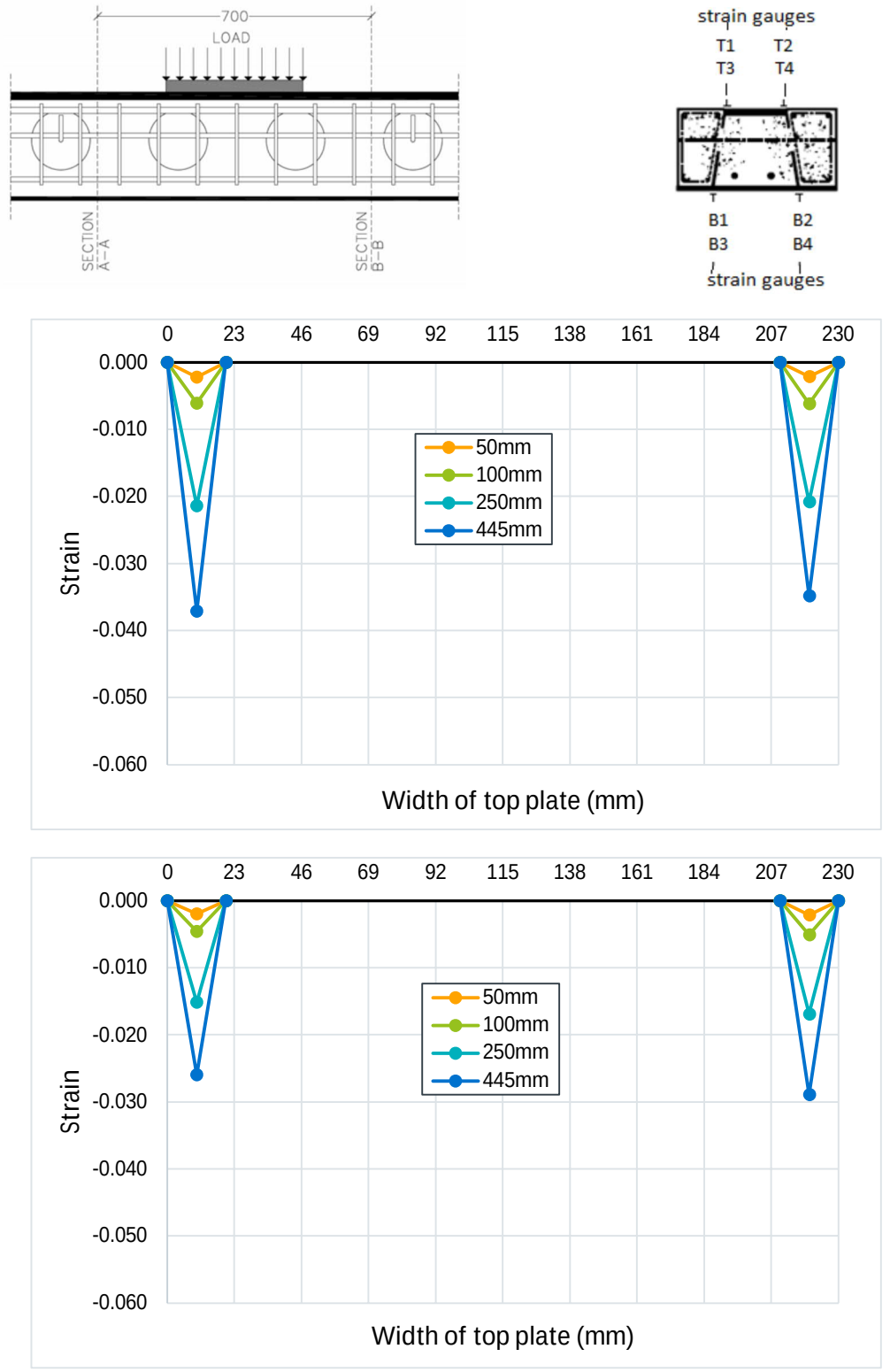

Fig. 5.77- S11- Strains along the top plate at sections A-A (top) and B-B (bottom) for various deflections

5.2.3 Specimen S12

The first cracks appeared at a deflection of 21 mm of the first and second serviceability circle (figure 5.78). The difference with the previous specimens of this type was that these initial cracks were developed at the top surface of concrete at both ends probably due to torsion. Also, some small gaps were visible between the interface of concrete and steel beam. In figures 5.79-5.81 the crack pattern at 50 mm, 100 mm and 180 mm is presented, respectively. The test ended at a deflection of 416 mm again because the loading actuator reached its maximum displacement capacity. The beam maintained its strength until the end of the test with no degradation (figures 5.85 and 5.86) and the damage at concrete was limited at the top cover (figure 5.82). Finally, due to the lack of symmetry the specimen at the end of the test was twisted. Torsion can be seen in pictures 5.83 and 5.84.

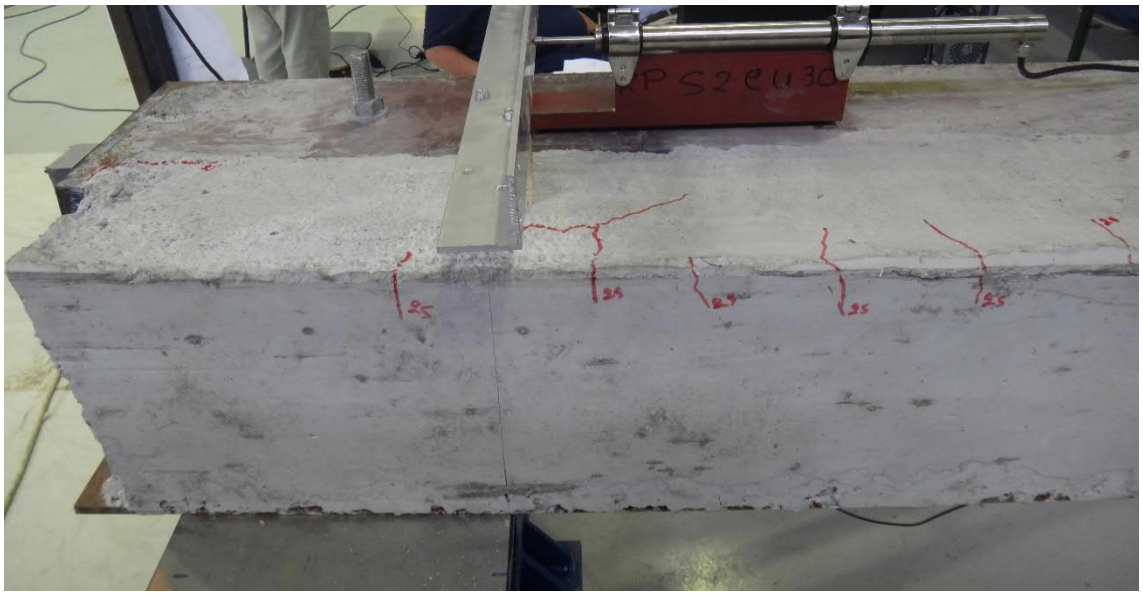

Fig. 5.78- S12- Cracks at deflection of 21 mm (fig. 5.85 and 5.86, points A and A')

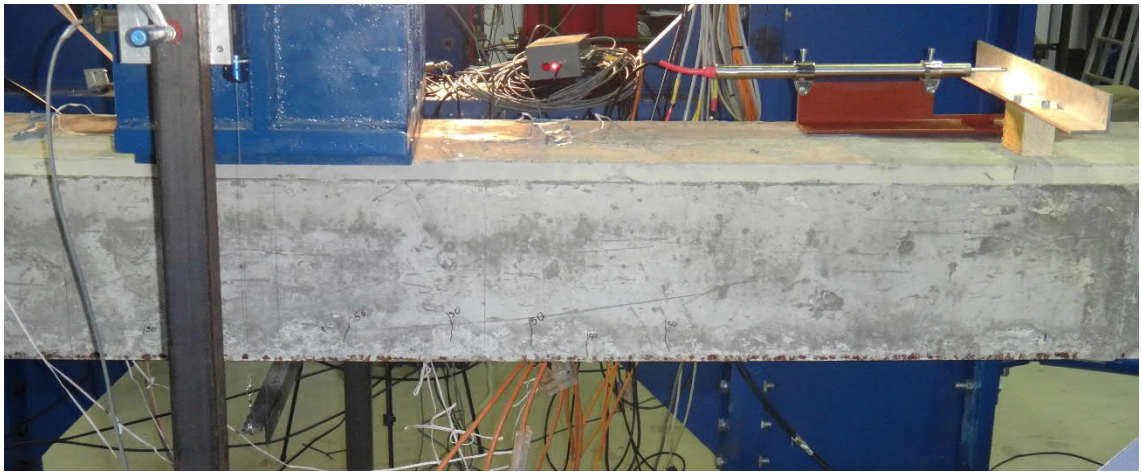

Fig. 5.79- S12- Cracks at deflection of 50 mm (fig. 5.85 and 5.86, points B and B')

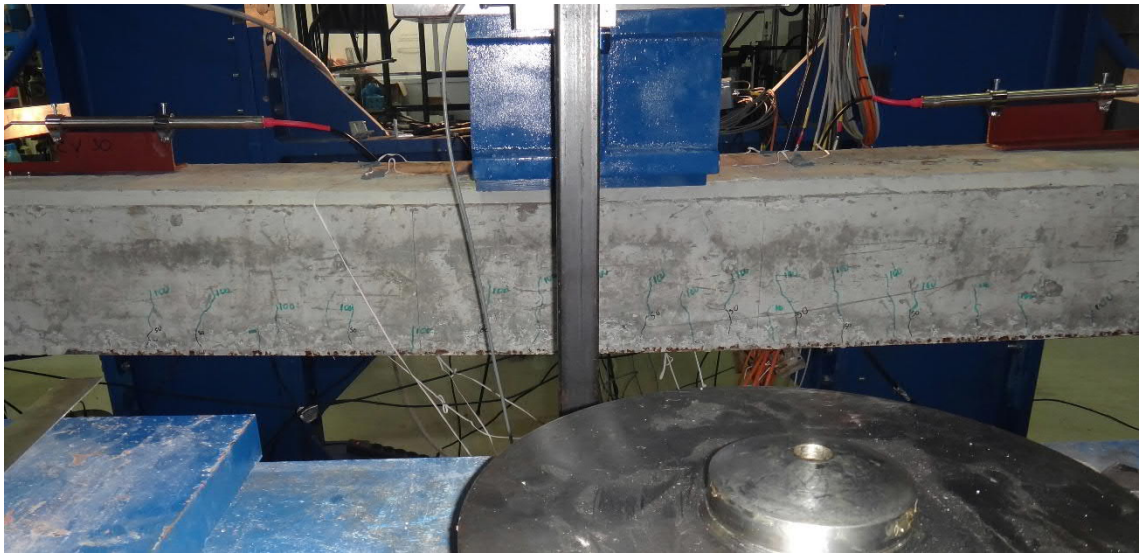

Fig. 5.80- S12- Cracks at deflection of 100 mm (fig. 5.85 and 5.86, points C and C')

Fig. 5.81- S12- Cracks at deflection of 180 mm (fig. 5.85 and 5.86, points D and D')

Fig. 5.82- S12- The specimen at the end of the test (fig. 5.85 and 5.86, points E and E')

Fig. 5.83- S12- Torsion at the end of the test (fig. 5.85 and 5.86, points E and E')

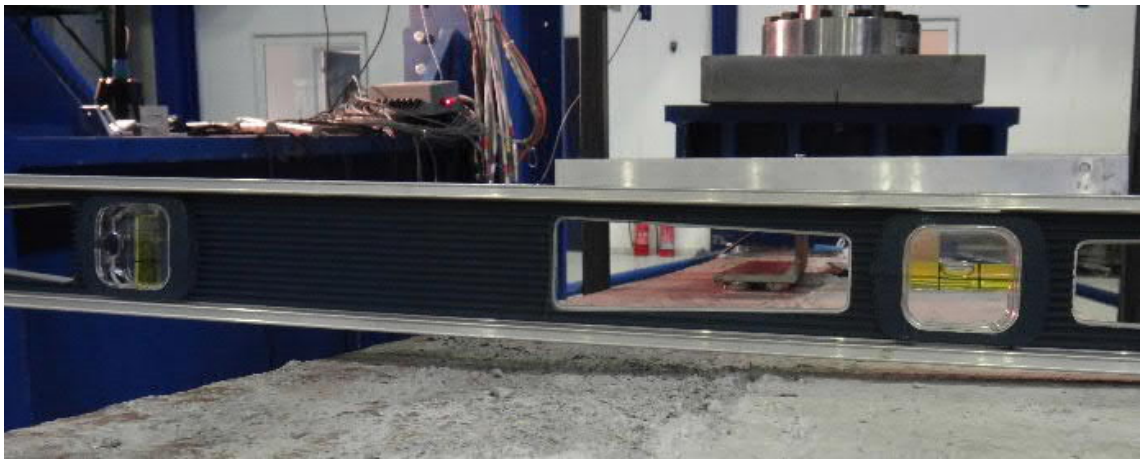

Fig. 5.84- S12- Torsion at the end of the test (fig. 5.85 and 5.86, points E and E')

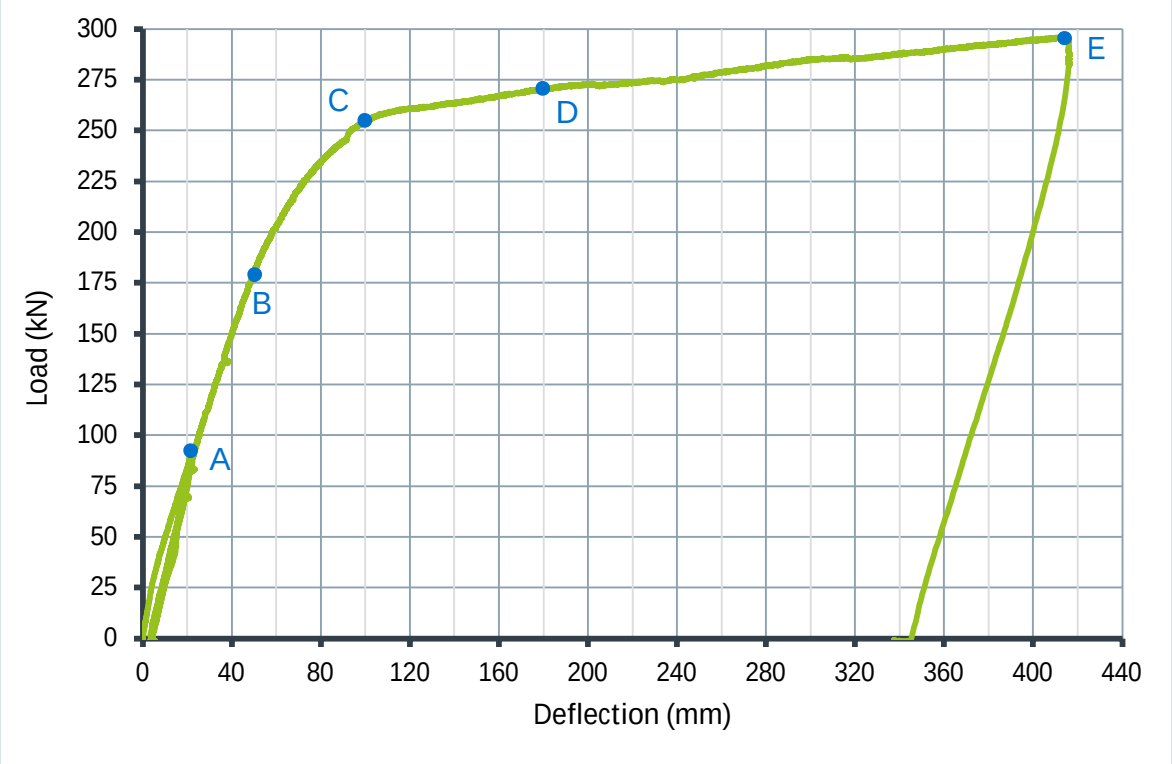

Fig. 5.85- S12- Average load- deflection curve

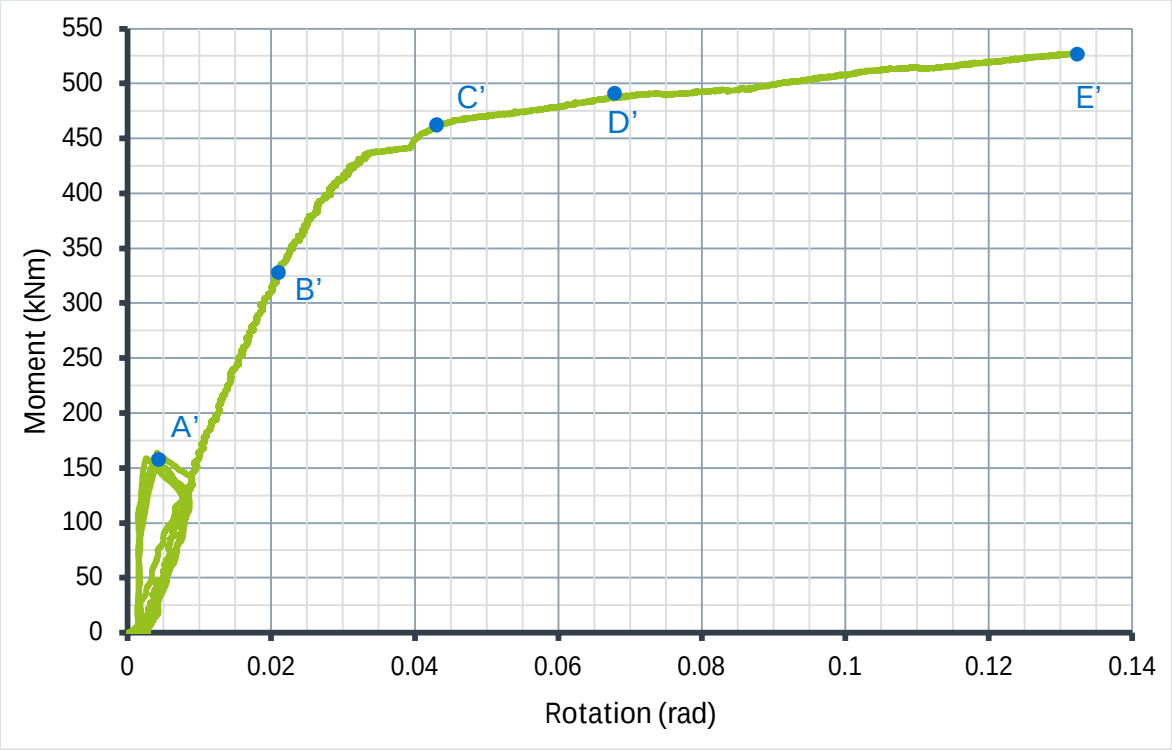

Fig. 5.86- S12- Average moment- rotation curve (Inclinometer)

The slips between the concrete and the steel beam remained in very low values (figure 5.87). As presented in figure 5.88, maximum slips were observed at S3 (0.27 mm). The very small values, almost zero, combined with the hardening behavior presented in figures 5.85 and 5.86, indicates that there is a full shear connection between the steel and concrete parts.

Load- strain curves are presented in figure 5.89. In figures 5.90 and 5.91 the propagation of strains is presented at the intersections of web plates with the bottom and top plates, for different deflection values. Because of the difference between the tensile strains at the bottom plate and the corresponding compressive strains at the top plate, it can be assumed that the neutral axis is closer to the top face of the beam.

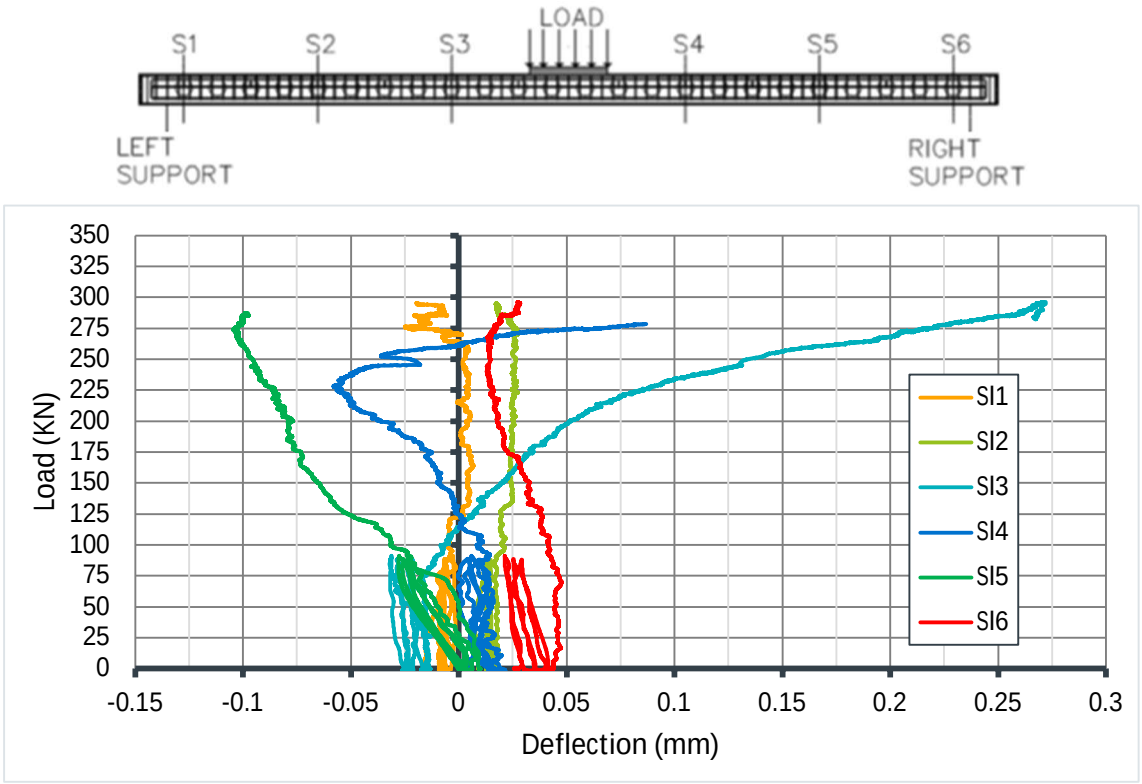

Fig. 5.87- S12- Load- slip curves

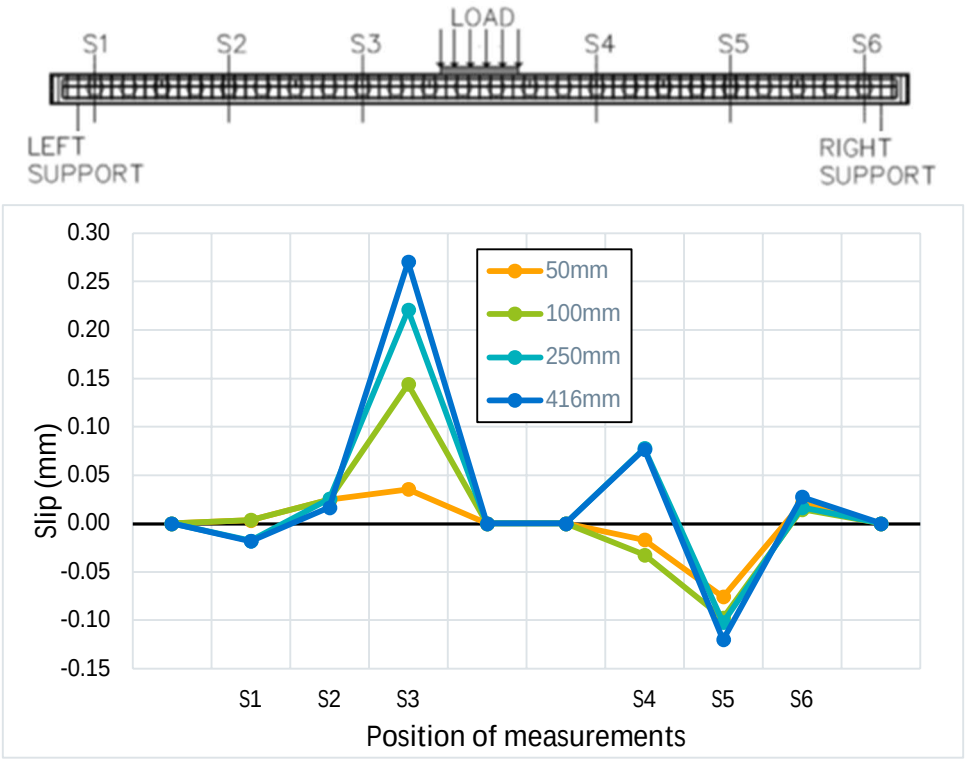

Fig. 5.88- S12- Slip propagation for different deflection values

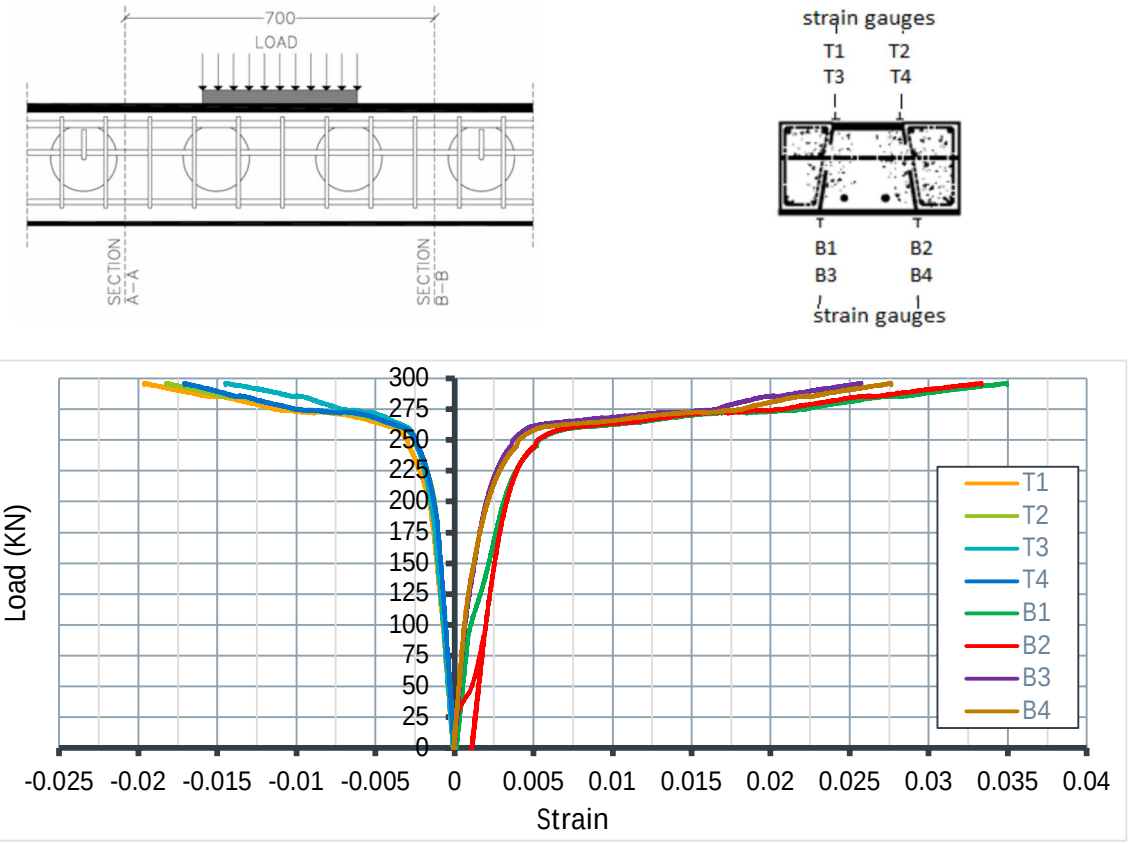

Fig. 5.89- S12- Strains at the top and bottom plates of the beam

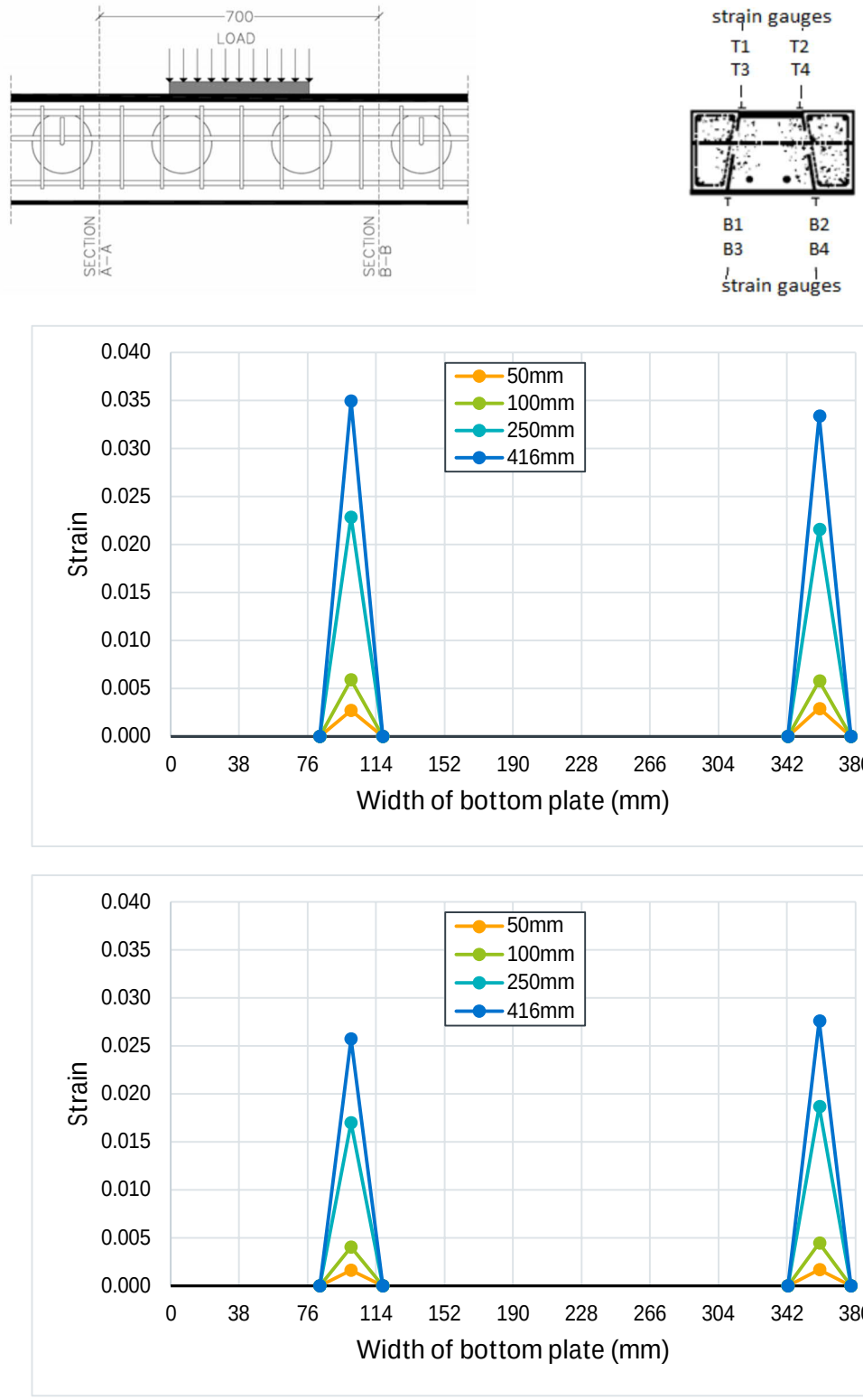

Fig. 5.90- S12- Strains along the bottom plate at sections A-A (top) and B-B (bottom) for various deflections

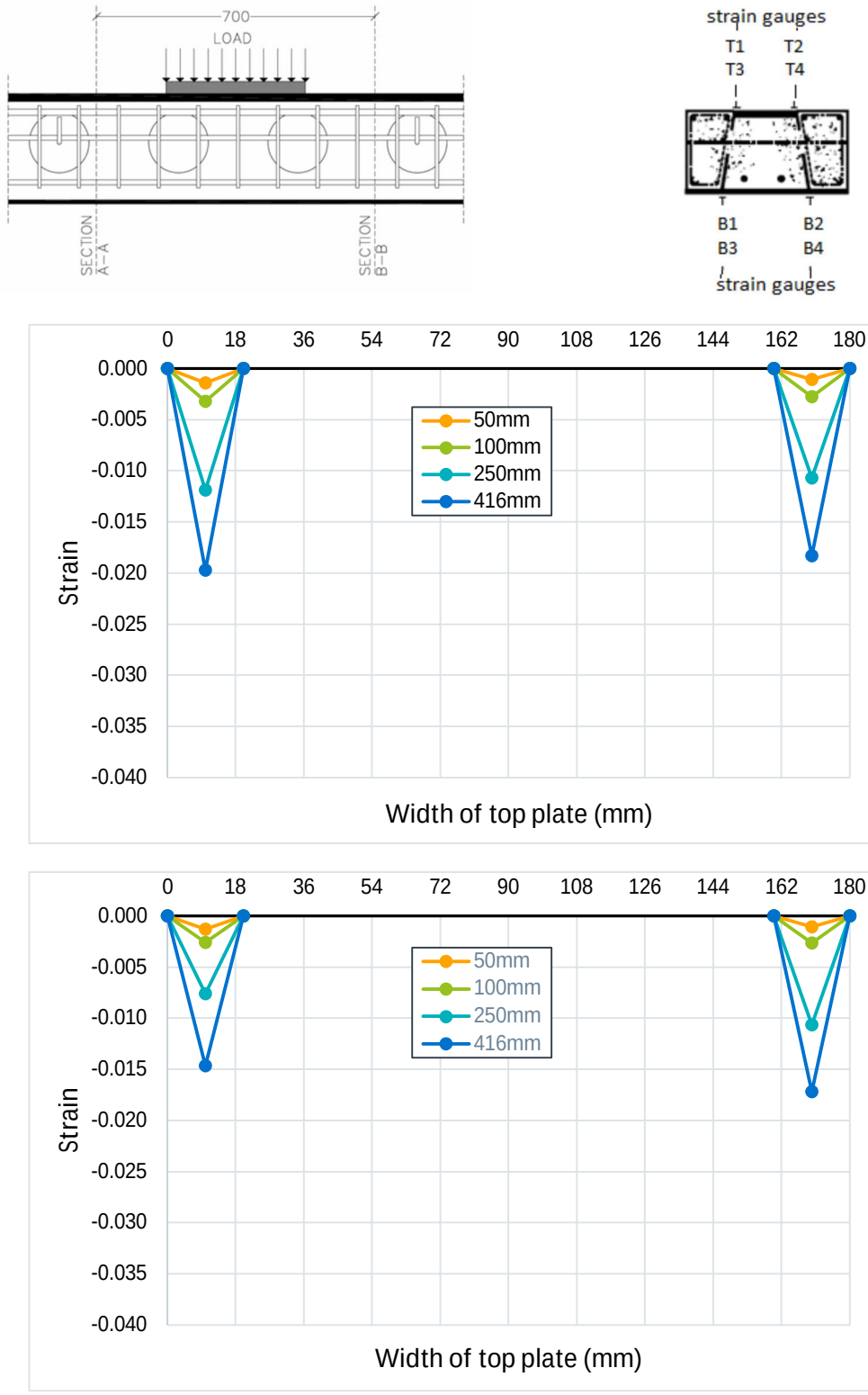

Fig. 5.91- S12- Strains along the top plate at sections A-A (top) and B-B (bottom) for various deflections

5.2.4 Comparative results

All Type 2 specimens manifested similar in form ductile behavior. After the yielding point, they acquired a hardening behavior until the end of the tests with no strength degradation (figure 5.92). The condition of the specimens at the end of the tests was very good with spalling of concrete limited at the top cover. It can be observed that the load value is proportional to the size of beams cross sections with S11 having the higher value. In figure 5.93 the normalized load- deflection curves are presented to make more obvious the similarities in the behavior of these three specimens.

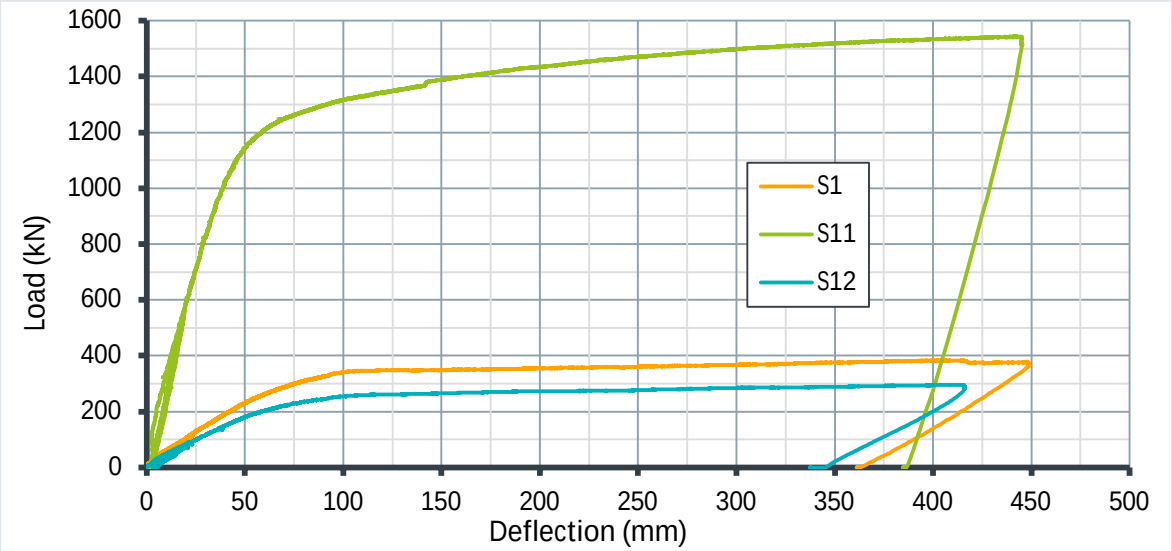

Fig. 5.92- Type 2 load- deflection curves

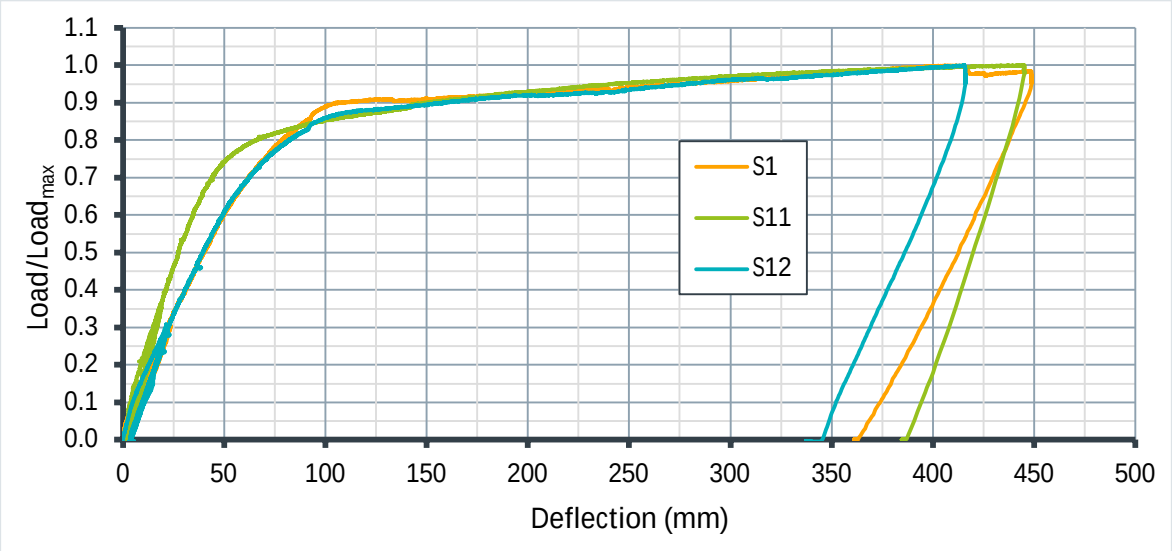

Fig. 5.93- Normalized Type 2 load- deflection curves

5.3 Type 3 sections

The tests with the Type 3 sections also manifested flexural hardening behavior. The small non-linearities at the load- deflection curves are caused by local crushing of the concrete, mainly located at the cover area outside the top reinforcement.

5.3.1 Specimen S6a

First cracks occurred at a deflection of 25 mm (305 kN) after the serviceability circles (figure 5.94). In figures 5.95 and 5.96 the crack pattern at 50 mm (545 kN) and 100 mm (750 kN) is presented. At a deflection of 110 mm (753 kN), under the loading area, a transverse bar from the top layer of the rebar mesh was bended, causing a crack at the top face of the concrete (figure 5.97). The bottom plate of the steel beam yielded at a deflection of 98 mm (748 kN). The test ended at a deflection of 452 mm because the loading actuator reached its maximum displacement capacity (figures 5.98- 5.100). The beam maintained its strength until the end of the test with no degradation (figures 5.104 and 5.105). In figures 5.101- 5.103 the condition of the beam can be seen after the removal of the crushed concrete. A local buckling was occurred at the longitudinal rebars, but due to the stirrups and the transversal bars the buckling length was small and did not affect the general behavior of the beam. The usage of stirrups prevented the crushing of the concrete and limited it at the cover area.

Fig. 5.94- S6a- Cracks at deflection of 25mm (fig. 5.104 and 5.105, points A and A')

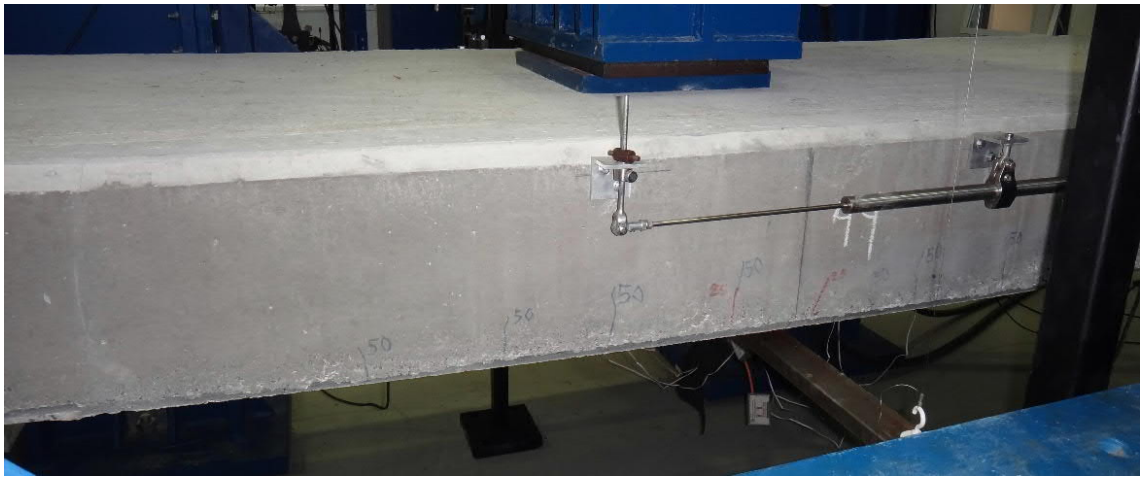

Fig. 5.95- S6a- Cracks at deflection of 50mm (fig. 5.104 and 5.105, points B and B')

Fig. 5.96- S6a- Cracks at deflection of 100mm (fig. 5.104 and 5.105, points C and C')

Fig. 5.97- S6a- Cracks at the top face of concrete (fig. 5.104 and 5.105, points C and C')

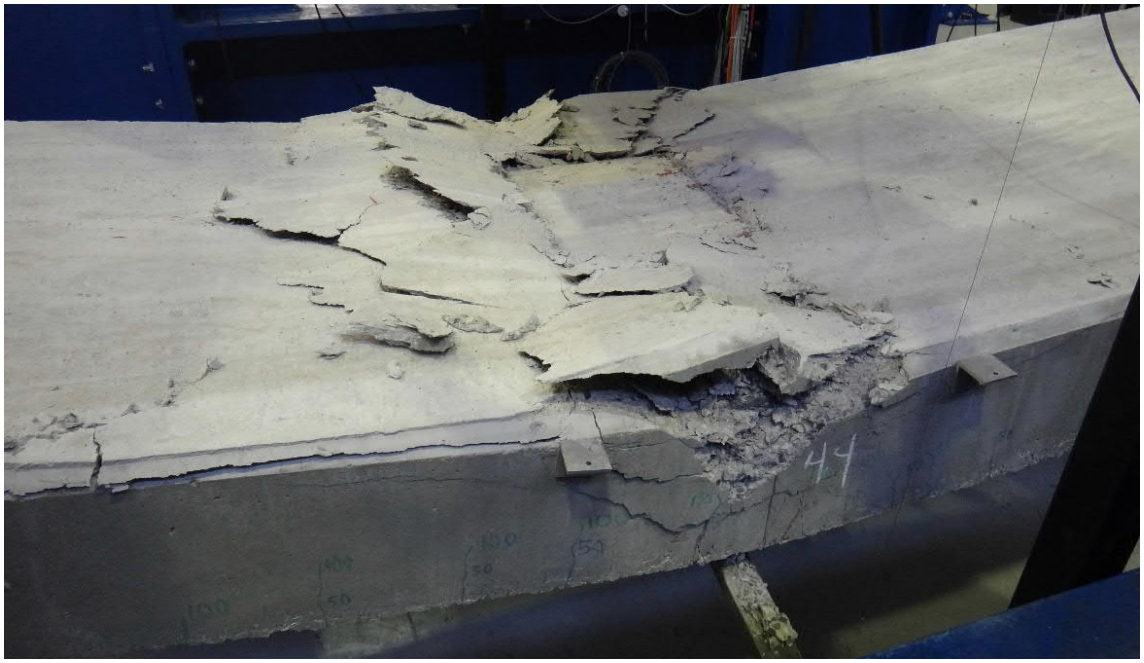

Fig. 5.98- S6a- The beam at the end of the test (fig. 5.104 and 5.105, points D and D')

Fig. 5.99- S6a- The beam at the end of the test (fig. 5.104 and 5.105, points D and D')

Fig. 5.100- S6a- Cracking of the specimens bottom and sides at the end of the test (fig. 5.104 and 5.105, points D and D')

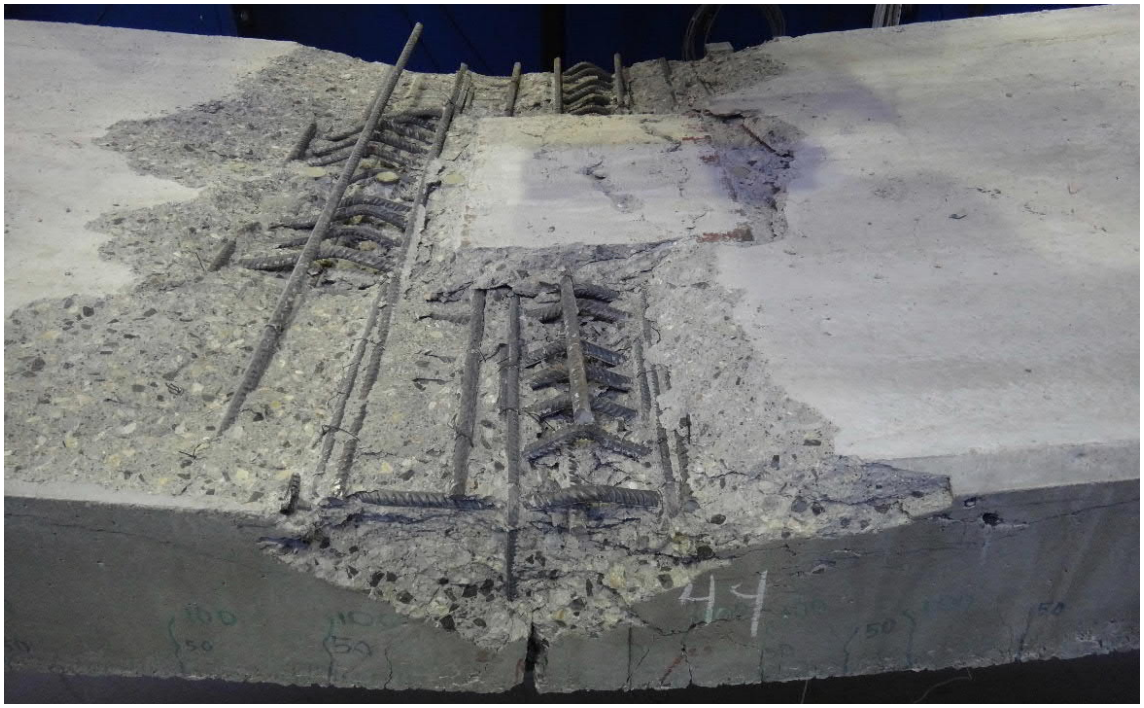

Fig. 5.101- S6a- The beam after the removal of loose concrete

Fig. 5.102- S6a- The beam after the removal of loose concrete

Fig. 5.103- S6a- The beam after the removal of loose concrete

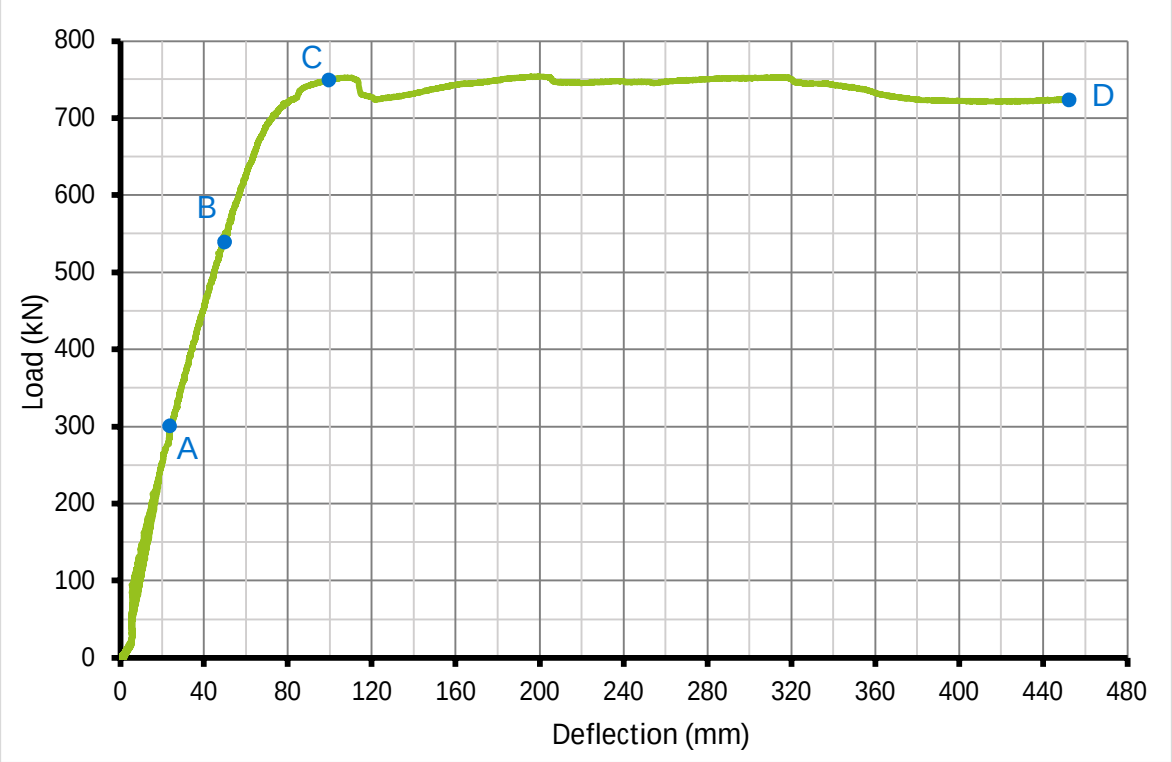

Fig. 5.104- S6a- Average load- deflection curve

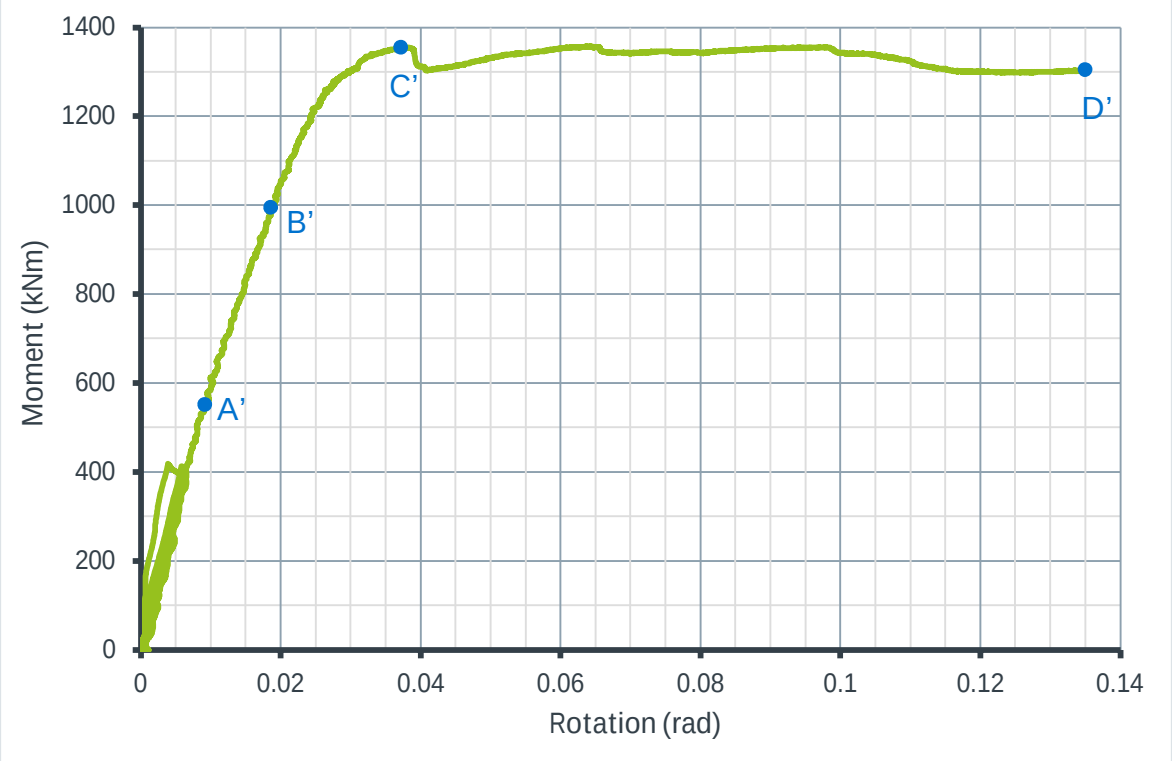

Fig. 5.105- S6a- Average moment- rotation curve (Inclinometer)

The slips between the concrete and the steel beam are presented in figure 5.106. The maximum slips were observed at S3 and S4, with absolute values equal to 4.74 and 3.61 respectively, by the LVTDs nearest to the loading area (figure 5.107). The values of the slips are reducing proportionally along the length of the beam, following the direction from the loading area to the supports

Load- strain curves are presented in figure 5.108. Highest strain values were measured at section A-A (figure 5.109). Up to a deflection equal to 100 mm, the strains were evenly distributed along the width of the bottom plate. At the final steps of the test the highest strain values were measured at the middle of the plate.

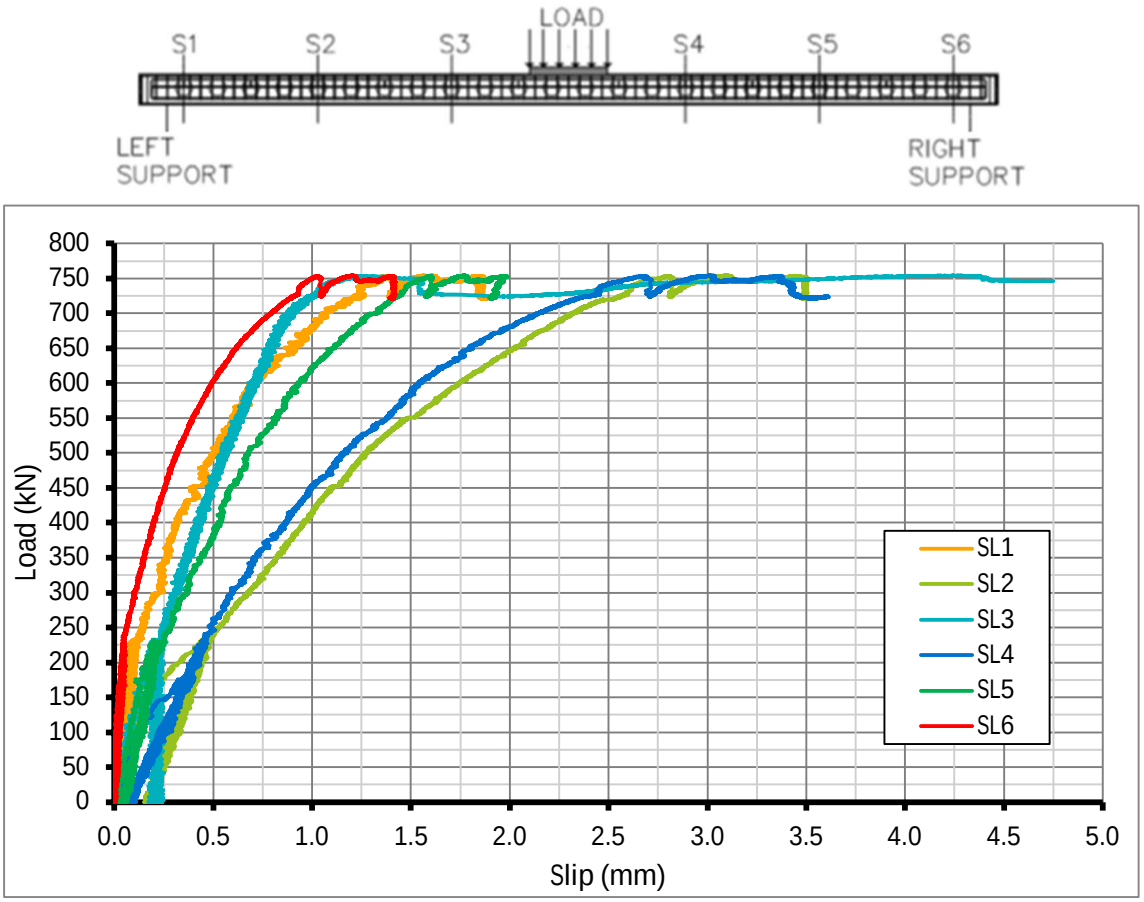

Fig. 5.106- S6a- Load- slip curves

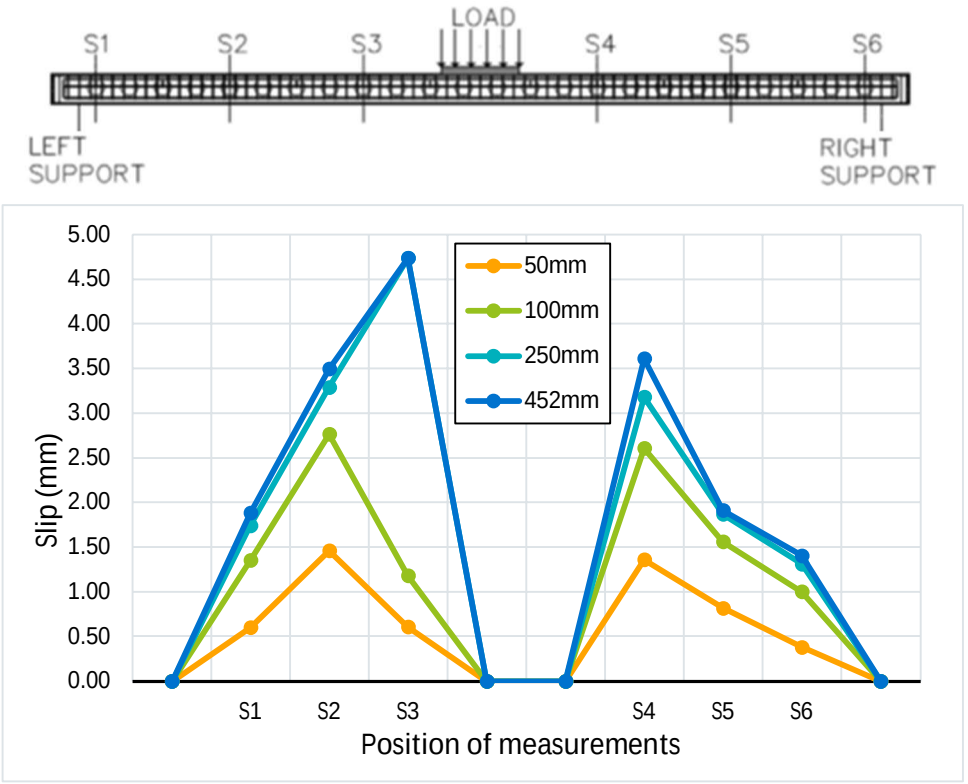

Fig. 5.107- S6a- Slip propagation for different deflection values

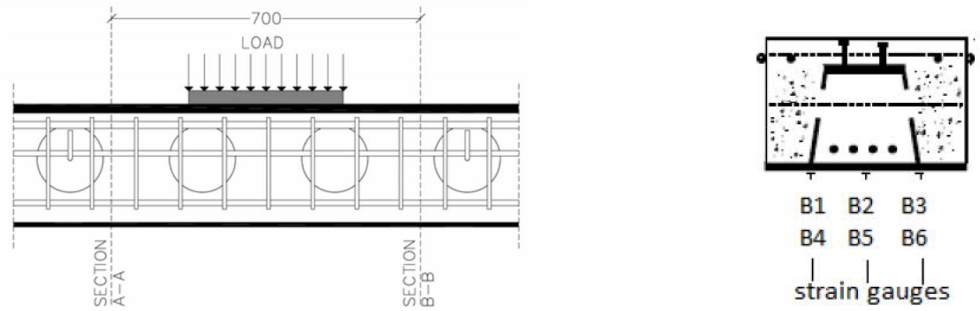

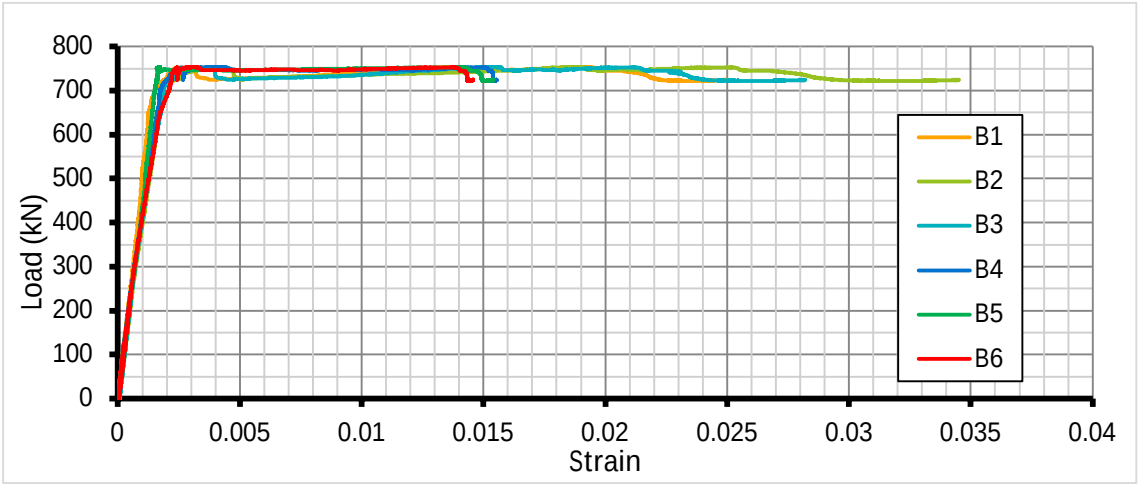

Fig. 5.108- S6a- Tensile strains at the bottom plate of the beam

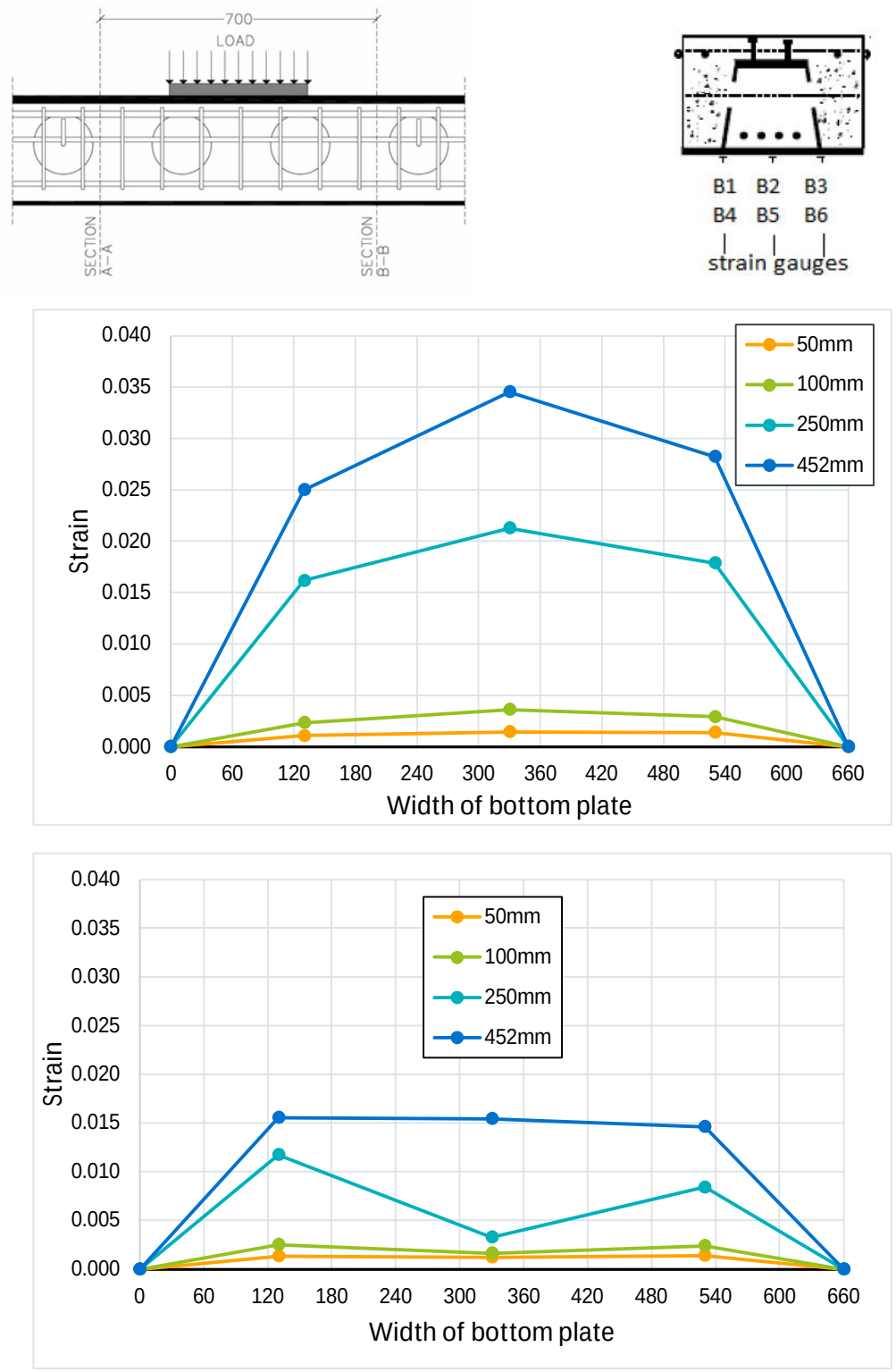

Fig. 5.109- S6a- Strains along the bottom plate at sections A-A (top) and B-B (bottom) for various deflections

5.3.2 Specimen S6b

First cracks occurred at a deflection of 25 mm (305 kN) after serviceability circles (figure 5.110). In figures 5.111- 5.113 the crack pattern at 50 mm (544 kN), 100 mm (741 kN) and 150 mm (746 kN) is presented, respectively. At a deflection of 119 mm (736 kN), under the loading area, a transverse bar from the top layer of the rebar mesh was bended, causing a crack at the top face of the concrete (figure 5.114). The test ended at a deflection of 447 mm because the loading actuator reached its maximum displacement capacity. The beam maintained its strength until the end of the test with no degradation (figures 5.117 and 118). A local buckling was occurred at the longitudinal rebars, but due to the stirrups and the transversal bars the buckling length was small and did not affect the general behavior of the beam (figures 5.115 and 5.116). The usage of stirrups prevented the crushing of the concrete and limited it at the cover area.

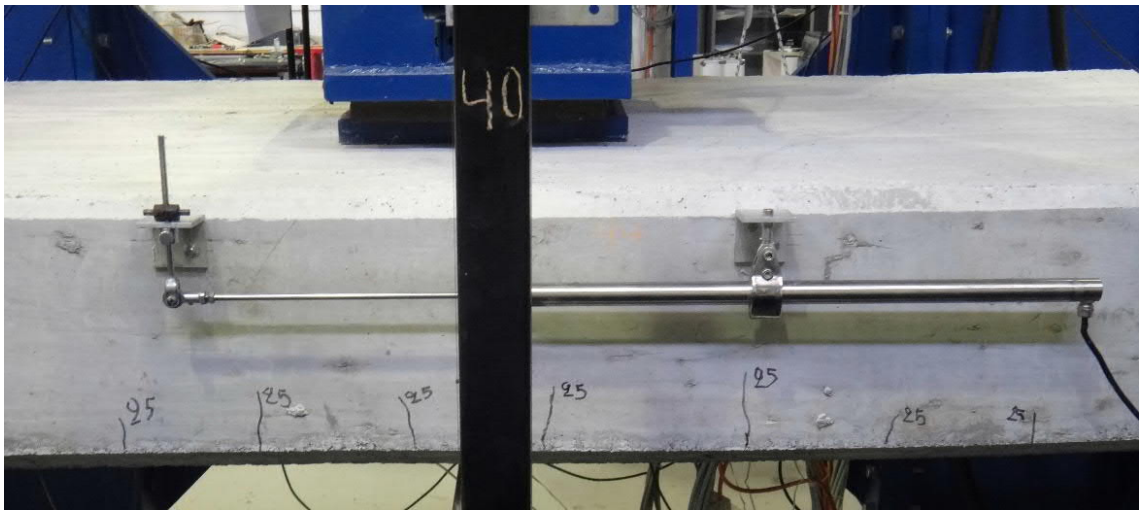

Fig. 5.110- S6b- Cracks at deflection of 25 mm (fig. 5.117 and 5.118, points A and A')

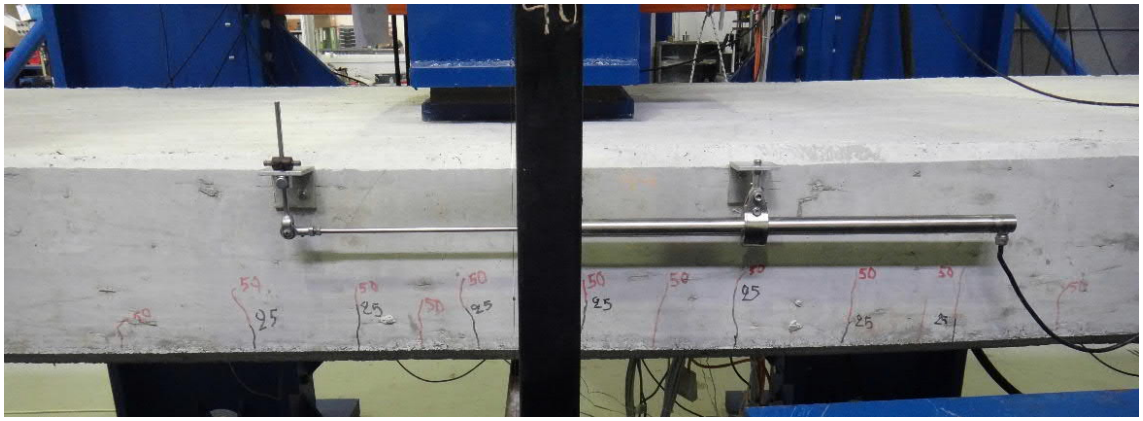

Fig. 5.111- S6b- Cracks at deflection of 50 mm (fig. 5.117 and 5.118, points B and B')

Fig. 5.112- S6b- Cracks at deflection of 100 mm (fig. 5.117 and 5.118, points C and C')

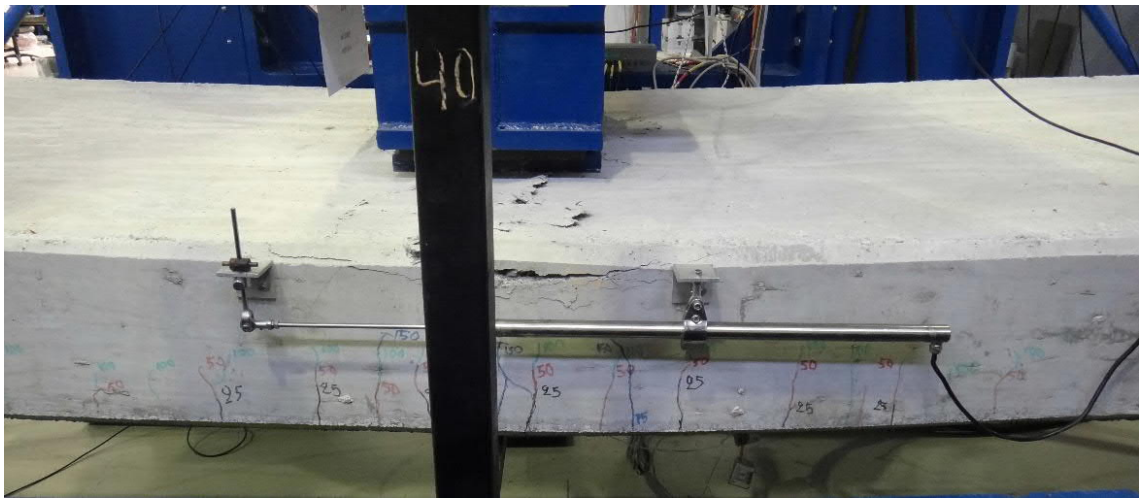

Fig. 5.113- S6b- Cracks at deflection of 150 mm (fig. 5.117 and 5.118, points E and E')

Fig. 5.114- S6b- Cracks at the top face of concrete (fig. 5.117 and 5.118, points D and D')

Fig. 5.115- S6b- The beam after the removal of loose concrete (fig. 5.117 and 5.118, points F and F')

Fig. 5.116- S6b- The beam after the removal of loose concrete (fig. 5.117 and 5.118, points F and F')

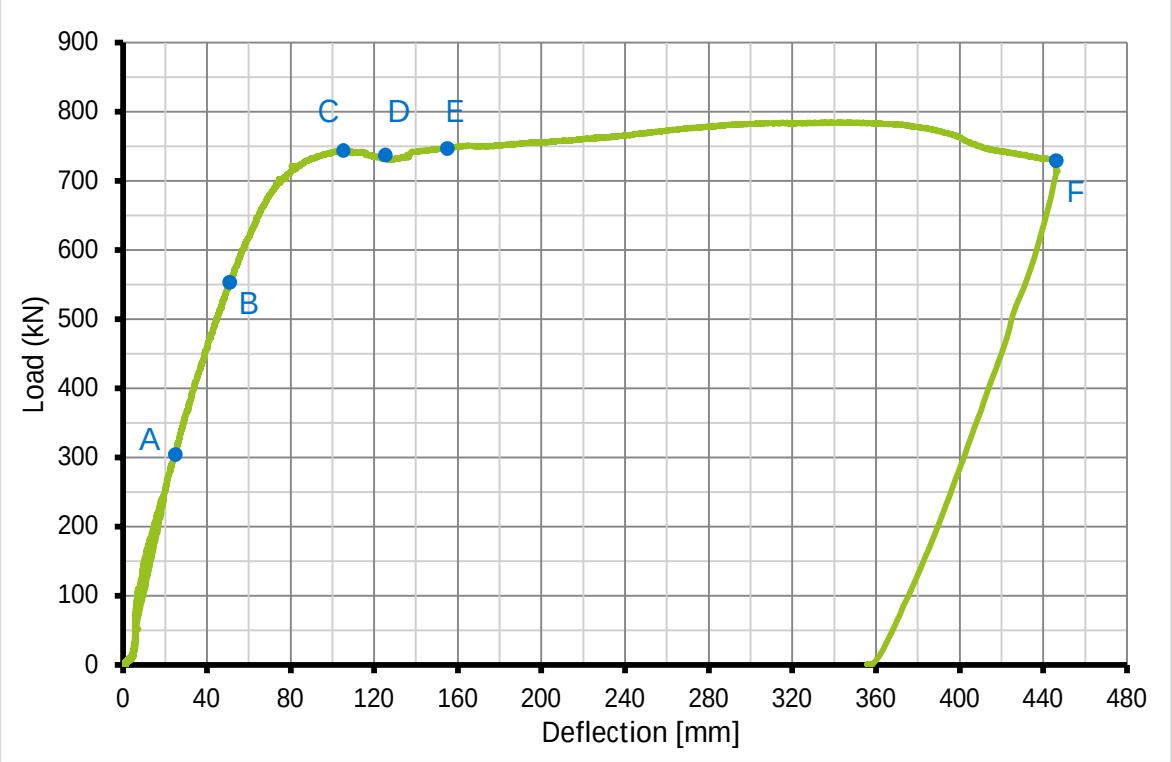

Fig. 5.117- S6b- Average load- deflection curve

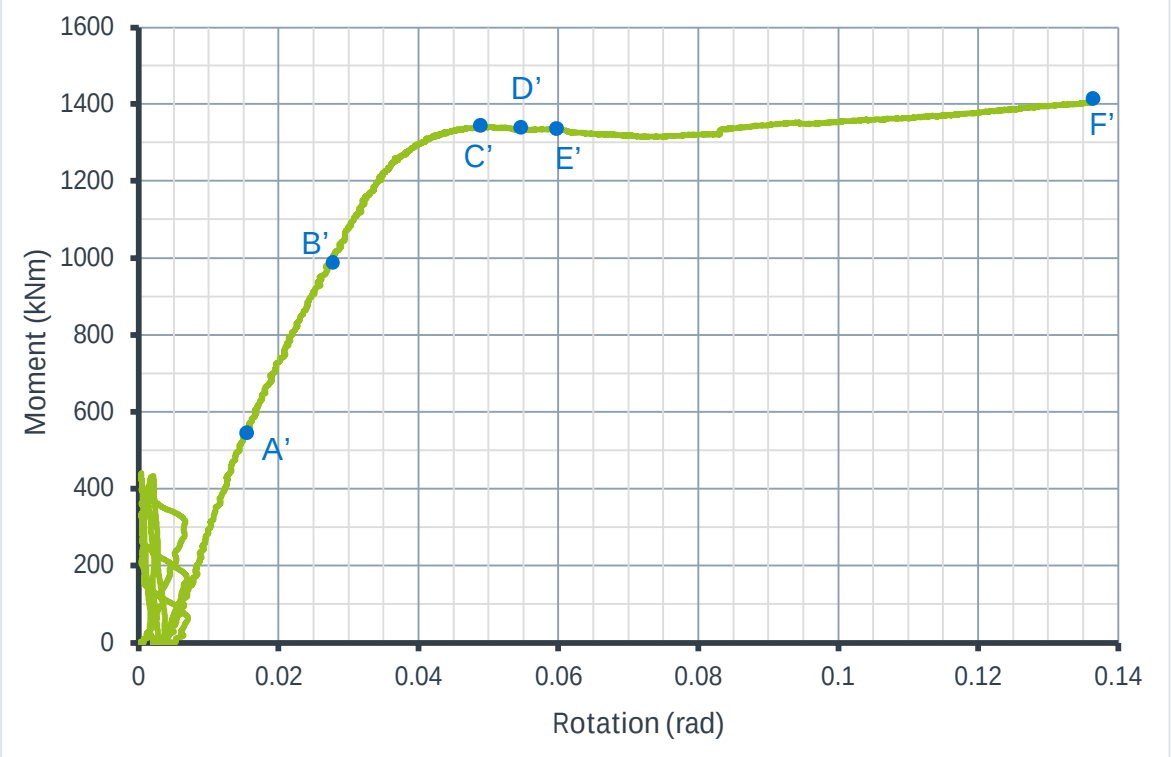

Fig. 5.118- S6b- Average moment- rotation curve (Inclinometer)

The slips between the concrete and the steel beam are presented in figure 5.119. The slips were symmetrical at both halves of the beam. The maximum slips were observed at S2, S3, S4 and S5 and measured almost equal to 1.6 mm (figure 5.120). The values were reduced towards the supports. Because of the two rows of shear studs the slips were reduced 65% related to the slips measured on S6a.

Load- strain curves are presented in figure 5.121. The strains were evenly distributed along the width of the bottom plate for all deflection values (figure 5.122). Strain values of both sides of the loading area, section A-A and B-B, were close.

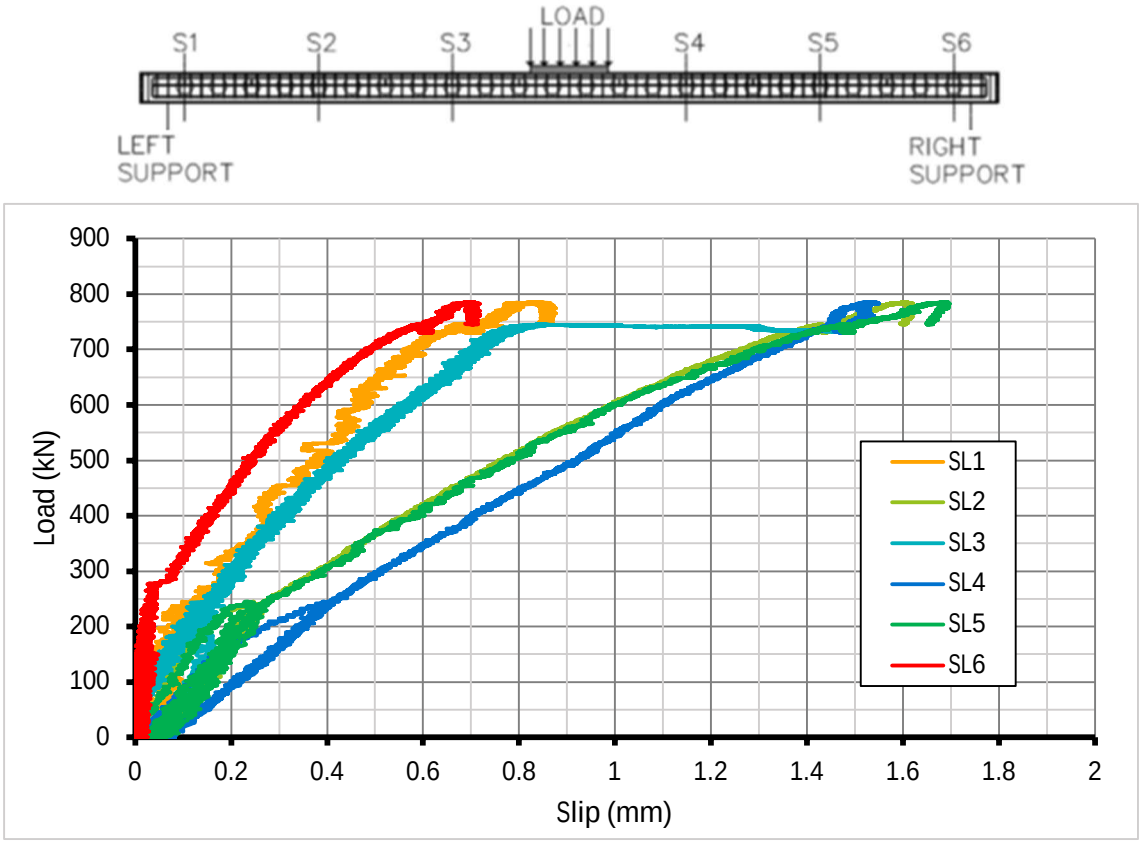

Fig. 5.119- S6b- Slips between concrete and steel beam

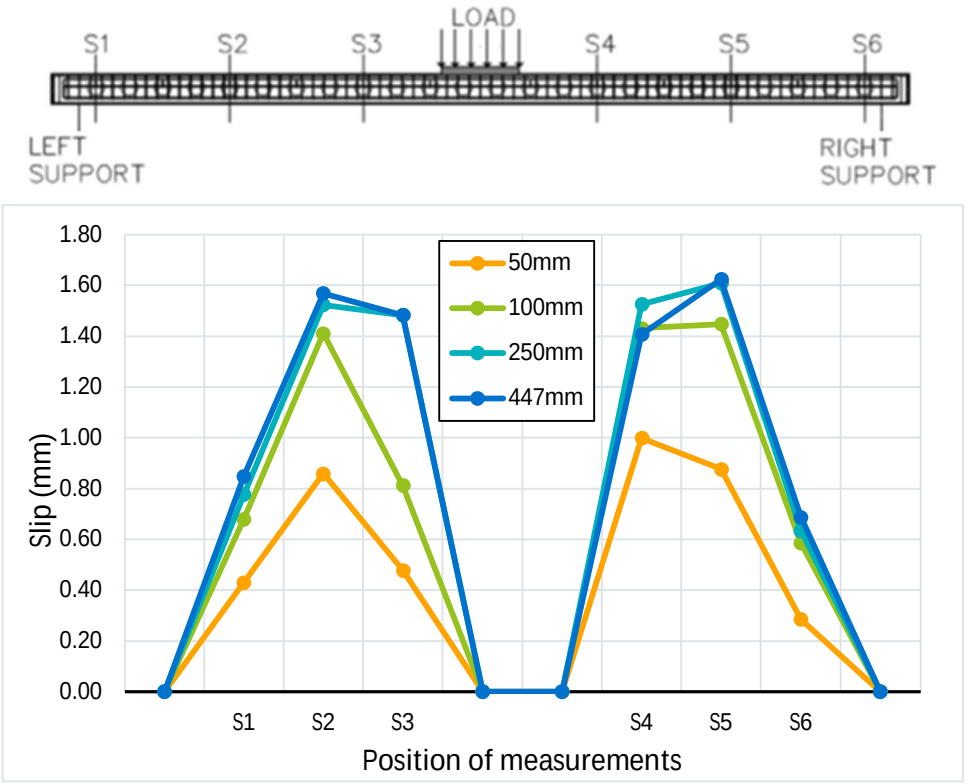

Fig. 5.120- S6a- Slip propagation for different deflection values

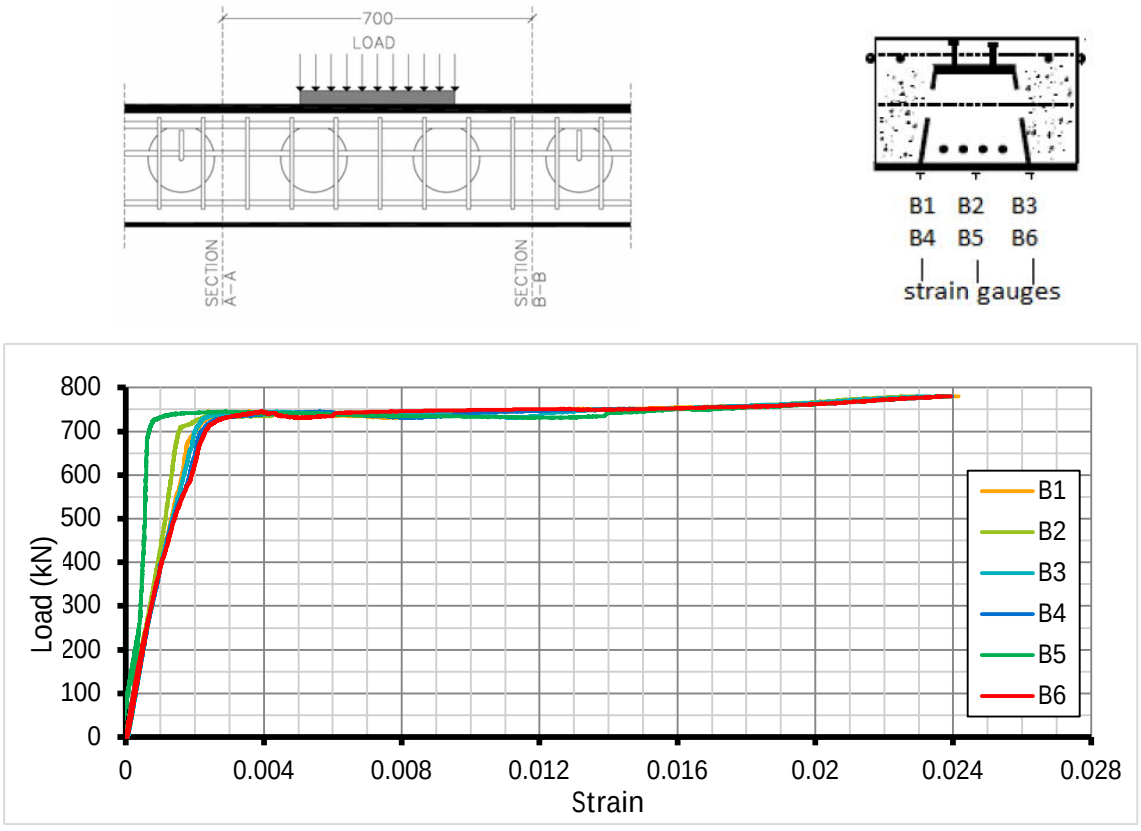

Fig. 5.121- S6b- Tensile strains at the bottom plate of the beam

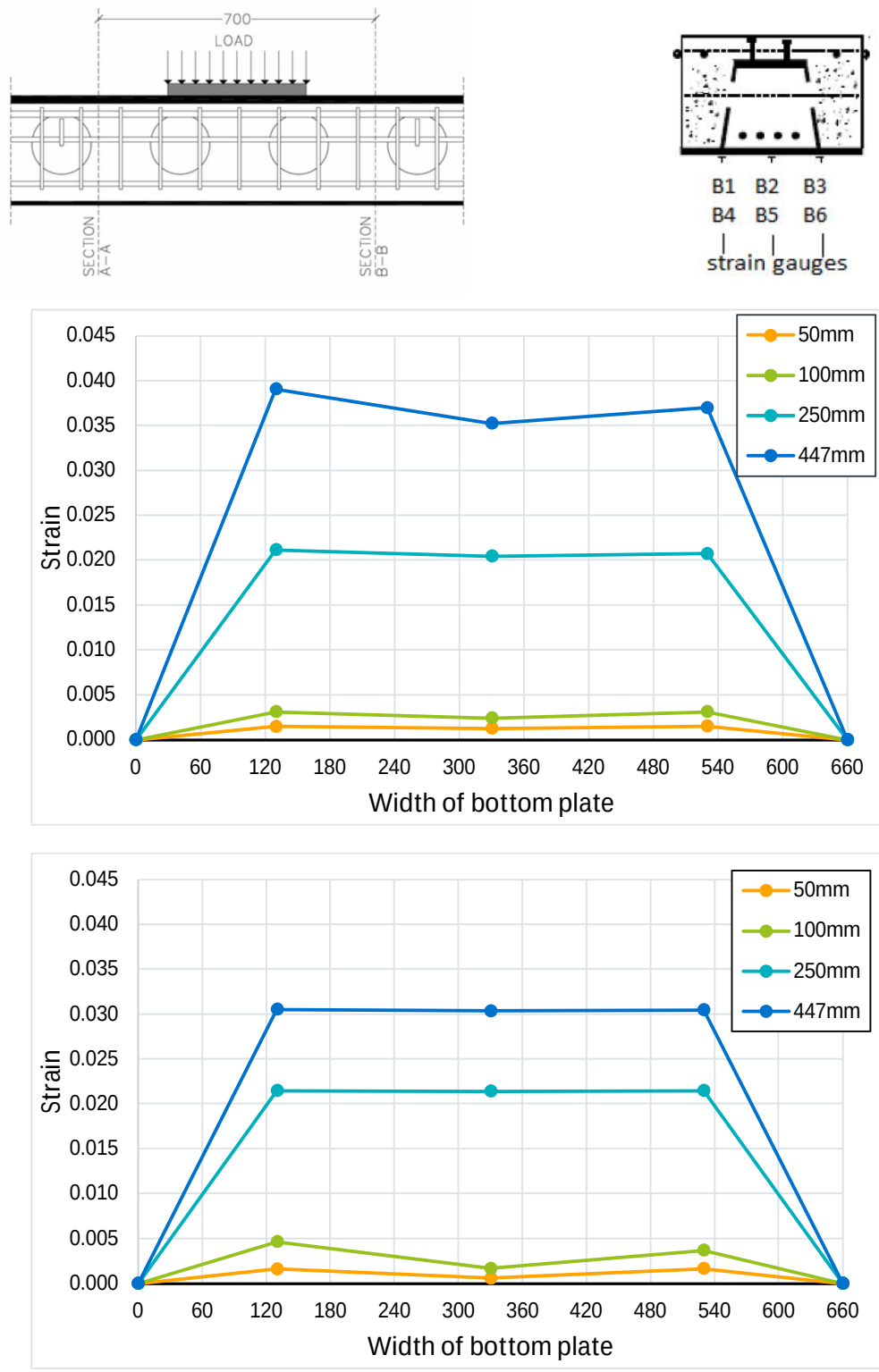

Fig. 5.122- S6b- Strains along the bottom plate at sections A-A (top) and B-B (bottom) for various deflections

5.3.3 Specimen S7

First cracks occurred at a deflection of 17 mm (282 kN) at the first serviceability circle (figure 5.123). In figures 5.124- 5.126 the tensile concrete cracks at deflection equal to 50 mm (734 kN), 100 mm (879 kN) and 150 mm (920 kN) are presented. At a deflection of 114 mm (881 kN), under the loading area, a transverse bar from the top layer of the rebar mesh was bended, causing a crack at the top face of the concrete (figure 5.127). The test ended at a deflection of 432 mm (870 kN) because the loading actuator reached its maximum displacement capacity. The beam maintained its strength until the end of the test with no degradation (figure 5.130). A local buckling was occurred at the longitudinal rebars, but due to the stirrups and the transversal bars the buckling length was small and did not affect the general behavior of the beam. The usage of the stirrups prevented the crushing of the concrete and limited it at the cover area as can be seen in figures 5.128 and 5.129.

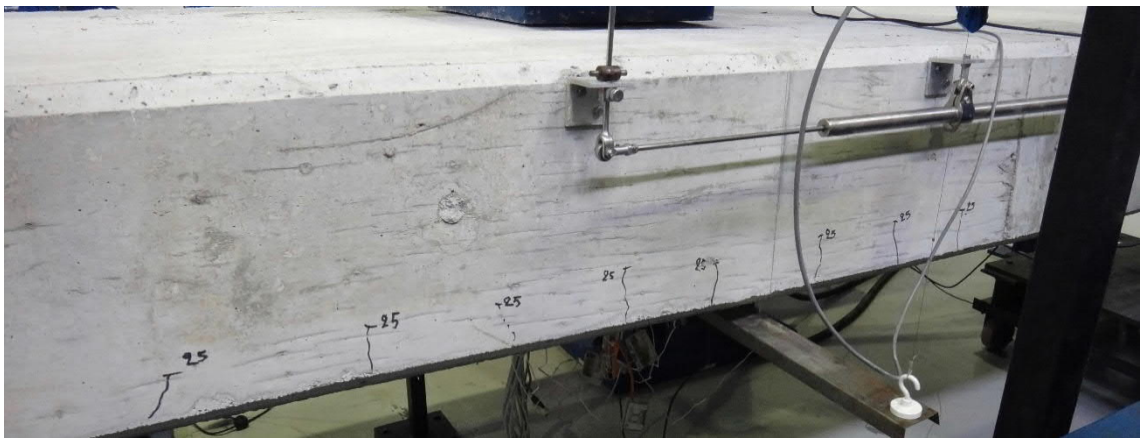

Fig. 5.123- S7- Cracks at deflection of 17 mm (fig. 5.130, point A)

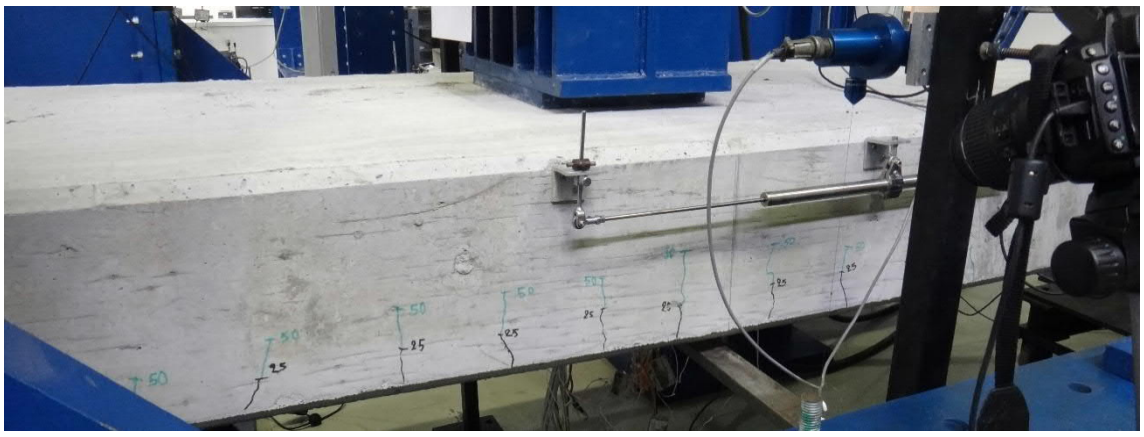

Fig. 5.124- S7- Cracks at deflection of 50 mm (fig. 5.130, point B)

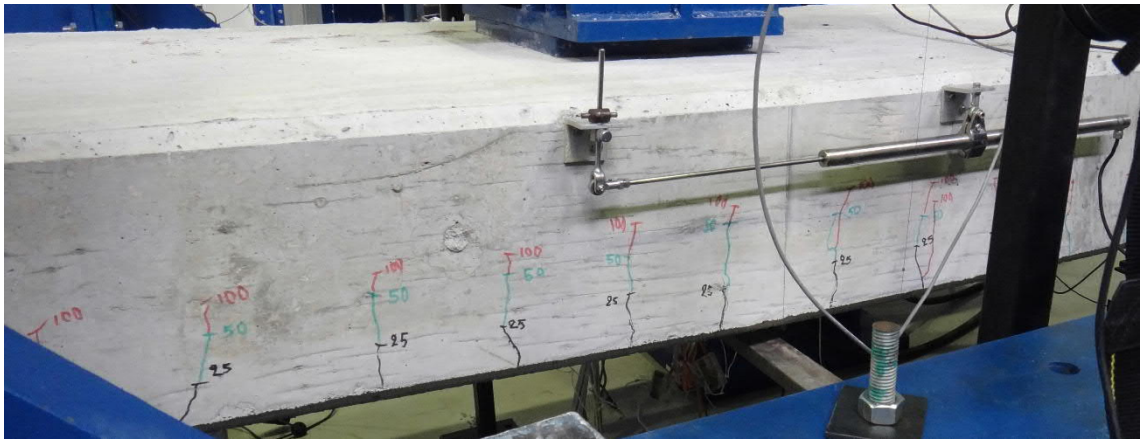

Fig. 5.125- S7- Cracks at deflection of 100 mm (fig. 5.130, point C)

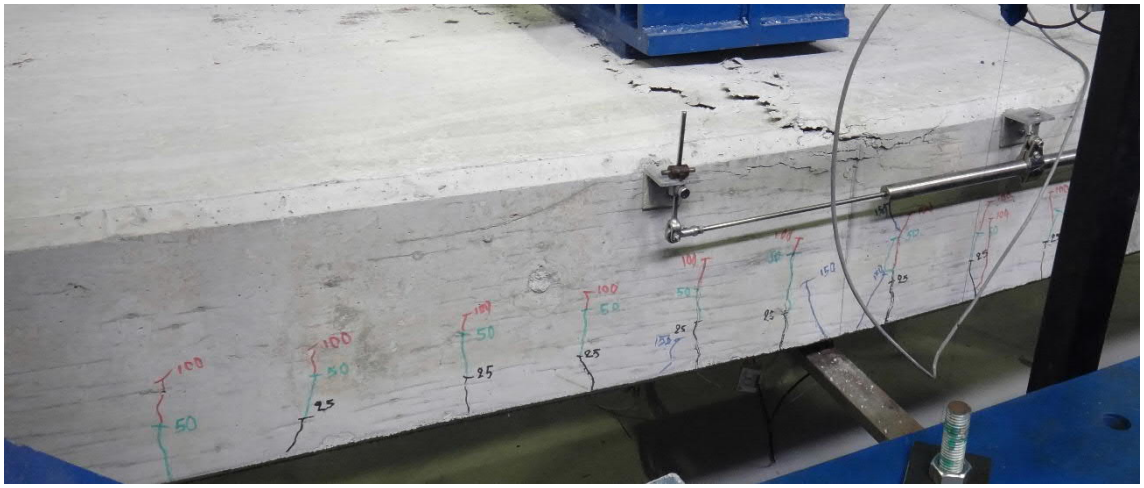

Fig. 5.126- S7- Cracks at deflection of 150 mm (fig. 5.130, point E)

Fig. 5.127- S7- Cracks at the top face of concrete (fig. 5.130, point D)

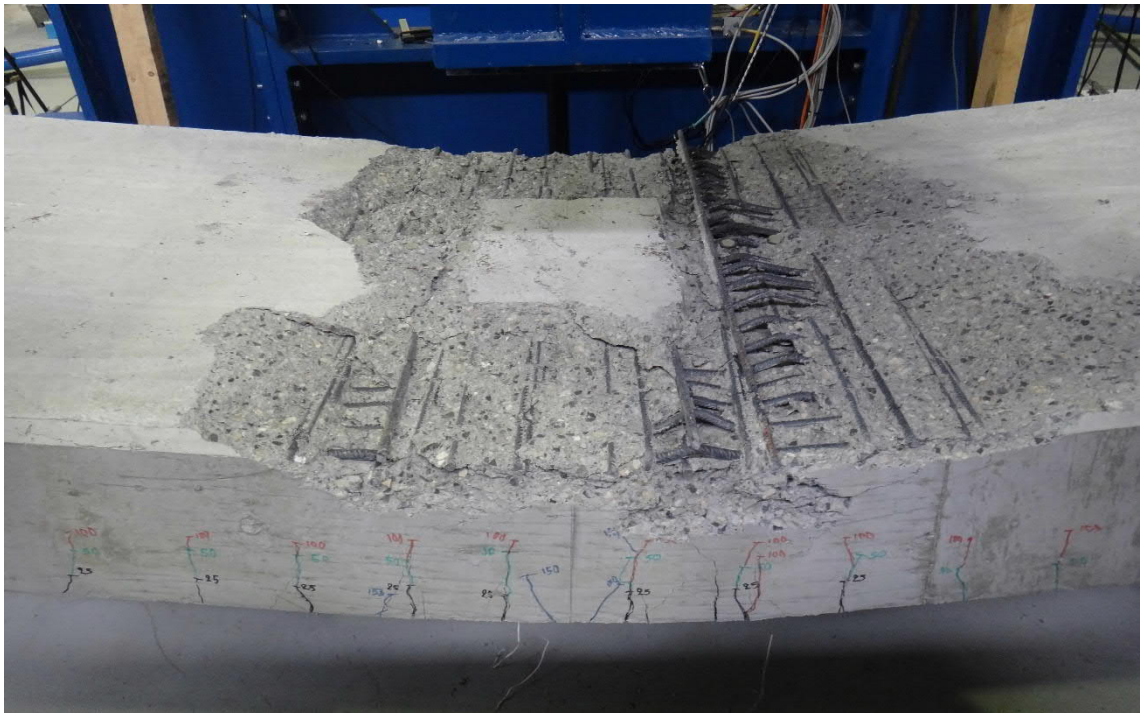

Fig. 5.128- S7- The beam after the removal of loose concrete (fig. 5.130, point F)

Fig. 5.129- S7- Cracks at the bottom of concrete plate at the end of the test (fig. 5.130, point F)

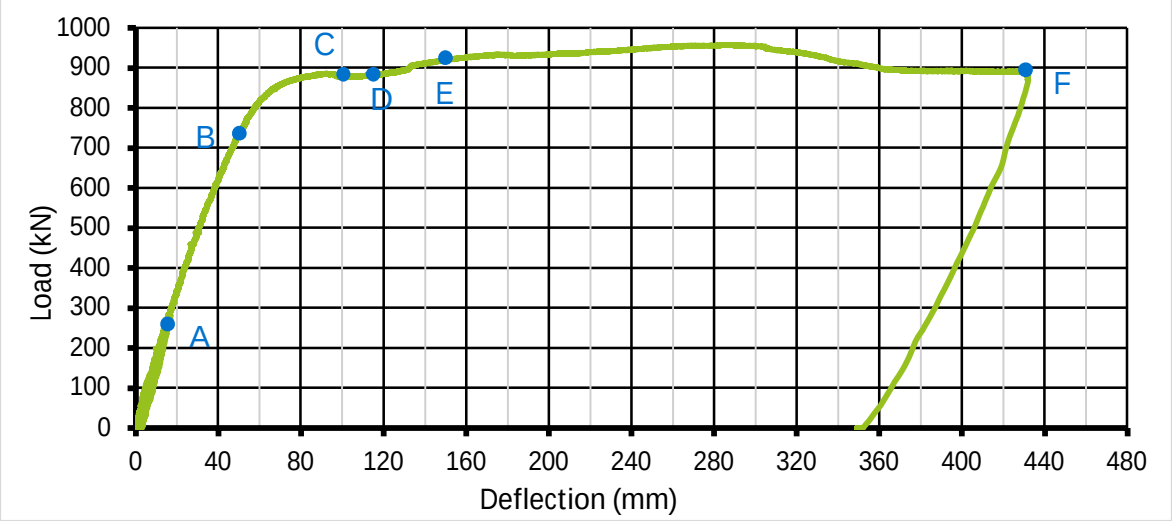

Fig. 5.130- S7- Average load- deflection curve

The slips between the concrete and the steel beam are presented in figure 5.131. The slips were symmetrical at both sides of the loading actuator. The maximum slips were observed at S3 and measured almost equal to 3.0 mm (figure 5.132). The values were reduced towards the supports.

Load- strain curves are presented in figure 5.133. The strains were evenly distributed along the width of the bottom plate for all deflection values (figure 5.134), with the value measured at the center of the plate being slightly higher. Strain values of both sides of the loading area, section A-A and B-B, were close.

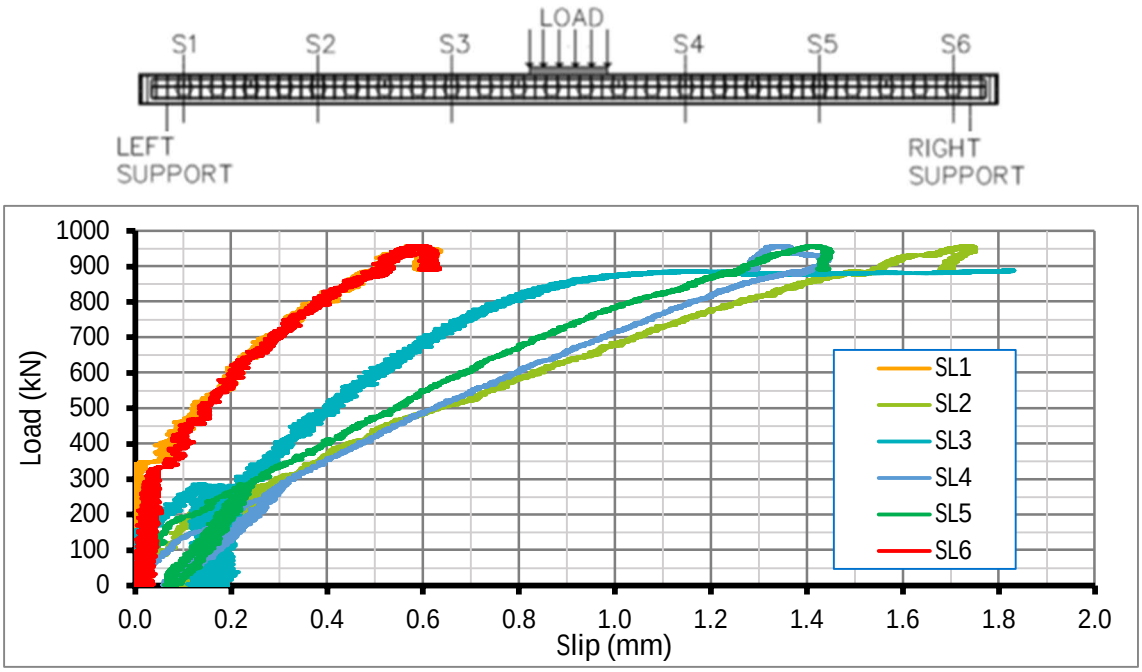

Fig. 5.131- S7- Slips between concrete and steel beam

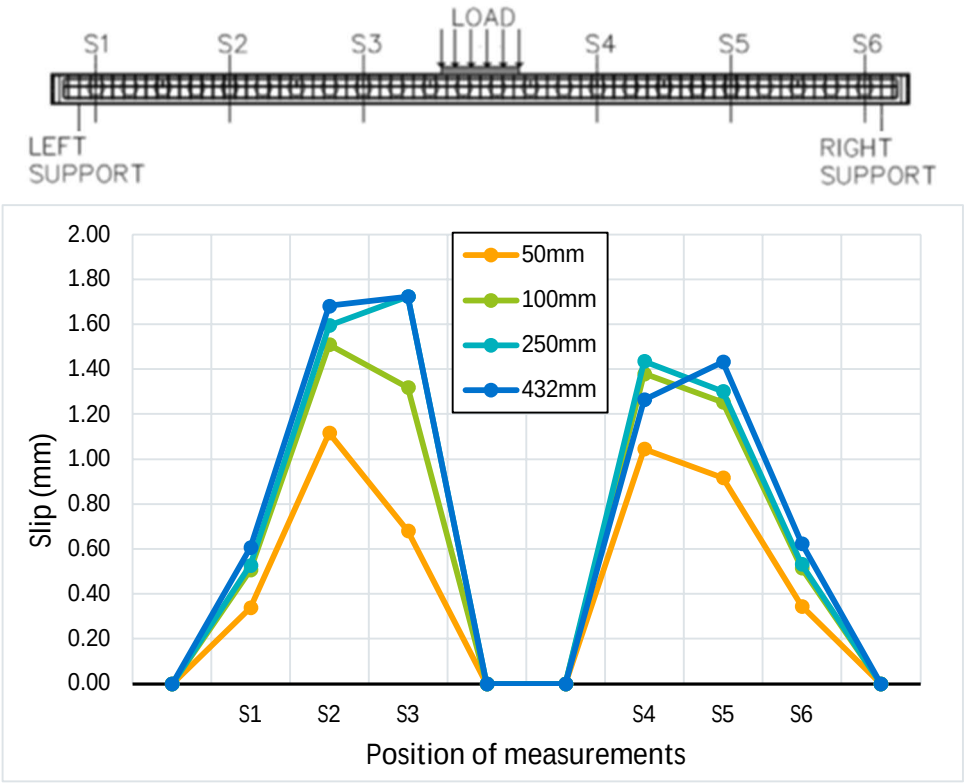

Fig. 5.132- S7- Slip propagation for different deflection values

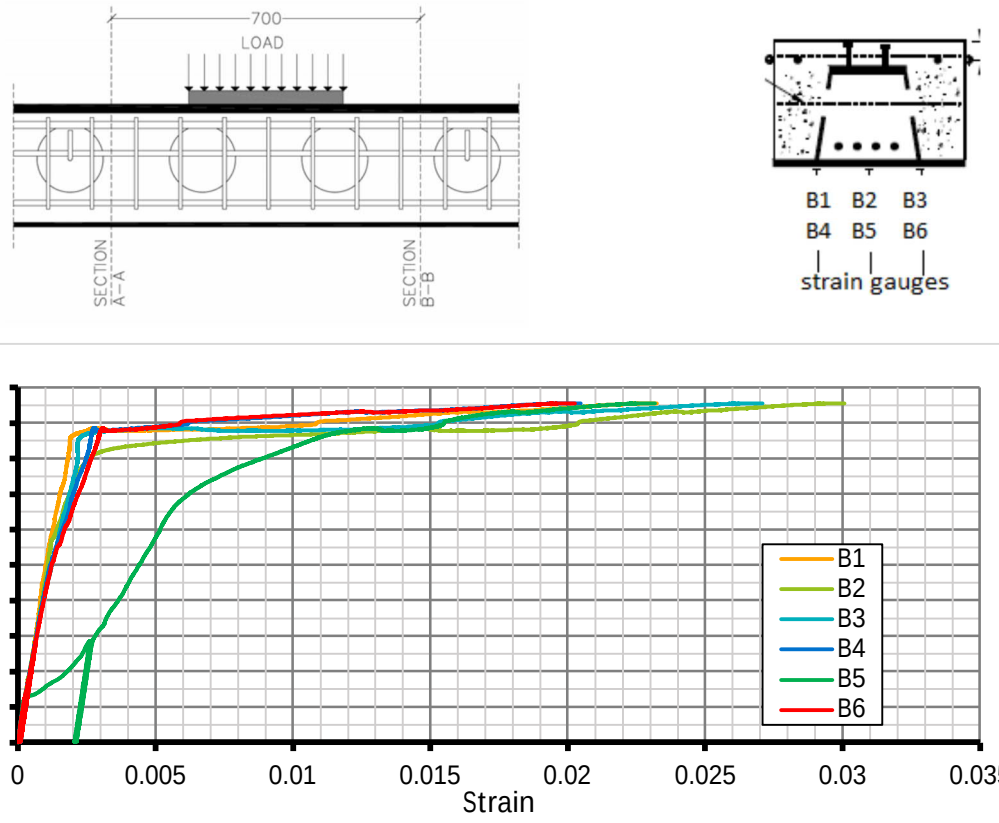

Fig. 5.133- S7- Tensile strains at the bottom plate of the beam

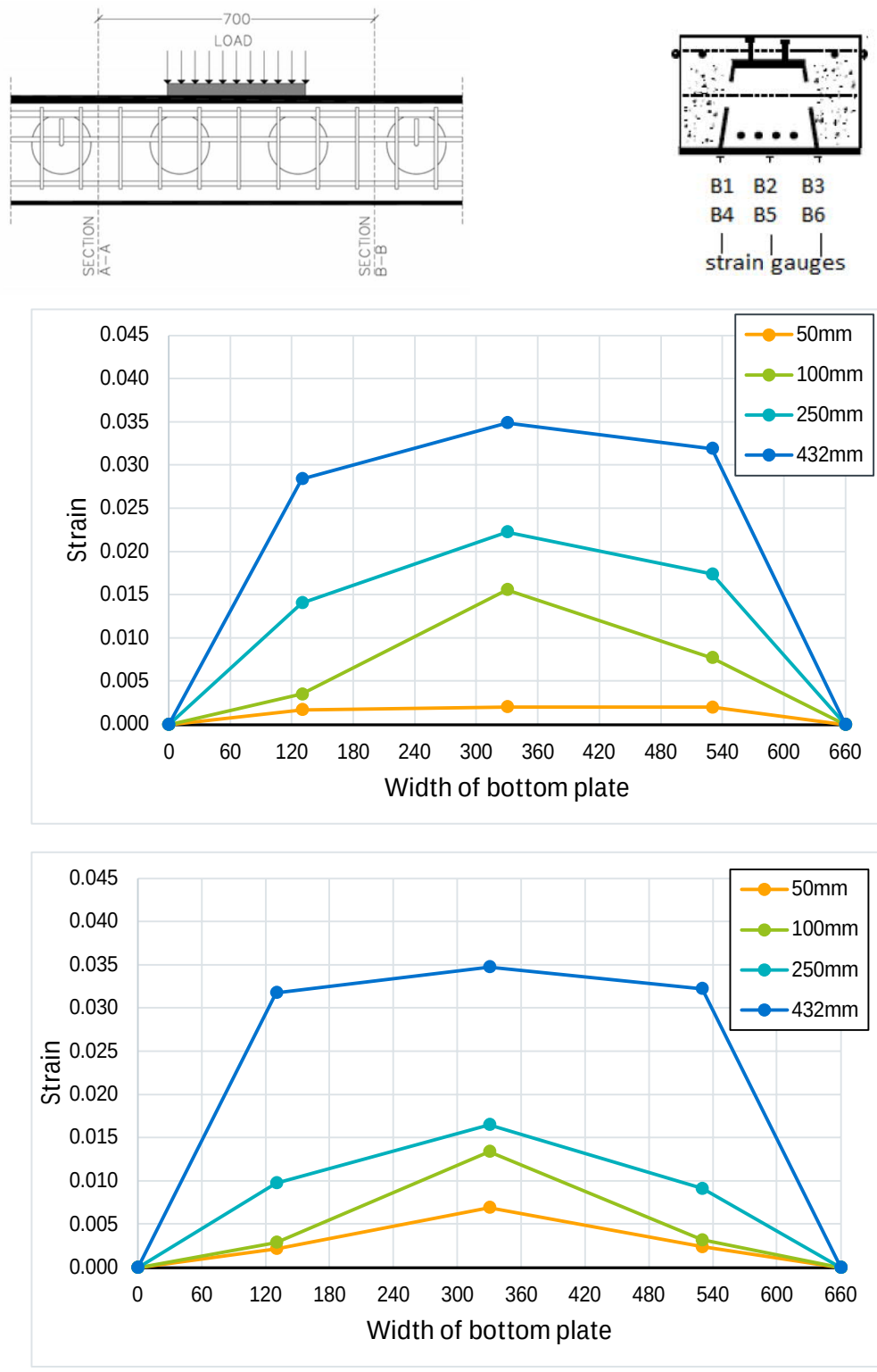

Fig. 5.134- S7- Strains along the bottom plate at sections A-A (top) and B-B (bottom) for various deflections

5.3.4 Specimen S8

The first tensile hair-line dimensioned cracks appeared at the bottom of the specimen at a deflection of 19 mm (483 kN), which was the maximum deflection of the serviceability circles (figure 5.135). In figures 5.136- 5.139 the tensile cracks at deflections of 25 mm (614 kN), 50 mm (999 kN), 100 mm (1091 kN) and 150 mm (1137 kN) are presented, respectively. At a deflection of 85 mm (1103 kN) the first compressive cracks appeared under the loading area (figure 5.140). The test ended at a deflection of 445 mm (1106 kN) because the loading actuator reached its maximum displacement capacity (figures 5.141- 5.142). The beam maintained its strength until the end of the test with no degradation (figures 5.144 and 5.145). A local buckling was occurred at the longitudinal rebars, but due to the stirrups and the transversal bars the buckling length was small and did not affect the general behavior of the beam. Due to the use of stirrups, the crushing of the concrete was limited at the cover area as can be seen in figure 5.143.

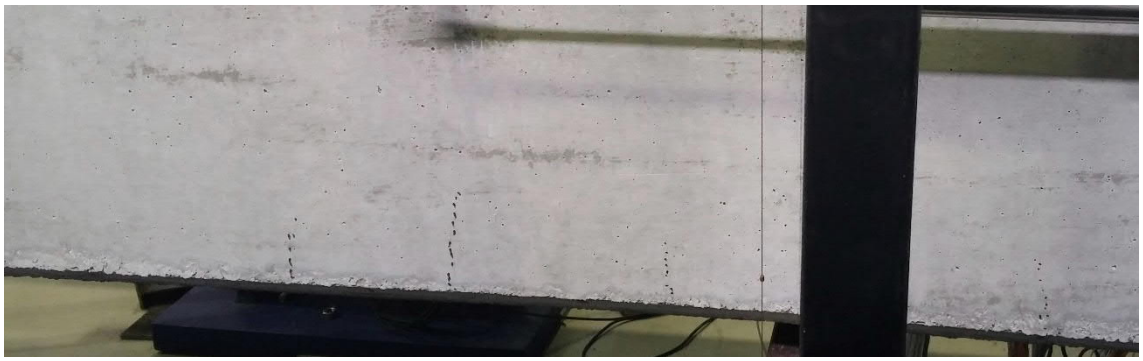

Fig. 5.135- S8- Hair-line cracks at deflection of 19 mm (fig. 5.144 and 5.145, points A and A')

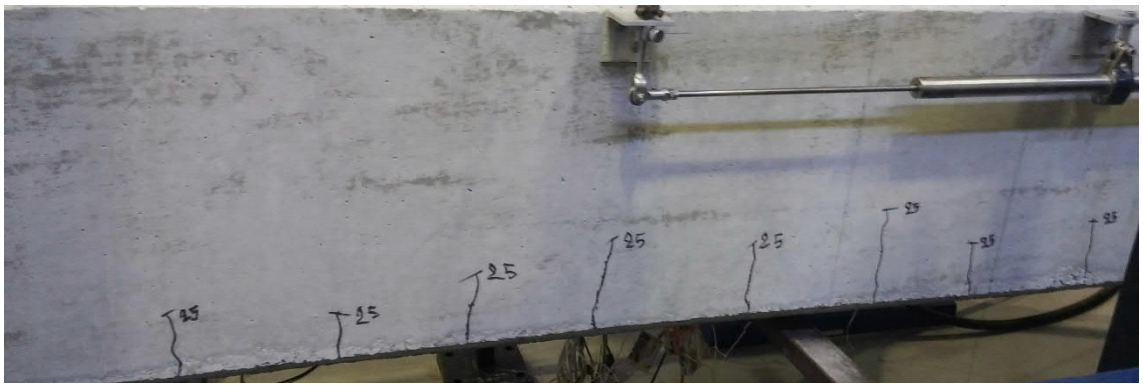

Fig. 5.136- S8- Cracks at deflection of 25 mm (fig. 5.144 and 5.145, points B and B')

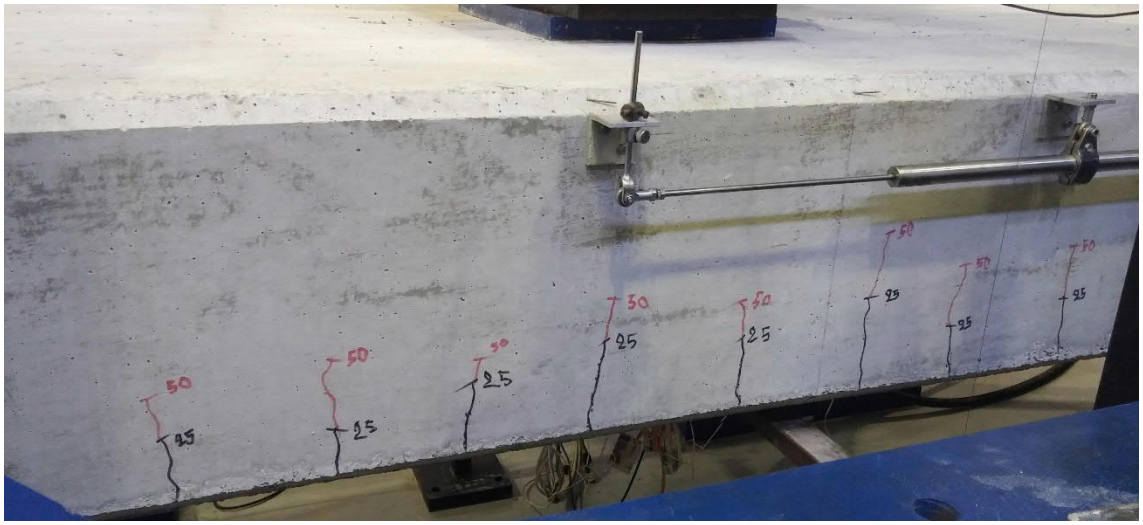

Fig. 5.137- S8- Cracks at deflection of 50 mm (fig. 5.144 and 5.145, points C and C')

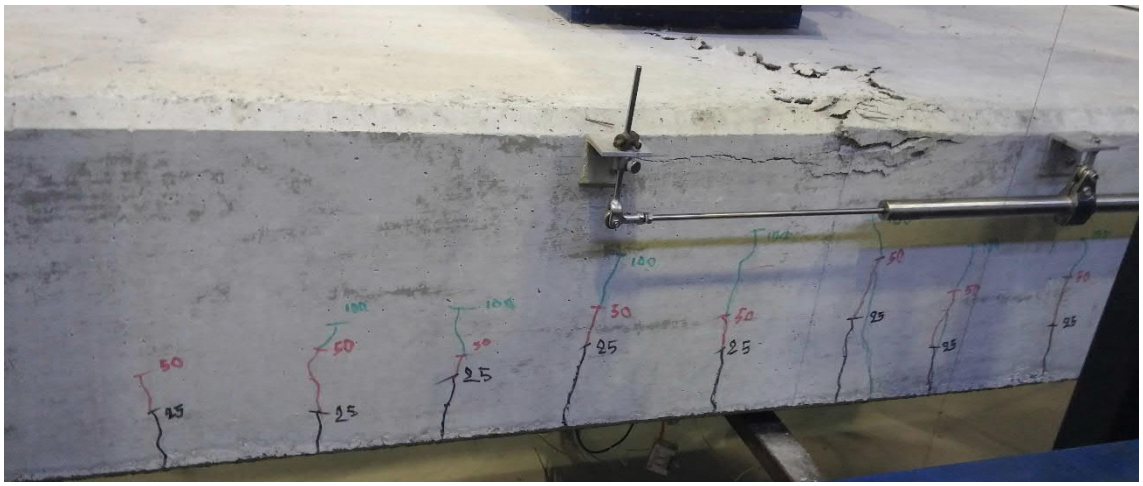

Fig. 5.138- S8- Cracks at deflection of 100 mm (fig. 5.144 and 5.145, points E and E')

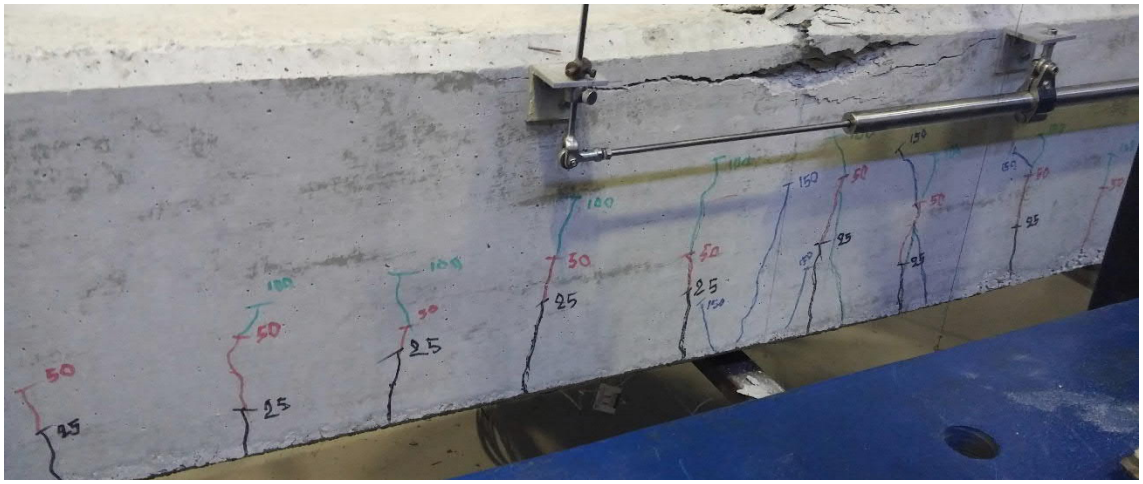

Fig. 5.139- S8- Cracks at deflection of 150 mm (fig. 5.144 and 5.145, points F and F')

Fig. 5.140- S8- Cracks at the top face of concrete (fig. 5.144 and 5.145, points D and D')

Fig. 5.141- S8- The beam at the end of the test (fig. 5.144 and 5.145, points G and G')

Fig. 5.142- S8- Bottom of concrete plate at the end of the test (fig. 5.144 and 5.145, points G and G')

Fig. 5.143- S8- The beam after the removal of loose concrete (fig. 5.144 and 5.145, points G and G')

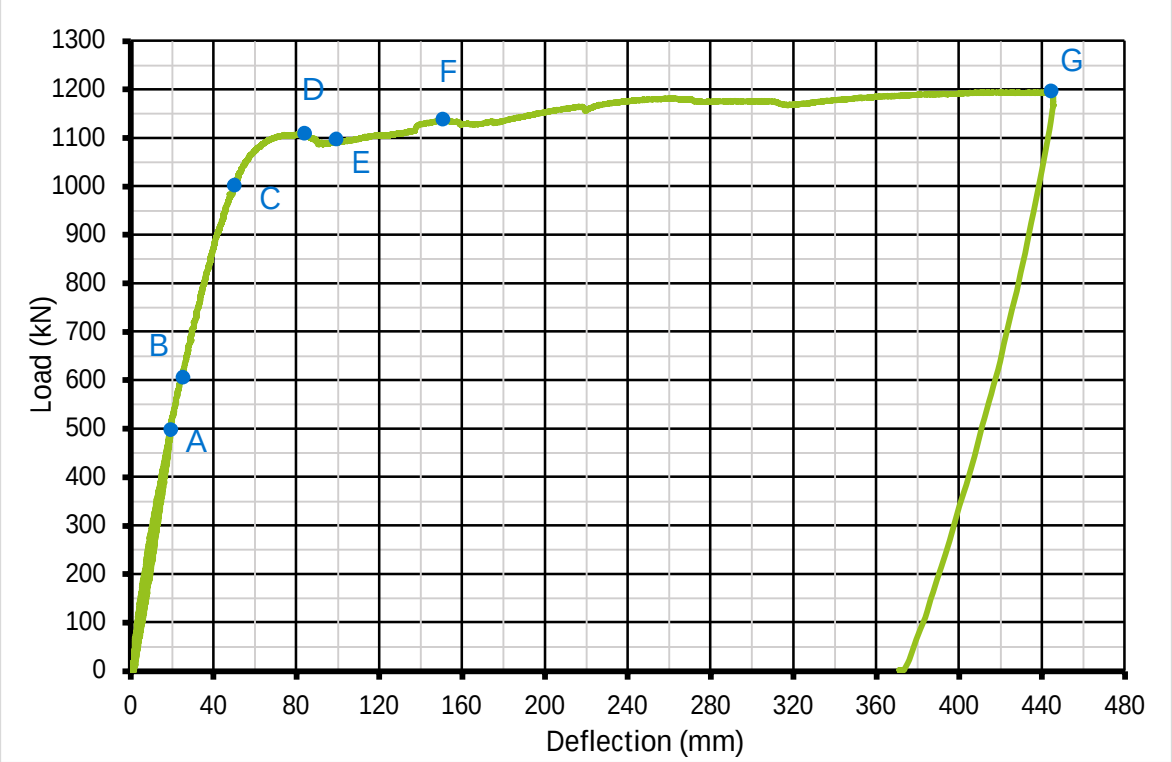

Fig. 5.144- S8- Average load- deflection curve

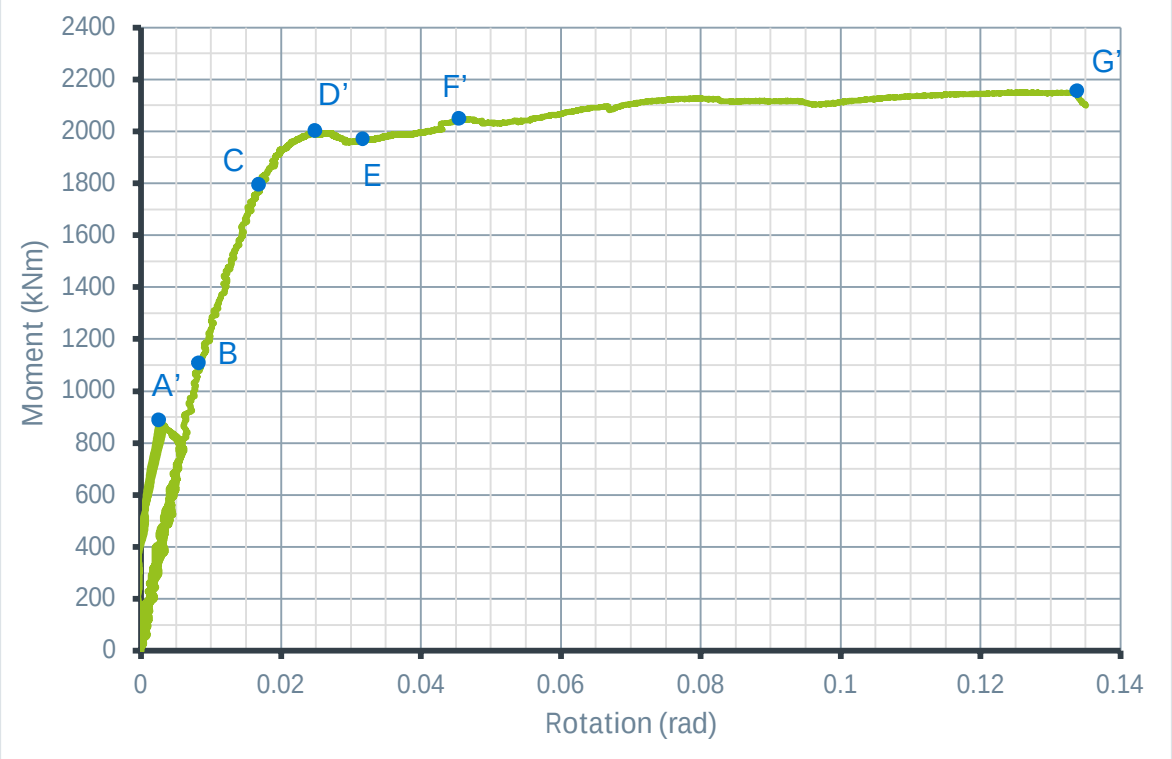

Fig. 5.145- S8- Average moment- rotation curve (Inclinometer)

The slips between the concrete and the steel beam are presented in figure 5.146. The maximum slips were observed at S3 and S4, measured equal to -3.6 mm and 3.89 mm, respectively (figure 5.147), while a change of slip direction between S2 and S3 is observed. The values were reduced towards the supports.

Load- strain curves are presented in figure 5.148. The strains were almost evenly distributed along the width of the bottom plate for all deflection values (figure 5.149), with slightly highest the strains at the intersections of the bottom plate with the web plates.

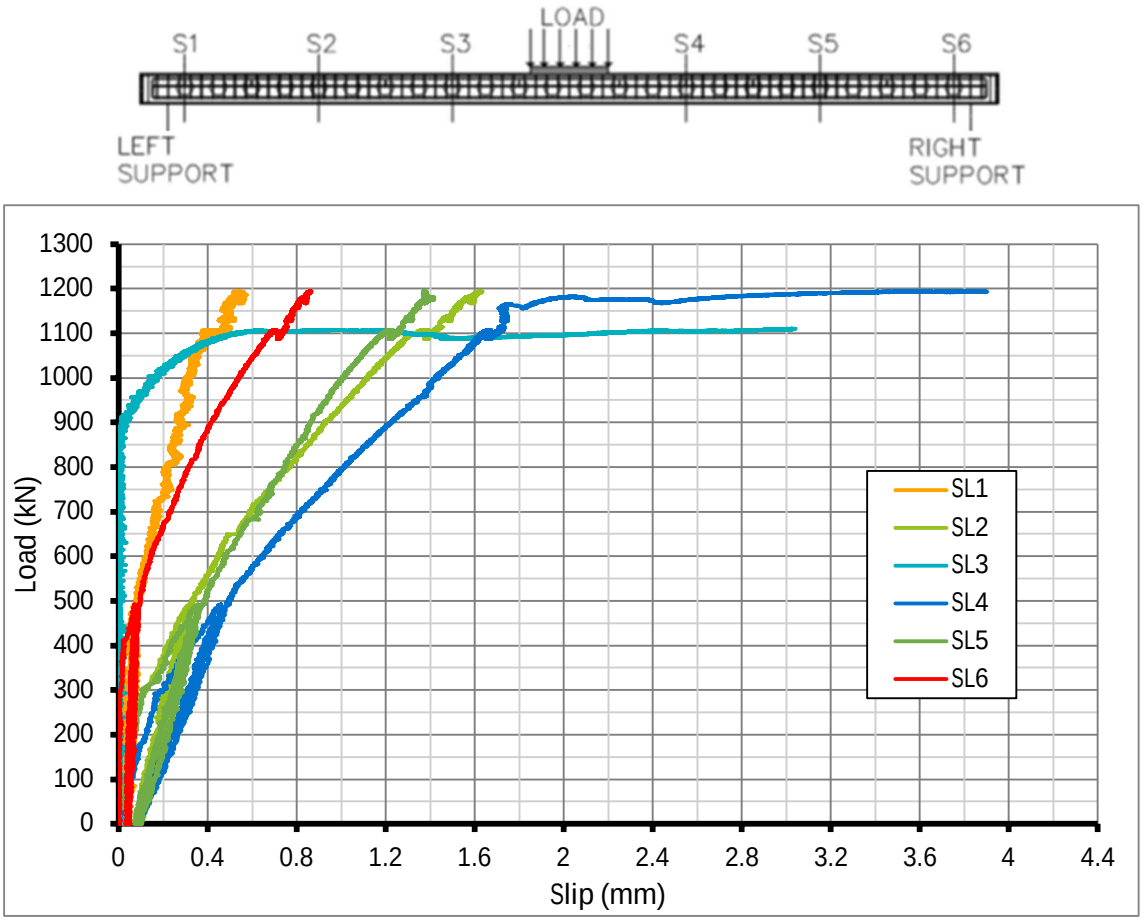

Fig. 5.146- S8- Slips between concrete and steel beam

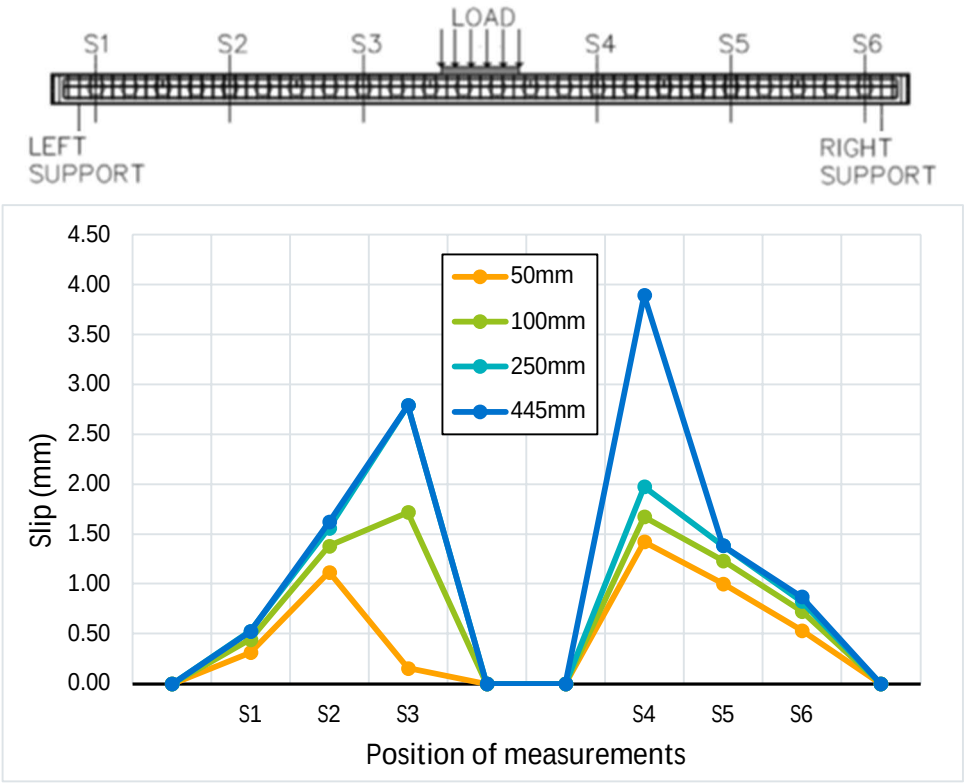

Fig. 5.147- S8- Slip propagation for different deflection values

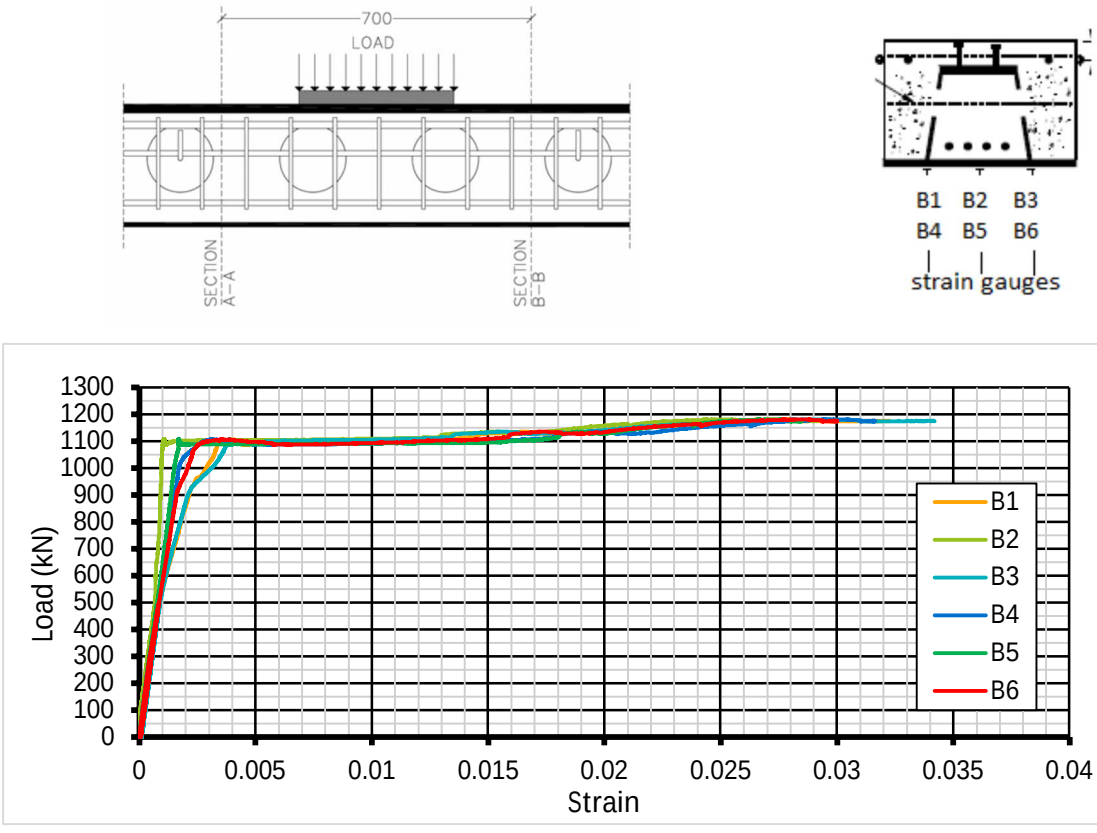

Fig. 5.148- S8- Tensile strains at the bottom plate of the beam

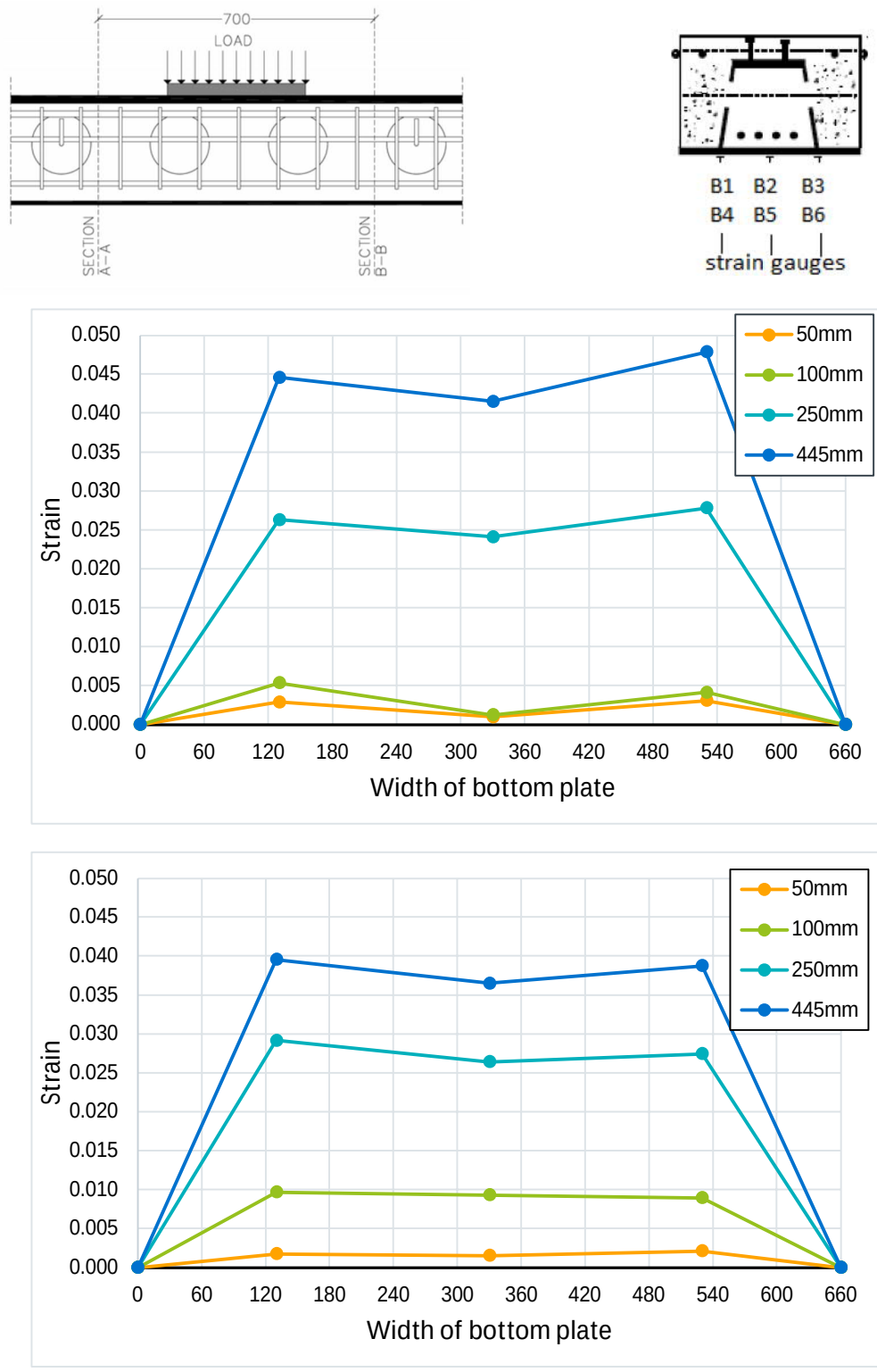

Fig. 5.149- S8- Strains along the bottom plate at sections A-A (top) and B-B (bottom) for various deflections

5.3.5 Comparative results

All Type 3 specimens were ductile. After the yielding point, they acquired an elastoplastic behavior until the end of the tests with no strength degradation (figures 5.150- 5.151). The small drops in strength at the curves are due to the spalling of concrete mainly, at the top cover. The condition of the specimens at the end of the tests was very good with spalling of concrete limited at the top cover. The buckling of the longitudinal rebars of the top mesh was not extensive and did not cause any significant reduction in the load bearing capacity of the specimens.

As can be seen in the following figures, S6a, with one row of shear studs and S6b with two rows of shear studs, had identical behavior. So, similarly with the cases of Type 1 specimens, the different number of shear studs' rows did not affect the global flexural behavior of the beams. On the contrary, this difference in detailing influenced the slips between the concrete and steel parts, where, in the case of two rows of shear studs (S6b) the slips were considerably reduced. The difference in height of the cross sections was the major factor that affected the behavior of the beams. S6a and S6b, the beams with the smaller cross section had the lowest strength while S8 had the highest. Given S6a (or S6b) as a control specimen due to its smallest height, an increase of 16.67% and 32.83% of height led to an increase of 26.88% and 58.35% of the peak load, for specimens S7 and S8, respectively.

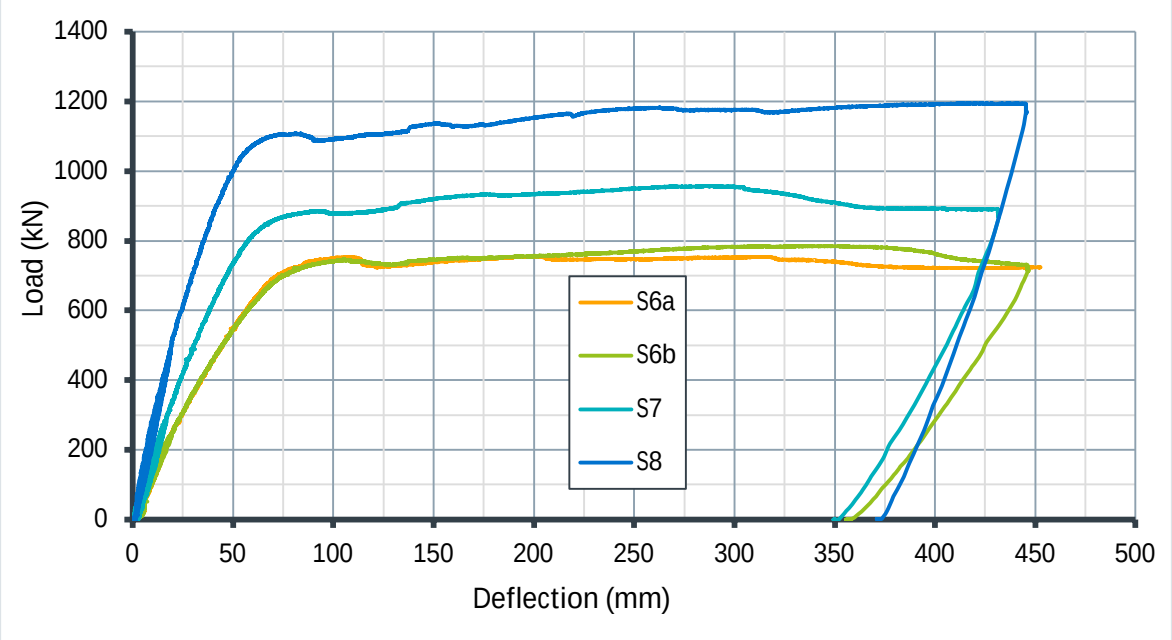

Fig. 5.150- Type 3 load- deflection curves

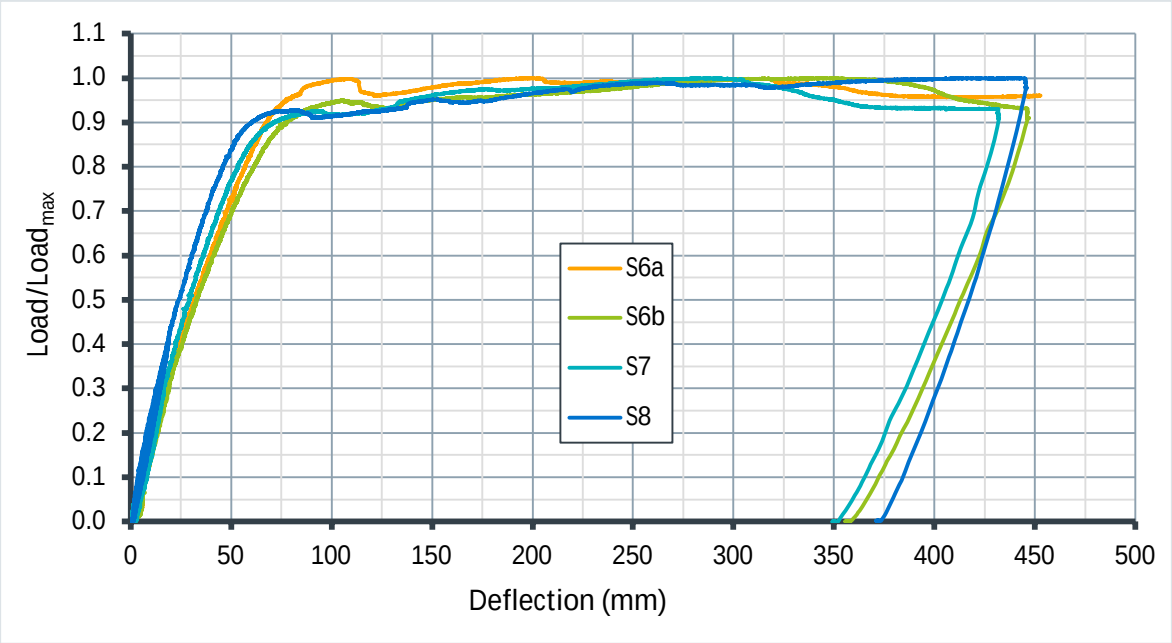

Fig. 5.151- Normalized Type 3 load- deflection curves

5.4 Type 4 sections

As can be seen in figure 4.5 these beams have two thin concrete ledges at the top at both sides. These specimens represent the combination of Deltabeam with precast prestressed HC floor with structural topping.

5.4.1 Specimen S9

First hair-line cracks appeared at the first serviceability circle (figure 5.152) at a deflection of 19 mm (479 kN). In figures 5.153- 5.155 the tensile concrete cracks at deflections of 25 mm (588 kN), 50 mm (1005 kN) and 75 mm (1124 kN) are presented, respectively. At a deflection of 90 mm (1140 kN) the first compressive cracks appeared at the one ledge of the concrete plate under the loading area (figure 5.156). Immediately after the appearance of the cracks the ledge failed under compression, causing a load reduction equal to 75 kN (figures 5.159 and 5.160). For the next approximately 100 mm the load was generally constant when a new load reduction equal to 80 kN occurred due to the failure of the second concrete ledge. After that the specimen manifested a hardening behavior up to the end of the test (463 mm- 1007 kN) where the loading actuator reached its maximum displacement capacity (figure 5.157). The open stirrups were effective and the confinement they provided was the reason for the good shape of the central concrete part (figure 5.158) and the overall ductile behavior.

Fig. 5.152- S9- Hair-line cracks at deflection of 19 mm (fig. 5.159 and 5.160, points A and A')

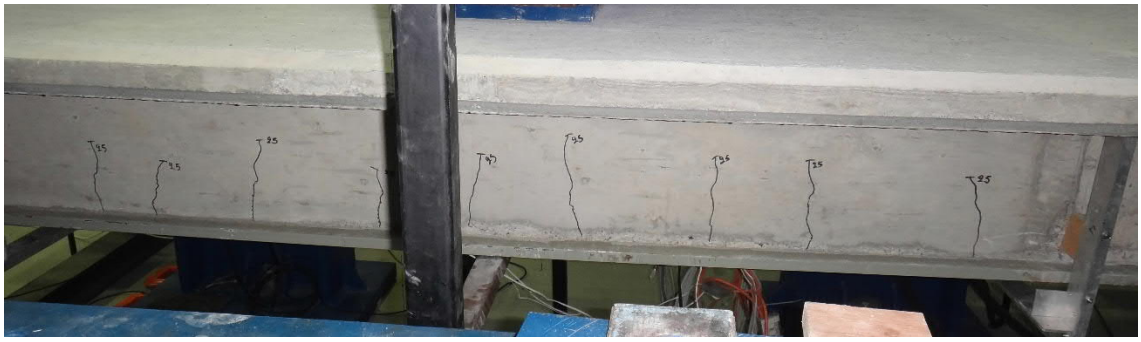

Fig. 5.153- S9- Cracks at deflection of 25 mm (fig. 5.159 and 5.160, points B and B')

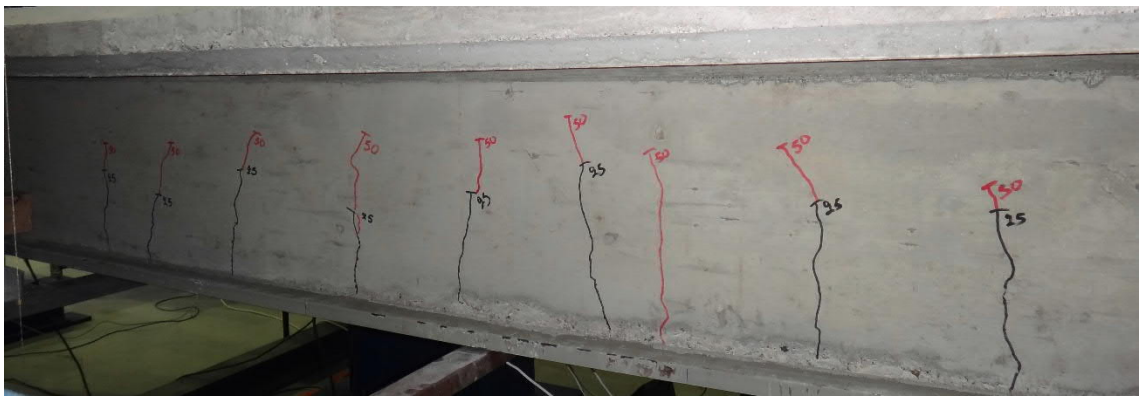

Fig. 5.154- S9- Cracks at deflection of 50 mm (fig. 5.159 and 5.160, points C and C')

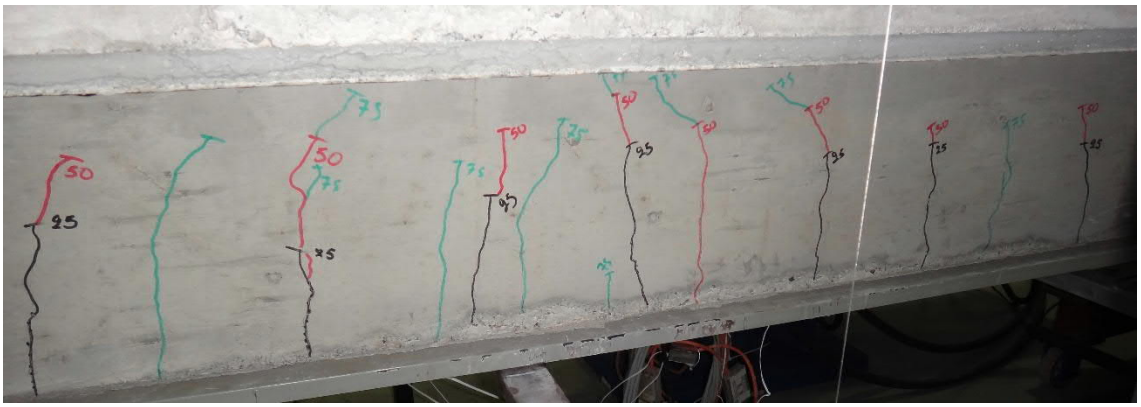

Fig. 5.155- S9- Cracks at deflection of 75 mm (fig. 5.159 and 5.160, points D and D')

Fig. 5.156- S9- Cracks at the top face of concrete (fig. 5.159 and 5.160, points E and E')

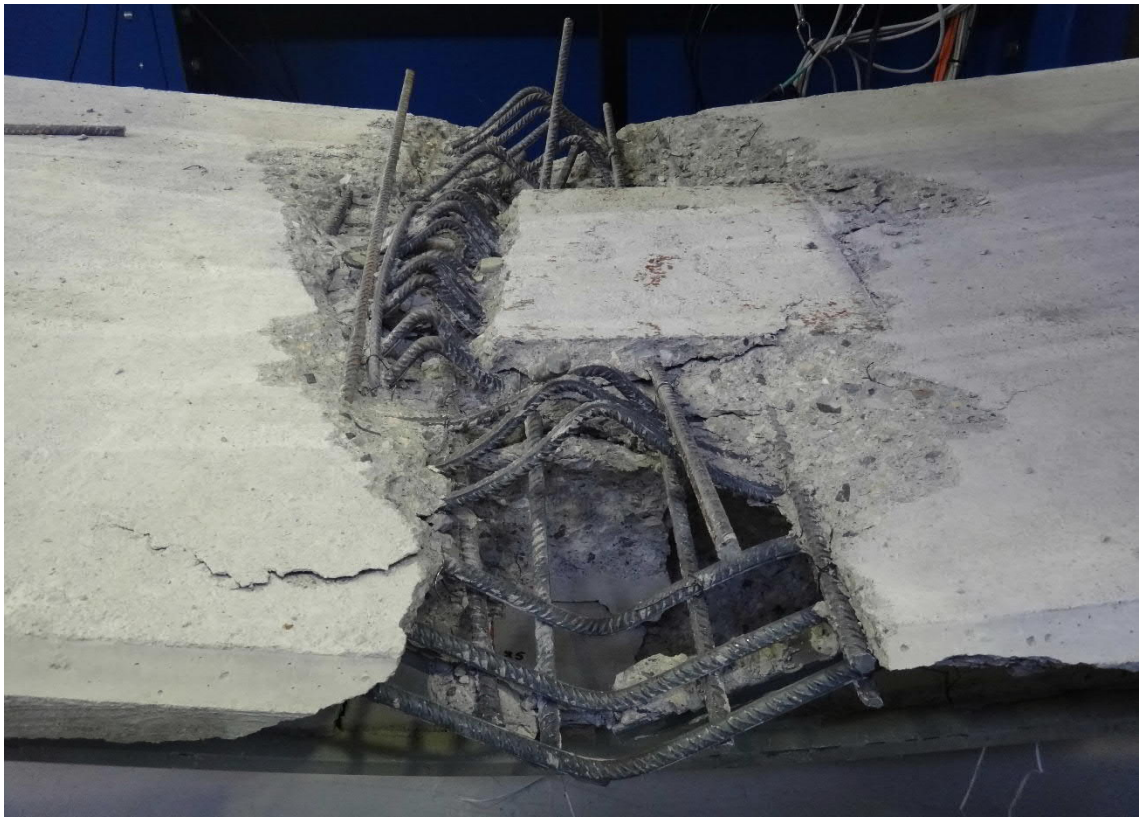

Fig. 5.157- S9- The beam after the removal of loose concrete (fig. 5.159 and 5.160, points F and F')

Fig. 5.158- S9- Cracks at the middle of the span at the end of the test (fig. 5.159 and 5.160, points F and F')

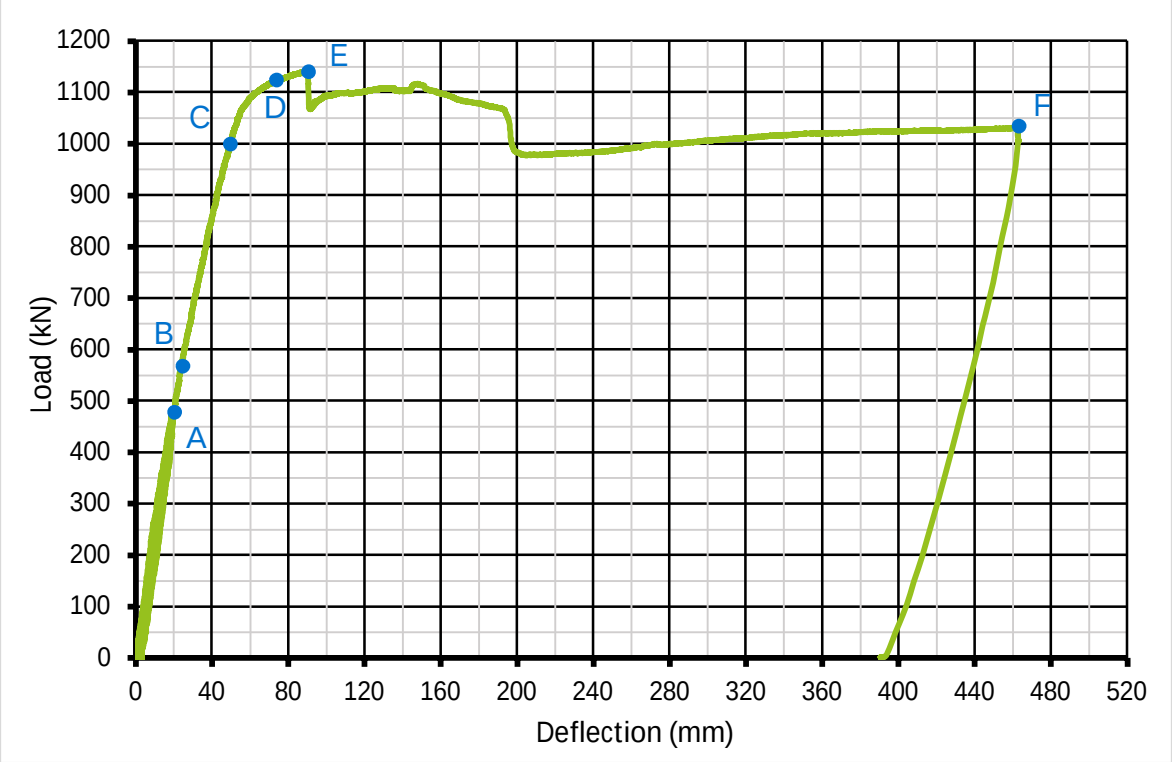

Fig. 5.159- S9- Average load- deflection curve

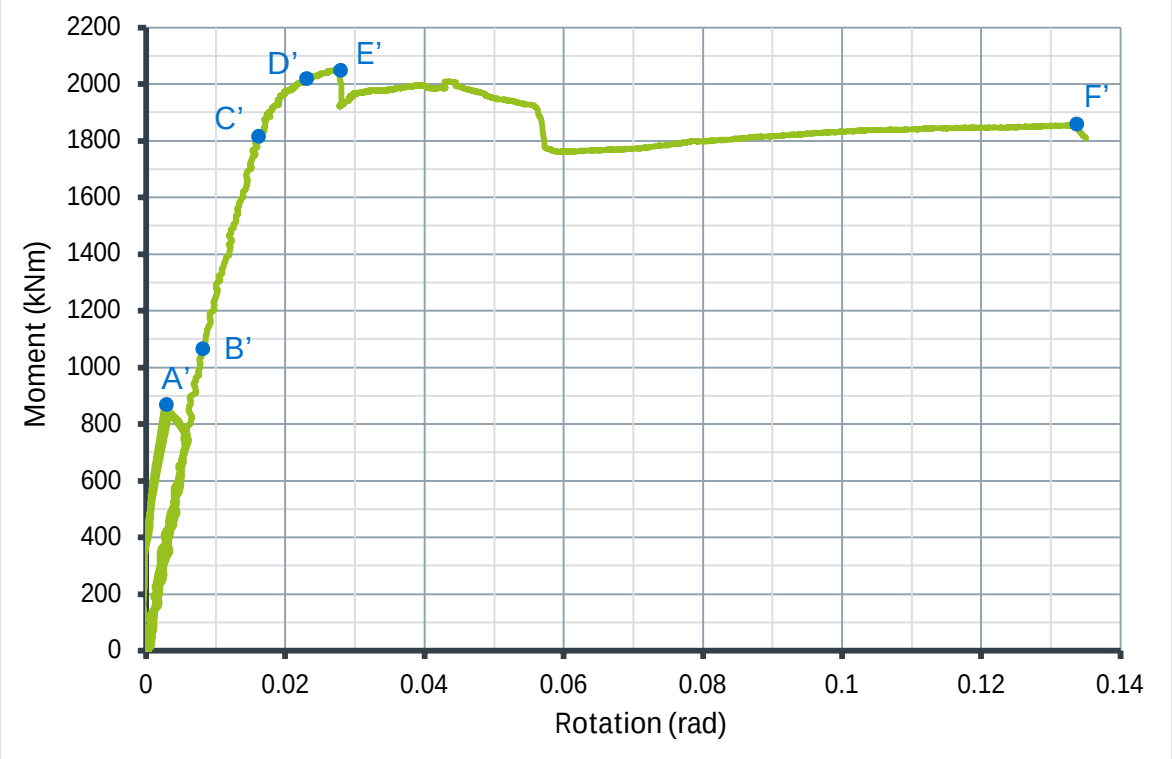

Fig. 5.160- S9- Average moment- rotation curve (Inclinometer)

The slips between the concrete and the steel beam are presented in figure 5.161. The maximum slips were observed at S2 and S4, measured equal to 2.20 mm and 3.02 mm, respectively (figure 5.162). The slip values are decreasing proportionally towards the supports.

Load- strain curves are presented in figure 5.163. The strains were almost evenly distributed along the width of the bottom plate for all deflection values (figure 5.164), with an unexpected peak at the middle of the plate at section B-B at the end of the test.

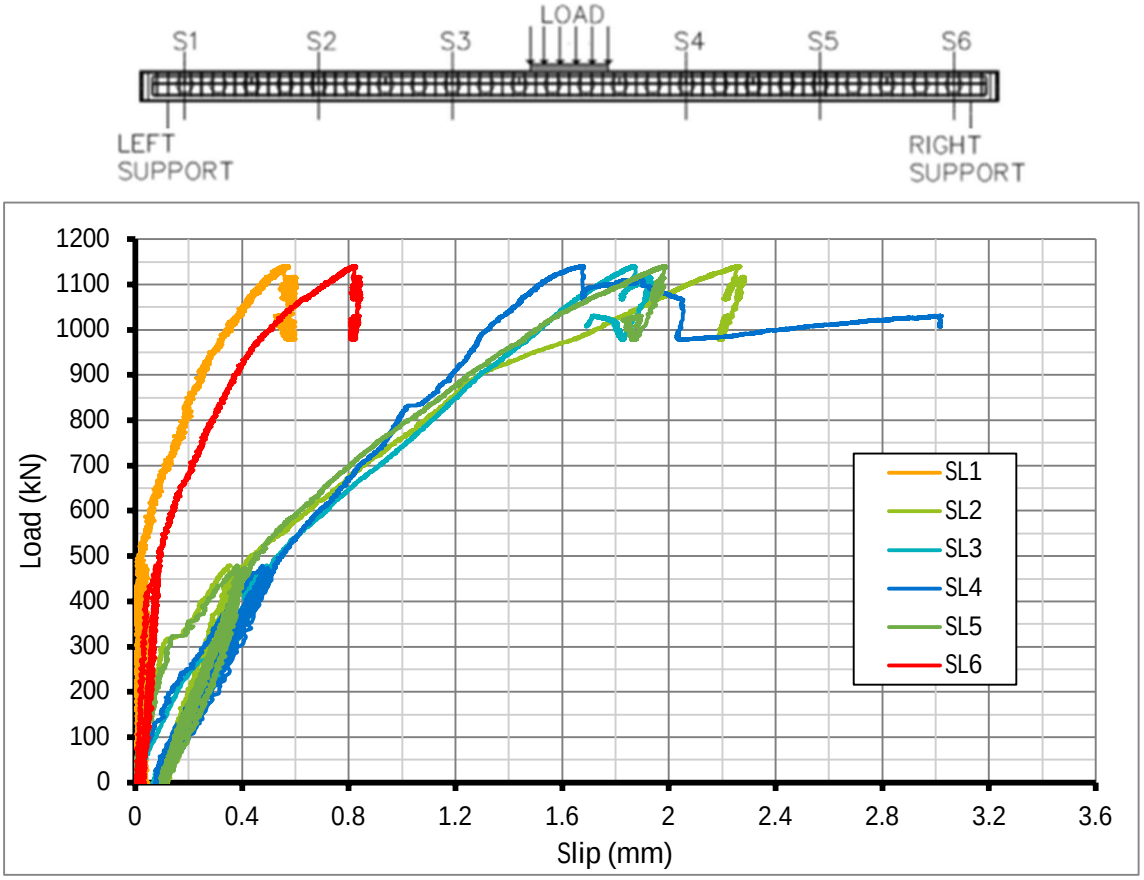

Fig. 5.161- S9- Slips between concrete and steel beam

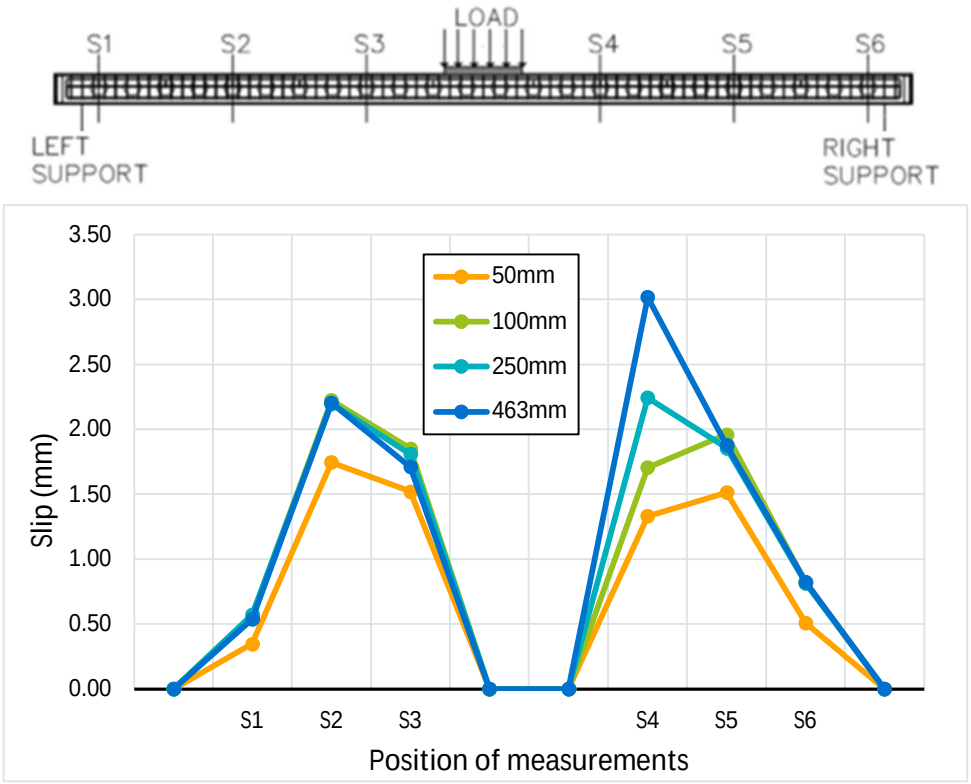

Fig. 5.162- S9- Slip propagation for different deflection values

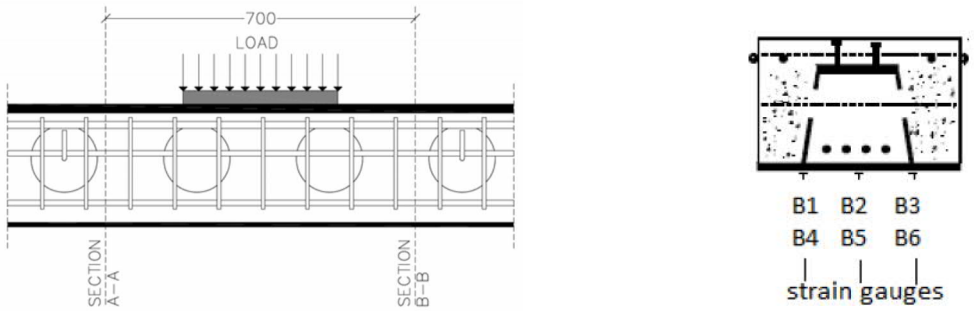

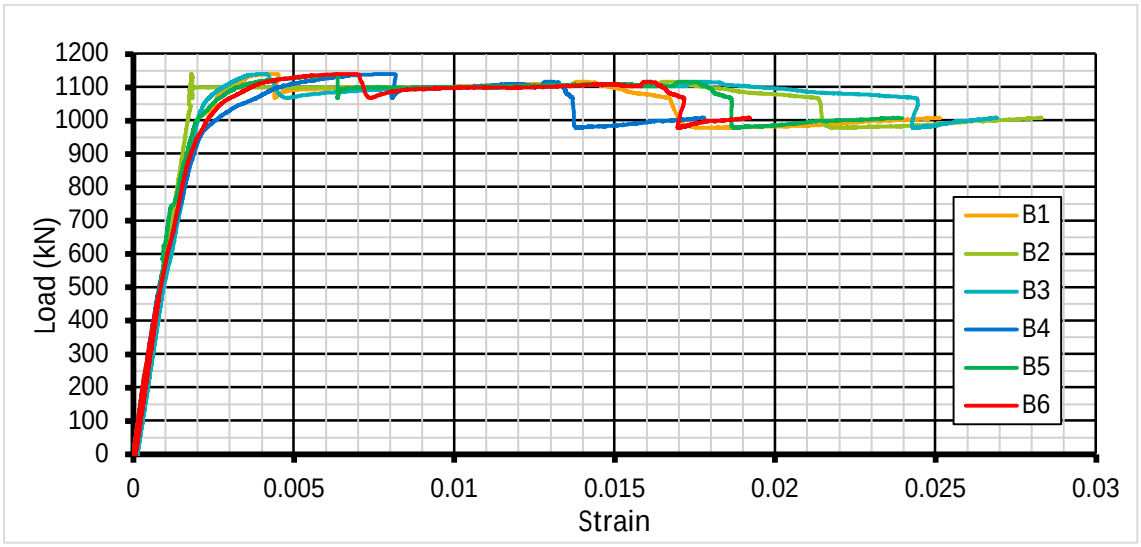

Fig. 5.163- S9- Tensile strains at the bottom plate of the beam

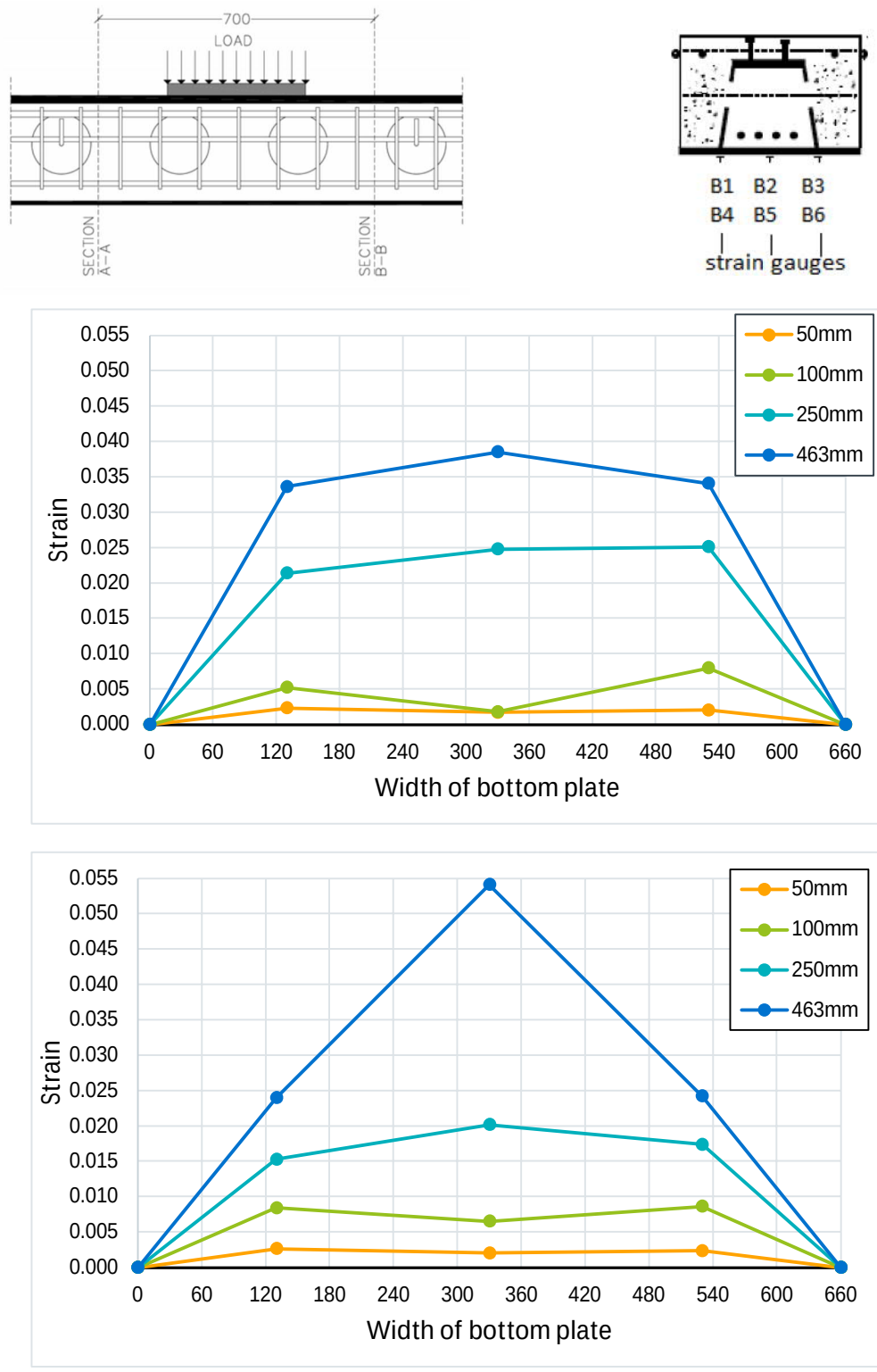

Fig. 5.164- S9- Strains along the bottom plate at sections A-A (top) and B-B (bottom) for various deflections

5.4.2 Specimen S10

First hair-line cracks appeared at the first serviceability circle (figure 5.165) at a deflection of 20 mm (605 kN). In figures 5.166 and 5.167 the tensile concrete cracks at deflection equal to 25 mm (679 kN) and 50 mm (1232 kN) are presented, respectively. At a deflection of 80 mm (1323 kN) the first concrete ledge failed leading to a 55 kN load loss (figure 5.168). For the next approximately 85 mm the load was generally constant when a new load reduction equal to approximately 100 kN occurred due to the failure of the second concrete ledge. After that point the remained constant with a value of 1150 kN up to the end of the test (460 mm- 1114 kN) where the loading actuator reached its maximum displacement capacity (figures 5.172 and 5.173). The open stirrups were effective again and maintained the central concrete part in a good shape (figures 5.169- 5.171).

Fig. 5.165- S10- Hair-line cracks at deflection of 20 mm (fig. 5.172 and 5.173, points A and A')

Fig. 5.166- S10- Cracks at deflection of 25 mm (fig. 5.172 and 5.173, points B and B')

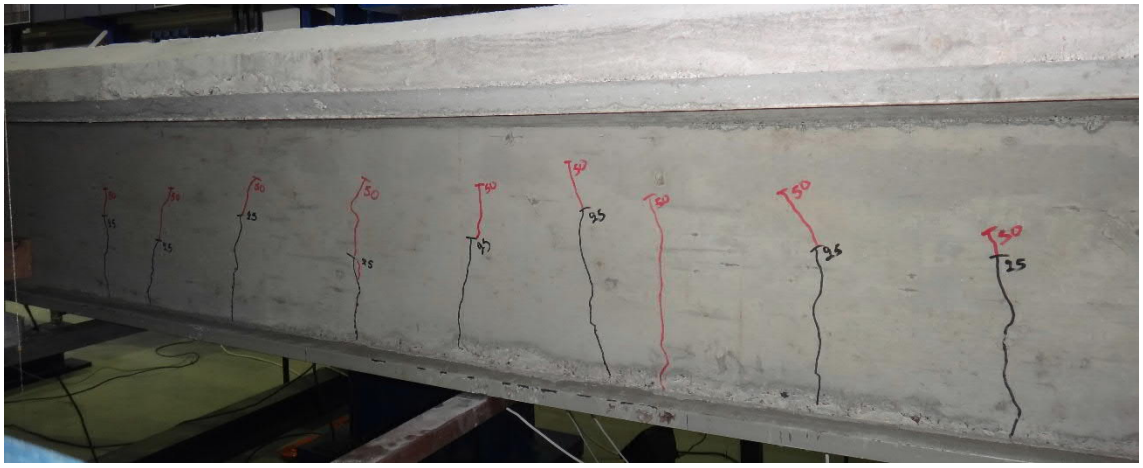

Fig. 5.167- S10- Cracks at deflection of 50 mm (fig. 5.172 and 5.173, points C and C')

Fig. 5.168- S10- Cracks at the top of the concrete (fig. 5.172 and 5.173, points D and D')

Fig. 5.169- S10- The beam at the end of the test (fig. 5.172 and 5.173, points E and E')

Fig. 5.170- S10- Cracks at the middle of the span at the end of the test (fig. 5.172 and 5.173, points E and E')

Fig. 5.171- S10- The beam after the removal of loose concrete (fig. 5.172 and 5.173, points E and E')

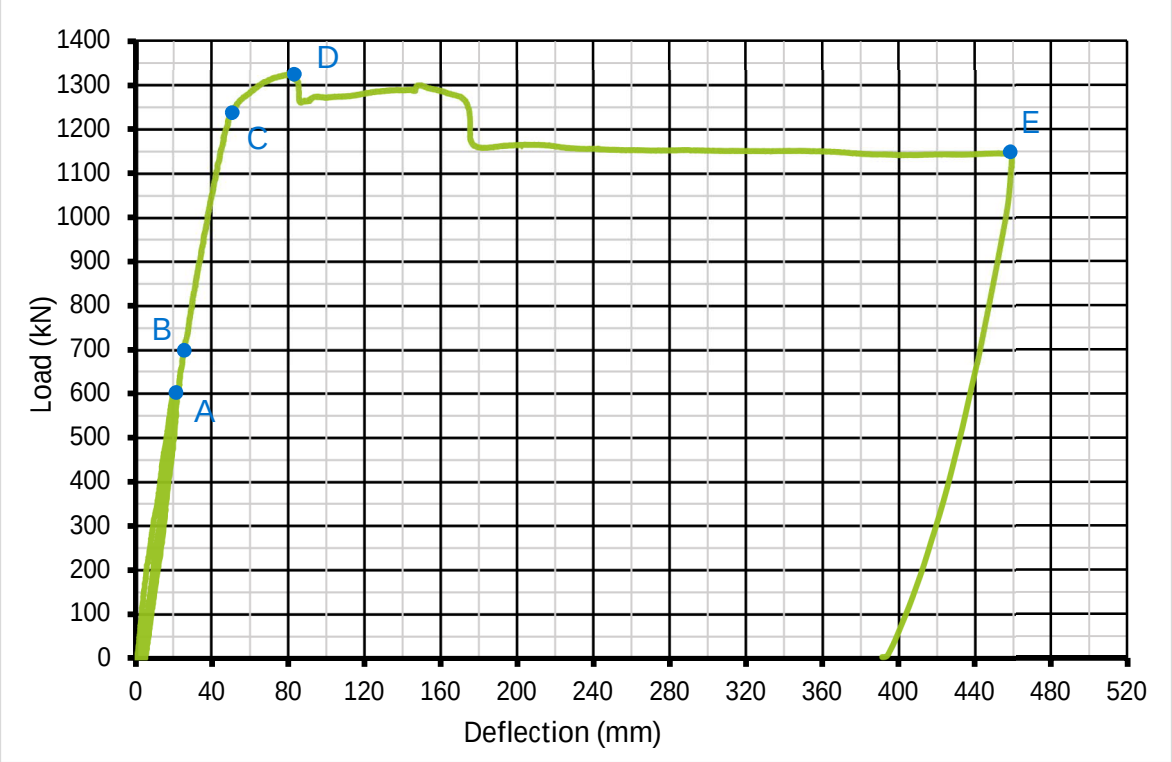

Fig. 5.172- S10- Average load- deflection curve

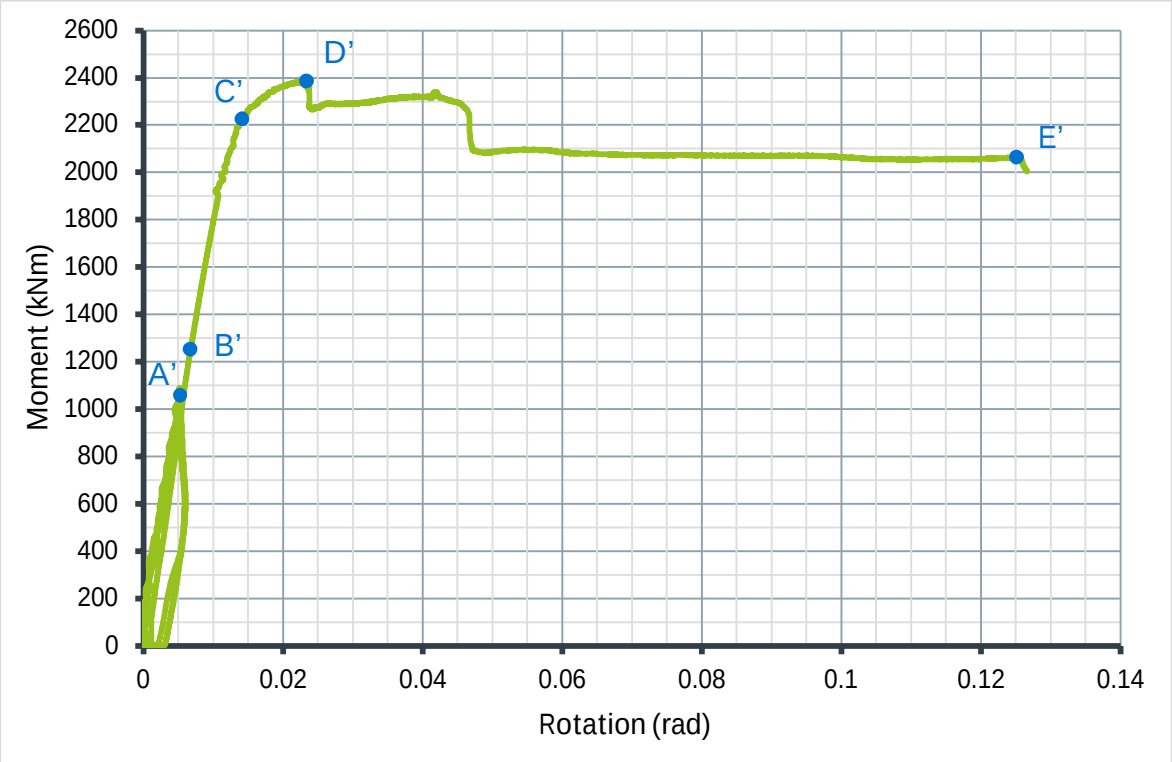

Fig. 5.173- S10- Average moment- rotation curve (Inclinometer)

The slips between the concrete and the steel beam are presented in figure 5.174. The maximum slips were observed at S3 and S4, measured equal to -3.00 mm and 3.35 mm, respectively (figure 5.175). The slip values are decreasing proportionally towards the supports in both sides of the beam.

Load- strain curves are presented in figure 5.176. The strains were almost evenly distributed along the width of the bottom plate for all deflection values (figure 5.177), with the value measured at the center of the plate being slightly higher. Strain values of both sides of the loading area, section A-A and B-B, were close.

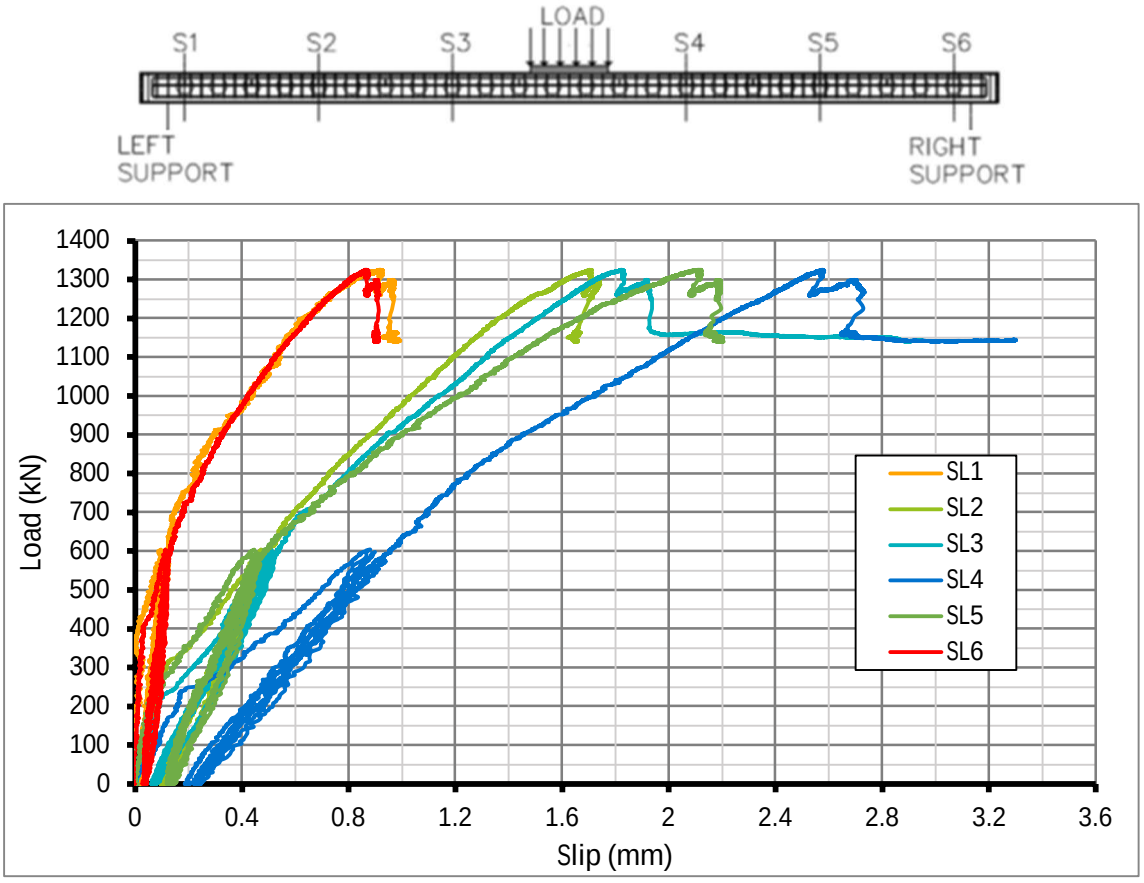

Fig. 5.174- S10- Slips between concrete and steel beam

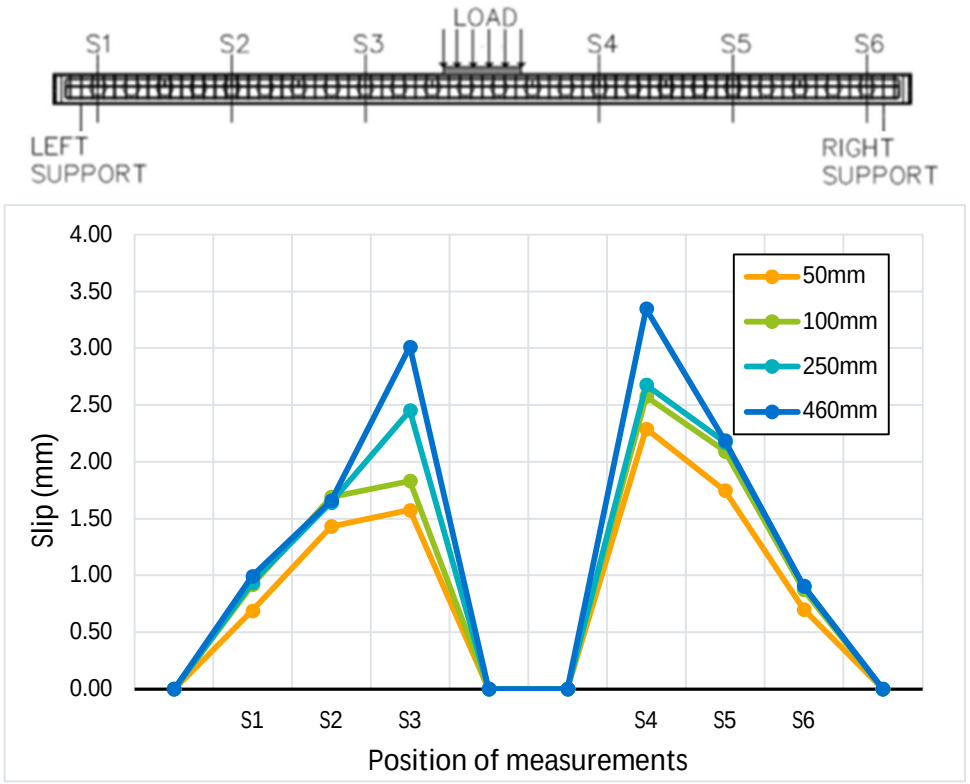

Fig. 5.175- S10- Slip propagation for different deflection values

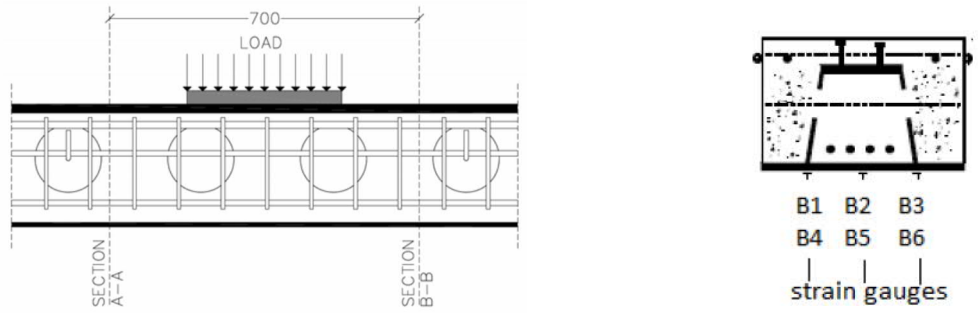

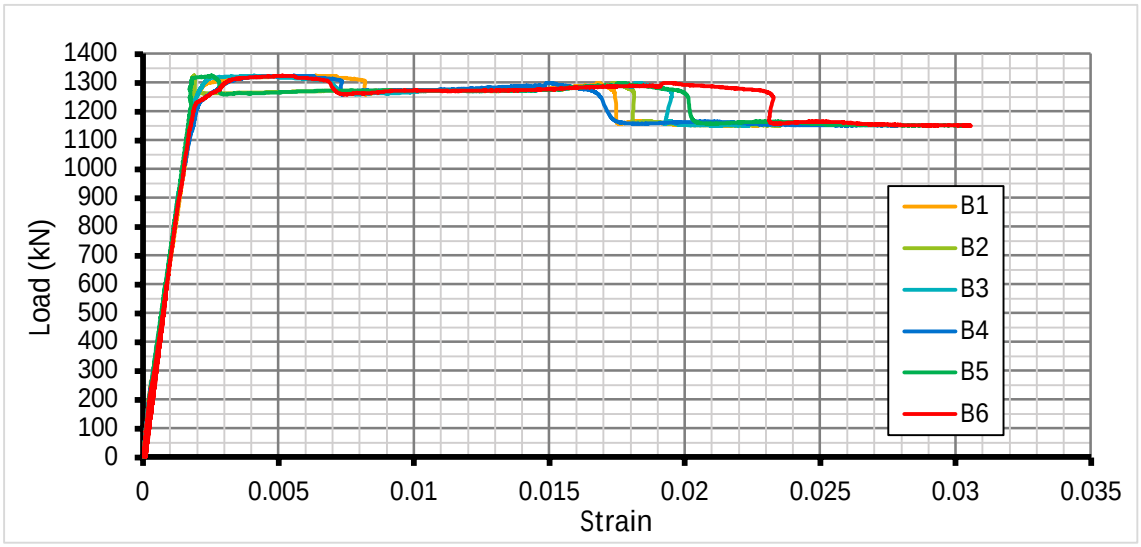

Fig. 5.176- S10- Tensile strains at the bottom plate of the beam

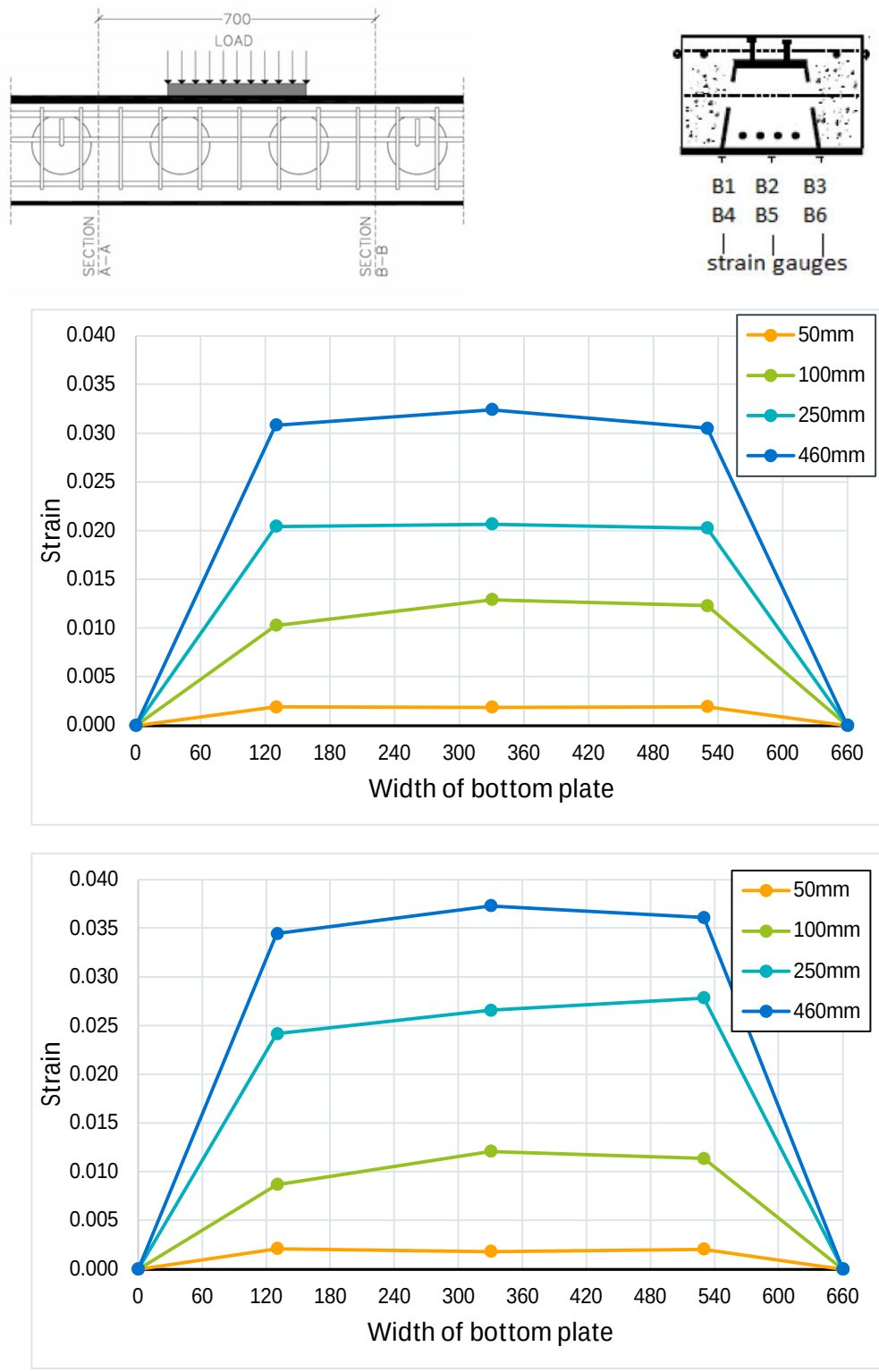

Fig. 5.177- S10- Strains along the bottom plate at sections A-A (top) and B-B (bottom) for various deflections

5.4.3 Comparative results

Both Type 4 specimens exhibited the same behavior. After the maximum load the two concrete ledges failed successively, causing two relatively significant reductions in the resistance of about 8.5% and 7%, for S9 and S10 respectively (figures 5.178 and 5.179). The fact that the concrete ledges had the same thickness and reinforcement in both beams led to the same reductions (about 100 kN). After that point, in both beams, the central part of the beam (steel beam, core concrete, outer concrete confined by the open stirrups) managed to maintain its strength, providing an overall ductile behavior. Finally, like in the previous cases the beam with the highest section was proved to be the one with the greatest resistance. S10 was 12.3% higher and had 16.2% higher strength than S9.

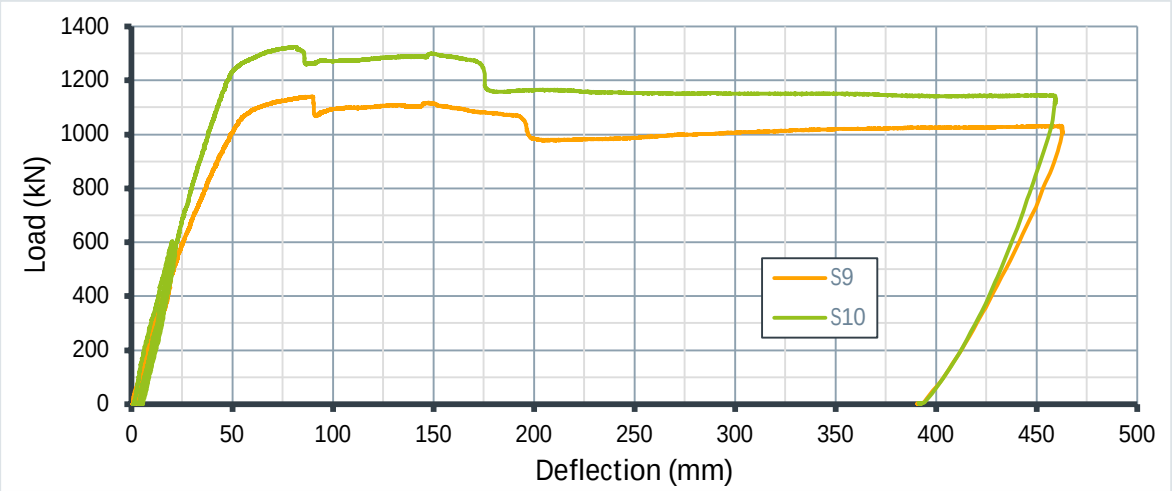

Fig. 5.178- Type 4 load- deflection curves

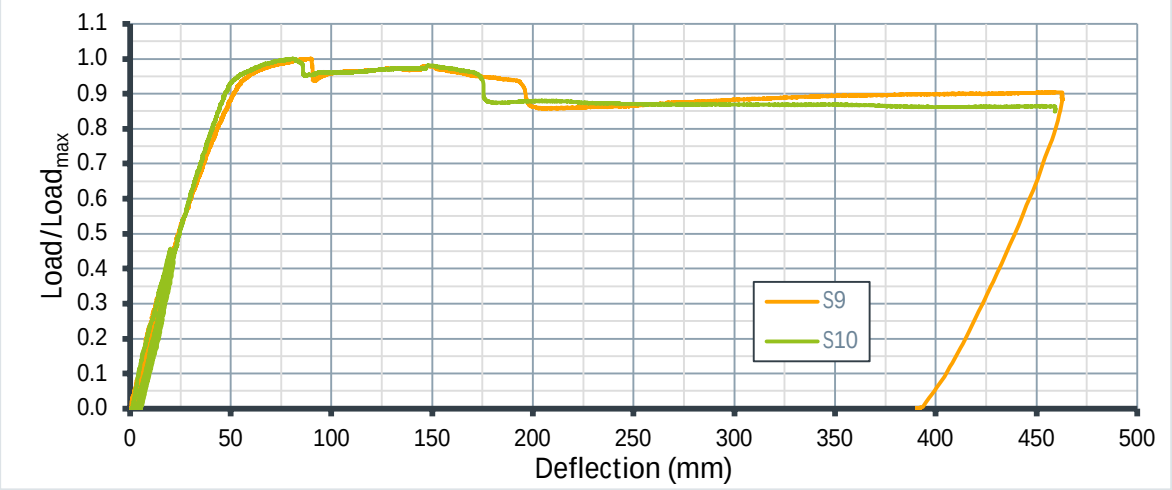

Fig. 5.179- Normalized Type 4 load- deflection curves

6

Analytical investigation with Finite element method

6.1 Introduction to Finite element method

The finite element method (FEM) is a computer-based procedure that can be used to analyze structures and continua. This numerical method, commonly applied by engineers, covers almost the whole spectrum of engineering analysis, including static, dynamic, thermal behavior of physical systems, fluid motions etc. Advances in computer hardware made in the last two decades, have made it easier and very efficient to use finite element software for the solution of complex engineering problems on personal computers [34, 35]. Since this method is a numerical approach, the results obtained by conducting a finite element analysis are rarely "exact" to the reality. Nevertheless, a very accurate solution can be obtained if a finite element model is used based on principles of FEM.

The scientific pillars of the finite element method are a direct result of the need to solve complex elasticity and structural analysis problems in civil and aeronautical engineering. The first development can be traced back to the work of A. Hrennikoff in 1941 [36] and R. Courant in 1943 [37]. Although these scientists followed different perspectives in their finite element approaches, they each identified the one common and essential characteristic: mesh discretization of a continuous domain into a set of discrete sub-domains, usually called elements. Another fundamental mathematical contribution to the FEM is represented by the book "An Analysis of the Finite Element Method" by Gilbert Strang and George Fix, first

published in 1973 [38]. Since then, FEM has been generalized to be used for the numerical modeling of physical systems in many engineering problems.

To summarize in general terms how the finite element method works, a list of the main steps of the finite element solution procedure, using the direct stiffness approach, is the following [39]:

i. Discretize the continuum- The first step is to divide the regions of the model into finite elements. The finite element mesh is typically generated by a preprocessor program. This first step is one of the most crucial in determining the accuracy of the results.

ii. Define the element properties- The matrix equation for the finite element should be established by defining the element properties and selecting the proper, for each problem, element type, which relates the nodal values of the unknown field approximation function to other parameters.

iii. Assemble the element equations- To find the global equation system for the whole solution region all the element equations must be assembled. Element connectivities are used for the assembly process. Before solution, boundary conditions (which are not accounted in element equations) and loads should be imposed.

iv. Solve the global equation system- The finite element global equation system can be solved with direct and iterative methods. The nodal displacement values of the sought function are produced as a result of the solution.

v. Compute additional results- In many mechanical problems additional parameters like strains and stresses are of interest in addition to displacements, which are obtained after solution of the global equation system.

6.2 Description of models

6.2.1 Assembly of models

The finite element analysis software Abaqus was used to simulate the behavior of the test specimens. The models were assembled by five 3D parts; one for concrete, one for the steel beam, one for the reinforcement and two rigid parts to simulate the supports and the loading plate (figure 6.1). This analytical investigation was conducted only for Type 2, 3 and 4 specimens (see § 4.3.1). The lack of reinforcement rebars in Type 1 beams made the concrete a very computationally unstable material and so the time increment of the analysis was reduced to a very small value making the completion of the analysis impossible.

A general contact option was chosen to simulate the interaction between the different parts. The general contact algorithm allows for very general characteristics in the surfaces that it uses. Abaqus automatically defines an all-inclusive surface that is convenient for prescribing the contact domain. In addition, to avoid physically unreasonable contact interactions and, thus, reduce the time of the analysis, contact exclusion pairs can be defined. The general contact algorithm generates contact forces to resist node-into-face, node-into-analytical rigid surface and edge-into-edge contact penetrations. To complete the definition of the interaction between the different regions of the model, an interaction property model must be applied to the interacting pairs. A hard contact was chosen along the normal direction of the interaction. The surfaces do not transmit any contact pressure unless the nodes of the slave surface contact the master surface and no penetration is allowed at each constraint location. Still, the two surfaces of the interaction pair are able to separate relative to each other after contact. The tangential behavior of the interacting surfaces was defined with two different property types. Between the concrete and the steel beam a friction with a factor equal to 0.4 was applied [40]. This value is commonly used in the literature. Also, during calibration procedure, the effect of this factor was assessed and this value gave the most optimal results. The friction factor had a more noticeable effect during the initial states of the analysis, when the beam maintained its elastic behavior with higher values of the friction factor resulting in a higher composite stiffness.

However, during the development of inelastic straining in the concrete, gaps will open between the material parts making the friction ineffective. Between the supports and the bottom plate of the steel part a friction factor equal zero was chosen to simulate the interaction between the steel and teflon plates.

Typical model of Type 2 specimens

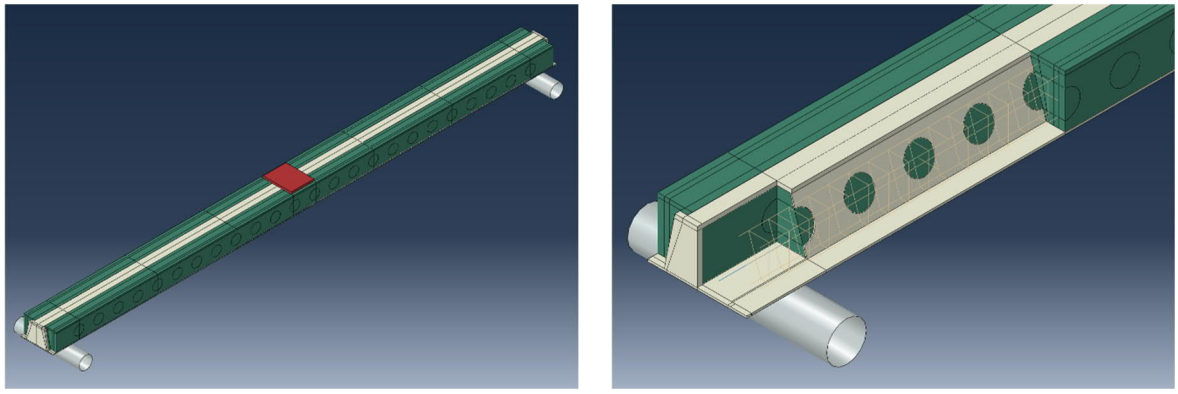

Typical model of Type 3 specimens

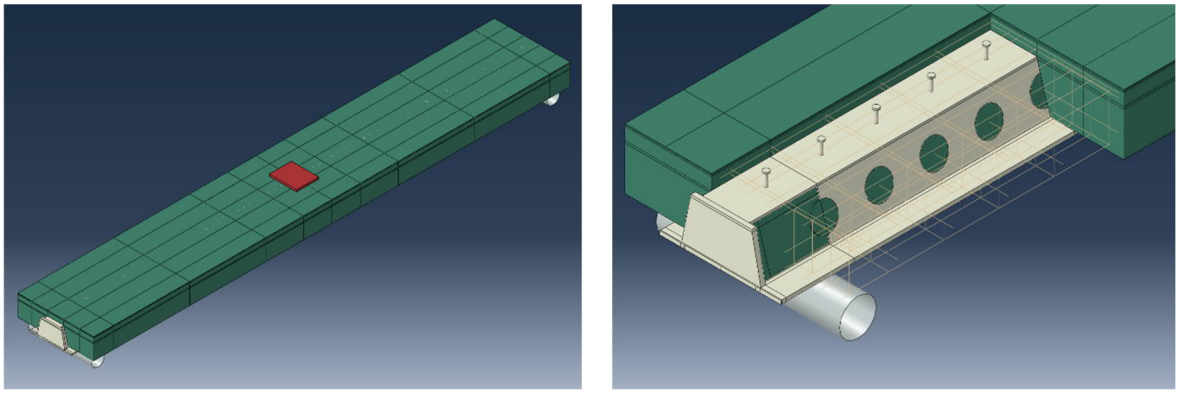

Typical model of Type 4 specimens

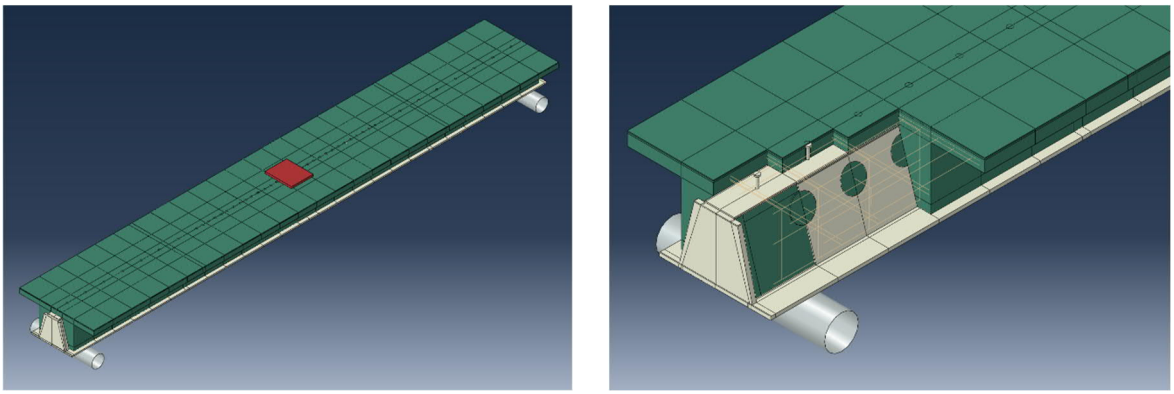

Fig. 6.1- Presentation of typical models for each section type

The embedded element technique is used to simulate the interaction between the concrete and the reinforcement bars. This technique specifies that an element or group of elements is

constrained (embedded) to “host” elements. Abaqus searches for the geometric relationships between the nodes of the embedded and the host elements. If a node of an embedded element lies within a host element, the translational degrees-of-freedom (dofs) at the node are eliminated and the node becomes an “embedded node”. The translational dofs of the embedded node are constrained to the interpolated values of the corresponding dofs of the host element. Embedded elements are allowed to have rotational dofs, but these rotations are not constrained by the embedding [41].

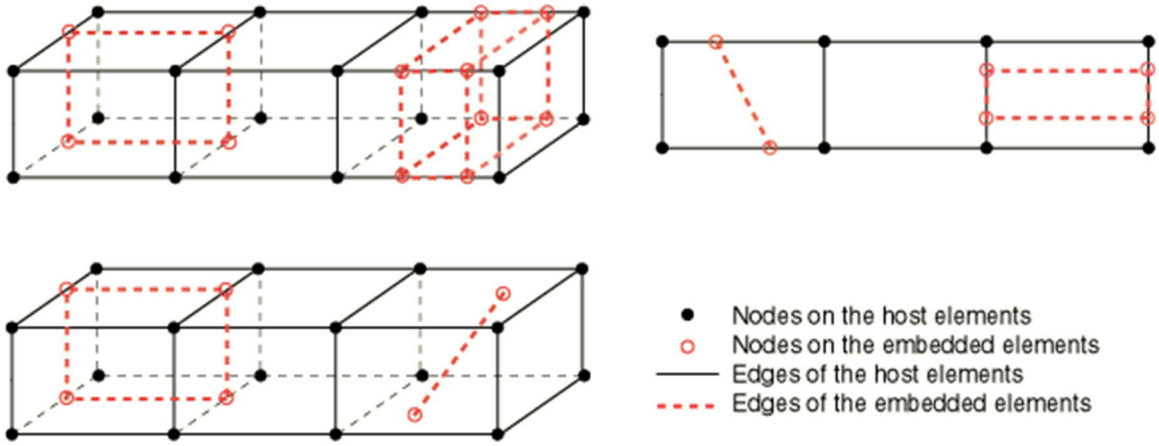

Fig. 6.2- Examples of embedded and host elements

6.2.2 Meshing of models

The meshes of each section type is presented in figures 6.3- 6.5 for Type 2, 3 and 4, respectively. Solid hexahedral elements were used to mesh the steel beam and concrete parts. For the supports and the loading steel plate rigid elements were used. Finally, the mesh of the reinforcement and the fire rebars was created with linear truss elements. More details about each element type are given in the following. The number of elements used to create the mesh of each model is presented in Table 6.1.

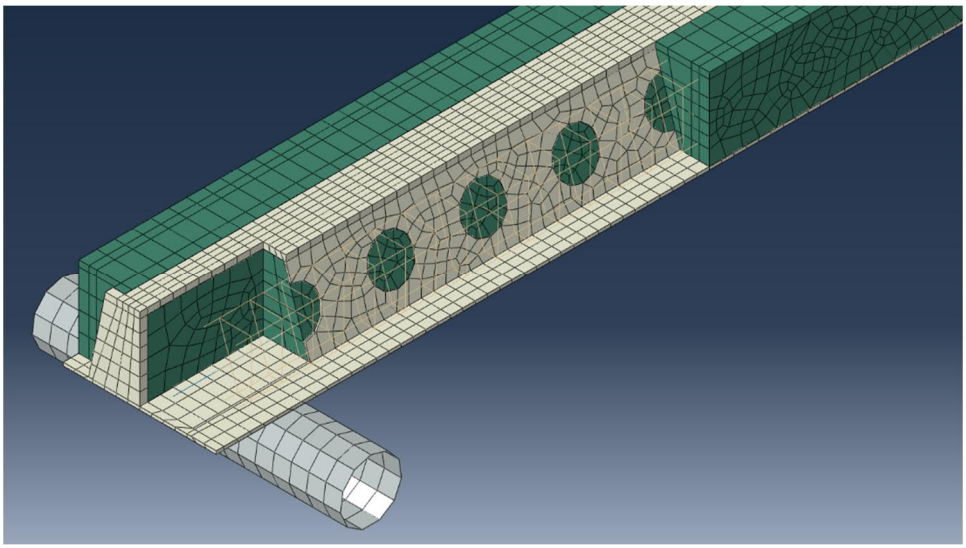

Fig. 6.3- Typical mesh of Type 2 specimens

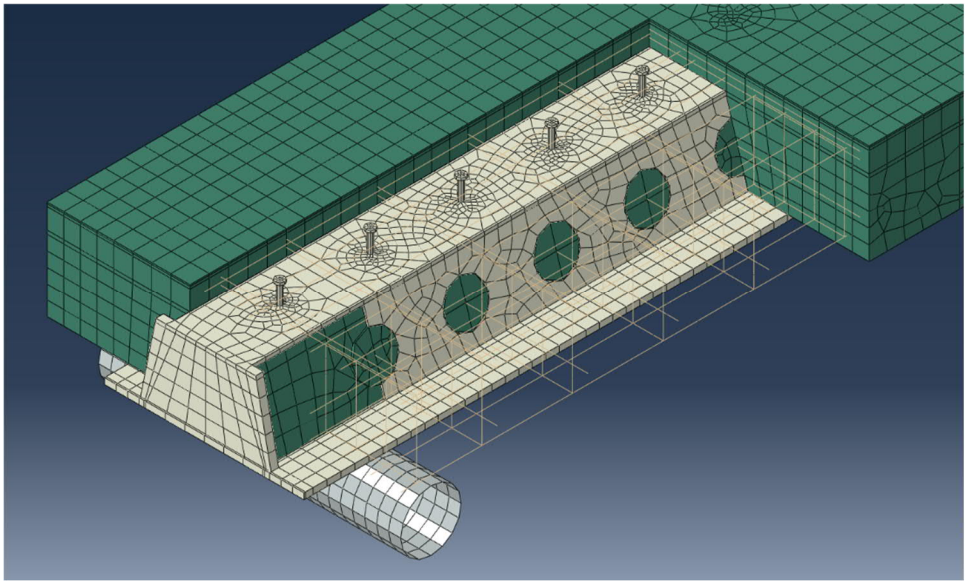

Fig. 6.4- Typical mesh of Type 3 specimens

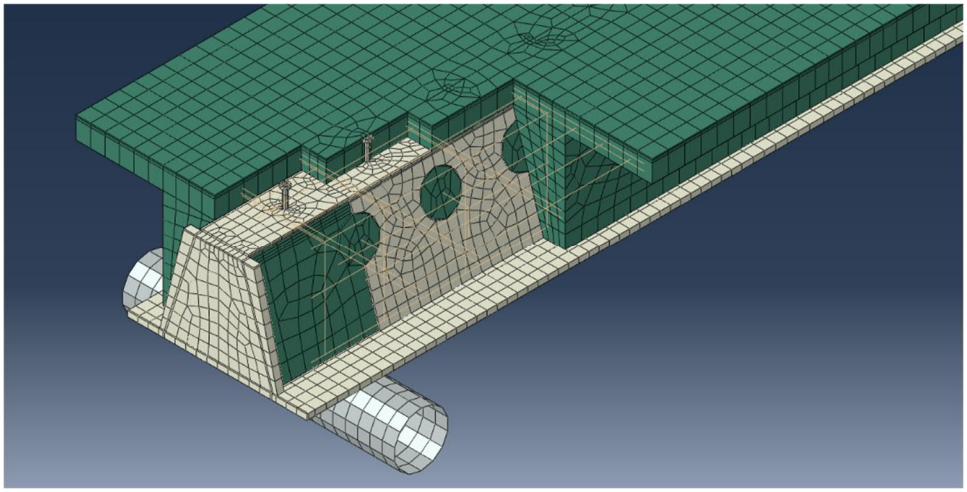

Fig. 6.5- Typical mesh of Type 4 specimens

- Solid element type C3D8R

Solid (continuum) elements are the standard volume elements of Abaqus. C3D8R are first-order (linear) interpolation elements (figure 6.6). In the name of the element the letter R stands for reduced-integration. The stiffness matrix is created by a lower- order integration, while full integration is used for the mass matrix and the loads.

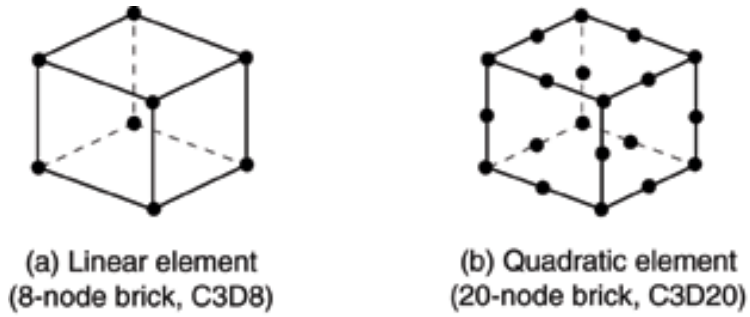

Fig. 6.6- First (linear) and second (quadratic) order elements

- Shell rigid element type R3D4

These elements in Abaqus are used to define the surfaces of rigid bodies for contact. R3D4 are 3-dimensional elements with 4 nodes. The positive normal is given by the right-hand rule going around the nodes of the element in the order that they are given in the element's connectivity (figure 6.7). The face on the side of the element with the positive outward normal is referred to as SPOS. The face on the opposite side is referred to as SNEG.

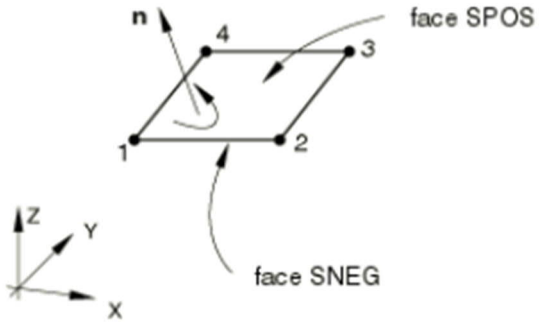

Fig. 6.7- Positive normal for R3D4 elements

- Truss element type T3D2

Truss elements are used in two and three dimensions to model line-like structures that support loading only along the axis or the centerline of the element. No moments or forces perpendicular to the centerline are supported.

Fig. 6.8- Node ordering on elements (left) and integration point for output

Table 6.1- Number of elements and nodes for each model

Section Type	Model	Solid elements (C3D8R)	Rigid elements (R3D4)	Truss elements (T3D2)	Total elements	Nodes
Type 2	S1	24673	506	3706	28885	40996
	S11	30489	506	5786	36781	45348
	S12	8713	506	2280	11499	18364
Type 3	S6a	104946	882	11482	117310	155103
	S6b	67182	882	9736	77800	102286
	S7	45642	882	12580	59104	78303
	S8	76266	882	10948	88096	112515
Type 4	S9	84184	698	6918	91800	125473
	S10	53616	698	8344	62658	88310

6.2.3 Definition of materials

6.2.3.1 Definition of steel material

The classical metal plasticity for isotropic materials (Von Mises yield criterion) in conjunction with a linear hardening model were used in Abaqus to define the structural and reinforcement steel materials. The Von Mises yield criterion is an updated version of Tresca's criterion [42] (figure 6.9). Henri Tresca, based on tests he conducted on metal specimens, proposed that yielding occurs when the maximum shear stress reaches a critical value. This value is equal to:

$$\tau_{max} = max\left(\frac{1}{2}|\sigma_1 - \sigma_2|, \quad \frac{1}{2}|\sigma_2 - \sigma_3|, \quad \frac{1}{2}|\sigma_3 - \sigma_1|\right)$$

where σ_1, σ_2 and σ_3 are the principal stresses.

Tresca's criterion predicted with sufficient accuracy the yielding of metals. Its only drawback was that it takes into account only the maximum shear stress. Von Mises proposed a criterion [43] that the yielding surface is calculated as the solution of the equation $f(\sigma) = \sigma_e - \sigma_0$. The equivalent stress σ_e is equal to

$$\sigma_e = \left[\frac{1}{2}(\sigma_1 - \sigma_2)^2 + \frac{1}{2}(\sigma_2 - \sigma_3)^2 + \frac{1}{2}(\sigma_3 - \sigma_1)^2 + 3\tau_{12}^2 + 3\tau_{23}^2 + 3\tau_{31}^2\right]^{\frac{1}{2}}$$

The linear kinematic hardening model used to model the behavior of metals subjected to cyclic loading is pressure-independent meaning that yielding of the material is independent of the equivalent pressure stress. The yield surface used in the linear kinematic hardening model is defined by the function

$$F = f(\sigma - \alpha) - \sigma^0 = 0$$

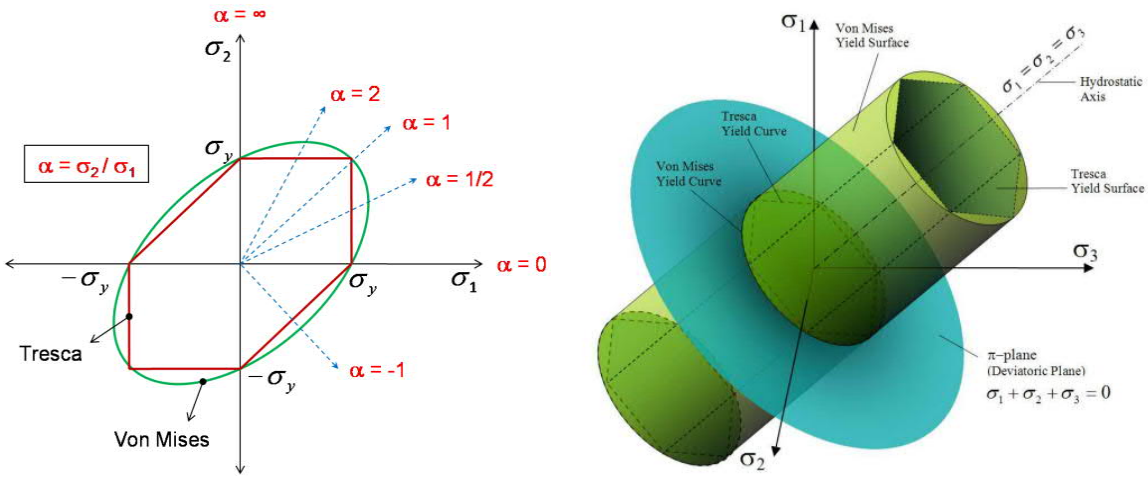

Fig. 6.9– Tresca's and Mises's yield surface

where σ^0 is the yield stress and $f(\sigma\text{-}\alpha)$ is the equivalent Mises stress with respect to the back-stress α in order to simulate the Bauschinger effect [44]. This effect, named after Johann Bauschinger (1834- 1893), refers to a property of materials where the material's stress/strain characteristics change as a result of the microscopic stress distribution of the material and is

generally related with conditions where the yield strength of a metal decreases due to the strain direction changes after the first cycle of loading [45].

Generally, a yield function is defined as $f(\sigma, \alpha) = 0$ where σ includes the stress components and α describes material's parameters. When f<0 the material behaves elastically (figure 6.10). The limit of the yielding surface (elastic limit) is obtained for f=0. Stress values resulting to f>0 are not acceptable. This means that in perfect plasticity, the values of stresses can only be redistributed in such a way that the resulting point moves along the boundary curve of the yielding surface.

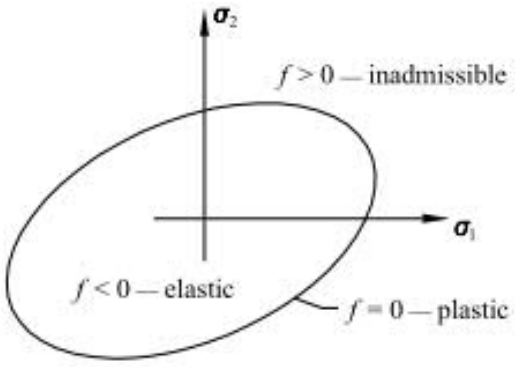

Fig. 6.10– Example of yield surface

The isotropic hardening model assumes that yield compression and tension strength remain equal as the yield surface develops if they were initially equal. In order to take into account the Bauschinger effect, where a hardening in tension leads to a softening in compression, the kinematic hardening rule should be applied. The shape and size of the yield surface remains the same but is translated in stress space. The yield surface is shifted according to the hardening parameter α, known as shift-stress or back-stress.

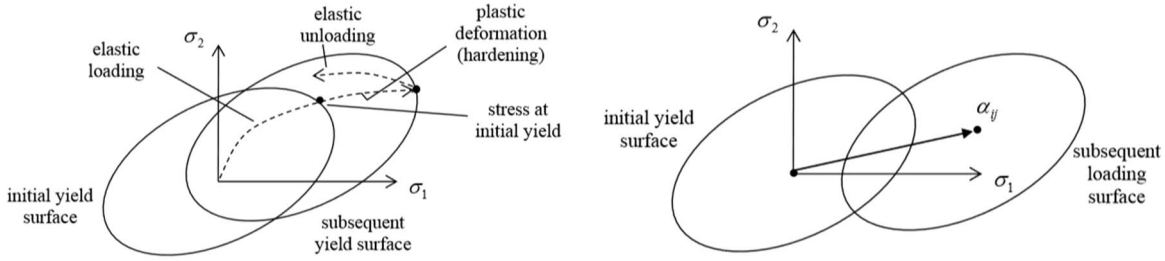

Fig. 6.11– a) Kinematic hardening b) Stress shift α

The true stress and strain values were obtained from the engineering values measured by the tensile tests and presented in section 4.5. The engineering values are calculated by dividing the experimental forces by the initial cross section area of the object under tension. But this area is not constant during the test. The analytical equations used to convert the engineering values to the equivalent true are given below:

$$\sigma_{true} = \sigma_{engineering} * \left(1 + \varepsilon_{engineering}\right)$$

$$\varepsilon_{true} = \ln\left(1 + \varepsilon_{engineering}\right)$$

6.2.3.2 Definition of concrete material

Concrete generally is a very complex material. The complexity is mainly due to non-linear stress-strain behavior of the concrete under multi-axial stress conditions, strain softening and anisotropic stiffness reduction, progressive cracking caused by tensile stresses and strains, bond between concrete and reinforcement, aggregate interlocks and dowel action of reinforcement, time dependent behavior as creep and shrinkage [46].

Advancement in computing techniques and the computational capabilities of modern computers resulted in the creation of various models with the mentioned above complexities included. To simulate the concrete behavior of the specimens, Abaqus' "Concrete damaged plasticity" (CDP) model was used. This model is a continuum, plasticity-based, damage model. The two main concrete failure mechanisms are cracking under tension and crushing under compression [47]. The model assumes that the uniaxial tensile and compressive response of concrete is characterized by damaged plasticity, as shown in figure 6.12.

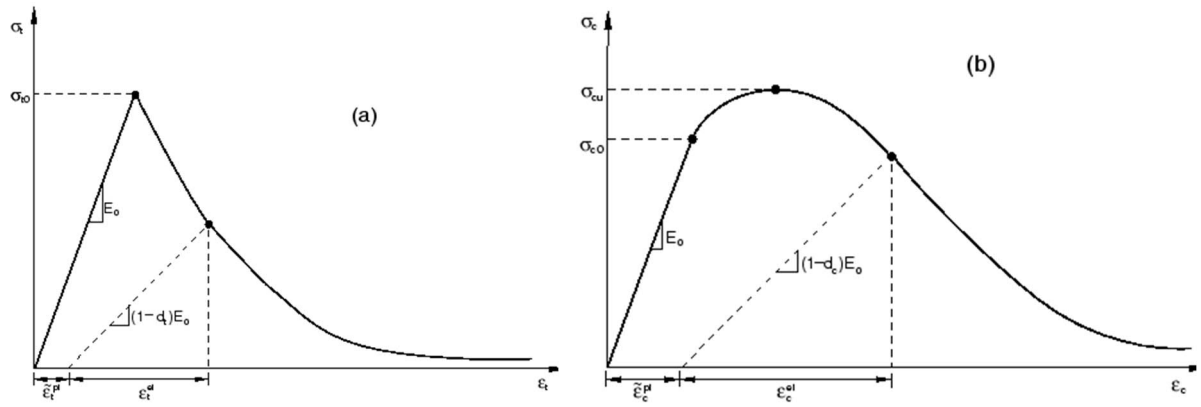

Fig. 6.12- Response of concrete to uniaxial loading in tension (a) and compression (b)

where $\bar{\varepsilon}_t^{pl}$ and $\bar{\varepsilon}_c^{pl}$ are the tensile and compressive equivalent plastic strains and d_t and d_c are tension and compression damage variables that characterize the degradation of the elastic stiffness. The damage variables can take values from zero, representing the undamaged material, to one, which represents total loss of strength. In order to create the non- linear stress-strain relation for the uniaxial compression, the formulas provided by Eurocode 2 (§3.1.5) were used. The post failure tensile behavior was defined by fracture energy (figure 6.13). Hillerborg [48] defines the energy G_f, required to open a unit area of crack. By defining the tension softening behavior with stress- displacement relation rather than using a stress- strain one, the material is not related to the cracked element length (mesh) and so convergence issues are avoided.

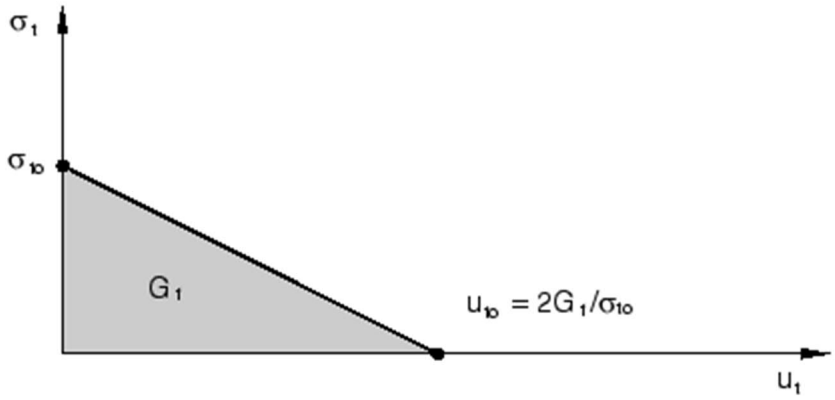

Fig. 6.13- Post-failure stress- fracture energy curve

The concrete damaged plasticity model assumes non-associated potential plastic flow implying that material stiffness matrix is asymmetric; therefore, the unsymmetrical matrix storage and solution implementation should be employed in ABAQUS software. The flow potential *G* in the effective $\bar{p}$ - $\bar{q}$ plane considered for CDP model is a modified Drucker-Prager hyperbolic function [49] given by the following formula:

$$G = \sqrt{(\varepsilon\sigma_{to}\tan\psi)^2 + \bar{q}^2} - \bar{p}\ \tan\psi$$

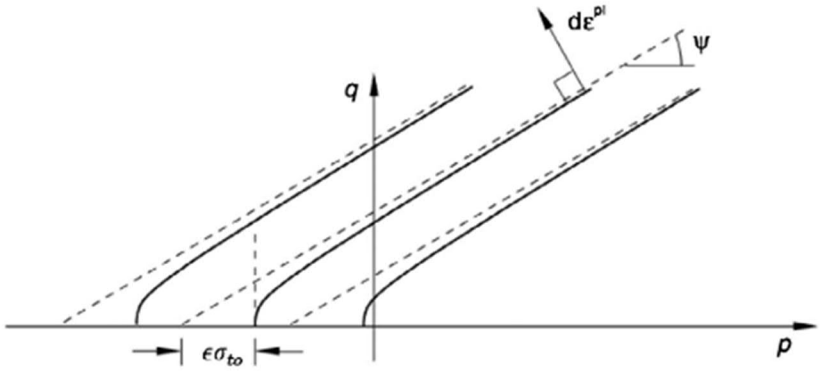

Fig. 6.14- Hyperbolic Drucker- Prager flow potential function

- $\bar{p}$ is the equivalent mean hydrostatic stress
- σ_{to} is the uniaxial tensile strength of concrete in hydrostatic tension state
- ψ is the Angle of dilatancy (or Dilation angle). The dilatancy parameter is important for characterizing concrete's behavior when it is deformed. This angle was introduced by Bent Hansen [50]. Dilatancy may be defined as an inelastic change in volume that is associated to shear distortion of an element in the material [51]. This factor that can be determined by proper tests and, according to the literature, can take values from 0 to almost 55, was one of the basic factors that its influence was investigated through this calibration procedure. A sensitivity analysis is presented in a following section.
- ε is an eccentricity parameter that defines the rate at which the function approaches the asymptote (figure 6.14). The flow potential tends to a straight line as the eccentricity tends to zero. The default value ε= 0.1, which implies that the material has almost the same dilation angle over a wide range of confining pressure stress values, was chosen.

The model makes use of the yield function of Lubliner et. al. [52], with the modifications proposed by Lee and Fenves [53] to account for different evolution of strength under tension and compression. In terms of effective stresses, the yield function takes the form

$$F = \frac{1}{1-a}\left[\bar{q} - 3\alpha\bar{p} \quad + \beta(\bar{\varepsilon}^{pl})\langle\hat{\bar{\sigma}}_{max}\rangle - \gamma\langle-\hat{\bar{\sigma}}_{max}\rangle - \bar{\sigma}_c\left(\bar{\varepsilon}_c^{pl}\right)\right] = 0$$

with

$$\alpha = \frac{(\sigma_{b0}/\sigma_{c0})-1}{2(\sigma_{b0}/\sigma_{c0})-1} \; 0, \qquad \beta = \frac{\bar{\sigma}_c\left(\bar{\varepsilon}_c^{pl}\right)}{\bar{\sigma}_t\left(\bar{\varepsilon}_t^{pl}\right)}(1-\alpha) - (1+\alpha), \qquad \gamma = \frac{3(1-K_c)}{2K_c-1}$$

where

- $\hat{\bar{\sigma}}_{max}$ is the maximum principal effective stress
- σ_{b0}/σ_{c0} is the ratio of the initial equibiaxial compressive yield stress to the initial uniaxial compressive yield stress. The default value is 1.16.
- K_c is the fraction of the second stress invariant on the tensile meridian, $q_{(TM)}$, divided with the second stress invariant on the compressive meridian, $q_{(CM)}$, at initial yield for any given value of the pressure invariant *p* such that the maximum principal stress is negative ($\hat{\sigma}_{max} < 0$). K_c must not exceed the following limits; $0.5 \leq K_c \leq 1$. The default value is 2/3 (figure 6.15). K_c was also one of the basic factors that affected the most the results of the analyses. A sensitivity analysis is presented in a following section as well.
- $\bar{\sigma}_c\left(\bar{\varepsilon}_t^{pl}\right)$ is the effective tensile cohesion stress
- $\bar{\sigma}_c\left(\bar{\varepsilon}_c^{pl}\right)$ is the effective compressive cohesion stress

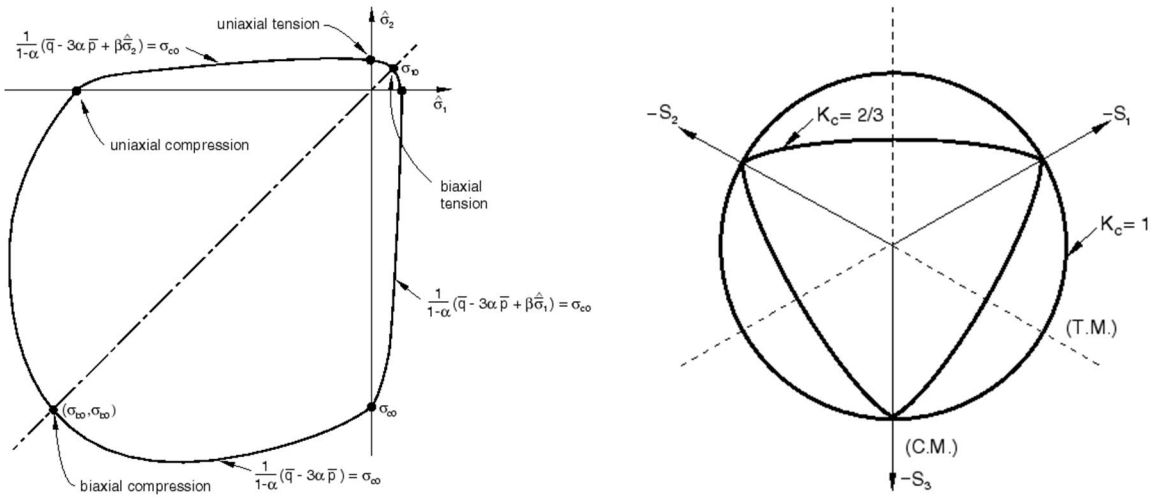

Fig. 6.15- Yield surface in plane stress (left) and in the deviatoric plane related to different values of K_c (right)

The final values used in all the models of the factors presented above that led to the optimum results, related to the experimental ones, are given in Table 6.2.

Table 6.2- Values used for the definition of CDP model

Dilation angle ψ	Eccentricity	σ_{b0}/σ_{c0}	K_c
10	0.1	1.16	0.8

Table 6.3- Parameters used for the definition of material models

Series 1 (S1, S12)					
Concrete		Structural steel		Reinforcement steel	
Compressive strength f_c (MPa)	36.23	Yielding stress f_{ay} (MPa)	416.22	Yielding stress f_{sy} (MPa)	537.24
Tensile strength f_{ct} (MPa)	3.28	Ultimate stress f_{au} (MPa)	680.18	Ultimate stress f_{su} (MPa)	705.16
Elastic modulus E_c (MPa)	32370	Elastic modulus E_a (MPa)	210000	Elastic modulus E_s (MPa)	200000
Fracture energy G_F (N/mm)	0.061				
Series 2 (S6a, S6b, S7, S8, S9, S10, S11)					
Concrete		Structural steel		Reinforcement steel	
Compressive strength f_c (MPa)	38.81	Yielding stress f_{ay} (MPa)	393.49	Yielding stress f_{sy} (MPa)	500
Tensile strength f_{ct} (MPa)	2.9	Ultimate stress f_{au} (MPa)	691.25	Ultimate stress f_{su} (MPa)	510
Elastic modulus E_c (MPa)	33045	Elastic modulus E_a (MPa)	210000	Elastic modulus E_s (MPa)	200000
Fracture energy G_F (N/mm)	0.064				

6.2.4 Load and boundary conditions

As described previously, the deflection was applied to the beam through a rigid part that simulates the steel plate located on the bottom of the loading actuator. The deflection was applied in four steps exactly like the tests; three steps for the loading- unloading phase up to the serviceability limit and one step for the maximum deflection allowed by the actuator. The

rigid part used to simulate the supports was restrained to move and rotate along all axes (figure 6.16).

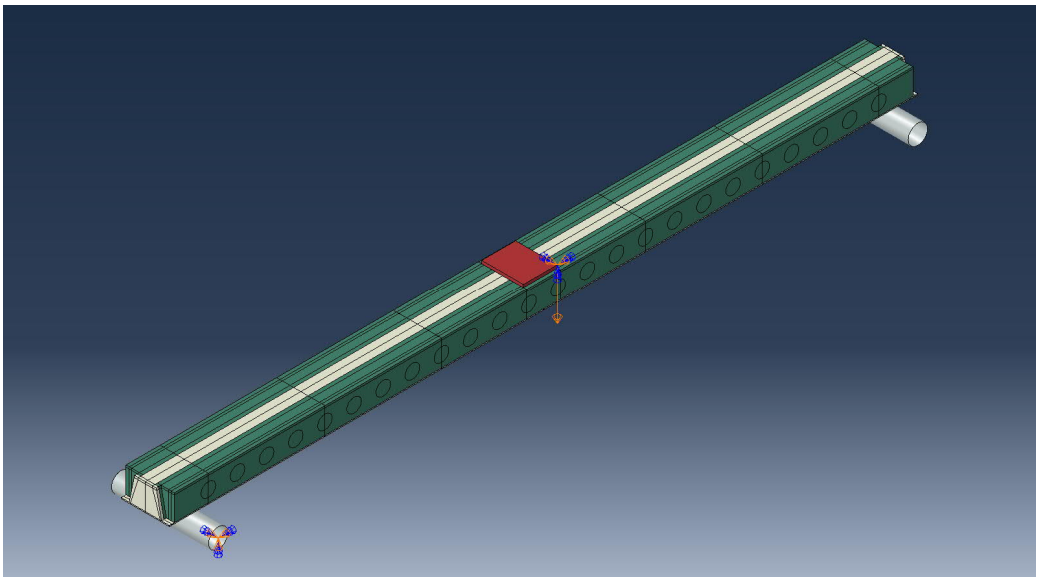

Fig. 6.16- Applied deflection and boundary conditions

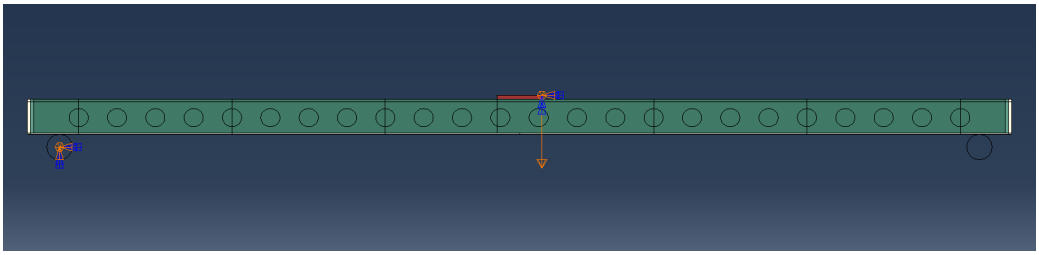

Fig. 6.17- Applied deflection and boundary conditions

6.3 Results of FEM analysis

In the following sections the results from the analyses are presented. More specifically, the load-deflection and load- strain curves of experimental measurements and analytical numerical predictions are compared. The strain curves present the average value of all the values measured for each specimen. Additionally, contour images showing the distribution of Von Mises stresses and nominal plastic strains along the longitudinal axis of the steel part are included. Finally, the average load- deflection curves for each type as well as for all the models are presented.

6.3.1 Type 2 sections

6.3.1.1 Specimen S1 (§5.2.1)

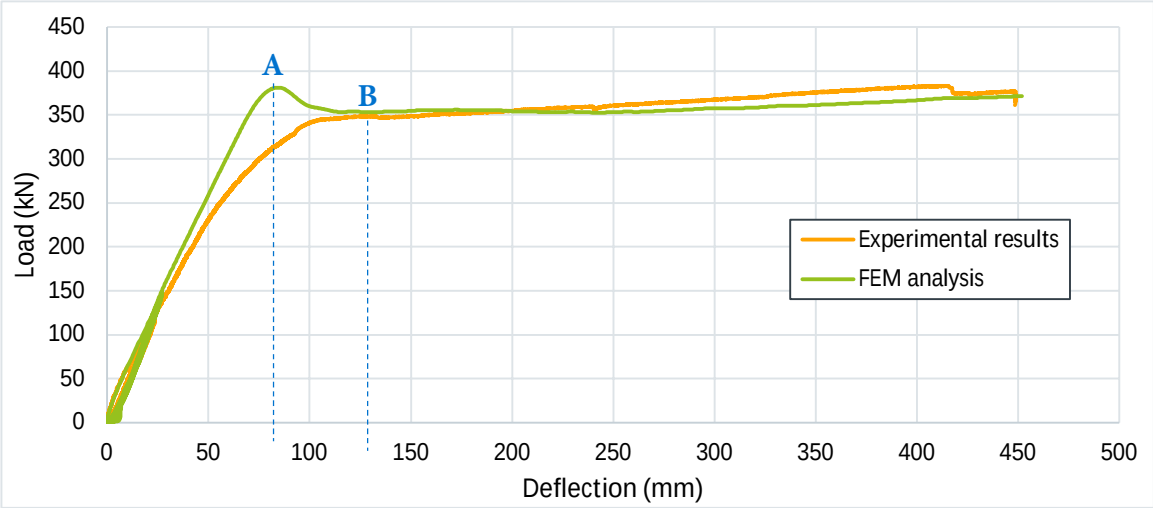

Fig. 6.18- S1- Comparison of load- deflection curves

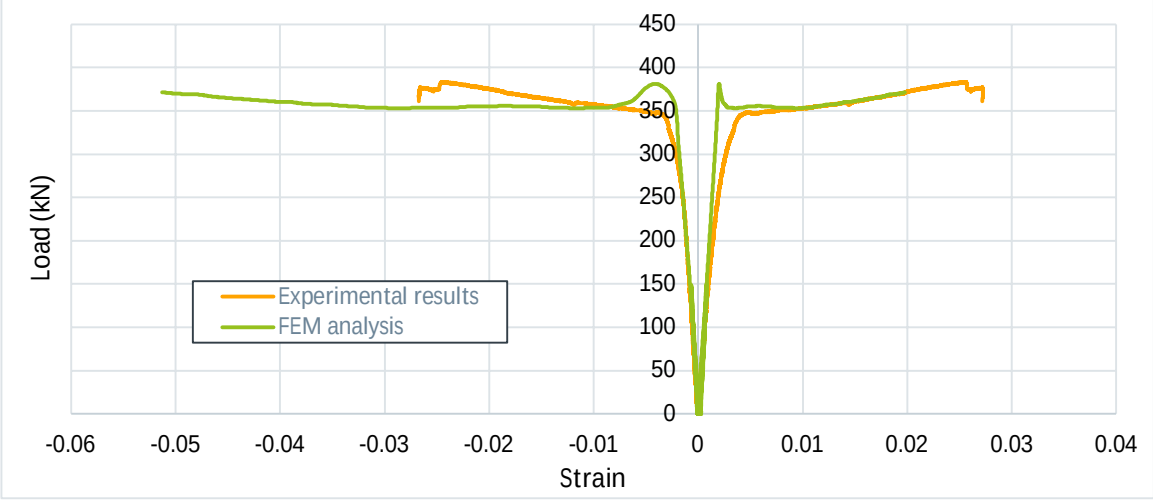

Fig. 6.19- S1- Comparison of load- strain curves

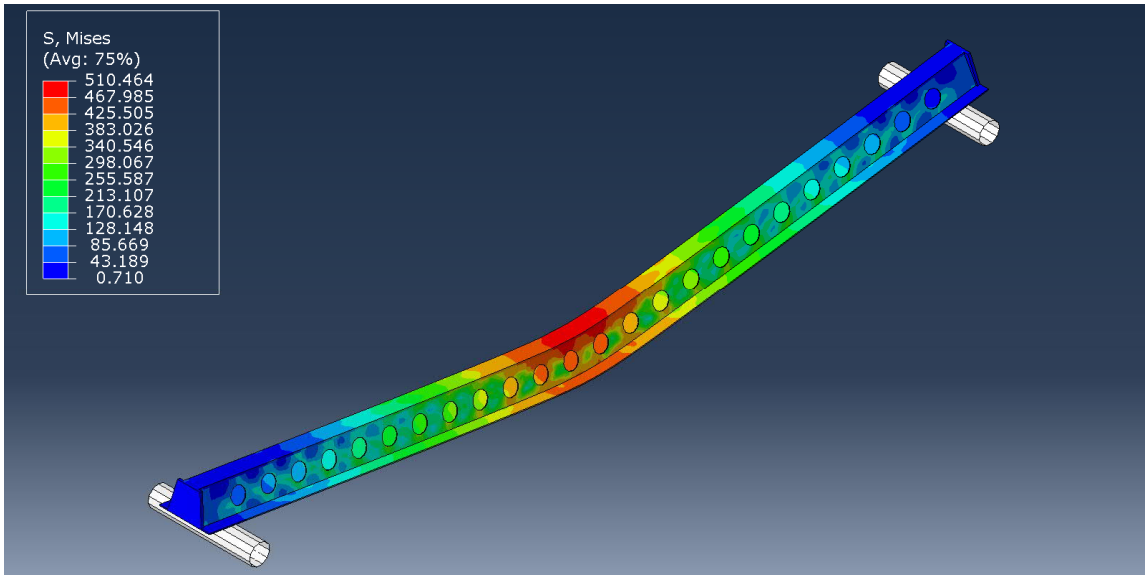

Fig. 6.20- S1- Von Mises stresses on steel part

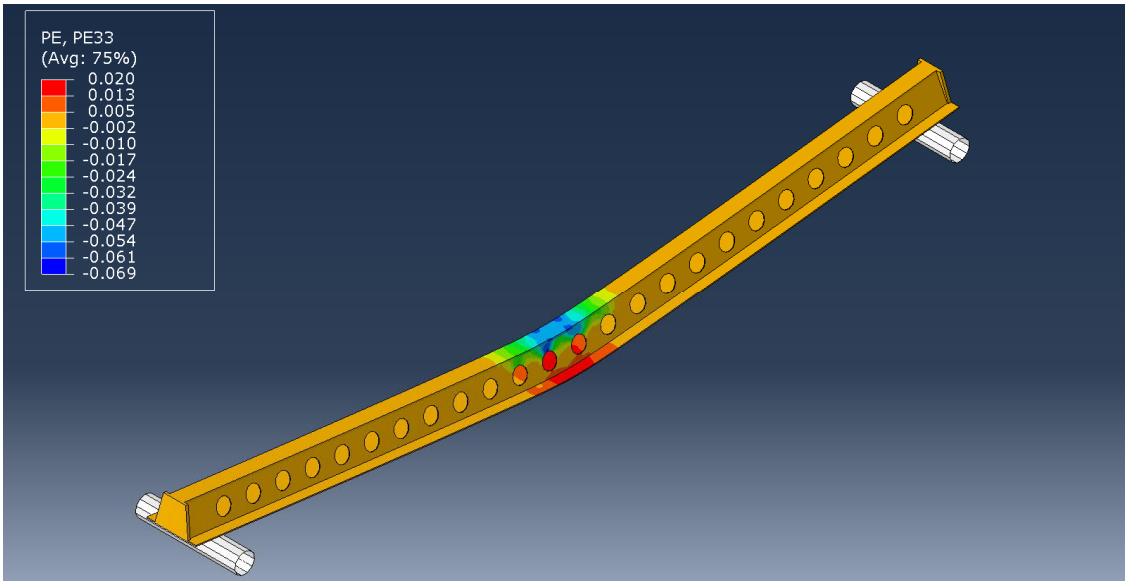

Fig. 6.21- S1- Plastic strains on steel part along longitudinal axis

The load- deflection curves (figure 6.18) correlate quite well. The elastic behavior of the model was simulated with high accuracy. The difference up to 125 mm (figure 6.18, point B), with maximum value equal to 69 kN at a deflection of 79 mm (figure 6.18, point A), is mainly due to the behavior of the concrete. The plastic behavior of the model is almost the same with the test. The load- strain curves (figure 6.19) follow the experimental ones, but they differ at the ultimate values. In figure 6.21, where the longitudinal nominal plastic strains are presented, it appears that there are still areas in the web at the mid span where the plastic strains are zero

(orange color). This means that the section is not fully plasticized providing a potential for additional deformation. Also, it can be seen at figure 6.20 that the stresses on that area of the webs are below the yielding stress of the steel (f_{ay}= 416.22 MPa).

6.3.1.2 Specimen S11 (§5.2.2)

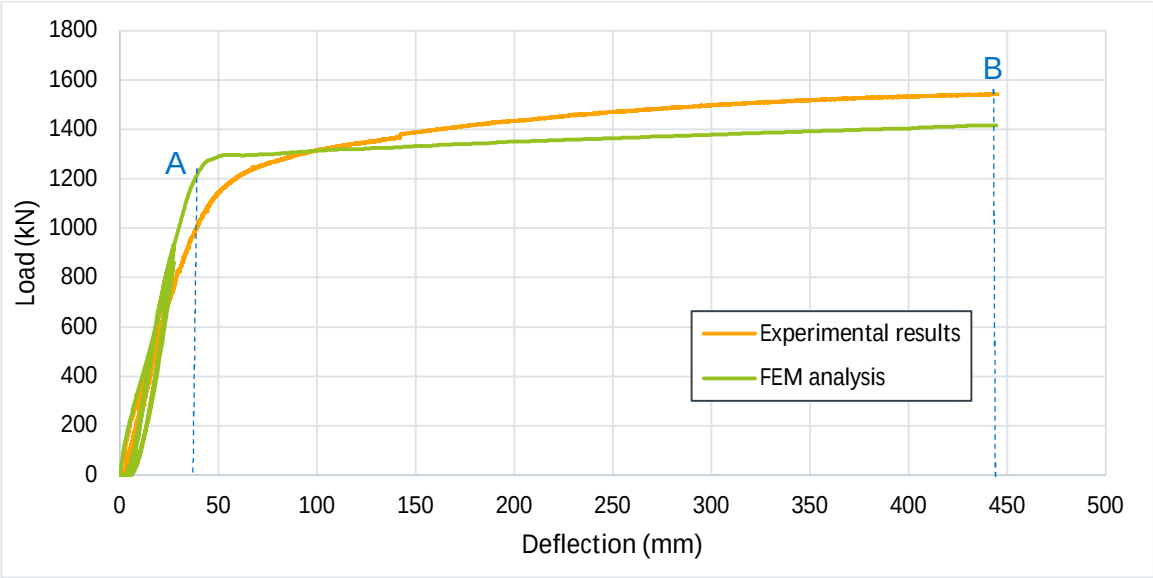

Fig. 6.22- S11- Comparison of load- deflection curves

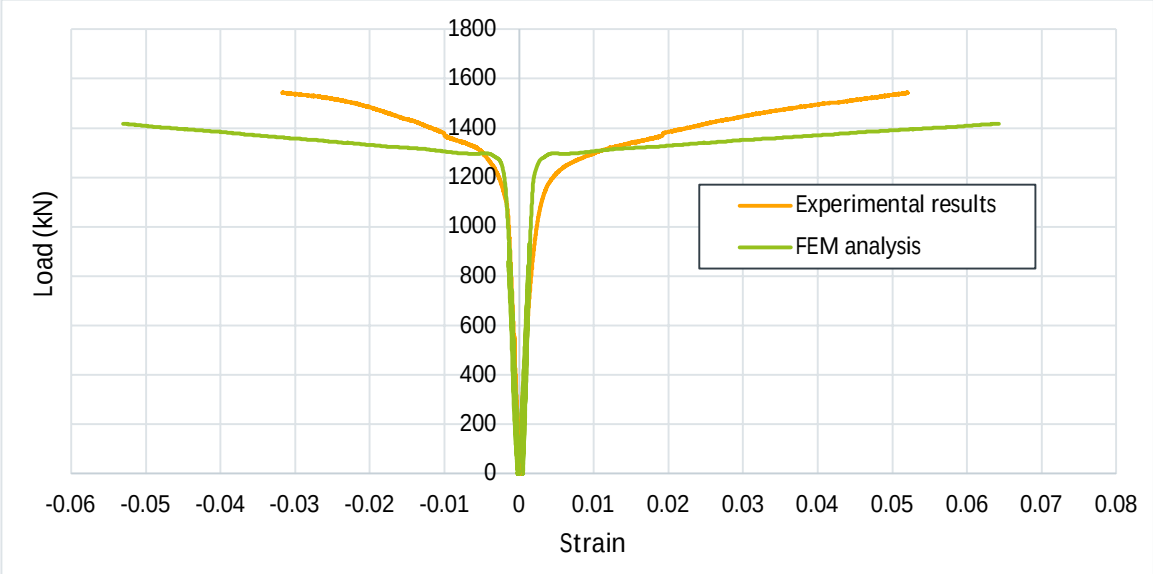

Fig. 6.23- S11- Comparison of load- strain curves

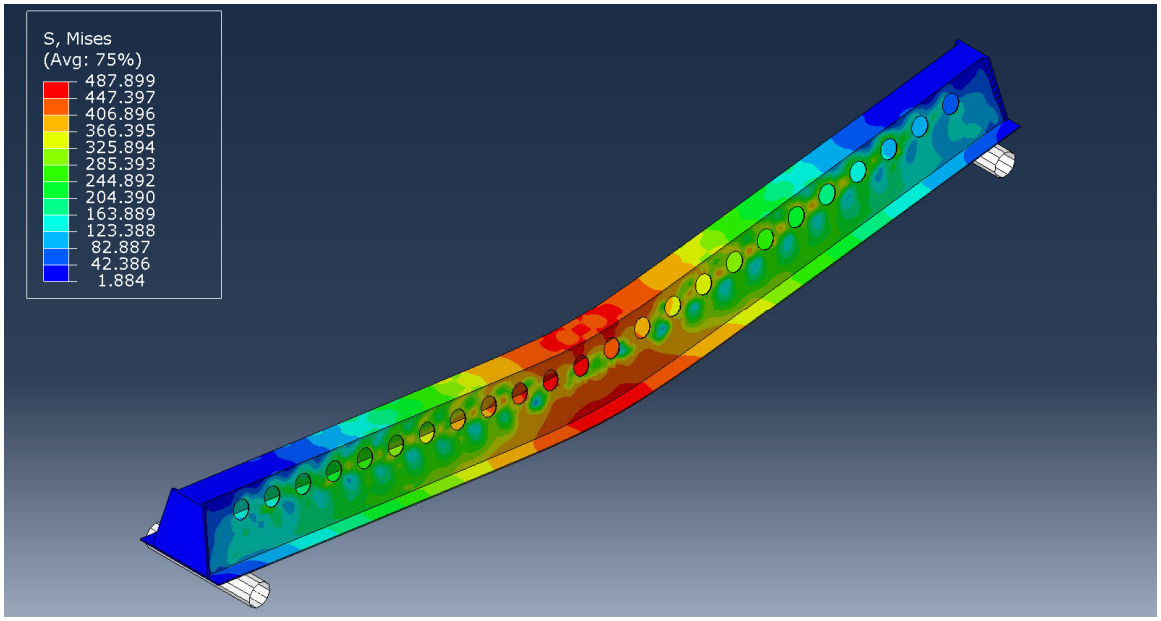

Fig. 6.24- S11- Von Mises stresses on steel part

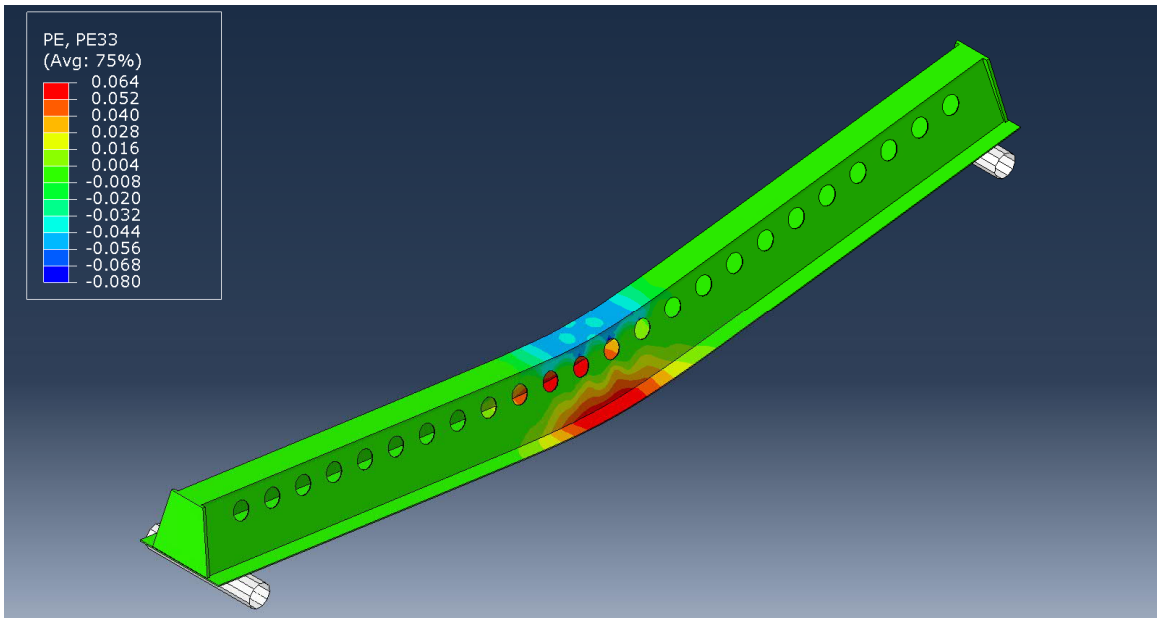

Fig. 6.25- S11- Plastic strains on steel part along longitudinal axis

The load- deflection curves (figure 6.22) are quite similar. Initial stiffness of the model was close to the stiffness of the test specimen. The maximum difference between the two curves is equal to 216.21 kN at a deflection of 37.6 mm (figure 6.22, point A) and the difference at the maximum deflection is 126.1 kN (figure 6.22, point B). The load- strain curves (figure 6.23) are close to the experimental ones with different ultimate values. The Von Mises stresses are presented in figure 6.24. Green colored areas at the webs of the mid span in figure 6.25 have elastic behavior and therefore the section is not fully plasticized.

6.3.1.3 Specimen S12 (§5.2.3)

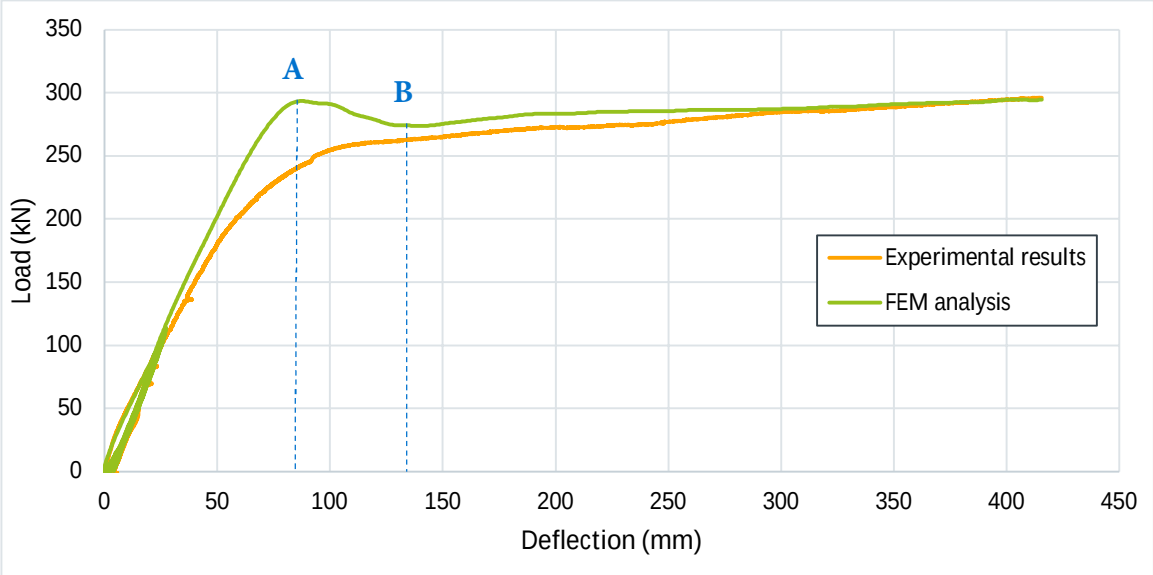

Fig. 6.26- S12- Comparison of load- deflection curves

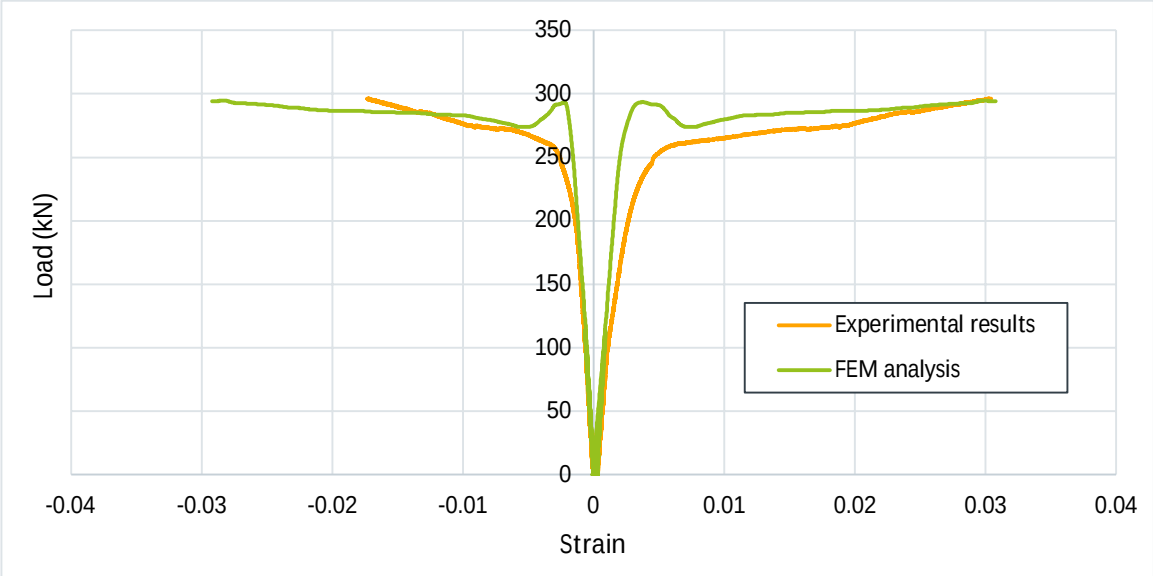

Fig. 6.27- S12- Comparison of load- strain curves

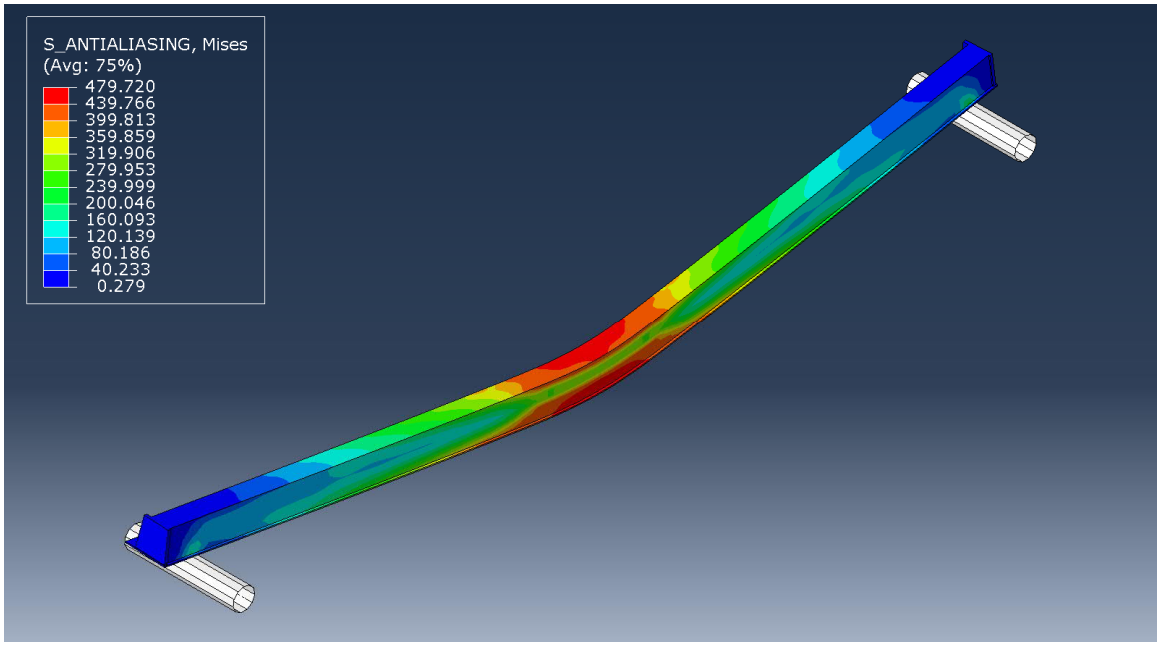

Fig. 6.28- S12- Von Mises stresses on steel part (View 1)

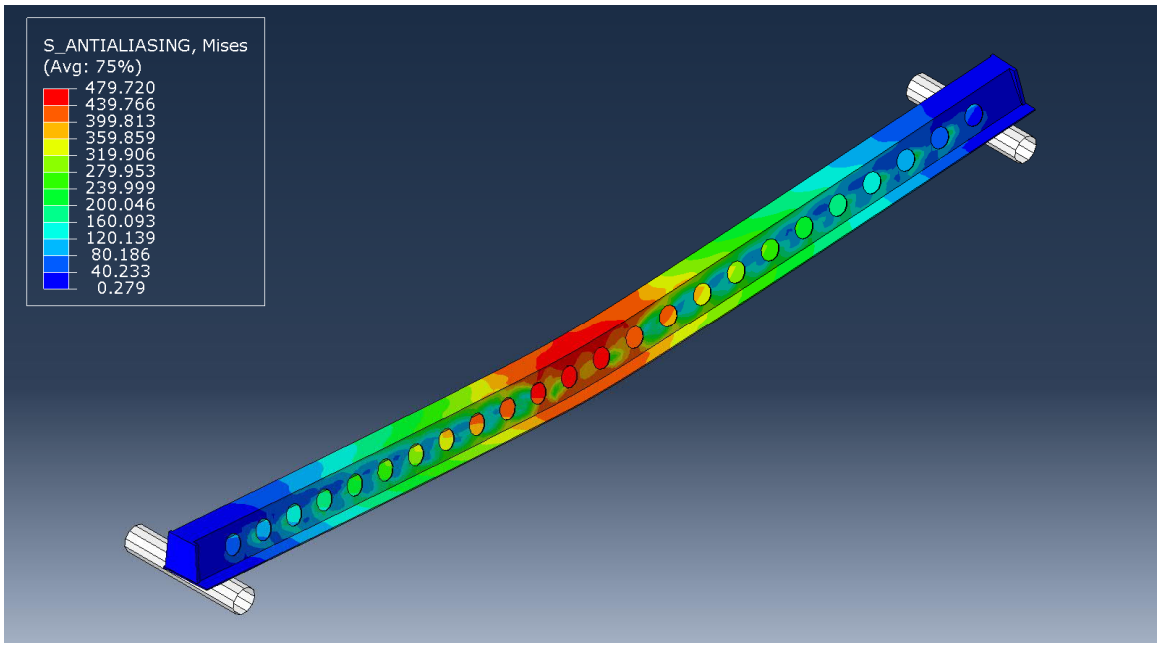

Fig. 6.29- S12- Von Mises stresses on steel part (View 2)

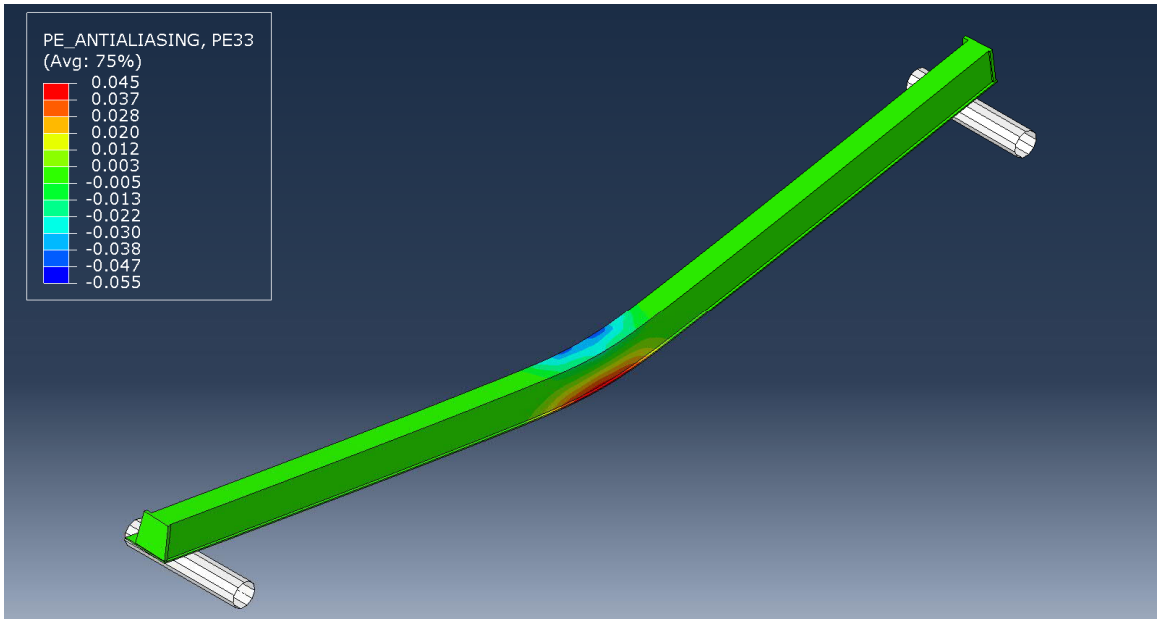

Fig. 6.30- S12- Plastic strains on steel part along longitudinal axis (View 1)

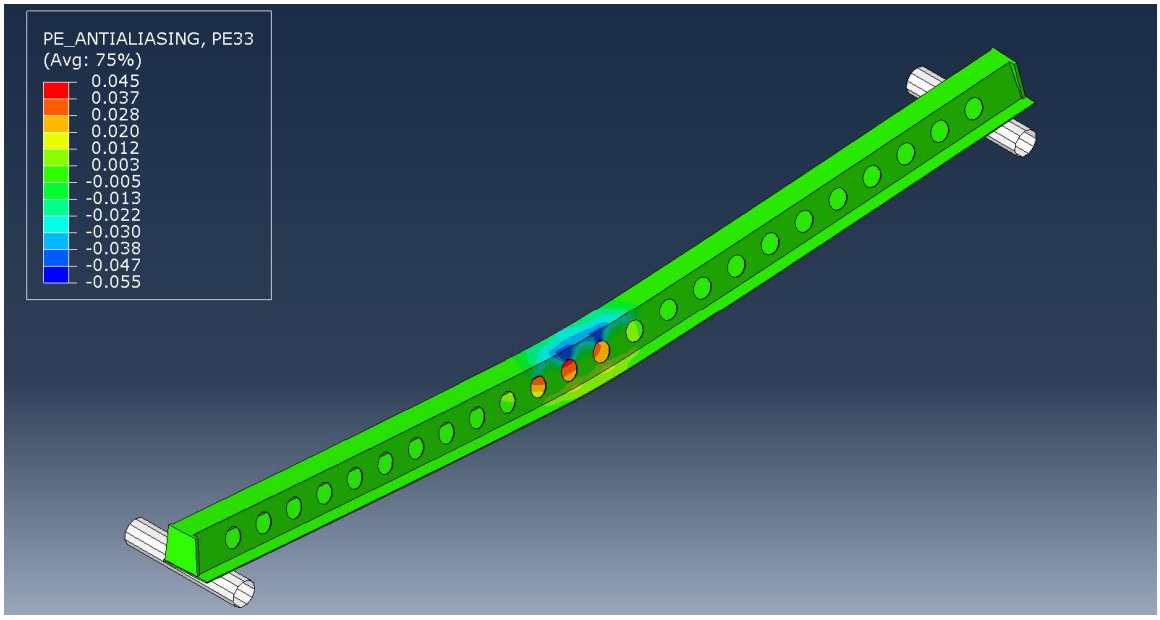

Fig. 6.31- S12- Plastic strains on steel part along longitudinal axis (View 2)

The model for the specimen S12 has similar behavior with the one for S1. The difference on the load- deflection curves is limited between the deflection values of 50-130 mm (figure 6.26, point B) with highest value equal to 54 kN at a deflection of 81.5 mm (figure 6.26, point A). Again, the elastic and plastic behavior seems to be the same. The load- strain curves (figure 6.27) follow the experimental ones, with same maximum tensile values. For this model, because it is not symmetric, contour images showing the distribution of Von Mises stresses (figures 6.28- 6.29) and plastic strains (figures 6.30- 6.31) are provided for both sides.

6.3.2 Type 3 sections

6.3.2.1 Specimen S6a (§5.3.1)

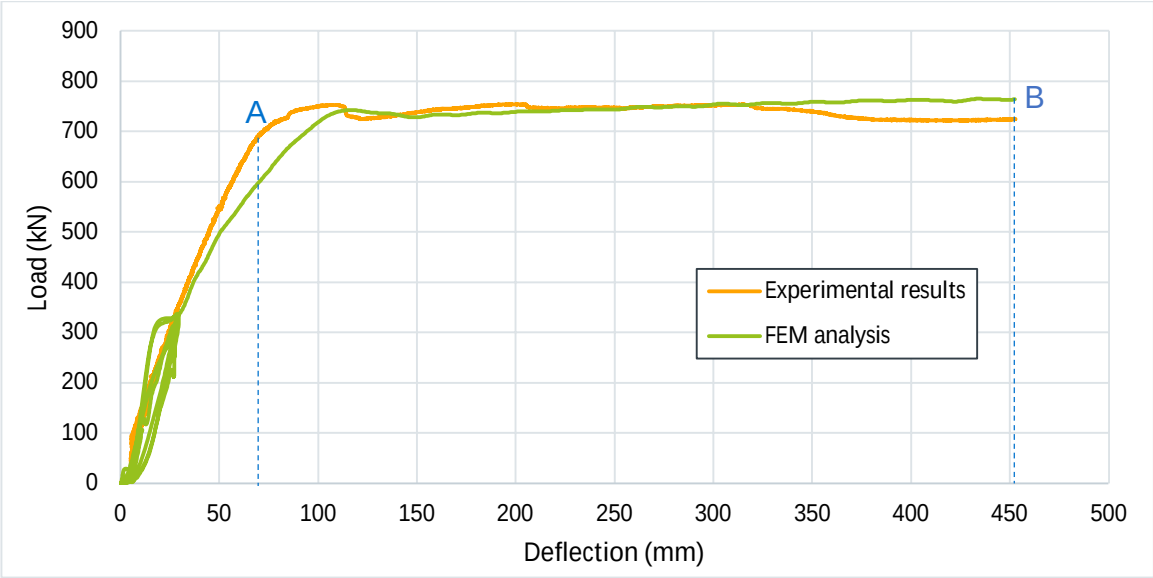

Fig. 6.32- S6a- Comparison of load- deflection curves

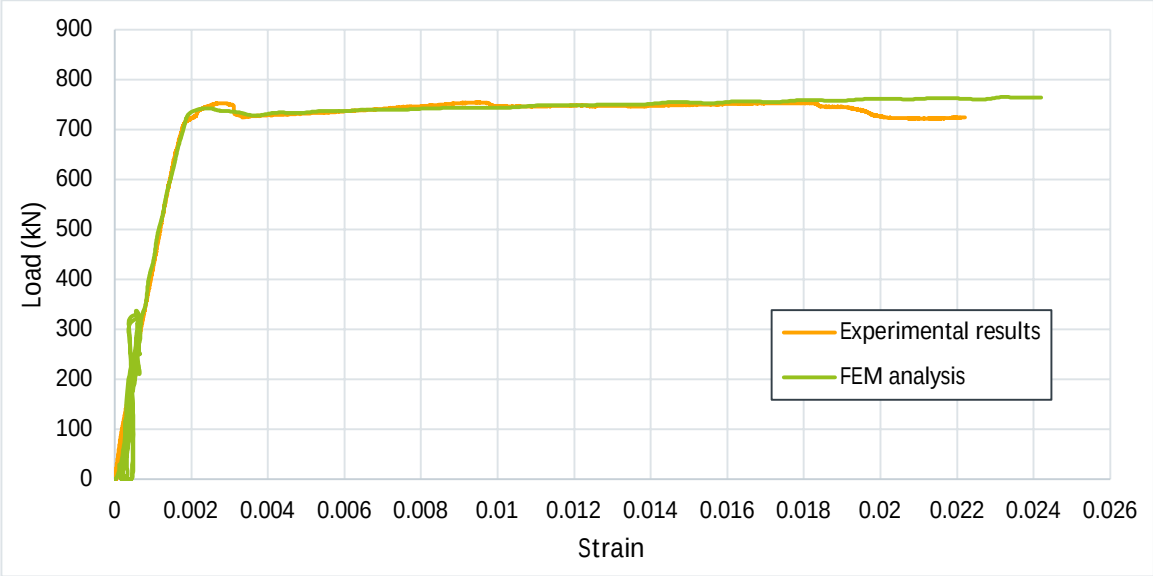

Fig. 6.33- S6a- Comparison of load- strain curves

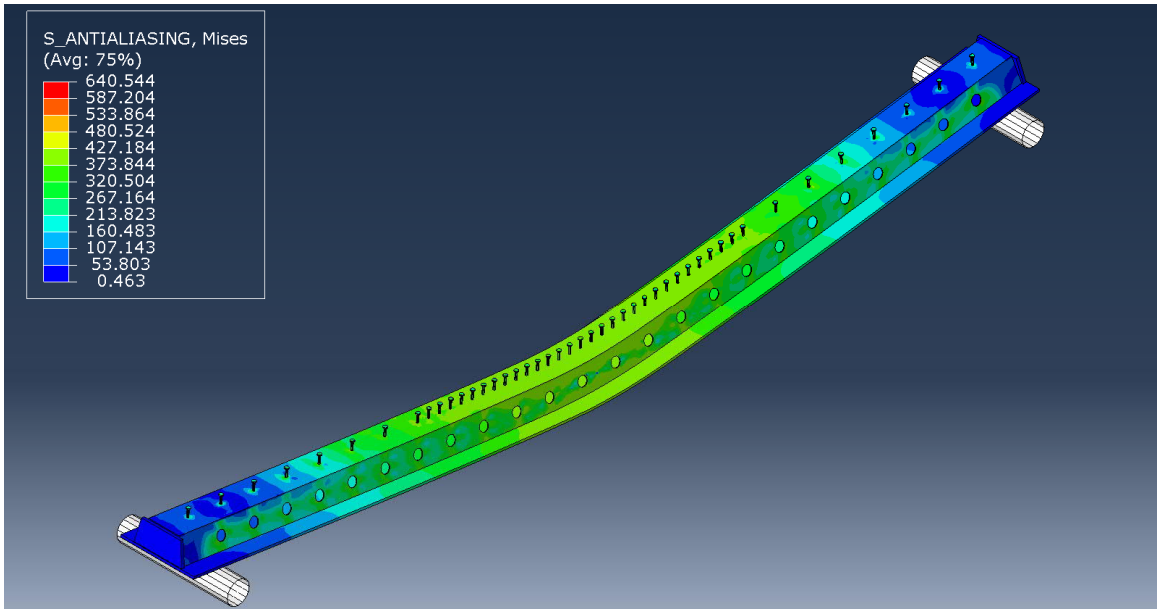

Fig. 6.34- S6a- Von Mises stresses on steel part

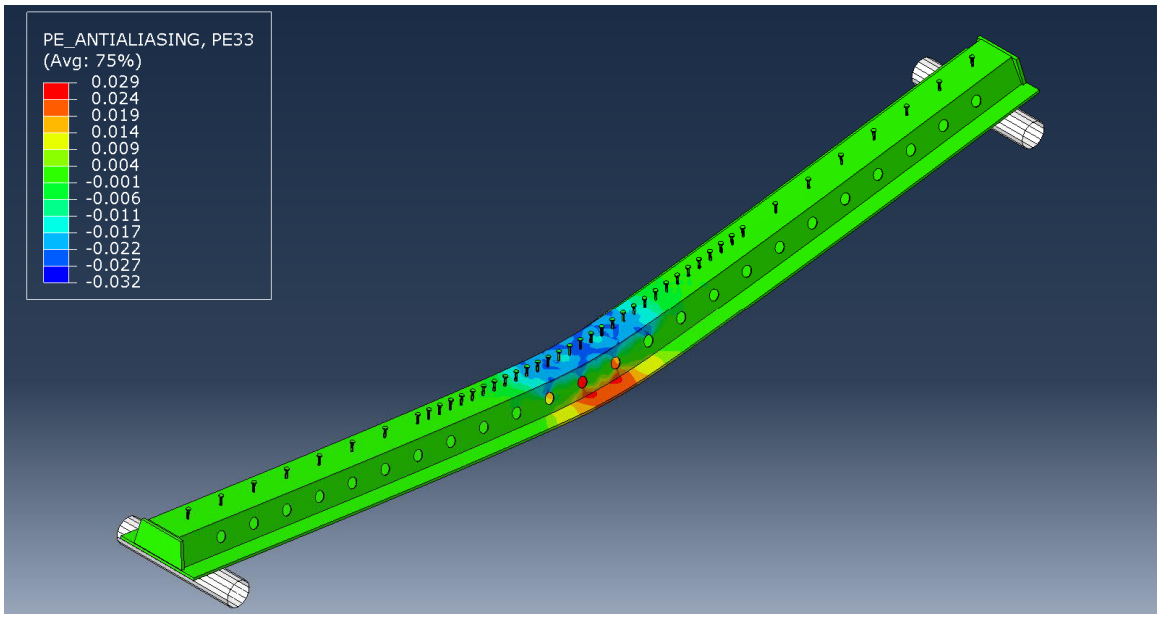

Fig. 6.35- S6a- Plastic strains on steel part along longitudinal axis

The load- deflection curves are very similar (figure 6.32). The yielding of the beam at the model, begins in a smaller deflection value, but this difference is not more than 25 mm. The maximum difference of the load is equal to 93.5 kN for a deflection of 69.3 mm (figure 6.32, point A). The load difference at maximum deflection is 39.3 kN (figure 6.32, point B). The load- strain curves (figure 6.33) are identical with the analytical ultimate value calculated really close to the experimental one. The plastic strains have relatively small values and are not spread in a wide area (figure 6.35) and so the Von Mises stresses on at the middle span of the beam, as presented in figure 6.34, have almost exceeded the yielding stress (f_{ay}= 393.49 MPa and f_{au}= 691.25 MPa).

6.3.2.2 Specimen S6b (§5.3.2)

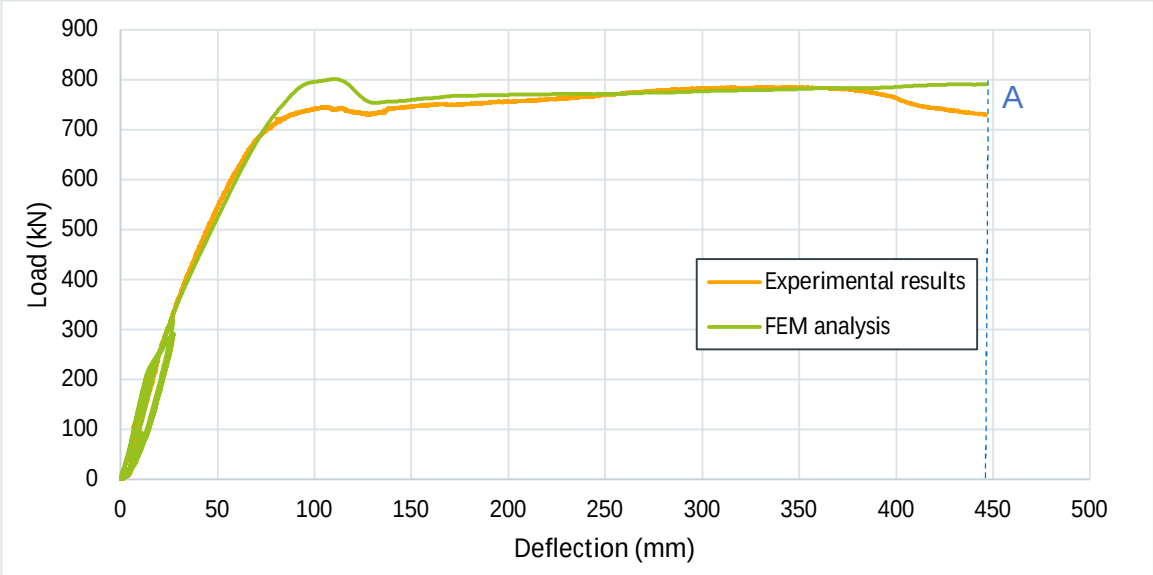

Fig. 6.36- S6b- Comparison of load- deflection curves

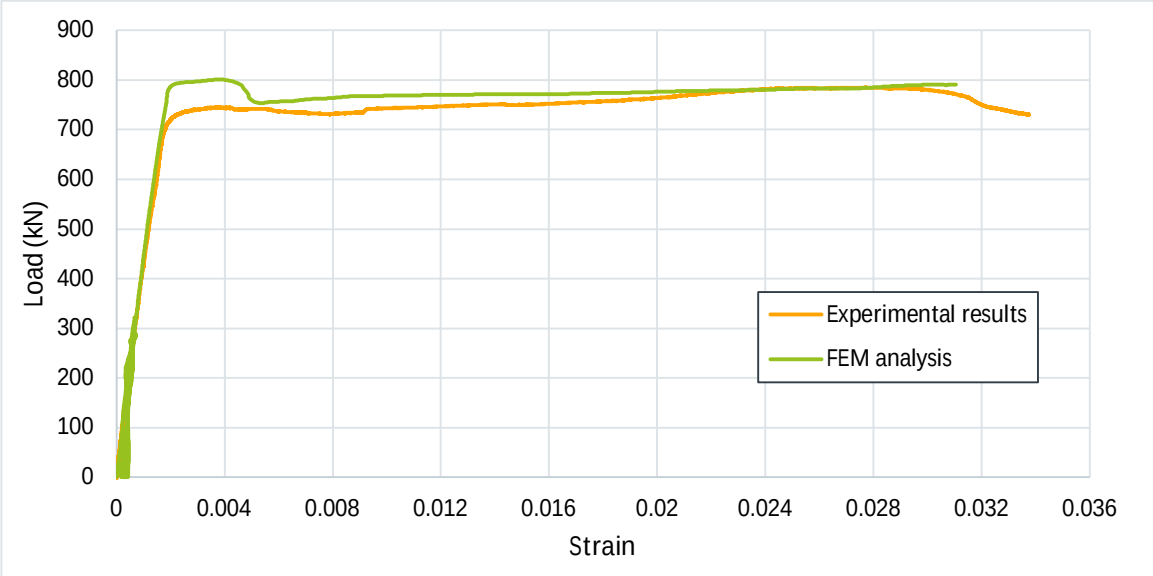

Fig. 6.37- S6b- Comparison of load- strain curves

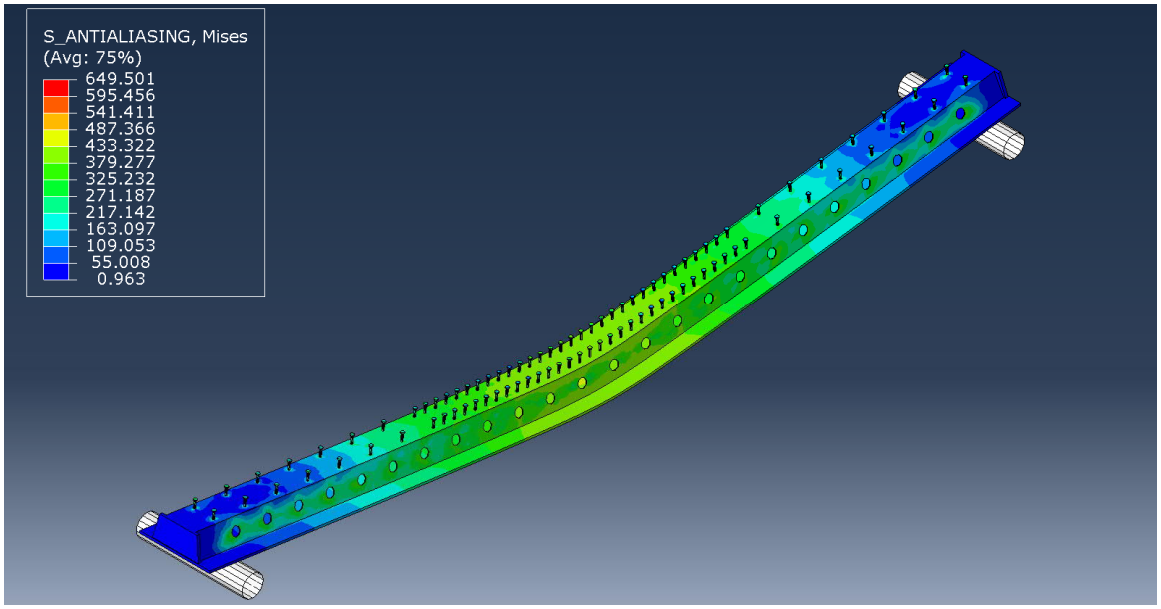

Fig. 6.38- S6b- Von Mises stresses on steel part

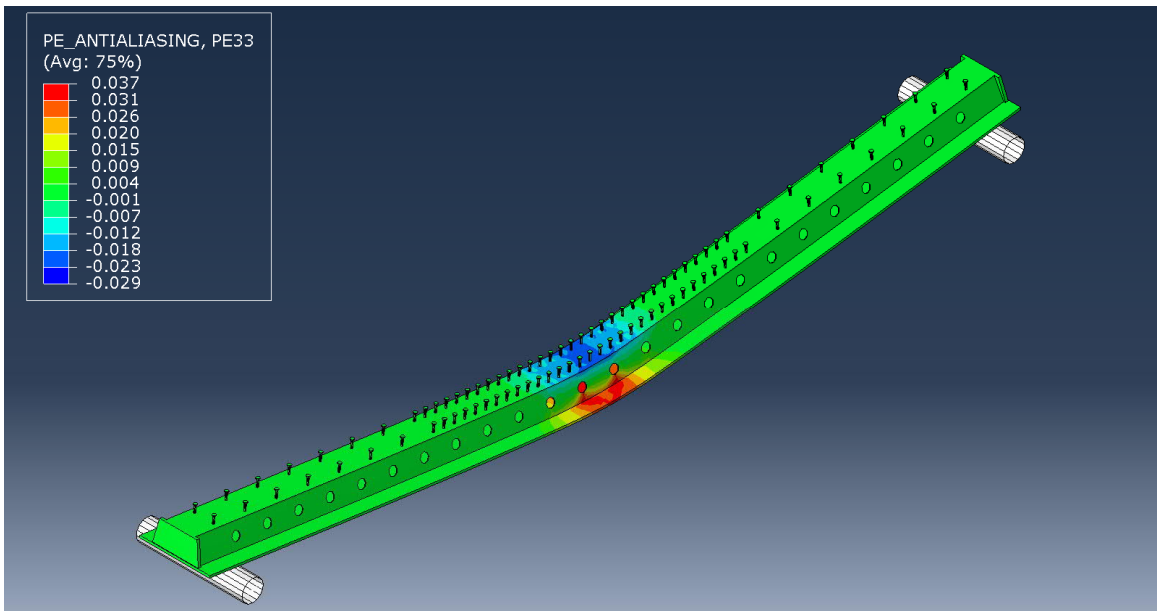

Fig. 6.39- S6b- Plastic strains on steel part along longitudinal axis

Same notes with the S6a can be made for S6b. As pointed in chapter 5.3.5, the difference in the number of shear studs rows did not affect the overall behavior of the beams. This was observed also for the FE model. Both load- deflection (figure 6.36) and load- strain (figure 6.37) curves are very similar with analytical ultimate strain calculated really close to the experimental one. The maximum load difference between the two curves is 61 kN and is located at the maximum deflection (figure 6.36, point A). The propagation of the “plastic hinge” is small (figures 6.38 and 6.39) Green colored areas at the webs of the mid span (figure 6.39) have elastic behavior and therefore the section is not fully plasticized.

6.3.2.3 Specimen S7 (§5.3.3)

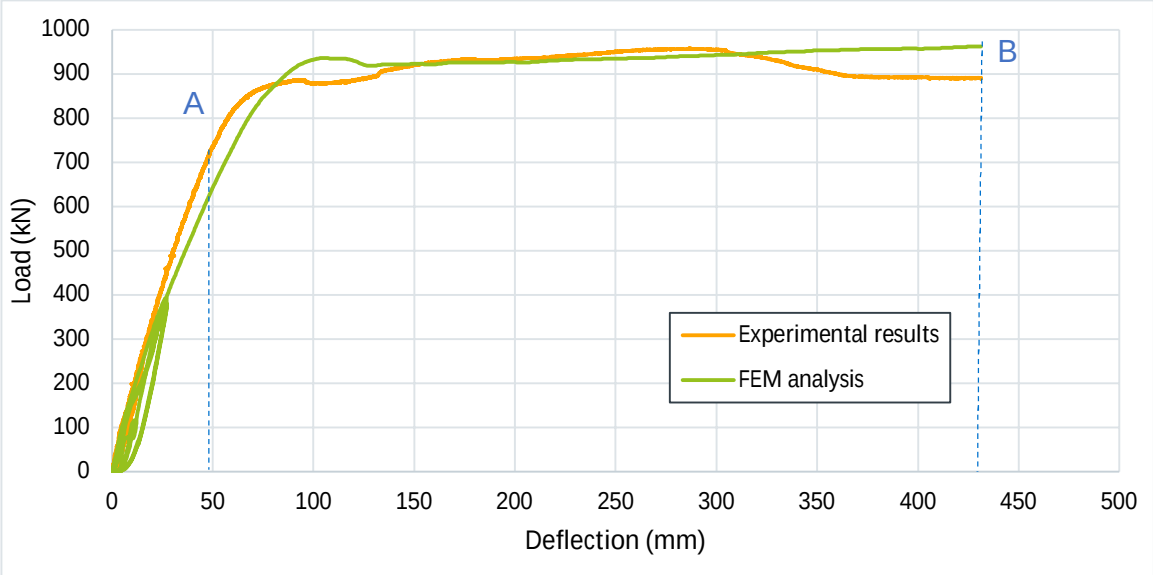

Fig. 6.40- S7- Comparison of load- deflection curves

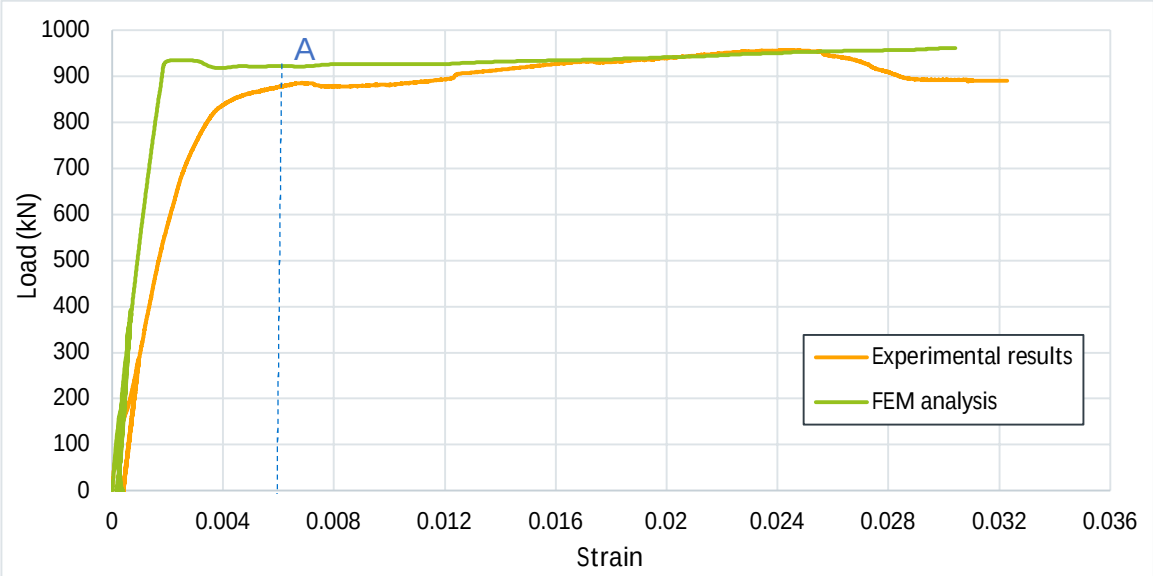

Fig. 6.41- S7- Comparison of load- strain curves

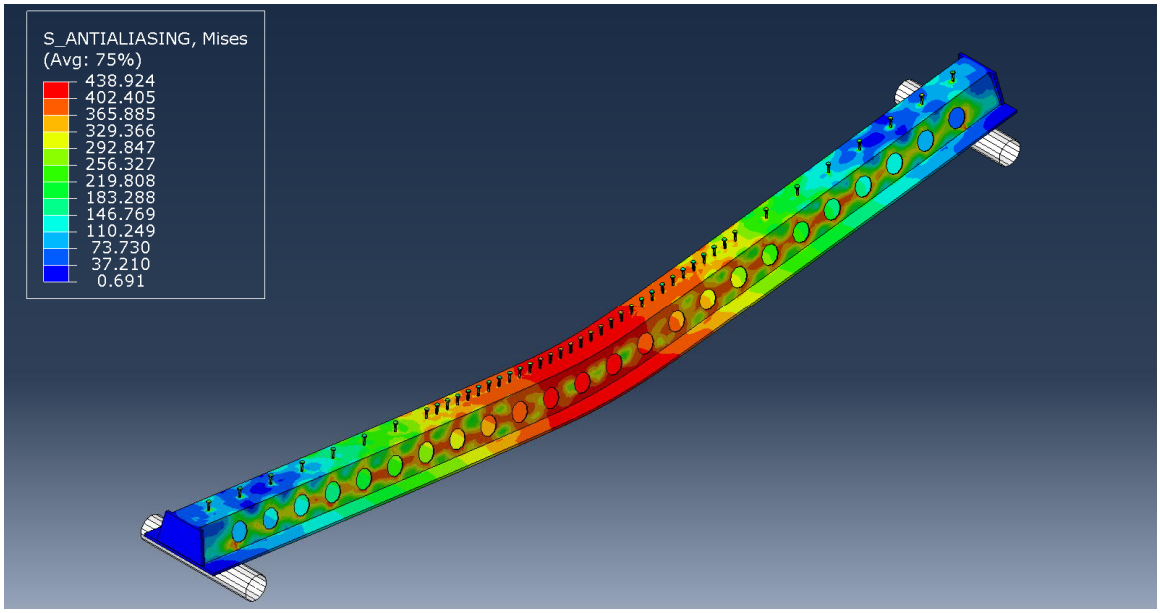

Fig. 6.42- S7- Von Mises stresses on steel part

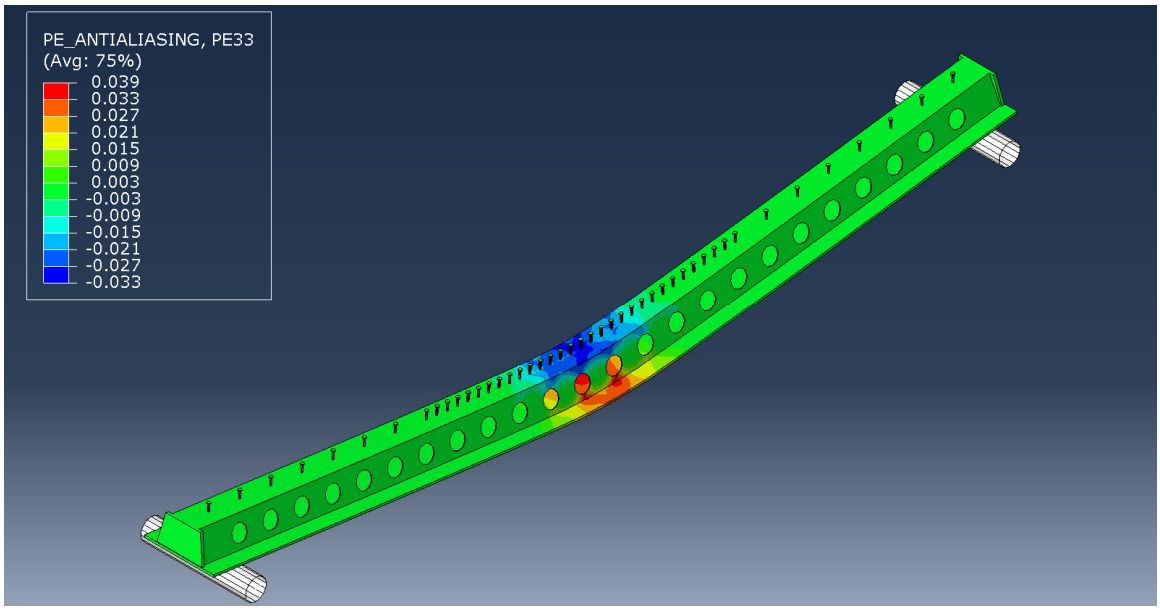

Fig. 6.43- S7- Plastic strains on steel part along longitudinal axis

The load- deflection curves are again very close (figure 6.40). The maximum load difference (figure 6.40, point A) and the difference at the maximum deflection (figure 6.40, point B) are 95.5 kN (at 49 mm deflection) and 71.8 kN, respectively. The load- strain curves (figure 6.41) are different up to a strain equal 0.006 (figure 6.41, point A), while the ultimate strain calculated is really close to the experimental one. Von Mises stresses and plastic strains are presented in figures 6.42 and 6.43, respectively. Green colored areas at the webs of the mid span (figure 6.43) have zero plastic strains and still an elastic behavior.

6.3.2.4 Specimen S8 (§5.3.4)

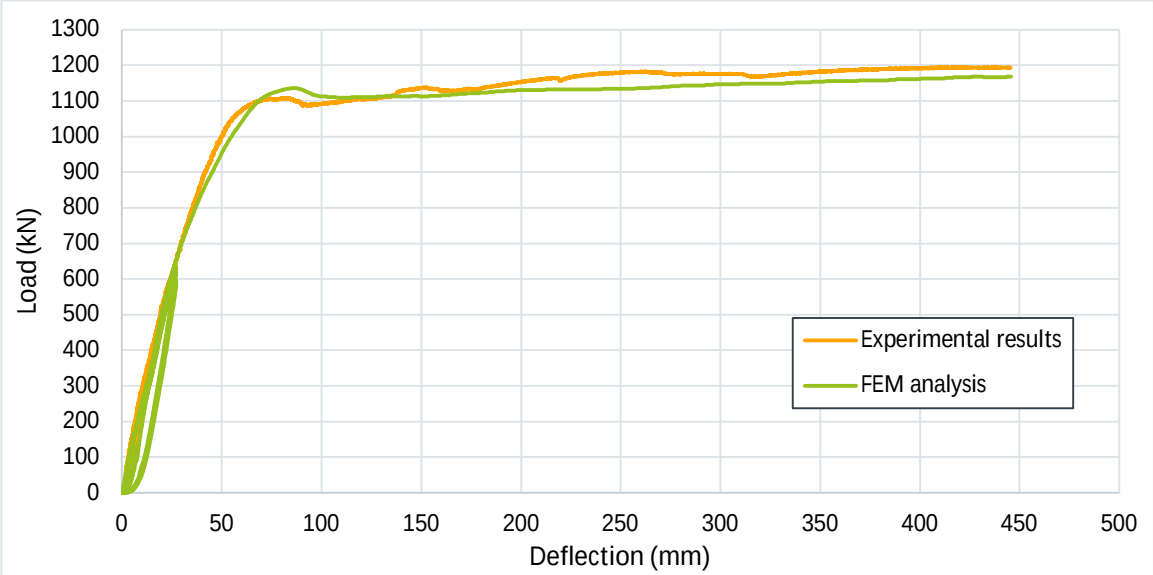

Fig. 6.44- S8- Comparison of load- deflection curves

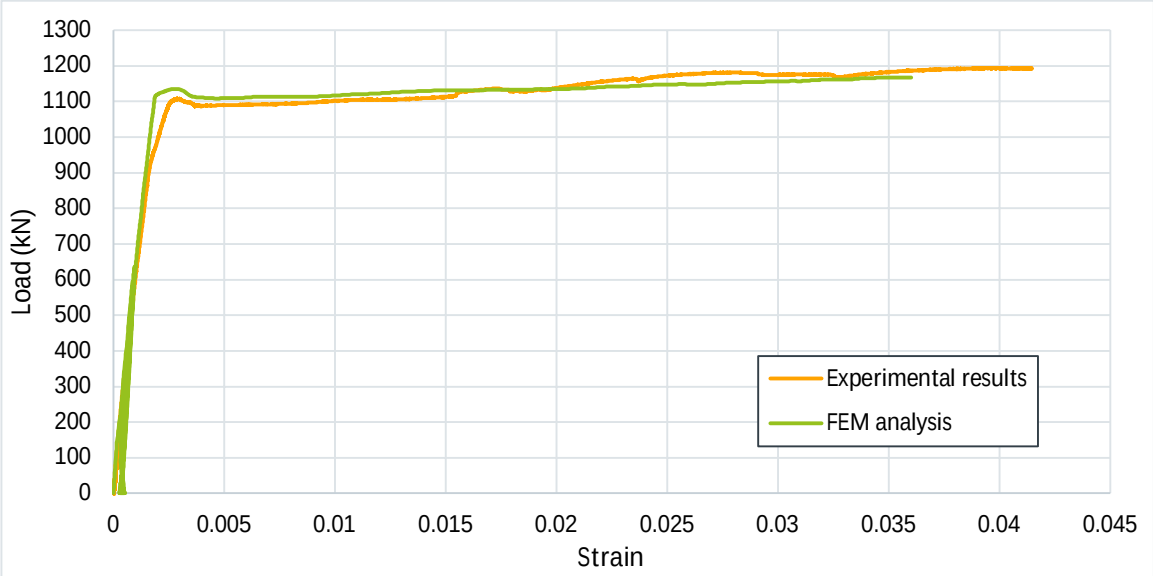

Fig. 6.45- S8- Comparison of load- strain curves

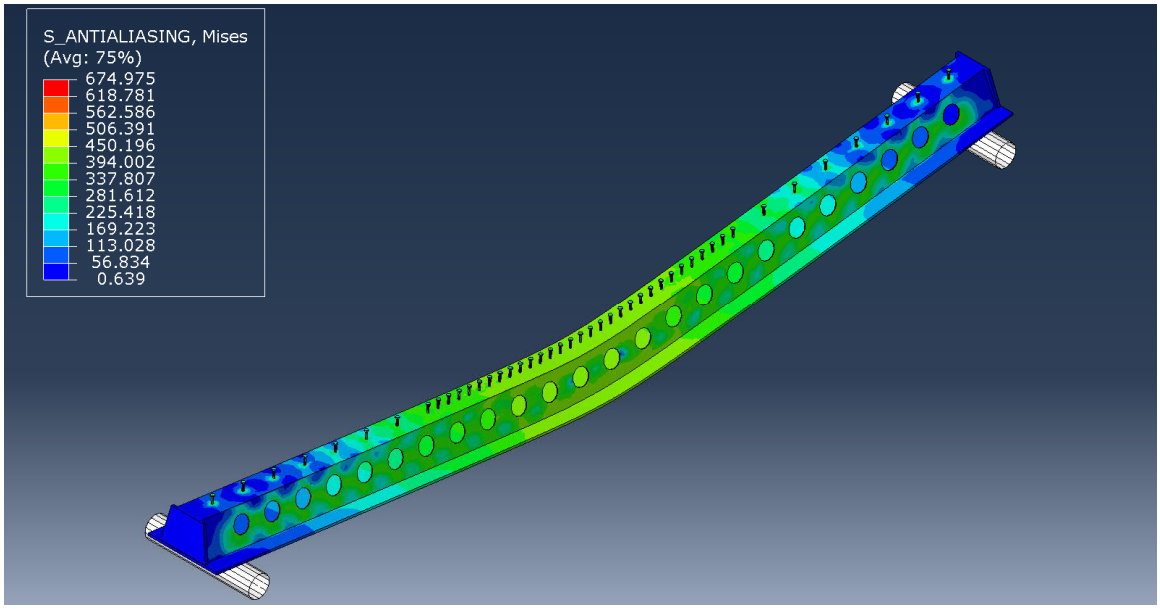

Fig. 6.46- S8- Von Mises stresses on steel part

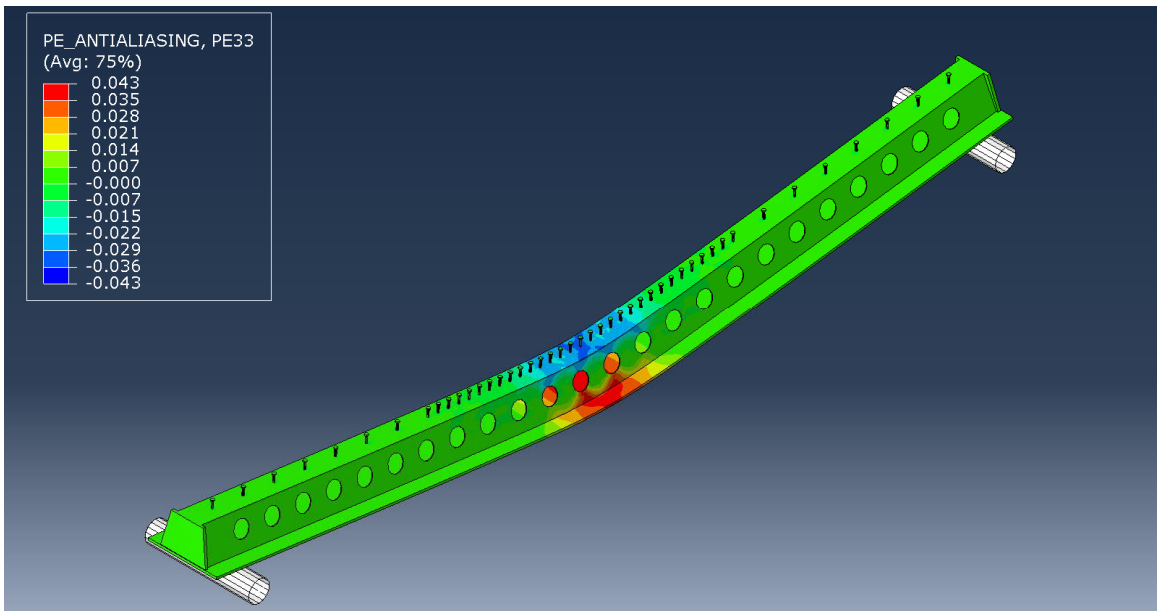

Fig. 6.47- S8- Plastic strains on steel part along longitudinal axis

Results of the last model of this section type had the best correlation with the experimental data. The load- deflection curves (figure 6.44) and load strain curves (figure 6.45) are identical. The ultimate calculated ultimate strain value was equal to 0.036, a little less than the experimental ultimate stain measured 0.041. Like all the previous models, at the mid span, there are areas of the web between the web holes (figure 6.47) that have zero plastic strain (green color) and behave elastically. The Von Mises stresses (figure 6.46) on the top and bottom plate at the middle of the span slightly exceeded the yielding stress of the steel beam (f_{ay}= 393.49 MPa).

6.3.3 Type 4 sections

6.3.3.1 Specimen S9 (§5.4.1)

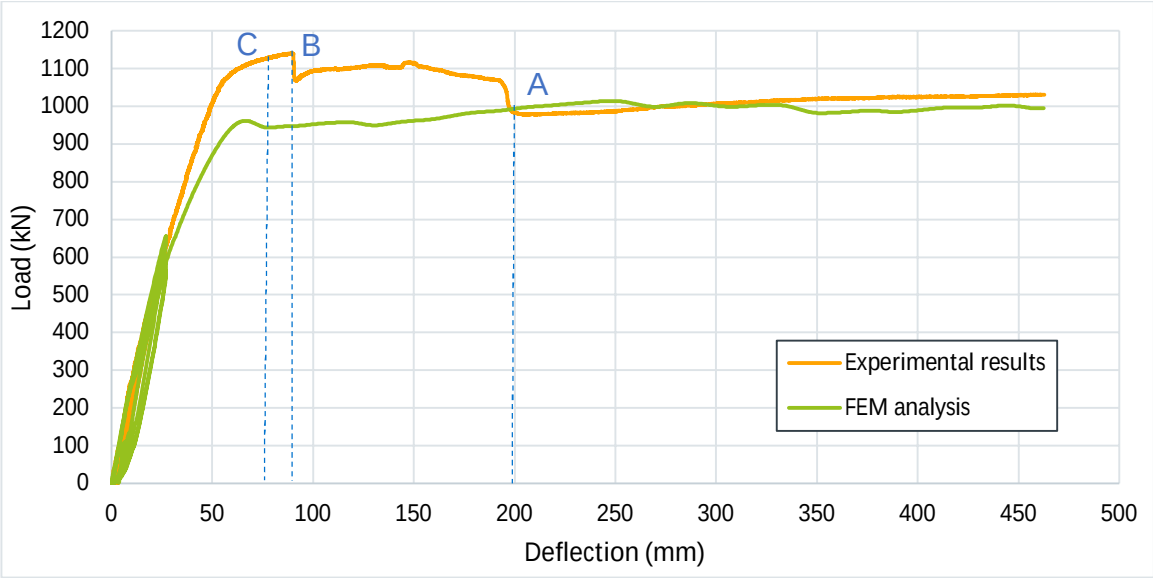

Fig. 6.48- S9- Comparison of load- deflection curves

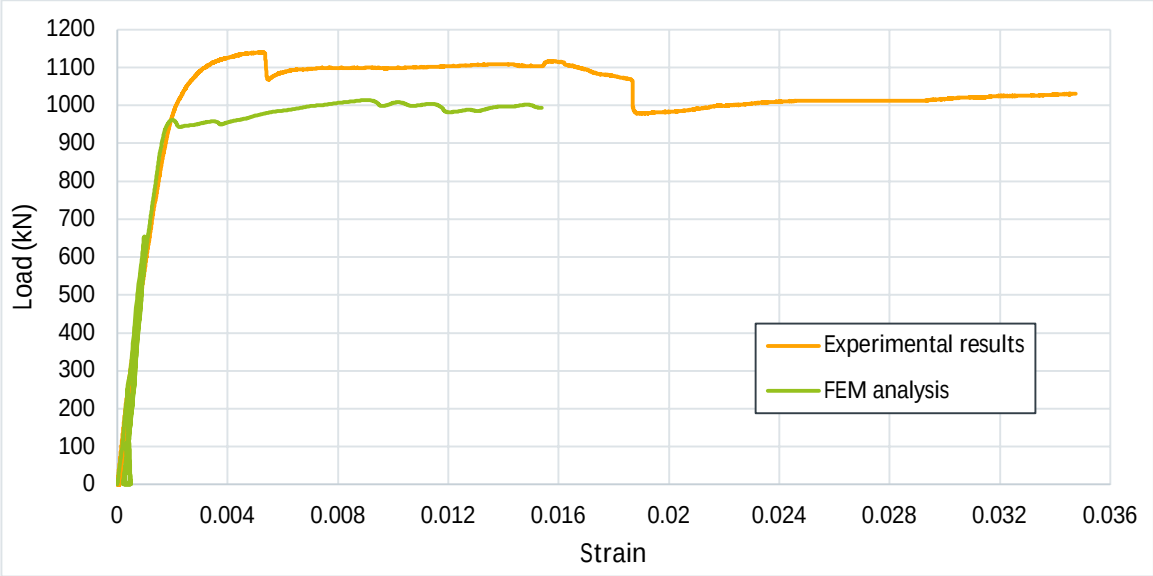

Fig. 6.49- S9- Comparison of load- strain curves

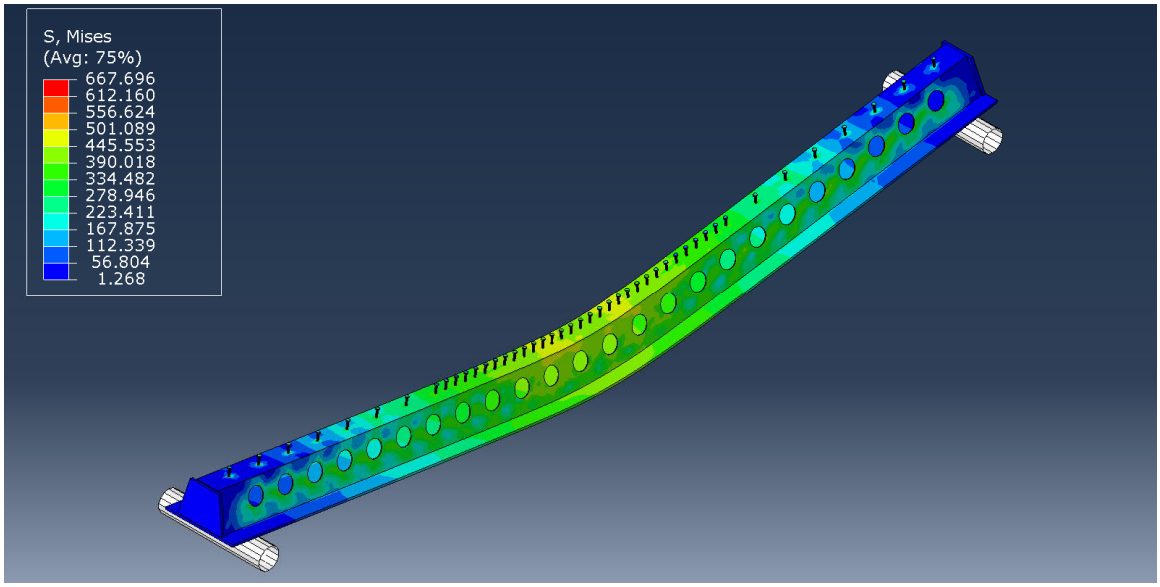

Fig. 6.50- S9- Von Mises stresses on steel part

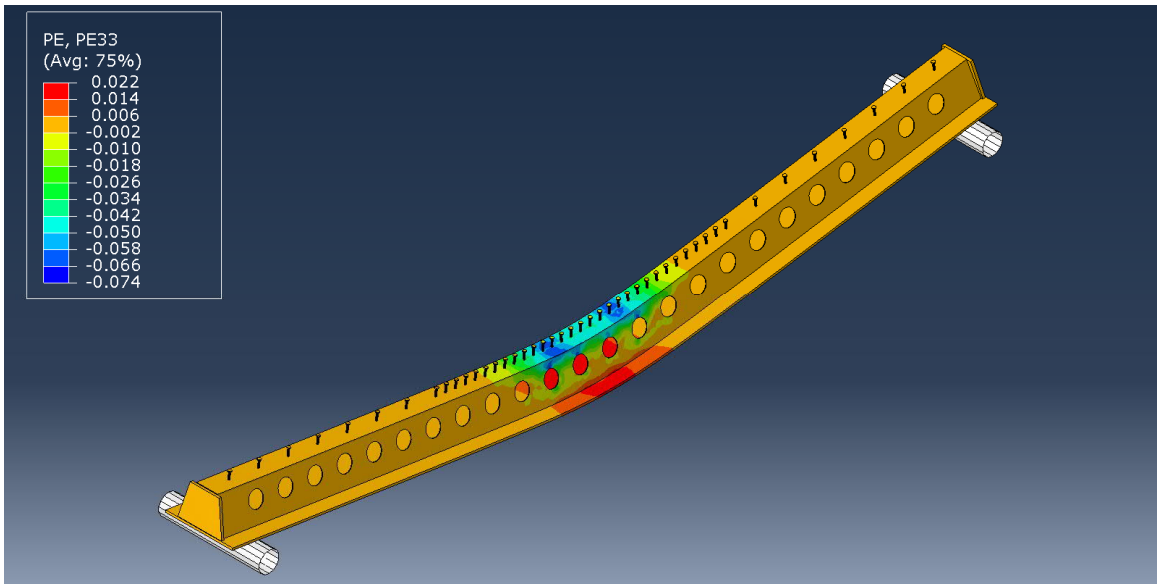

Fig. 6.51- S9- Plastic strains on steel part along longitudinal axis

As can be seen in the load- deflection curve (figure 6.48) there is a difference at the load values up to the deflection of 200 mm (figure 6.48, point A). The maximum difference is 192.8 kN and is located at deflection of 88.65 mm (figure 6.48, point B). This value is equal to 17% of the experimental load at that point. As explained in the chapter related to the experimental results of type 4 beams (§5.4.1), the two subsequent load reductions are due to the failure of the two concrete ledges on the top part of the beams. The first impression given by the comparison of the two curves is that this behavior was not properly predicted by the FE model. Figure 6.52

and 6.53 show that these concrete ledges actually failed at the FE model. Processing of the analytical results shows that the failure of both ledges begun simultaneously at a deflection of about 75 mm (figure 6.48, point C). After the second reduction where the section able to carry the load was diminished to the steel part, the concrete core and the concrete confined by the open stirrups, the two curves are identical. For specified maximum deflection of 450 mm, the FE model calculated a smaller strain (figure 6.49). Finally, Von Mises stresses and plastic strains are presented in figures 6.50 and 6.51, respectively.

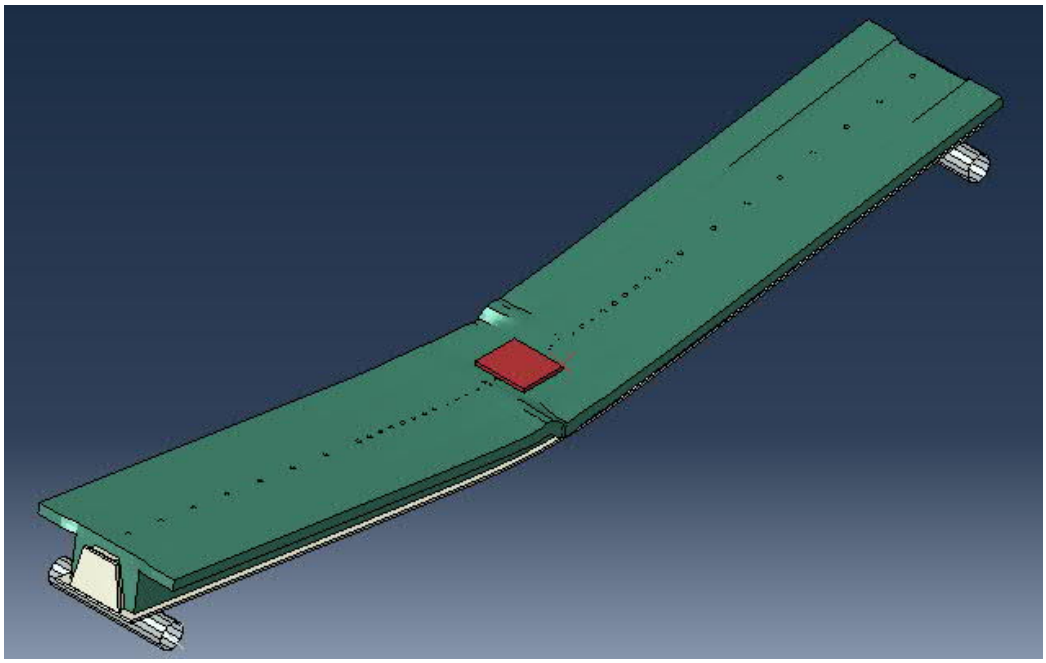

Fig. 6.52- S9- Deformation of the model

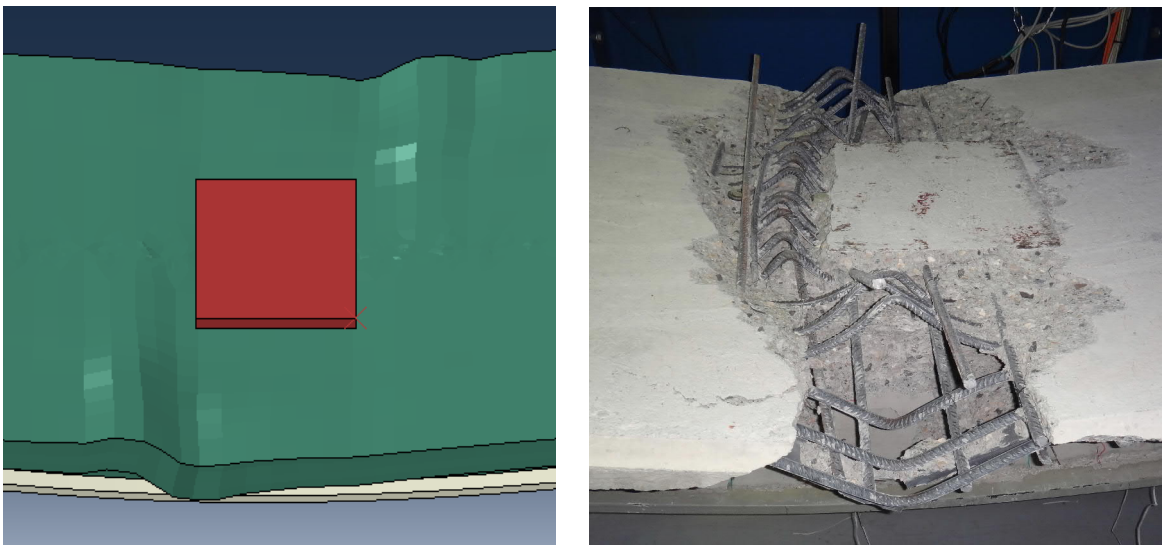

Fig. 6.53- S9- Deformed shape on FE model (left) and specimen at the end of the test (right)

6.3.3.2 Specimen S10 (§5.4.2)

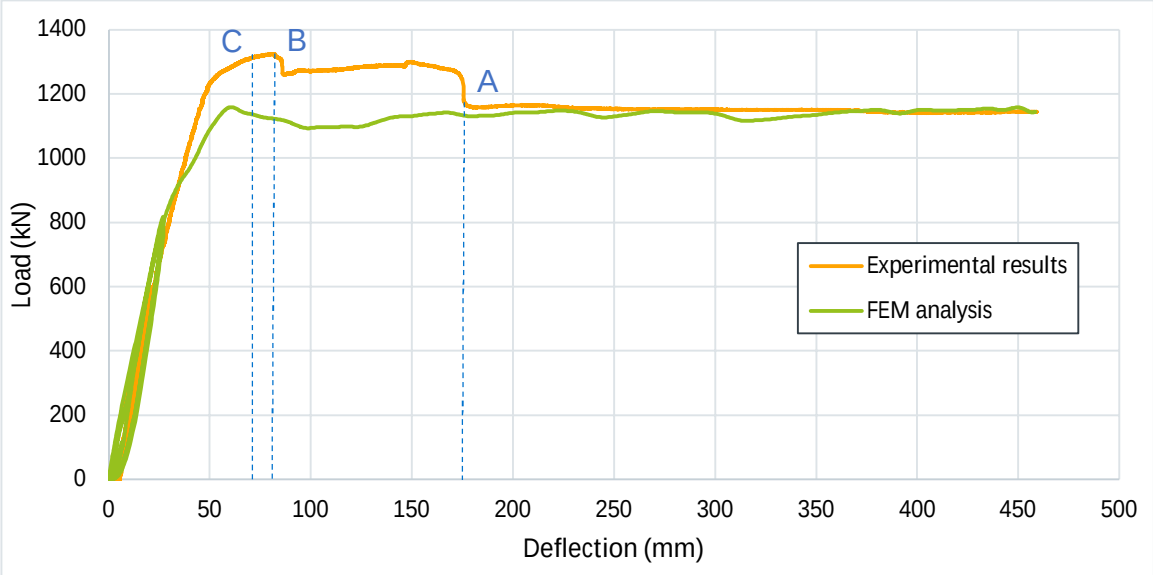

Fig. 6.54- S10- Comparison of load- deflection curves

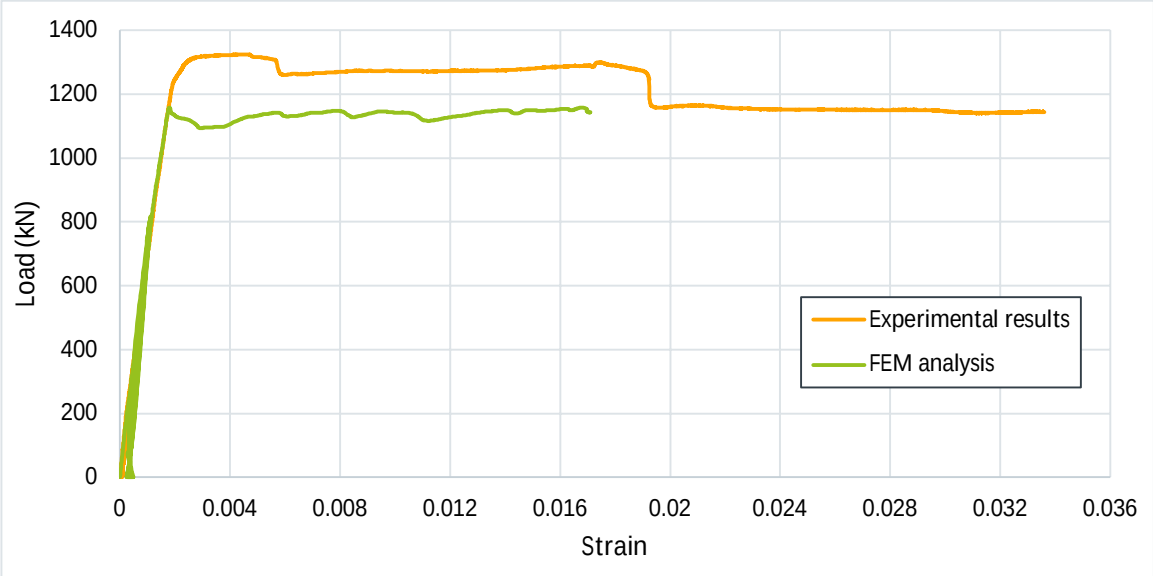

Fig. 6.55- S10- Comparison of load- strain curves

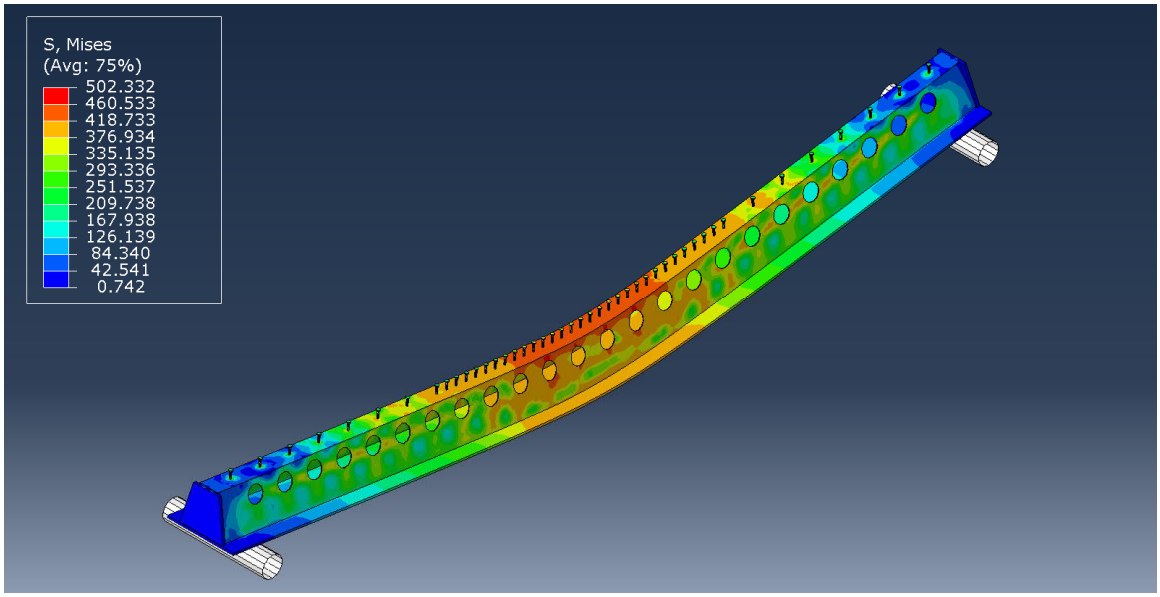

Fig. 6.56- S10- Von Mises stresses on steel part

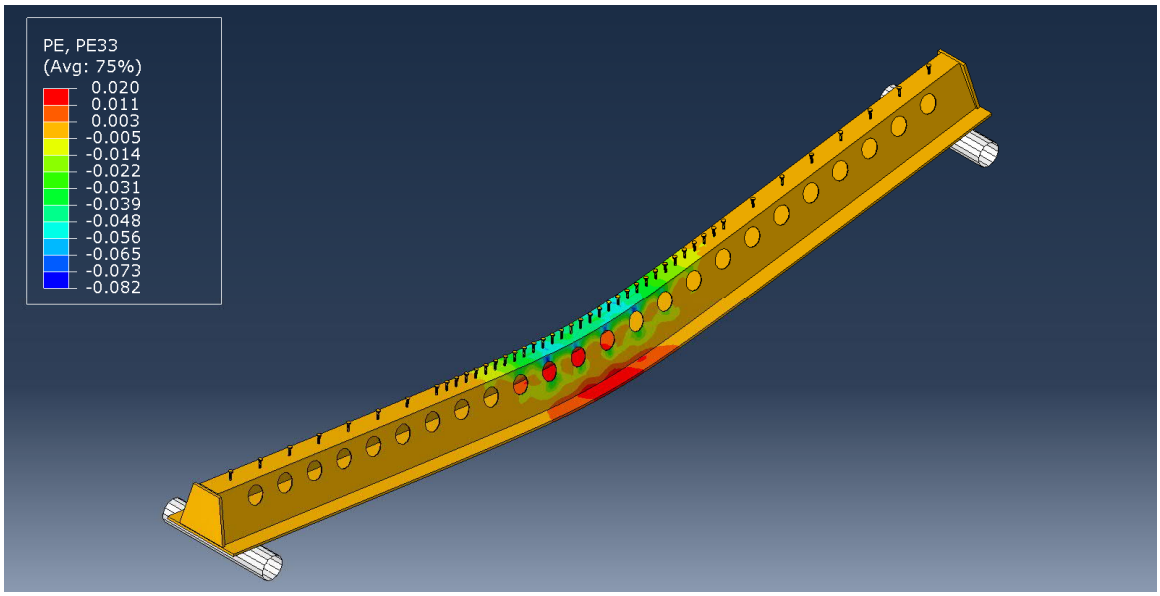

Fig. 6.57- S10- Plastic strains on steel part along longitudinal axis

As can be seen in the load- deflection curve (figure 6.54) there is a difference at the load values up to the deflection of 175 mm (figure 6.54, point A). The maximum difference is 201.5 kN and is located at deflection of 82 mm (figure 6.54, point B). This value is equal to 15% of the experimental load at that point. Figure 6.58 and 6.59 show that the concrete ledges of the concrete plate failed. That happened simultaneously at a deflection of about 70 mm (figure 6.54, point C). After the second reduction where the section able to carry the load was diminished to the steel part, the concrete core and the concrete confined by the open stirrups,

the two curves are identical. Again, the model did not calculate and predict the strains at the bottom plate of the steel beam for inelastic measured deformations. However, the elastic part correlated very well with the experimental results (figure 6.55). Finally, Von Mises stresses and plastic strains are presented in figures 6.56 and 6.57, respectively.

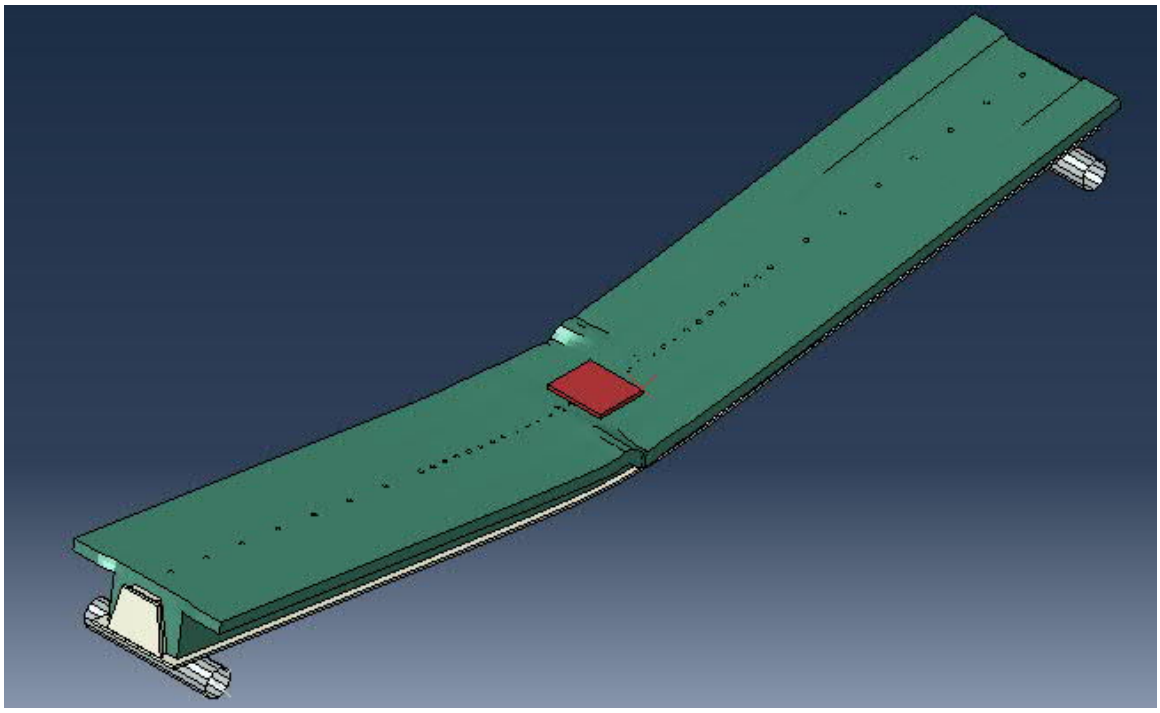

Fig. 6.58- S10- Deformation of the model

Fig. 6.59- S10- Deformed shape on FE model (left) and specimen at the end of the test (right)

6.3.4 Average results

With the proper interpolation procedure, the average load- deflection and load- strain curves were created. To do that, the curves for each specimen had to be transformed into "new" with predefined deflection step. The average results are presented for each section type (load-deflection curves in figures 6.60, 6.62, 6.64 and load- strain curves in figures 6.61, 6.63, 6.65). Finally, an average load- deflection curve for all the specimens is presented (figure 6.66).

- Type 2 sections

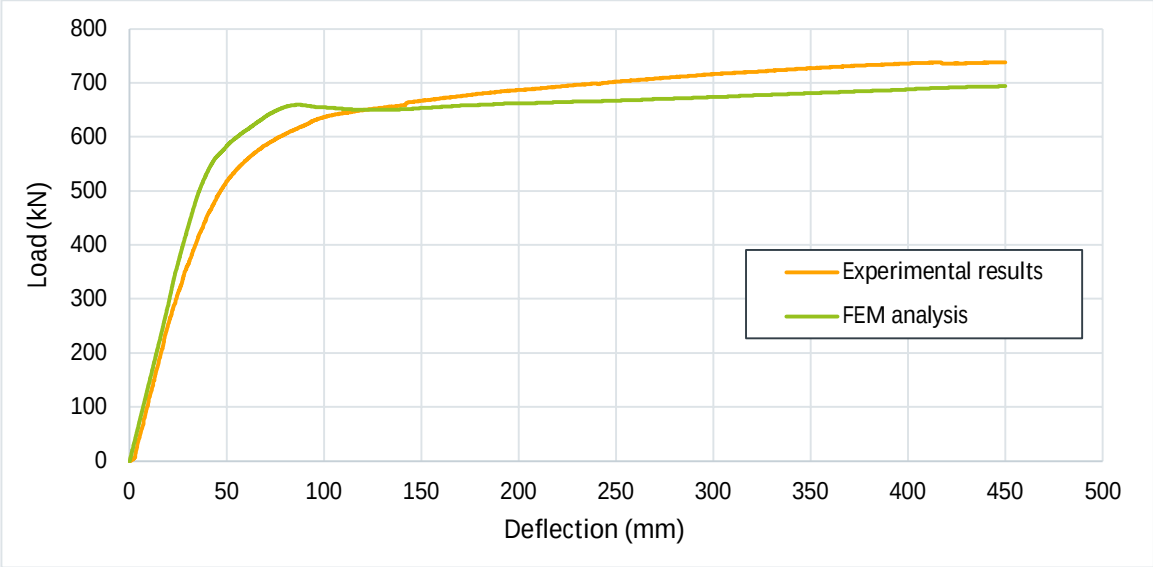

Fig. 6.60- Average load- deflection curves for Type 2 section beams

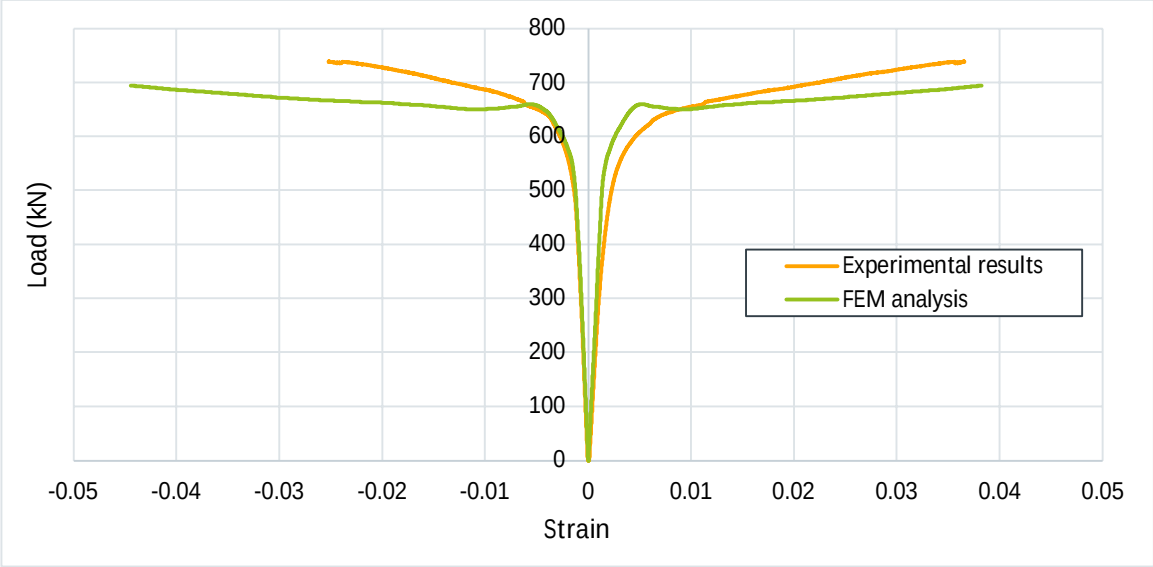

Fig. 6.61- Average load- strain curves for Type 2 section beams

- Type 3 sections

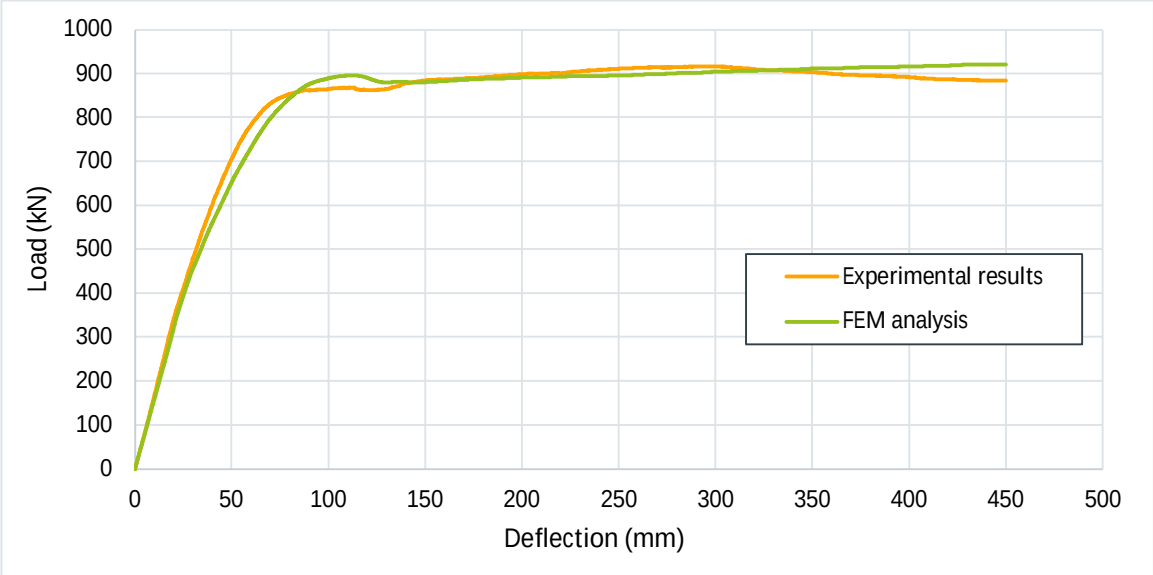

Fig. 6.62- Average load- deflection curves for Type 3 section beams

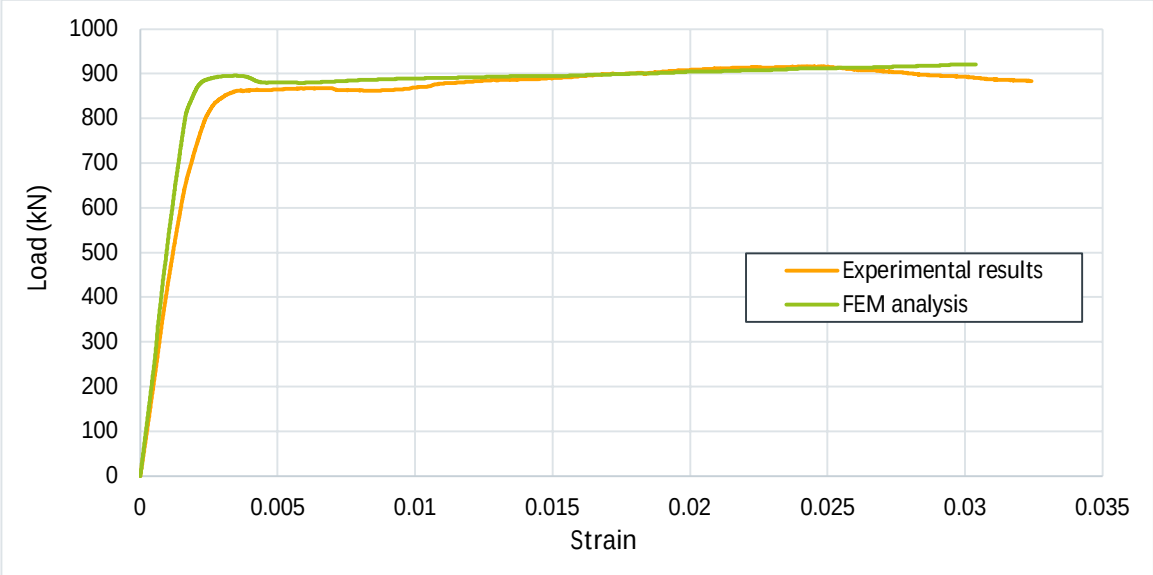

Fig. 6.63- Average load- strain curves for Type 3 section beams

- Type 4 sections

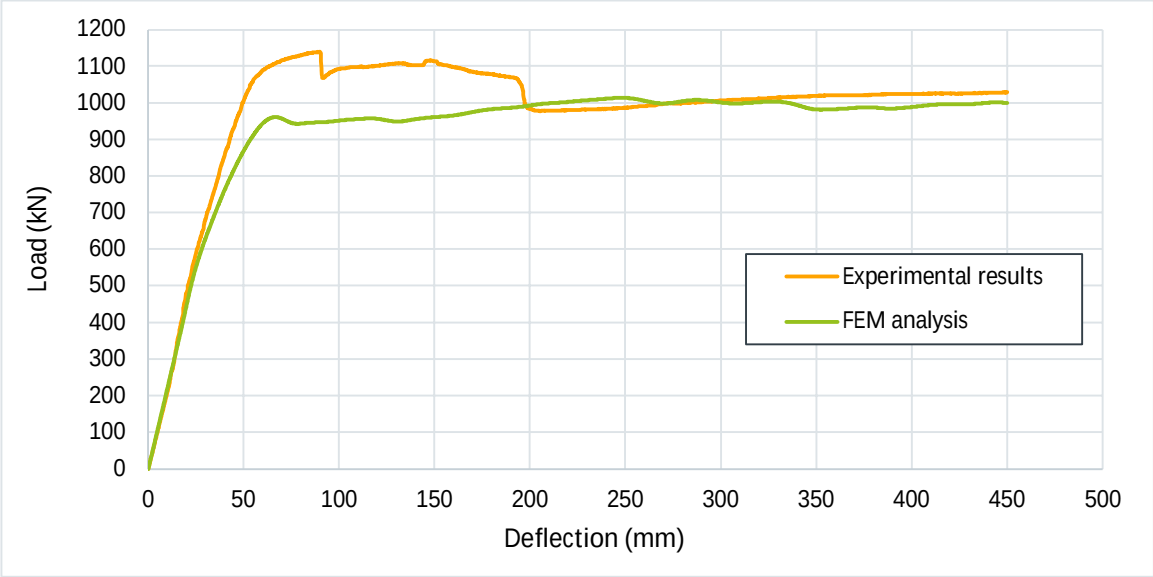

Fig. 6.64- Average load- deflection curves for Type 4 section beams

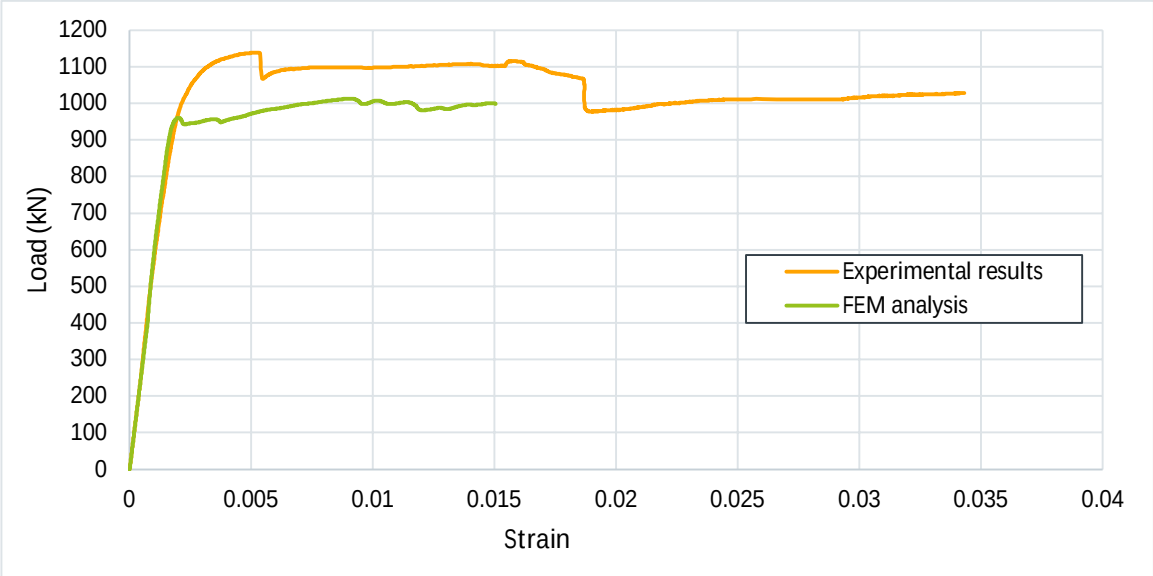

Fig. 6.65- Average load- strain curves for Type 4 section beams

- Total average results

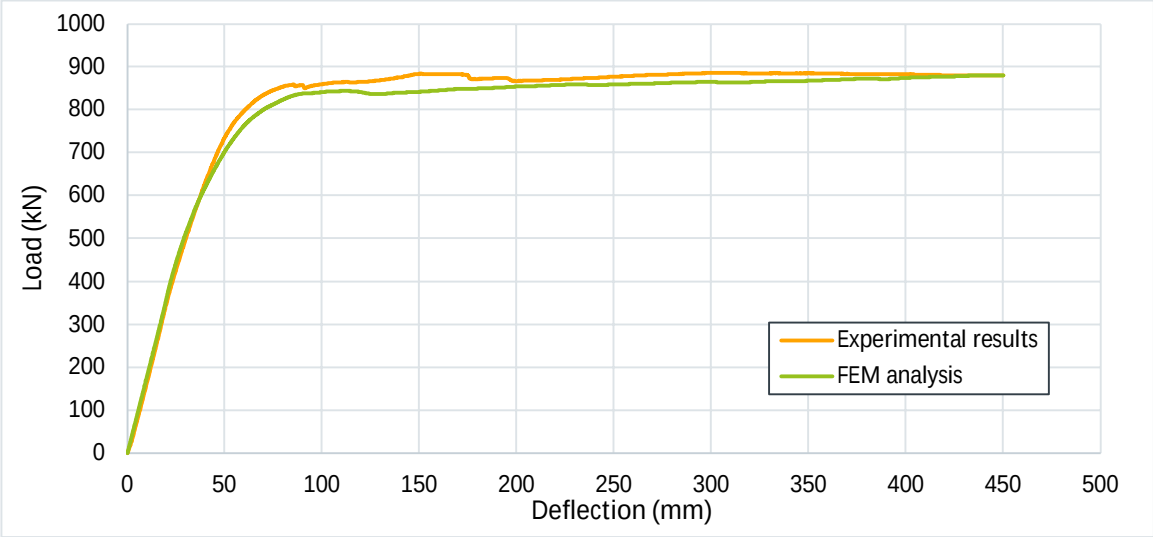

Fig. 6.66- Average load- deflection curves for all specimens

In figure 6.67 the error (%) and the difference between the experimental and analytical results are presented. The formulas used for the calculations are the following:

$$Residual = P_{experimental} - P_{analytical} \quad \text{and} \quad Error = \frac{P_{experimental} - P_{analytical}}{P_{experimental}}$$

The error is less than 5%. At the beginning of the curves up to a deflection of about 25 mm the error seems to be quite high. The actual difference as can be seen in figure 6.66 is not so significant (maximum 17 kN) This can also be observed at the comparison of load deflection curves in figure 6.66 where this difference is not noticeable.

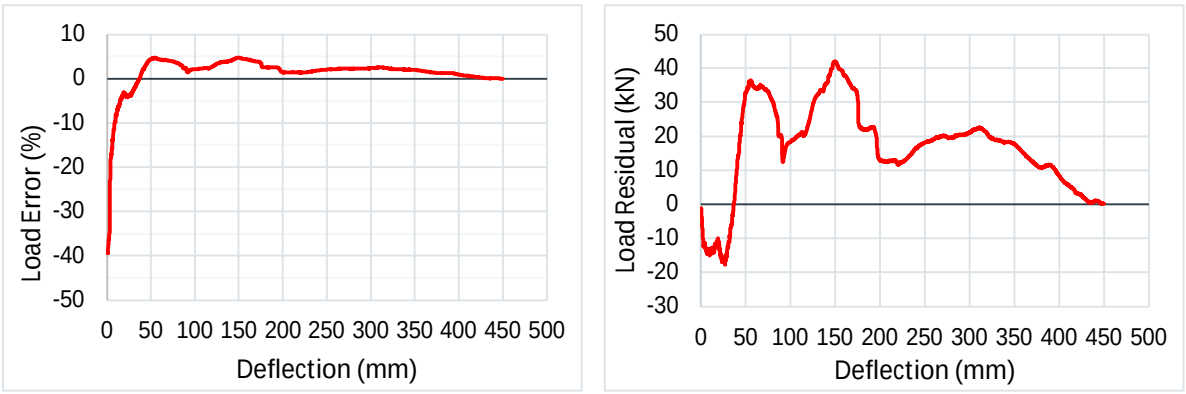

Fig. 6.67- Error (left) and residual (right) between the experimental and analytical load data

In order to have a better estimation of the correlation between the experimental and analytical results, coefficient of determination was calculated using Pearson's formula [54]. The coefficient of determination is used to explain how much variability of one factor can be caused by its relationship to another factor and is represented as a value between 0 and 1. A value of 1.0 indicates a perfect match, and therefore a very reliable model for future predictions. A value of 0, on the other hand, would indicate that the model fails to accurately model the data at all. The closer the value is to 1, the better the relationship between the two factors. In this case the coefficient is equal to 0.998. This proves that the FEM model can predict with high accuracy the behavior of other beams with the same configuration. In figure 6.68 the almost perfect correlation is presented graphically. In figure 6.69 the area of ±5% error for the analytical values is presented.

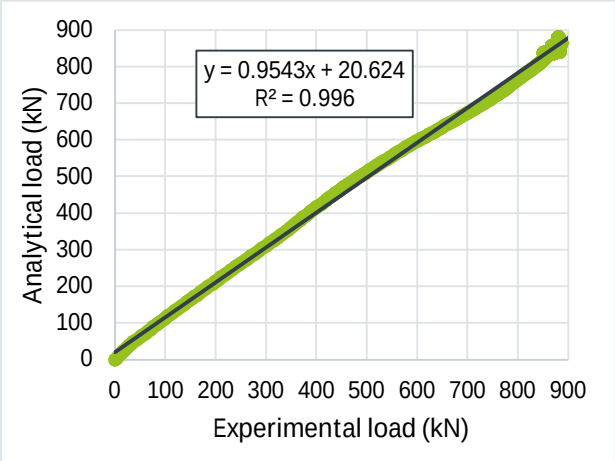

$$r = \frac{n\sum xy - (\sum x)(\sum y)}{\sqrt{n(\sum x^2) - (\sum x)^2}\sqrt{n(\sum y^2) - (\sum y)^2}}$$

Fig. 6.68- Correlation between the experimental and analytical values

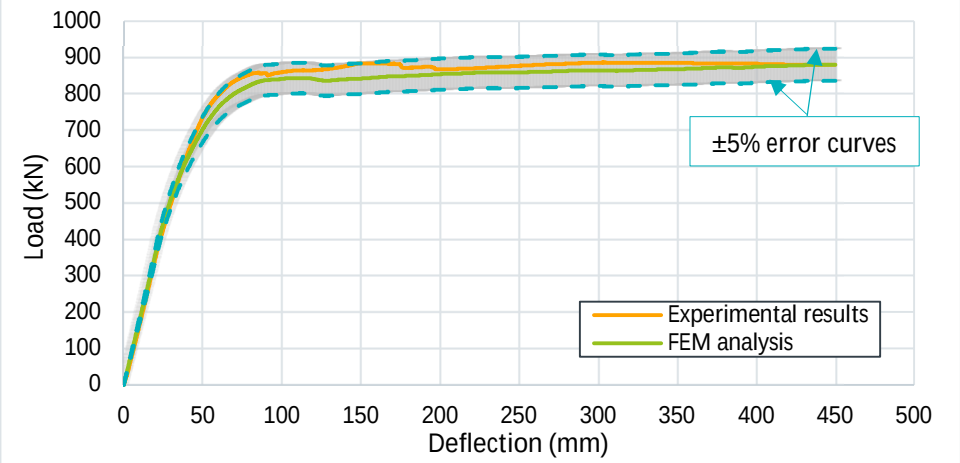

Fig. 6.69- Area of ±5% error for the analytical values

6.4 Sensitivity analysis

In order to demonstrate the effect of the concrete parameters, i) dilation angle and ii) K_c factor, there being the two concrete factors that mostly affected the behavior of the FE models, load-deflection curves for different values of each factor are presented (figures 6.70- 6.73) for the representative specimen S6a.

6.4.1 Dilation angle **ψ**

This factor has an effect on the strength of concrete (figure 6.70). At deflections where the strains have exceeded the ultimate strain of concrete, approximately 100 mm, the contribution of this factor is not so important. Higher angle values led to higher resistance. In order to elucidate the effect of this factor an additional figure with a fraction of the load values is presented (figure 6.71).

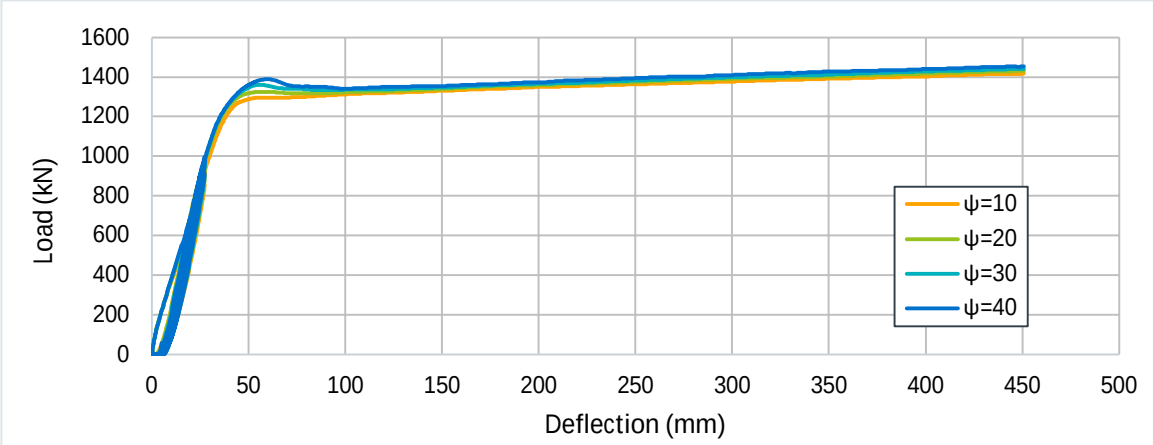

Fig. 6.70- Load- deflection curves for different values of dilation angle

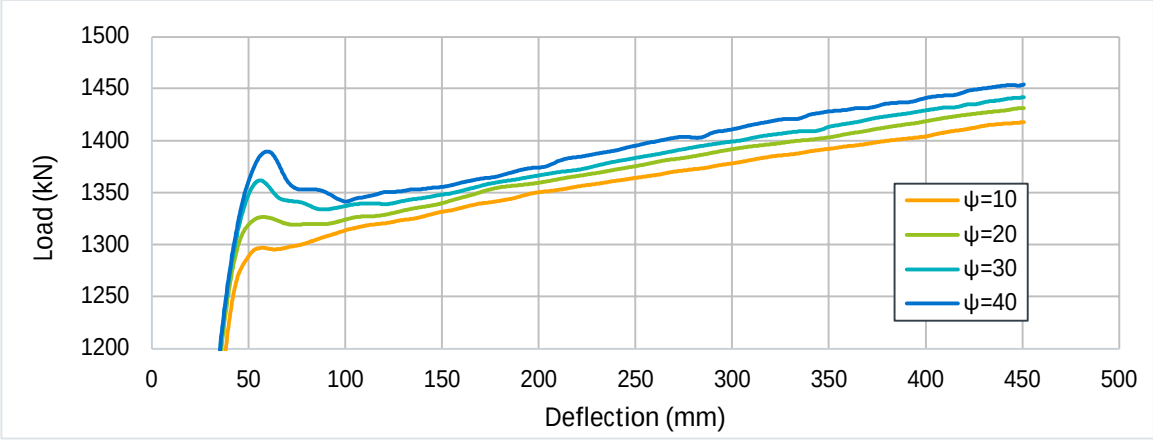

Fig. 6.71- Load- deflection curves for different values of dilation angle, detail at peak resistance

6.4.2 K_c factor

This factor had an effect at the overall behavior of concrete and its deformation capacity. Lower factor values led to a bigger load shift when the beam entered the plastic zone. Figures 6.72 and 6.73 are the reciprocal of figures 6.70 and 6.71.

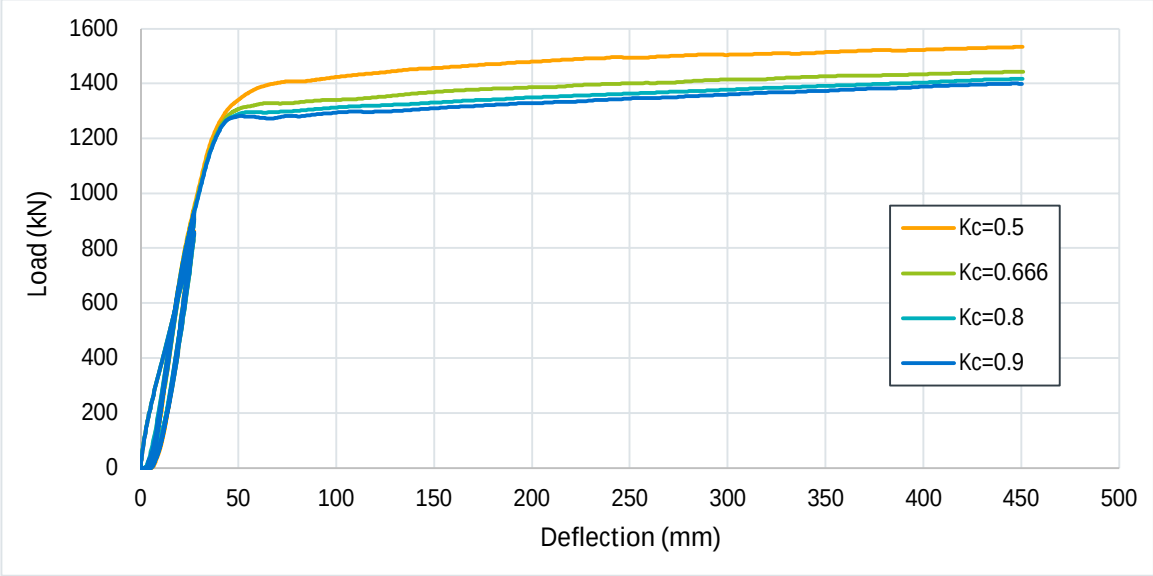

Fig. 6.72- Load- deflection curves for different values of K_c

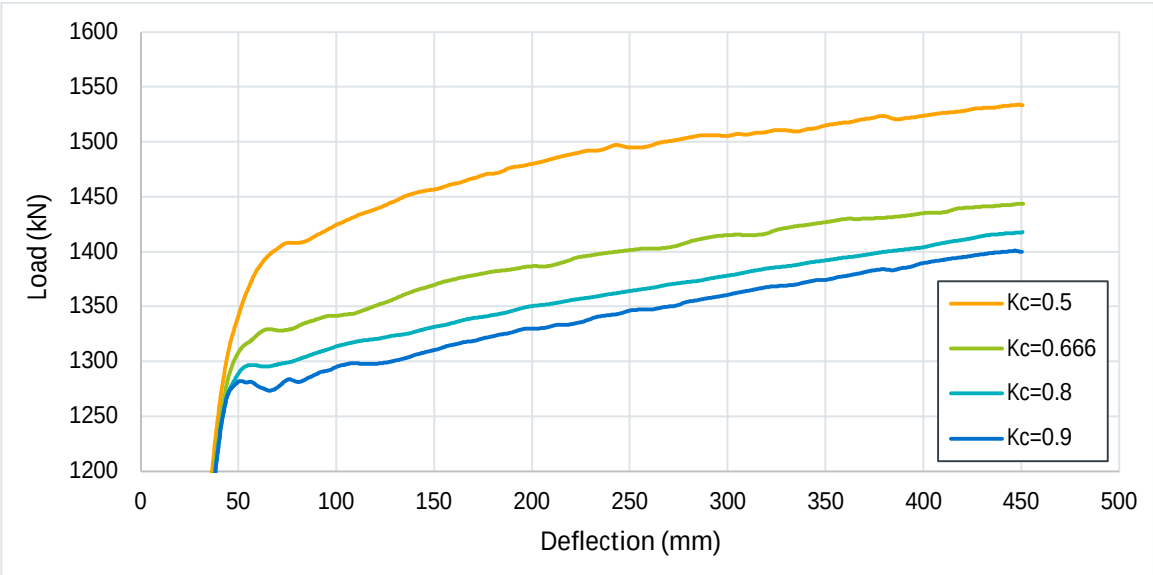

Fig. 6.73- Load- deflection curves for different values of K_c, detail at peak resistance

6.5 Additional investigation

An additional analytical investigation was conducted that reveals the importance of the lateral protection provided by the external confined concrete to the steel webs, as this affects the global behavior of the beam. The investigation was carried out on specimen S11. The tested cross-section was used as a control model. The main alteration of the additional models was the lack of external concrete. The parameter under investigation through this sensitivity analysis was the thickness of the web plates. The cross-sections of the models are presented in figure 6.74. Model 2 has the same steel profile as model 1 (web plate thickness equal to 6 mm in both models). In model 3, two rebars with diameter 20 mm were welded above and below the web holes at both sides. Finally model 4 has a thicker web plate with thickness equal to 8 mm. In Table 6.3 the basic differences between the model are summarized.

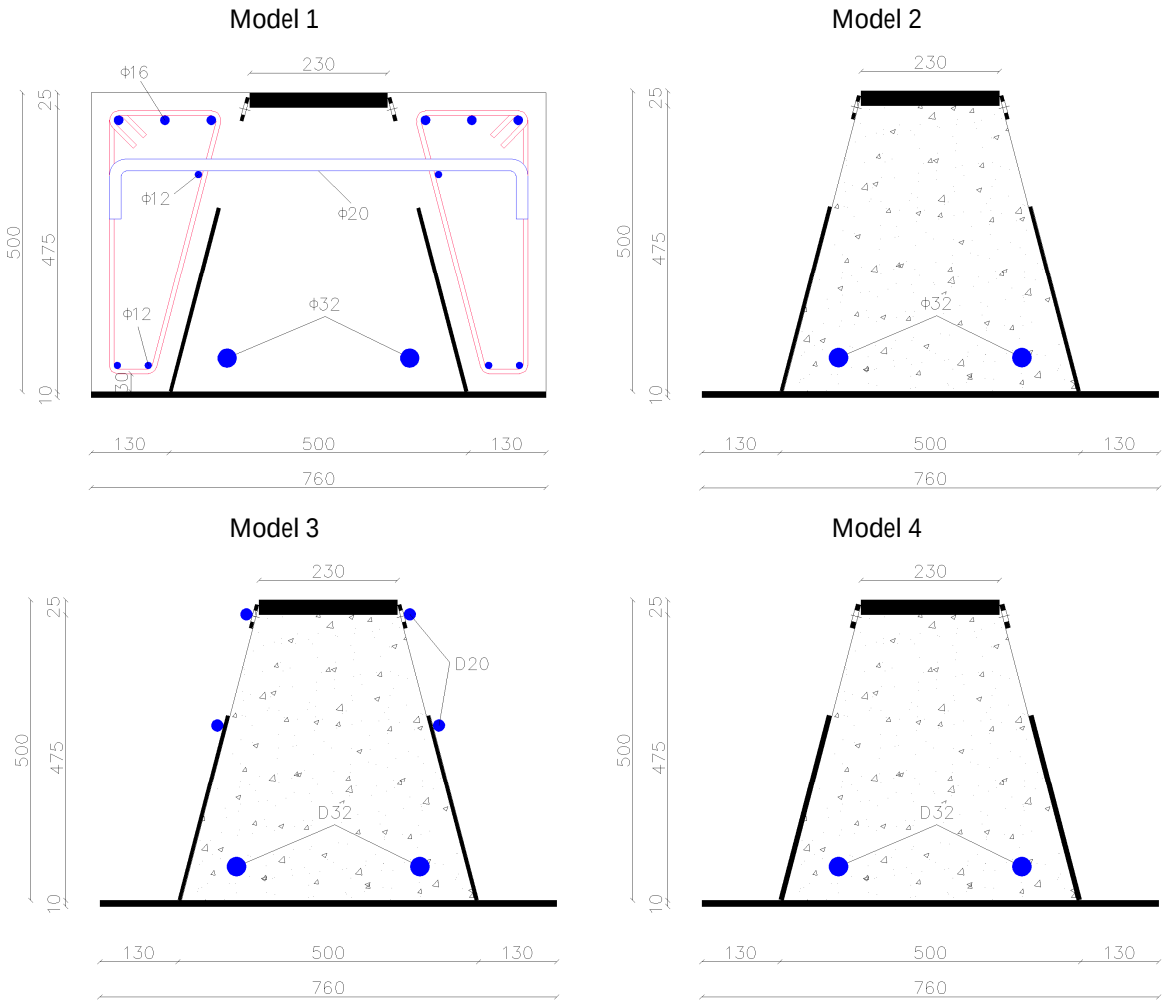

Fig. 6.74- Sensitivity analysis models

Table 6.4- Details of the models

Models	Reinforced external concrete	Thickness of top plate	Thickness of web plates	Welded rebars on webs
Model 1	Yes	25	6	No
Model 2	No	25	6	No
Model 3	No	25	6	4D20
Model 4	No	25	8	No

6.5.1 Model 1

Model 1 was calibrated with the experimental data and, as mentioned before, was the control model for the comparison with the other models. In figure 6.75, the displacements along the transverse direction for the maximum deflection of 500 mm are presented. As certified from the test, no buckling occurred at the top and web plates.

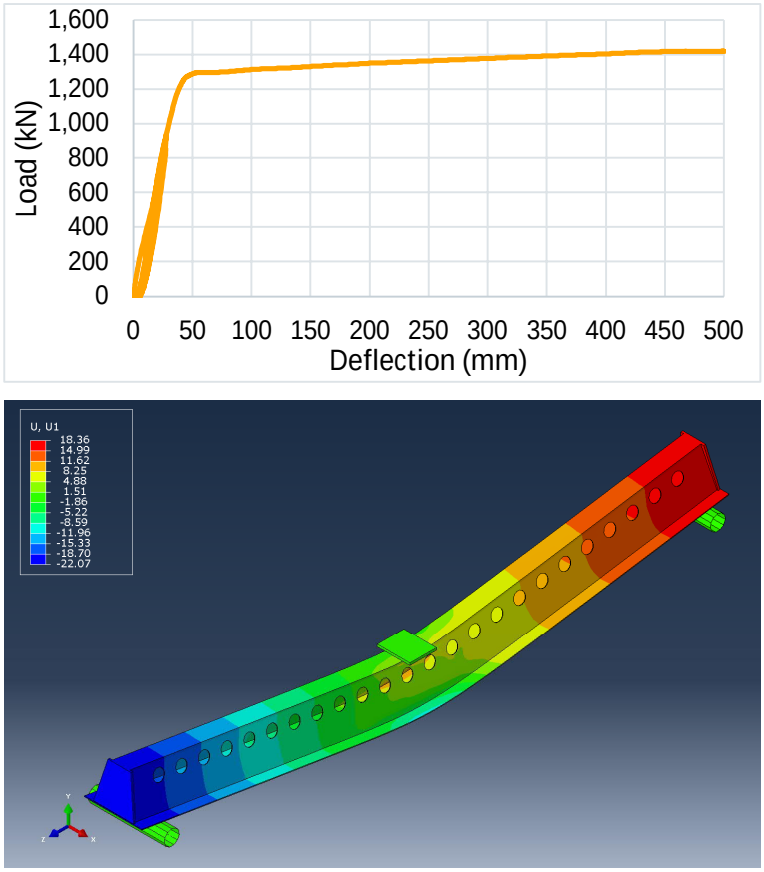

Fig. 6.75- Transversal deformation of Model 1

6.5.2 Model 2

When the maximum load was reached at a deflection of 42 mm (figure 6.76- Point A), the web plates locally buckled at the loading area and a small reduction occurred at the load-deflection curve. Afterwards, the model adopted a hardening behavior until a deflection of 250 mm when the top plate buckled (figure 6.76- Point B) and the beam lost its ability to carry additional load. The reduction in the load-deflection curve continued until the end of the analysis at a deflection value equal to 500 mm (figure 6.76- Point C).

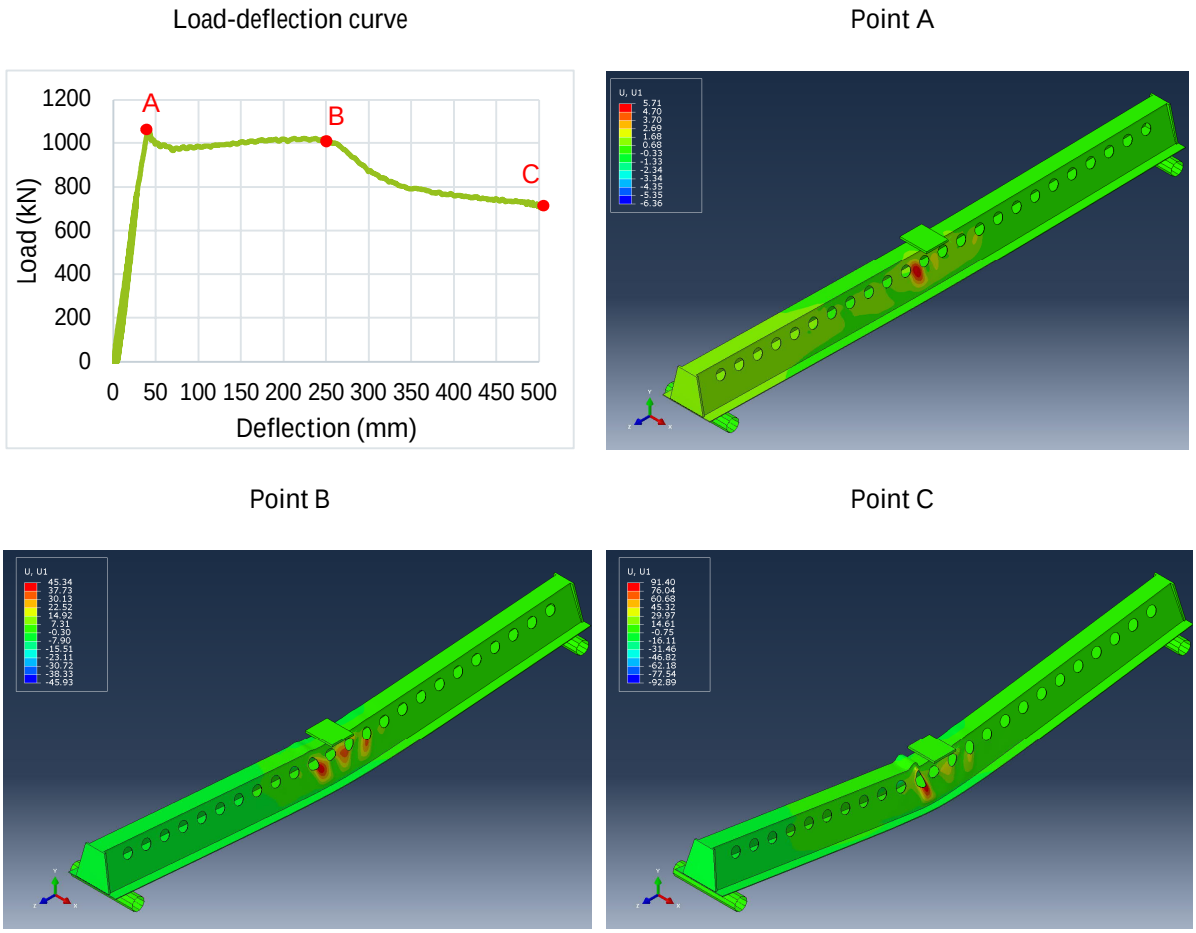

Fig. 6.76- Transversal deformation of Model 2

6.5.3 Model 3

Model 3 exhibited similar behavior with model 2. At a deflection of 50 mm (figure 6.77- Point A), the web plates buckled. In this case the compressive stresses were distributed to a wider area and the extent of the buckling was larger because of the rebars contribution. Therefore, the reduction of the load was small and immediately a plastic behavior with hardening began. Eventually, at a deflection of 325 mm (figure 6.77- Point B) the top plate buckled which caused strength degradation and failure of the beam. The analysis stopped at a deflection of 500 mm (figure 6.77- Point C) where the buckling of the top plate is more obvious.

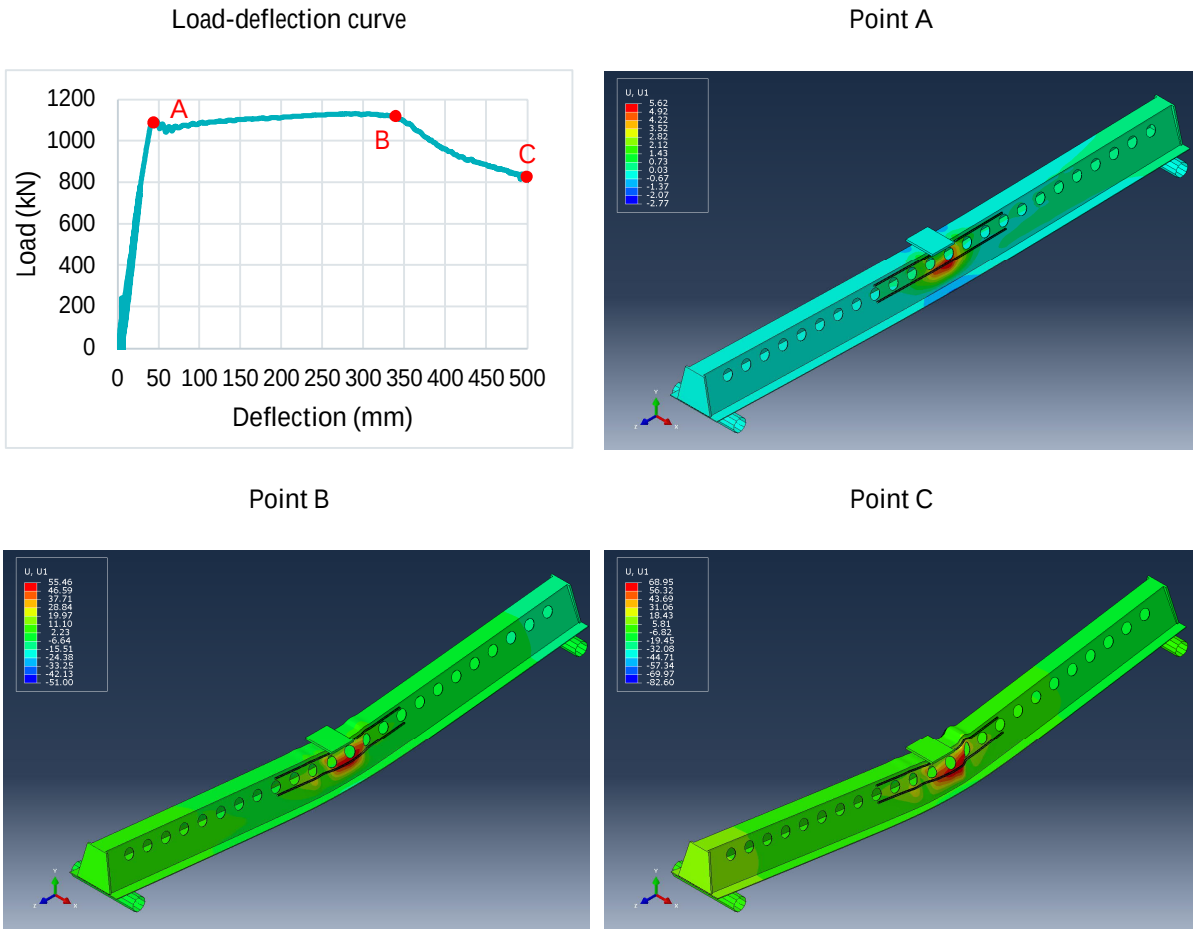

Fig. 6.77- Transversal deformation of Model 3

6.5.4 Model 4

The beam of the fourth and final model buckled as in the previous models. Nevertheless, this model displayed a better behavior than models 2 and 3. The local buckling on the webs occurred at the yielding point, at a deflection of 48 mm (figure 6.78- Point A). The post-yielding behavior consisted of an ascending branch with constant slope up to a deflection of 450 mm (figure 6.78- Point C) where the top plate buckled. At that point and for the next 50 mm until the end of the analysis, the load began to decline (figure 6.78- Point C).

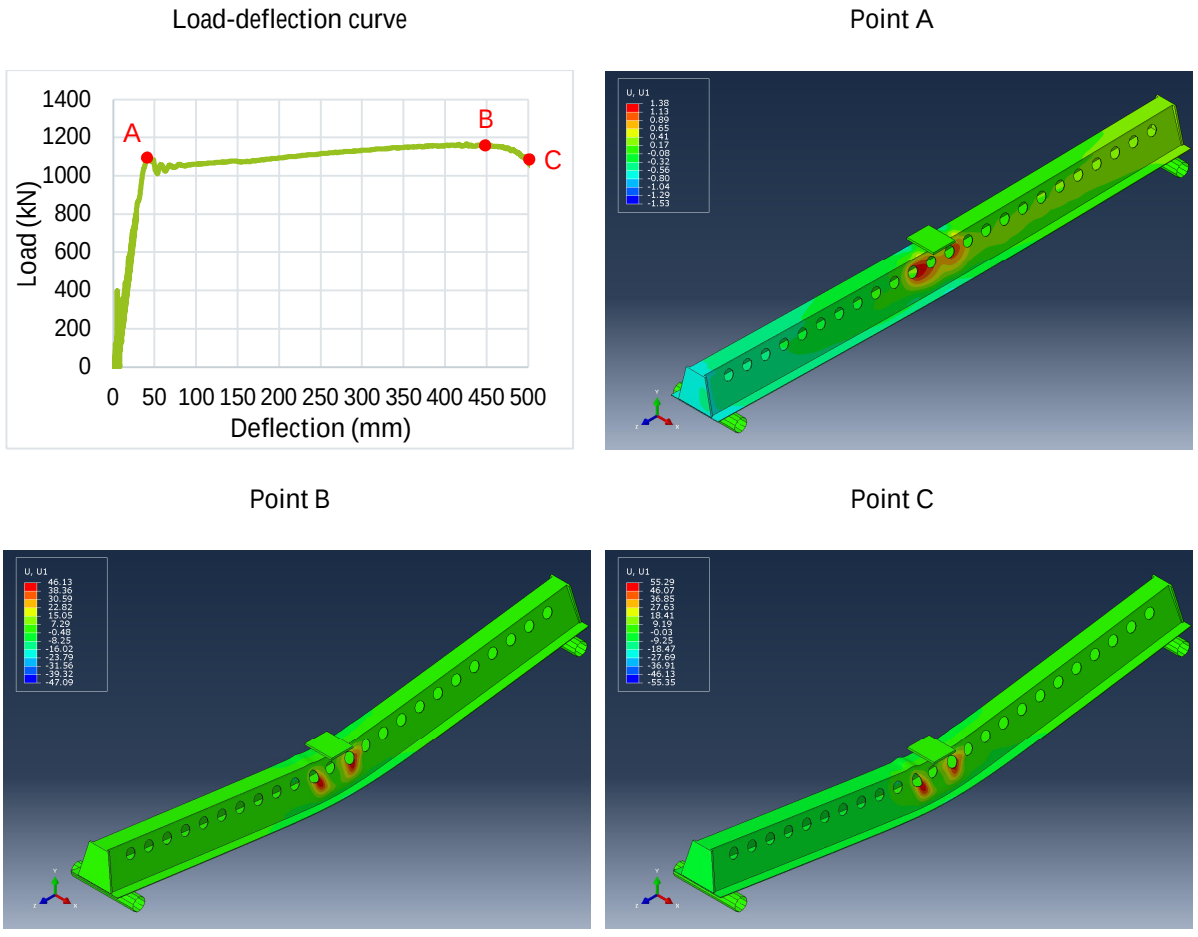

Fig. 6.78- Transversal deformation of Model 4

6.5.5 Comparison of the results

In figure 6.79 the comparison of the load-deflection curves of all four models is presented. All models without external reinforced concrete buckled locally. Initially, buckling appeared at the web plates and this subsequently led to the buckling of the top plate. Results showed that when the web plates were “stronger” the global behavior of the beams was improved and buckling of the top plate occurred at a higher deflection value. Nonetheless, risk of buckling is eliminated completely only when the webs are restrained to move laterally. This lateral restrain is provided by the reinforced external concrete part and the confinement due to stirrups.

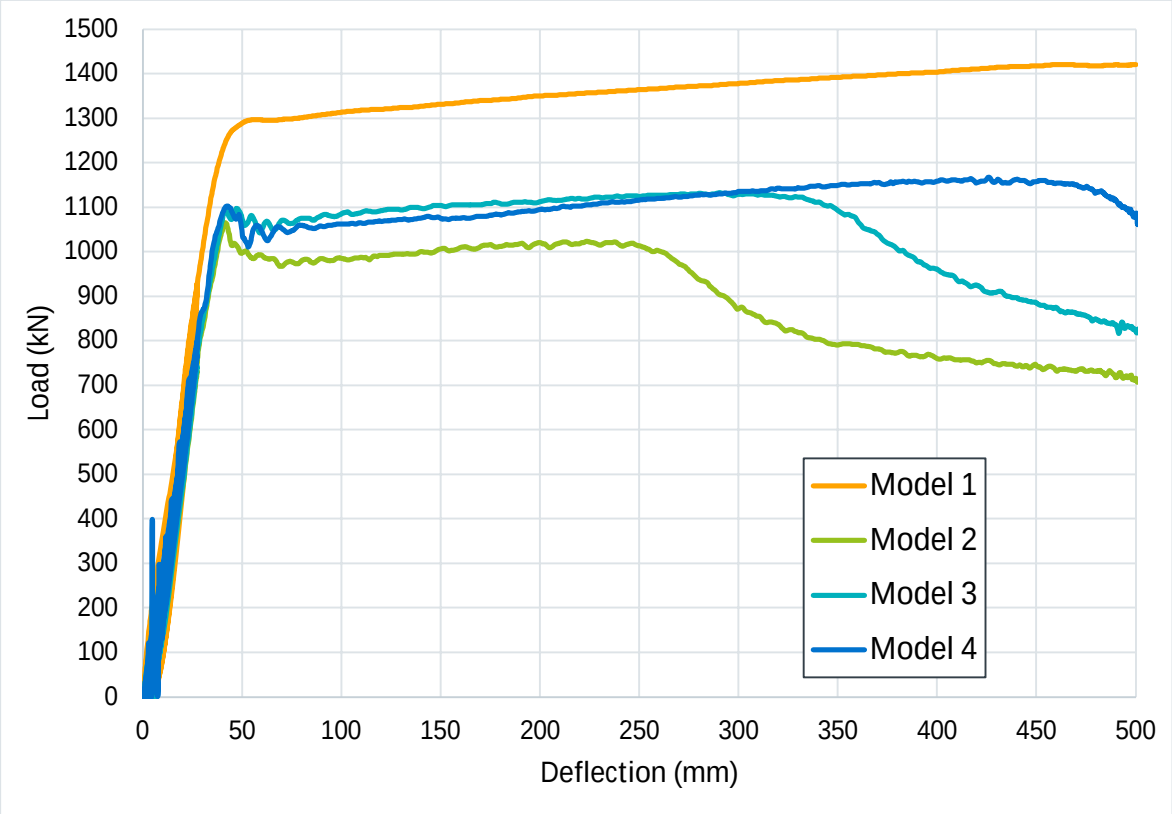

Fig. 6.79- Comparison of load- deflection curves

7

Seismic design of office building

In the present chapter, a design of a building, which is meant to house offices, is presented. Two different analyses were conducted and compared. In the first one Deltabeams were used, while the second one made use of reinforced concrete beams with monolithic concrete slabs. It should be noted that not all the steps of an in-detail design are included in this presentation, as this would be out of the scope of this investigation. Nevertheless, the complete procedure and all the instructions of the related Eurocodes were thoroughly followed and applied.

7.1 Description of the building

The initial architectural plan view of a typical level of the building is presented in figure 7.1. Its length is 21.25 m and its width 17.80 m. The clear height between each level is 3.00 m, a factor that is decided to remain constant between the two design models, as usually for offices it is vital for their proper functionality.

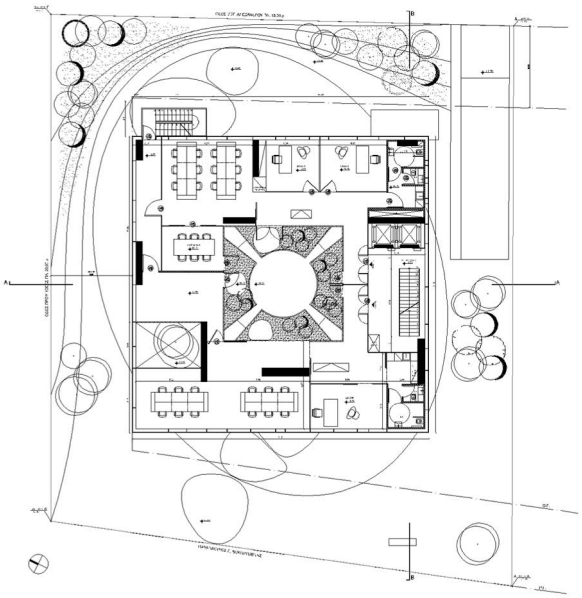

Fig. 7.1- Plan view of the typical level

The equivalent model used for the building design is shown in figure 7.2. Slight modifications were made in order to simplify the design models.

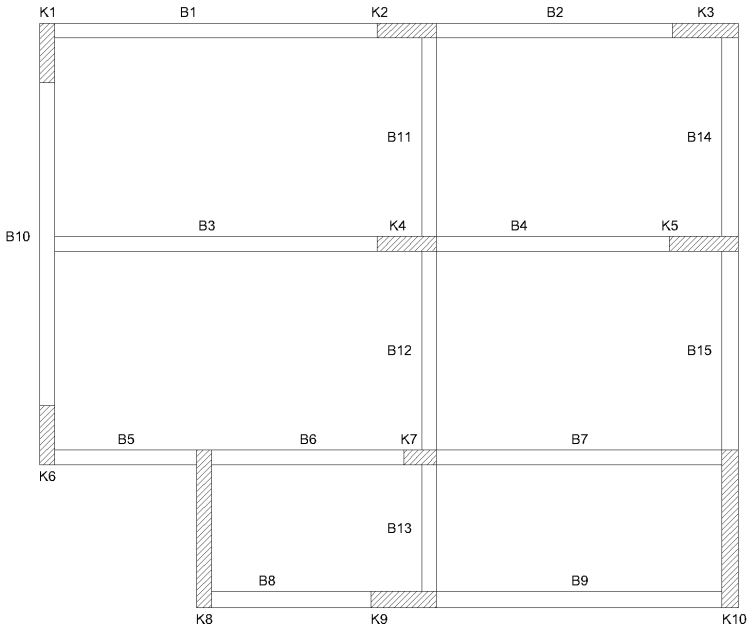

Fig. 7.2- Plan view of the design model

7.2 Details for the seismic design

The site of the building is located to the seismic zone with a design ground acceleration value equal to 0.16g. The ground type chosen was type B. According to Table 5.1 of EN 1998-1:2004 the behavior factor for the calculation of the horizontal design component was chosen equal to 3.0. Correspondingly, the behavior factor used to create the design spectrum curve for the vertical component was chosen equal to 1.5. The calculated horizontal and vertical response spectrum curves are shown in figure 7.3.

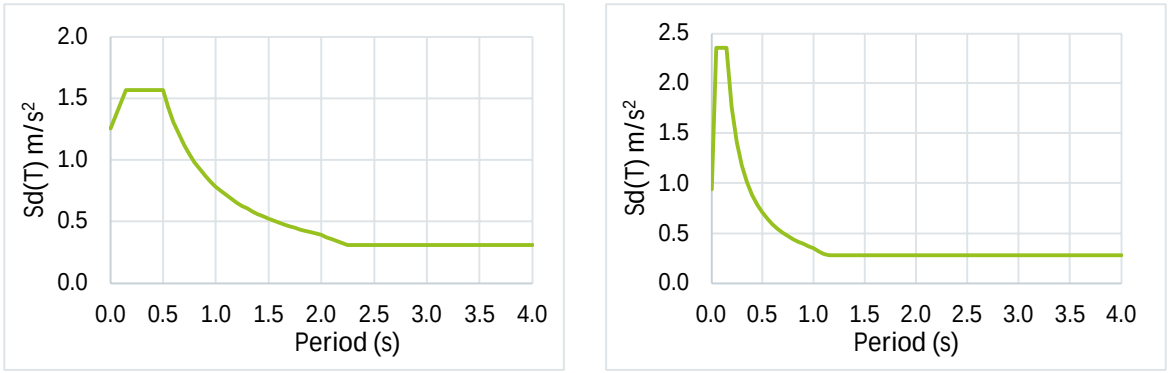

Fig. 7.3- Response spectrum curves for the horizontal (left) and vertical (right) seismic components

7.3 Description of the models

7.3.1 Analysis using Deltabeams

As explained in § 4.2, Deltabeams are connected to the vertical shear walls in such a way that only vertical forces can be successfully transferred from the beams to the walls. So, practically, the Deltabeams should only be designed against the static combination of permanent and live loads. The design of this building was divided into two parts. Initially, the model was created in "Peikko Designer Deltabeam" [55], a software especially created for the design of Deltabeams by Peikko. Subsequently, the same model was created in SAP2000 [56] for the design of the shear walls. The procedure and the models are described in detail in the following sections.

7.3.1.1 Design of Deltabeams

A model was created, according to the plan view shown in figure 7.2, in order to design the Deltabeams (figure 7.4). The beams are modelled as simply supported under static loads and, thus, only the analysis of a typical level is required. At the first stage, when the beams are connected to the walls, they are behaving as steel beams. Afterwards, in stage two, hollow core concrete slabs are placed on the ledges of the bottom plate of the beams. Finally, the third stage includes the addition of a concrete layer (topping) above the beams and the slabs. Consequently, checks were made for all stages of construction. The beams were checked and designed against moment and shear loads, fire and for the serviceability limit state.

The thickness of the hollow core slabs and the concrete topping was 200 mm and 80 mm, respectively. The geometry of the Deltabeams is presented in detail in Table 7.1. In Table 7.2, the bending resistance and the capacity ratio are presented. The grade of the concrete used for the infill of Deltabeams and the topping layer was C30/37, while the concrete grade of the hollow core slabs was C50/60. The structural steel grade of the Deltabeams was S355.

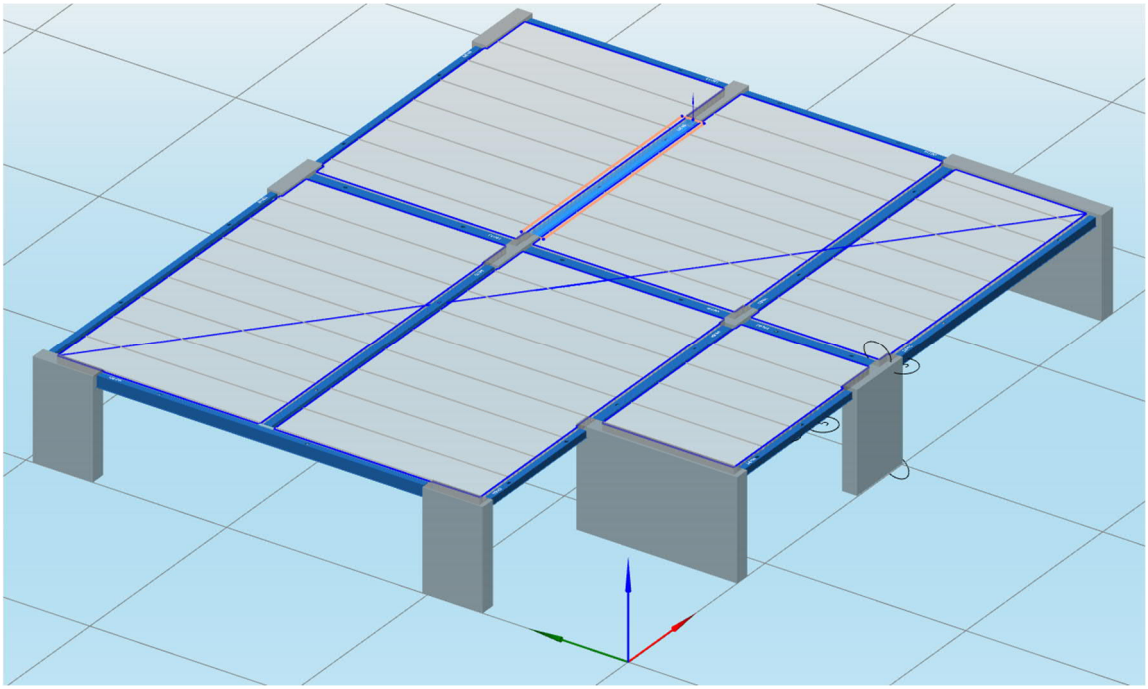

Fig. 7.4- 3D view of model in Peikko Designer

Table 7.1- Geometry of Deltabeams

Beam	Deltabeam	Top plate width (mm)	Top plate thickness (mm)	Bottom plate width (mm)	Bottom plate thickness (mm)	Web plate thickness (mm)	DB height (mm)	Concrete topping height (mm)	Total height (mm)
B1	DR30-270	180	14	390	7	5	300	80	380
B2	DR20-245	180	14	365	7	5	200	80	280
B3	D30-400	230	25	660	14	5	300	80	380
B4	D22-400	270	16	660	12	5	220	80	300
B5	DR20-245	180	10	365	5	5	200	80	280
B6	D20-400	278	10	660	8	5	200	80	280
B7	D22-400	270	16	660	10	5	220	80	300
B8	DR20-245	180	10	365	5	5	200	80	280
B9	DR25-260	180	10	380	5	5	250	80	330
B10	DR32-285	180	30	405	16	6	320	80	400
B11	D20-400	278	10	660	5	5	200	80	280
B12	D20-400	278	10	660	5	5	200	80	280
B13	D20-400	278	10	660	5	5	200	80	280
B14	DR20-245	180	10	365	5	5	200	80	280
B15	DR20-245	180	10	365	5	5	200	80	280

Table 7.2- Bending resistance and capacity ratio

Beam	Deltabeam	Design Moment (kNm)	Bending Resistance (kNm)	Capacity ratio (%)
B1	DR30-270	413.4	486.15	85.0
B2	DR20-245	211.8	276.86	76.5
B3	D30-400	809.6	952.52	85.0
B4	D22-400	410.7	561.47	73.1
B5	DR20-245	76.3	182.66	41.8
B6	D20-400	231.4	405.06	57.1
B7	D22-400	518.9	555.86	93.4
B8	DR20-245	65.5	182.63	35.9
B9	DR25-260	217.8	304.16	71.6
B10	DR32-285	822.5	882.36	93.2
B11	D20-400	66.3	297.82	22.3
B12	D20-400	67.5	297.82	22.7
B13	D20-400	26.9	297.82	9.0
B14	DR20-245	36.1	182.63	19.8
B15	DR20-245	36.7	182.63	20.1

7.3.1.2 Design of the concrete shear walls

As mentioned previously, the second step of the design was to create the same model with the selected Deltabeam sections in SAP2000 and proceed with the design of the shear walls. The model consisted of ten storeys as presented in figure 7.5. In Table 7.1, it is seen that the maximum total height of Deltabeams is 0.38 m. Keeping the clear height between levels constant and equal to 3 m, leads to a storey total height equal to 3.4 m. The total height of the model is 34 m. The base nodes of the frames used to simulate the shear walls were fixed, restrained to move or rotate along any direction.

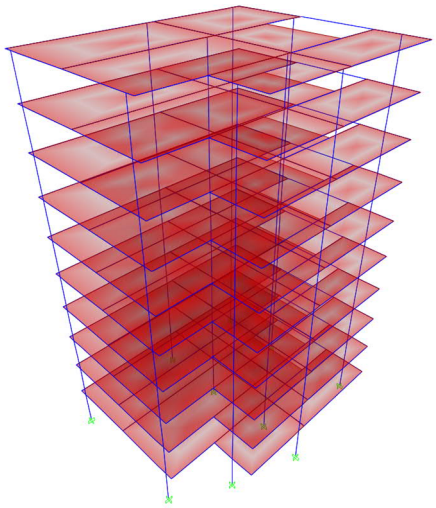

Fig. 7.5- 3D view of model in SAP2000

- Deltabeams

To import Deltabeams as a section property for the frame objects simulating beams, Section Designer was used. Section Designer is an integrated utility built into SAP2000 that enables modeling and analysis of custom cross sections. The cross sections were created with steel S355 as the base material and two typical examples are presented in figure 7.6.

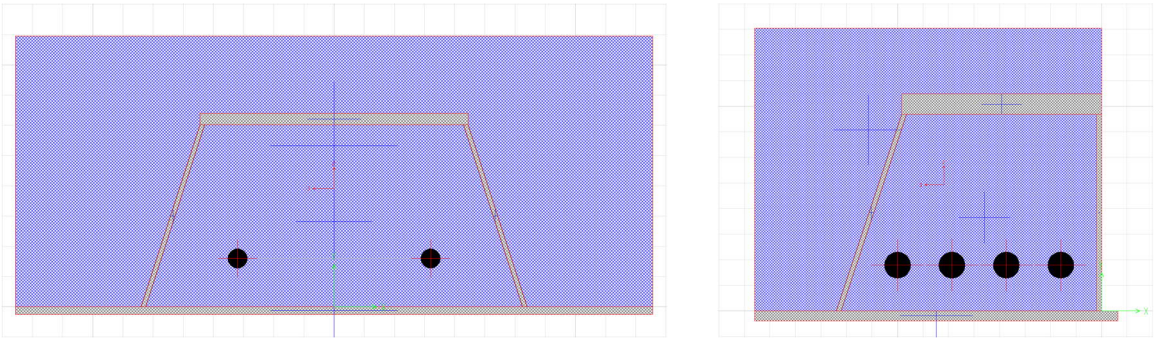

Fig. 7.6- Typical cross sections of Deltabeams in SAP2000 Section Designer

- Concrete shear walls

The dimensions and the area of vertical reinforcement of the concrete shear walls are described in Table 7.3. Each wall was modeled with a line element at its central axis (figure 7.7). The cross sections of these elements, which were also created with the Section Designer utility, have the actual geometry and reinforcing details of the corresponding wall (figure 7.8).

Table 7.3- Details of concrete shear walls

Wall	Length (m)	Width (m)	Vertical reinforcement $A_{s,v}$ (cm^2)
K1	1.80	0.45	137.44
K2	1.80	0.45	169.90
K3	2.00	0.45	117.81
K4	1.80	0.45	117.81
K5	2.10	0.45	197.04
K6	1.80	0.45	137.44
K7	1.00	0.45	49.09
K8	4.80	0.45	221.67
K9	2.00	0.50	197.04
K10	4.80	0.50	246.30

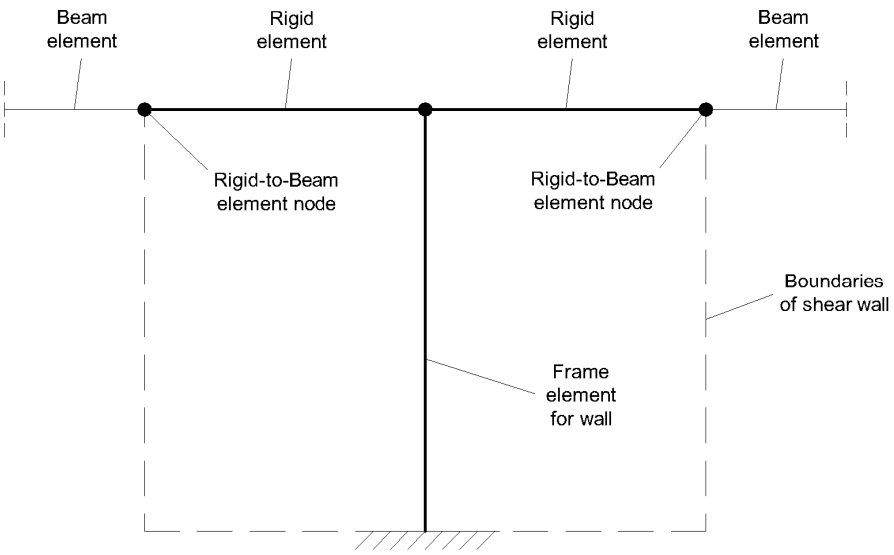

Fig. 7.7- Structural model used for the design of shear walls

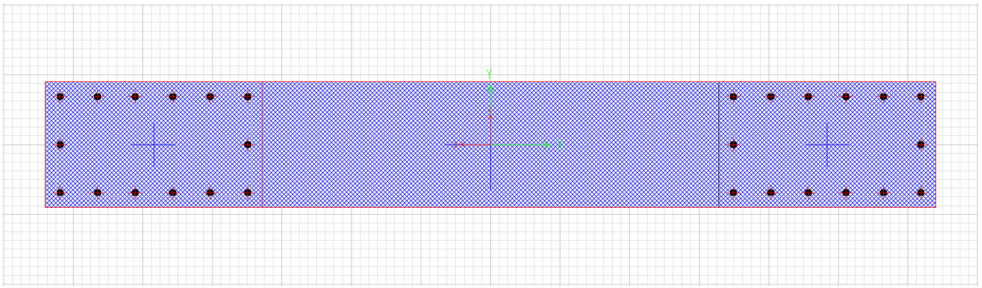

Fig. 7.8- Typical cross sections of concrete walls in SAP2000 Section Designer

The rigid elements have the same cross section with the adjoining beams. Their mass and weight were set to zero in order to avoid consideration of their mass twice in the analysis. For each Deltabeam, the moments along both directions at both ends (connection nodes with rigid elements) as well as the torsion at one end were released to simulate the behavior of a simply supported beam.

- Concrete slabs

An equivalent cross section was used for the concrete plate because of the lack of hollow core slabs in the section types selection list of SAP2000. A thick plate element with thickness equal to 0.194 m was defined, in order to have equal mass with the “original” one. In addition, a modifier equal to 2.41 was used to adjust the bending stiffness of the plate. A specific diaphragm constraint was not assigned at the nodes of each level, because it was considered that with the use of the selected plate type, the contribution of the diaphragm action could be estimated by the analysis.

7.3.1.3 Results

Response Spectrum analysis was conducted using the first 100 modes to calculate the seismic loads. The eigenperiods of the first three modes as well as the modal mass participating ratios along each direction is included in Table 7.4. Additionally, the sum of all the ratios is calculated for all the modes. For the two horizontal directions and the rotational one along the vertical axis, the total participating ratios are higher than the required 90%. The modal shapes for the first three modes are presented in figure 7.9.

Table 7.4- Modes and mass participating ratios

Mode	Period (sec)	UX	UY	UZ	RX	RY	RZ
1	1.275	0.753	0.002	0.000	0.001	0.190	0.001
2	1.175	0.002	0.668	0.000	0.259	0.000	0.006
3	0.962	0.001	0.009	0.000	0.002	0.000	0.688
Total	Using 100 modes	0.980	0.977	0.773	0.882	0.859	0.960

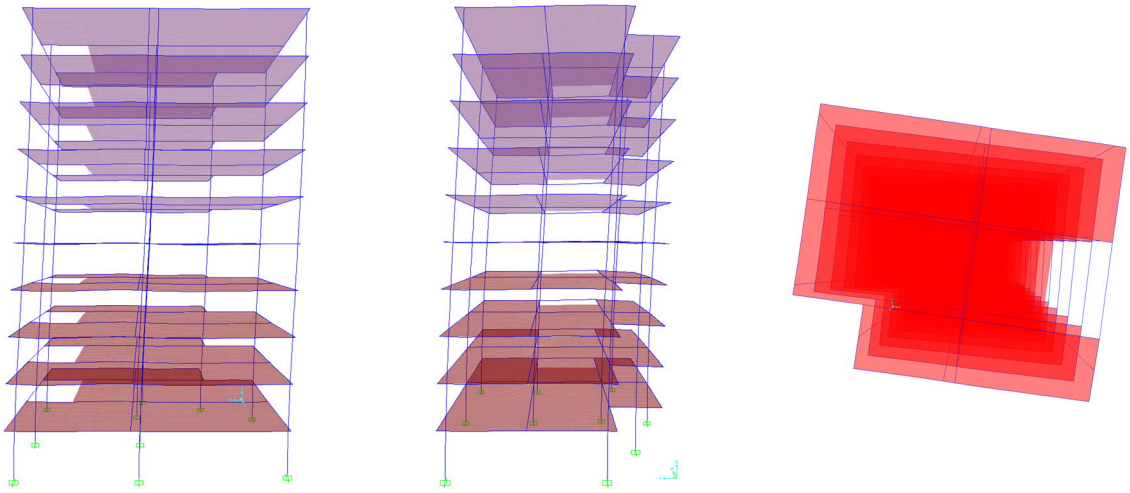

Mode 1 Mode 2 Mode 3

Fig. 7.9- Modal shapes for the first three eigenmodes

In the following Table 7.5 the design axial loads, the M2 and the M3 design moments of the critical combination are included for each vertical element. Furthermore, in the last column the maximum P-M-M interaction ratio is presented, which, as can be observed, is smaller than one for all elements, meaning that the criteria for the combination of axial load and moments is fulfilled. It should be noted that the design is not the optimal but an initial attempt to prove that this system with the proper beam-to-column connection can carry successfully seismic

and static loads. Hence, the dimensions of the walls were decided to be the same with the initial drawings, even though there is possibility for their reduction as shown from the analysis.

Table 7.5- Maximum design loads and P-M-M interaction ratio

Shear wall	Vertical reinforcement A_s (cm^2)	Axial Load P (kN)	Moment M2 (kNm)	Moment M3 (kNm)	P-M-M Interaction ratio
K1	98.17	-4336.17	377.71	-65.81	0.262
K2	98.17	-3364.15	1297.36	38.38	0.291
K3	98.17	-2234.10	914.22	-19.86	0.291
K4	98.17	-9797.73	22.26	2.87	0.563
K5	98.17	-3461.19	1907.09	-24.04	0.297
K6	98.17	-3697.73	81.83	-43.96	0.232
K7	49.09	-5000.81	84.48	4.20	0.521
K8	221.67	-6149.72	3707.53	46.45	0.329
K9	137.44	-2434.99	812.19	23.75	0.283
K10	246.30	-3668.31	10509.24	-98.74	0.335

7.3.2 Analysis using concrete beams

7.3.2.1 Design of the building using SAP2000

In this case with the common concrete beams only one analysis was conducted with SAP2000. The geometry of the walls and the reinforcement remained the same with the previous analysis. Again, for simplicity, one cross section was used for the beams which was calculated based on the loads of the most critical one.

- Concrete beams

The cross section of the beams was designed in Section Designer (figure 7.10). The height and width of the beam were 0.7 m and 0.35 m, respectively. As longitudinal reinforcement 12 bars with diameter of 18 mm (A_s=30.54 cm^2) were used for both bottom and top faces. The selection of these dimensions led to a new storey height equal to 3.7 m. As a result, the model consists of nine storeys and a total height of the building is equal to 33.3 m.

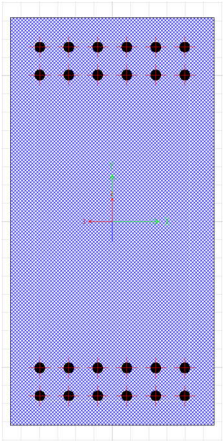

Fig. 7.10- Cross sections of concrete beams in SAP2000 Section Designer

7.3.2.2 Results

Once more, Response Spectrum analysis was used with the first 100 modes to calculate the seismic loads. The eigenperiods of the first three modes as well as the modal mass participating ratios along each direction is included in Table 7.6.

The sum of all the mass participating ratios is presented in the last line of the Table 7.6. For all directions the total participating ratios are higher than 90%. The mode shapes for the first three eigenmodes are presented in figure 7.11.

Table 7.6- Modes and mass participating ratios

Mode	Period (sec)	UX	UY	UZ	RX	RY	RZ
1	0.949	0.065	0.640	0.000	0.210	0.014	0.004
2	0.907	0.720	0.058	0.000	0.021	0.160	0.002
3	0.683	0.001	0.009	0.000	0.001	0.000	0.730
Total	Using 100 modes	0.990	0.990	0.900	0.940	0.930	0.970

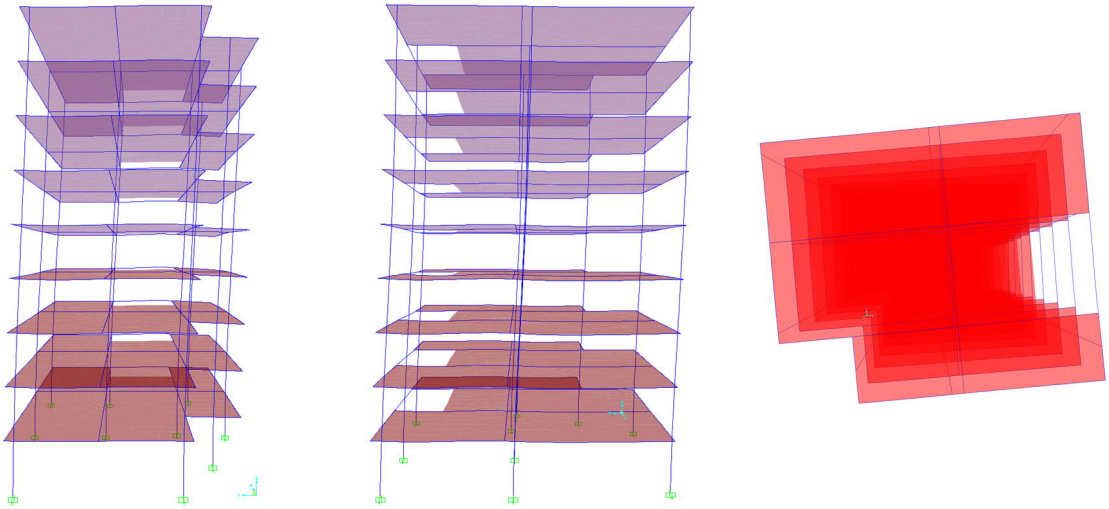

Model 1 Mode 2 Mode 3

Fig. 7.11- Mode shapes for the first three eigenmodes

In Table 7.7, similar to the previous analysis, the design axial loads, the M2 and the M3 design moments of the critical combination are presented for each vertical element. Furthermore, the maximum design axial loads, the M2 and the M3 design moments of the most critical beam are included. Again, the checking of the design was conducted in terms of the P-M-M interaction ratio.

Table 7.7- Maximum design loads and P-M-M interaction ratio

Element name	Longitudinal reinforcement A_s (cm^2)	Axial Load P (kN)	Moment M2 (kNm)	Moment M3 (kNm)	P-M-M Interaction ratio
K1	98.17	-4074.35	916.99	-80.20	0.285
K2	98.17	-4679.06	1425.94	51.39	0.360
K3	98.17	-3208.15	400.33	-31.74	0.395
K4	98.17	-2962.35	110.01	33.73	0.632
K5	98.17	-325.39	427.01	-259.47	0.330
K6	98.17	-199.57	836.04	125.91	0.281
K7	49.09	-4795.71	82.26	2.39	0.500
K8	221.67	-6527.23	7558.45	107.02	0.292
K9	137.44	-3320.12	2268.62	39.96	0.302
K10	246.30	-4515.51	9447.81	-127.24	0.386
Beam	61.08	-1244.85	21.37	-409.66	0.957

7.4 Comparison of the results

Processing of the results and comparison between the two analysis reveal some interesting conclusions. Primarily, the major difference is located at the number of storeys. The model with Deltabeams consists of 10 storeys with a total height 34.00 m, in contrast to the 9 storeys of the model with the concrete beams and a total height equal to 33.30 m.

As expected, the building with the monolithic frames was stiffer than the one with the Deltabeams. The increase of the stiffness, and thus the reduction of the eigenperiods, is important because it can lead to higher seismic loads. The comparison of the three first modes is shown in Table 7.8. Furthermore, the direction of the first two modes changed as can be observed by the mass participation ratios in Tables 7.4 and 7.6 for the model with Deltabeams.

The ratios of the modal mass participating in the seismic response for both models were almost the same and only the sum values of the second model were higher for the first 100 modes. Finally, a different distribution of the loads was observed because of the different static system between the two models. Nevertheless, no great differences appeared in the P-M-M interacting ratios.

Table 7.8- Comparison of eigenperiods between the two models

Mode	Period (sec)		Difference (%)
	Deltabeams	Concrete beams	
1	1.275	0.949	25.57
2	1.175	0.907	22.81
3	0.962	0.683	29.00

7.5 Application of the current research

To implement the findings of the described research a model was created to calculate the bending resistance of the reinforced Deltabeams with the method of plastic rigid analysis. As explained in Chapter 2 (§2.1.2.1), external loads are distributed to the individual parts of the cross-section according to their resistance, given that the cross-section is Class 1 or 2 and full interaction exists between the individual parts.

The most common method to calculate the plastic flexural resistance is to divide the cross-section into smaller rectangle shapes with thickness equal to Δz. Each shape corresponds to an area $\Delta A_i = b_i \Delta z_i$, according to the width of the shape, and to one ultimate stress f_i relative to the material. The bending moment relative to the neutral axis is:

$$\Delta M_i = \Delta A_i f_i (z_i - z_o)$$

where z_o and z_i are the distances of the neutral axis and the central axis of each shape from the outer fiber, respectively.

The final bending resistance is the sum of these individual moments.

$$M_{pl,Rd} = \sum \Delta M_i$$

The initial section is substituted by an equivalent one. The partition of the cross-section to shapes according the varied materials is presented in figure 7.12.

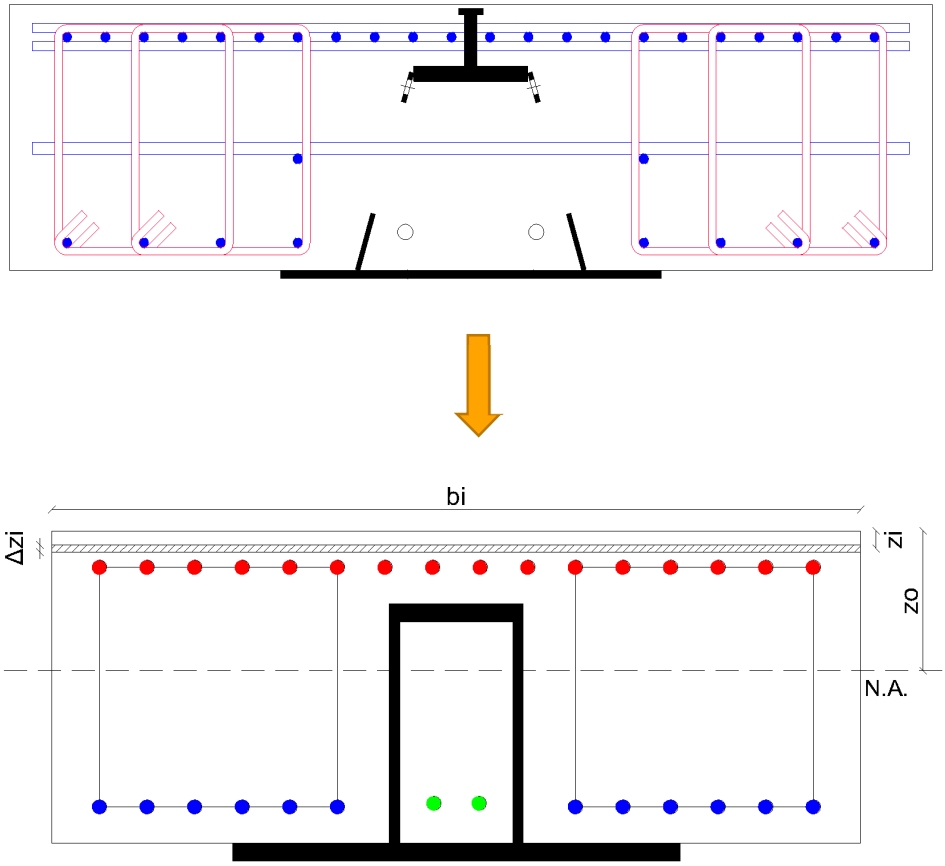

Fig. 7.12- Equivalent section for the calculation of plastic flexural resistance

In order to validate the model, the resistance of the tested specimens, described in detail in Chapters 4 and 5, was calculated using the true material strengths instead of the characteristic ones and all design factors were taken equal to one. Afterwards the calculated values were compared with the experimental curves. Comparison of the results is shown in the following figures 7.13- 7.16. The blue horizontal line is the one calculated using the numerical model.

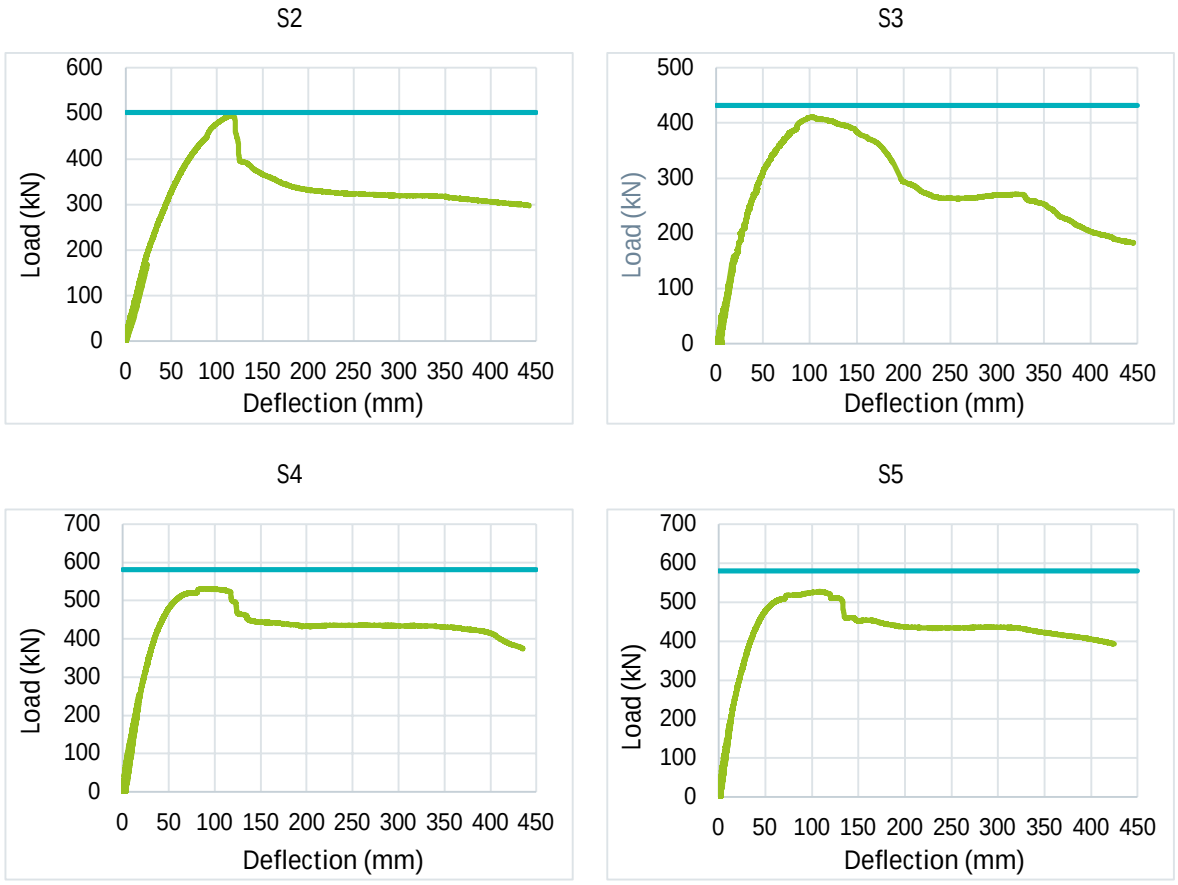

Fig. 7.13- Comparison of the numerical and experimental results for Type 1 specimens

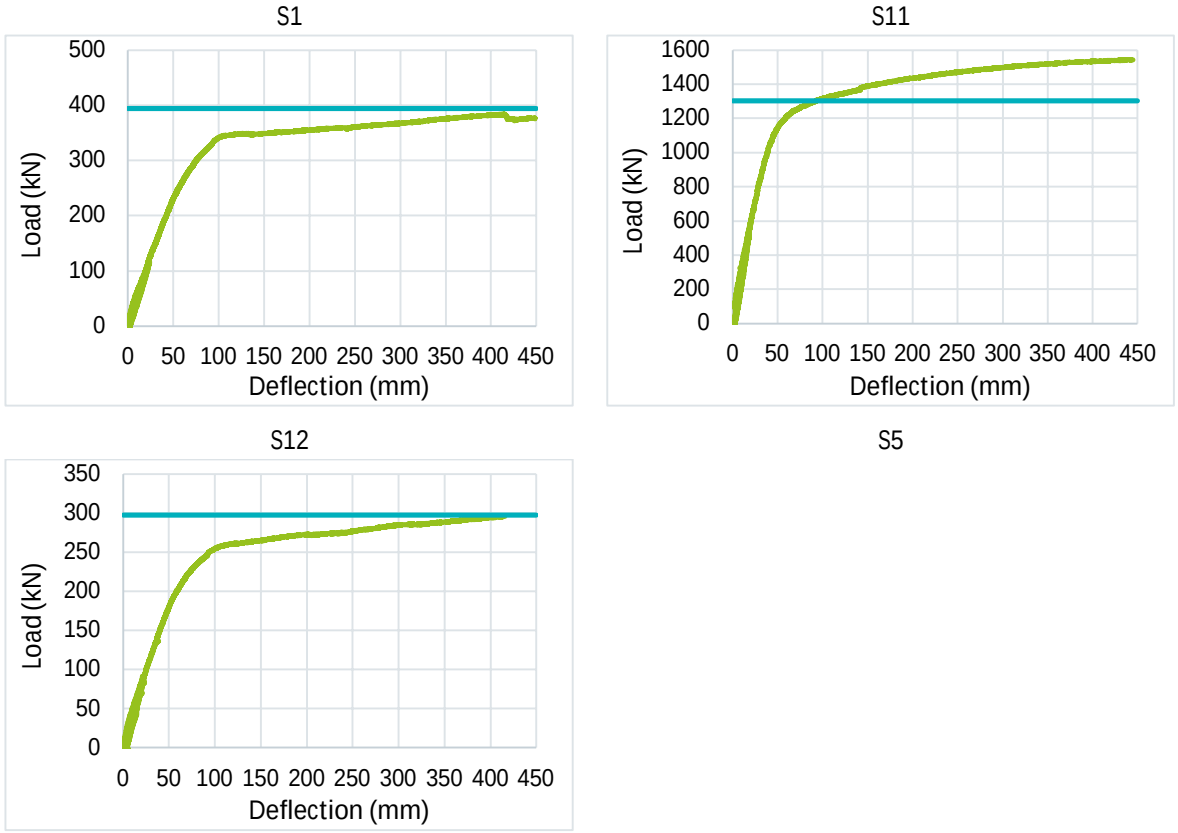

Fig. 7.14- Comparison of the numerical and experimental results for Type 2 specimens

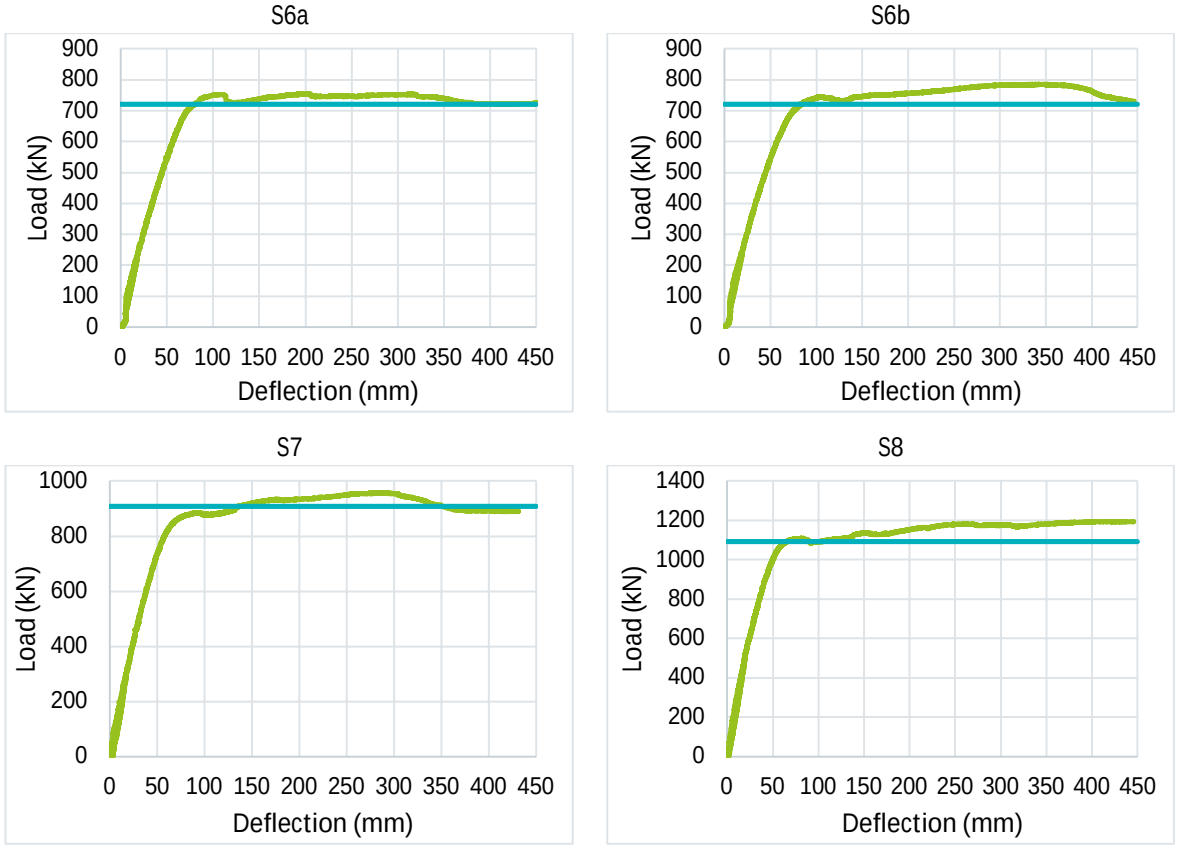

Fig. 7.15- Comparison of the numerical and experimental results for Type 3 specimens

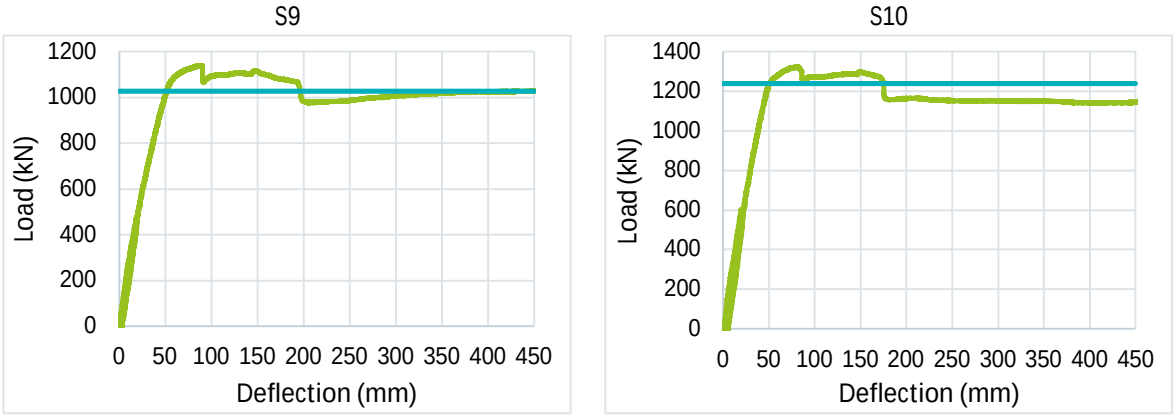

Fig. 7.16- Comparison of the numerical and experimental results for Type 4 specimens

The good correlation of the calculated results with the experimental ones validates the accuracy of the numerical model. The next step will be to update the cross-sections of the Deltabeams used in the first building (§7.3.1), to a type 3 (figure 7.12 top) cross-section in such a way that smaller Deltabeams will be able to carry the same loads. It should be noted that these calculations refer only to the flexural design of the beams and not to additional load cases like shear or fire. The intention is to demonstrate the potential of this new reinforced configuration. The new Deltabeams are presented in Table 7.9. In Table 7.10 the flexural plastic resistances for both cases in conjunction with their heights are shown. With the use of the reinforced sections the total height of each storey is reduced from 3.4 m to 3.33 m leading to a reduction of the total height equal to 0.7 m.

Table 7.9- New cross-sections of Deltabeams

Beam	Deltabeam	Top plate width (mm)	Top plate thickness (mm)	Bottom plate width (mm)	Bottom plate thickness (mm)	Web plate thickness (mm)	DB height (mm)	Concrete topping height (mm)	Total height (mm)
B1	DR22-250	180	10	370	5	5	220	80	300
B2	DR20-245	180	14	365	7	5	200	80	280
B3	D22-400	230	14	660	7	5	220	80	300
B4	D20-400	270	10	660	5	5	200	80	280
B5	DR20-245	180	10	365	5	5	200	80	280
B6	D20-400	278	10	660	5	5	200	80	280
B7	D20-400	278	10	660	5	5	200	80	280
B8	DR20-245	180	10	365	5	5	200	80	280
B9	DR20-245	180	10	365	5	5	200	80	280
B10	DR25-260	180	20	380	15	5	250	80	330
B11	D20-400	278	10	660	5	5	200	80	280
B12	D20-400	278	10	660	5	5	200	80	280
B13	D20-400	278	10	660	5	5	200	80	280
B14	DR20-245	180	10	365	5	5	200	80	280
B15	DR20-245	180	10	365	5	5	200	80	280

Table 7.10- Comparison of the deigned beams with the strengthened ones

Beam	Design Moment (kNm)	Deltabeam	Total height (mm)	Bending Resistance (kNm)	Deltabeam	Total height (mm)	Bending Resistance (kNm)
B1	413.4	DR30-270	380	486.15	DR22-250	300	436.33
B2	211.8	DR20-245	280	276.86	DR20-245	280	412.46
B3	809.6	D30-400	380	952.52	D22-400	300	839.19
B4	410.7	D22-400	300	561.47	D20-400	280	667.80
B5	76.3	DR20-245	280	182.66	DR20-245	280	279.20
B6	231.4	D20-400	280	405.06	D20-400	280	507.20
B7	518.9	D22-400	300	555.86	D20-400	280	612.44
B8	65.5	DR20-245	280	182.63	DR20-245	280	279.20
B9	217.8	DR25-260	330	304.16	DR20-245	280	344.01
B10	822.5	DR32-285	400	882.36	DR25-260	330	886.07
B11	66.3	D20-400	280	297.82	D20-400	280	429.83
B12	67.5	D20-400	280	297.82	D20-400	280	429.83
B13	26.9	D20-400	280	297.82	D20-400	280	429.83
B14	36.1	DR20-245	280	182.63	DR20-245	280	279.20
B15	36.7	DR20-245	280	182.63	DR20-245	280	279.20

8

Summary and conclusions

8.1 Short summary

Deltabeam is a slim-floor composite beam that is integrated into a floor. It is designed to be used as structural element combined with all general concrete slab types: hollow-core slabs, filigree slabs, composite steel decking, trapezoidal steel decking slabs and cast-in-situ concrete slabs. Deltabeams act as steel beams before the infill concrete has reached the required strength. After placement of the slabs, the beams are completely filled with concrete on-site through regularly spaced web openings; thus forming a composite structure after the concrete has hardened. Shear resistance of the composite cross-section is considerably higher than that of the steel part because of the contribution of the core concrete. Multiple fire tests have proven Deltabeam to have an excellent fire resistance (rate higher than R180). These resistance values depend on the thickness of the bottom plate and the number of fire rebars placed inside the boxed core of the beam. The fire rebars compensate the strength loss of the bottom plate, meaning that additional external fire protection is not normally needed.

Deltabeams can be used as single-span beams or in multi-span beam construction. In multi-span beam construction, Gerber connections are used to connect the beams. Connection of Deltabeams with columns is currently achieved with corbels or with bolts and welds at the top of a column. In that way only vertical reactions can be successfully transferred to the vertical structural elements from the beams.

The ultimate goal of the current project is to create a full moment frame that will provide adequate ductility and resistance in order to be used for designs against seismic loads or column

loss scenarios. In this dissertation, the first part of the project, which is related to the investigation of the positive (sagging) bending resistance of the beams, was presented. The experimental part of this investigation consisted of 13 specimens with various geometry and reinforcing details. The 3-point bending tests were conducted in the Institute of Steel Structures of NTUA.

The experimental set-up consisted of a test rig, a computer controlled hydraulic cylinder and test specimens. The supports were specifically designed and fabricated for these tests in order to represent “hinged” supports. The distance between the central axes of the supports was 7200 mm. The maximum load capacity of the actuator was 2.5MN and its maximum stroke 500 mm. The load was introduced to the specimen by means of a rigid construction. Deflection at middle-span, strains at bottom and top flanges, slips between steel and concrete and rotations of the specimens were monitored throughout the tests. Also, test frame and supports were constantly monitored with LVDTs to take into account unwanted displacements and settlements.

The loading of the tests was displacement-controlled. Two loading protocols were used. The loading protocols were divided in three parts. The first part included three (3) cycles at serviceability displacements 27 mm, which is approximately L/260. The second and third parts included monotonical loading with two different speeds up to the end of the tests. The specimens were divided in four types regarding the detailing of their section. With these four types, various parameters, such as different steel profiles, reinforcing details, arrays of shear studs and concrete shapes were investigated during the experiments.

Type 1 sections were the least reinforced specimens and represented the common configuration of the beams. This factor had a greatly influential effect on their behavior. When maximum load was reached, failure occurred. The concrete under compression was crushed due to the lack of longitudinal and transversal reinforcement and that led to buckling of the web and the top plates. All specimens of type 2 sections had a hardening behavior. Strength was maintained until the end of the tests. It should be noted that all tests of type 2 were

terminated at a deflection of 450 mm because the maximum stroke of the actuator was reached. Specimens at the end of the tests were in perfect condition. The concrete did not crash because of the confinement produced by the stirrups. This behavior leads to the conclusion that even higher displacement values could be reached. The tests with the Type 3 sections also manifested hardening behavior. Again, the tests were terminated at the maximum displacement capacity of the actuator at approximately 450 mm. These specimens represented the combination of Deltabeam with precast prestressed HC floor with structural topping. The small strength reductions that appeared at the load-deflection curves indicated the failure of the thin concrete ledges of the structural topping. Then, the strength remained constant until the end of the tests providing again an overall ductile behavior. The core part of the section was maintained in perfect shape due to confinement provided by the open stirrups.

The finite element analysis software Abaqus was used to simulate the behavior of the beams. This analytical investigation was conducted for Type 2, 3 and 4 specimens. The models were assembled by five parts; one for concrete, one for the steel beam, one for the reinforcement and two rigid parts to simulate the supports and the loading plate. In order to develop a finite element mesh for the concrete and the steel parts, linear hexahedral elements with reduced integration (C3D8R) were used. Accordingly, reinforcement bars were modelled with linear truss elements (T3D2). Load- deflection curves were obtained and compared with the experimental results. The experimental and analytical curves correlated well. Subsequently, using the proper interpolation procedure, the average curves for experiments and FE models were created. The resemblance of these two curves indicated that the models with this configuration can predict with substantial accuracy the behavior of the beams.

Finally, a design of a building, which was meant to house offices was presented. Two different analyses were conducted and compared. In the first one Deltabeams were applied while the second one was conducted with reinforced concrete beams. To implement the findings of the current research a model was created to calculate the bending resistance of the reinforced Deltabeams with the method of plastic rigid analysis. The next step was to update the cross-

sections of the Deltabeams used in the building with a new cross-section in such a way that smaller Deltabeams would be able to carry the same loads.

8.2 Conclusions

The main conclusions of this dissertation can be summarized as follows:

1. The small number of publications related to shallow floor beams subjected to bending loads combined with the lack of any reference or design guidance on Eurocodes as well as the numerous possibilities and combinations of steel sections and shapes, indicates that this topic should be investigated more extensively.

2. The experimental results showed that Deltabeams, in conjunction with proper steel reinforcement exhibit a highly ductile behavior. The slips between concrete and structural steel were very small and the integrity of the specimens was maintained up to the end of the tests.

3. Specimens with the same cross-section and different number of shear studs rows demonstrated the same behavior, meaning that the shear connection between steel and concrete was full and the additional row of shear studs did not affect the results.

4. Nine finite element models were created and calibrated with the experimental data. Correlation between the experimental and analytical results was very good, with a difference less than 5%. The coefficient of determination (R^2) was equal to 0.996, validating the model as a very dependable one for further predictions of similar composite beams.

5. A sensitivity investigation was conducted related to the dilation angle ψ and the K_c factor, the two concrete factors that mostly affected the behavior of the FE models. Dilation angle affected the strength of concrete with higher values leading to higher loads. At deflections where the strains have exceeded the ultimate strain of concrete the contribution of this factor is not significant. The K_c factor had a major impact on the

overall behavior of concrete and its deformation capacity. Lower factor values led to a bigger load shift when the beam entered the plastic zone.

6. An additional analytical investigation was conducted that revealed the importance of the lateral restriction to movement provided by the external confined concrete to the steel webs which affects the global behavior of the beam. All models without external reinforced concrete buckled locally. Initially, buckling appeared at the web plates that subsequently led to buckling of the top plate. Results showed that when the web plates were thicker, and thus had a greater resistance, the behavior of the beams was better and buckling of the top plate occurred in a higher deflection value. Nonetheless, risk of buckling is eliminated completely only when the webs are restrained to move laterally. The lateral restrain is provided by the reinforced external concrete part and the confinement due to stirrups.

7. Deltabeams were successfully used as simply supported beams for the seismic design of an office building. Comparison of the results with a second model made by conventional monolithic concrete frames revealed the beneficial effect of the swallow floor construction, since, because of the lower height of Deltabeams, there was space for ten storeys instead of nine of the construction with the concrete beams for the same total height.

8.3 Concise list of proposed future work

1. The first part of the ongoing project to create a full moment frame using Deltabeams has been successfully concluded. The next step of the research should be the experimental and numerical investigation of the flexural behavior of Deltabeams under negative (hogging) moments for the critical areas near the beam-to-column connections. Finally, a moment connection must be designed in order to ensure that stability, ductility, robustness and redundancy levels requested by Eurocodes for extreme cases like earthquake loading and column loss scenarios are achieved.

2. Chapter 7 revealed that it is possible to use Deltabeams as simply supported beams in conjunction with strong vertical elements in designs accounting for earthquakes. Consequently, the beam-to-column connection must be thoroughly investigated both experimentally and analytically.

3. The calibrated finite element models can now be used for an in-depth investigation of aspects and factors (confinement of core concrete, interaction between concrete and steel, shear connection, forces acting at the web-holes of the beams, stress and strain distribution etc.) that couldn't be measured during the tests. That knowledge is important for the comprehensive understanding of the performance of these beams under a rage of loading conditions.

References

[1] Jean-Pierre Birat, “The relevance of Sir Henry Bessemer's ideas to the steel industry in the twenty-first century”, Ironmaking & Steelmaking 31(3):183-189, June 2004.

[2] Robert H. Thurston, “Sir Charles William Siemens”, American Association for the Advancement of Science, Science, Vol. 3, No. 49 (Jan. 11, 1884), pp. 34-36.

[3] Alan Blanc, Michael McEvoy, Roger Plank, “Architecture and Construction in Steel”, Taylor & Francis, ISBN 978-1-135-82839-4, 2003.

[4] Jo Ann Rayfield, "Tragedy in the Chicago Fire and Triumph in the Architectural Response", Illinois History Teacher, 1997, Retrieved September 25, 2018 – via Illinois Periodicals Online.

[5] Skalomenos K., “Seismic performance of plane moment resisting frames with concrete filled steel tube columns and steel I beams”, PhD Dissertation, University of Patras, April 2014

[6] Christophe Paul, “Le béton armé et ses applications. Deuxième edition”. Paris et Liège: Libraire Polytechnique, Ch. Beranger, 1902.

[7] Eberhard Pelke, Karl-Eugen Kurrer, “On the evolution of steel-concrete composite construction”, 5th International Congress on Construction History, Chicago, 2015.

[8] Bach C., “Versuche über den Gleitwiderstand einbetonierten Eisens”, Mitteilungen über Forschungsarbeiten, Verein Deutscher Ingenieure, Kommissionsverlag von Julius Springer; Berlin, 22, 1-41, 1905.

[9] Kahn Julius, Composite Beam Construction. US-Patent No. 1,597,278, 1926

[10] AASHO, “Standard specifications for highway bridges”, Association General Offices 917 National Press Building, Washington D.C., 1949.

[11] Walter Borgogno, “Tragverhalten von Slim Floor Decken mit Betonhohlplatten bei Raumtemperatur und Brandeinwirkungen”, Institute of Structural Engineering, Swiss Federal Institute of Technology, Zurich, December 1997

[12] Zhongcheng Ma, “Fire safety design of composite slim floor structures”, Helsinki University of Technology Laboratory of Steel Structures Publications 18, TKK-TER-18, Espoo 2000

[13] SBI- Swedish Institute of Steel Construction, “Office buildings in steel- The Swedish Method”, Publication No. 80, December 1983, Revised in 1991

[14] CEN (European Committee for Standardization). (2004). Eurocode 4: Design of composite steel and concrete structures - Part 1-1: General rules and rules for buildings, EN 1994-1-1:2004

[15] CEN (European Committee for Standardization). (2005). Eurocode 3: Design of steel structures- Part 1-1: General rules and rules for buildings, EN 1993-1-1:2005

[16] Kuhlmann Ulrike, “Design of composite beams according to Eurocode 4-1-1. Ultimate Limit States.”, Institute of Structural Design, University of Stuttgart

[17] Vayas Ioannis, “Composite structures”, Klidarithmos Publ., 1996, 2nd Edition, 2010

[18] CEN (European Committee for Standardization). (2004). Eurocode 2: Design of concrete structures- Part 1-1: General rules and rules for buildings, EN 1992-1-1:2004

[19] Classen Martin, Stark Alexander, Hegger Josef, “Steel-HSC composite beams with partial shear connection and miniaturized limited-slip-capacity connectors”, Steel Construction, 11(1):94-103, February 2018

[20] Peikko Group Corporation, “Behavior and design of steel-concrete composite structures”, M&P Paino Oy Publ., 1st edition, 2017

[21] CEN (European Committee for Standardization). (2004). Eurocode 8: Design of structures for earthquake resistance - Part 1: General rules, seismic actions and rules for buildings, EN 1998-1:2004.

[22] Myong-Keun Kwak, Byung-Wook Heo, Kyu-Woong Bae, Keung-Hwan Kim and Tae-Sup Moon, "Flexural capacity of the encased (slim floor) composite beam with deep deck plate", Council on tall buildings and urban habitat, CTBUH 2004 Seoul Conference, October 10-13, 2004

[23] Yuanqing Wang, Lu Yang, Yongjiu Shi, Ruhang Zhang, "Loading capacity of composite slim frame beams", Journal of Constructional Steel Research 65 (2009) 650–661

[24] Shiming Chen, Toi Limazie, Jianyao Tan, "Flexural behavior of shallow cellular composite floor beams with innovative shear connection", Journal of Constructional Steel Research 106 (2015) 329-346

[25] T. Sheehana, X. Daia, J. Yanga, K. Zhoua and D. Lam, "Flexural behavior of composite slim floor beams", 12th International Conference on Advances in Steel-Concrete Composite Structures (ASCCS 2018), Universitat Politècnica de València, València, Spain, June 27-29, 2018

[26] Nadia Baldassino, Giacomo Roverso, Gianluca Ranzi, Riccardo Zandonini, "Service and Ultimate Behaviour of Slim Floor Beams- An Experimental Study", Structures, Volume 17, February 2019, Pages 74-86

[27] Leskela M.V., Peltonen S., Iliopoulos A. and Kiriakopoulos P., "Numerical and experimental investigations on the vertical shear resistance of boxed steel cross-sections with concrete infill (Deltabeams)". Eurosteel 2014 Conference Papers /08/27-039, 6 p.

[28] Peltonen S., Plum C.M., "Brandveiligheid- Druckboog en schurfweerstand helpen onbeschermde ligger bij brand", Bouwen met staal 215, 50-52, June 2010.

[29] EN 10025-1, Hot rolled products of structural steels - Part 1: General technical delivery conditions. CEN 2004.

[30] ISO 6892-1:2016, Metallic materials- Tensile testing- Part 1: Method of test at room temperature

[31] ISO 15630-1:2010, Steel for the reinforcement and prestressing of concrete- Test methods- Part 1: Reinforcing bars, wire rod and wire

[32] ISO 13918:2017, Welding- Studs and ceramic ferrules for arc stud welding

[33] EN 12390-3, Testing hardened concrete - Part 3: Compressive strength of test specimens, CEN 2012

[34] C.C. Spyrakos, "Finite Element Modeling in Engineering Practice", Pittsburgh PA, 1994.

[35] C.C. Spyrakos, J. Raftoyiannis, "Linear and Nonlinear Finite Element Analysis in Engineering Practice", Pittsburgh PA, 1997.

[36] A. Hrennikoff, "Solution of problems of elasticity by the framework method", Journal of applied mechanics 8.4: 169–175, 1941

[37] R. Courant, "Variational methods for the solution of problems of equilibrium and vibrations", Bulletin of the American Mathematical Society 49: 1–23, 1943

[38] G. Strang, G. Fix, "An Analysis of the Finite Element Method", Prentice Hall, 1973

[39] G. P. Nikishkov, "Introduction to the Finite Element Method", University of Aizu, Japan, 2004

[40] Rinker MW, SP Pilli, NK Karri, JE Deibler, KI Johnson, JD Holbery, OD Mullen, and DE Hurley, "Structural Integrity of Single Shell Tanks at Hanford- 9491", WM2009 Conference, Phoenix, AZ, March 1-5, 2009

[41] ABAQUS: Abaqus analysis user's manual, Version 2018, Dassault Systemes.

[42] Henri Tresca, Appendix C: “Note on the form which it is advisable to adopt for the metres to be constructed by the International Commission”, pp 77-93, in Second Report of the Commissioner of Inland Revenue of the Inspection of Weights, Measures and Gas, in Sessional Papers, Volume 2, Second Session of the Third Parliament of the Dominion of Canada, Session 1875, Volume VIII (English translation of Tresca's French paper on Tresca section)

[43] Von Mises, R. (1913). Mechanik der festen Körper im plastisch deformablen Zustand. Göttin. Nachr. Math. Phys., vol. 1, pp. 582–592.

[44] Bauschinger J 1886 Mitteilung XV aus dem Mechanisch-technischen Laboratorium der Königlichen Technischen Hochschule in München 13 115

[45] Dieter, George E. (1988). Mechanical Metallurgy. McGraw Hill Book Company. pp. 236, 237. ISBN 0-07-084187-X.

[46] S.V.Chaudhar, M.A.Chakrabarti, “Modeling of concrete for nonlinear analysis using Finite Element Code ABAQUS”, International Journal of Computer Applications (0975- 8887), Volume 44– No.7, April 2012.

[47] P. Kmiecik, M. Kamiński, “Modelling of reinforced concrete structures and composite structures with concrete strength degradation taken into consideration”, Archives of civil and mechanical engineering, Vol. XI, No. 3, 2011

[48] Hilleborg A, Modéer M., Peterson PE., “Analysis of crack formation and crack growth in concrete by means of fracture energy mechanics and finite elements”, Cement Concrete Res, 6:773-82, 1976

[49] D. C. Drucker, W. Prager, “Soil mechanics and plastic analysis or limit design, Q.”, Applied Math. 10, No.2, 157-165, 1952.

[50] Hansen, C. E. Bent, “Line ruptures regarded as narrow rupture zones - Basic equations based on kinematic considerations”, Proc. Brussels Conf. 58 on Earth Pressure Problems, Vol. I, 39-48, 1958.

[51] Vermeer PA, De Borst R, 'Non-associated plasticity for soils, concrete and rock." HERON 29(3), 1984

[52] J. Lubliner, J. Oliver, S. Oller, and E. Oñate, "A Plastic-Damage Model for Concrete," International Journal of Solids and Structures, vol. 25, pp. 299–329, 1989.

[53] J. Lee and G. L. Fenves, "Plastic-Damage Model for Cyclic Loading of Concrete Structures," Journal of Engineering Mechanics, vol. 124, no. 8, pp. 892–900, 1998.

[54] Pearson, K., "Notes on the History of Correlation", Royal Society Proceedings, 58, 241, Biometrika, 13, 25-45, 1920.

[55] Peikko Group Corporation, Peikko Designer Deltabeam

[56] SAP2000, Integrated software for structural analysis and design, Computers and Structures, Inc., Berkeley, California, USA